MAX '91

Workshop #2:

Developments in Observations and Theory for Solar Cycle 22

Laurel, Maryland, 8-9 June 1989

MAX '91

Workshop #2:

Developments in Observations and Theory for Solar Cycle 22

Laurel, Maryland, 8-9 June 1989

Edited by
Robert M. Winglee
University of Colorado
Boulder, Colorado

Brian R. Dennis
NASA Goddard Space Flight Center
Greenbelt, Maryland

Cover

An eruptive prominence associated with the X1.6 3B flare of June 20, 1989. This event and its coronal mass ejection were well observed during the first Max '91 Campaign. This digital H-alpha image was obtained at 15:04 UT (4 minutes before the peak of the event in soft X-rays) by the Holloman Solar Observatory of the USAF SOON system.

TABLE OF CONTENTS

High Energy Flare Physics

Theory and Modelling

Observations of AR 5395

Observatory Reports

PREFACE

More than 100 scientists attended the second workshop of the Max '91 program held at the Johns Hopkins Applied Physics Laboratory in Laurel, Maryland, on June 8 and 9, 1989, in conjunction with the meeting of the Solar Physics Division of the American Astronomical Society. The success of the workshop was due in large part to the excellent facilities at the Kossiakoff Center of the Johns Hopkins Applied Physics Laboratory and the support of the local organizing committee chaired by David Rust.

The purpose of the Max '91 program is to gather coordinated sets of solar flare and active region data and to perform interpretive and theoretical research aimed at understanding flare energy storage and release, particle acceleration, flare energy transport, and the propagation of the flare effects to Earth. Instruments for long-duration balloon flights are being funded by NASA and ground-based instruments are being funded by NSF. Coordination of Max '91 observations is being carried out by Alan Kiplinger at the Space Environment Laboratory in Boulder, CO. The Max '91 program is part of the SCOSTEP sponsored international FLARES 22 program led by Marcos Machado (Argentina) and Ernest Hildner (USA).

Four discussion groups were organized during the workshop on the following subjects: high-energy flare physics, coordinated magnetograph observations, flare theory and modelling, and Max '91 communications and coordination. A special session also took place on observations of Active Region 5395 and the associated flares during March 1989. These proceedings of the workshop contain the group leaders' summaries of the discussions that took place in the different group meetings, papers resulting from the contributed oral and poster presentations, and outlines of talks that were presented by invited speakers on topics such as the scientific objectives of solar gamma ray observations, the solar capabilities of each of the four instruments on the Gamma Ray Observatory, and access to Max '91 information.

Discussions focussed on developments in observations and theory, particularly in relations to plans for future space, rocket, balloon, and ground-based observations and their coordination, and theoretical questions relevant to the Max '91 program. The magnetograph group discussed observations made during the International Solar Month on September 16 and 17, 1988, when observatories around the world participated in comparative magnetograph observations of active regions AR 5148, 5105, and 5106. Clear difficulties were identified in calibrating measurements from the different observatories.

Recent observations of the March '89 Active Region 5395 were presented. This active region was one of the largest flare producing active regions on record with 11 class

X flares and 48 class M flares. Four great geomagnetic storms were produced by flares associated with the active region; one of these storms caused the Hydro-Quebec power system to fail. Preliminary results detailing these and other terrestrial effects were presented. Ground-based and satellite observations were also presented showing some of the unique characteristics of the active region and its associated flares.

Capabilities of future observations from several new satellite and balloon instruments and their impact on solar physics were discussed in the high energy flare physics group. The satellites include the Gamma Ray Observatory, SOLAR-A, and Ulysses; the balloon instruments include GRID and SOUP. Scientists from many of the ground-based observatories also gave presentations of new facilities. These discussions and presentations are summarized in this proceedings.

Theoretical discussions concentrated on flare research currently being undertaken by various groups. Central issues include evolution of the magnetic field, electron and ion energization and the properties of beams and current systems during a flare. With the higher time and spatial resolution of the new instruments coming on line, important new constraints will be placed on the modelling, and an exciting time is expected as the modelling and observational capabilities develop during Max '91.

It is expected that several Max '91 workshops will be organized in the future. The next general Max '91 workshop will be held in conjunction with the AAS/SPD meeting in Albuquerque, NM, in June, 1990. A separate workshop is planned to discuss observations made during the first Max '91 observing campaign held in June, 1989. Future workshops will be held to address results of more coordinated space and ground-based campaigns with specific scientific objectives.

HIGH ENERGY FLARE PHYSICS GROUP SUMMARY

J.M. Ryan[1] *and J.D. Kurfess*[2]

[1]University of New Hampshire, Durham, NH
[2]Naval Research Laboratory, Washington, D.C.

Abstract

We review the contributions of the High Energy Flare Physics Special Session in the American Astronomical Society Solar Physics Division Meeting in Laurel, Maryland on 8, 9 June 1989. Oral and poster papers were presented on observatories and instruments available for the upcoming solar maximum. Among these are the space-based Gamma Ray Observatory, the Solar Flare and Cosmic Burst Gamma Ray Experiment on the Ulysses spacecraft, the Soft X-Ray Telescope on the spacecraft Solar-A and the balloon-based Gamma Ray Imaging Device. Ground based observatories with new capabilities include the new BIMA, Owens Valley Radio Observatory and the Very Large Array. The highlights of the various instrument performances are reported and potential data correlations and collaborations are suggested.

1. Max '91 Objectives

In the 1988 Kansas City Max '91 Workshop there was no specific session on High Energy Flare Physics; rather sessions were devoted to specific scientific questions such as particle acceleration and energy release. As the next maximum approaches we must be ready to design and implement real observing programs. It is appropriate then that special attention be paid to solar physics from the perspective of the type of measurements to be made. Toward this end the High Energy Flare Physics session in the 1989 Laurel Max '91 Workshop brought experimenters together who will be conducting such observations focussing on the high energy aspect of the flare problem.

As has been the situation for many years, gains in understanding flare physics often derives from the merging of complementary data sets and coordinated observations with common scientific goals. The upcoming solar maximum can be studied with new instrumentation starting from ideas based upon our accumulated knowledge of past solar cycles.

Effective coordinated observations are difficult to conduct. As pointed out by Rust (1988), the early success of such coordinated observations early in the Solar Maximum Mission serves as a warning that despite our best intentions our target data sets will not

be easily obtained. This problem is most severe for the case of high energy flares, i.e. where X-rays, γ-rays and emissions typical of high energy particles are present. The occurrence rate of such events is significantly lower than that of flares in general and their predictability remains a problem. For example, no joint observation of a γ-ray flare between GRS on SMM and the VLA comes to mind despite numerous opportunities.

However, the payoff of a few such coordinated observations can be large thus motivating us to pursue them. Such observations during the last cycle include the simultaneous measurements of OV ultraviolet emission and hard X-rays (Woodgate et al. 1983), relating the OV excitation to the energetic electron population; the γ-ray/white light measurements of the 1 July 1980 and 24 April 1981 flares (Ryan et al. 1983; Kane et al. 1985; Zirin and Neidig 1981), constraining the role of energetic protons with respect to electrons in the production of the optical continuum emission; and the measurements of neutron-decay protons (Evenson et al. 1983) and direct energetic neutrons (Chupp et al. 1983) from the 3 June 1982 flare, yielding a neutron spectrum over a wide energy range and over a wide emission angle.

For studying high energy flares in this next maximum, the community will have new powerful instrumentation. This instrumentation includes the Gamma Ray Imaging Device (GRID), the Gamma Ray Observatory (GRO), the Solar Flare and Cosmic Gamma-Ray Experiment (HUS) on Ulysses, HIGRES and the Soft X-Ray Telescope (SXT) on Solar-A. Ground based observations will be possible with improved capabilities of the VLA and Owens Valley Radio Observatory (OVRO) and the construction of BIMA. Although our goals for studying high energy flares are similar to those in 1980, our starting point is well along. Our instrumentation is more sensitive and our questions are more directed. For example, in 1980 a major question was whether or not the electrons which produce the hard X-rays are the same ones which produce the microwave and radio emission. After observing many flares from which both emissions were measured, we now know that there is no simple answer which applies to all events. A better question today might be "Can we identify in frequency or space the emission best correlated with the X-radiation $>$ 100 keV and associate this with the magnetic structure of the active region"? Answering such questions requires detailed and coordinated observations. The purpose of this special session was to gather together the experimentalists who will be responsible for obtaining these detailed data so as to spawn ideas on how to conduct such measurements. It was also hoped that theorists would contribute suggestions on new observations; however, the special session on theory conflicted in time and we enjoyed only one theory contribution to the session. This contribution by Batchelor (1989) did, in fact, directly, addressing the causative agent for impulsive bursts. Relating the physics of the flare process to observational signatures is a difficult task with certainly less than a 100% probability of success. The exercise, however, is a useful one. By observing in multiple wavelengths the

progression or evolution of moving plasma and electron distributions, one should be able to eliminate some transport processes from the realm of potential flare producing agents. One most easily identified, and perhaps eliminated, is the propagating modes of magnetic reconnection due to the wide range of Alfven speeds within different coronal structures. By proposing such observations to the experimentalists, one must discuss the limitations of the measurements and alternatives which may be offered which address the same problem. The interplay between the theorists and the experimentalists is important in formulating a program for the upcoming maximum.

The remainder of this review paper addresses only the contents of the contributed talks and poster papers. The details of each presentation can be found elsewhere in this volume. We only address the global aspect of the session.

2. The Gamma Ray Observatory

The Gamma Ray Observatory (GRO) will carry four large instruments whose main objectives are to undertake comprehensive observations of astrophysical sources throughout the 15 keV to 30 GeV energy range. However, GRO will also provide significant capabilities for observations of energetic solar gamma rays and neutrons, and therefore be an integral part of the MAX '91 program. GRO is scheduled for launch in June 1990, near the peak of the current sunspot cycle. A 6-10 year mission lifetime is expected.

2.1 Solar Physics with GRO

The GRO instruments, briefly described below, provide enhanced capabilities for solar flare observations relative to previous high-energy instruments (Kurfess, 1988). Improved sensitivities and time resolutions will be available over a broad range of gamma ray energies. The capability to measure unambiguously the flux and spectrum of solar neutrons is also available. With these capabilities, GRO will provide dramatically improved measurements of the temporal histories for the acceleration and interaction of electrons and ions in the flare. Correlation of these measurements with X-ray, microwave and mm-wave observations, particularly new imaging instruments, will be particularly beneficial to our understanding of the flare acceleration mechanism.

The improved high-energy gamma-ray and neutron observations will provide, for the first time, high-quality spectra of the most energetic particles in the flare. When combined with spectral information derived from nuclear line ratios at lower energies, these will provide our best data on the nature of the acceleration processes producing these high-energy particles.

GRO will significantly extend the studies begun with SMM regarding the isotropy of the energetic ions. The shape of the $\sim$ 450 keV ^{7}Li and ^{7}Be feature from α–α fusion can be

used to investigate the nature of the ion beam, whether isotopic, fan beam, or pencil beam by studying γ-ray spectra vs. heliospheric longitude (Murphy et al. 1990). Correlation of these observations with lower energy imaging detectors should yield information on the spatial extent of ions in the flare region.

Finally, we mention the unique capability for line γ-ray observations to determine elemental composition and compositional anomalies in the flare region. These studies, also initiated with SMM (Murphy et al. 1985a,b), can be greatly expanded, and with other MAX '91 observations, should provide improved insight into the sites of particle acceleration and interactions.

2.2 The GRO Mission

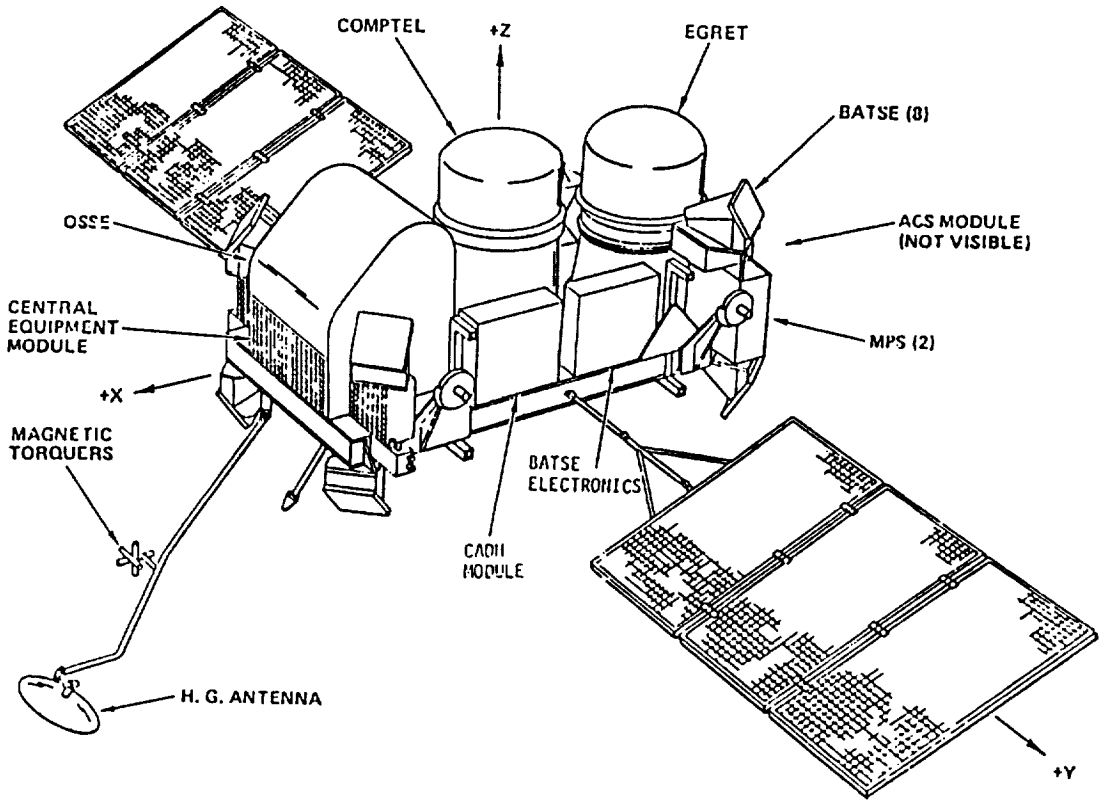

Figure 1. Illustration of the Gamma Ray Observatory and associated instruments. Three instruments (OSSE, COMPTEL, and EGRET) are mounted on the +Z side of the spacecraft. The Eight BATSE modules are located on the corners of the S/C to provide full sky coverage. The solar panels can rotate + 90 degrees about the Y-axis. The Sun is constrained to be located in the +X hemisphere and is further constrained to be not closer than 48 degrees to the Y axis.

The general configuration of the GRO is shown in Figure 1. Three of the instruments (OSSE, COMPTEL and EGRET) are located on the +Z side of the spacecraft. GRO is a three-axis stabilized spacecraft with solar panels that can rotate ± 90 degrees about the Y-axis, and with the Sun generally restricted to the +X hemisphere in the S/C coordinate system. This enables the +Z instruments to be pointed to any position on the sky at any time, including the Sun. The fourth instrument, BATSE, is designed to provide a full sky monitor for transient sources and consists of eight modules located on the corners of the spacecraft.

Following the initial on-orbit check-out of the GRO spacecraft and instruments, a 15-month phase will be conducted during which a complete sky survey will be obtained by the wide field-of-view EGRET and COMPTEL instruments. This will be accomplished using a sequence of about 30 two-week viewing periods during which the Z-axis of the spacecraft (see Figure 1) is held fixed at pre-selected positions on the sky. The viewing program is currently under development, and is subjected to a number of constraints (Bertsch, 1989). Solar observations can be incorporated during this period by selecting a viewing program that achieves a uniform sky survey while also placing the Z-axis near the Sun for selected viewing periods. If the periodicity and phase of the 155-day cycle observed during the last solar cycle (Rieger et al. 1984) can be determined, this can be used to optimize solar observations within the overall sky survey. It is also possible to consider "targets of opportunity" wherein the GRO viewing program is interrupted by a high- priority event, which could include a period when solar activity is expected to be high. Reorientation of GRO in response to a target-of-opportunity can be accomplished in less than 1 day (Kniffen, 1989).

2.3 GRO Instruments

A brief description of the four GRO instruments is given in the following sections. Characteristics of the instruments are listed in Table I.

2.3.1 BURST AND TRANSIENT SOURCE EXPERIMENT (BATSE)

The Burst and Transient Source Experiment (BATSE) consists of eight detector modules positioned on the GRO spacecraft to provide full coverage of the sky for cosmic gamma-ray bursts and transients (Fishman et al. 1985). Each module contains two uncollimated NaI scintillation detectors; a large area detector (2025 cm2), to provide high sensitivity and directional capability and a 125 cm^2 by 3.0"-thick NaI crystal which provides better energy resolution. The energy range covered is 15 keV to 100 MeV.

BATSE will have extensive capabilities for solar flare observations (Fishman et al. 1989) due to its large sensitive areas, versatile data system for handling transient phenomena, and continual observation of the Sun during daylight portions of the orbit. During

TABLE I. GRO INSTRUMENT SUMMARY

Instrument	BATSE	OSSE	COMPTEL	EGRET
Energy Range (MeV)	0.15–1.0(LAD) 0.15–100 (spect.)	0.05–10.0 10–150 (solar)	1–30	20–30000
Energy Resolution	30% (LAD) 8.0% (spect.)	8.0% (.6 MeV) 3.2% (6.1 MeV)	5–8%	15%
Time Resolution				
Broad-Band Spectroscopy	10μsec 1 sec	125μsec 4 sec	125μsec	100μsec
Effective Area (cm2) (maximum) (per module)	1800 (LAD) 125 (spect.)	1950 (0.5 MeV)	30	1000
Field-of-View (degrees)	Full Sky	3.8x11.4	45 FWHM	45x51

normal operations, BATSE will accumulate 16-channel spectra with 2-second resolution from all detector systems. Full 256-channel resolution spectra are acquired from each detector every one minute. Upon detection of a transient event, as defined by a programmable burst trigger algorithm, up to 4Mb of dedicated data can be stored for subsequent transmission to the ground. These data will provide the best time-resolved solar flare spectra available at high energies. This can include, for example, 192 high-resolution spectra from the spectroscopy detectors with time resolutions as short as 64 msec based on a time-to-spill algorithm. Higher time resolution can be obtained in an event-by-event mode which can store up to 64k events with a time resolution of 128 microseconds.

The burst trigger algorithm can determine the start of a transient event with a minimum timescale of 64 msec, clearly adequate for most solar phenomena. BATSE provides a burst trigger signal to the other three instruments on GRO which can use this signal to reconfigure operating modes for acquisition of burst data. Comparative rates in the four LAD's viewing the Sun can be used to determine the solar origin of an event. This information is also provided as part of the burst trigger signal to OSSE and COMPTEL which can establish operating modes specifically dedicated to solar phenomena.

2.3.2 ORIENTED SCINTILLATION SPECTROMETER EXPERIMENT (OSSE)

The Oriented Scintillation Spectrometer Experiment is designed to provide high sensitivity in the nuclear line region of the spectrum (Kurfess et al. 1989). Each of the four identical OSSE detectors is mounted in a single-axis pointing system which provides

rotational freedom of 192 degrees about the spacecraft Y-axis. The OSSE is located on the +X (solar) end of the spacecraft, which will enable the drive capability to be used to point the OSSE detectors at the Sun without disturbing the Z-axis objectives of the COMPTEL and EGRET instruments.

The total OSSE detector area is 2685 cm^2, about 10 times that of the SMM gamma ray detector. A tungsten alloy passive collimator provides a 3.8° by 11.4° field-of-view for the study of localized sources. This requires OSSE detectors to be pointed at the Sun for primary solar flare observations. Pulse-shape discrimination is used distinguish gamma-ray and neutron interactions in the NaI and to provide a positive detection of solar flare neutrons in the energy range above about 20 MeV.

Spectra in the 0.1-10 MeV energy range are processed by two 256-channel PHA's; individual spectra are accumulated every four seconds. Above 10 MeV, 16-channel gamma-ray and neutron energy-loss spectra are accumulated, also with typical 4-second time resolutions. An event-by-event data mode for selected energy ranges (e.g. the 4.4 MeV and/or 6.1 MeV lines for ^{12}C or ^{16}O) with a time resolution of 0.125 milliseconds is available for high time resolution observations. Thus, solar flare spectra in the nuclear line region will be acquired with much improved sensitivity and time resolution when compared with SMM.

The operation of the OSSE instrument is controlled by redundant on-board micro-processors. In response to a BATSE burst signal indicating detection of a solar flare, the four detectors can automatically re-orient to the Sun if the Sun is located near the X-Y plane, (see Figure 1), which due to solar panel attitude constraints, will often be the case.

2.3.3 IMAGING COMPTON TELESCOPE (COMPTEL)

COMPTEL is designed to observe gamma rays in the 1-30 MeV energy range in a broad (approx. 1 sr) field-of-view centered on the spacecraft Z-axis. COMPTEL also provides and excellent neutron detection capability in the 20-200 MeV energy range. The instrument consists of two detector arrays; and upper array, D1, comprised of seven 28-cm diameter NE213A liquid scintillation detectors, and a lower array, D2, which consists of fourteen 28-cm diameter x 3" thick NaI scintillation detectors. The basic properties of the instrument are described in Schoenfelder et al. (1981). Solar capabilities are discussed by Ryan and Lockwood (1989). Operationally, an incoming gamma ray or neutron scatters in detector array D1, and the scattered particle is detected in array D2. See Figure 2. In those events where the scattered gamma ray is totally absorbed in D2, the energy of the incident gamma ray is the sum of the energy losses in the upper and lower detectors, and the arrival direction is confined to a cone whose axis is determined by the locations of the interactions in D1 and D2 and the Compton scattering angle derived from the scattering kinematics. For events of solar origin, the requirement that the Sun lie on the angular

acceptance cone results in a gamma-ray spectrum with non-photopeak events strongly suppressed.

COMPTEL is sensitive to solar flares in three different operating modes. In the normal operating mode, COMPTEL provides high sensitivity to flares when the Sun is within the instrument field-of-view. This mode will provide excellent sensitivity for line and continuum gamma-ray emissions in the 1-30 MeV region. In addition, COMPTEL has the capability to observe transient phenomena, including solar flares, in a "single detector mode". In this mode, two of the fourteen NaI detectors are used to accumulate 256-channel pulse-height spectra in the 0.1 to 20 MeV region on programmable time scales of 0.1 to 25 seconds. The BATSE burst trigger signal is used initiate the acquisition of these spectra.

In the neutron detection mode a neutron elastically scatters on a hydrogen nucleus in a D1 detector and then interacts in a D2 detector. The energy loss in D1 and the time of flight between the upper and lower detector arrays is used to determine the neutron energy. The TOF information and pulse-shape discrimination in the D1 array are used to distinguish neutrons from gamma rays. The neutron mode is entered in response to a solar trigger signal from BATSE and will provide excellent neutron spectroscopy with a large signal-to- noise ratio for large flares.

2.3.4 ENERGETIC GAMMA RAY EXPERIMENT TELESCOPE (EGRET)

EGRET covers the high-energy portion of the spectrum from 20 MeV to 30 GeV (Fichtel et al. 1983). The instrument consists of two spark chamber modules which convert incoming gamma rays to positron-electron pairs. The arrival directions of incident gamma rays can be determined to several degrees at 100 MeV and to less than one degree at 1 GeV. EGRET's field-of-view is centered on the +Z axis and has a full-width-at-half- maximum of about 45° x 51°. A total absorption calorimeter below the spark chambers provides $\sim$ 15% energy resolution for gamma rays extending into the several GeV region.

EGRET provides solar flare capability in two modes. First, when the +Z axis of GRO is pointed to within 45 degrees of the Sun, EGRET provides high sensitivity to gamma radiation in the primary spectral region of the instrument. This will represent the first experiment to have good sensitivity in this spectral region for solar flares and will provide the opportunity to investigate the most energetic phenomena on the Sun through the gamma rays associated with neutral pion decay and the production of bremsstrahlung from the highest energy electrons in the flare region. In the second mode, the NaI crystal assembly is used to monitor transient events in the energy range from 0.6 MeV to 167 MeV. Upon receiving a BATSE burst trigger signal, 256-channel spectra will be acquired every 65.5 seconds during the flare or burst.

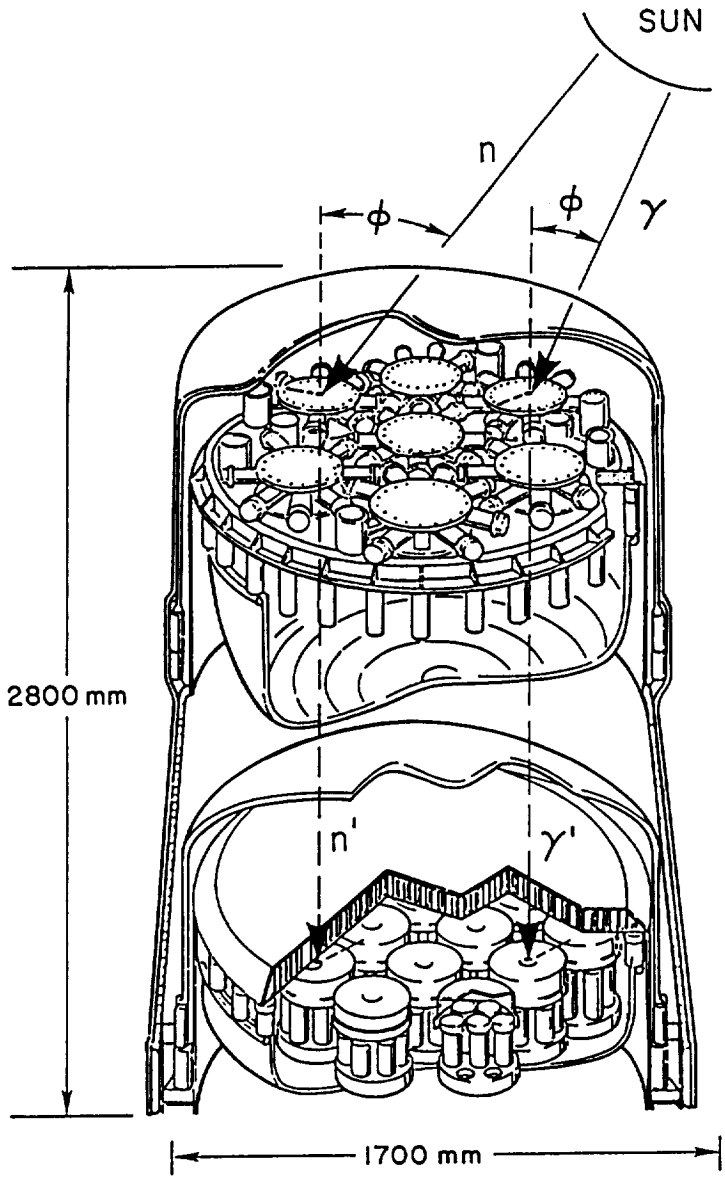

COMPTEL
IMAGING COMPTON TELESCOPE

Figure 2. Imaging Compton Telescope (COMPTEL). Imaging is accomplished by reconstruction of event cones from incident gamma rays which scatter in a liquid scintillator array (D1) followed by detection of the scattered photon in detector array D2.

2.4 GRO Guest Investigator Program

A vigorous Guest Investigator program will be implemented on GRO. The GI program will be initiated during the 15-month sky survey phase and will reach full level about three years into the mission. During the sky survey phase about 50% of the BATSE data on flares will be made available for Guest Investigator studies. Also, a selected rate history from the BATSE detectors will be provided to the solar physics community, through the HXRBS/SMM analysis center at GSFC. OSSE opportunities will include OSSE data on selected flares (probably those same flares available from BATSE) and opportunities to participate on an OSSE Solar Flare team. These opportunities will be available through GRO a NASA Research Announcement.

To support GRO investigators, a GRO Science Support Center (GROSSC) is being established at GSFC (Kniffen, 1989). This Center will be the central point of contact between the GI and the GRO data, and will assist GI's and prospective GI's by providing access to selected GRO data, past and planned GRO observations, data analysis software, etc. A Center employee for each GRO instrument (Instrument Specialist) will be located at a PI institution to assist GI's with the detailed aspects of their investigations.

3. Hard X-ray and Gamma-Ray Imaging - GRID

To date, imaging solar flares above soft X-ray energies has been accomplished with limited sensitivity and with angular resolutions barely adequate to detect flare morphology. No gamma-ray imaging has been attempted. Such observations are critically needed to determine the precise locations of particle acceleration and interaction in the flare region for comparison with observations at lower energies. One of the three instruments selected for the MAX '91 Balloon Program, GRID, is designed to provide such observations.

GRID, Gamma Ray Imaging Device, is currently under development by a consortium led by Dr. C.J. Crannell of GSFC (Orwig et al. 1989). The instrument uses the technique of Fourier transform imaging and employs a 22-set scanning modulation grid collimator optical system and NaI non-position sensing detectors. Full Sun imaging in the 20-700 keV spectral region will be obtained with a limiting spatial resolution of 1.9 arc-seconds and time resolutions down to 100 ms.

The first flight of GRID is scheduled for a 8-14 day long-duration balloon flight to be launched from Antarctica in January, 1992. During a two-week balloon flight, it is estimated that $\sim$ 40 flares can be imaged at energies above 100 keV. These images, in conjunction with microwave imaging and high-energy observations provided by GRO, should provide critically needed information on the location and mechanisms for particle acceleration in solar flares.

4. The Soft X-Ray Telescope (SXT) on Solar-A

In studying the effects of high energy particles it is necessary that measurements be made at other wavelengths where manifestations of these particles may be found. The importance of soft X-ray measurements cannot be underestimated. The interplay between the thermal and non-thermal processes is not fully understood, so measuring the thermal plasma temperature in space and time is critical to constraining the role of particles in heating the solar atmosphere. As a rule soft X-rays always precede the impulsive phase of the flare, but only by a few seconds in many cases. The Soft X-Ray Telescope (SXT) on Solar-A should be capable of improving our coverage in this wavelength domain (Brown et al. 1989).

Solar-A is scheduled to be launched in September 1991 and thus is well timed with respect to the availability of GRID, GRO and Ulysses. SXT, a grazing incidence telescope with an intrinsic resolution of better than 4 arc-sec, will image in 64 $\times$ 64 pixels the field-of-view (6.25 arc-min^2) in several wavelengths. The five wavelength windows have been chosen to be most sensitive to variations in plasma temperature. Thus, a temperature image can be constructed in the limit with a angle resolution approaching that of GRID.

The telemetry of Solar-A is limited, so that the 64 x 64 image budget is restricted to 8000 per day coming from 5 accessible orbits per day. SXT will also construct up to 5 large images (1024 x 1024 pixels) of almost the full Sun at these same wavelengths.

5. The Solar Flare and Cosmic Gamma-Ray Experiment on Ulysses

For the experimental gamma-ray astronomer, solar flares are much like cosmic gamma-ray bursts. Both are emitters of transient gamma-ray fluxes with solar flares generally lasting somewhat longer. With the measurement techniques being identical, cosmic gamma ray burst detectors such as BATSE on GRO and the Solar Flare and Cosmic Gamma-Ray Experiment (HUS) on Ulysses can provide excellent high-energy photon data on flares. The HUS on Ulysses will provide the opportunity to measure gamma-ray fluxes from flares at large aspect angles with respect to the earth direction with virtually a 100% duty cycle. The trajectory of Ulysses takes the spacecraft first past Jupiter and then over the south and then the north solar pole. With such a configuration of Ulysses, GRO and perhaps GRID, we will have a situation similar to that of PVO and ISSE-3. That is, spacecraft at different heliographic latitudes will be making observations of the same solar flare, measuring the differential gamma ray flux from different aspect angles (e.g. Kane et al., 1979). These stereoscopic observations can provide data on the altitude dependence of the flux and the emission measure as a function of heliographic latitude.

HUS consists of two detectors, a Si surface barrier detector and a CsI omnidirectional scintillator (Boer et al. 1989). The CsI detector is probably most adaptable to

solar flare studies. It has an area of 20 cm^2 operating in the range of 30 to 200 keV. This instrument on Ulysses is small, but has the advantage of spending a long period within 1 A.U. and observing the Sun almost continuously. In the burst mode, the mode in which flare data will be obtained, the detector accumulates 16-channel spectra at different accumulation times beginning with 1 s and progressing to 16 s for a total period of 496 s. The beginning of the burst (for 16 s) has the detector transmitting the total counting rate at an 8 ms cadence. At the end of this 496 s period the telemetry buffer is full and readout begins with continued monitoring of the total count rate every 0.5 s. But for the small area factor, the HUS instrument characteristics match well with BATSE. The period for which the spacecraft will be at high latitudes (> 70 degrees) is roughly 230 days.

The launch of Ulysses is to take place in October 1990. From there the trajectory takes it out to the orbit of Jupiter (5 AU), after which it begins its path over the south solar pole. The passage over the south pole takes place in 1994 with a similar passage over the north pole in 1995. The sensitivity of the HUS will, of course, be reduced at large solar radii, but the exposure towards the Sun will be well coordinated with the GRO and Solar- A. The prospect for obtaining complementary data sets is good.

6. Radio and Microwave Observations

6.1 Millimeter-Wave Imaging - BIMA

Millimeter wave observations provide information on the highest energy electrons in solar flares, and enable observations of this component into the chromosphere. Operating in an atmospheric window from 70 - 115 GHz, a consortium consisting of the Univ. of California (Berkeley), Univ. of Illinois and the Univ. of Maryland have established the BIMA mm-wave interferometer (Kundu et al. 1989) and plan to devote extended observing periods to solar flare observations.

BIMA will provide (by late 1990 or early 1991) a 6-element array. With 15 baselines, BIMA will be able to generate maps of solar flares with a temporal resolution of 0.1 sec and spatial resolution of $\sim$ 1 arc sec. Thus, BIMA will provide detailed maps indicting the electron acceleration and emission region with high-time resolution. Correlating these images with the maps obtained with GRID, Solar A, or with other high energy observations obtained, e.g. by GRO instruments will provide much greater insight into the acceleration region and mechanism.

6.2 Microwave Imaging and Spectroscopy - OVRO

The Owens Valley radio interferometer (OVRO) is currently undergoing an expansion which will provide a 5 antenna array (10 baselines) dedicated to solar observations. This system, to be operational in October 1990 (Hurford and Gary, 1989), will include

two existing 27m antennae and three 2m antennae. Each antenna will be equipped with frequency agile receivers which can be tuned to 86 discrete frequencies in the 1-18 GHz band in rapid succession (10-30 frequencies/second).

With this expansion, the Owens Valley solar array will provide simultaneous imaging and spectroscopy. Two-dimensional microwave images with $\sim$ 2 arc-second resolution will be acquired in the 1-18 GHz band. This combination of spectroscopy and imaging will enable the acquisition of magnetograms at the base of the corona. The microwave spectrum is sensitive to the nature of the energetic electrons (thermal vs. non-thermal) and also provides information on the plasma properties in the flare region. This dedicated data set will be an integral part of many MAX '91 correlative studies.

6.3 The Very Large Array (VLA)

During the Solar Maximum Mission, the coincidence of positive VLA and GRS observations of a gamma ray flare did not occur (Kundu, priv. comm., 1989; Lang, priv. comm., 1989). For the purpose of coordinating radio/microwave telescope data with those from a gamma ray instrument, the VLA is in effect an unexploited instrument. Its imaging capability offers a real chance to relate the electron bremsstrahlung emission above 1 MeV to the optically thin microwave emission perhaps originating from the same original electron population. The populations responsible for these emissions could, in principle, be the same; but, more likely derive from the same population, fractionating by some unknown process. Recent work by Lang and Willson (1989) indicates that different parts or phases of a flare exhibit radio emissions from different sites. Until recently (GRID), all hard X-ray ($>$ 200 keV) and gamma ray instruments integrated over the entire solar disk. It has thus been difficult to identify the elements of the flare's temporal structure with physical processes or structures on the Sun. Spatial information has always been lacking. The new feature of the VLA which was not present in the last solar maximum is the ability to observe the full Sun at both 20 and 90 cm. The two wavelengths probe different depths of the corona and view different coronal structures.

To a high degree the emission of nuclear gamma rays is well correlated to the emission of electron bremsstrahlung $>$ 300 keV. We can use this fact with the spatial information provided by the VLA to locate the sites of electron activity in a flare, and thus the sites of energetic proton activity. What is required is dedicated and coordinated observing. Max '91 can provide the environment for such observing. The small field-of-view in earlier configurations of the VLA made the observation of a gamma ray flare an improbable event. With full Sun coverage, the likelihood of obtaining coordinated data sets is dramatically increased.

7. Conclusion

As compared to the last solar maximum, there will be new and different instrumental power being trained on the Sun. These instruments require different observing plans and goals to study the elusive high-energy solar flare. It is imperative that an organized effort be initiated to refine these goals and to devise the appropriate observing plan. The Max '91 Workshop is one of the first steps in that direction. Further work is necessary, before the maximum and before the first of the balloon-based and space-based instruments described above becomes operational.

What potential collaborations and data correlations may be possible with the instruments described above? The following are a few suggestions.

1) BIMA, OVRO and VLA with GRID

These radio and microwave telescopes each will offer better than 2 arcsec spatial resolution over a wide range of frequencies. Any of these data can be correlated with the images produced by GRID. All are sensitive to energetic electrons giving rise to gyrosynchrotron radiation and bremsstrahlung.

2) BIMA, OVRO and VLA with any or all of the GRO instruments

The GRO provides unprecedented sensitivity to electron bremsstrahlung radiation above 5 MeV. At these energies there is no confusion between thermal and non-thermal origins of the radiation. These energetic electrons in reasonable solar magnetic fields will radiate at optically thin frequencies observable to all the radio telescopes. The bremsstrahlung gamma-ray flux over a wide range of energies can be directly compared or contrasted with the radio and microwave images over a wide range of frequencies.

3) HUS with BATSE

The continuous coverage of the Sun by HUS at large solar aspect angles combined with the sensitivity of BATSE offer considerable prospects for a new set of stereoscopic observations of flares from different heliographic latitudes.

4) SXT with any or all of the GRO instruments

The role of energetic particles in heating the lower solar corona is still in question. If rapid images could be obtained by SXT, they could be compared to the gamma ray (electronic or nuclear) light curves to search for and study any correlations.

References

Batchelor, D. 1989, *Proceedings of the Second MAX '91 Workshop*, 8-9 June 1989, Laurel, MD, this volume.

Bertsch, D.L. 1989, *Proceedings of the Second MAX '91 Workshop*, 8-9 June 1989, Laurel, MD, this volume.

Boer, M., Sommer, M., and Hurley, K. 1989, *Proceedings of the Second MAX '91 Workshop*, 8-9 June 1989, Laurel, MD, this volume.

Brown, W.A., Acton, L.W., Bruner, M.E., Lemen, J.R., and Strong, K.T. 1989, *Proceedings of the Second MAX '91 Workshop*, 8-9 June 1989, Laurel, MD, this volume.

Chupp, E.L. 1984, Ann. Rev. Astron. Astrophys., 22, 359.

Chupp, E.L., Forrest, D.J., Kanbach, G., and Share, G.H. 1983, Proceedings of the 19th Intl. Cosmic Ray Conf. (Bangalore), late papers, p. 334.

Evenson, P., Meyer, P., and Pyle, K.R. 1983, Ap. J., 274, 875.

Fichtel, C.E., Bertsch, D.L., Hartman, R.C., Kniffen, D.A., Thompson, D.J., Hofstadter, R., Hughes, E.B., Campbell-Finman, L.E., Pinkau, K., Mayer-Hasselwander, H., Kanbach, G., Rothermel, H., Sommer, M., Favale, A.J., and Schneid, E.J. 1983, 18th Int'l Cosmic Ray Conference, Vol 8, p.19.

Fishman, G.J., Meegan, C.A, Parnell, T.A., Wilson, R.B., Paciesas, W., Matteson, J.L., Cline, T., and Teegarden, B. 1985, 19th Internat. Cosmic Ray Conf. Papers, 3, 343.

Fishman, G.J., Meegan, C.A., Wilson, R.B., Parnell, T.A., Paciesas, W.S., Pendleton, G.N., Hudson, H.S., Matteson, J.L., Peterson, L.E., Cline, T.L., Teegarden, B.J., and Schaefer, B.E., 1989, *Proceedings of the Second MAX '91 Workshop*, 8-9 June 1989, Laurel, MD, this volume.

Hurford, G.J. and Gary, D.E. 1989, *Proceedings of the Second MAX '91 Workshop*, 8-9 June 1989, Laurel, MD, this volume.

Kane, S.R., Anderson, K.A., Evans, W.D., Klebesadel, R.W., and Laros, J. 1979, Ap. J. (Letters), 233, L151.

Kane, S.R., Love, J., Neidig, D.F., and Cliver, E.W. 1985, Ap. J. (Letters), 290,.L45.

Kniffen, D.A., 1989, *Proceedings of the Second MAX '91 Workshop*, 8-9 June 1989, Laurel, MD, this volume.

Kundu, M.R., White, S.M., Gopalswamy, N. and Bieging, J.H., 1989, *Proceedings of the Second MAX '91 Workshop*, 8-9 June 1989, Laurel, MD, this volume.

Kurfess, J.D. 1988, Solar Physics, 118, 347.

Kurfess, J.D., Johnson, W.N., Share, G.H., Matz, S.M and Murphy, R.J., 1989, *Proceedings of the Second MAX '91 Workshop*, 8-9 June 1989, Laurel, MD, this volume.

Lang, K.R., and Willson, R.F. 1989, *Proceedings of the Second MAX '91 Workshop*, 8-9 June 1989, Laurel, MD, this volume.

Murphy, R.J., Forrest, D.J., Ramaty, R. 1985a, 19th Internat. Cosmic Ray Conf. Papers, 4, 253.

Murphy, R.J., Ramaty, R., Forrest, D.J., and Kozlovsky, B. 1985b, 19th Internat. Cosmic Ray Conf. Papers, 4, 249.

Murphy, R.J., Hua, X.-M., Kozlovsky, B. and Ramaty, R. 1990 Ap. J. (submitted).

Orwig, L.E., Crannell, C.J., Dennis, B.R., Starr, R., Hurford, G.J., Prince, T.A., Hudson, H.S., van Beek, F., Greene, M.E., Johnson, W.N., Norris, J.P., Wood, K.S and Davis, J.M., 1989, *Proceedings of the Second MAX '91 Workshop*, 8-9 June 1989, Laurel, MD, this volume.

Rieger, E., Share, G.H., Forrest, D.J., Kanbach, G., Reppin, C., and Chupp, E.L. 1984, Nature, 312, 623.

Rust, D.M., Max '91 Flare Research at the Next Solar Maximum, Workshop 1: Scientific Objectives, Summary and Reports, Ed. Canfield, R.C. and Dennis, B.R., 1988.

Ryan, J.M., Chupp, E.L., Forrest, D.J., Matz, S.M., Rieger, E., Reppin, C., Kanbach, G., and Share, G.H. 1983, Ap. J. (Letters), 272, L61.

Ryan, J.M. and Lockwood, J.A., 1989, *Proceedings of the Second MAX '91 Workshop*, 8-9 June 1989, Laurel, MD, this volume.

Woodgate, B.E., Shine, R.A., Poland, A.I., and Orwig, L.E. 1983, Ap. J., 265, 530. Zirin, H. and Neidig, D. 1981, Ap. J. (Letters), 248, L45.

MAGNETOGRAPH GROUP SUMMARY

Harrison P. Jones

NASA/Goddard Space Flight Center
Laboratory for Astronomy and Solar Physics

Introduction.

The Magnetograph Group evolved from the Energy Buildup and Storage Group, chaired by T. Tarbell at the 1988 Max '91 Workshop in Kansas City. The suggestion was advanced at the 1988 Workshop that observing campaigns specifically designed to obtain magnetic field measurements from many participating sites should be conducted as part of the FLARES 22/Max '91 program. It was felt that such campaigns would provide cross-calibration of instrumentation, would allow studies of active region evolution over periods of several days, and would permit extrapolation of coronal fields and inference of magnetic energy content.

The discussion at the 1989 Max '91 Workshop at Laurel, Md. began with oral presentations by Harvey, who discussed a much earlier magnetograph comparison program conducted by J. Beckers under IAU sponsorship early in the 1970's; by Zirin, who discussed the successful two-station magnetograph network with Big Bear Solar Observatory and Huairou Solar Observatory in China; by Jones, who discussed a recent cooperative observing effort during the International Solar Month (Sep. 1988); and by Chapman who described new instrumental developments at the San Fernando Observatory.

Open informal discussion followed the oral presentations. The intent of the original agenda was to develop specific guidelines and action items for further magnetograph campaigns. However, actual attention focussed on the techniques and many practical problems of interleaving ground-based measurements of magnetic fields from diverse sites and instruments to address the original scientific objectives.. The predominant view of the discussion group was that present instrumentation and analysis resources do not warrant immediate, specific plans for further worldwide campaigns of cooperative magnetograph observing. The several reasons for this view, together with many caveats, qualifications, and suggestions for future work are presented in the following summary of the Magnetograph Group discussion.

The IAU Campaign.

Under sponsorship of the IAU, Jacques Beckers coordinated a program to compare then extant magnetographs. Observations began with a pilot study in 1970, continued with a primary campaign in 1971, and ended with an unsuccessful attempt to observe active regions in June, 1972. A brief summary of the results appears in *IAU Transactions* **XVA** (1973), p.108, and an extensive unpublished report was also prepared. Target regions were observed by the participating instruments in the FeI 5250 Å line; data were prepared at each site on punched cards in a common fixed format and were sent to Beckers for analysis. Eventually, both point-by-point and "scatterplot" comparisons of data from pairs of instruments were prepared. All the instruments were longitudinal field magnetographs, mostly of more or less conventional Babcock design.

The initial studies showed some large discrepancies (factors of order 2) which led to better understanding of calibration procedures and correction of several errors. One discrepancy in algebraic sign was not firmly resolved until in-situ measurements of the interplanetary field at 1 A.U. were correlated with the polarity of fields at the solar surface. After correction of the calibration errors, general agreement at roughly the ± 25% level was found between instruments for the 5250 Å line in weak-field regions. The agreement in strong-field areas near sunspots was much worse, almost certainly because of "saturation" effects induced by line-profile changes. Harvey pointed out that, although the full report was not published, the studies did identify

calibration problems and induced a healthy appreciation of the observable effects of line-profile variations on the relation between Zeeman shifts and measurements of intensity differences in polarized light. The preparation and intercomparison of the data were extremely laborious, particularly for the coordinator.

The Big Bear-Huairou Network

More recent and quite successful efforts at cooperative magnetograph observing have been conducted using video magnetographs at Big Bear Solar Observatory and the Huairou Observatory near Beijing. Long-term magnetogram movies displayed at the discussion session and elsewhere unmistakably demonstrate the advantage of nearly continuous coverage of magnetic evolution over periods of days--the natural time scale of the phenomenon. Movement of many magnetic patterns can be easily followed in the time series of networked magnetograms which would be impossible to identify across the night-time interruptions at a single site. As a general rule, Zirin felt that eight-hour coverage is clearly not adequate for these studies while sixteen-hour coverage is nearly sufficient.

Zirin identified three important elements in the success of this network in addition to the obvious fact that the observing sites are strategically dispersed in longitude. First, the instruments are similar (the Huairou design being based on the Big-Bear video magnetograph) and comparatively simple. Second, the observing campaigns are most successful when there is interchange of scientific staff between sites. Finally, a powerful image processing system and a dedicated expert to run it are available to reduce and interleave the observations into a coherent single time series. This very considerable data reduction and analysis capability is necessary even though the geometric and scaling corrections are minimized by the similarity of the instruments.

Cooperative Magnetograph Observations during the International Solar Month.

In response to the "charge" developed at the 1988 Max '91 workshop, Jones noted that the International Solar Month--a period of observing campaigns originally planned for simultaneous observation of the Sun from the Soviet Phobos mission, the Solar Maximum Mission, the VLA, and many ground-based observatories--provided an early opportunity to use an existing infrastructure for communication and target selection to obtain comparative magnetograph observations.

Accordingly, under the auspices of the National Solar Observatory, an exploratory letter was sent to many observatories with appropriate instrumentation. The primary goals were to identify potential participants, to establish communications links, to identify peculiarities in data sets, and, in general, to learn how to organize better campaigns. Responses expressing interest in the project were received from eleven groups; however, communications were too slow for actual participation in many cases, and several instruments were either not ready for observations or were undergoing repairs and renovation. A target region near disk center was selected for intensive observation on 16 and 17 September, 1988, and was announced over the standard e-mail communications network used by the organizers of the International Solar Month. By the time of the Laurel workshop, data from five groups were available (Hawaii-Mees Observatory (MO); Mount Wilson Observatory (MW); Lockheed Palo Alto Research Laboratories (LPARL) operating the Solar Optical Universal Filter and Polarimeter (SOUP) breadboard instrument at the Swedish Telescope on La Palma; the San Fernando Observatory (SFO) of California State University at Northridge (CSUN); and the National Solar Observatory/Kitt Peak (NSO/KP). Observations from the San Fernando Observatory were of two regions (NOAA ARs 5105 and 5106) on a different date (11 August 1988) but could be compared with NSO/KP full-disk data. A summary of relevant observing parameters is shown in Table I.

With some difficulty, the various data sets (all on standard magnetic tape) were read at the National Optical Astronomy Observatories (NOAO) central computing facilities in Tucson and were coverted to IRAF (Interactive Reduction and Analysis Facility) format. One can identify common features in grey scale displays of the various magnetograms without great difficulty,

but the large disparities in field of view (82 X 82 arc-seconds to full-disk) and pixel size (1/6 to 20 arc-seconds) are immediately obvious. The images were interpolated onto grids of square pixels where necessary and were rotated (approximately) to "standard" heliographic orientation with solar north at the top, west to the right.

Table 1.

Observatory	Instrument	Line	Region	Time	Pixel Size (arc-sec)	FOV (arc-sec)
LPARL La Palma	SOUP/OSL Breadboard	6303	AR5148	09/17/88 16:36	0.16x0.16	82x82
MO	Stokes Polarimeter	6303	AR5148	09/17/88 17:39	5.6x5.6	196x140
MW	150-ft Tower Magnetograph	5250	AR5148	09/17/88 19:20	12.7x20.2	Full Disk
NSO/KP	512-Channel Diode Array Magnetograph	8688	AR5148	09/17/89 16:10-22:10 (every 5 min.)	1.0x1.0	256x512
			AR5105, AR5106	08/11/89 16:10	1.0x1.0	Full Disk
CSUN/SFO	Dual Reticon Magnetograph	6303	AR5105	08/11/89 22:05	1.9x1.9	486x480
			AR5106	08/11/89 22:22	1.9x1.9	486x477

It proved easier to "stretch", rotate, and register the three higher resolution magnetograms (LPARL, NSO, SFO). As of the workshop and this writing, pixel-by-pixel and scatterplot comparisons have only been carried out for these three sites. The NSO/KP magnetograms have been used as the "standard" primarily because of the relatively high spatial resolution and long historical record of the instrument. Figure 1 shows the comparison of a sample line from the LPARL (at full spatial resolution) and the NSO data (magnified by interpolation to the same pixel size and masked to the same field of view). Allowing for the different spatial resolution, the overall correspondence between the two data sets appears reasonably good except that the reported field strength of the LPARL data seems systematically higher. This effect is shown somewhat better in the pseudo scatter-plot of Figure 2. A direct point-by-point scatterplot would simply show a saturated black area due to the large number of points in the images. Thus Figure 2 shows instead a half-tone rendering of log(1+N) where N is the two-dimensional histogram (20 x 20 Gauss bins) of the images. The mean (solid curve) and $\pm$ 1 σ (dashed curves) of the one-dimensional slices of the histogram at each bin of the NSO data are plotted to give a more quantitative view of the systematic variation and the spread of the data. A substantial portion of the spread of points may be attributed to the large discrepancy in spatial resolution (many localized features in the LPARL data are not seen in the NSO magnetograms) and errors in spatial registration. The instruments also seem to respond rather differently to strong umbral fields. The negative spike at zero field in the NSO data is an artifact of boundary interpolation during the image rotation process. The systematic correlation between the data sets is

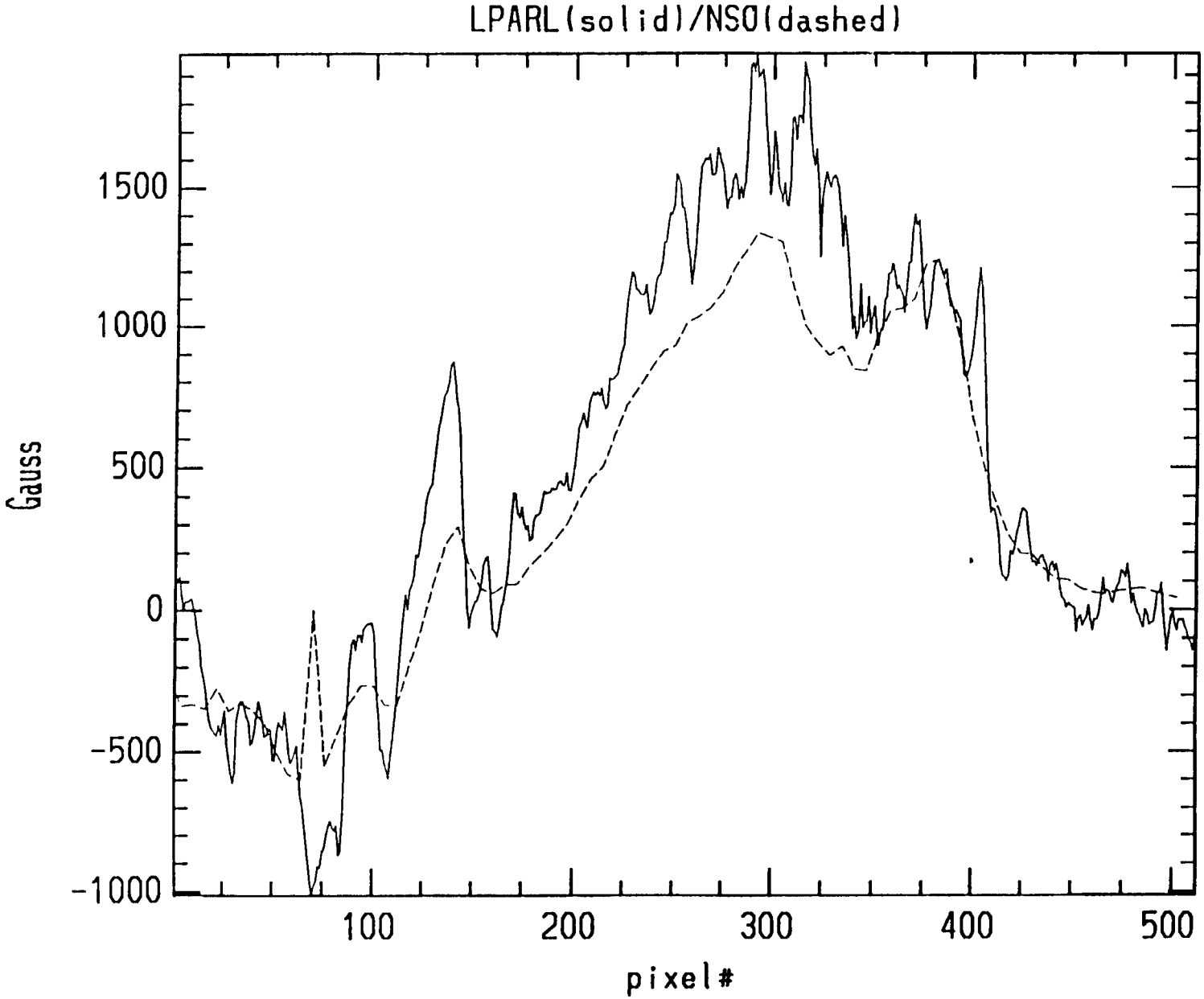

Figure 1. - Longitudinal magnetic fields from a sample line of regstered images of AR 5148 from LPARL (solid) and NSO/KP (broken).

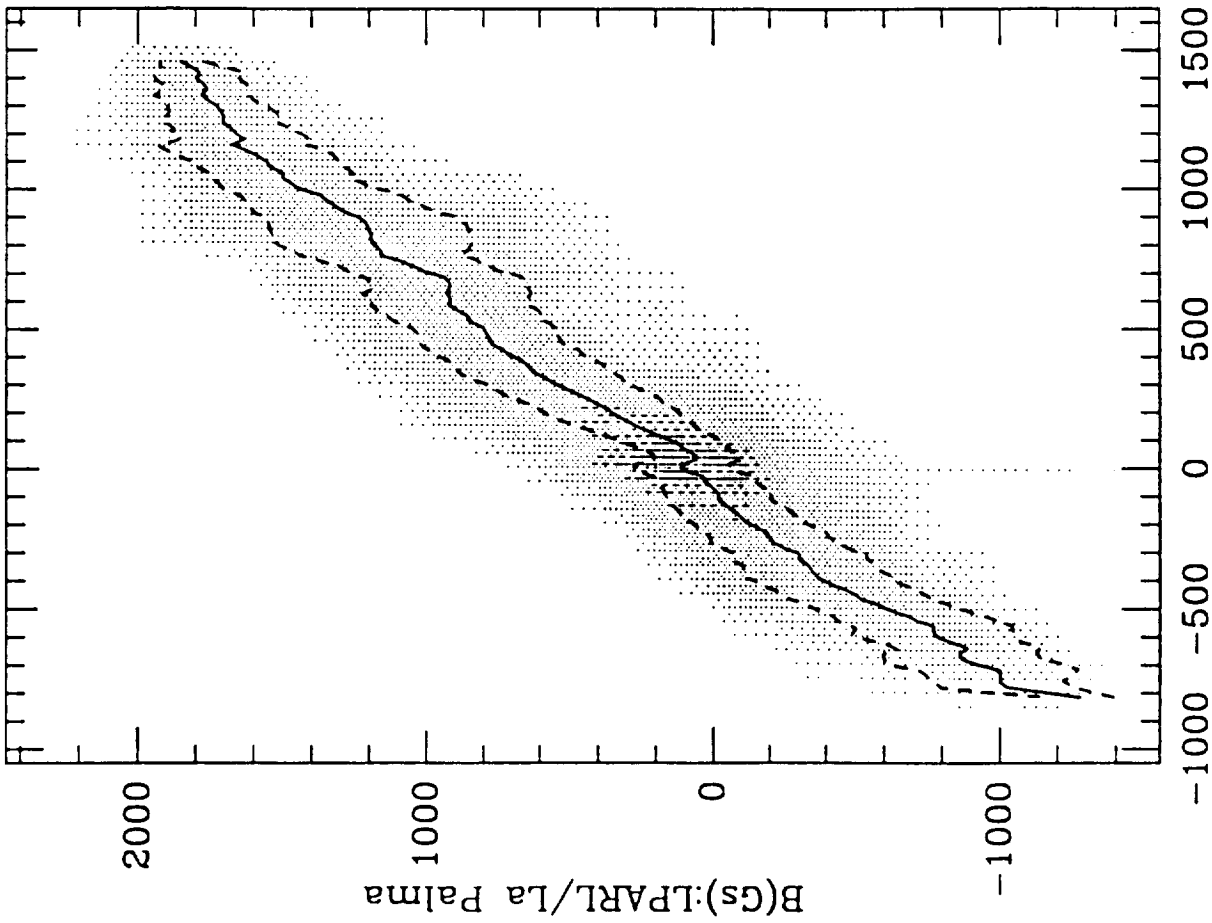

Figure 2. - "Scatterplot" diagram of LPARL and NSO/KP magnetic fields from registered images of AR 5148. The density of plotted points is determined from the two-dimensional histogram (see text), and the curves show the mean ± 1 σ of histogram slices.

quite linear, but the slope (LPARL vs. NSO) is 1.2.

Figure 3 compares sample image lines from the SFO and NSO data for one of the observed active regions, and Figure 4 shows the corresponding "scatterplot". There is a similar anomalous negative spike at zero NSO field, but the overall spread of points is reduced when compared to the LPARL-NSO plots, presumably because of the similar spatial resolution of the two instruments. However, the SFO instrument saturates at smaller field values than the NSO magnetograph, and the slope (SFO vs. NSO) is approximately 0.75.

Both the LPARL and SFO instruments are new so that it is perhaps not surprising to find calibration constants in disagreement. The specific reasons for the discrepant slopes are not clear, however, and further investigation of the calibration procedures will be undertaken. Loosely speaking, the spread in field values is consistent with the ± 25% found in the IAU study. Thus, the basic quantitative correlation properties between magnetographs, when the data are compared pixel by pixel, have not changed much between the previous and current generations of instruments. Since the instruments which have been compared so far are still basically Babcock magnetographs which are sensitive to line profile effects, this is a result which might be anticipated. On the other hand, the visual correspondence between actual magnetogram images is quite good which suggests that networks of similar instruments can in principle be used for long-term studies of magnetic field evolution. Moreover, it should be noted that "today's pixel" typically has much greater spatial resolution, linearity, uniformity of response, sensitivity, and dynamic range than could be found in data from fifteen or twenty years ago.

Finally, although media for interchange of digital data and image processing hardware and software are vastly improved in the last fifteen years, actual reduction, analysis, and comparison of diverse data is still laborious and time-consuming, particularly in the exploratory stages. The rotation and magnification of dissimilar images for precise registration can be particularly difficult and may require several iterations by an intelligent and knowledgeable analyst. Once the rotation and magnification parameters have been established, sequences of similar images may be shifted in a more automated fashion to complete the registration process.

New Magnetograph Instrumentation at the San Fernando Observatory

G. Chapman presented preliminary data from two new instruments at the San Fernando Observatory operated by the California State University at Northridge (CSUN). The first of these is a Babcock magnetograph using dual Reticon arrays to span segments of the solar image (similar to the NSO/Kitt Peak magnetograph); the second is a Video Spectra-Spectroheliograph which records full long-slit spectra from a two-dimensional CCD detector on video tape. Some analysis of sunspot Stokes V-profiles derived from the latter instrument was discussed. In particular, the discussion emphasized that the wavelength separation of the extrema in Stokes V is more a reflection of line width than field strength. More importantly in the context of the group discussion, the instrumentation is representative of a new generation of both line-of-sight and vector magnetographs which are likely to be completed in the next year or two--a circumstance which considerably influenced subsequent discussion of the desirability and timing of future magnetograph campaigns.

Discussion

The open discussion centered less on the desirability of the scientific goals mentioned in the introduction and more on the practicality of achieving them with Max '91 campaigns scheduled in the next year or so.

Considerable attention was given to formats and image projection protocols which might facilitate data handling and comparison. The FITS format is convenient for image processing at NSO so long as the "standard" is rigidly observed (fixed 2880 byte blocks, header keywords blank-padded to eight characters, partial trailing blocks padded to full fixed size, etc.) but has a block length which is too small for efficient transfer of large images and which is wasteful of space on new high-density media such as heliscan video tape cartridges (e.g., Exabyte). The Lockheed group has developed an efficient storage format for Exabyte cartridge tapes, and a

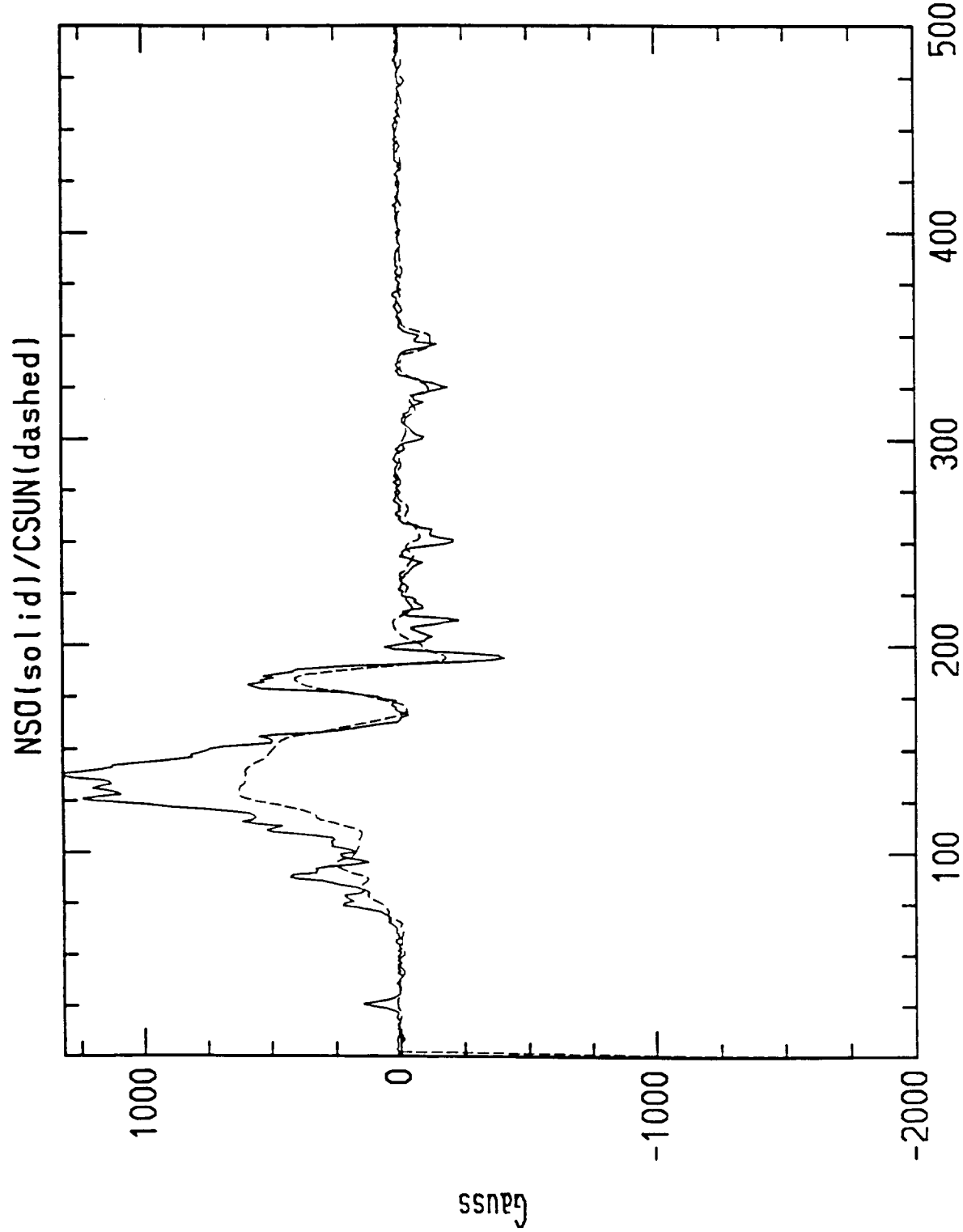

Figure 3. - Longitudinal magnetic fields from a sample line of regstered images of AR 5105 from NSO/KP (solid) and SFO (broken).

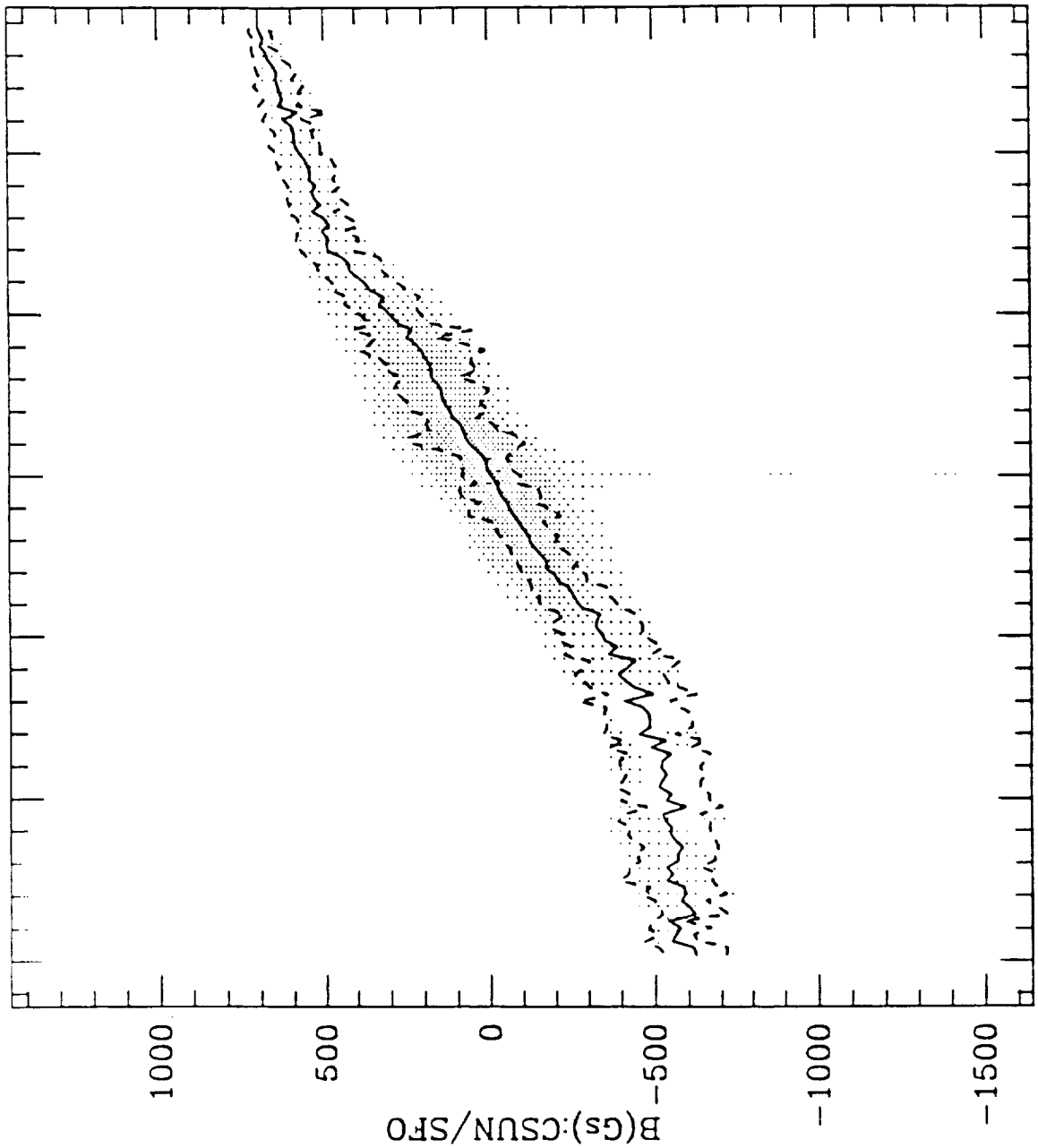

Figure 4. - "Scatterplot" diagram of SFO and NSO/KP magnetic fields from registered images of AR 5105.

long-block FITS format is being developed at NOAO partly for archiving full-disk magnetograms on Exabyte tapes. Rabin (NSO) and Shine (LPARL) agreed to explore possibilities for a useful standard. It was also suggested that a standard coordinate system (e.g. Carrington) be adopted for data interchange and that local sites interpolate their data onto such a grid before export. Many reservations were expressed about both the practicality and need for such a standard, and no specific action was agreed upon.

Some discussion was devoted to the comparability of vector field measurements. The transverse component of the field is ordinarily much more difficult to measure since it has a weak linear polarization signature, and preliminary comparison of results between the Marshall Vector Magnetograph and the Hawaii Stokes polarimeter seem to reflect this. A new Advanced Stokes Polarimeter is being developed by the High Altitude Observatory and NSO/Sacramento Peak which should be less subject to some of the current measurement uncertainties since it will record full Stokes profiles at high spatial and spectral resolution. An alternative method for measuring vector fields which partly avoids the difficulties of weak polarization is to observe infrared lines whose widths are small compared to the magnetic splitting. Work is proceeding on two infrared magnetographs at the NSO McMath telescope. One will operate near the opacity minimum at 1.6 μm (Rabin *et al.*) while the other will make use of the 12 μm emission lines (Deming,*et al.*). Other characteristics of the infrared (improved seeing, less scattered light, simplicity of interpretation, linear dependence of source function on temperature, etc.) help to make this an attractive spectral regime, and the detector technology to make such devices possible is rapidly maturing. Both instruments are in fairly early stages of development, and their impact on studies during the current maximum of activity is uncertain.

Conclusions.

From the results of the oral papers and the tenor of the ensuing discussions, a general consensus developed that existing optical magnetographs do not yield measurements of solar magnetic fields which can be intercompared with high quantitative precision. Many of the reasons for this are known (line profile effects; seeing; different spatial resolution), and new instruments are nearing completion which should be less sensitive to at least some of the problems. Thus campaigns to calculate evolution of magnetic energy content in an active region volume using magnetograms from multiple sources are at present ill-posed. Extrapolation of photospheric fields to coronal heights, while still uncertain given the scatter in measurements by different instruments, may be a better posed problem simply because the dominant contribution is from low-order multipoles whose measurement is less sensitive to seeing, spatial resolution, and line profile effects.

Given the high degree of geometric fidelity achievable with modern detector systems, magnetograms taken at different locations with similar resolution have a very high degree of visual comparability and can be used to observe many elemental processes of magnetic field evolution (transverse motions of flux concentrations, flux emergence, subsidence, bipolar encounters, evolution of network boundaries, etc.). However, with the notable exception of the La Palma instrument, the magnetographs which participated in the International Solar Month are clustered in the American Southwest and are too narrowly dispersed in longitude for effective networking. Moreover, the elements which have led to the successful operation of the Big Bear-Huairou network (especially simplicity and similarity of instruments) will be difficult to develop for other existing magnetographs over a wide geographic distribution. Thus, although magnetograms will continue to be essential planning tools and will provide necessary data for Max '91 studies of solar activity, the current state of the art does not justify a near-term campaign organized around magnetographs. One limited "mini-campaign" was suggested--the intensive observation of the kinematics and dynamics of the polar field reversal. Zirin agreed to lead such an effort.

Cross-calibration of instrument pairs continues be a useful endeavor. J. Schmelz agreed to contact international observatories to see if further such comparisons might be undertaken with NSO data. Although the NSO magnetograph will be replaced with the new NSO/NASA

Spectromagnetograph which will use full line profiles instead of two-slit detection, both the old and new instruments will be operated together long enough to allow thorough cross-calibration between new and old standards. There was general agreement that all the issues should be revisited in about a year's time after many of the "next generation" instruments have become operational.

N90-12462

Theory and Modeling Group

Gordon D. Holman
Laboratory for Astronomy and Solar Physics
NASA/Goddard Space Flight Center
Greenbelt, Maryland

The primary purpose of the Theory and Modeling Group meeting was to determine who is doing (or is interested in doing) theoretical work pertinent to the MAX '91 Program, and to encourage theorists to pursue modeling which is directly relevant to data which can be expected to result from the Program. The number of scientists participating in the Group ranged from ~ 25–30. The morning 1.5 hours of the Group meeting was devoted to determining the research interests of those present at the meeting. Each participant briefly summarized the research he or she is doing relevant to active regions and flares. The afternoon (2 hours) was devoted to open discussion of several topics pertinent to the science as well as the organization of the MAX '91 Program. The discussion was sometimes rambling, but generally lively.

A list of participants and their institutions is contained in the table on the following page. The table is organized by subject areas in which the participants expressed interest, so a few are listed more than once. Since the catagorization was determined on the basis of interests expressed at the meeting, it does not necessarily represent the full range of interests of each scientist. Likewise, since the categories are somewhat broad, the table does not reflect the specific research interests of each participant. This information can be found in the contributions from the individual scientists that follow this summary. The catagorization does provide, however, an overview of the range of subject areas represented at the meeting.

In contrast to the strong attendance at the Theory Group meeting, only 5 theoretical papers had been submitted to the MAX '91 Workshop: 2 from Goddard (S. Benka and G. Holman), 2 from Colorado (M. McKean and R. Winglee), and one from Stanford (J. Klimchuck). Much of the afternoon discussion was concerned with the existence and formation of multiple current channels and their return currents in flaring regions, since this was a common theme in the papers from Colorado and from Goddard, as well as other papers presented at the SPD meeting. There is clearly increasing interest in how these current channels might be formed, and the observational consequences of their presence. This will be an important issue in the interpretation of MAX '91 data.

Magnetic Field Strength, Structure, and Evolution	
G. Holman	NASA/Goddard
J. Klimchuck	Stanford U.
Z. Mikic	SAI, San Diego
Reconnection Theory	
P. Liewer	JPL
Electron Energization	
S. Benka	U. North Carolina & NASA/Goddard
G. Holman	NASA/Goddard
G. Roumeliotis	U. Alabama, Huntsville
Electron Beam, Return Current Properties	
G. Emslie	U. Alabama, Huntsville
M. Karlicky	Astronomical Inst., Prague
M. McKean	U. Colorado
P. McNeice	STX, at NASA/Goddard
D. Spicer	NASA/Goddard
R. Winglee	U. Colorado
Electron Trapping and Escape	
R. Hamilton	Stanford U.
E. Lu	Stanford U.
Ion Acceleration and Beam Properties	
P. Cargill	U. Maryland
F. Lang	Catholic U., at NASA/Goddard
M. McKean	U. Colorado
C. Werntz	Catholic U., at NASA/Goddard
R. Winglee	U. Colorado
Chromospheric Evaporation	
G. Emslie	U. Alabama, Huntsville
R. Falciani	Inst. di Astronomia, Florence
D. Zarro	ARC, at NASA/Goddard
White Light Emission	
G. Fisher	U. Hawaii
Soft X-ray Observations	
D. Batchelor	NASA/Goddard
J. Saba	Lockheed, at NASA/Goddard
K. Strong	Lockheed, Palo Alto
Radio Observations	
N. Gopalswamy	U. Maryland
E. Schmahl	U. Maryland
G. Thejappa	U. Maryland
S. White	U. Maryland
Laboratory Experiments	
T. Tamano	General Atomics, San Diego

A couple of solar flare paradigms were discussed, with neither of them receiving any strong support from those present. One of these was the importance of magnetic reconnection in flares. Although it is generally agreed that magnetic reconnection plays a role in flares, it is not apparent that magnetic reconnection need be the primary mode of energy release in flares. Magnetic reconnection is often taken as a starting point for flare models, but no arguments were found for why this need be the case. It is also often stated that the primary release of flare energy occurs at the top of coronal loops. Although observational evidence from the last solar maximum seemed to indicate this, it is now apparent that this need not be the case.

Another topic of discussion was the applicability of numerical simulation results to solar flares. Clearly, the results of a numerical simulation are only as good as the physical processes and conditions that can be (or have been) included in the code. For those not directly involved in the simulation, this is often difficult to judge. The detailed discussion and comparison of numerical simulations may be an appropriate topic for a group meeting at a future MAX '91 Workshop.

Given the observations planned for this solar maximum, in what areas might significant progress in our understanding of the physics of solar flares be expected? Improved imaging and spectral information in soft X-rays and microwaves and the availability of vector magnetograph observations should yield much better information about pre- and post-flare active region structures, magnetic field strengths, and plasma properties. Improved X-ray and microwave observations should lead to significant progress in determining the balance between heating and electron acceleration in flares, and to tighter constraints on the properties of the acceleration region. More detailed information about the evolution of plasma heated during flares should become available. A better understanding of the importance and properties of microflares should also become available. Gamma-ray observations should lead to more detailed information about the spatial, directional, and spectral distribution of the energetic electrons and ions responsible for this emission, and about ion abundances in the solar atmosphere. All of these areas are ripe for further theoretical work.

On the other hand, it is not likely that significant information will be obtained relevant to the role and properties of magnetic reconnection in flares. (In the upper atmosphere, at least, where the magnetic pressure is dominant. Improved optical observations may provide some information about this at photospheric and chromospheric levels.) Likewise, there is not likely to be any conclusive information about the possible role played by energetic protons in flares, except for the high-energy particles involved in the production of nuclear γ-ray emission.

The impression left from this Workshop is that it would not be productive to have any further Theory and Modeling Group meetings. Rather, it would be better to have a variety of topical sessions promoting interaction among theorists and observers. It would, however, be useful to have occasional special working groups on specific theoretical topics relevant to the MAX '91 program. These groups would have to be well-planned and small enough to make significant progress. Topics for

these working groups might include the theoretical extrapolation of vector magnetic field measurements, comparison of electron beam/return current simulations, or modeling of chromospheric evaporation. Also, a number of investigators in both Europe and the U.S. have recently been working on the magnetic trapping, scattering, and precipitation of particles in flares. It would undoubtedly be worthwhile for these researchers to compare their methods and results. These special working groups should not interfere with the need for theorists and observers to interact, however, as is required for a strong, healthy scientific program.

Summary of Observations of AR 5395

D. M. Zarro[1] *and R. M. Winglee*[2]

[1] Applied Research Corporation/ Lockheed Palo Alto Research Laboratories

[2] Dept. of Astrophysical, Planetary and Atmospheric Sciences, University of Colorado

Active Region 5395 of March 1989 was one of the largest active regions observed to transit the disk of the sun. It was extraordinary in the number and intensity of flares it produced, including 11 X-class flares and 48 M-class flares. It was also responsible for one of the largest geomagnetic storms ever recorded on Earth. The second MAX'91 workshop held at Applied Physics Laboratory in Laurel, Maryland during 7-9 June 1989 provided a first opportunity for scientists from many observatories, both national and international, to come together to present and discuss preliminary results.

Terrestrial effects associated with flares from AR 5395 were reported by *D. Speich* and *Gaizauskas, Hughes, and Tapping.* The most famous effect was the 13-14 March geomagnetic storm which caused the Hydro-Quebec power system to fail. A total of four great geomagnetic storms were produced by AR 5395. These storms produce strong modification of the earth's ionosphere which can cause dropouts in radio communications and enhanced drag on satellites. In addition, two intense interplanetary shocks swept by the earth (March 8 and 13) (*Sarris and Krimigis*). These shocks play a major role in determining fluxes of energetic ions in the earth's magnetosphere. The fluxes observed by the IMP-8 spacecraft during the March 13 shock in the energy channel 0.3 – 0.5 MeV was the highest recorded by the spacecraft.

The Solar Maximum Mission (SMM) satellite observed many of the flares associated with AR 5395. Characteristics of some of the flares in ultraviolet, soft and hard X-rays, and gamma rays were reported by *Drake and Gurman*, *Slater*, *Schwartz and Dennis*, and *Forrest*, respectively. The SMM soft X-ray Polychromator (XRP) obtained high quality spectra and images of many of the events. Ironically, several of the X-class flares were so intense that the XRP instruments had to be offset from the active region in order to avoid detector saturation. Some of the flares showed extremely fast time structures, particularly in hard X-rays (*Schwartz and Dennis*) and gamma rays (*Forrest*), with rise and fall times of the order of a second. In a flare that occurred on March 10 the implied electron spectrum was extremely hard with a peak at possibly MeV energies. Equally interesting, there appeared to be no delay between hard X-ray emission at $\sim$ 50 keV and gamma-ray emission at $\sim$ 50 MeV within the the 2 s time resolution of the SMM Gamma Ray Spectrometer.

Several groups presented ground-based observations from the NSO/Coronal Photometer (*Altrock*), Big Bear Solar Observatory (*Zirin*), and the NSO/Hα Vacuum Tower

Telescope (*Neidig, Wülser and Canfield*). In particular, two X-class flares which occurred on March 11 were the largest ever observed with Hα imaging spectroscopy at NSO. Radio observations from Owens Valley (*G. Hurford*), the Berkeley-Maryland-Illinois Array (*Kundu, White, Gopalswamy and Bieging*) and Radio Solar Telescope Network (*Cliver and Gentile*) were also reported. Magnetic field observations obtained with the Kitt Peak Magnetograph (*Jones*) and the Big Bear Magnetograph (*H. Zirin*) showed the evolution of many distinct features in the active region. Their relation with overall dynamics of the active region and flare production is currently being investigated.

Collaborative studies amongst various groups are currently underway to compare emissions in radio, Hα, UV, hard X-rays and gamma rays. These studies seek to isolate the source of the energetic electrons and the characteristics of the electron acceleration.

Scientific Objectives of Solar Gamma-Ray Observations

R. E. Lingenfelter

University of California, San Diego

Solar flare neutrons and gamma rays are produced by nuclear interactions of flare accelerated ions in the solar atmosphere. A rich variety of such gamma ray and neutron observations have been made by the SMM, other satellite, balloon and ground based detectors, and they have provided a wealth of unique information on the nature of particle acceleration in flares and on flare process itself. What we have learned from these observations was were briefly reviewed, and what we can hope to learn from more sensitive new observations to be made with the Gamma Ray Observatory (GRO), the MAX 91 balloon program, and the Nuclear Astrophysics Explorer was outlined.

The observations have shown that the observed gamma rays and neutrons were produced mainly in thick target interactions of accelerated ions trapped on magnetic loops and running their range in solar atmosphere; they could not have been produced in thin target interactions of ions which escaped into the interplanetary medium because the abundances of spallation products, such as Li, B, T and D, would exceed those observed. Comparisons of the number of accelerated protons required to produce the observed gamma rays and neutrons with the number observed in the interplanetary medium show that the fraction of accelerated protons that escape into the interplanetary medium from impulsive flares varies greatly from 0.002 to 0.98 with the largest escape fractions occuring in the largest flares, where the accelerated ion energy density can exceed that of the confining magnetic field.

The neutron and gamma ray observations also show that the energy spectra of the accelerated protons trapped at sun have a form consistent with an exponential or a Bessel function in momentum, as would be expected from stochastic acceleration, rather than a power law as would be expected from shock acceleration. The energy spectra of the accelerated protons in the interplanetary medium also generally seem to be roughly the same as that of those trapped at the Sun suggesting that the process of proton escape from most impulsive flares is energy independent. In the longer duration flares, however, the protons observed in the interplanetary medium may have power law spectra suggesting subsequent shock acceleration of the escaping ions. The observed time dependence of the prompt gamma ray line emission also requires that the ions trapped on converging magnetic loops be precipitated rapidly by MHD turbulent pitch angle scattering, which may also be responsible for their acceleration.

The forthcoming solar flare gamma-ray and neutron observations with the more sensitive detectors of BATSE, OSSE, COMPTEL and EGRET on the GRO should give a wealth of important new information. In particular:

New constraints on ion acceleration, pitchangle scattering, magnetic mirroring, energy spectra and angular distributions should be obtained from measurements of the time-dependence of the nuclear lines versus that of the π° decay and $\pi^{\pm}$ bremsstrahlung gamma rays, as well as from direct measurements of the neutron spectra versus time and solar longitude.

Direct determinations of the accelerated alpha particle to proton ratio can be obtained from measurements of the alpha-particle produced Be and Li deexcitation gamma rays versus those of the predominantly proton-excited C and O.

A unique determination of the photospheric density scale heights in flare regions can be obtained from measurements of the Compton scattered continuum just below the 2.223 MeV line from deep neutron capture on hydrogen.

More extensive and more precise chromospheric/photospheric abundances can be determined from more sensitive measurements of nuclear deexcitation lines from a wider range of elements, and better determinination of the photospheric ^{3}He/H ratio can be made from more sensitive measurements of the time dependence of the 2.223 MeV line.

In addition, high resolution gamma-ray spectroscopy of solar flares from Ge spectrometers flown in the MAX-91 ballon program and on the Nuclear Astrophysics Explorer will give much more sensitive measurements of all of the properties discussed above and provide much unique new information, such as:

Independent determinations of the angular distributions and energy spectra of interacting accelerated ions from high resolution measurements of the nuclear deexcitation line profiles and asymmetries.

Direct determinations of the temperature, density and ionization fraction in the flare interaction regions from high resolution measurements of the shape and temporal evolution of the 511 keV line and 3-photon positronium continuum.

Time-dependent determinations of the properties of both the thermal and nonthermal plasmas in flares from high resolution measurements of the hard X-ray continuum spectrum versus time.

THE GAMMA-RAY OBSERVATORY: AN OVERVIEW

Donald A. Kniffen
NASA Goddard Space Flight Center
Greenbelt, Maryland 20771

ABSTRACT

The Gamma-Ray Observatory (GRO) is a 16,000 kg spacecraft containing four instruments which span almost six decades of energy from about 50 KeV to about 30 GeV. It will provide the first opportunity to make simultaneous observations over such a broad band of gamma-ray energies. GRO is assembled and undergoing testing prior to its scheduled June 4, 1990 launch aboard the Space Shuttle. The orbit will be circular with an altitude of 450 km and with an inclination of 28 degrees. Data will be recorded at 32 kilobits per second and dumped once per orbit via the Tracking and Data Relay Satellite System (TDRSS). The spacecraft is three-axis stabilized and timing will be maintained to .1 ms. The Observing schedule will begin with an all sky survey, consisting of 30 two week pointings, covering the first 15 months of science operations. Following observations will emphasize source studies and deep searches. Originally selected as a Principal Class spacecraft with a two year mission, extension of the mission to six to ten years makes a vigorous Guest Investigator Program both possible and desirable. Such a program will be fully in place by the third year of the mission, with limited opportunities earlier. Each of the four instruments has a capability for observing both gamma-ray bursts and solar flare gamma-rays, and there is some solar neutron capability. Correlated observations with those at other wavelengths is also receiving considerable attention in the mission planning.

INTRODUCTION

The Gamma-Ray Observatory (GRO) was announced in 1977 as an opportunity for gamma-ray experiments to be included on a free-flying observatory to be launched aboard the space shuttle. The mission was planned as a 3-axis stabilized platform containing four instruments with a planned two year lifetime on orbit. A 1983 launch was anticipated. GRO was envisioned to be the first of a series of five astrophysical missions emphasizing gamma-ray astronomy, x-ray astronomy and cosmic-ray astrophysics.

The GRO is a 16,000 kg spacecraft (Figure 1) which provides an oriented platform for a complement of four instruments to make observations of the gamma-ray sky spanning 6 decades of energy, from 30 KeV to 30 MeV (Figure 2). The very wide dynamic range

requires the use of different instruments with a number of detection techniques. Specifics of the instrument capabilities, especially with regard to solar flare observations, will be given in separate papers in later sessions.

The Z-axis of the spacecraft may be pointed to any region of the sky at any time. However, once chosen, the X-axis must be selected to satisfy sun angle constraints which affect the power from the solar panels and the thermal environment of various spacecraft components.

As GRO developed, it became clear that the science return could be significantly enhanced by extending the duration of orbital operations. By the time such an option was considered, the development of the instruments had already begun , and the design of the spacecraft was underway. Studies showed that the only consumable quantity preventing a lifetime of from six to ten years, without major changes to the design and some existing hardware, was the propellant gas required to maintain the operational orbit in the face of atmospheric drag. A decision was made to provide GRO with a dedicated launch so that it could be taken directly to its operational altitude of 450 kilometers at the beginning of the mission. This provides sufficient fuel savings to allow the orbit to be maintained between 440 and 450 kilometers for up to ten years.

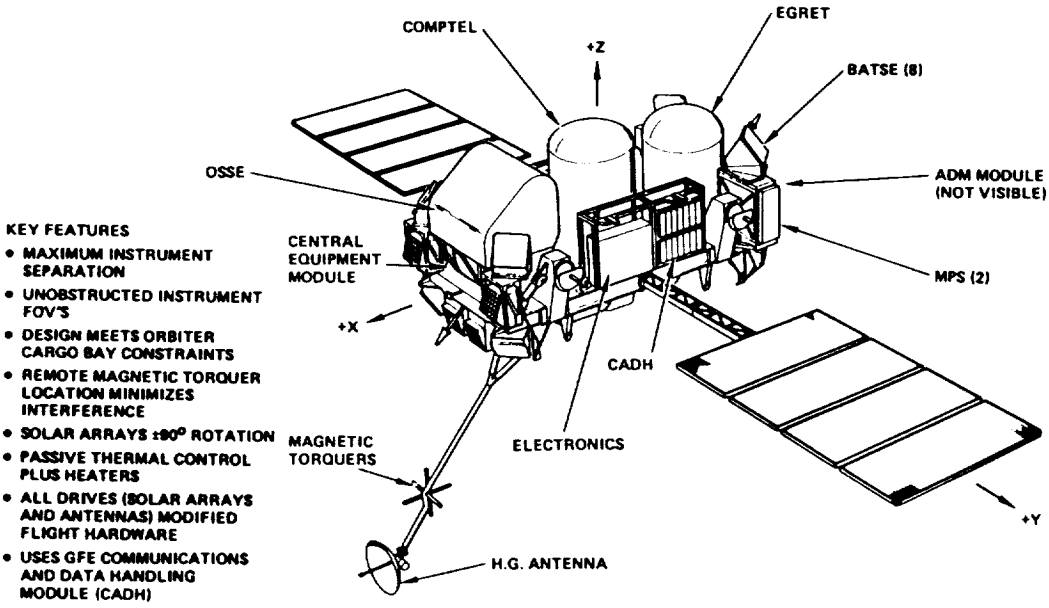

Figure 1. The Gamma-Ray Observatory

The extension of the mission lifetime not only makes it possible, but indeed very desirable to expand the scientific involvement beyond the original Principal Investigators (PIs) and their Co-Investigators. This not only spreads the access to the data and observing opportunities, but it also enhances the scientific return by the infusion of ideas from a broader community. However, since the data analysis systems were designed for a PI class mode of operation, a program to involve those from outside the PI teams must be done in a manner that carefully considers the difficulties in analyzing and interpreting the data, with care to ensure that reliable results are obtained. The program must at the same time provide access to the data for qualified researchers. In this paper, I will briefly describe the mission, the Guest Investigator Program and the organizational structure that is planned to manage the Project during the operations and to implement the Guest Investigator Program.

THE GAMMA-RAY OBSERVATORY MISSION

The Gamma-Ray Observatory is now totally integrated and is undergoing Observatory environmental testing at the Mission Contractor

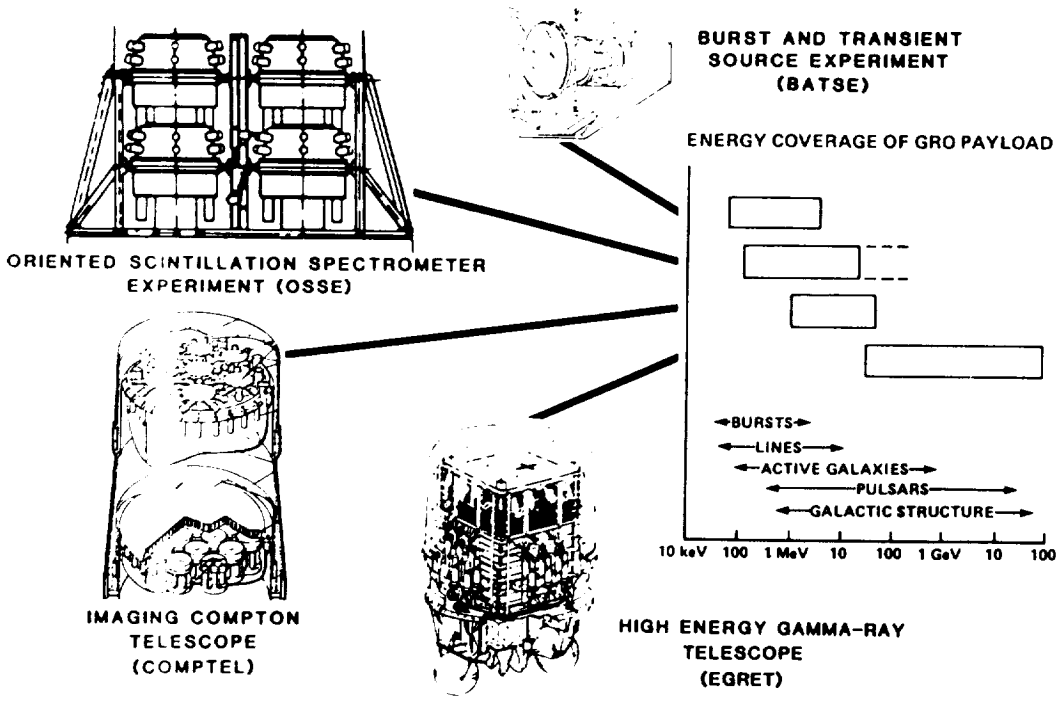

Figure 2. Energy Coverage of the GRO Experiments

facility. GRO is scheduled for launch in June 1990. GRO will be carried directly to its operational altitude of 450 km. Although the orbital altitude is degraded by atmospheric drag, it will be maintained between 440 and 450 km (Figure 3) by the on-board propulsion system. At the end of the mission the spacecraft will either be retrieved by the Space Shuttle, or will receive a controlled reentry, using the propulsion system .

During the orbit operations data will be recorded at a 32 kilobit per second data rate, and these data will be telemetered via the Tracking and Data Relay Satellite (TDRS) once every two orbits at a 512 kilobit rate. Uplink commanding of both the experiments and the spacecraft will also be sent during these TDRS contacts. The mission operations profile is indicated in Figure 4. The Control Center will be at the Goddard Space Flight Center. Data will be received in packetized form with all ancillary information required to analyze the data already inserted on board the spacecraft. Time ordering, overlap elimination and quality checks will be done on ground before the data are forwarded, within 48 hours of receipt, to the experiment data analysis facility sites.

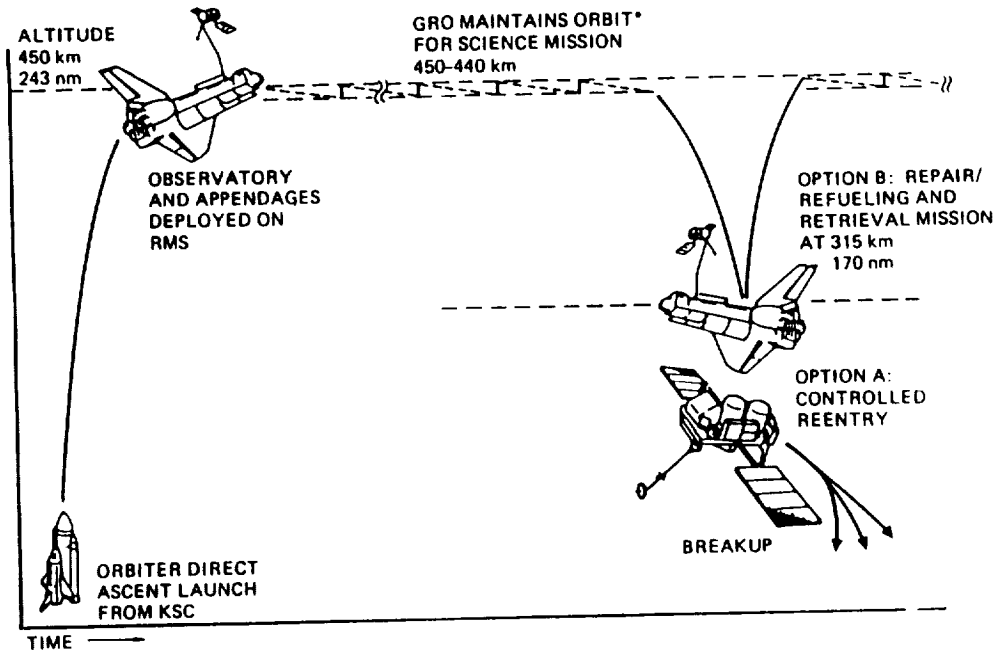

*REQUIRED MISSION LIFE IS 2.25 YEARS – ESTIMATED LIFE GREATER THAN 8 YEARS

Figure 3. The GRO Mission Profile

The viewing program for the first 15 months will consist of a nearly-uniform full sky survey of two weeks exposures for the two wide field instruments (EGRET and COMPTEL). The narrow aperture instrument (OSSE) will select 30 primary and secondary targets for discrete source studies during this 15 month period, and, of course, the burst instrument (BATSE) covers the entire unocculted sky at all times. The viewing program will be discussed in detail in a later paper.

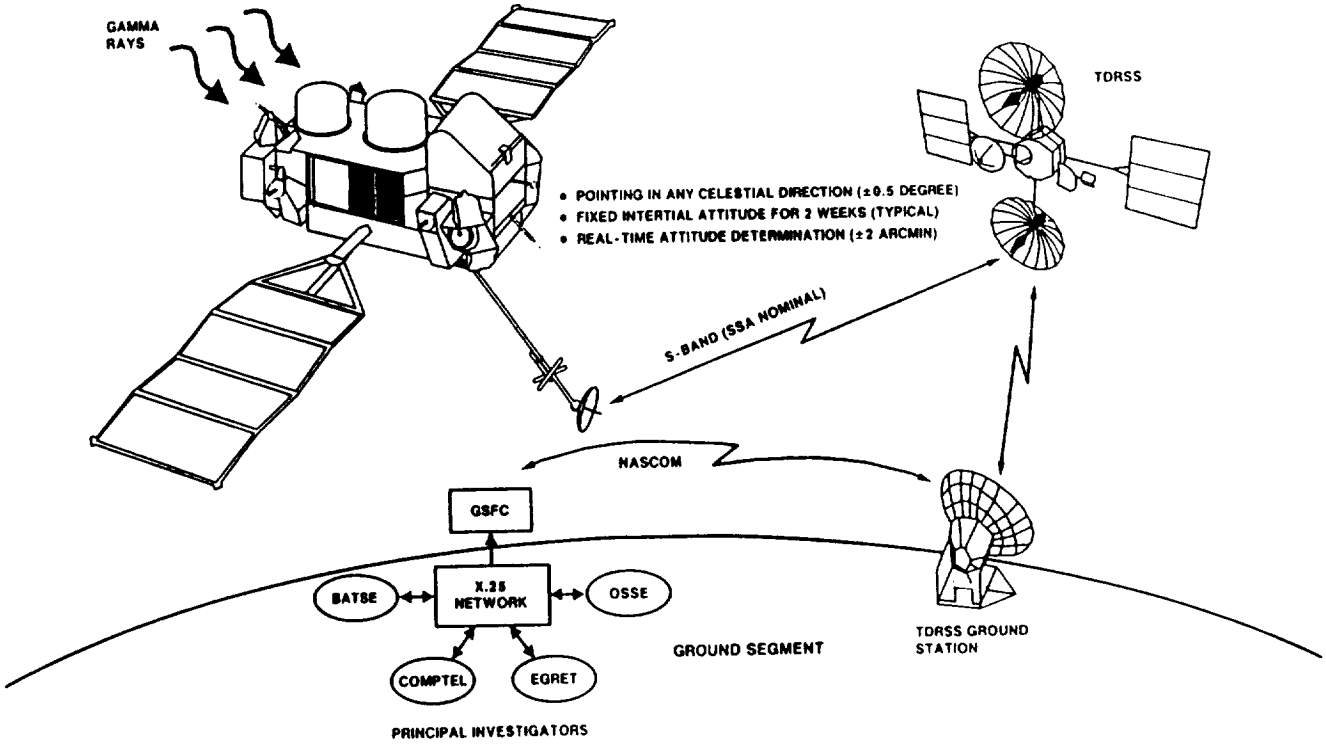

Figure 4. GRO Mission Operations

THE GUEST INVESTIGATOR PROGRAM

As discussed above, the extended GRO mission presents an opportunity for expanded participation beyond that of the Principal Investigators and their Co-Investigator teams. Recognizing the value of increasing the involvement of the broader scientific community NASA plans to implement a vigorous GRO Guest Investigator Program, which will be phased in starting in the first year of the mission, and reaching the full level in the fourth year of

the mission when Guest Investigators will have access to about half of the viewing time.

NASA is planning to release a NASA Research Announcement for the first phase of the Guest Investigator Program later this year. This phase will involve limited opportunities with two of the GRO Instruments. In the second phase, opportunities will include about 30 percent of the viewing time, and the opportunity to work with data a various levels of processing as the proposer desires. The Investigator will be able to visit one of the GRO PI institutions and work for an extended period of time with the PI teams, or he can choose to work independently with higher level archival data products. There will also be opportunities for coordinated observations and for theoretical studies related to GRO.

THE SCIENCE SUPPORT CENTER

The central point of contact for Guest Investigator support will be the GRO Science Support Center, located on-site within the Laboratory for High Energy Astrophysics at the Goddard Space Flight Center. The Center will be a source of information for potential users at all stages of their involvement, from the preproposal stage, through the analysis phase. The Center will provide information on the availability and timing of opportunities, and give technical support in the implementation of the contract with the Guest Investigator.

The Science Support Center will be a source for technical information on the GRO instruments, for scientific and technical information on the GRO spacecraft and mission, for catalogs of data on GRO and other astrophysics and astronomy observations, for the status of GRO observations, for availability of useful analysis software, and other such information of use for GRO investigations.

The Center will come under the GRO Project Scientist, and will provide support to him and the Assistant Project Scientist in promoting the greatest possible scientific return from the mission. The Chief Scientist will also act as a science spokesman for GRO.

THE SCIENTIFIC OUTLOOK FOR GRO

The Scientific Objectives of the Gamma-Ray Observatory are:

A study of discrete objects such as black holes, neutron stars, and objects emitting only at gamma-ray energies.

A search for evidence of nucleosynthesis - the funda-

mental process in nature for building up the heavy elements and other gamma-ray lines emitted in astrophysical processes.

The exploration of the Galaxy in gamma rays to study the origin and dynamic pressure effects of the cosmic-ray gas and the structural features revealed through the interaction of the cosmic rays with the interstellar medium.

A study of the nature of other galaxies as seen at gamma-ray wavelengths, with special emphasis on radio galaxies, Seyfert galaxies, and quasi-stellar objects.

A search for cosmological effects through observations of the diffuse gamma radiation and for the possible primordial black-hole emission.

Observation of gamma-rays bursts, their luminosity distribution, the spectral and temporal characteristics, and their spatial distribution.

These objectives cover a very wide range of outstanding problems in astrophysics, from local sources to extragalactic sources of both localized and extended emissions, involving the most massive and dynamic objects and most energetic astrophysical processes known. The relative immaturity of observations at these wavelengths makes the potential for new knowledge commensurate with the large increase in observing capability.

GRO represents a great step in sensitivity, over and order of magnitude improvement over previous observations, and with much greater exposure to the entire celestial sphere. There is a hope for a mission lifetime greater than any previous gamma-ray mission, and great improvements in angular resolution will be made across the spectrum. Coordinated Observations , already planned by observers at many other wavelengths, will bring the very great advantages of synergism to all of the observations. So, in this context of great expectations, let us revisit the historical record for a moment.

The first great milestone of observational gamma-ray astronomy occurred in 1968 with the launch of the OSO-3 satellite with gamma-ray spectrometer experiment of Kraushaar et al. (1972). This pioneering experiment gave us the first unambiguous observation of the diffuse gamma-ray emission from the plane of our galaxy. As shown in Figure 5, both the observed longitude and latitude distributions gave clear indications of this dominating feature of the gamma-ray sky. Although the angular resolution of the instrument was limited, the emission was clearly resolved in longitude. The discrete source contribution, if any, could not be

discerned, but it was concluded that a major portion of the observed emission resulted from the decay of neutral pions resulting from the interaction of galactic cosmic rays with the interstellar gas.

Observations with much better resolution followed with the spark chamber instruments flown aboard SAS-2 (Fichtel, et al.,1975) and COS-B (Mayer-Hasselwander, et al., 1982) (Figure 6). Now clear evidence for many local variations in the central galactic enhancement can be seen, some due to known discrete sources, some to as yet identified local excesses. These may be additional point sources, or indications of localized enhancements in matter, cosmic rays, or both. Better resolution and sensitivity is required to resolve these questions, and the GRO observations will provide this. However, the most significant conclusion of the comparison of the OSO-3 and COS-B figures is the significant improvement in the detail of our knowledge of the emission from such regions that comes with major increases in observational capability. While COS-B represented increase in effective area of about a factor of five compared to OSO-3, the GRO EGRET instrument provides almost a factor of 40 increase over COS-B. Improvements in spatial and spectral resolution and dynamic range are equally dramatic. Considering the improvement in detail COS-B provided, the implications for GRO on this and other observations are enormous.

The GRO instrument and science contributions will expand on these points., and so it is only redundant to discuss them further here. The program before us looks very exciting. Those of us who have been involved in the difficult task of building the instruments look forward to hearing the many ideas the community will present on ways to maximize the return on these long and intense efforts. We all look forward to a very stimulating Workshop, and an even more stimulating involvement of astronomy and astrophysics community in the most exciting opportunities that the Gamma-Ray Observatory will provide for all.

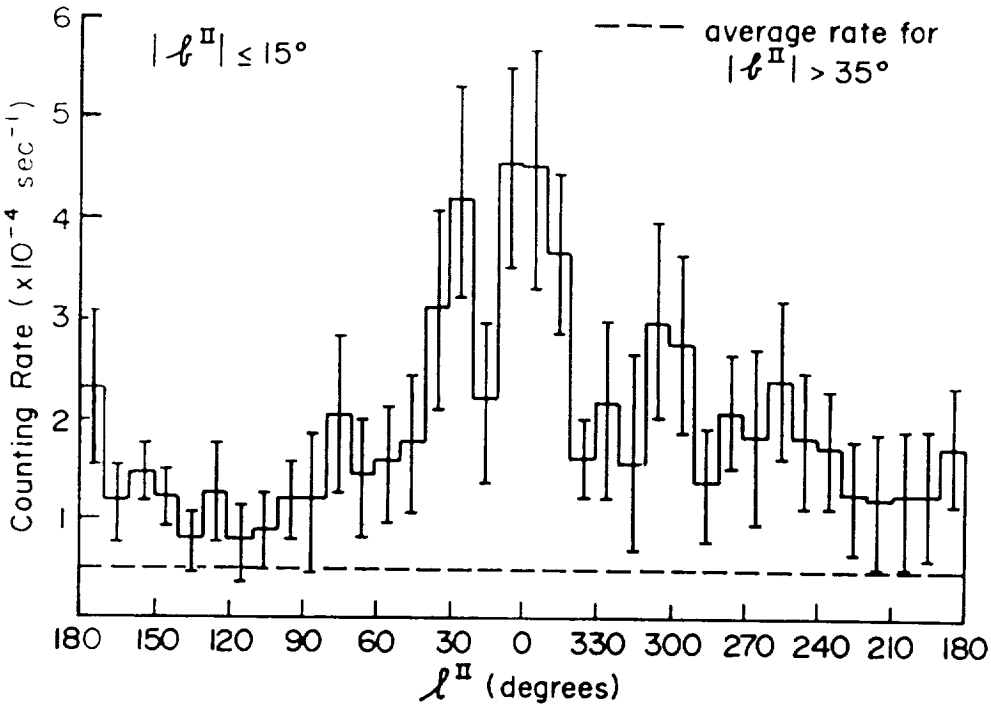

(a)

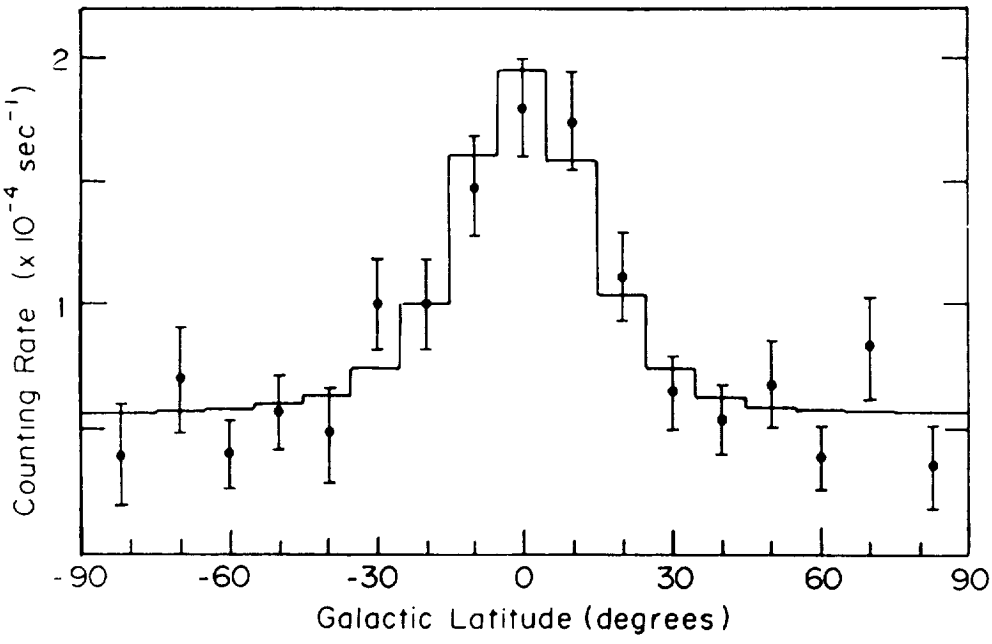

(b)

Figure 5. OSO-3 Longitude (a) and Latitude (b) Distributions of the Galactic Diffuse Gamma-Ray Emission above 100 MeV. (Mayer-Hasselwander, et al., 1982)

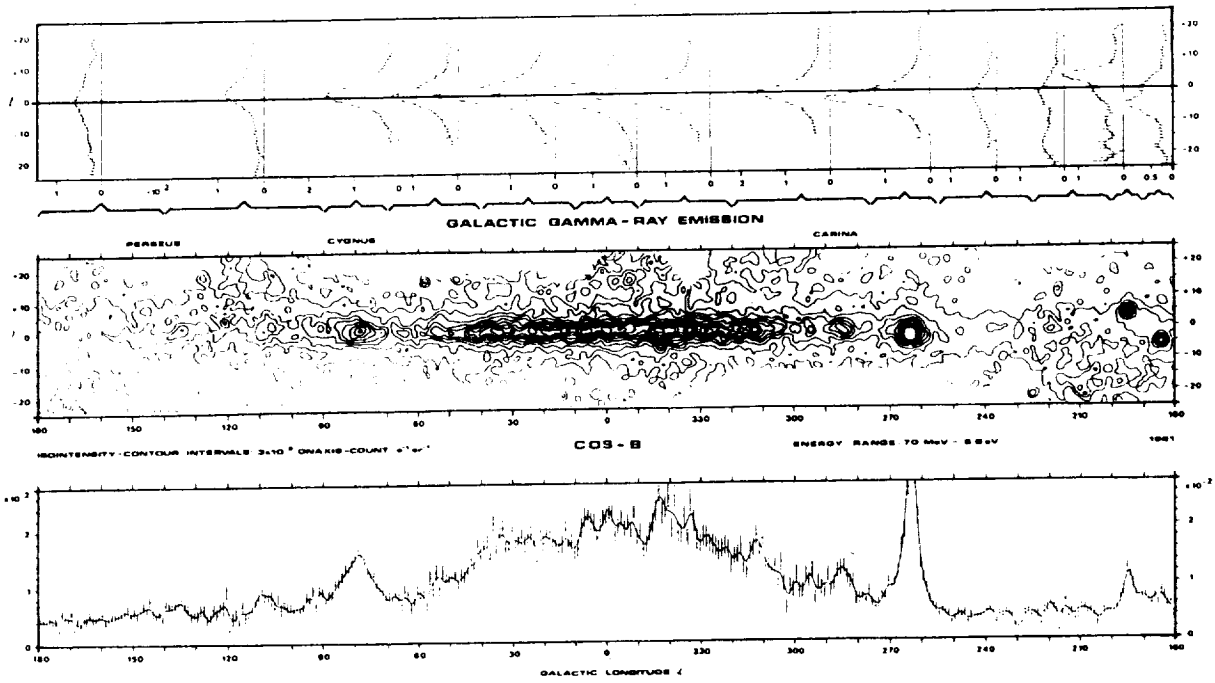

Figure 7. The COS-B Latitude (Top) and Longitude (bottom) distributions and contour plot of the diffuse galactic gamma-ray emission above 70 MeV.

Each of the GRO instruments has a capability for observing solar flare gamma-rays and neutrons, spanning the full range of energies for GRO. The capabilities include good sensitivity and time resolution and good energy resolution throughout the entire spectrum. These capabilities will be discussed in detail in later sessions, but perhaps the most important thing to point out here is that GRO has the capability to point to any region of the sky with the full instrument complement within a few hours. Furthermore the BATSE instrument will provide continuous observations of the Sun for transient events when it is not occulted by the Earth, and with proper advanced planning, the OSSE instrument can be oriented in the spacecraft X-Z plane to view the Sun within three hours.

The great increase in observing capability offered by GRO provides the opportunity for it to be one of NASA's most exciting and productive missions. Our knowledge in all areas of gamma-ray astrophysics will be greatly increased. Our study of the gamma-ray emission from solar flares should teach us much about the process of production, acceleration, storage and propagation of particles in solar flares.

REFERENCES

Fichtel, C. E., Hartman, R. C., Kniffen, D. A., Thompson, D. J., and Bignami, G. F. 1975, Ap. J., **198**, 163.

Kraushaar, W. L., Clark, G. W., Garmire, G. P., Borken, R., Higbie, P., Leong, V., and Thoros, T. 1972, Ap. J.,**177**, 341.

Mayer-Hasselwander, H. A., Bennett, K., Bignami, G. F., Buccheri, R., Caraveo, P. A., Hermsen, W., Kanbach, G., Lebrun, F., Lichti, G. G., Masnou, J. L., Paul, J. A., Pinkau, K., Sacco, B., Scarsi, L., Swannenburg, B. N., and Wills, R. D. 1982, Astron. and Astrophys., **105**, 164.

WHEN AND WHERE TO LOOK TO OBSERVE MAJOR SOLAR FLARES?

T. Bai

Stanford University

Abstract

When and where to look is an important issue to observers planning to observe major solar flares. Prediction of major flares is also important because they influence the Earth's environment. This paper discusses how to utilize recently discovered solar "hot spots" and a solar activity periodicity of about 154 days in determining when and where to look to catch major flares.

HOT SPOTS FOR FLARE ACTIVITY

It has been discovered that solar flares are not uniformly distributed in longitude, but that there exist "hot spots" or "active zones," where flare activity is much higher than elsewhere (Bai 1987, 1988). Figure 1 shows the longitude distribution of major flares of the Northern Hemisphere in a system rotating with a synodic period of 26.72 days (from Bai 1988). Here major flares mean flares with comprehensive flare indices (CFI) greater than 5 for cycle 19 and those with CFIs greater than 6 for the 1965-1979 period. Compilation and indexing of CFIs are given by Dodson and Hedeman (1971, 1975, 1981). For the period since the launch of the *Solar Maximum Mission* (*SMM*), major flares mean flares with peak rates greater than 1000 count/s measured by the Hard X-Ray Burst Spectrometer (HXRBS). In this figure we find two longitude intervals where the flare

distribution is higher than the average; they are called "hot spots" or "active zones." One around 120° is very prominent for cycles 20 and 21; the other around 300° is not very distinctive for cycle 20, nevertheless four superactive regions appeared in the 270-330° interval during cycle 20. These two hot spots were about 180° apart in longitude and remained at the same locations during cycles 20 and 21. They rotated with a synodic period of 26.72 days.

For this figure, the Central Meridian at 00:00 UT on January 1, 1965 was taken as the zero longitude. With this convention, the relationship between Carrington longitude, l_c, and the relative longitude, l_n, of Figure 1 is given by

$$l_n = 1.021 l_c - (N_{cr} - 1489)\, 7.48 + 106 + 360 m_1 , \qquad (1a)$$

or

$$l_n = 1.021 l_c - (N_{cr} - 1812)\, 7.48 + 210 + 360 n_1 \qquad (1b)$$

where N_{cr} is the Carrington rotation number and m_1 and n_1 are integers to make l_n be in the 0-360° range.

Figure 2 shows the longitude distribution of major flares of the Southern Hemisphere in a system rotating with a synodic period of 26.61 days (from Bai 1988). Here also we find two longitude intervals, 10-60° and 170-260°, where the flare distribution is higher. The enhancement in the first interval is very prominent for cycle 21, weak for cycle 19, and nonexistent for cycle 20. The enhancement in the second interval can be seen through all three cycles. These two hot spots in the Southern Hemisphere rotated with a synodic period of 26.61 days, and they were also separated by

about 180° in longitude. Here the same convention was used for the zero longitude as for Figure 1. The relation between l_c, and l_s of Figure 2 is given by

$$l_s = 1.025 l_c - (N_{cr} - 1489)\, 9.00 + 105 + 360 m_2, \qquad (2a)$$

or

$$l_s = 1.025 l_c - (N_{cr} - 1812)\, 9.00 + 78 + 360 n_2, \qquad (2b)$$

where m_2 and n_2 are integers to make l_s be in the 0-360° range.

It is of great interest to find out what causes hot spots lasting two or three solar cycles. Whatever the physical mechanism is, the hot spots may be useful in determining where to point our instruments to observe major flares. It is often criticized with a hind sight that we have not done well in pointing *SMM* detectors to very prolific active regions. Before relying on hot spots, let us see the longitude distribution of major flares in cycle 22. Figure 3 shows the longitude distribution of major flares with HXRBS peak count rates above 1000 counts/s for the period from January 1, 1986 to March 31, 1989. We find a huge concentration of flares in the 90-150° interval. This is due mainly to flares from three superactive regions: AR 5278, AR 5355, and AR 5395. The last one produced 27 major flares. AR 5470, which produced a series of major flares in early May (private communication, Don Neidig; Bill Marquett) was located at (N30, l_c=263°). It was right at the prominent hot spot with l_n=96°. AR 5528 produced an X-class flare in early June, and its relative longitude is l_n=275°, putting it squarely in the less prominent hot spot of the Northern Hemisphere for cycles 20 and 21 (see Figure 1).

Thus, so far, the Northern Hemisphere flare distribution for cycle 22 looks very similar to those for cycles 20 and 21.

The longitude distribution of major flares of the Southern Hemisphere is shown in Figure 4 for the same period as for Figure 3. This distribution does not resemble that of Figure 2 at all. It is too early to say whether the Southern Hemisphere will develop hot spots at new locations or at the same locations as in earlier cycles.

From the above discussions, the Northern Hemisphere hot spot around l_n=100° is the most promising place to look. This hot spot rotates with a 26.72-day synodic period and crossed the Central Meridian on May 31, 1989. It should be remembered that a hot spot is not active continuously, but major flare activity comes and goes every several months. A hot spot that has been quiet for several months does not burst suddenly into violent flare activity, but it becomes very active usually one or two rotations after forming interesting active regions (see Figures 5, 9, and 13 of Bai 1988). If an interesting active region begins to develop in a hot spot, therefore, we should pay attention.

A 154-DAY PERIODICITY

It has been recently discovered that solar activity exhibits a periodicity of about 154 days. This periodicity appears not only in the rate of occurrence of solar flares but also in various indicators of solar activity (Rieger *et al.* 1984; Kiplinger *et al.* 1984; Bogart and Bai 1985; Ichimoto *et al.* 1985; Bai and Sturrock 1987; Lean and Brueckner 1989; Droege *et al.* 1989).

This periodicity can be used in determining when to observe the Sun to catch major flares. Between June 1980 and December 1983, the increase of flare activity with the 154-day period was very regular (Rieger et al 1984; Bogart and Bai 1985; Bai and Sturrock 1987). If such a regularity is repeated in the future, the 154-day periodicity is going to be a good guide in planning for major solar flare observations. However, a recent analysis of the occurrence of proton flares (Bai, Cliver, and Kile 1989) shows that the periodicity is intermittent by appearing in the interval between April 1957 and December 1971 and in the interval between April 1978 and October 1983. My analysis of the occurrence of HXRBS major flares shows that the periodicity is not present in the interval from January 1984 to June 1989 (Fig. 5). Therefore, the observations so far are not so encouraging.

But we have to wait for the reappearance of the periodicity. If we see a great increase of flare activity in early August, five months after the burst of major flares in AR 5395 in March 1989, we may expect a reappearance of the 154-day periodicity.

TYPES OF ACTIVE REGIONS

Predicting major solar flares based on the periodicity and hot spots is like predicting the weather based on the climate. It is good for long-term predictions and for the average behavior. For short-term predictions, knowing the types and development histories of active regions on the solar disk is necessary, because more than 99% of flares occur in active regions. Therefore, it is important to know

what types and morphology of sunspot groups produce large numbers of major flares. There has been a large amount of work on this subject, and a proper review is beyond the scope of this paper (see McIntosh 1981; Sawyer, Warwick, and Dennett 1986; references therein).

Since January 1972 a revised Zurich classification scheme has been adopted by the *Solar Geophysical Data* (McIntosh 1981). The first letter in this three-letter classification scheme indicates whether the group is unipolar or bipolar and what is the longitudinal extent in the case of a bipolar group. The second letter indicates the area of the largest sunspot in the group. The third letter indicates the sunspot distribution in the group. It is of interest to find out what classes superactive regions belong to. Bai (1988) gives three-letter classifications of superactive regions at the peak of their development. Table 1 gives the frequencies of different classes among the superactive regions given by Bai (1988). We find that 37 of the 49 superactive regions for the 1972-1985 period have "E" or "F" as their first letters of the classification. This means that for a large majority of superactive regions their longitudinal extents are greater than 10°. Forty four of the 49 superactive regions have "k" as their second letters of the three-letter classification. This means that for a large majority of superactive regions the penumbral diameters of their largest sunspots are greater than 5° in heliographic angle ($>6 \times 10^4$ km). Twenty five of the 49 superactive regions have "c" as their third letter of the three-letter classification. This means that superactive regions are compact, which indicates that the magnetic field gradient is large somewhere in superactive regions. Therefore,

if an active region belongs to Ekc or Fkc class, it is more likely to produce major flares.

TABLE 1
SUNSPOT GROUP CLASSES OF SUPERACTIVE REGIONS

First Letter	A	B	C	D	E	F	H
No. of A. R.	0	0	1	11	22	15	0

Second Letter	x	r	s	a	h	k
No. of A. R.	0	0	3	1	1	44

Third Letter	x	o	i	c
No. of A. R.	0	4	20	25

SUMMARY

We have discussed how to utilize the 154-day periodicity and the existence of hot spots in determining when and where to look to observe major flares. The two Northern Hemisphere hot spots that persisted at the same locations through cycle 20 and 21 seem to persist at the same locations until now (June 1989). Therefore, the Northern Hemisphere hot spots---especially the prominent one---are good places to watch to observe major flares. Especially when complex active regions appear within the hot spots, we should expect major flares from there. The longitude distribution of southern hemisphere flares for cycle 22 until now is different from those of the preceding cycles. It is not certain at this time whether or not the distribution for the Southern Hemisphere will resemble those of the

preceding cycles as more flares are produced. Therefore, southern hemisphere hot spots are, as of now, less reliable.

The 154-day periodicity does not appear in the occurrence rate of major flares for the time interval from the beginning of 1984 until now. A recent study shows that the periodicity is intermittent appearing in certain epochs and not appearing in other epochs. Therefore, when the 154-day periodicity resumes its regularity, we can use it for planning observations of major solar flares.

REFERENCES

Bai, T. 1987, Astrophys. J. **314**, 795.

Bai, T. 1988, Astrophys. J. **328**, 860.

Bai, T., and Sturrock, P. A. 1987, Nature **327**, 601.

Bogart, R. S., and Bai, T. 1985, Astrophys. J. (Letters) **299**, L51.

Dodson, H. W., and Hedeman, E. R. 1971, World Data Center for Solar-Terrestrial Physics Report UAG-14, (Boulder: NOAA).

Dodson, H. W., and Hedeman, E. R. 1975, World Data Center for Solar-Terrestrial Physics Report UAG-52, (Boulder: NOAA).

Dodson, H. W., and Hedeman, E. R. 1981, World Data Center for Solar-Terrestrial Physics Report UAG-80, (Boulder: NOAA).

Droege, W. Gibbs, K., Grunsfeld, J. M., Meyer, P., and Newport, B. J. 1989, Ap. J. Suppl. (in press)

Ichimoto, K., Kubota, J., Suzuki, M., Tohmura, I., and Kurokawa, H. 1985, Nature **316**, 422.

Kiplinger, A. L., Dennis, B. R., and Orwig, L. E. 1984, Bull. A. A. S. **16**, 891.

Lean, J. L., and Brueckner, G. E. 1988, Astrophys. J. **337**, 568.

McIntosh, P. S. 1981, in *The Physics of Sunspots*, ed. L. E. Cram and J. H. Thomas, (Sunspot: Sacramento Peak Observatory), 3—54.

Rieger, E., Share, G. H., Forrest, D. J., Kanbach, Reppin, C., and Chupp, E. L. 1984, Nature **312**, 623.

Sawyer, C., Warick, J. W., and Dennett, J. T. 1986, *Solar Flare Predicition*, (Boulder: Colardo Associated Univ. Press)

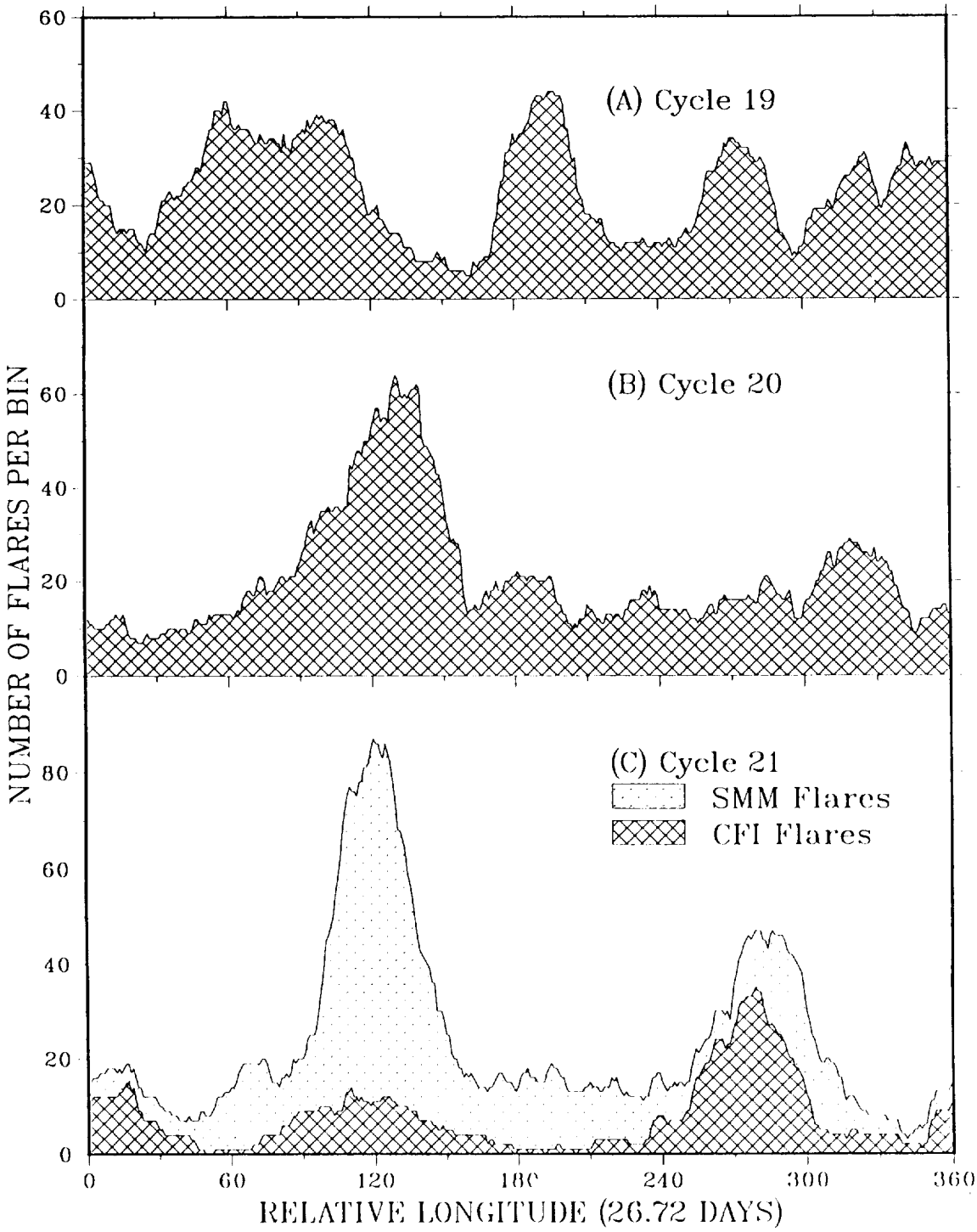

Fig. 1. Longitude distribution of northern hemisphere major flares for cycle 19(a), cycle 20(b), and cycle 21(c) in a system rotating with a synodic period of 26.72 days. For cycle 19, flares with CFI>5 are selected, and for the 1965—1979 period, flares with CFI>6 are selected. For years from 1980, *SMM* flares with peak HXRBS rate >1000 counts/s are selected. (Figure from Bai 1988)

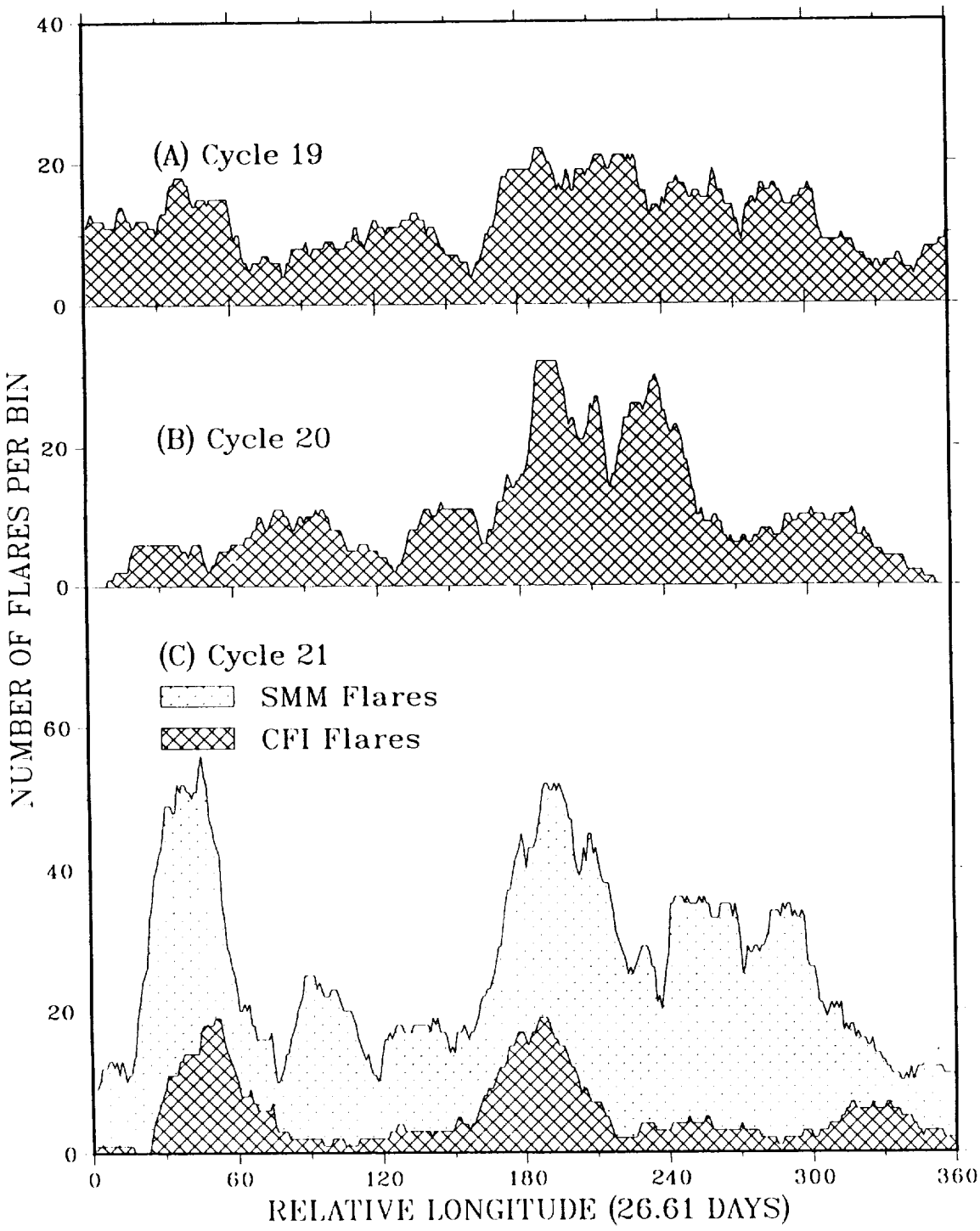

Fig. 2. Longitude distribution of southern hemisphere major flares for cycle 19(a), cycle 20(b), and cycle 21(c) in a system rotating with a synodic period of 26.61 days. The same selection criteria for major flares were used as for Fig. 1. (Figure from Bai 1988)

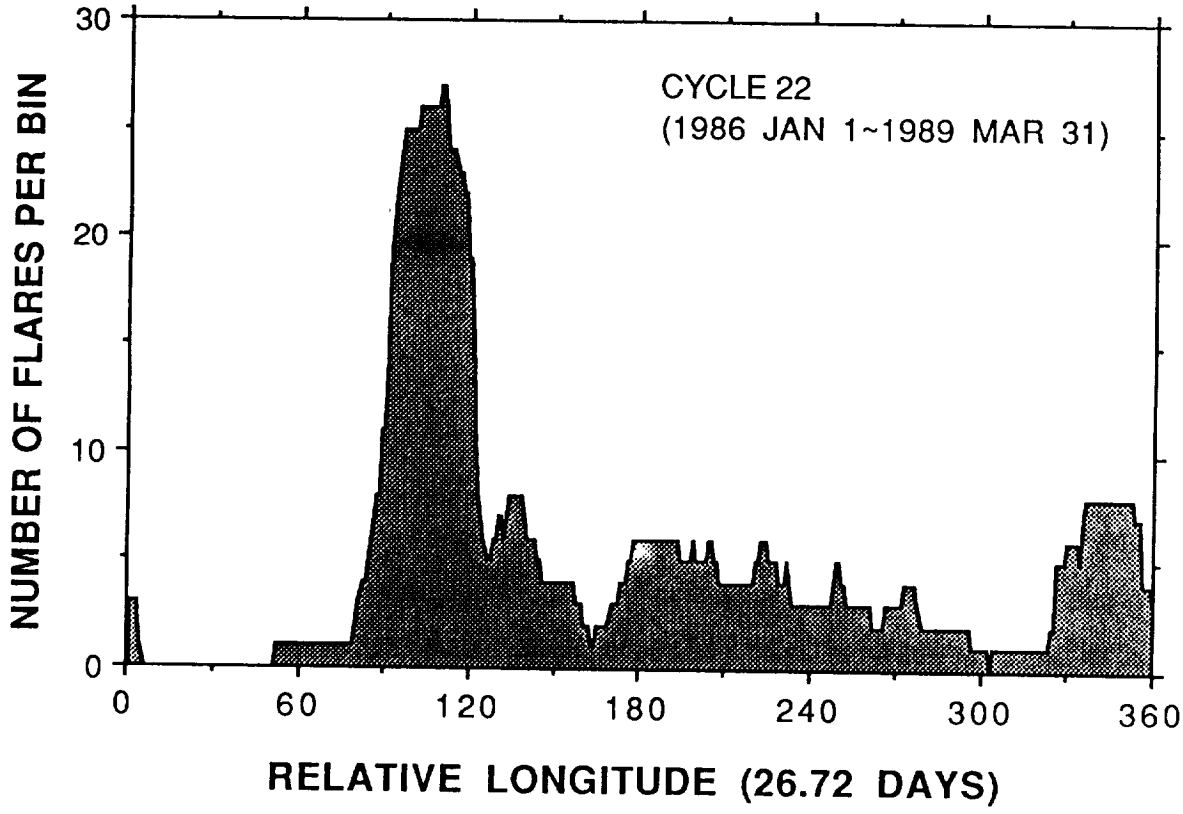

Fig. 3. Longitude distribution of northern hemisphere major flares for cycle 22 in a system rotating with a synodic period of 26.72 days.

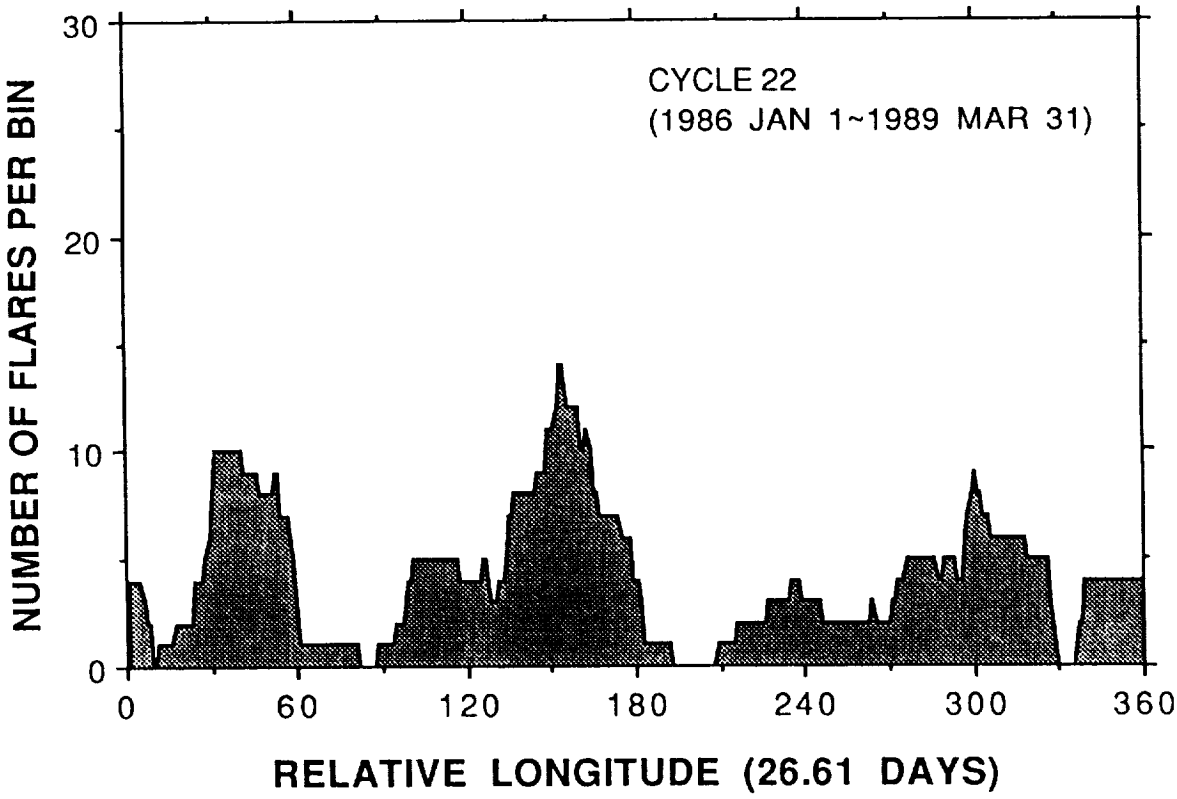

Fig. 4. Longitude distribtuion of southern hemsiphere major flares for cycle 22 in a system rotating with a synodic period of 26.61 days.

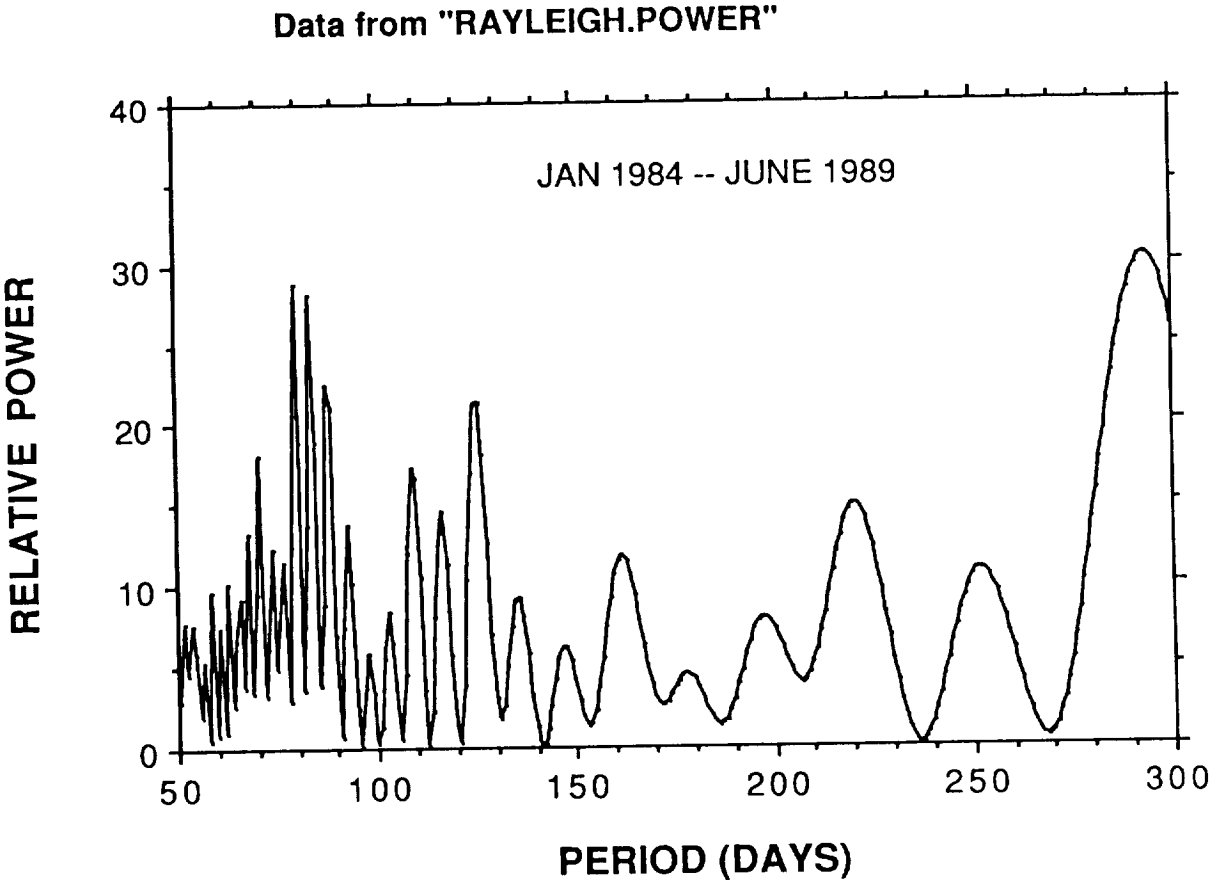

Fig. 5. Fourier power spectrum for the occurrence of major flares for the 1986 January 1 to 1989 June 8 interval. There is no peak at all near 154 days.

N90-12466

Access to MAX '91 Information via Computer Networks

Alan L. Kiplinger[1,2]

[1]Department of Atmospheric, Planetary and Astrophysical Sciences
University of Colorado, Boulder, CO 80309-0391

[2]NOAA/Space Environment Laboratory, Boulder, CO 80303

Various types of flare information, activity, active region reports, x-ray plots and daily Campaign Action notices are now available on SPAN, and INTERNET. Although this system was developed for use of Max '91 participants during campains, it is updated daily and maintained at times outside of campaigns. Thus it is available for general use outside of campaigns.

The Space Environment Laboratory maintains VAX and Apollo systems, both of which are on INTERNET. The VAX is also on the SPAN network as node SELVAX or 9555. Details of access to files on the VAX are given below.

I. Types of Information

The following types of information are available in conveniently labeled files on the VAX and Apollo systems.

** Daily Event Listings*

Single line listings of solar flares compiled at 03:00 UT for the previous day. These files are composed in near-real-time by forecasters at NOAA's Space Environment Laboratory. Associations of optical and X-ray events are generally established through time coincidences of GOES data with optical identifications provided by the U.S. Air Force SOON network.

** Solar Forecasts*

Probabilities of flare production for the sun as a whole, activity summaries and geomagnetic forecasts.

** Solar Activity Reports*

Listings of significant activity from various regions as well as particle events and recent geomagnetic activity.

** Region Reports*

Descriptions of various active regions including positions, areas and spot classifications and announcements of returning regions.

** Plots of GOES soft X-rays with tagged optical events*

Since Textronix emulation is available for almost all computers, Textronix 4010 compatible plot files which show the GOES hard and soft channels in standard 6-hour plots are available. There are four plots per day generated at 3:00 UT for the previous day. The files may be copied or plotted directly over the networks.

** Campaign Action*

Perhaps the most important information to be distributed during campaigns (and the only daily information which that is directly distributed to participants via EMAIL) are the daily Campaign Action notices. These bulletins will contain daily target information, status of primary instruments, observing itineraries, solar activity reports and brief reminders of scientific objectives. The distribution will be primarily through electronic mail and the GEOALERTS. Action notices are also saved in files as described below, thus if the message is not delivered promptly, then the participant should be able to retrieve the daily ACTION notice in the same manner as the other types of data.

II. SPAN Access to MAX '91 Information and Action Notices (VAX VMS)

On the SPAN network, node SELVAX:: or 9555:: has available a variety of files with various types of information as shown in Table I.

To receive Max '91 information files over SPAN (VAX VMS) one should type:

SET DEFAULT 9555::sys$userroot:[max91]

Entering a command such as

TYPE 21JUN89.EVENTS

will display the event listing for June 21st on the display. One may also type DIR to list the files that are available. Note that the complete file description with node can be specified in the TYPE statement without setting the default directory but this may be cumbersome if more than one file is accessed.

GOES Soft X-Ray Plots
(for TEXTRONIX-4010 compatible terminals and printers)

The SPAN Node 9555:: also has copies of GOES plots - Textronix files that are available at 9:00 UT for the previous day. A Textronix 4010 terminal or an equivalent emulation is required. On SPAN to receive a plot type:

TYPE 9555::SYS$USERROOT:[MAX91]08JUN89A.SAV (You may also COPY it to your directory)

Table I. Types of Max'91 Information and File Syntax

Type of information	Filename Syntax	Example
Daily Event Listings	DDMMMYY.EVENTS	21JUN89.EVENTS
Solar Forecast	FORECAST.REPORT	FORECAST.REPORT (name never changes, File is replaced daily)
Region Report	REGION.REPORT	FORECAST.REPORT (name never changes)
Activity report	ACTIVITY.REPORT	ACTIVITY.REPORT (name never changes)
GOES Plots	DDMMMYY*.SAV where *=A,B,C,or D A = 00 - 06 UT B = 06 - 12 UT C = 12 - 18 UT D = 18 - 00 UT	21JUN89C.SAV (i.e. the 6 hour plot starting at 18:00 UT on 21 JUNE)
Campaign Action Notices	DDMMMYY.ACTION	21JUN89.ACTION

You will receive a 6-hour GOES plot 0:00 - 6:00 UT for 08 Jun 89 as the name suggests. The suffixes A,B,C or D in the file name indicates 0-6, 6-12, 12-18 and 18-24 UT, respectively, for the day described in the file name. The data in the upper and lower curves represent one minute averages of the 1-8A and 0.5-4A data respectively. To provide the most complete soft x-ray coverage (in case of losses of data) data from both the GOES-6 and GOES-7 sattelites are presented. Data from GOES-6 is drawn as a dotted line while data from GOES-7 (the primary sattelite) is drawn as a solid line.

IMPORTANT NOTE: ON VAX VMS SYSTEMS: for plots to work be sure that your terminal is set to NOWRAP. If it is not, then issue the command: SET TERM/NOWRAP

(Note that data more than 1 month old will be deleted from the disk in order to conserve disk space.)

Additional means of receiving the Daily Action Notices (during campaigns only)

A backup communications system for SELVAX:: has been established on the node SOLARX:: at the University of Colorado. Only the daily ACTION notices are stored on this account and they may be accessed by entering commands like:

TYPE SOLARX::UP:[MAX91]23JUN89.ACTION

Note also that a third method of receiving the action notices is to send any mail message to the solarmail address - SOLAR::maxaction. In this case, a mail message containing the current action notice will be transmitted back to requesting party in most instances.

III. INTERNET Access using TELNET and FTP

** TELNET access*

By far the easiest way to access Max '91 information over INTERNET is to log onto SELVAX directly and to access the files as described above for SPAN. It is also possible to copy the files to your computer by using FTP as described at the end of this section.

For TELNET access to SELVAX type:

telnet 192.163.244.10

When the system prompts for the USERNAME:, type MAXT (a mnemonic for Max' 91 and TELNET). No password is needed. Typing the various files as described for SPAN will bring the reports and plots to your screen. To terminate the connection type LOGOFF.

Note that this is a very restricted account and it cannot be used to connect to SPAN or access other directories on SELVAX. It is not intended for SPAN users to use the MAXT account since SET DEFAULT as described above accomplishes the same results.

** FTP access*

(The following assumes that anyone on INTERNET has FTP file transfer protocol available.)

INTERNET access to NOAA's SELVAX computer to acquire the Max '91 event listings, region reports, goes plots etc. is available.

To your system type the numeric address (lower case recommended): (On some systems the name address: *selvax.bldr.nist.gov* may be required instead of the numeric address.)

ftp 192.163.224.10

The system should respond with a USER: request. If it does request a username, type- *ftp*.

If a password is requested, simply type a carriage return since no password is required.

You then should have FTP access to SELVAX.

One should type: *cd [max91] or perhaps cd max91* ; to change defaults to the proper directory.

If your system fails to accept this you might try going to a higher level by:

ftp> cd .. ftp> cd max91

One of these steps should put you on the proper directory. Entering "dir" or "ls" or a similar command should provide a list of the files that are available. One can then "get" files from SELVAX as you desire since the SELVAX MAX91 account is open to file outgoing file transfers. (Note to transfer GOES plots one should type "binary" before the "get" command so as to correctly transfer the file.)

eg.: *ftp> binary* ; sets file transfer mode
ftp> get 25jun89a.sav ; should bring plot the file to your system

With the exception of the ACTION notices that are only issued during campaigns, the remainder of information described above is planned to be available on a continuous basis throughout the Max '91 program. Thus observatories can receive GOES plots or region summaries at anytime desired. However, due to a limited amount of disk space on SELVAX, some files may only be retained for one or two weeks. Campaign data will reside on the disk longer than files that are generated outside of campaigns.

CAPABILITIES OF GRO/OSSE FOR OBSERVING SOLAR FLARES

J.D. Kurfess, W.N. Johnson, and G.H. Share
E.O. Hulburt Center for Space Research
Naval Research Laboratory
Washington, DC 20375

S.M. Matz
Department of Physics and Astronomy
Northwestern University
Evanston, IL 60208

R.J. Murphy
Universities Space Research Association
Columbia, MD 21044

ABSTRACT

The launch of GRO near solar maximum makes solar flare studies early in the mission particularly advantageous. The Oriented Scintillation Spectrometer Experiment (OSSE) on GRO, covering the energy range 0.05-150 MeV, has some significant advantages over the previous generation of satellite-borne gamma-ray detectors for solar observations. The OSSE detectors will have about 10 times the effective area of the Gamma-Ray Spectrometer (GRS) on SMM for both photons and high-energy neutrons. OSSE also has the added capability of distinguishing between high-energy neutrons and photons directly. The OSSE spectral accumulation time (~4s) is four times faster than that of the SMM/GRS; much better time resolution is available in selected energy ranges. These characteristics will allow the investigation of particle acceleration in flares based on the evolution of the continuum and nuclear line components of flare spectra, nuclear emission in small flares, the anisotropy of continuum emission is small flares, and the relative intensities of different nuclear lines. The OSSE observational program will be devoted primarily to non-solar sources. Therefore, solar observations require planning and special configurations. The instrumental and operational characteristics of OSSE will be discussed in the context of undertaking solar observations. The opportunities for Guest Investigators to participate in solar flare studies with OSSE will be presented.

INTRODUCTION

Observations during the last solar maximum greatly increased our knowledge about solar flares. The Gamma-Ray Spectrometer (GRS) on the Solar Maximum Mission satellite, in particular, made a number of discoveries which relate directly to the process of particle acceleration in flares (for a review of GRS observations see Chupp 1984; for an overview of the current state of flare research and future prospects see the papers in volume 118 of Solar Physics as well as contributions in these proceedings). GRO will be able to observe the peak of the current solar cycle following its scheduled launch in June, 1990, and OSSE has the capabilities to extend the GRS observations to smaller flares and faster timescales, and to

measure separately the high energy photon and neutron spectra. Thus, OSSE should help give a clearer picture of the flare process.

The Gamma-Ray Observatory (GRO) represents NASA's next major mission in high-energy astrophysics. GRO will carry four large instruments whose main objectives are to undertake comprehensive observations of astrophysical sources throughout the 20 keV to 30 GeV energy range. The general configuration of GRO is shown in Figure 1. GRO is a three-axis stabilized spacecraft. The solar panels can rotate ± 90 deg about the Y-axis, with the Sun restricted to the +X hemisphere relative to the S/C coordinate system. The movable solar panels enable the Z-axis of GRO (common axis of EGRET and COMPTEL) to be pointed to any position on the sky at any time, including the Sun. GRO will launched into a 450-km orbit with an inclination of 28.5 deg. The baseline mission duration is two years, although plans are being implemented for an extended mission.

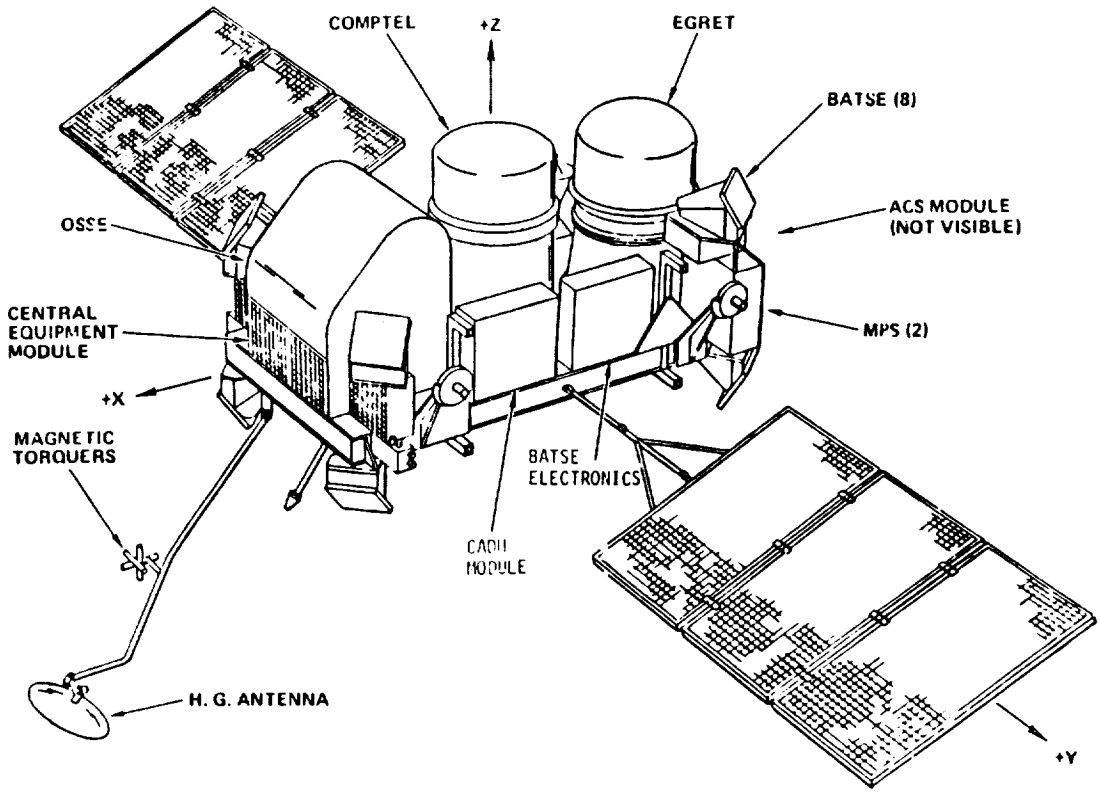

Figure 1. Illustration of the Gamma Ray Observatory and associated instruments. Three instruments (OSSE, COMPTEL, and EGRET) are mounted on the + Z side of the spacecraft. The eight BATSE modules are located on the corners of the S/C to provide full sky coverage. Other systems include the High Gain Antenna for communications with the TDRSS, Modular Power Systems (MPS), Command and Data Handling (CADH) system, and the Attitude Control System (ACS). The solar panels can rotate ± 90 deg about the Y-axis. The Sun is constrained to be located in the +X hemisphere and is further constrained to be not closer than about 50 deg to the Y-axis.

II. THE OSSE INSTRUMENT

The OSSE instrument is described in detail elsewhere (Kurfess et al. 1983, Johnson et al. 1989), and the use of OSSE for solar observations has been discussed by Kurfess (1988). Figure 2 illustrates the overall OSSE instrument and Figure 3 is a diagram of an OSSE detector. Briefly, OSSE consists of four large NaI-CsI phoswich detectors, passively collimated, actively shielded on the sides with 3.35-inches of NaI and on the back by the CsI portion of the phoswich. Each detector can be independently rotated about an axis parallel to the spacecraft Y-axis, the axis of the solar panels (see Figure 1). This gives OSSE the ability to observe a number of different sources in a single GRO pointing. Normally, two or three celestial sources will be targets in a two-week interval; each target object will usually be observed by making measurements alternately with the source in and outside the detector field-of-view to obtain both source and background data.

Table 1: COMPARISON OF SMM/GRS AND GRO/OSSE CAPABILITIES

	GRS	OSSE
Energy Range (main detectors)	0.3-10 MeV	0.05-10 MeV
Effective area at 511 keV	150 cm^2	1950 cm^2
Spectral time resolution	16.384 s	4.096 s
Field of view (FWHM, at 511)	130°	3.8° x 11.4°
Fast spectral windows	300-350 keV 64 ms	8 selectable 4-512 ms

In Table 1 we have summarized some of the important characteristics of the OSSE instrument and compared them to those of the GRS (Forrest et al. 1980). Both instruments cover similar energy ranges and have similar energy resolutions. OSSE extends to a lower energy in its main spectral range; this range was covered by GRS with auxiliary X-ray detectors. Both instruments have the ability to measure high energy (>10 MeV) photons and neutrons. However, because of the pulse-shape discrimination employed on the OSSE phoswich detectors, OSSE has the additional capability of directly separating the neutron and photon signals. OSSE is much larger, with a total effective area (all four detectors) more than ten times that of the GRS at 511 keV. The normal spectral time resolution of OSSE is four times faster than that of the GRS. The fastest GRS time resolution was 64 ms in an energy window near 300 keV. In contrast, OSSE has eight programmable energy windows with time resolution of 4-512 ms.

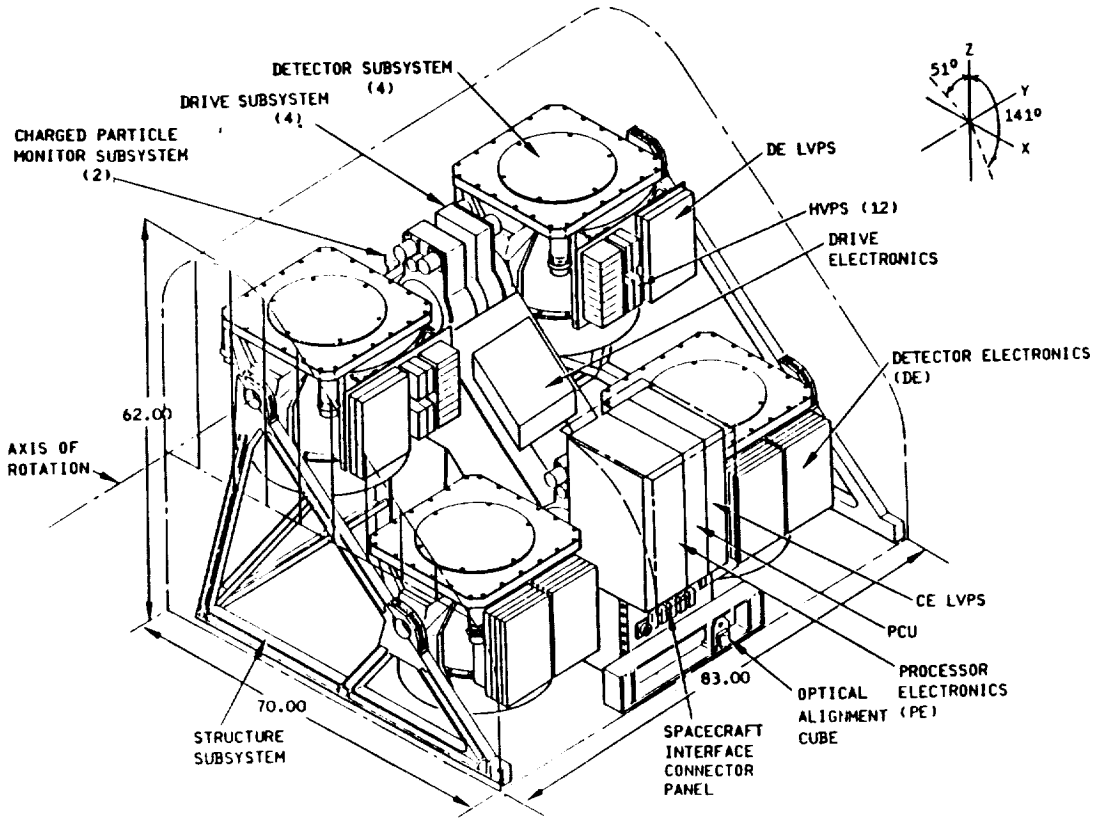

Figure 2. OSSE instrument for GRO. OSSE includes four identical scintillation detector assemblies. Each detector has an independent single-axis pointing system which has a 192° range of motion in the X-Z plane.

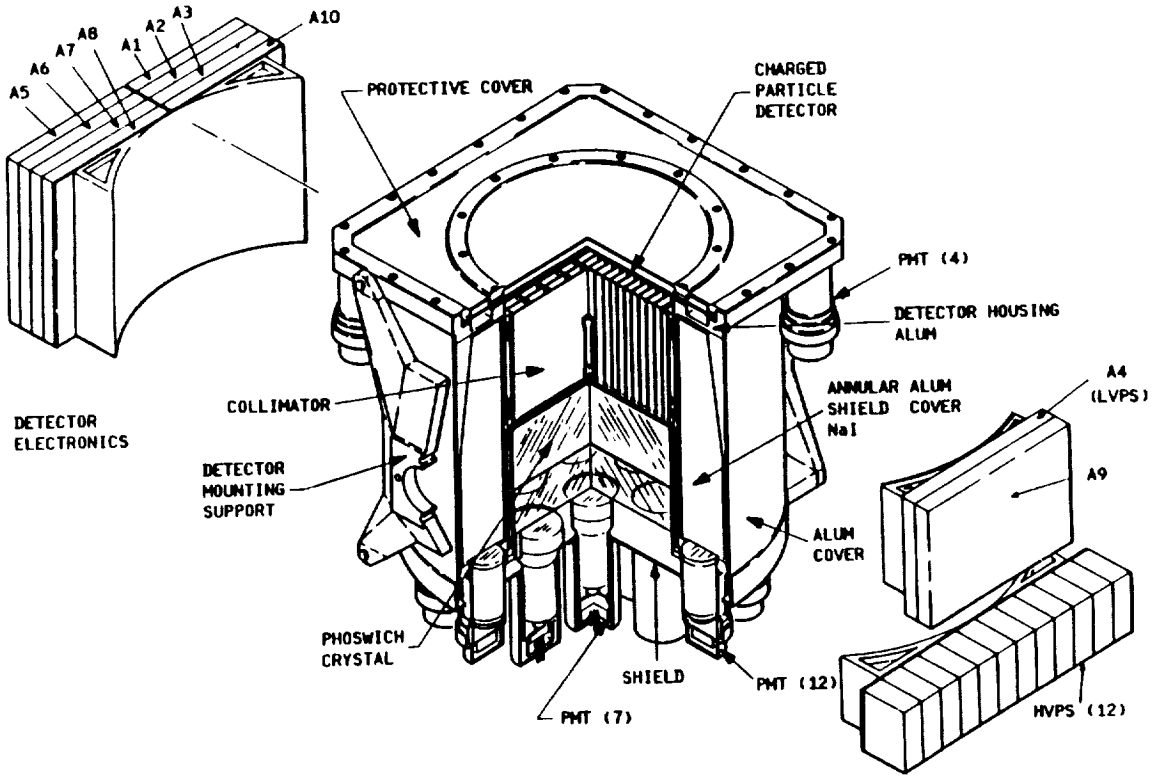

Figure 3. Cut-away view of an OSSE detector assembly.

Figures 4 and 5 compare the sensitivities of OSSE and SMM for the detection of γ-rays and neutrons respectively.

III. SOLAR OBSERVING MODES

As described above, OSSE has a number of characteristics which make it valuable for solar observations: large effective area, fast time resolution, good spectral range, and the ability to distinguish between high energy photons and neutrons. This gives it the promise of significantly extending the work done with the GRS. However, unlike the GRS, it has a small field-of-view (defined by its collimator) and it is not a dedicated solar-pointing instrument. It is necessary therefore to plan observations specifically to acquire solar data with the main detectors.

There are three principal modes which can be used to observe solar flares. In the first case, the Sun may be selected as one of the OSSE sources for a GRO pointing. This implies that (typically) 50% of the time during a two-week viewing period would be dedicated to solar observation, with the Sun in the field-of-view of one or more of the OSSE detectors. The GRS discovered (Rieger et al. 1984) a 154-day period in the occurrence of gamma-ray flares, with 35% of such flares occurring in the 15.4 days at the peak of the cycle. If the coming solar maximum is as active as the last, and the 154-day cycle is present, we can choose our dedicated solar observations at the peak of the flare cycle. We would then expect to observe approximately 5 GRS-class flares in a two-week observation. We would also detect (presumably) a large number of flares which would have been too weak to be classified as gamma-ray flares by the GRS.

In addition to the pre-planned observations, solar activity may cause the Sun to be considered a target of opportunity. For example, a period of solar observing could be initiated by predictions of flare activity. Since the Sun can often be placed in the OSSE field-of-view simply by a detector rotation about the Y-axis, such observations will often be possible without requiring any re-orientation of the GRO spacecraft.

In the second mode OSSE would not have the Sun as one of the selected sources for a two-week observation. However, BATSE will provide, in addition to the normal transient event triggers, a flag signaling an event of solar origin, based on count ratios in the four BATSE detectors viewing the Sun. OSSE can be configured so that one or more of its detectors will be repositioned to point at the Sun after receiving a flare trigger from BATSE. Since the OSSE detectors can move at a rate of 2° per second over a maximum angular range of 192°, solar pointing can be achieved within 45-90 s after the trigger.

Finally, when it is not possible or desirable to re-orient the detectors to put the Sun in the field-of-view, photon spectra can still be taken from the detector shield elements. In this mode we would choose to analyze the shield elements with the best solar exposure. This would allow dedicated monitoring of the Sun with large effective areas, ~ 600 cm^2 at 511 keV for each shield element. A small number of shield spectra that cover 0.1-8 MeV in 256 channels can be acquired at 4 s time resolution.

In any of these modes OSSE can be set up to change configuration electronically after a flare trigger to enhance observations. For example, the detectors could be commanded to stop chopping, or to transmit more detailed neutron data.

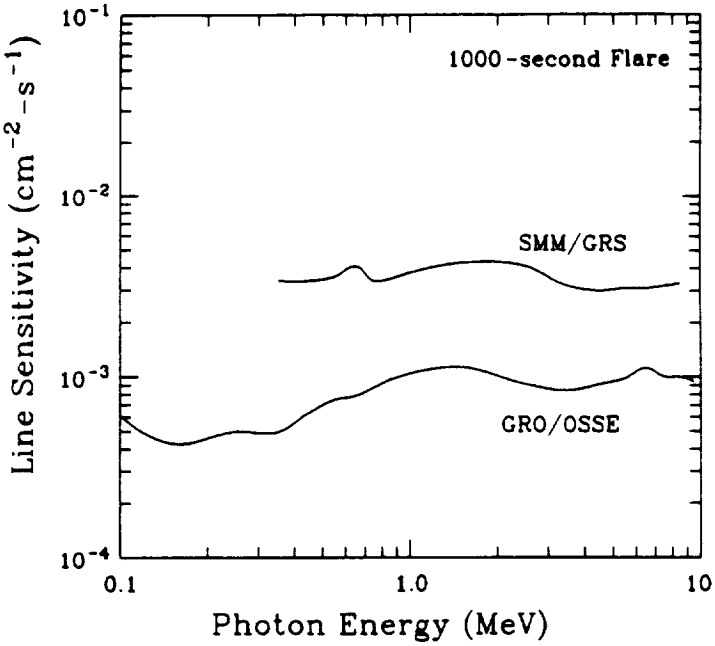

Figure 4. Comparison of the line gamma-ray sensitivities of the OSSE instrument on the Gamma-Ray Observatory with the SMM Gamma-Ray and Neutron Monitor. A flare duration of 1000 s was assumed, and the limiting sensitivities utilize nominal detector background but do not include any consideration of underlying solar continuum.

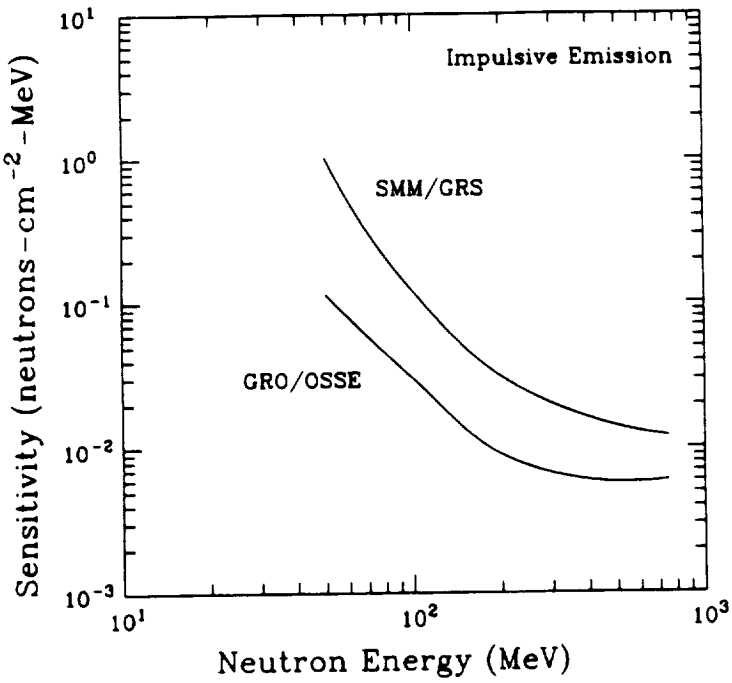

Figure 5. Comparison of neutron detection capabilities of the OSSE instrument on the Gamma-Ray Observatory with the SMM Gamma-Ray and Neutron Monitor. An impulsive neutron emission at the Sun is assumed, with no continuing high-energy solar gamma flux at the time of arrival of neutrons at the Earth.

IV. OSSE SOLAR PHYSICS CAPABILITIES

Although OSSE is not optimized for viewing transient sources such as solar flares, its design characteristics nevertheless offer significant advantages over the previous generation of solar-flare-dedicated detectors. The increased sensitivity due to the large effective area of OSSE will provide substantial advancements in several areas in solar research. For example, it will allow the extension of the study of the electron and nuclear emission correlation discovered by the SMM/GRS (Forrest 1983) to much smaller flare sizes. This will help determine whether a threshold for ion acceleration exists.

The study of solar abundances, begun with the analysis (Murphy et al. 1985a,b) of the SMM/GRS data from the 27 April 1981 solar flare, can be extended to include a large number of flares. Data exists from several flares in the SMM data base, but the usefulness of these data is limited by its statistical quality. The high sensitivity of OSSE will improve this situation. The increased sensitivity will also allow for a search for ion acceleration by the quiet Sun, evidenced by the detection of the 2.223 MeV neutron-capture line or nuclear de-excitation lines such as the 4.44 MeV line from ^{12}C.

Finally, the larger area could help resolve the issue of accelerated-ion anisotropy addressed by the analysis (Murphy et al. 1990) of the ~450 keV ^{7}Li and ^{7}Be lines from α-α fusion observed by SMM from the 27 April 1981 limb flare. Observations of a disc-centered flare with sufficient statistical quality could distinguish an isotropic distribution from a fan-beam distribution; this is impossible for a limb flare except with a high-resolution detector. Associated with this analysis would be a determination of the fraction of flare-generated positrons which decay via positronium, as evidenced by the positronium continuum below the 511 keV annihilation line. This positronium fraction can provide information on the density and temperature at the annihilation site. The positronium continuum makes a contribution to the <511 keV emission comparable to that from the α-α lines and the improved statistical quality of OSSE data will help distinguish between these two sources.

Another advantage of OSSE is improved time resolution. In some SMM/GRS events, electron and ion emissions were observed (Forrest and Chupp 1983, Kane et al. 1986) to have rapid fluctuations which were simultaneous to within the GRS temporal resolution (~2 seconds). Shorter timescales have been observed (e.g., Kiplinger et al. 1983) in hard X-ray electron emission but there are no corresponding measurements for nuclear emission. The high time resolution modes and large area of OSSE can be used to constrain relative electron and ion acceleration timescales to within several milliseconds.

The energy of the protons responsible for the production of nuclear line emission is 10 to 30 MeV while that of the protons responsible for producing the pions which yield the 100 MeV pion-decay emission is ~1 GeV. In the 3 June 1982 flare, these two emissions were observed (Ramaty and Murphy 1987) to be simultaneous to within the SMM/GRS temporal resolution of 16 seconds implying the simultaneous acceleration of the associated protons. The increased temporal resolution of OSSE will improve the constraint to within 4 seconds. This constraint is important for understanding the energy dependence of ion acceleration in solar flares.

One additional advantage of OSSE is the ability to directly distinguish between >10 MeV photons and neutrons. The SMM/GRS was able to do this to some degree either by arrival-time considerations or by appealing to the statistical nature of the detection process (Chupp et al. 1987). The former is inadequate when the gamma-ray and neutron production is extended in time and the latter has uncertainties inherent in the statistical approach. In addition, OSSE can directly determine the neutron energy spectrum which was accomplished by SMM through time-of-flight measurements, again inadequate when the emission is extended.

An important aspect of any effective observing program is correlation with observations made by other detectors at both similar and different wavelengths. Such correlated observations can directly address important issues of solar-flare research. For example, evidence for the anisotropy of relativistic electron bremsstrahlung, and therefore of the relativistic electrons themselves, has been obtained through statistical studies (Rieger et al. 1983, Vestrand et al. 1987, Rieger 1989, Dermer and Ramaty 1986) of flare locations on the solar disc. This anisotropy can be tested directly in individual flares through simultaneous observations by two spacecraft viewing the Sun from significantly-different directions; e.g. by GRO/OSSE and the proposed Ulysses mission (Cotin et al. 1983) which will view the Sun from out of the ecliptic plane.

Whether the hard X-ray emission from solar flares arises from thermal or non-thermal processes is a continuing controversy. Evidence for a non-thermal origin would be the unambiguous detection of footpoint emission from a flaring magnetic loop. Correlating OSSE observations with an imaging detector like the proposed GRID instrument (Crannell et al. 1988) would help resolve this issue.

Another question concerning particle acceleration is the relationship between flare protons observed in interplanetary space and the protons responsible for the gamma-ray emission. Proton kinetic-energy spectra deduced from gamma-ray observations by OSSE can be compared to direct spectral measurements of the protons escaping from the flare by spacecraft such as IMP-8 (assuming it continues to operate during some fraction of the OSSE mission) or the proposed CRRES mission (Gussenhoven, Mullen and Sagalyn 1985).

The upper energy limit for the detection of neutrons by OSSE is about several hundred MeV. This limit can be extended for large flares by correlating OSSE observations with those of ground-based neutron monitors. These monitors generally do not have energy resolution but can provide upper limits to the neutron energy spectrum (e.g., Murphy, Dermer and Ramaty 1987) and thus to the proton spectrum responsible for neutron production.

The relativistic electrons responsible for the hard X-ray and gamma-ray emission via bremsstrahlung also can produce microwave emission via the synchrotron process. Electron kinetic-energy spectra deduced from the hard X-ray and from the microwave measurements can be compared with OSSE data to provide insight into the physical properties of the common (if any) regions of emission. Observations with the VLA or from VLBI can also provide imaging of the microwave emission region.

V. GRO GUEST INVESTIGATOR PROGRAM

A Guest Investigator program for GRO will be implemented with release of an initial NASA Research Announcement (NRA) planned for later this year. GI opportunities for the 15-month phase I (sky-survey) period of the mission will be limited primarily to opportunities on OSSE and BATSE. Increasing GI opportunities will be available during the second and third years of the mission, and beyond.

Since GRO will be launched at the peak of solar activity, interest in using GRO data for solar flare work is expected to be high. In order to accommodate representation from the solar physics community, both in terms of planning and implementing solar observations with OSSE, and in analysis and interpretation of solar data, GI representation on an OSSE Solar Physics Science Team will be solicited as part of the NRA. Questions relating to solar opportunities with OSSE should be directed to J. Kurfess, OSSE Principal Investigator, or R. Murphy, Team Leader for the OSSE Solar Physics Science Team.

VI. CONCLUSIONS

OSSE can make significant observations of transient sources, but these observations require planning. This planning is in progress, although a number of issues are unresolved. Attempts to synchronize solar observations with peaks of solar activity depend on the presence and phase of the 154-day period. These have not been determined for the current solar cycle. In addition, we need to examine other predictors of flare activity which could be used to define target of opportunity criteria for the Sun. There may be difficulties in observing large flares, where the intense low-energy flux could swamp the detector (pulse pile-up, gain changes, etc.). Most importantly, we need to look at what are the most interesting solar and burst questions we can address, and what observing modes (physical and electronic) are optimum to test them.

VII. REFERENCES

Chupp, E.L. 1984, Ann. Rev. Astron. Astrophys., **22**, 359.

Chupp, E.L., Debrunner, H., Fluckiger, E., Forrest, D.J., Golliez, F., Kanbach, G., Vestrand, W.T., Cooper, J., and Share, G.H.: 1987, Ap. J. **318**, 913.

Cotin, et al. 1983, ESA SP-1050, p. 209.

Crannell, C.J., et al. 1988, Proposal to NASA for a Gamma-Ray Imaging Device on a Balloon.

Dermer, C.D., and Ramaty, R. 1986, Ap. J., **301**, 962.

Forrest, D.J. et al. 1980, Solar Phys., **65**, 15.

Forrest, D.J. 1983, in "Positron-Electron Pairs in Astrophysics", ed. M.L. Burns, A.K. Harding and R. Ramaty (New York:AIP), p. 3.

Forrest, D.J., and Chupp, E.L. 1983, Nature, **305**, 291.

Gussenhoven, M.S., Mullen, E.G., and Sagalyn, R.C. 1985, AFGL-TR-85-0017.

Johnson, W.N. et al. 1989, Proceedings of the Gamma Ray Observatory Science Workshop.

Kane, S.R., Chupp, E.L., Forrest, D.J., Share, G.H., and Rieger, E. 1986, Ap. J. (Letters), **300**, L95.

Kiplinger, A.L., Dennis, B.R., Emslie, A.G., Frost, K.J., and Orwig, L.E. 1983, Ap. J. (Letters), **265**, L99.

Kurfess, J.D., Johnson, W.N., Kinzer, R.L., Share, G.H., Strickman, M S., Ulmer, M.P., Clayton, D.D., and Dyer, C.S.: 1983 Adv. Space Res. **3**, No. 4, 109.
Kurfess, J.D. 1988, Solar Phys., **118**, 347.
Murphy, R.J., Dermer, C.D., and Ramaty, R. 1987, Ap. J. Suppl., **63**, 721.
Murphy, R.J., Forrest, D.J., Ramaty, R., and Kozlovsky, B. 1985a, 19th Internat. Cosmic Ray Conf. Papers, **4**, 253.
Murphy, R.J., Ramaty, R., Forrest, D.J., and Kozlovsky, B. 1985b, 19th Internat. Cosmic Ray Conf. Papers, **4**, 249.
Murphy, R.J., Hua, X.-M., Kozlovsky, B. and Ramaty, R. 1990, Ap. J. (submitted).
Ramaty, R., and Murphy, R.J. 1987, Sp. Sci. Rev., **45**, 213.
Rieger, E., Share, G.H., Forrest, D.J., Kanbach, G., Reppin, C., and Chupp, E.L. 1984, Nature, **312**, 623.
Rieger, E., 1989 Solar Phys. (in press).
Rieger, E., Reppin, C., Kanbach, G., Forrest, D.J., Chupp, E.L., and Share, G.H. 1983, 18th Internat. Cosmic Ray Conf. Papers, **10**, 338.
Vestrand, W.T., Forrest, D.J., Chupp, E.L., Rieger, E., and Share, G.H. 1987. Ap. J., **322**, 1010.

The Solar Gamma Ray and Neutron Capabilities of COMPTEL on the Gamma Ray Observatory

James M. Ryan and John A. Lockwood

Institute for the Study of Earth, Oceans and Space
University of New Hampshire
Durham, NH

Abstract

The imaging Compton telescope COMPTEL on the Gamma Ray Observatory has unusual spectroscopic capabilities for measuring solar γ-ray and neutron emission. The launch of the GRO is scheduled for June 1990 near the peak of the sunspot cycle. With a 30 - 40% probability for the Sun being in the COMPTEL field-of-view during the sunlit part of an orbit, a large number of flares will be observed above the 800 keV γ-ray threshold of the telescope. The telescope energy range extends to 30 MeV with high time resolution burst spectra available from 0.1 to 10 MeV. Strong Compton tail suppression of instrumental γ-ray interactions will facilitate improved spectral analysis of solar flare emissions. In addition, the high signal to noise ratio for neutron detection and measurement will provide new neutron spectroscopic capabilities. Specifically, a flare similar to that of 1982 June 3 will provide spectroscopic data on > 1500 individual neutrons, enough to construct an unambiguous spectrum in the energy range of 20 to 200 MeV. Details of the instrument and its response to solar γ-rays and neutrons will be presented.

1. Introduction

The launch of the Gamma Ray Observatory during the solar maximum in 1990 will provide powerful tools with which to examine the γ-ray and neutron emissions from solar flares. COMPTEL, the imaging double Compton scatter telescope, has unique capabilities for measuring the flux and energy of both the solar γ-ray and neutron emissions. With its field-of-view (FOV) of about 60° for γ-rays and 90° for neutrons, the Sun will be in the field-of-view ~ 40% of the time. In this paper we first describe the detection technique and the physical instrument and then present a preliminary response of COMPTEL to γ-rays and neutrons. Finally, we predict the COMPTEL response to the γ-ray and neutron emissions of the 1982 June 3 solar flare.

2. Compton Telescope Basics

A Compton telescope is a γ-ray detector in which the Compton scattering process is used to measure the photon's energy and incident direction. In this type of detector a γ-ray must scatter in two physically independent detecting elements or planes, nominally a forward and rearward detector. A precise time-of-flight (TOF) measurement establishes the general forward or backward direction of the scattered photon. The measured TOF must be consistent with the light travel time, identifying and, when desired, discriminating against scattered neutrons. Pulse shape discrimination techniques can further isolate the effects of neutrons. This delayed coincidence requirement efficiently suppresses contributions from internal radioactivity and backward scattered particles. These selection criteria can be adjusted to select neutrons, as opposed to photon events, as discussed below. Charged particles are normally rejected via thin active charged particle shields. The Compton scatter kinematics impose an additional geometrical constraint upon the scattering process using the energy deposits in the two detectors to provide the photon scatter angle as described below and illustrated in Fig. 1.

$$\phi = \cos^{-1}(1 - \varepsilon/E_2 + \varepsilon/(E_1 + E_2)) \qquad (1)$$

Here, ε is the electron rest mass energy, E_1 is the energy deposit in the forward detector, E_2 is the energy deposit in the second or rearward detector and ϕ is the Compton scatter angle provided $E_1 + E_2$ is the full incident γ-ray energy. Although the constraints of coincidence, timing and scatter angle greatly reduce the background contribution to the instrument count rate, they simultaneously reduce the detecting efficiency. Consequently, Compton telescopes are generally large in order to compensate for the reduced efficiency while retaining a high signal to noise ratio. Because of the large size, it is fortunate that Compton telescopes often have a large ratio of active to passive material. The necessity of collimation, it can be argued, is obviated by the inherent directionality of the TOF and scatter angle criteria, eliminating the mass associated with active or passive γ-ray shielding.

The basic scattering process for photons is illustrated in Fig. 1. The quantities that one measures are the position A of the Compton scatter in the forward detector, the energy E_1 of the scattered electron, the position B of the scatter in the rearward detector and the energy deposit E_2 in that detector. One computes from these quantities the direction of the scattered photon's velocity vector, i.e. the axis of the cone in Fig 1. From the energy deposits, one computes the scatter angle ϕ, the half angle of the cone and the total γ-ray

energy ($E_1 + E_2$). Without measuring the direction of the scattered electron at point A, only the polar angle of the scatter is known. From inspection one sees that the direction information suffers from an azimuthal degeneracy; that is, for a given energy, photons from any source lying on the cone mantle shown, as shown in Fig. 1, produce identical signatures in the instrument. The azimuth information is solely contained in the direction of the scattered electron in the forward detector; this direction is not measured.

3. COMPTEL Gamma Ray Response

COMPTEL, designed for the Gamma Ray Observatory, is a Compton telescope as described above. It will be the first Compton telescope to be placed on-orbit and will provide us with the opportunity to perform observations of weak cosmic sources for extended periods of time. The mechanical design of COMPTEL is illustrated in Fig. 2 (Schönfelder *et al.* 1984). An incoming γ-ray scatters off an electron in one of 7 D1 detectors and proceeds down to one of 14 D2 detectors scattering again. Such events constitute the ideal type of γ-ray interaction. The material in D1 is a liquid organic scintillator, NE213A, with the properties of low density and low Z. The detector is a fraction of a mean free path thick, meaning that the incident γ-ray (or neutron) can usually scatter in D1 and leave D1 without scattering again. For the case of small angle γ-ray scatters ($< 30°$), the incident γ-ray can deposit a large part of its energy in the D2 detector which is comprised of NaI (high density, high Z).

The liquid organic scintillator in D1 (NE213A) possesses pulse shape discrimination properties, in that proton ionization tracks produce pulses with long rise times in the emitted visible light. Conversely, electrons and other minimum ionizing particles produce pulses with short rise times. The Pulse Shape Discrimination circuit, in effect, measures this rise time, whereby the events can be, in large part, segregated into two groups, proton scatters and electron scatters. This capability of the instrument allows for efficient identification of signals from recoil or knock-on protons produced by fast neutrons scattering off hydrogen in D1. Any reaction producing a recoil proton can be identified by these means, such as inelastic scattering of fast neutrons off carbon producing a γ-ray and either a knock-on proton or neutron (which then can elastically scatter off hydrogen). Pure γ-ray producing neutron reactions off carbon in D1 are also possible and represent an intrinsic background.

The D1 and D2 subsystems of the telescope are each completely surrounded by charged particle detectors (see Fig. 2). These 4 domes of plastic scintillator NE110 are 1.5

cm thick and do not significantly attenuate the incident γ-ray or neutron fluxes, yet are virtually 100% efficient in identifying charged cosmic rays.

The incident photon direction is constrained to a cone mantle, as illustrated in Fig. 2. In order to translate this geometrical feature to the the coordinate system of the telescope we require knowledge of the positions of the γ-ray or neutron scatters in D1 and D2. This is accomplished not only by knowing in which detectors the scatters occurred, but also by using a process to locate an event within a detector by comparing the relative pulse heights of the attached photomultiplier tubes. This provides spatial information within the triggered detectors in D1 and D2.

Errors in the measured energy and scatter angle occur via uncertainties in the measured energies in D1 and D2 and uncertainties in the measured interaction positions in D1 and D2. Partial energy absorption in D2 (resulting in an escaping γ-ray) yields a low value for the total γ-ray energy and a large value for the scatter angle ϕ.

Distinguishing features of COMPTEL are summarized below.

1) Liquid scintillator NE213A is used in the upper or forward detecting array. This liquid has pulse shape discrimination properties and high light output with the chemical properties of low density and low atomic weight, minimizing multiple scattering in D1.

2) No γ-ray shields are employed. Charged particle shields provide 4π sr rejection of charged cosmic rays.

3) NaI is used in D2 for higher photopeak efficiency and better energy resolution. A high photopeak efficiency provides better angle information since less energy is lost from the system.

4) In both D1 and D2 the position of the photon (or neutron) interaction is determined via the Anger camera technique, i.e. using the relative pulse heights of the photomultiplier tubes in that module.

5) Photomultiplier tube gains are continuously monitored using standard light sources. A Light Emitting Diode in each detector module provides short term gain information, while β^- tagged ^{60}Co sources provide long term gain information with monoenergetic on-board γ-rays (Snelling *et al.* 1986).

6) The threshold of the D1 detector is nominally 50 keV providing a small scatter angle threshold, increasing total efficiency and efficiency in the on-axis direction.

7) The threshold in the D2 detection array is nominally 500 keV, which lowers the total overall energy threshold of the system to approximately 800 keV for γ-ray scatters $< 30°$.

C-2

8) A quantity related to the γ-ray scatter angle is computed on-board to determine if the event is worthy of transmission. The parameters associated with this computation are adjustable by ground command providing the capability to maximize the good event rate.

The total geometrical area of the forward detector array D1 is approximately 4300 cm^2, while the effective area for γ-ray double scatters in the range of 1 to 10 MeV is < 40 cm^2. The spatial resolution (1 σ) in a D1 module (~ 1 MeV) is ~ 2 cm, while that in a D2 module is ~ 1 cm. Although a function of incident energy and angle, the energy resolution of the system is between 5 and 10%.

COMPTEL as an imaging photon telescope relies on the full energy deposit of the γ-ray to estimate correctly the scattering angle ϕ of the photon in the instrument (Schönfelder *et al.* 1984). For a solar flare γ-ray interacting in COMPTEL the inferred scatter angle ϕ about the vector of the scattered γ-ray must be such that the photon is assigned a solar origin as indicated schematically in Fig. 2. Hence, we know that the photon deposited its full energy in the detector. The response of the telescope to such events is simple. The energy or pulse height distribution is basically Gaussian in shape with a heavily suppressed Compton tail at low energies. Since the solar γ-ray spectra are rich in continuum and lines from C, N, O, Ne, Mg etc., a simple instrumental response function will facilitate correct de-convolution of the pulse height spectra. The response of the telescope to monoenergetic photons from a ^{24}Na source is shown in Fig. 3.

The effective detector area of COMPTEL to 5 MeV solar photons incident at 30° is about 25 cm^2, decreasing to about 10 cm^2 at 1 MeV and 20 MeV (Schönfelder *et al.* 1984). For the solar γ-ray flare which occurred on 1982 December 7 we estimate that the average γ-ray flux > 1 MeV was about 1 photon cm^{-2} s^{-1} over a period of ~ 1000 s. With COMPTEL's sensitive area this would result in a count rate of 25 s^{-1}, just exceeding the telemetry rate of COMPTEL of 20 s^{-1}. For a 1000 s event duration this yields ~ 20 000 counts for good spectroscopy statistics.

4. COMPTEL Burst Measurements

The burst mode of the COMPTEL instrument can also be used to detect the first fast burst of solar γ-rays. The programmable Burst Spectrum Analyzer (BSA) continually integrates γ-ray spectra from two separate D2 detector modules in a background mode at a programmed cadence and integration time (nominally 30 s). One detector covers the energy interval from 0.1 to 1 MeV and the other the interval from 1 to 10 MeV. Each detector has an unobscured field-of-view of about 2.5 sr and an area of ~ 600 cm^2. Outside this field-of-view varying amounts of intervening material exists attenuating the solar γ-ray flux.

The capabilities of COMPTEL for burst detection are discussed by Winkler *et al.* (1986). The sequence of spectra integration is illustrated in Fig. 4. When the burst system on COMPTEL receives a signal from the Burst and Transient Source Experiment (BATSE) indicating a burst of any origin, it starts accumulating spectra in these two modules at programmed time intervals, here shown as every 1.7 s, for a total of six spectra, after which it switches to a so-called tail mode integration time of ~ 10 s as indicated schematically in Fig. 4. This fast accumulation rate provides information about the initial solar burst of γ-rays. These integration times are tentative and doubtless will be adjusted on-orbit.

5. COMPTEL Operation During Solar Flares

Within 5 s after the burst start, BATSE sends a second signal to the On-Board Computer (OBC) if the burst originated from the general direction of the Sun. Within the next two minutes, depending on the timing of the BATSE signal relative to the OBC telemetry frame, the OBC commands COMPTEL into a solar neutron mode for a time interval of 90 minutes or one orbit. In the solar neutron mode the Time-of-Flight (TOF) acceptance window for events is shifted from a (pre-flight) nominal range of - 20 ns to + 20 ns (+ corresponding to downward-moving γ-rays and neutrons) to 0 to + 40 ns. A TOF measurement of 0 ns corresponds to simultaneous events in D1 and D2 with forward-moving γ-rays having a TOF of ~ 5 ns. This change in operating mode is also shown schematically in Fig. 4. COMPTEL still accumulates spectra in two D2 detector modules, each with a geometrical area of about 600 cm^2.

Double scatter telescope events are assigned a telemetry priority depending upon the measured event characteristics. The priority γ_1 is the highest priority, reserved for cosmic γ-ray events, with other events, γ_2 priority, (e.g. neutrons) largely filling the remainder of the telemetry stream. While the instrument is in the solar neutron mode γ_1 (priority) events are still in the data stream as indicated in Fig. 4. Solar neutrons, γ_2 events, are separated from the γ-rays by pulse height requirements in D1 and D2, Pulse Shape Discrimination (PSD) in the D1 detectors and TOF criteria (Fig. 4).

6. COMPTEL Neutron Response

The ideal type of neutron interaction in COMPTEL occurs when the incoming neutron elastically scatters off a hydrogen nucleus in the D1 detector. The scattered neutron then proceeds to the D2 detector where it may interact, depositing some of its energy to produce a trigger signal as indicated in Fig. 2. The energy of the incident neutron is

computed by summing the proton recoil energy E_1 in the D1 detector with the energy of the scattered neutron E_s deduced from the TOF from the D1 to the D2 detector. The scatter angle for non-relativistic neutrons (< 150 MeV) can be computed by the formula:

$$\phi = \cos^{-1} \{E_s/(E_s+E_1)\}^{0.5}.$$

The neutron can be traced backwards from D2 to D1 through the angle ϕ to a cone mantle restricting the incident direction to include the Sun. This is a geometrical constraint identical to that of the γ-ray measurements. The pulse shape information about energy deposits in D1 is sufficient to reject more than 95% of electron recoil events greater than about 1 MeV, the energy threshold in D1 for neutron detection. This method of detecting and measuring the neutrons is clean, in that a delayed coincident scatter with the correct pulse shape in D1 is required, yielding a large signal to noise ratio. Other inelastic reactions with C also occur in the liquid scintillator, particularly at energies greater than about 50 MeV. The C interactions in D1 often produce γ-rays, deuterons or alphas which can be identified. These can be included to further increase the instrument response to neutrons. These interactions are difficult to interpret, but in the case of a solar neutron event, can be used to supplement the information obtained from the elastic scatters.

With COMPTEL in the solar neutron mode (see Fig. 4) neutron interactions appear in the γ_2 channel, covering the TOF interval from about 10 to 40 ns. The PSD and TOF criteria in this channel are such that solar neutrons incident on D1 in the energy range from about 10 MeV to 200 MeV are recorded. In this energy interval COMPTEL can observe neutrons from about 14.5 to 55 minutes after release from the Sun. This corresponds to a minimum observed delay time of 6 to 47 minutes after the onset of the γ-ray flash (assuming neutrons are not produced without accompanying γ-rays).

A prototype of COMPTEL (Science Model 3) consisting of two D1 and three D2 modules was exposed at the Indiana University Cyclotron Facility to calibrated pulsed neutron beams from 20 to 200 MeV incident at various angles to the telescope. The fluxes as measured by the beam monitor and the D1 detector in the singles mode and the flux calculated from the beam current in the cyclotron using the known neutron production cross sections agreed to within ~ 50%. The resulting data were inspected to select events obeying the proper kinematic relationship for elastic scatters. These events were then tabulated to compare with Monte Carlo calculations performed to predict the efficiencies for elastic (n,p) scattering reactions. The calculated efficiencies were systematically about 1.95 greater than those measured. This discrepancy probably arises from the various approximations used in the calculations, such as neglecting the material in front of and

internal to the telescope, underestimating the attenuation of the neutrons by C interactions in D1, and assuming that every scattered neutron incident on D2 with an energy greater than the threshold energy produces an output signal from D2. The in-flight sensitivity of COMPTEL was then modeled in the full instrument configuration. The resulting effective area of COMPTEL for neutrons incident at 30° as a function of energy is shown in Fig. 5 where the calculated area is scaled by the above factor. The heavy line indicates the calibrated energy range.

6. COMPTEL Response to the 1982 June 3 Solar γ -Ray Flare

We can use these calculated efficiencies to estimate the response of COMPTEL to the solar neutrons from a flare event such as that of 1982 June 3. The reader is referred to the paper of Lockwood *et al.* (1989) presented at the NASA/GRO Workshop from which much of this material is derived. The calculated neutron energy spectrum in total neutrons produced per MeV at the Sun as a function of neutron energy according to Murphy *et al.* (1987), assuming that the neutrons are impulsively produced, is plotted in Fig. 6. A power law in rigidity times an exponential in energy is assumed for the solar neutron production spectrum, i.e.

$$dN/dE = A\, p^{-5} \exp(-E/1000), \qquad (2)$$

where p is in Mv and E in MeV. We further assume that the relativistic neutron energy spectrum is identical to the relativistic proton spectrum. The resulting neutron energy spectrum at the earth corrected for the neutron lifetime is also shown. The energy range of COMPTEL for solar neutrons, as indicated by the heavy line from about 10 MeV to 200 MeV, covers the maximum in the neutron energy spectrum at earth. An event such as that of 1982 June 3 would have produced about 1800 clean neutron events in COMPTEL over a time interval of about 40 minutes or an average event rate of $\leq 2\ s^{-1}$, within the telemetry bandwidth of γ_2 events.

Neutrons were detected from this event by the Solar Maximum Mission/Gamma Ray Spectrometer (SMM/GRS) (Forrest *et al.* 1980) and by ground level neutron monitors (Chupp *et al.* 1987; Debrunner *et al.* 1983; Efimov *et al.*1983). In Fig. 7 we have reproduced Fig. 1 from Chupp *et al.* (1987) showing the count rates of several energy channels of the GRS on SMM and the relative excess count rate of the Jungfraujoch neutron monitor. Chupp *et al.* (1987) state that the 56 - 199 keV X-ray channel responds predominantly to electron bremsstrahlung X-rays, while the 4.1 - 6.4 MeV photons originate largely from nuclear γ-ray line emissions indicative of energetic proton

interactions in the chromosphere and corona. In these energy bands the event started at 1142.7 UT (Forrest *et al.* 1985) and reached a maximum at 1143.5 UT. The High Energy Matrix (HEM) of the GRS responds to energy losses of > 25 MeV, a result of high energy photon and neutron interactions. The count rate of the HEM has a first peak with onset at 1143.0 UT and a maximum between 1143.0 and 1143.5 UT. A second peak is observed to start at 1145 UT, with a maximum at 1146 UT and a prolonged lower level excess count rate terminated by satellite sunset. The HEM count rate has a time structure different from those at lower energies. A fraction of this excess high-energy count rate (> 25 MeV) is due to > 50 MeV neutrons with the remainder (second peak) attributable to photon emission from charged and neutral π mesons (Forrest *et al.* 1985). The excess rate of the Jungfraujoch neutron monitor for 1 minute intervals shown in Fig. 7 is expressed in percent of the average count rate determined from the two reference intervals 1110 - 1140 UT and 1200 - 1230 UT.

The difference in the responses of the SMM detector and the Jungfraujoch neutron monitor to solar neutrons was used by Chupp *et al.* (1987) to estimate the time-averaged neutron emissivity at the Sun. Since neither the SMM detector nor the Jungfraujoch neutron monitor measure the neutron energy, the evolution of the emitted neutron spectrum in not known. One can, in the simplest case, assume either impulsive solar neutron production at a specified time or a time extended solar neutron production starting at a specified time, and following a particular intensity-time profile while maintaining a constant spectral shape at the Sun. The time-extended count rate profile seen at Jungfraujoch in Fig. 7 indicates that the solar neutron production at the Sun must have been time-extended rather than impulsive. This is supported by the conclusions of Forrest *et al.* (1985) that π meson decay produced γ-rays more than 2 minutes after the impulsive phase. In Fig. 9 we show the count rate of the SMM GRS detector and the Jungfraujoch neutron monitor (taken from Fig. 1 in Chupp *et al.* (1987)) as a function of the time of arrival of the neutrons assuming that the solar neutron production started at 1143:26 UT. Clearly, a time extended solar neutron production which has an intensity-time profile given by that of the > 25 MeV channel shown in Fig. 7 and being a power law in energy with an index of - 2.4 gives a good fit to both sets of count rates. An impulsive neutron production at 1143:26 UT also shown in Fig. 8, however, does not give a good fit to the SMM GRS and Jungfraujoch count rates. For comparison we show in the upper panel of Fig. 8 the predicted count rate ($\times$ 10) of COMPTEL to impulsive solar neutron production with the energy spectrum given by Murphy *et al.* (1987) shown in Fig. 6.

It is important to point out that since COMPTEL measures the solar neutron energies directly, a neutron energy spectrum at earth can be constructed. For impulsive

neutron production at the Sun with the neutron energy spectrum shown in Fig. 6, COMPTEL would have measured the spectrum shown in Fig. 9.

7. Conclusions

During a two year period after mid-1990, the projected launch date for GRO, we should expect a large number of solar γ-ray events with emission of photons > 0.8 MeV. From February 1980 to December 1982 Rieger *et al* (1983) found ~ 130 solar flares with emission > 0.3 MeV, of which 8 emitted > 10 MeV γ-rays. Two of these events emitted measurable neutrons > 50 MeV. Consequently, we should expect to find many solar flares with both high energy γ-rays (> 1 MeV) and neutrons (> 10 MeV) present, since the energy threshold of COMPTEL for neutrons is much lower than that of the SMM detector and since the neutron response curve of COMPTEL is well-matched to the solar neutron energy spectrum at earth.

By combining the normal imaging capabilities of COMPTEL with its burst mode operation and solar neutron spectroscopic abilities, definitive information should be obtained about the spectral evolution of nucleonic and electronic processes in solar flares. Neutron energy measurements provide more precise and extensive data about proton acceleration. For the unusual solar flare occurring on the west limb of the Sun in which prompt, energetic solar protons (> 500 MeV), γ-rays and neutrons are observed and measured, we should be in a position to understand better the relative roles of stochastic and diffusive shock acceleration processes at the Sun.

Acknowledgements

The COMPTEL experiment is the result of the efforts of the Max Planck Institut für Extraterrestrische Physik, Garching, FRG; the Space Research Organization of the Netherlands, Leiden, The Netherlands; the University of New Hampshire, Durham, New Hampshire and the Space Science Department of ESA/ESTEC, Noordwijk, The Netherlands. The work of the authors has been funded by NASA contract NAS5-26645.

References

Chupp, E. L., H. Debrunner, E. Flückiger, D. J. Forrest, F. Golliez, G. Kanbach, W. T. Vestrand, J. Cooper, and G. Share 1987, *Ap. J.*, **318** : 913-925.

Debrunner, H., E. Flückiger, E. L. Chupp, and D. J. Forrest 1983, *Proc. 18th Internat. Cosmic Ray Conf.*, **4** : 75.

Efimov, Yu E., G. E. Kocharov, and K. Kudela 1983, *Proc. 18th Internat. Cosmic Ray Conf.*, **10** : 276.

Forrest, D. J., E. L. Chupp, J. M. Ryan, M. L. Cherry, I.U. Gleske, C. Reppin, K. Pinkau, E. Rieger, G. Kanbach, R. L. Kinzer, G. Share, W. N. Johnson, and J. D. Kurfess 1980, *Solar Phys.*, **65** : 15-23.

Forrest, D. J., W. T. Vestrand, E. L. Chupp, E. Rieger, J. Cooper, and G. Share 1985, *Proc. 19th Internat. Cosmic Ray Conf.*, **4** : 146-149.

Lockwood, John, V. Schönfelder, K. Bennett, G. Eymann, J. M. Ryan, D. Morris, J. Macri, and B. Swanenburg 1989, to be published in Proceedings of GRO Workshop, Greenbelt MD.

Murphy, R. J., C.D. Dermer, and R. Ramaty 1987, *Ap. J.*, **316** : L41-56.

Rieger, E., C. Reppin, G. Kanbach, D. J. Forrest, E. L. Chupp, and G. H. Share 1983, *Proc. 18th Internat. Cosmic Ray Conf.*, **10** : 338.

Schönfelder, V., R. Diehl, G. Lichti, H. Steinle, B. N. Swanenburg, A. Deerenberg, H. Aarts, J. A. Lockwood, W. R. Webber, J. M. Ryan, G. Simpson, B. G. Taylor, K. Bennett, and M. Snelling 1984, *IEEE Trans. Nucl. Sci.*, **NS-31** (1) : 766-770.

Snelling, M., K. Bennett, and J. Clear 1986, *Nucl. Instr. Meth.*, **A248** : 545-549.

Winkler, C., V. Schönfelder, R. Diehl, G. Lichti, H. Steinle, B.N. Swanenburg, H. Aarts, A. Deerenberg, W. Hermsen, J. A. Lockwood, J. M. Ryan, G. Simpson, W. R. Webber, K. Bennett, A. v. Dordrecht, and B.G. Taylor 1986, *Adv. Space Res.*, **6** (4) : 113-117.

Figure Captions

1. The kinematics of a Compton scatter, the principle of measurement for a Compton telescope.

2. The mechanical structure of COMPTEL, illustrating the detection method for γ-rays and neutrons.

3. The energy response of COMPTEL to 1.37 and 2.75 MeV photons under the conditions of ideal scattering kinematics, i.e. ϕ is the true scatter angle.

4. The sequence of spectra integrations of the COMPTEL burst system. Shown is the *Background*, *Burst* and *Tail* spectra integrations relative to the trigger signal from BATSE. Also shown are the time-of-flight spectra used during normal operations and during solar flare measurements. The function of γ_1 and γ_2 event data is illustrated on the lower part of the figure.

5. COMPTEL effective area for neutron detection at 30° incident angle. The solid line indicates the calibration range.

6. The time integrated neutron spectrum at the Sun (Murphy *et al.* 1987) and at earth.

7. Intensity-time profiles of several GRS data channels and count rate of Jungfraujoch neutron monitor, reproduced from Chupp *et al.* (1987).

8. Count rates of the SMM/GRS data and Jungfraujoch neutron monitor superimposed on the predicted count rate for COMPTEL for the same event, assuming both impulsive and extended emissions of neutrons.

9. Predicted COMPTEL count rate spectrum due to a neutron flux as illustrated in Fig. 6.

PRINCIPLE OF MEASUREMENT

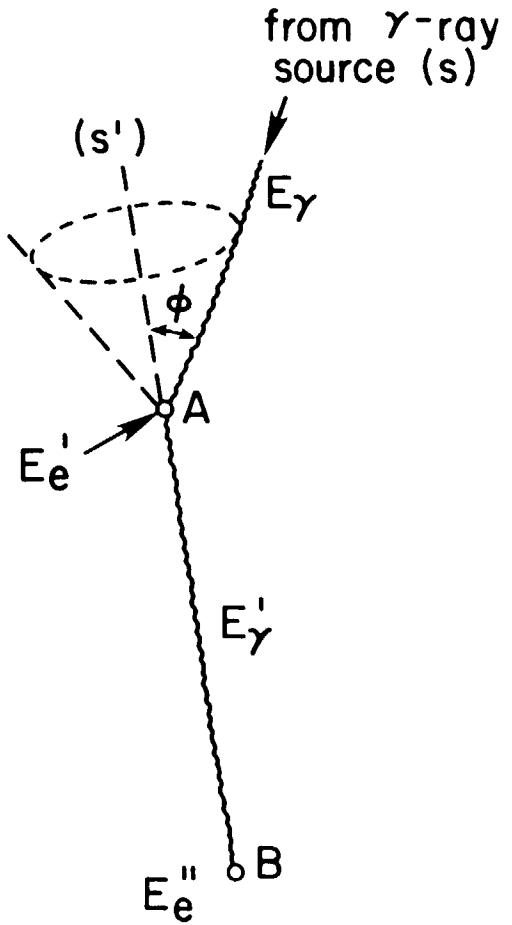

if $E_\gamma' = E_e''$

$\Longrightarrow$

$$E_\gamma = E_e' + E_e''$$

$$\cos\phi = 1 - \frac{m_0c^2}{E_e''} + \frac{m_0c^2}{E_e' + E_e''}$$

Figure 1

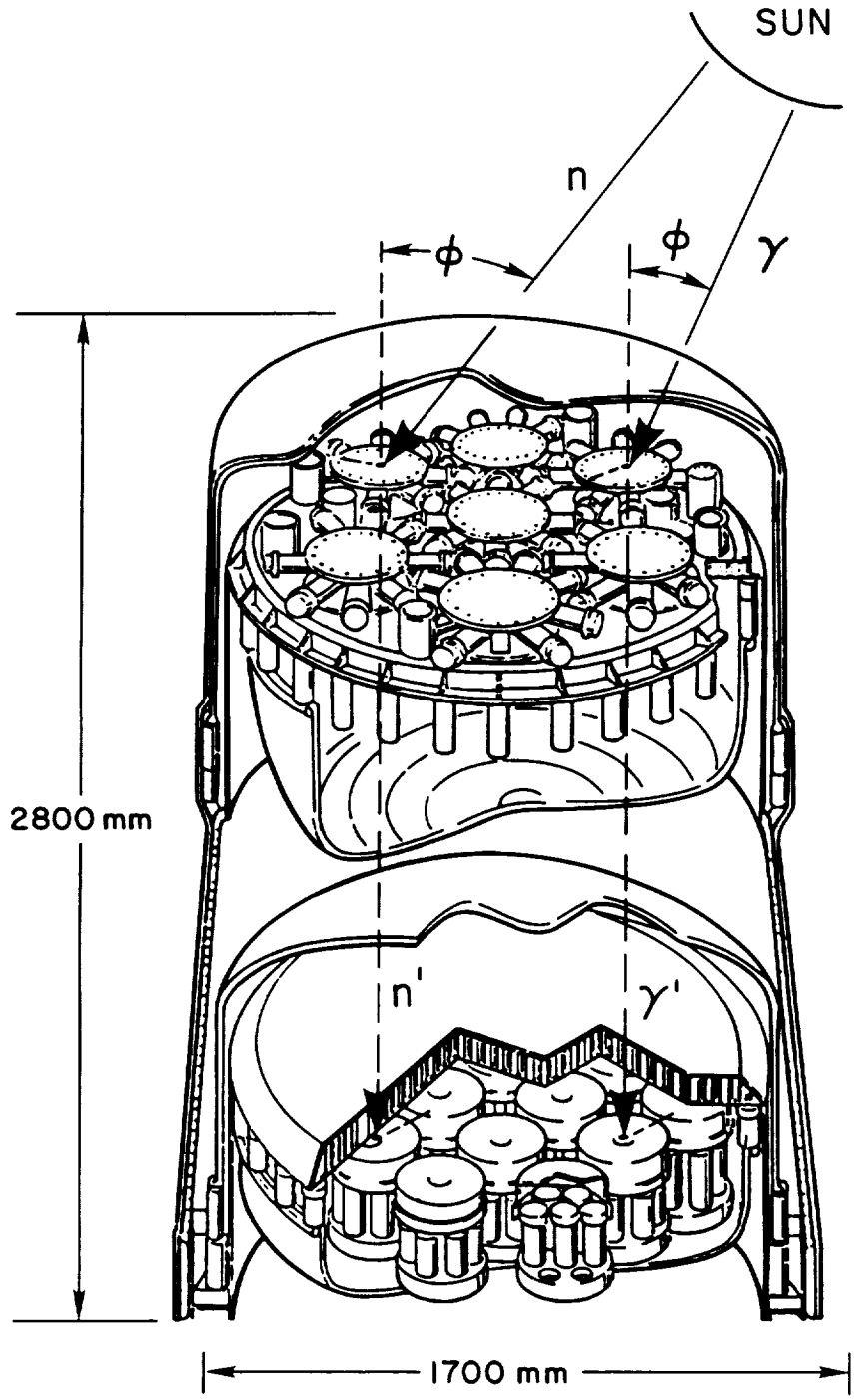

COMPTEL
IMAGING COMPTON TELESCOPE

Figure 2

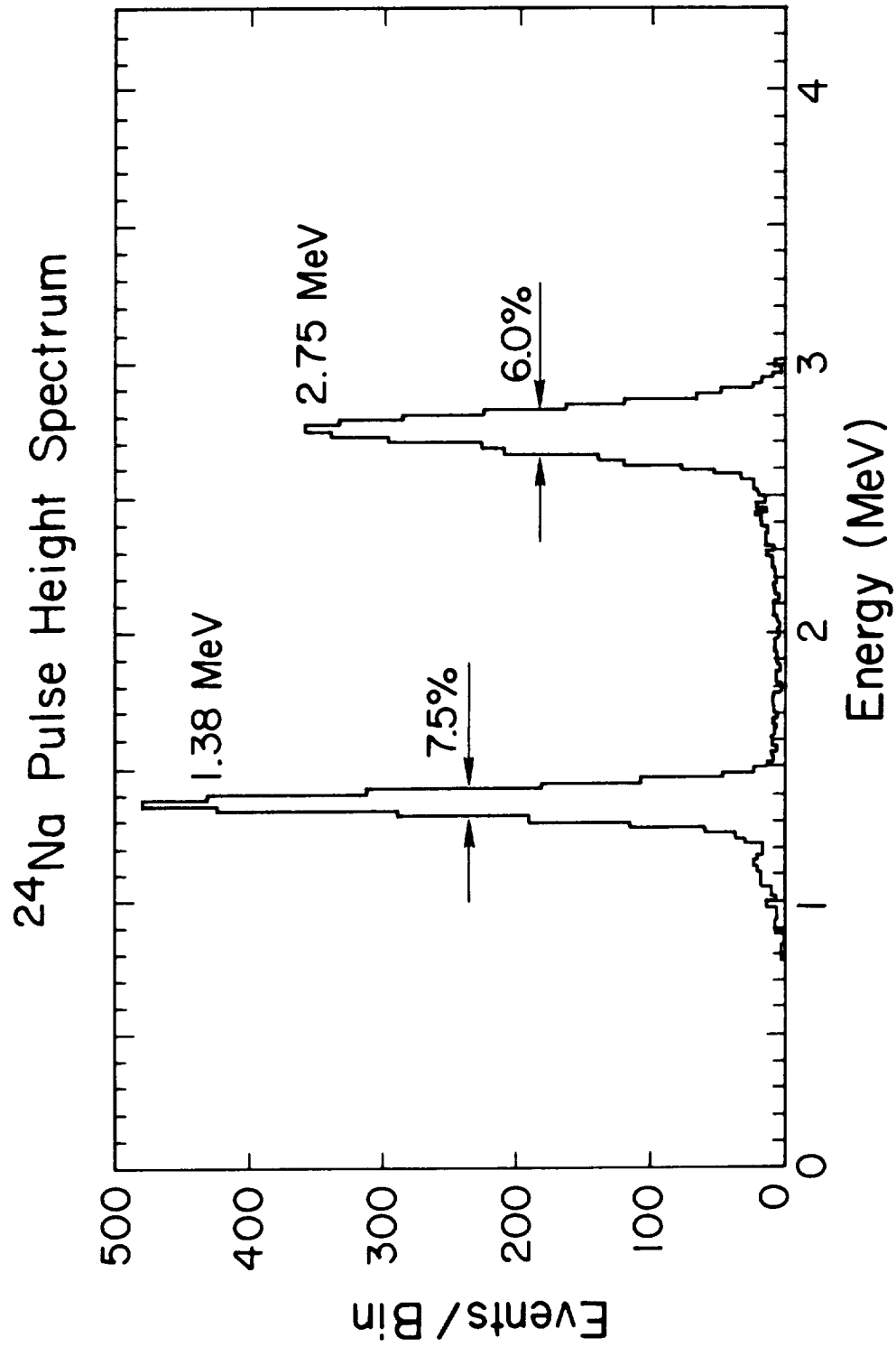
^{24}Na Pulse Height Spectrum
1.38 MeV
7.5%
2.75 MeV
6.0%
Events / Bin
Energy (MeV)
0
100
200
300
400
500
1
2
3
4

Figure 3

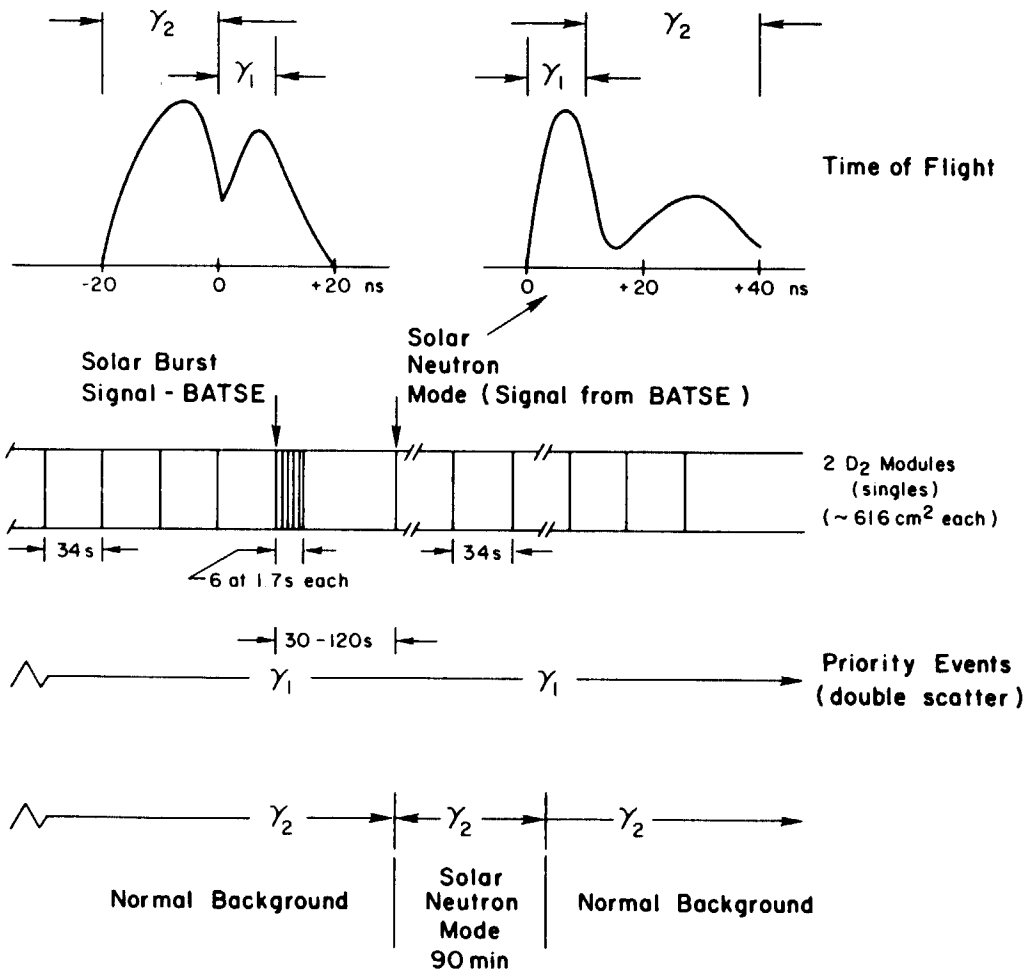
γ_2
γ_1
-20
0
+20 ns
γ_1
γ_2
0
+20
+40 ns
Time of Flight
Solar Burst Signal - BATSE
Solar Neutron Mode (Signal from BATSE)
2 D_2 Modules (singles) (~616 cm^2 each)
34 s
6 at 1.7s each
34 s
30 - 120s
γ_1
γ_1
Priority Events (double scatter)
γ_2
γ_2
γ_2
Normal Background
Solar Neutron Mode 90 min
Normal Background

Figure 4

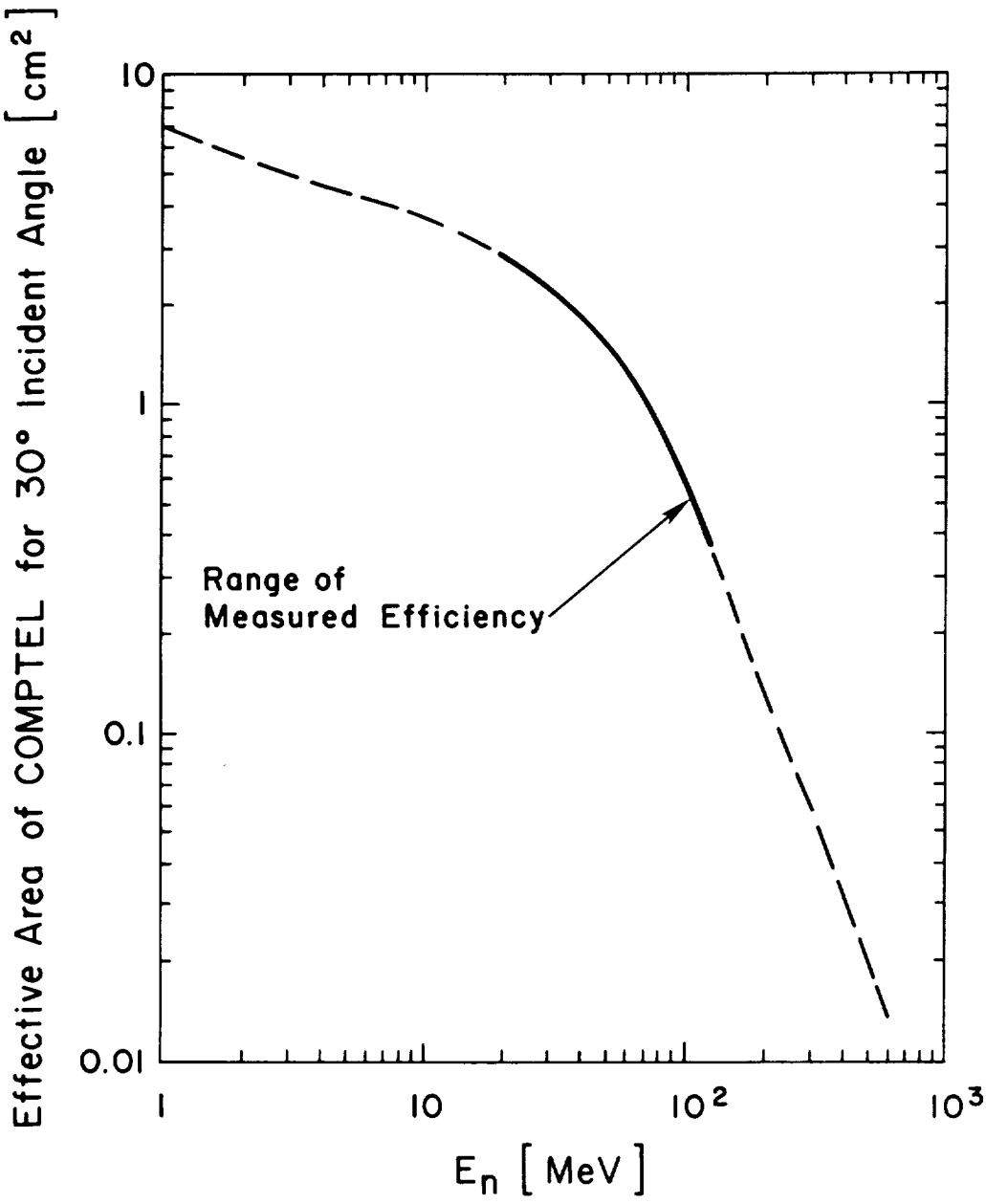
Effective Area of COMPTEL for 30° Incident Angle [cm²]
10
1
0.1
0.01
1
10
10²
10³
Range of
Measured Efficiency
Eₙ [MeV]

Figure 5

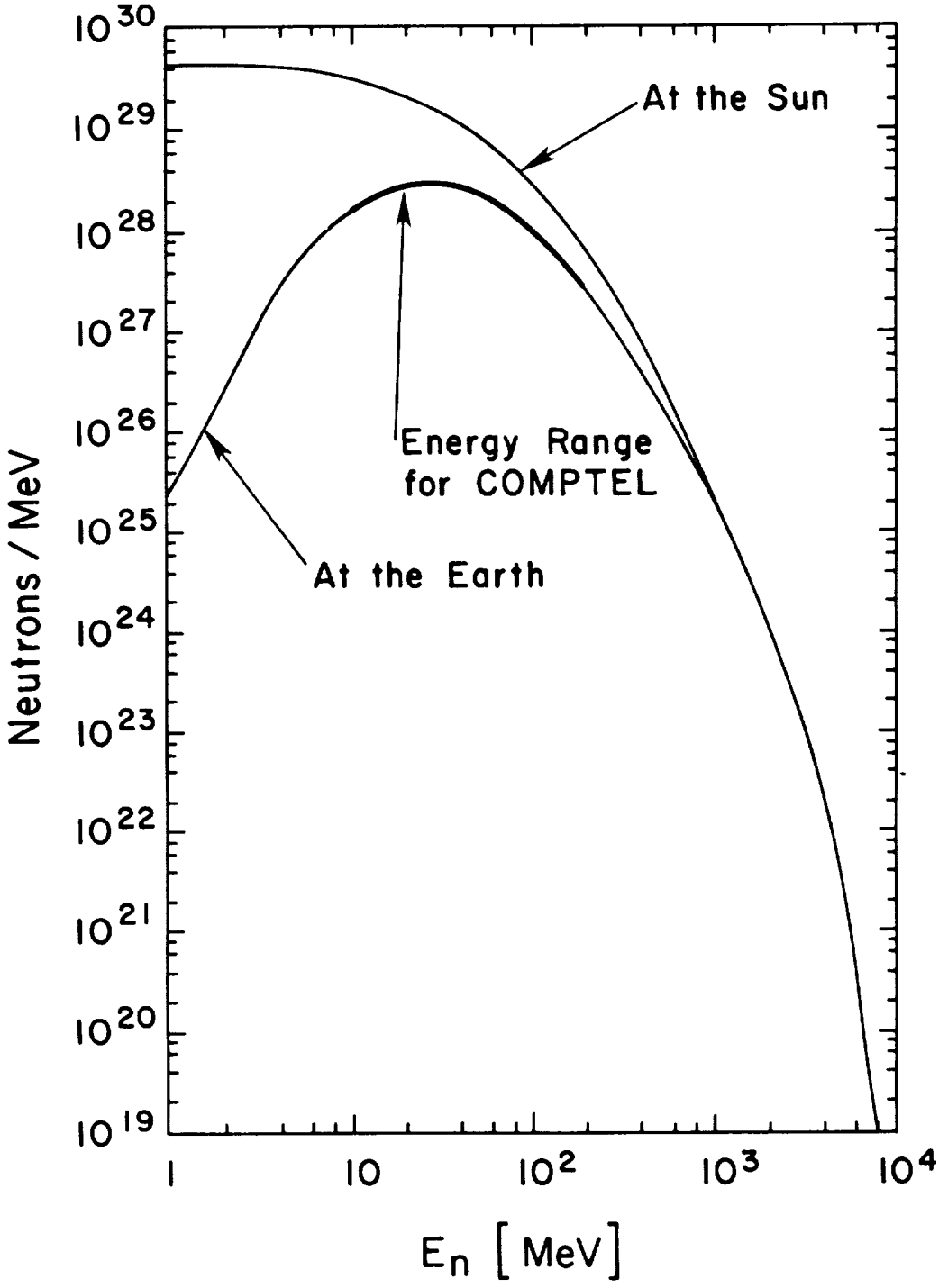
10^{30}
10^{29}
10^{28}
10^{27}
10^{26}
10^{25}
10^{24}
10^{23}
10^{22}
10^{21}
10^{20}
10^{19}
Neutrons / MeV
At the Sun
Energy Range
for COMPTEL
At the Earth
1
10
10^2
10^3
10^4
E_n [MeV]

Figure 6

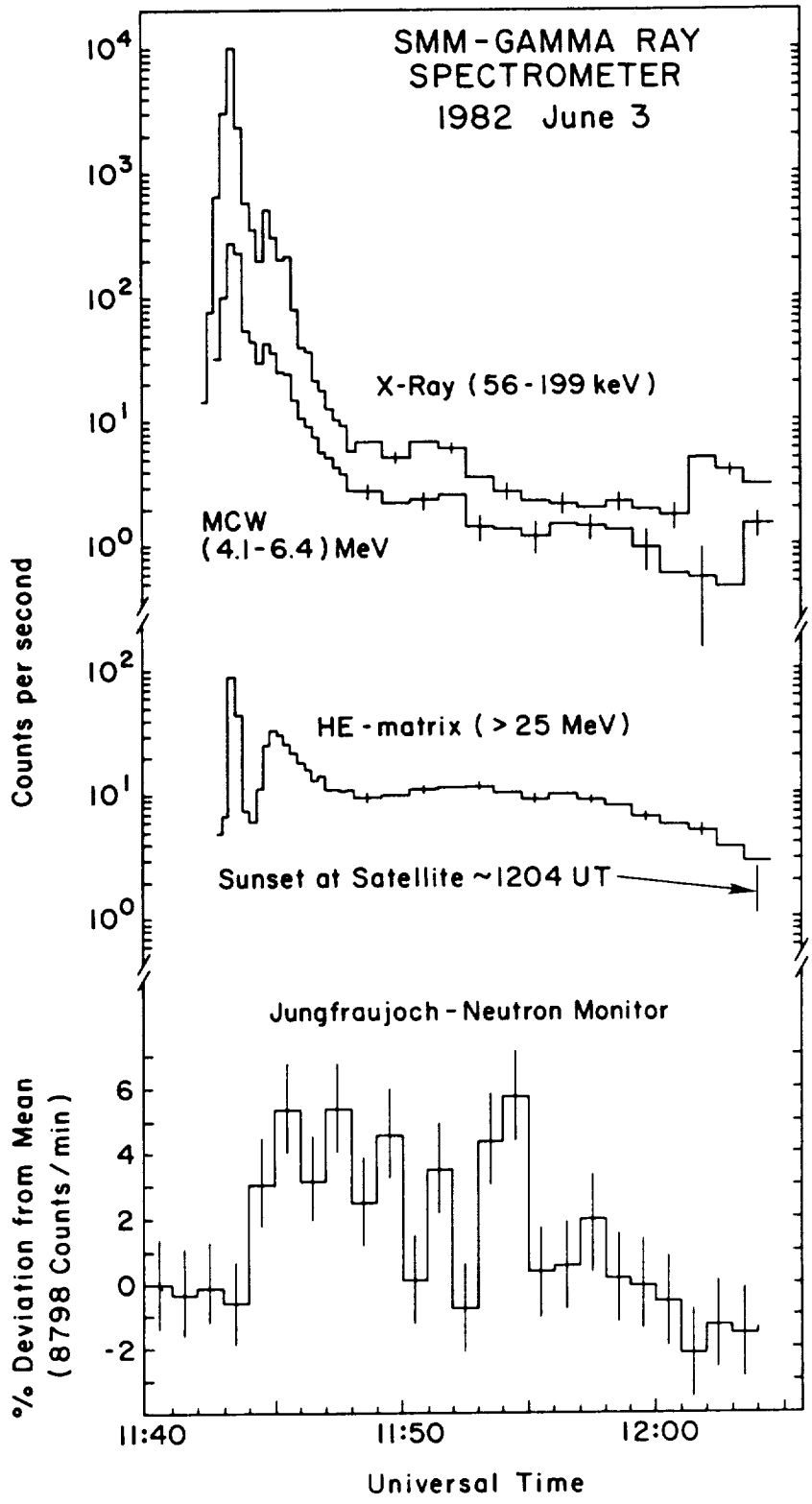

From Figure 1 in Chupp et al. (1987)

Figure 7

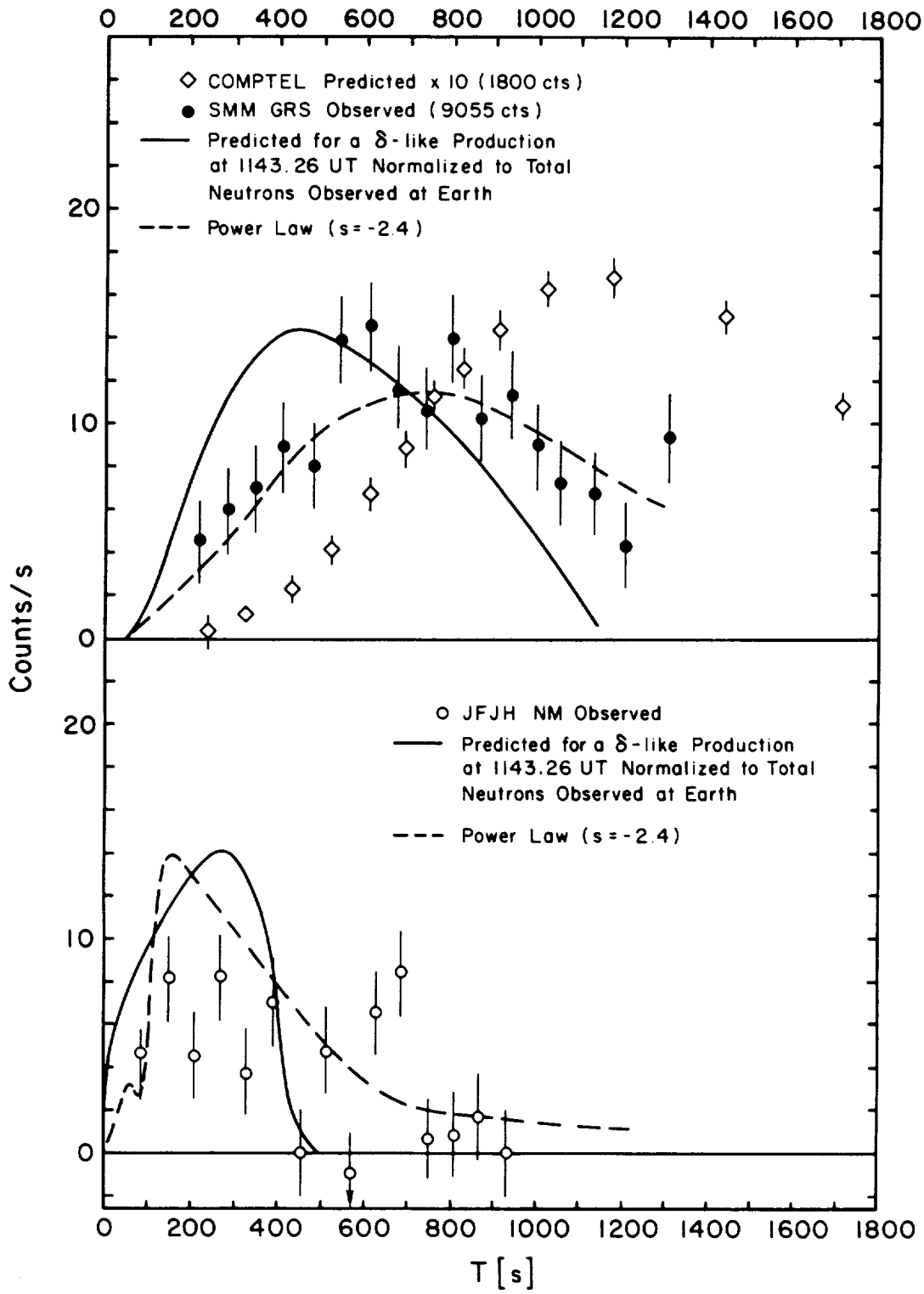
0 200 400 600 800 1000 1200 1400 1600 1800
◇ COMPTEL Predicted x 10 (1800 cts)
● SMM GRS Observed (9055 cts)
Predicted for a δ-like Production at 1143.26 UT Normalized to Total Neutrons Observed at Earth
Power Law (s=-2.4)
20
10
0
Counts/s
o JFJH NM Observed
Predicted for a δ-like Production at 1143.26 UT Normalized to Total Neutrons Observed at Earth
Power Law (s=-2.4)
20
10
0
0 200 400 600 800 1000 1200 1400 1600 1800
T [s]

Figure 8

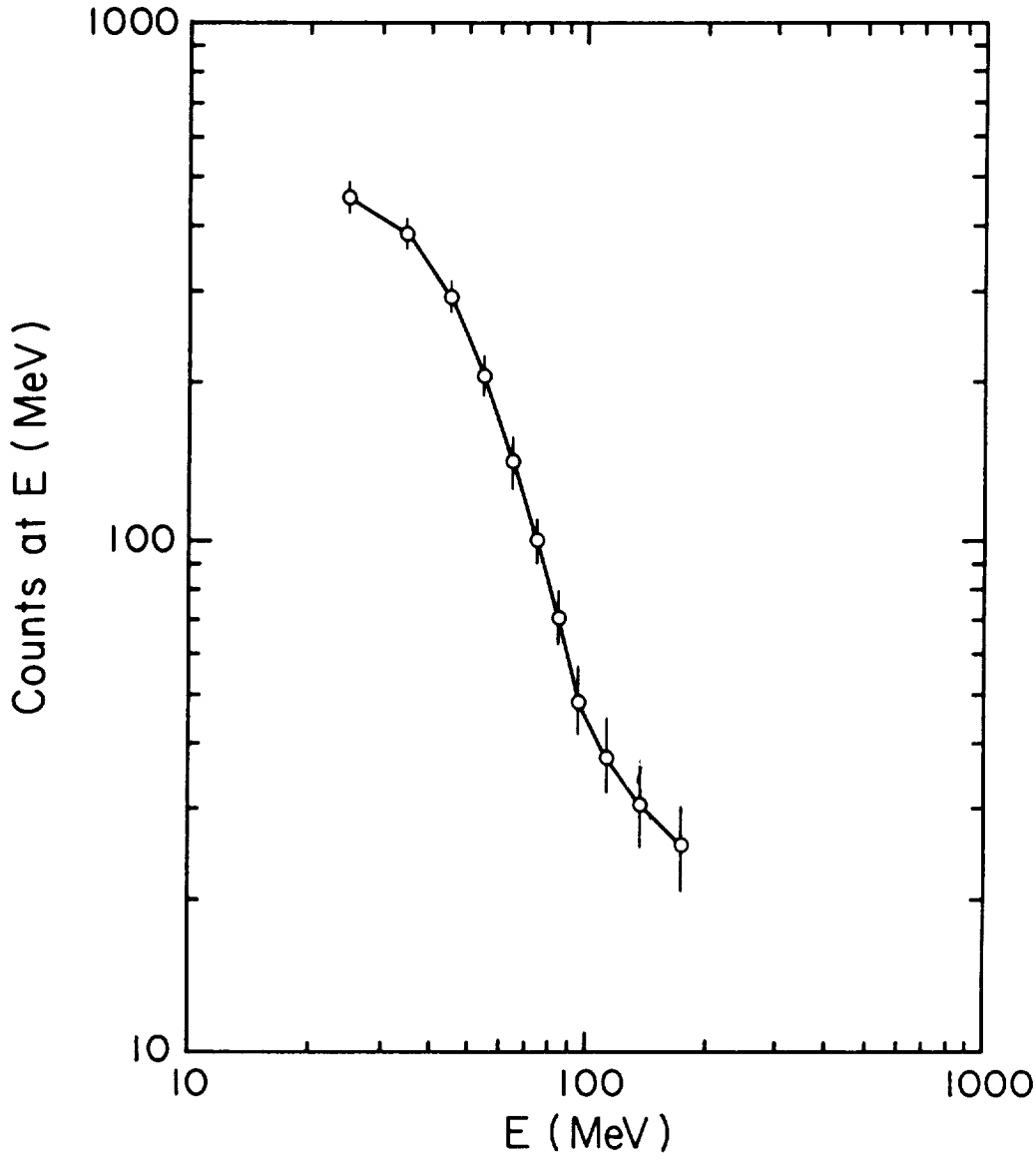

Figure 9

5/5-92

N90-12469

The BATSE Experiment on the Gamma Ray Observatory: Solar Flare Hard X ray and Gamma-Ray Capabilities

G.J. Fishman, C.A. Meegan, R.B. Wilson, T.A. Parnell (NASA/MSFC); W.S. Paciesas, G.N. Pendleton (UAH); H.S. Hudson, J.L. Matteson, L.E. Peterson (UCSD); T.L. Cline, B.J. Teegarden, B.E. Schaefer (NASA/GSFC)

ABSTRACT

The Burst and Transient Source Experiment (BATSE) for the Gamma Ray Observatory (GRO) consists of eight detector modules that provide full-sky coverage for gamma-ray bursts and other transient phenomena such as solar flares. Each detector module has a thin, large-area scintillation detector (2025 cm^2) for high time-resolution studies, and a thicker spectroscopy detector (125 cm^2) to extend the energy range and provide better spectral resolution. The total energy range of the system is 15 keV to 100 MeV. These 16 detectors and the associated onboard data system should provide unprecedented capabilities for observing rapid spectral changes and gamma-ray lines from solar flares. The presence of a solar flare can be detected in real-time by BATSE; a trigger signal is sent to two other experiments on the GRO. The launch of the GRO is scheduled for June 1990, so that BATSE can be an important component of the MAX '91 campaign.

1. INTRODUCTION

The Gamma Ray Observatory (GRO), the second of NASA's Great Observatories, is scheduled for launch in June, 1990. The four experiments of the GRO are at least an order of magnitude more sensitive than their predecessors, and it is expected that the GRO will bring the field of gamma-ray astronomy into a mature observational phase. The four experiments have different yet complementary goals, with overlapping energy ranges and distinct observational techniques.

Although the primary scientific objective of BATSE is the study of gamma-ray bursts and other transient phenomena, it has design features which will enable it to make significant contributions to solar physics. For strong solar flares, its large effective area will permit hard x-ray and gamma-ray observations with a sensitivity greater than both the HXRBS and the GRS experiments on SMM. These observations will be especially important in the upcoming solar maximum when, following the end of the SMM, the U.S. has no other long-term high-energy solar monitoring

capability. This paper is derived from several papers that were recently presented at the GRO Science Workshop held at Goddard Space Flight Center in April 1989 (Fishman et al. 1989a,b; Paciesas et al. 1989a; Pendleton et al. 1989). It concentrates on a description of the BATSE instrumentation and data analysis system--both of which would be of interest to potential users of BATSE for solar investigations. The papers of the GRO Workshop describe in more detail the scientific objectives and capabilities of BATSE and contain more information on the instrument and data analysis system being developed. Copies of those papers are available upon request.

2. EXPERIMENT CONFIGURATION

BATSE consists of eight uncollimated detector modules arranged on the corners of the Gamma Ray Observatory (GRO) to provide the maximum unobstructed view of the celestial sphere. Each detector module contains a large-area detector (LAD), optimized for sensitivity and directional response, and a spectroscopy detector (SD) optimized for broad energy coverage and energy resolution.

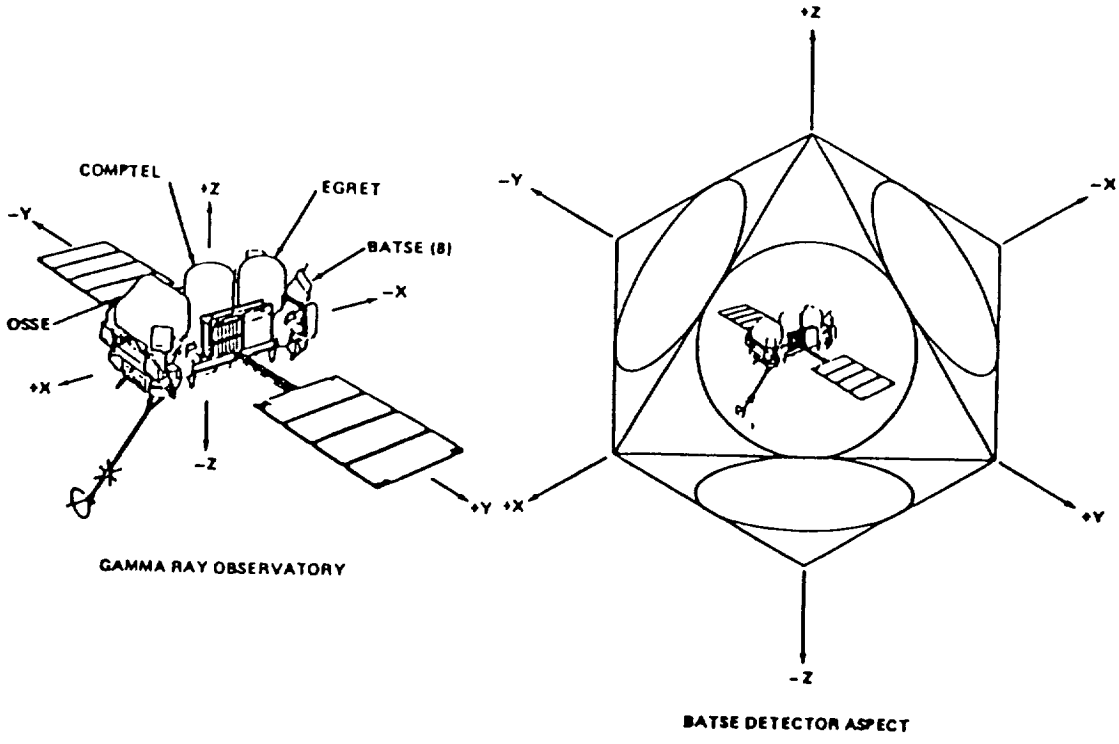

Figure 1. Illustration showing the co-alignment of the principal axes of the Gamma Ray Observatory with the octahedron geometry of the BATSE detectors.

The eight planes of the LADs are parallel to the eight faces of a regular octahedron, thus providing nearly uniform sky coverage. As shown in Figure 1, the three primary axes of the octahedron are parallel to the three principal axes of the spacecraft. Since the faces of a regular octahedron comprise four pairs of intersecting planes, every detected burst will be viewed by four detectors. Similarly, four detectors will always view the Sun during the daytime portions of each orbit.

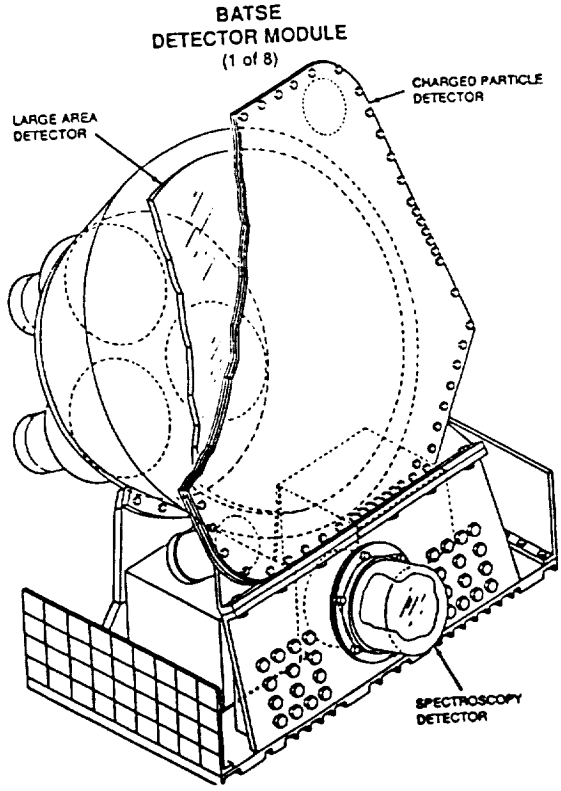

Figure 2. Pictorial representation of a BATSE detector module.

2.1. Large-Area Detector (LAD)

As shown schematically in Figure 2, the LAD contains a NaI(Tl) crystal 50.8 cm (20 in.) in diameter and 1.27 cm (0.5 in.) thick. The large diameter-to-thickness ratio of the scintillation crystal produces a detector angular response similar to that of a cosine function at low energies where the crystal is opaque to incident radiation. At energies above about 300 keV, the angular response is flatter than a cosine. The LADs are uncollimated in the forward hemisphere and passively shielded in the rear hemisphere.

Scintillation light from the detector crystal is viewed by three 12.7 cm (5 in.) photomultiplier tubes (PMTs). The signals from the three tubes are summed at the detector. A large light-integrating housing is used to collect the scintillation light in a relatively uniform manner (Figure 2). The housing is lined with passive lead/tin shielding and is coated with a barium sulphate-based white reflector. The passive shielding is effective up to energies of about 200 keV. The front of the LAD is covered by plastic scintillator (BC400, 0.63 cm thick) that rejects charged-particle-induced events in the LAD. Detailed performance characteristics of the LAD's are given by Paciesas et al. (1989b).

2.2. Spectroscopy Detector (SD)

The SD is an uncollimated NaI(Tl) scintillation detector 12.7 cm in diameter by 7.62 cm thick (5 in. x 3 in.). A single 12.7 cm diameter PMT is directly coupled to the scintillation detector window. The housing of the PMT has a passive lead/tin shield similar to that of the LADs. The crystal housing has a 3 in. diameter beryllium window, in order to provide high efficiency at energies as low as 15 keV. The axis of symmetry of a SD is offset by 19 degrees from the LAD axis, for mechanical reasons. The angular response of the SD is more nearly isotropic, so that alignment of the axes is not required.

Properties of the BATSE detectors are summarized in Table 1. The sensitive area and resolution of the detectors are shown in Figures 3 and 4, respectively.

	BATSE DETECTORS	
	LARGE AREA	SPECTROSCOPY
Material:	NaI(Tℓ)	NaI(Tℓ)
Frontal Area:	2,025 cm^2	127 cm^2
Thickness:	1.27 cm	7.62 cm
Energy Range:	30 - 1900 keV	15 keV - 110 MeV*
Energy Resol.:	27% @ 88 keV typ.	7.2% @ 662 keV typ.
		*Detector gain dependent

Table 1. BATSE Detector summary chart.

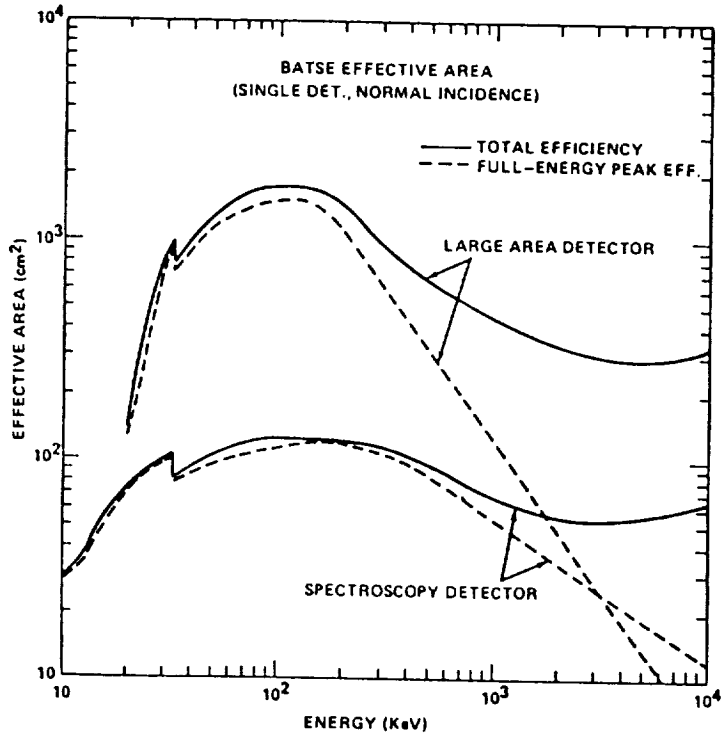

Figure 3. Effective areas of the BATSE LAD and SD as functions of energy.

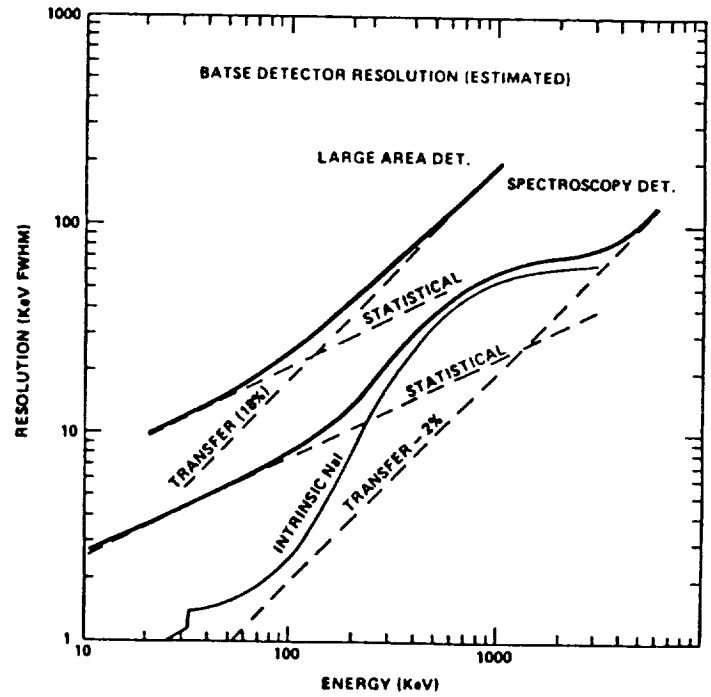

Figure 4. Energy resolutions of the BATSE LAD and SD as functions of energy.

2.3. Analog Electronics

Scintillation pulses from the detectors are processed by a gated baseline restoration circuit which minimizes the spectral distortion that usually accompanies high counting rates in detectors of this type. Pulses are processed in parallel by a high-speed, four-channel discriminator circuit and by a slower pulse-height analyzer system. The pulse-pair resolution of the discriminators is approximately 300 ns. The nominal equivalent energies of the upper three discriminators for the LADs are 50, 100, and 300 keV. The lower-level discriminator is programmable, with a typical level of 30 keV. Two of the fast discriminators for the SDs are set at energies above the energies analyzed by the pulse height system. The gain of each detector system is determined by the high voltage applied to the PMTs. The SDs will be operated at different gains, in order to span from 15 keV to greater than 100 MeV. The nominal energy ranges of the SDs are shown in Table 2.

BATSE SPECTROSCOPY DETECTORS
Energy Ranges

GAIN	NUMBER OF DETECTORS	DISPERSION	SPECTRAL ANALYSIS	HIGH ENERGY DISCRIMINATORS
High (4X)	4	1 KeV/ch.	15 keV – 2.7 MeV	5 MeV, 11 MeV
Medium (1X)	2	4 KeV/ch.	60 keV – 11 MeV	22 MeV, 45 MeV
Low (0.4X)	2	10 KeV/ch.	150 keV – 27 MeV	54 MeV, 110 MeV

Table 2. Spectroscopy Detector planned operating gains.

2.4. Digital Data System

Each of the eight BATSE detector modules sends data to the Central Electronics Unit (CEU). The CEU contains hardware and software that accumulates the data into several large RAM memory buffers. Extensive use of commandable parameters, plus the capability to reprogram the flight software after launch, insures that BATSE will have the flexibility to respond to unforeseen conditions in orbit, or newly discovered gamma-ray phenomena. The functions of the BATSE data system are summarized in Figure 5. Signals from the pulse-height converters are used to construct 128-channel spectra from the LADs and 256-channel spectra from the SDs. Each of the spectra are subdivided into ranges with different dispersions to increase the dynamic range and to efficiently use the available telemetry space. These energy channels are also mapped into 16 coarse

energy channels using programmable look-up tables, one for the LADs and one for the SDs. This permits the trade of time resolution for energy resolution in several of the data types. Discriminator events are accumulated in the hardware every 64 ms. The CEU hardware constructs various data types from the discriminators, 16-channel, 128-channel, and 256-channel spectral data.

BATSE provides a signal to the other GRO instruments if a triggered burst appears to be a solar flare. This signal may be used by COMPTEL to enter the neutron detection mode and by OSSE to point to the Sun, if available to the OSSE detectors. The main criterion for generating the solar flare trigger signal is that the relative count rates are consistent within upper and lower limits for a burst coming from the direction of the Sun. Other criteria are that the detectors most directly facing the Sun must be triggered, that the hardness ratio must be between specified limits, and that the maximum count rate must be above a specified lower limit. These criteria are applied after data have been accumulated for a specified time, nominally 2 s after the burst trigger. The OSSE team will specify the values of the various parameters.

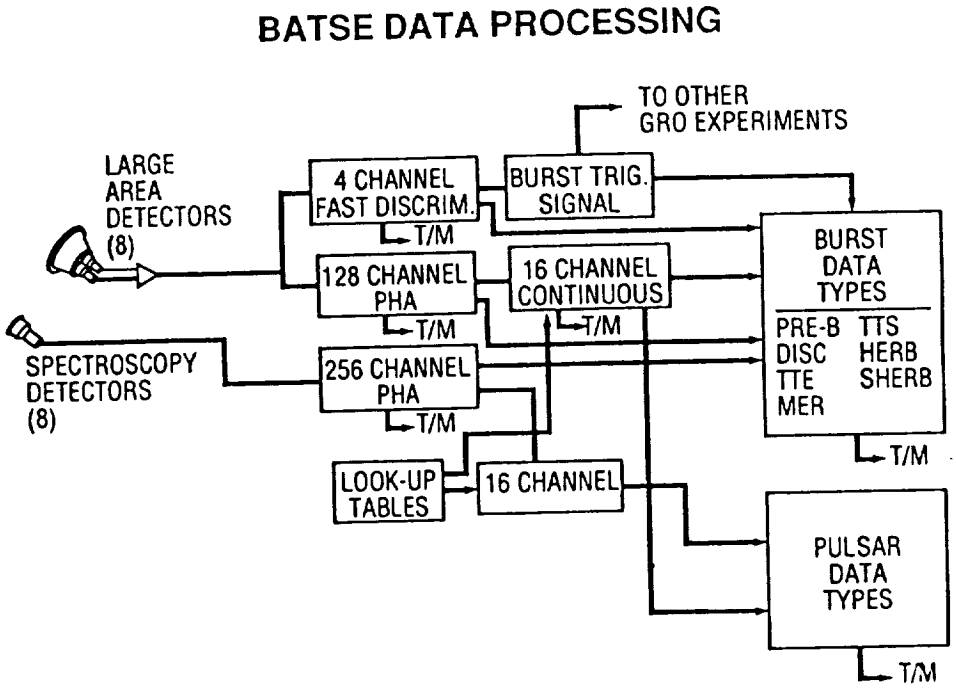

Figure 5. Overview of the BATSE onboard data system, showing principal data flows.

3. EXPERIMENT OPERATIONS AND SOLAR HARD X RAY MONITORING

BATSE is the only one of the four GRO instruments that can receive and analyze a large fraction of the data within days after observation. An extensive body of mission operations and data analysis software is being developed to derive gamma-ray burst locations, spectra, and counting rate histories soon after triggered events occur. Principal characteristics of the stronger gamma-ray bursts and solar flares will be made available to the scientific community in a timely manner via a common electronic bulletin board. We also expect to make available to the solar community hard x-ray data from the large-area detectors with 1 s resolution. This may be accomplished through the HXRBS/SMM analysis system at GSFC, according to recent discussions (B. Dennis, personal communication).

4. DATA ANALYSIS OPERATIONS

The primary facility for analysis of BATSE data will be located at NASA/Marshall Space Flight Center (MSFC). Additional facilities at NASA/Goddard Space Flight Center (GSFC) and the University of California, San Diego (UCSD), will be capable of implementing a subset of the functions of the primary facility. Guest Investigator support will be available at the primary analysis facility during the GRO mission.

The BATSE data archive is stored on the Marshall Archival System (MARS), an optical disk storage system which is maintained by MSFC for archival of flight data from various experiments. The other components of the primary data base are stored initially on magnetic disk, with archival backups to either local optical disk or magnetic tape. Analysis using a particular technique generally will proceed by generation of the appropriate secondary data base using the archived raw data combined with the calibration data, quality criteria, spacecraft parameters, and the BATSE instrument model. Subsequent analysis results and processed data are stored in tertiary Processed Data Bases (PDBs) which are managed using the commercially-available INGRES data base management system. Burst and solar flare catalogs are maintained and will be made available for public access. Software analysis tools consist primarily of display programs, spectral analysis functions such as line-fitting, and temporal search algorithms. A primary component of all data analysis is spectral analysis, including line searches and spectral deconvolution. A software package, the BATSE Spectral Analysis Software (BSAS) is being developed for this purpose by BATSE co-investigators at GSFC and it will be transported to other BATSE team facilities at MSFC and UCSD. Though primarily intended for analysis of burst spectra, the package will also be used for any spectral studies in the other analysis modes.

Three types of secondary data bases are produced for data analysis: the Individual Burst Data Base (IBDB), the Background Data Base (BDB), and the Pulsar Corrected Data Base (PCDB). At MSFC, these are created as needed for a specific application from the Primary Production Data Base and generally not archived. The IBDB and BDB formats are used to distribute a subset of the BATSE data to co-investigators at GSFC and UCSD, where local archives of these data bases are maintained. Within the GRO Guest Investigator (GI) program (Bunner 1989) a significant distinction is made between high-level and low-level data. The high-level data products will be analyzable in a relatively independent manner whereas use of low-level data will require close collaboration with the Principal Investigator (PI) team, typically involving a period of residence at a PI institution.

Any data which can be stored in a BATSE PDB are, in principle, available as high-level data. Standard sets of time histories and pulse-height spectra (with associated response matrices and calibration parameters) will be produced for each burst, solar flare, pulsar (onboard folding only), and bright occultation source. High-level data will be available either in Flexible Image Transport System (FITS) format or in the BATSE PDB format. The latter will be useful if the BSAS package is transported to another system.

The remaining BATSE data are available to Guest Investigators as low-level data. Once the GI attains sufficient familiarity with the instrument characteristics and analysis techniques, arrangements to transport relevant software and/or low-level data to another institution will be considered on a case-by-case basis. Catalogs of BATSE observations/investigations of bursts, solar flares, occultation sources, and pulsar sources will be generated during data analysis. Data analysis catalogs of bursts, solar flares, occultation sources, and pulsar sources will be available for public inspection via remote logon over the Space Physics Analysis Network (SPAN). Access via other means is being considered.

Access to low-level data will be available at MSFC beginning in the first year. We anticipate supporting from two to four Guest Investigators during the first year. Standard high-level data products will be available from MSFC during the second year. The standard high-level data products will also be incorporated into NASA's Astrophysics Data System (ADS). We plan to deliver data in FITS format to the appropriate ADS node within one year after receipt of data in usable form.

5. GUEST INVESTIGATIONS FOR SOLAR STUDIES

Numerous opportunities will exist for detailed studies of individual flares from solar flare-triggered BATSE data. The BATSE experimenters intend to make approximately 50% of the solar data available to guest investigators. For those flares that trigger the BATSE burst data system, hundreds of spectra will be accumulated over the duration of the flare. During the intense portions of many flares, time resolutions of tens of microseconds should be available with some limited spectral information. This should put severe constraints on the spatial distribution and evolution of high energy electron populations within the flare region. In addition to the electron component of flares, the high energy ion component from several MeV to several GeV can be studied through the emission of gamma-ray lines, pion decay, the decay of positron-emitting isotopes, and neutrons. Each of these species will have different temporal relationships with the flares, permitting additional insight into the spatial and temporal characteristics of the high energy ions within the flare regions. Gamma-ray line and neutron observations will be available with a higher time resolution than were possible from the GRS experiment on SMM.

Although not designed as a solar experiment, BATSE should be able to provide extensive, sensitive coverage of high-energy emission from the Sun during the present solar maximum.

References:

"BATSE: The Burst and Transient Source Experiment on the Gamma Ray Observatory", G.J. Fishman, C.A. Meegan, R.B. Wilson, W.S. Paciesas, T.A. Parnell, R.W. Austin, J.R. Rehage, J.L. Matteson, B.J. Teegarden, T.L. Cline, B.E. Schaefer, G.N. Pendleton, F.A. Berry, Jr., J.M. Horack, S.D. Storey, M.N. Brock, and J.P. Lestrade, GRO Science Workshop, GSFC, Proceedings to be published (1989a).

"The Burst and Transient Source Experiment (BATSE) Scientific Objectives and Capabilities", G.J. Fishman, C.A. Meegan, R.B. Wilson, W.S. Paciesas, T.A. Parnell, J.L. Matteson, B.J. Teegarden, T.L. Cline, G.N. Pendleton, and B.E. Schaefer, GRO Science Workshop, GSFC, Proceedings to be published (1989b).

"The BATSE Data Analysis System and Implementation of the Guest Investigator Program", W.S. Paciesas, G.N. Pendleton, G.J. Fishman, C.A. Meegan, R.B. Wilson, M.N. Brock, F.E. Roberts, and B.E. Schaefer, GRO Science Workshop, GSFC, Proceedings to be published (1989a).

"The BATSE Detector Response Matrices", G.N. Pendleton, W.S. Paciesas, J.P. Lestrade, G.J. Fishman, R.B. Wilson, and C.A. Meegan, GRO Science Workshop, GSFC, Proceedings to be published (1989).

"The Gamma Ray Observatory Guest Investigator Program", A.N. Bunner, GRO Science Workshop, GSFC, Proceedings to be published (1989).

"Performance of the Large Area Detectors for the Burst and Transient Source Experiment (BATSE) on the Gamma Ray Observatory", W.S. Paciesas, G.N. Pendleton, J.P. Lestrade, G.J. Fishman, C.A. Meegan, R.B. Wilson, T.A. Parnell, R.W. Austin, F.A. Berry, Jr., J.M. Horack, and S.D. Storey, SPIE Proceedings Vol. 1159, paper #1159-18, in press (1989b).

N90-12470

THE SOLAR FLARE AND COSMIC GAMMA-RAY BURST EXPERIMENT ABOARD THE ULYSSES SPACECRAFT

Michel Boer, Michael Sommer

Max Planck Institut fuer Extraterrestrische Physik,
8046 Garching bei Muenchen, West Germany

Kevin Hurley
Space Sciences Laboratory,
University of California, Berkeley, CA 94720
(on behalf the HUS-Ulysses team)

Abstract

The HUS-Ulysses team has prepared an instrument for the Ulysses spacecraft consisting of 2 Csi detectors and 2 Si surface barrier detectors for measuring X-rays in the range 5-200 keV with up to 8 ms time resolution. The prime objectives of the experiment are the study of solar flares and cosmic gamma-ray bursts. The Ulysses mission will leave the ecliptic during the forthcoming solar maximum. The total time above ecliptic latitudes +-70 degrees is expected to be 230 days. The solar data can be used in conjunction with other experiment to measure the directivity of the emission and for correlative studies.

The Cosmic Gamma-Ray Burst Experiment

The HUS X-ray flare and cosmic gamma-ray burst detector aboard the Ulysses spacecraft was designed by 3 european institutes, namely the Centre d'Etude Spatiale des Rayonnements,Toulouse (France), the Max Planck Institute fuer Extraterrestrische Physik, Garching bei Muenchen (West Germany), and the Astronomical Institute of Utrecht (The Netherlands). The launch is planned for october 1990. the primary objectives are the study of solar X-ray flares and of cosmic gamma-ray bursts.

The experiment consists of 2 detectors: 2 Si sensors operating in the range 5 to 20 keV with a field of view of 75 degrees (half cone, centered on the earth) and two CsI(Tl) scintillators for the range 15-200 keV with an all-sky field of view. The bit rate allowed in the Ulysses telemetry for HUS is 40 bit/second and the time resolution is up to 4 seconds for the Si sensors and up to 8ms for the scintillators.

The HUS 2B sensors are surface barrier detectors each 500 microns thick and 0.5 cm2 in area with a Be front window to reject low energy X-rays. The energy band channels are shown in the following table:

ENERGY BAND CHANNELS OF THE SOFT X-RAY DETECTORS

Channel	D0	D1	D2	D3	D4	D5
Energy limits (keV)	>3.5	5-7.1	7.1-10	10-14	14-20	>20

The count rates from the six channels D0 to D5 from the sum of the two sensors are accumulated over times which depends on the spacecraft telemetry as shown in the next table

ACCUMULATION TIMES FOR THE SOFT X-RAY DETECTORS

Channel	D0	D1	D2	D3	D4	D5
Accumulation times (sec.)						
Tracking mode	8	8	4	4	16	16
Storage mode 1	16	16	8	8	32	32

The HUS 2A sensor consists of 2 hemispherical CsI(Tl) scintillator cristals 3mm thick, optically coupled to 2 PM tubes. The effective area is about 20 cm2. In the absence of a flare, HUS2A has two waiting modes selectable by command. In mode 1, the Integral Count Rates (ICR sum of the two CsI detectors in the range 15-200 keV) are transmitted every 0.25 sec, in tracking mode (twice this value in storage mode 1). In mode two, the nominal mode for the mission, ICR are transmitted every 0.5s in tracking mode and, in addition, 4 channel energy spectra are transmitted everyach 8s (16s). The instrument switches automatically into burst mode when the count rate between 30 and 200 keV exceed a preset value during time intervals selectable by command between 0.125 and 2s. In this mode the time history of the flare is recorded with an integration time of about 8ms during 16s. These 16s begin 2 seconds prior to the trigger instant in order to keep the onset of the flare or a possible precursor. Energy spectra in 16 channels are also stored with 1s time resolution for 16s, 2s time resolution for 32s, and 16s time resolution for 448 seconds (total 8mn 16s). After the 32 kbit memory has been filled, the contents are sent to the telemetry. This burst readout mode lasts 34 mn in tracking mode. During this time count rates are transmitted every 0.5s in tracking mode. Then the experiment goes into a calibration mode. In this mode 32 spectra analysed in 32 channels are transmitted for each of the 2 CsI detectors

The two sensors (Si and CsI) are located on the radial boom of the spacecraft, in order to reduce the RTG background. After a launch in 1990, Ulysses will encounter Jupiter in 1992 and after a gravity assist maneuver will go out of the ecliptic to make 2 solar passes in 94 and 95 The total time spent at ecliptic latitudes more than +-70 degrees will be on the order of 230 days. As there is a shift in time between the maximum number of X-ray and optical flares, it is expected that Ulysses will record a large number of flares during its flight out of the ecliptic. Note that the overall mission takes place during the forthcoming solar maximum and that the experiment will work with almost 100

In addition of the normal data treatment of the experiment telemetry the PIs will have access to quick look data from selected data sets using a remote connection to JPL.

To conclude we mention (not exhaustively) two items for which the Ulysses contribution may be useful:

1. Multispacecraft observations: Ulysses (out of the ecliptic or far from the earth) may record a flare with an in-ecliptic spacecraft (e.g. GRO/BATSE or SOLAR A). This allows the determination of the direct of the emission or the height of the emitting region.

2. Ulysses data may be compared with data taken at other wavelengths from the earth, leading to useful correlations.

Acknowledgments: The Ulysses team consists of K. Hurley, M. Niel and G. Vedrenne (CESR, Toulouse France), M. Sommer and G. Pashmann (MPE, Garching FRG), C. de Jager and J. Reise (SRL, Utrecht The Netherlands), J.-C. Henoux (Obs. de Meudon France) and T. Cline (NASA/GSFC, Greenbelt MD)

VLA-MAX 91 TESTS OF HIGH ENERGY FLARE PHYSICS

Kenneth R. Lang and Robert F. Willson
Department of Physics and Astronomy
Tufts University, Medford, MA 02155

Abstract

The potential for VLA contributions during the coming maximum in solar activity is illustrated by unpublished observations of solar flares on 28 May, 8 June, 24 June and 30 September, 1988; some of this data will appear in the two papers by Willson et al. (1989a,b) referenced at the end of this article. The VLA can be used to spatially resolve flaring active regions and their magnetic fields; these results can be compared with simultaneous X-ray and gamma ray observations from space. We provide examples in which spatially separated radio sources are resolved for the pre-burst, impulsive and decay phases of solar flares. The emergence of precursor coronal loops probably triggers the release of stored magnetic energy in adjacent coronal loops. Noise storm enhancements can originate in large-scale coronal loops on opposite sides of the visible solar disk. An interactive feedback mechanism may exist between activity in high-lying 90 cm coronal loops and lower- lying 20 cm ones.

VLA Studies of Solar Flares

The VLA can be used to spatially resolve the various com- ponents of the active solar atmosphere, thereby improving our understanding of highly energetic, eruptive phenomena such as solar flares, erupting filaments, and coronal mass ejections. This can be done by observing activity across the entire solar disk at 20 cm and 90 cm wavelength. The 20 cm observations resolve coronal loops within active regions, while the 90 cm ones detect larger-scale coronal systems such as filaments and loops that interconnect two active regions or connect one active region with remote regions on the Sun. This capability was not available during the past solar maximum.

Solar flares, or bursts, can be imaged with VLA snapshot maps over times as short as 1.67 seconds. This is possible because microwave flares have a relatively simple structure and high bright- ness relative to the background Sun. The potential of such observations is illustrated by unpublished 20.7 cm observations that resolve the preburst, impulsive and decay phases of a microwave burst into three spatially separated coronal loops or systems of loops. (Figures 1,2,3 and 4).

In this case, the hot, precursor source apparently interacted with an adjacent one, leading to the explosive release of energy during the impulsive phase. The system of coronal sources then seems to have relaxed to a more stable state when yet another nearby source emitted the decay phase. Such studies are related to recent X-ray satellite observations by Machado et al. (1988). They showed that X-ray flaring activity usually involves two or more interacting magnetic bipoles within an active region with an initiating bipole impacting against the adjacent one.

Another unpublished observation (Figures 5 and 6) shows 20.7 cm precursor source seen with the VLA and not detected at hard X-rays. This precursor source is unpolarized and spatially separated from the subsequent impulsive burst which is dipolar and has a time profile that is well-correlated with the hard X-ray emission.

The soft X-ray data (GOES) indicate that the precursor source cannot be due to thermal bremsstrahlung; it is interpreted as the thermal gyroresonance radiation of emerging magnetic loops that trigger subsequent impulsive bursts from nearby coronal loops. Both the temperature and dipolar structure of the impulsive radiation are explained by the gyrosynchrotron radiation of energetic electrons in a dipolar loop. The injection of these electrons also explains the simultaneous hard X-ray emission.

VLA observations will also provide insight to other explo- sive solar phenomena such as coronal mass ejections and/or filament eruptions that may not be associated with impulsive solar flares. Current theoretical scenarios invoke instabilities and the eruption of large-scale magnetic arcades, or helmut streamers, that drive a coronal mass ejection and initiate sub- sequent filament eruption and/or flare emission (Priest 1988). If these models are correct, then the initiating source and driving mechanism for coronal mass ejections may occur in the low solar corona and they might be only weakly coupled to the visible solar surface. Because the low solar corona is blocked by the occulting disks of coronagraphs, the VLA will provide one of the only ways of studying the triggering of coronal mass ejections during the coming maximum. These ejections will be subsequently viewed by coronagraphs as they propagate out through the middle and upper corona.

There is also uncertainty about the unknown source that ini- tiates and continually excites solar noise storms for hours. Stewart, Brueckner and Dere (1986) have shown that the onset or cessation of noise storm activity is correlated with changes in large-scale coronal magnetic fields within an active region. VLA observations during MAX 91 at 20 cm and 90 cm wavelengths will provide insight to these phenomena.

Summary

The VLA can provide information on the location and method of energy release during explosive solar flares, and specify brightness and polarization structure during their

preflare, impulsive, and post-flare stages. Information on preburst heating and magnetic flare triggering can be obtained, and theoretical models for solar flares can be tested. The location of primary energy release at micro- wave wavelengths can be established. Thermal and magnetic evolution in the low solar corona can also be studied, perhaps establishing an initiating mechanism for coronal mass ejections. As discussed in another part of these workshop proceedings, in a paper entitled "VLA Capabilities for MAX 91" the VLA should be used for two-week observing campaigns in support of NASA solar observing flights. The VLA observations should also be coordinated with other ground-based telescopes to fully exploit the scientific return of the MAX 91 campaign.

References

Machado, M.E., Moore, R.L., Hernandez, A.M., Rovira, M.G., Hagyard, M.J., and Smith, J.B. 1988, "The Observed Character- istics of Flare Energy Release. I. Magnetic Structure and the Energy Release Site." Astrophysical Journal 326, 425-450.

Priest, E.R. 1989, "The Initiation of Solar Coronal Mass Ejections by Magnetic Non-Equilibrium." Astrophysical Journal 328, 848- 855.

Stewart, R.T., Brueckner, G.E., and Dere, K.P. 1986, "Culgoora and Skylab EUV Observations of Emerging Magnetic Flux in the Lower Corona." Solar Physics 106, 107-130.

Willson, R.F., Lang, K.R., Kerdraon, A., Klein, L., and Trottet, G. 1989, "Multi-wavelength Observations of Energy Release During a Solar Flare." Submitted to Astronomy and Astrophysics.

Willson, R.F., Lang, K.R., Schmelz, J.T., and Smith, K.L. 1989, "Multiple-wavelength SMM-VLA Observations of an M2-Class X-ray Flare and an Associated Coronal Mass Ejection." Submitted to the Astrophysical Journal.

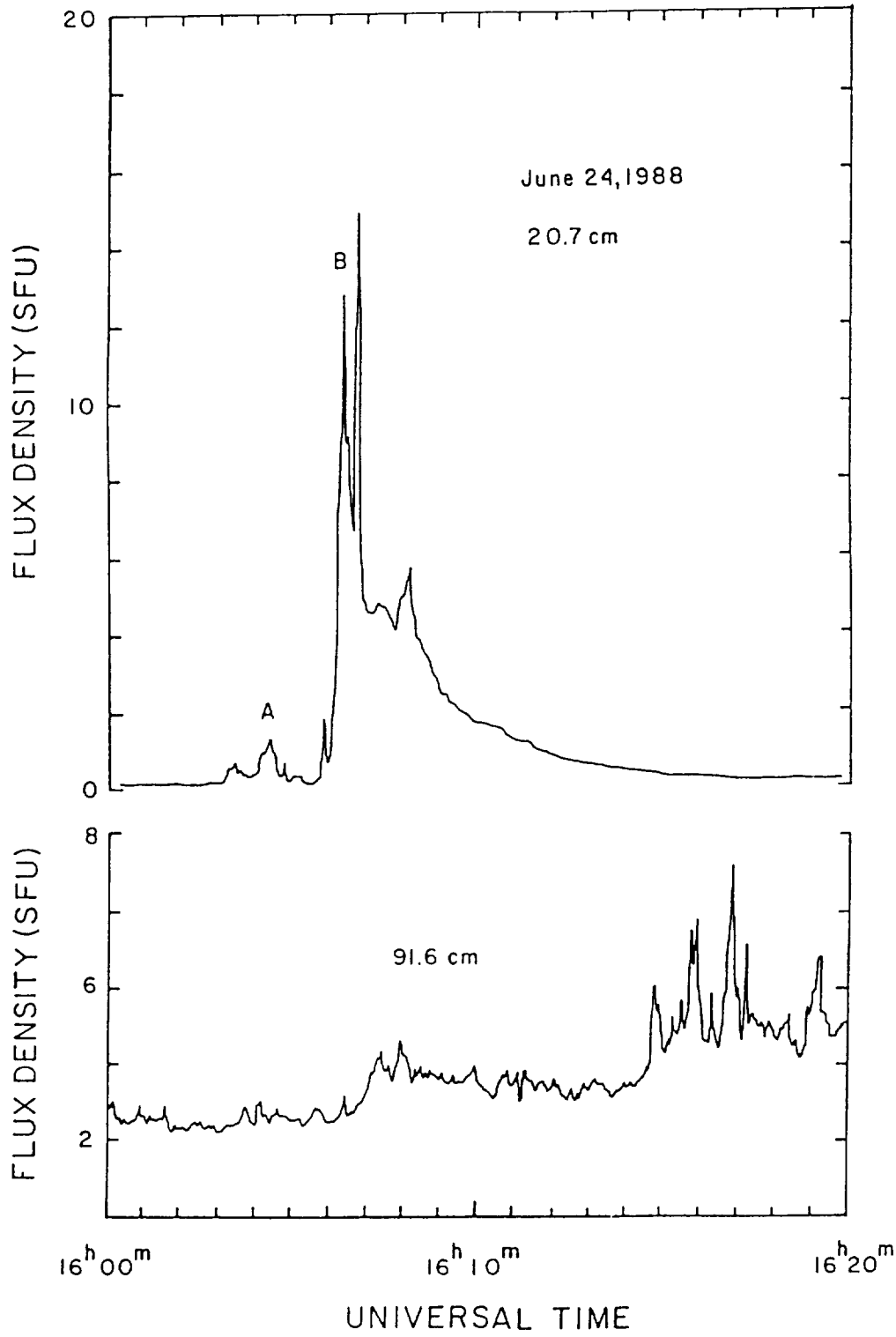

Fig. 1. The time profile of a 20.7 cm (1446 MHz) flare has a pre-burst (A), impulsive (B) and post-burst components that are spatially resolved with the VLA in different coronal sources (Figures 2 and 4). The bottom profile shows the impulsive burst and a subsequent noise storm at 91.6 cm wavelength (327.5 MHz).

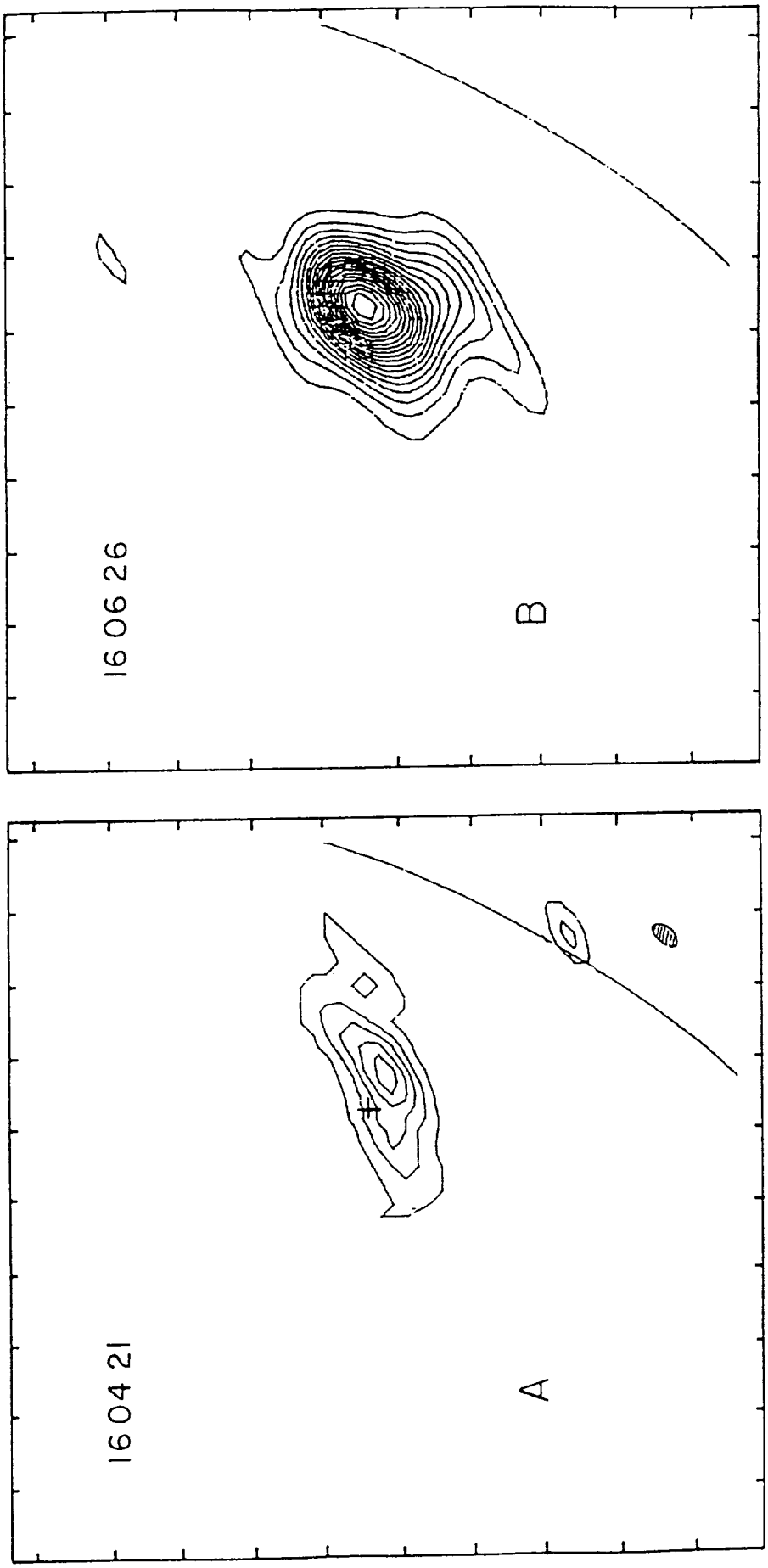

Fig. 2. The VLA resolves the preburst (A) and impulsive (B) components of a 20.7 cm flare into spatially seperated components with peak brightness temperatures of $T_{B_{max}}$ = 4.4 x 10^6 K and 1.0 x 10^8 K, respectively, and respective angular sizes of θ= 90" x 180" and 180".

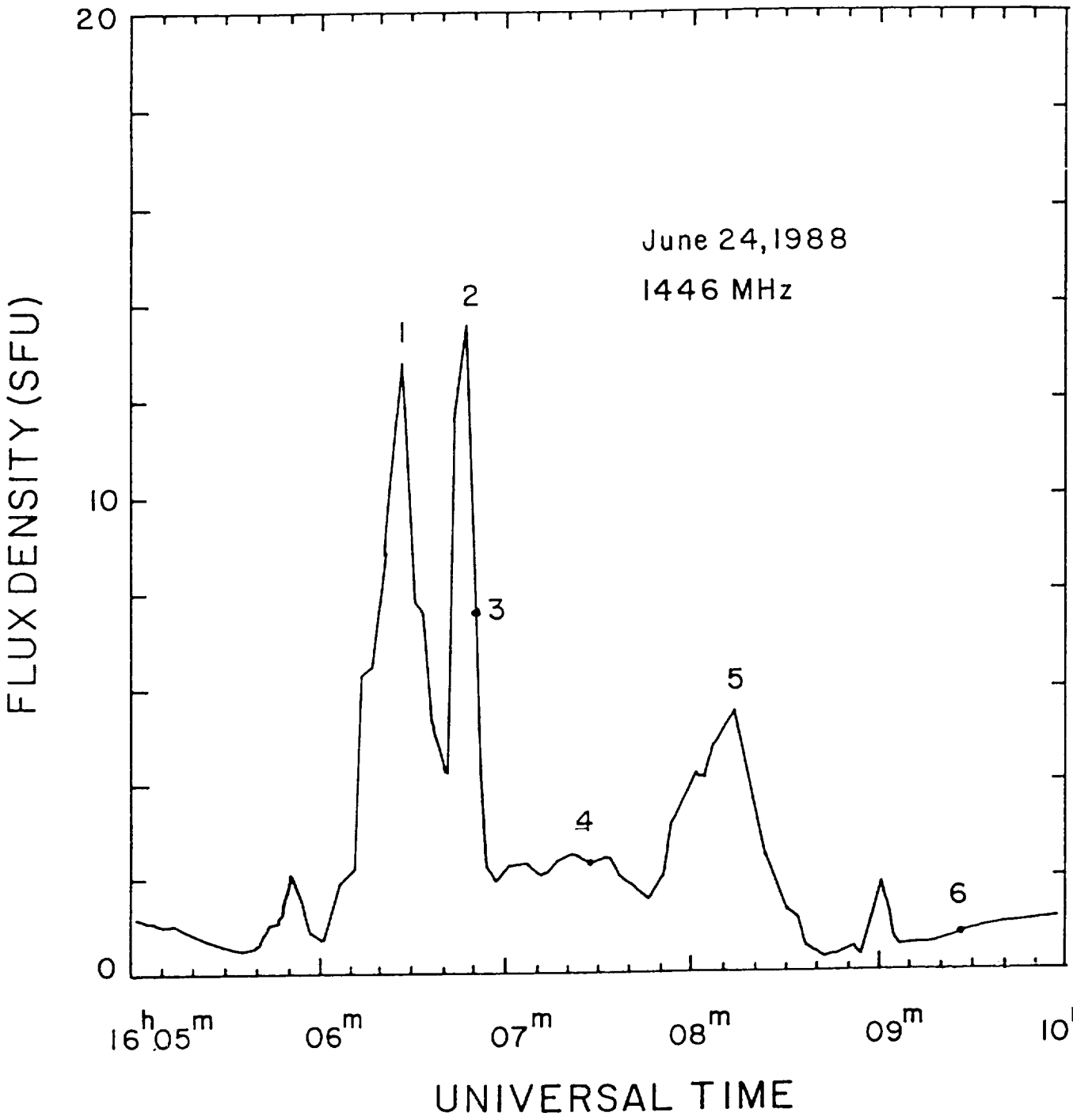

Fig. 3. An expanded time profile of the impulsive (1 and 2) and post-burst (3,4,5 and 6) components of a 20.7 cm flare. The two components come from spatially separated sources (see Figure 4).

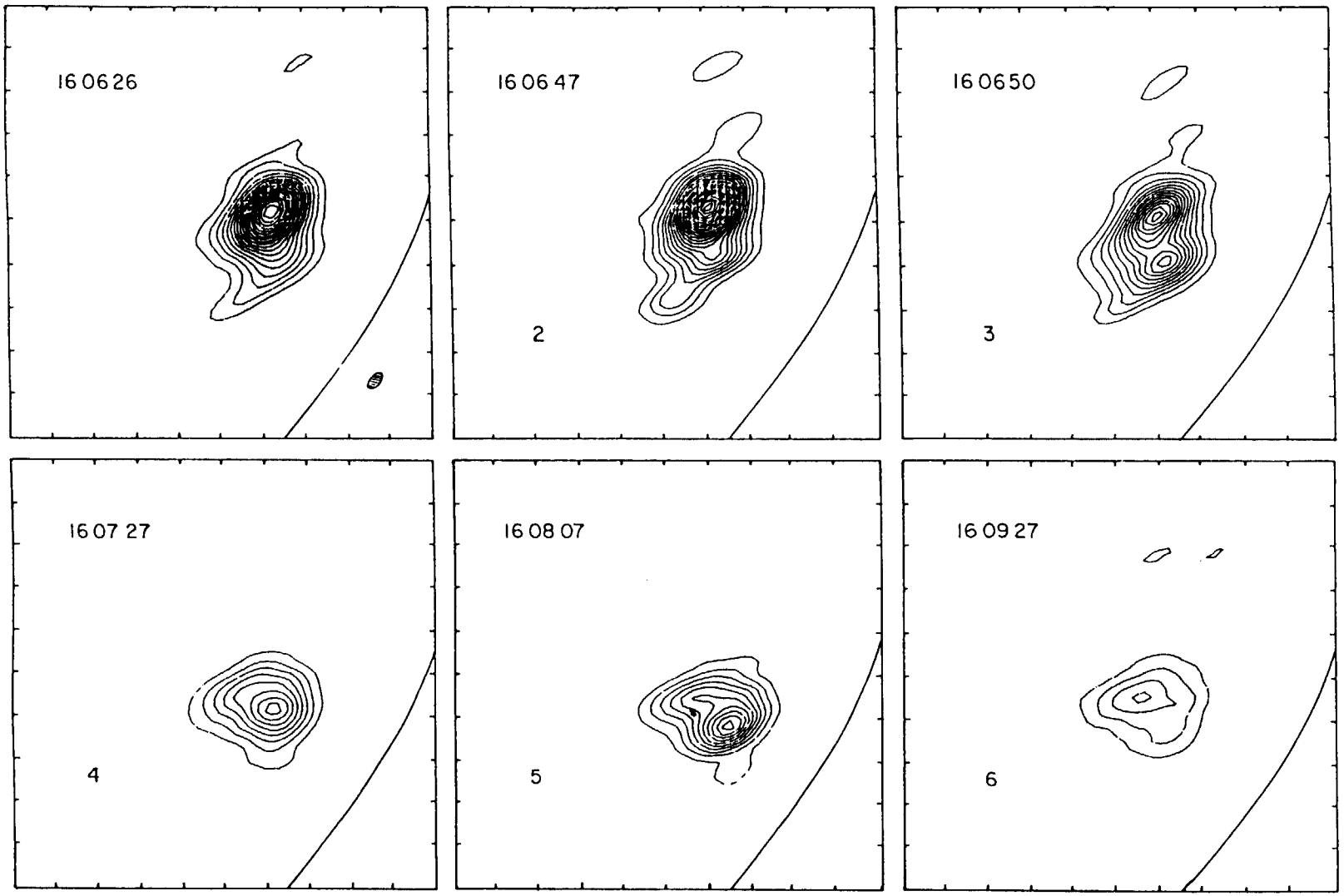

Fig. 4. The impulsive components (1 and 2) of a microwave burst are resolved with the VLA; they come from the same source with a peak brightness temperature of $T_{B_{max}} = 1.0 \times 10^8$ K and an angular extent of $\theta = 180''$. The post-burst emission comes from a spatially separated source that was first detected during the decay of the impulsive source 2 at time 3, and remained fixed in position and size for all subsequent times 4,5,and 6.

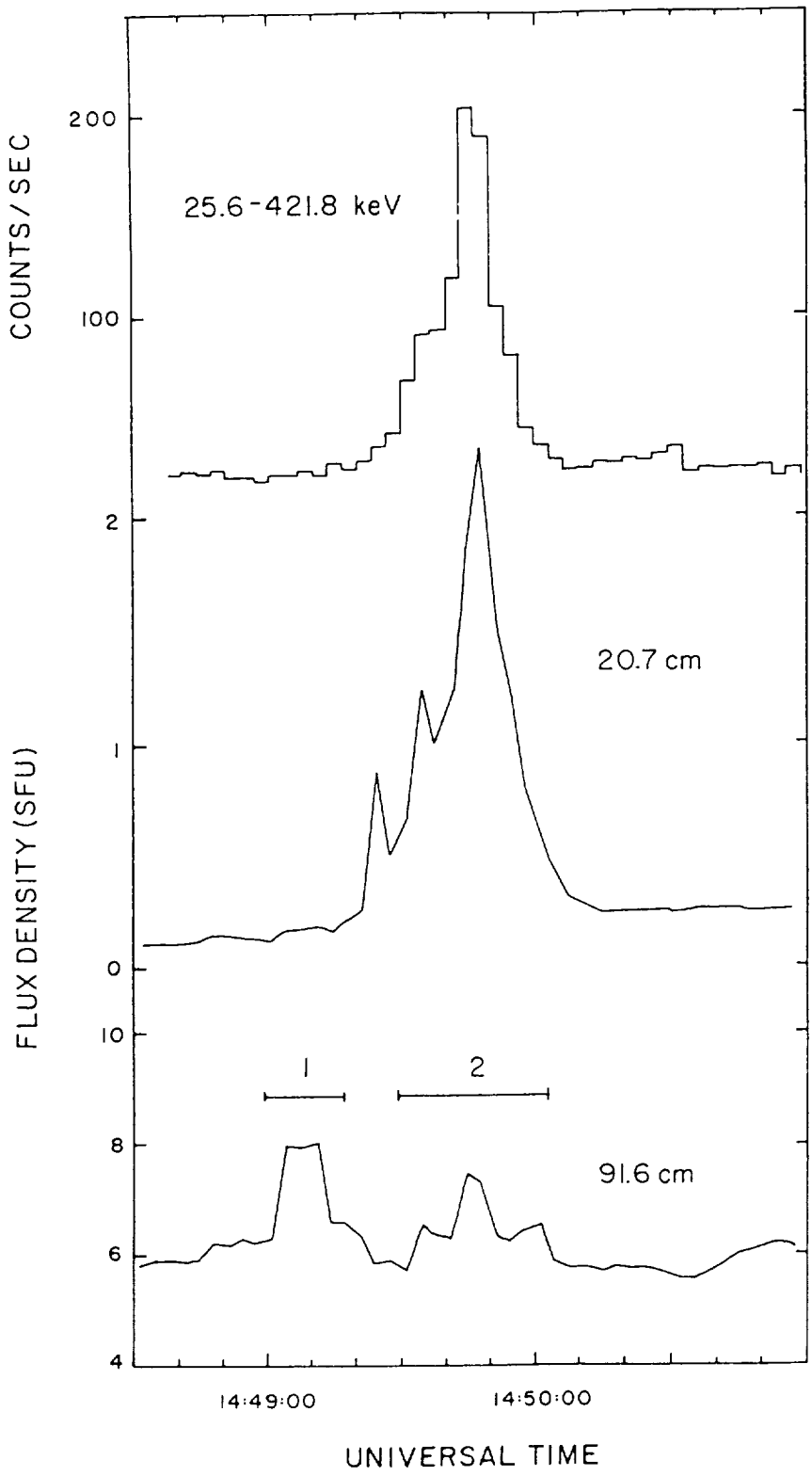

Fig. 5. The time profile of a 20.7 cm burst (middle) exhibits precursor emission that is not detected at hard X-ray wavelengths (top). Subsequent burst emission in the two spectral domains is well-correleted and is attributed to energetic electrons within a dipolar loop. The preburst and impulsive components are resolved by the VLA into two spatially separated components (see Figure 6).

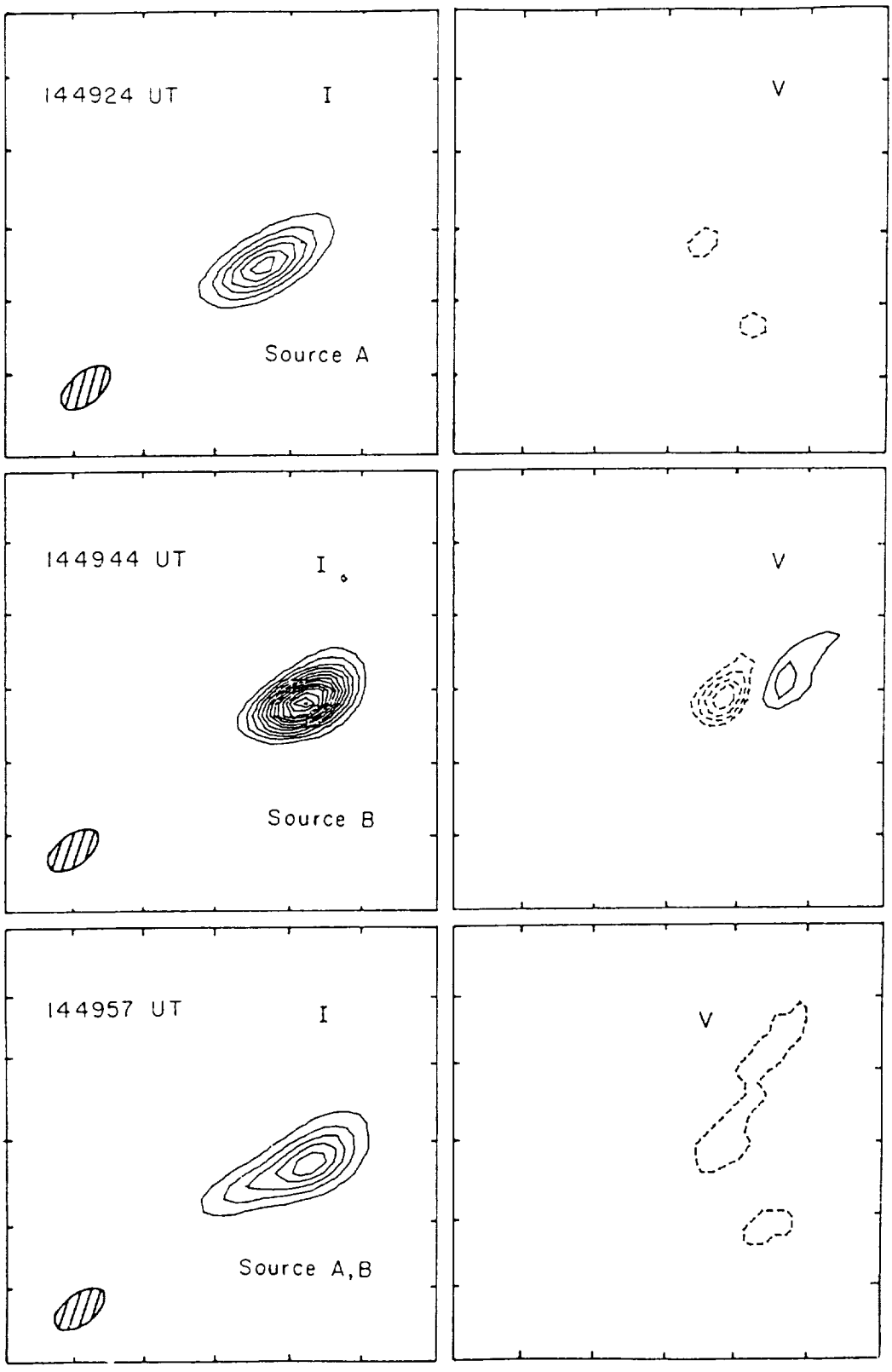

Fig. 6. The preburst emission A, is attributed to emerging coronal loops that triggered subsequent impulsive radiation from the dipolar source B. Both components have been resolved with the VLA with peak brightness temperatures of $T_{B_{max}}$ = 6.6×10^6 K and 1.5×10^7 K and angular sizes of θ= 30" x 60".

FIRST INTERFEROMETRIC OBSERVATIONS WITH ARC-SEC. RESOLUTION OF SOLAR RADIO BURSTS AT MILLIMETER WAVELENGTHS

M.R. Kundu, S.M. White, N. Gopalswamy
(U. Maryland)

and

J.H. Bieging
(U.C., Berkeley)

ABSTRACT

We provide a brief description of the Berkeley-Maryland-Illinois Array (BIMA) in the context of solar observations. Specific areas of research that could be attempted using BIMA during the Max'91 period are outlined. Finally, some preliminary results of flare observations during March 1989 are presented.

The Astronomy Program of the University of Maryland has recently joined the Universities of California (Berkeley) and Illinois in a consortium to upgrade the Hat Creek millimeter-wave interferometer (to be known as the Berkeley-Illinois-Maryland Array, or BIMA). The improved array will become available during the coming Solar Maximum, and we will have guaranteed time for solar observing as part of the consortium. We plan to make quasi-dedicated observations for long periods (10-15 days at a time), depending on solar activity.

(i) BIMA Array

The Hat Creek millimeter interferometer presently consists of three 6-m diameter antennas which can be located at various stations along a T-shaped road-way which extends 300 m East-West and 200 m North-South. Current operation is in the 2.5 - 4 mm wavelength atmospheric window. The receivers employ cooled Schottky diode mixers. The receivers can be tuned by a solid state oscillator from 70 to 115 GHz. Retuning takes about 5 - 15 minutes. Both sidebands of the first mixer are received and are separated by phase switching of the local oscillators. Thus, two frequencies separated by 2.3 GHz can be observed simultaneously. One linear polarization is received. A quarter-wave plate to produce circular polarization around 90 GHz is available. The receiver, antenna and atmosphere contribute to the system temperature. Scaled to above the atmosphere, the temperature is typically 300 to 500 K SSB over most of the band, rising to about 1000 K at 115 GHz where the opacity is greater.

The BIMA consortium will expand this interferometer into a 6-element array with 15 baselines. Work is already in progress for this expansion, and it is expected to be completed in late 1990 or early 1991. This array with 15 baselines will permit us to produce synthesized snapshot maps of solar flares at one or more frequencies in the range 70 - 240 GHz. Before this expansion is

completed, however, we shall use the instrument as a 3-element interferometer. This will be useful to find the positions of strongest burst sources with temporal resolution $\gtrsim$ 0.1 sec and spatial resolution $\gtrsim$ 1" arc. When the imaging instrument (6-element array) is completed, we will have a seventh antenna at our disposal which we plan to use at 3 or 4 wavelengths (20 mm, 10 mm, 3 mm and 1.3 mm) in order to obtain spectral information of mm burst sources.

ii) Science Objectives

The millimeter region has been perhaps the most under-utilized observing wavelength range in solar physics, due to the lack of telescopes which can match the temporal and spatial resolution available at other wavelengths. Millimeter wave observations are sensitive to both the highest-energy electrons in flares as well as to cool material in the chromosphere. Since we have only 3 antennas available at the present time, we shall concentrate on studies of flares.

ii (a) Flare Physics

Highly energetic particles accelerated in flares radiate strongly at millimeter wavelengths: in particular, since gamma-ray imaging is presently difficult, a millimeter array is the only method of imaging the most energetic particles in flares, and we propose many important studies using this fact. Using high time ($\gtrsim$ 0.1 sec) and spatial ($\lesssim$ 1") resolution, we will study particle acceleration in the impulsive phase, and the location of acceleration region in relation to other flare features. In gamma ray-mm wave flares recent evidence (from Solar Maximum Mission and mm wave observations) has demonstrated that electrons and protons are accelerated almost simultaneously to very high energies. In particular, electrons attain energies of 10 to 100 MeV within one or two seconds of flare onset, and emit both mm waves and continuum gamma rays of high intensity. This continuum radiation is accompanied by nuclear gamma ray lines at energies less than ~ 10 MeV due to protons, and neutrons are somtimes

detected at Earth (Chupp, E.L., Ann. Rev. Astr. Ap. 22, 359, 1984). At the present time there is no widely accepted explanation for this very rapid acceleration. Some argue that there must be a "first phase" process because of the very short time scale, possibly involving electric fields in double layers. Others argue that shock acceleration can act on short enough time scales (Decker, R.B., and Vlahos, L., Prompt Acceleration of Ions By Oblique Turbulent Shocks in Solar Flares, International Cosmic Ray Conference, La Jolla 1985). In the radio range, the spectral characteristic of gamma ray-mm wave flares is that the flux density increases with frequency.

We hope to add greatly to the understanding of prompt acceleration in flares using temporal and spatial resolution previously unavailable. Delays between gamma-ray and millimeter peaks will be studied in conjunction with spatial information on the location of the millimeter sources, which, along with information in microwaves, will allow us to investigate the propagation of energy from the corona to the chromosphere during the impulsive phase. We will also establish whether gamma-rays and millimeter-waves come from identical regions by studying the anisotropy of millimeter-wave flares on the disk.

ii (b) Electron Beams

In many flares, brightenings occur in Hα, EUV and even white light simultaneously with hard X-ray bursts. There is a controversy over the cause of these brightenings, whether due to electrons, protons, or an ion acoustic conduction front. Each method has problems: it is uncertain whether electrons are able to penetrate deeply enough into the dense atmosphere; we do not know how to accelerate an adequate number of protons in the required 1 s; and heat conduction by an ion acoustic front may be too slow (Dulk, G.A., Gary, D.E., Hjellming, R.M., and Kundu, M.R., Report of the Working Group on the Sun and Stars, Proc. NRAO Millimeter Array Workshop 1986).

Observations of mm waves can help answer these questions because they originate in the relevant region of the atmosphere, namely the low chromosphere, in contrast to cm waves which originate in the lower corona. If the mm wave emission in some flares is due to thermal bremsstrahlung from the heated plasma, it is relatively easy to relate radio wave brightness to the density-temperature structure in the heated region. The relative timing of mm wave vs. cm wave bursts should help distinguish among the possible causes.

iii) Preliminary Results From Interferometric Observations at 3 mm Wavelength

Using the presently available 3-element BIMA telescope we were able to observe the active region 5395, which produced an X-15 flare and many X- and M-class flares, during the period March 12-18, 1989 (the second half of its disk passage). For most of this time only one base line was available (because one receiver was not operational), and the weather was not good enough to measure the phase. Thus, positional data are not available. BIMA was in its widest configuration (spatial resolution ~ 1" arc), but the time resolution was only 10 seconds. With this system we observed several X- and M-class flares - all associated with optical Hα flares and/or microwave burst emission (as observed with the Owens Valley microwave inteferometer). The most striking result that has come out of these observations is that most millimeter bursts are spiky (that is unresolved with 10 sec time resolutions, see Fig. 1); there is a considerable amount of burst emission from sources of size < 1" arc. Three-base-line observations show that the source structure is not symmetric (Fig. 2). Corresponding to a typical microwave burst observed at OVRO with 3 sec time resolution with an impulsive phase followed by a post-burst, we observed a complex 3 mm burst with many spikes both during the impulsive and the post-burst phase (Fig. 1a). This suggests that at mm wavelengths we are really observing

different flare kernels which brighten up sequentially, so that spatial structure is seen as time structure as schematically illustrated in Fig. 1c.. We have observed one spike corresponding to a hard X-ray spike (Fig. 3) and UV-emission (Fig. 3a) observed by the SMM-HXRBS and SMM-UVSP experiments. There is good correspondence between the two time profiles (within 10 sec time resolution); hard X-rays were observed up to 100 Kev. The power-law spectrum (Fig. 3b) is not particularly hard - somewhat softer than what is observed in Y-ray flares.

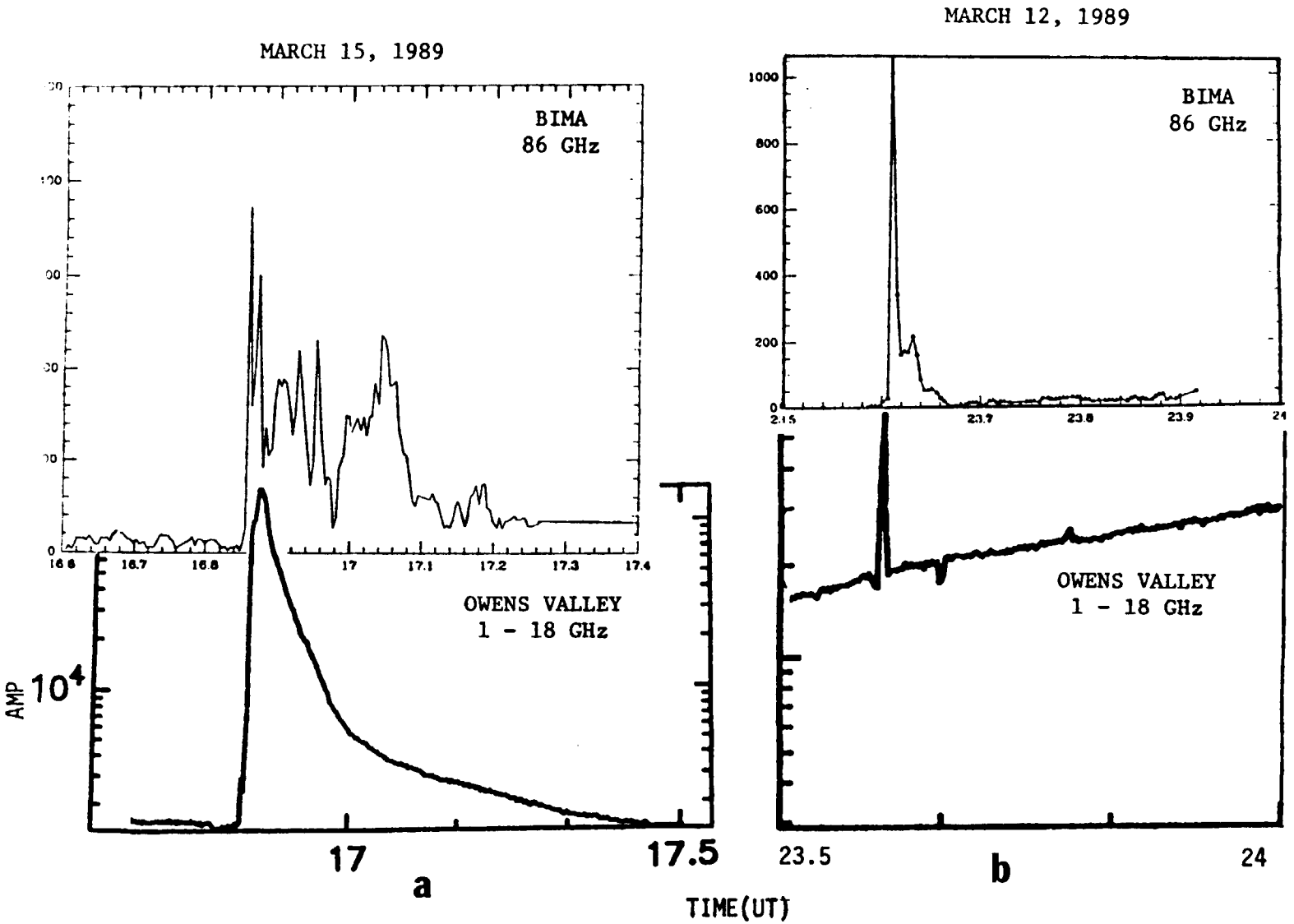

Fig. 1: With 1" arc spatial and 10 sec temporal resolution 3 mm bursts apppear as intense spikes - sometimes simple, sometimes complex. A significant part (probably a few percent) of the total flare emission at this wavelength appears to originate from kernels < 1" arc or < 700 km. This is the first direct measurement of such small scale structures in flaring regions. We believe that the flare kernel brightens up sequentially and appear as temporal structures.

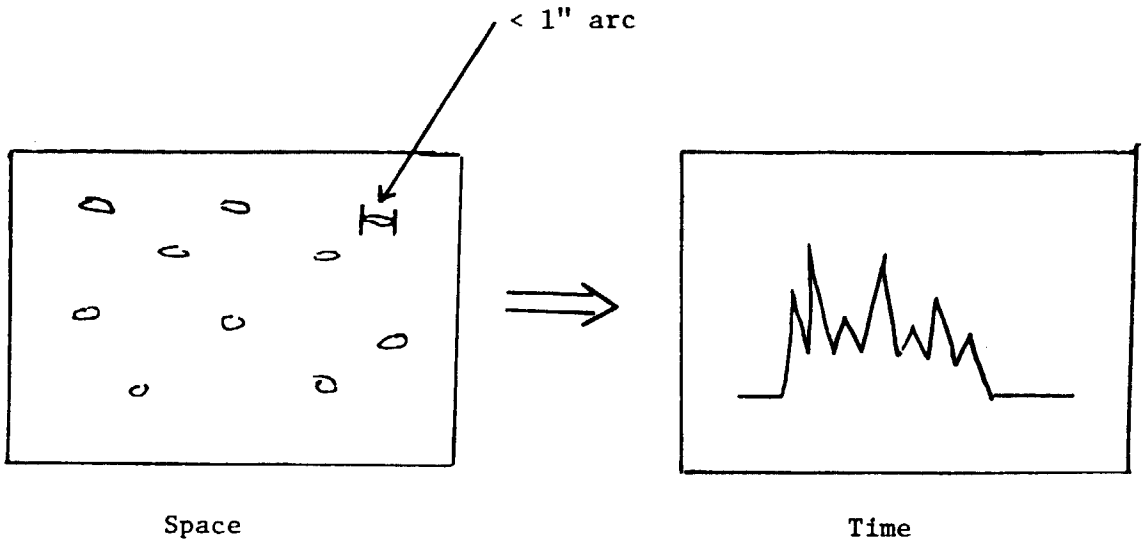

126

FIG. 1C

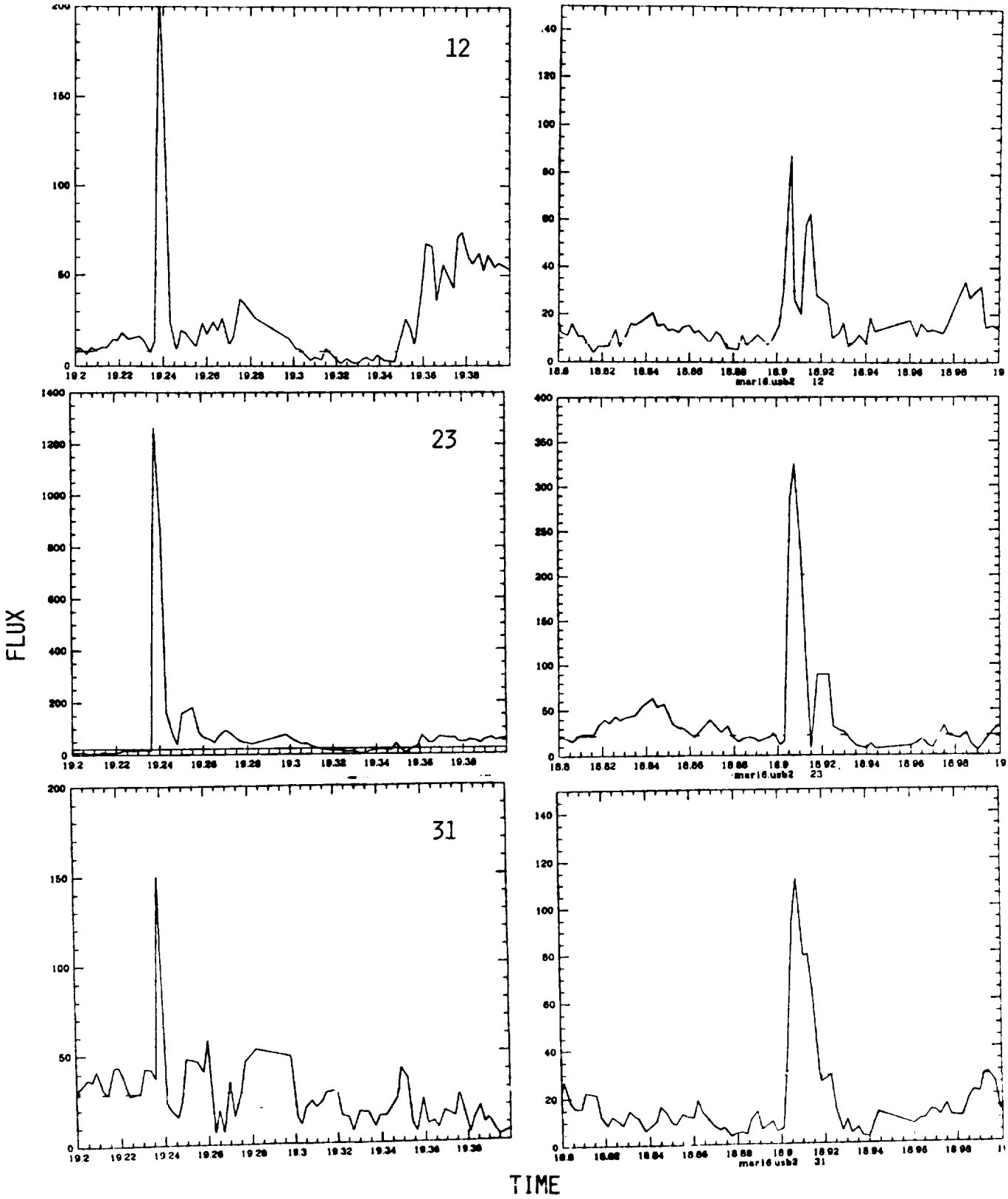

Fig.2 : Time profiles of two flares on March 16 1989 indicating assymmetry in the source. Note that the flux is larger by factors of 3 (right) and 10 (left) in the 2-3 base line compared to 1-2 and 3-1.

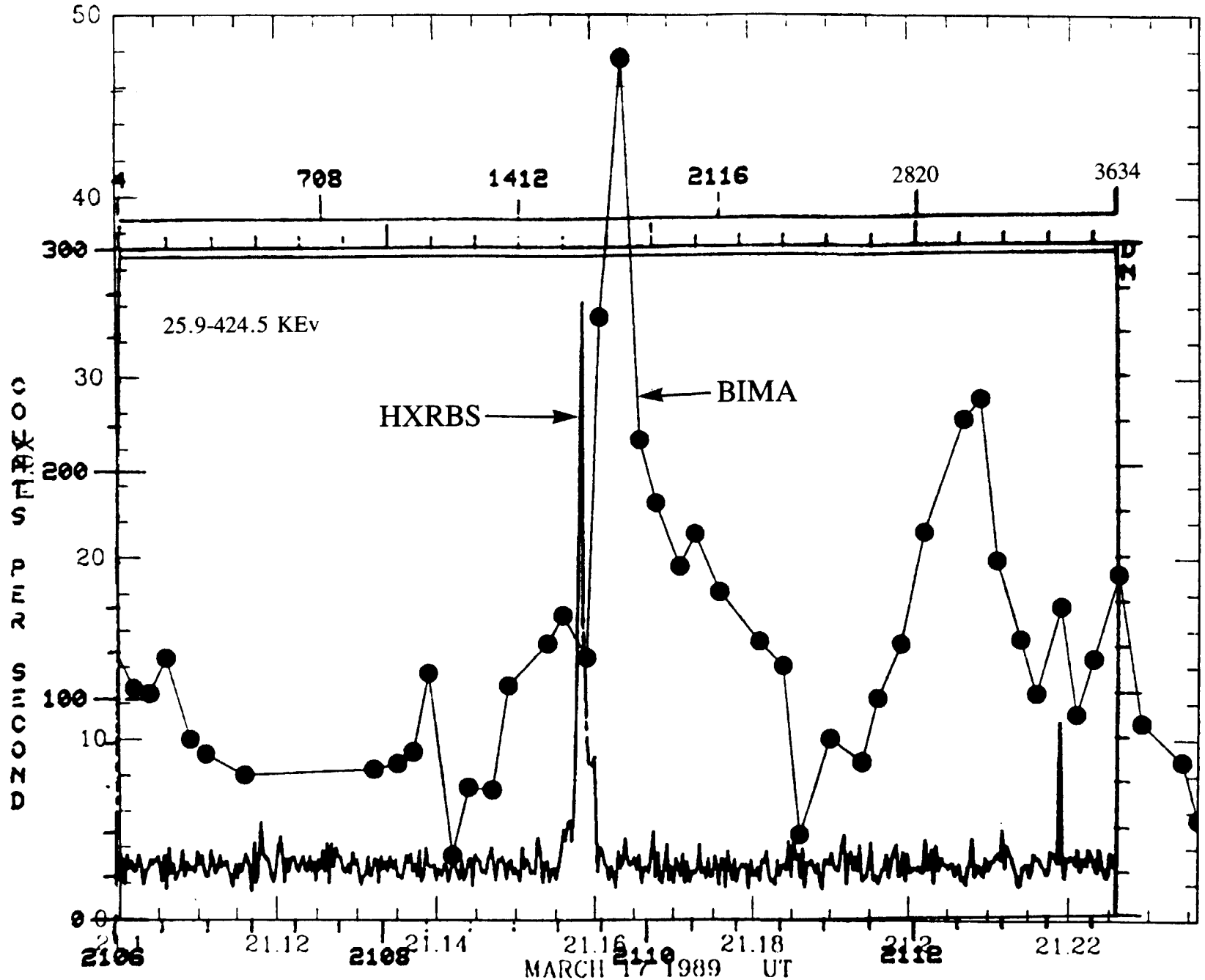

Fig.3 : Comparison between mm(BIMA) and SMM-HXRBS time profiles of March 17 1989 Flare. (Courtesy of R. Schwarts and B. Dennis for HXRBS data).

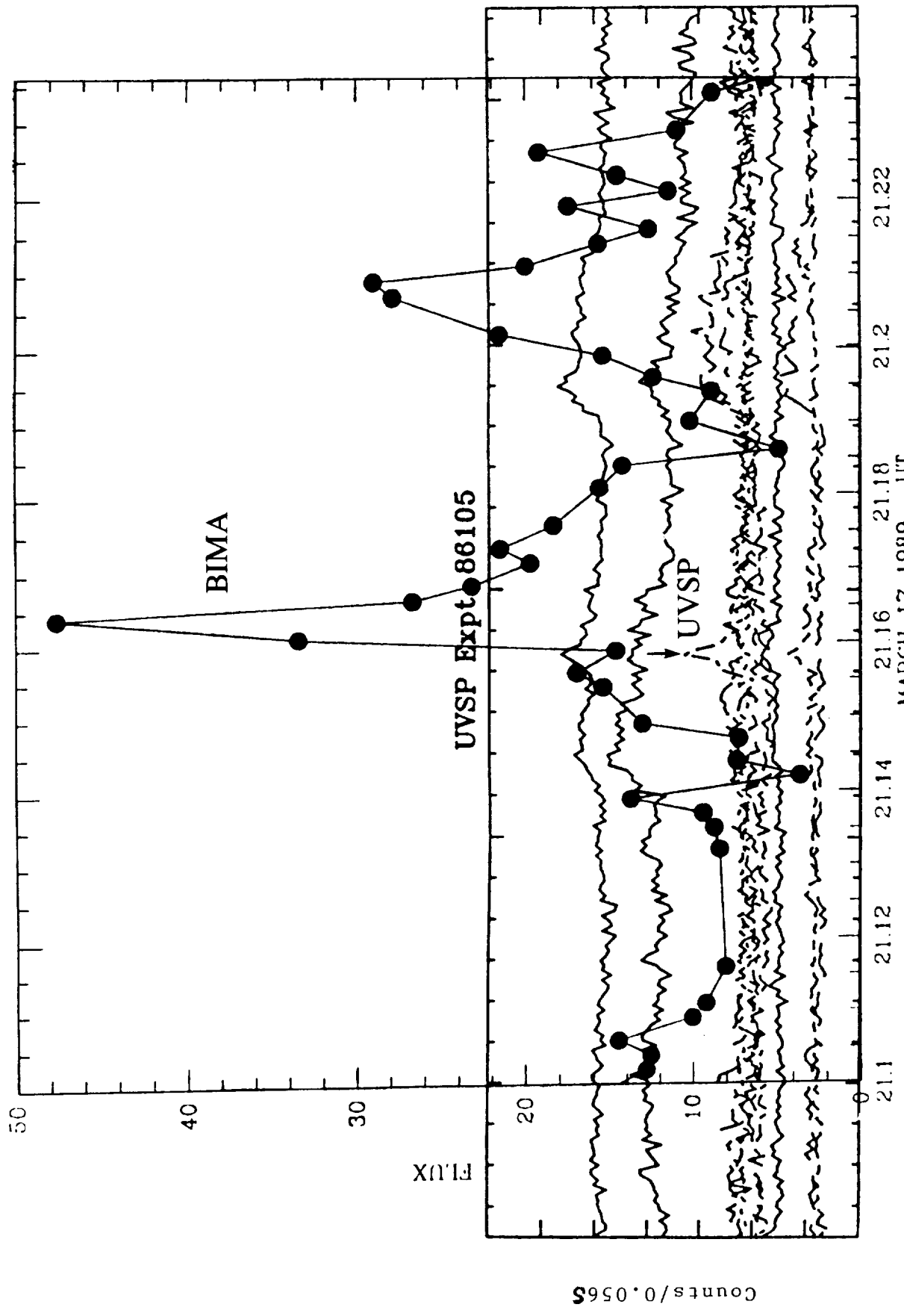

Fig.3a : Comparison between mm(BIMA) and UVSP time profiles for March 17 1989 Flare. (Courtesy of J. Gurman for UVSP data).

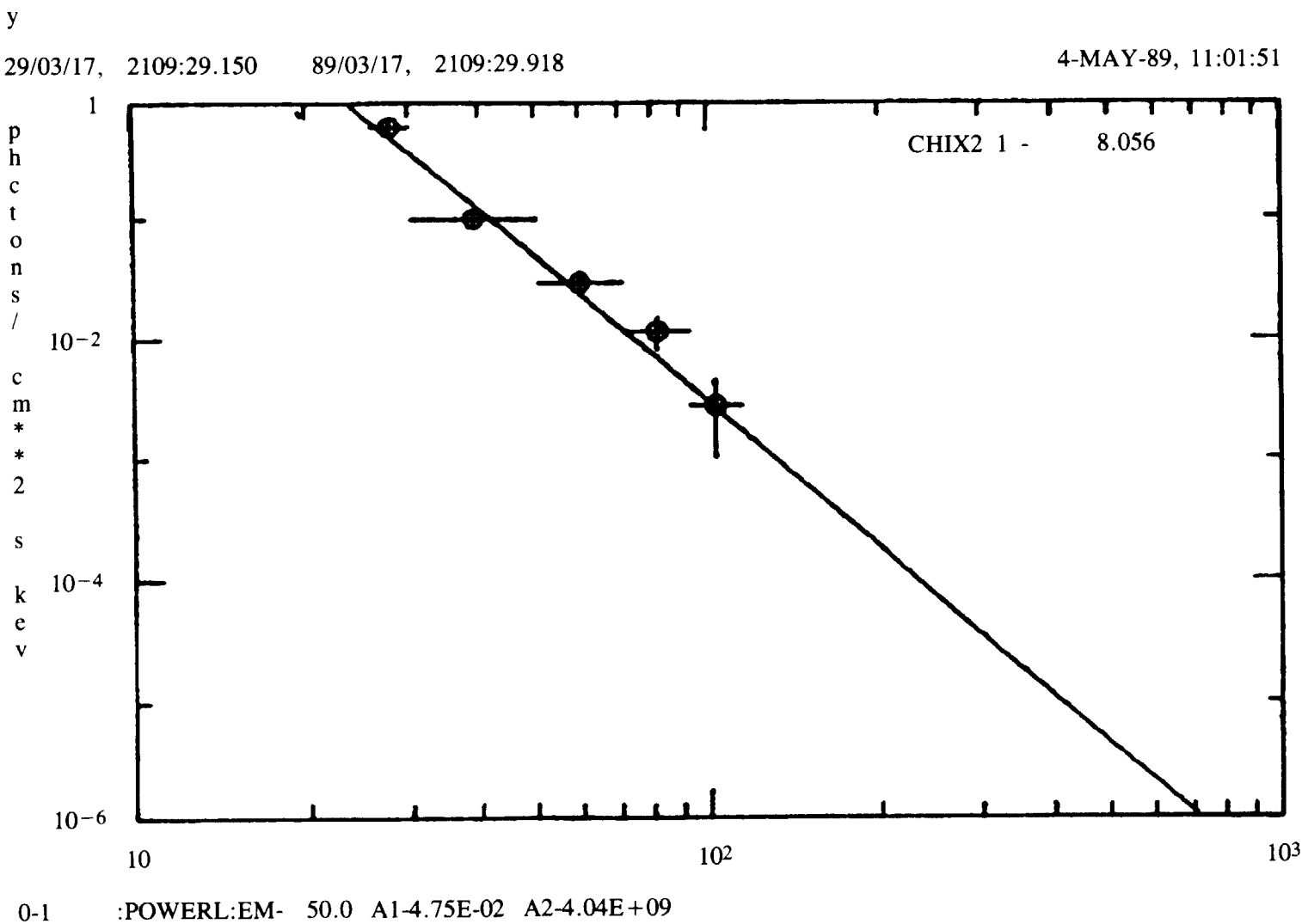

Fig.3b : Power spectrum of the March 17 1989 Flare from HXRBS.
(Courtesy of R. Schwartz and B. Dennis)

Observational Goals for Max '91 to Identify

the Causative Agent for Impulsive Bursts

D. A. Batchelor (NASA/GSFC)

Recent studies of impulsive hard X-ray and microwave bursts suggest that a propagating causative agent with a characteristic velocity of order 1000 km s^{-1} is responsible for these bursts. In this presentation, the results of those studies will be summarized and observable distinguishing characteristics of the various possible agents will be highlighted, with emphasis on key observational goals for Max '91 campaigns. The most likely causative agents suggested by the evidence are shocks, thermal conduction fronts, and propagating modes of magnetic reconnection in flare plasmas (although other possible agents cannot as yet be ruled out). With the new instrumentation planned for Max '91, high spatial-resolution observations of hard X-ray sources have the potential to identify the agent by revealing detailed features of source spatial evolution. Coordinated observations with the Very Large Array and other radio imaging instruments are also obviously of great importance, as well as detailed modeling of coronal loop structures to place limits on density and temperature profiles in the loops. With the combined hard X-ray and microwave imaging observations, aided by loop model results, the simplest causative agent to rule out would be the propagating modes of magnetic reconnection. To fit the observational evidence, reconnection modes would need to travel at approximately the same velocity (the Alfvén velocity) in different coronal structures that vary in length by a factor of 10^3. Over such a vast range in loop lengths, it is difficult to believe that the Alfvén velocity is constant. Thermal conduction fronts would be suggested by sources that expand along the direction of **B** and exhibit relatively little particle precipitation. Particle acceleration due to shocks could produce more diverse radially expanding source geometries with precipitation at loop footpoints.

I. INTRODUCTION

The main objective of research on solar and stellar flares is the discovery of the process responsible for the unpredictable, rapid, enormous releases of energy that occur in flares. The clearest observational clues are the impulsive X-ray and microwave radiations emitted during flares because these radiations offer the most direct information about the energy release process that boosts the radiating particles to an energy per particle E $\geq$ 25 keV (see Fig. 1).

There is ample evidence that simultaneous impulsive bursts of hard X rays (photon energy range from 25 keV to 500 keV) and microwaves (3 GHz $\leq f \leq$ 100 GHz band) both radiate from one distribution of energetic electrons (Takakura and Kai 1966; Mätzler 1978; Gary 1985; Schmahl, Kundu, and Dennis 1985; Kai 1986). The X rays are bremsstrahlung and the microwaves are gyrosynchrotron radiation. Crannell *et al.* (1978) made the assumption of a common source electron distribution, interpreted the hard X-ray spectra as thermal bremsstrahlung, and introduced a method to derive a characteristic length scale of a burst source. Their analysis showed that the rise times of solar impulsive bursts were correlated with spatial length scales of the sources. The correlation was confirmed by Batchelor *et al.* (1985) and Batchelor (1987), using *SMM* observations of hard X rays and microwave observations from Bern, Toyokawa, and Itapetinga observatories. The correlation is linear, consistent with the thermal conduction front model (TCF, see Brown, Melrose, and Spicer 1979).

A similar method for deriving source lengths was used in the work described herein, but it was adapted for use with *nonthermal* source models. The observations analyzed by Batchelor *et al.* (1985) and Batchelor (1987) were re-analyzed, employing the standard nonthermal models in the literature, the thick-target model (TT, Brown 1971) and trap-plus-precipitation model (TP, Melrose and Brown 1976).

II. METHOD OF ANALYSIS

The analysis method is briefly described in this section; a more detailed description of the method was given by Batchelor *et al.* (1985) and Batchelor (1989). The hard X-ray observations were made with the Hard X-ray Burst Spectrometer (HXRBS, see Orwig, Frost, and Dennis 1980). The microwave observations were made at Bern (Magun *et al.* 1981), Toyokawa (Torii *et al.* 1979), and Itapetinga (Kaufmann *et al.* 1982).

If the microwave spectrum of a burst is known throughout a sufficiently broad band, it generally exhibits a low-frequency segment with positive spectral index α (*i.e.* flux density $S \propto f^{\alpha}$, where f is frequency in Hz) and a high-frequency segment with negative α (the full spectrum is termed "C-type", Guidice and Castelli 1975; see Fig. 2 for examples). The positive-α segment is usually attributable to emission that is optically thick, due to self-absorption, and the negative-α segment to emission that is

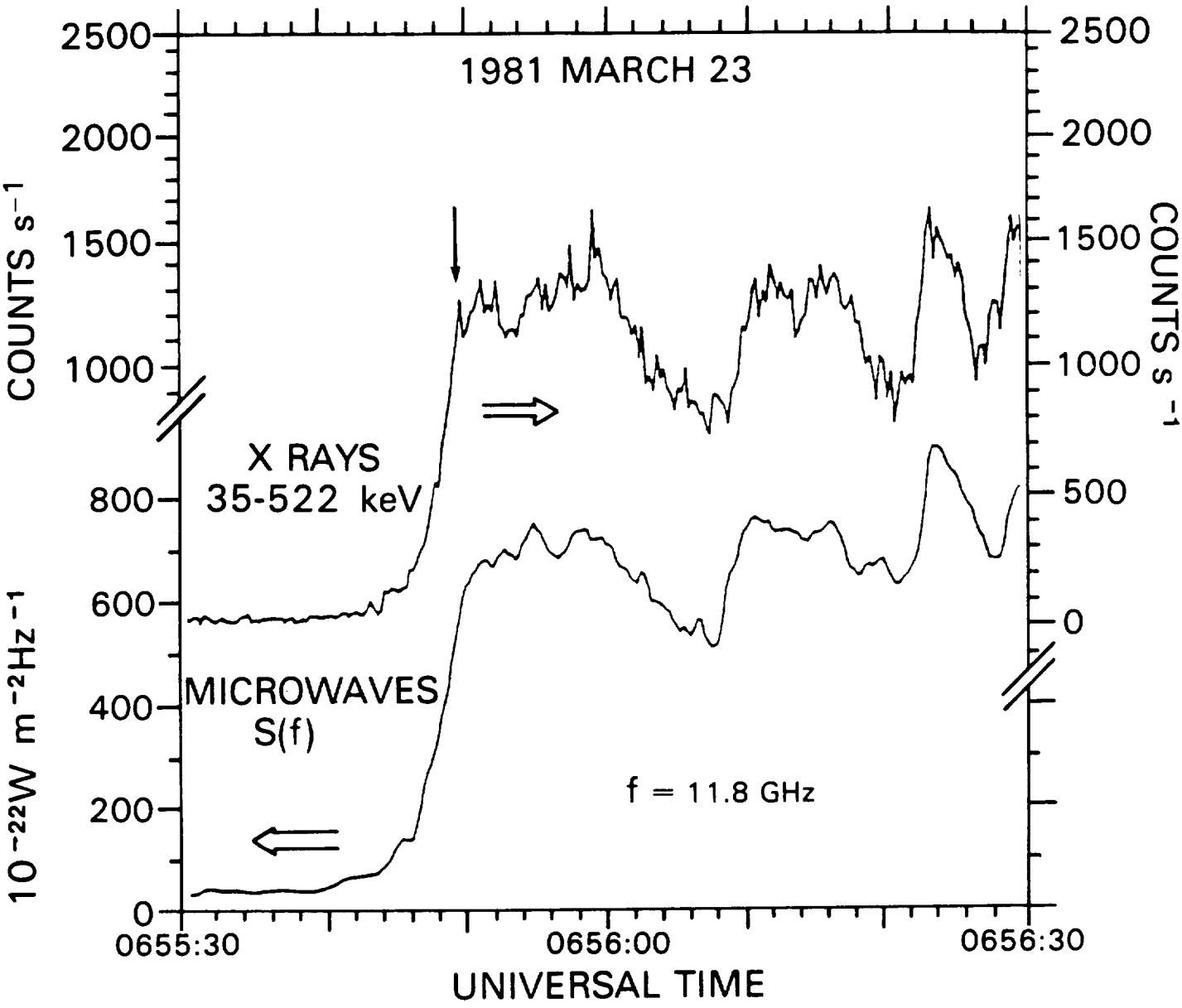

Figure 1. An impulsive solar burst of hard X rays and microwaves (HXRBS and Bern data respectively). The descending arrow marks the end of the first steady, impulsive rise during this burst, and the flux at this time was used to determine t_r (see text).

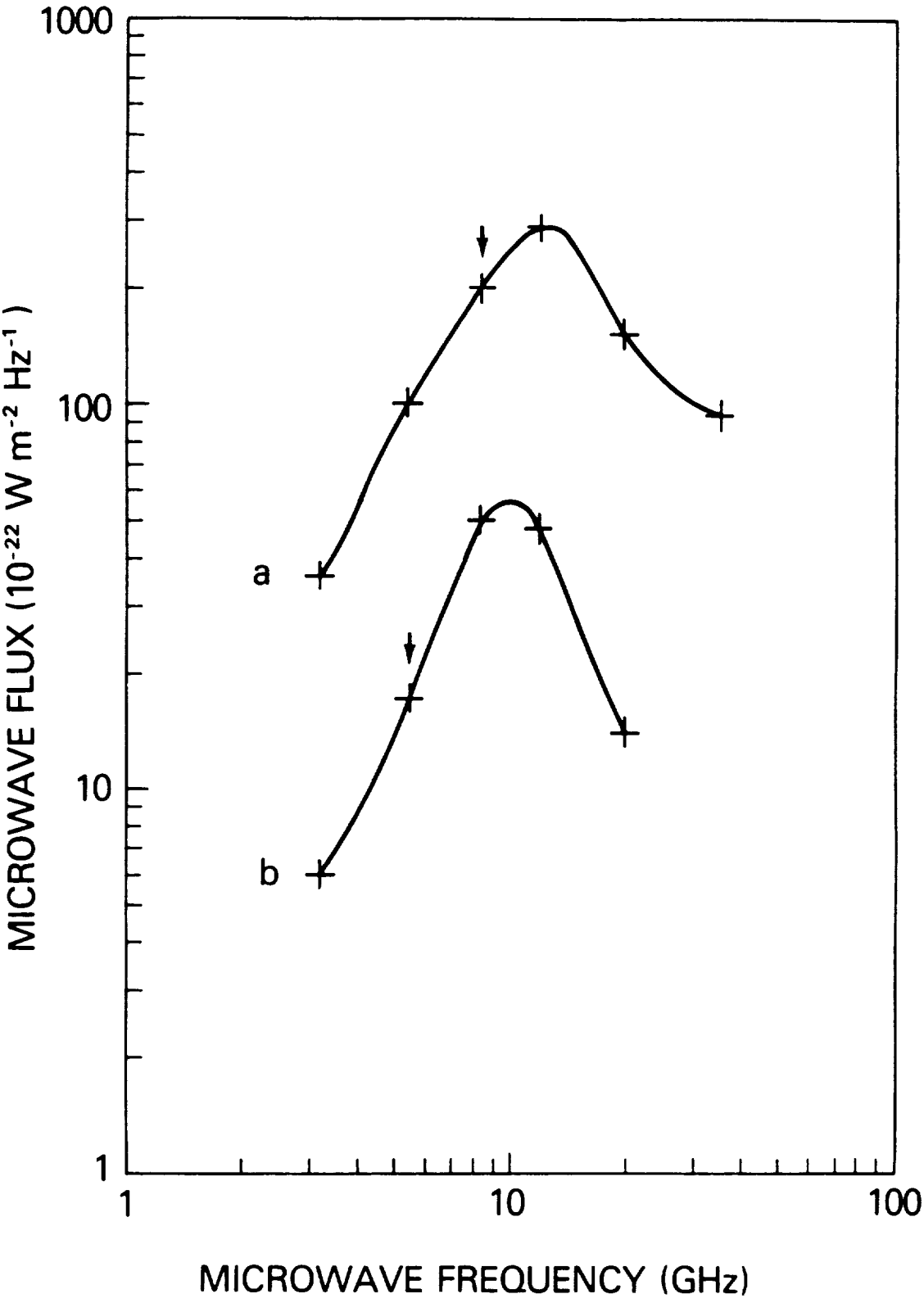

Figure 2. Examples of two microwave burst spectra, each at the time of hard X-ray burst maximum (Bern data). (a) 1981 August 10, (b) 1981 May 4. Arrows indicate points used to determine S_2 and f_2 (see text).

optically thin (Mätzler 1978; Ramaty 1969). The optically-thick emission was used here to derive an area of each source at the time when the counting rate summed over the whole HXRBS energy range was maximum.

First, 30 bursts observed with HXRBS and the radiotelescopes were selected. Bursts were selected with steady rises to a peak or plateau in their time histories ($t_r \leq$ 30 s), and microwave spectra observed in the positive-α segment. (Twice the time from half-maximum to maximum was defined as t_r.) For each burst, values denoted S_2 and f_2 were selected at the highest-frequency observation on the positive-α segment (see Fig. 2). The X-ray spectrum from HXRBS of each burst at its peak flux was fitted with the power law $I(\varepsilon) = A_1\ \varepsilon^{-\gamma}$ photons cm^{-2} s^{-1} keV^{-1}, in order to obtain the hard X-ray spectral index γ.

The approximate formulae derived by Dulk and Marsh (1982) for optically-thick microwave flux from a power law distribution of electrons ($N(E) \propto E^{-\delta}$ electrons cm^{-3}) were used to compute the effective emission temperature of the nonthermal microwave source T_{eff} (deg K) and A, the area of each source (cm^2):

$$T_{eff} = 2.2 \text{ x } 10^9\ 10^{-0.31\ \delta} \cdot$$

$$\cdot\ (\sin\ \theta)^{-0.36-0.06\ \delta}\ (f/f_B)^{0.50+0.085\ \delta} \quad (1)$$

$$A = 7.5 \text{ x } 10^{43}\ S\ f^{-2}\ T_{eff}^{-1}, \quad (2)$$

In Eq. (1), δ is the power-law index of the electron distribution. In the TT model, $\delta = \gamma + 1$, and in the TP model, $\delta = \gamma - \frac{1}{2}$. B is the magnetic field, the variable f_B = 2.8 x 10^6 B is the gyrofrequency (Hz), and θ is the angle between the **B** vector and the line of sight. In Eq. (2), the Sun-Earth distance is accounted for, and the units of S are solar flux units (1 SFU = 10^{-22} W m^{-2} Hz^{-1}).

The uncertainties in B and θ were treated as follows. Typical values of B in flares, deduced from other solar observations, generally range from 100 to 1000 gauss (Švestka 1976; Brown, Smith, and Spicer 1981). In this work, two values of $L \equiv A^{1/2}$ were computed for each burst, with B set equal to each of those two limits; the range in results was treated as the $\pm 1\sigma$ uncertainty. L is admittedly a crude approximation of the characteristic source dimensions, but its large range of variation – more than three orders of magnitude – makes it useful despite uncertainties in length-to-width ratio of the sources that it incorporates. The angle θ could not be measured. Gyrosynchrotron radiation is emitted most intensely in directions $\approx 90°$ from **B** (see Eq. (1)), so that the part of each source with θ nearest to 90° contributes most of the radiation. The dependence of L on θ is slight in the range $45° \leq \theta \leq 90°$, so $\theta = 45°$ was assumed for each burst, as an estimate of the mean value. Little error is incurred since bursts with small θ would have low T_{eff}, and tend not to be observed.

III. RESULTS

The observational parameters and results appear in Table 1. Figure 3 shows the plot of L vs. t_r for the TT model. The TP results make a very similar plot in Figure 4, except for a reduction of the L values by about 30%. Three of the flares occurred on or beyond the solar limb, and are marked with square symbols. Because these bursts might have been partially occulted by the limb, altering A, only the other 27 were included in the least-squares fit (Bevington 1969), drawn as the straight line in the plot. The slope of the best fit line, 1.07 ± 0.05, is unity within the uncertainties.

At least one of the limb bursts, the 1981 Dec. 7 event, has a value of L that is markedly displaced from the correlation, appearing in Fig. 3 with a square symbol well below the best fit line. The displacement of its value of L is in the direction consistent with partial occultation of a flare located just beyond the solar limb. This is an important test of consistency in the interpretation of A as representative of the true source area; displacement of a limb flare value of L in the other direction relative to unocculted burst values would have been an unresolvable conflict with geometry.

As described by Batchelor *et al.* (1985), the parameters entering the correlation were checked to reveal possible more fundamental underlying correlations. Of particular concern was the "Big Flare Syndrome" (Kahler 1982), the possible association of larger flare intensities with larger source sizes, harder X-ray spectra, etc. No underlying parameter correlations were capable of accounting for the close least-squares fit of the relation in Fig. 3. The "Big Flare Syndrome" in particular was ruled out by broad scatter in the plot of S_2 vs. t_r.

IV. DISCUSSION

The deduction that $L \propto t_r$ if one chooses the TT or TP model has important implications for the interpretation of impulsive flare phenomena. The correlation of L with t_r was already known on the basis of thermal flare models. The differences between thermal and nonthermal models for impulsive microwave and X-ray emission are substantial, and the (L, t_r) correlation must result in disparate ways from each of these models. The key inference from these results is: whether one chooses a model from either the nonthermal or thermal alternatives, there is clear evidence in each case that all impulsive bursts in the $0.1 \leq t_r \leq 30$ s range are due to one *type* of causative agent, characterized by a velocity of order 10^8 cm s^{-1}. A precise single velocity for the agent is not implied by the data, of course, given the crudeness of L and the scatter of the values; nevertheless, a *type* of agent that travels at speeds within less than an order of magnitude range is suggested by Fig. 3, and this will be termed "a characteristic velocity" hereafter.

TABLE I

Observational and Derived Parameters
of Solar Hard X-ray/Microwave Bursts

Date	UT	γ	t_r (s)	S_2 (SFU)	f_2 (GHz)	L: TT model (cm)	L: TP model (cm)
80 Mar 29	0918:09	3.3	3.0	510.	10.4	6.5×10^8	4.4×10^8
80 Mar 29	0955:06	2.8	5.2	210.	10.4	3.6×10^8	2.5×10^8
80 Jun 04	0654:19	3.8	7.0	320.	8.4	8.0×10^8	5.3×10^8
80 Jun 29	1041:35*	3.6	3.6	31.	8.4	2.4×10^8	1.6×10^8
80 Jul 01	1626:53	2.8	0.8	135.	19.6	1.2×10^8	8.4×10^7
80 Jul 01	1626:56	2.9	0.9	460.	19.6	2.3×10^8	1.6×10^8
80 Jul 01	1626:59	3.2	0.8	39.	19.6	7.1×10^7	5.0×10^7
80 Jul 01	1627:02	2.8	1.0	82.	35.0	4.1×10^8	3.0×10^7
80 Jul 01	1627:04	3.0	0.8	486.	28.0	1.4×10^8	1.0×10^8
80 Jul 01	1627:08	2.6	1.0	894.	35.0	1.3×10^8	9.5×10^7
80 Jul 01	1627:13	2.6	1.4	1330.	35.0	1.6×10^8	1.2×10^8
80 Oct 09	1123:58	4.2	5.2	100.	5.2	1.0×10^9	6.5×10^8
80 Nov 05	2233:02	3.8	24.	2400.	9.4	1.9×10^9	1.2×10^9
80 Nov 06	0650:51	4.5	20.	910.	8.4	1.6×10^8	1.1×10^9
80 Nov 08	1450:25	5.9	7.	33.	8.4	4.6×10^7	3.0×10^8
80 Nov 18	0718:08*	3.4	2.2	44.	19.6	7.9×10^8	5.5×10^7
80 Dec 17	0845:37	3.2	3.2	280.	8.4	6.3×10^8	4.2×10^8
81 Mar 23	0655:49	3.5	6.0	260.	8.4	6.6×10^8	4.4×10^8
81 Apr 10	1644:53	4.3	10.	120.	5.2	1.1×10^9	7.3×10^8
81 Apr 15	0643:09	4.7	3.8	14.	5.2	4.4×10^8	2.8×10^8
81 Apr 18	1049:28	4.5	5.0	55.	8.4	4.0×10^8	2.7×10^8
81 Apr 26	1115:31	4.	11.	75.	3.2	1.7×10^9	1.0×10^9
81 May 04	0838:03	4.2	1.8	17.	5.2	4.2×10^8	2.7×10^8
81 Jul 19	0533:25	3.9	12.	1400.	19.6	5.0×10^8	3.5×10^8
81 Jul 20	1311:27	4.5	22.	170.	2.8	3.6×10^9	2.2×10^9
81 Aug 10	0658:50	3.9	2.6	200.	8.4	6.5×10^8	4.3×10^8
81 Dec 07	1451:02*	3.1	10.0	240.	19.6	1.7×10^8	1.2×10^8
84 May 21	1326:29	2.7	0.2(m)	20.	90.0	5.3×10^6	4.1×10^6
84 May 21	1326:30	2.4	0.1(m)	50.	90.0	7.9×10^6	6.1×10^6
84 May 21	1326:37	3.2	0.1(m)	30.	90.0	7.0×10^6	5.4×10^6

* Limb flares, excluded from length-rise time correlation due to possible limb occultation.

m The 1984 May 21 bursts had rise times shorter than HXRBS time resolution. The microwave rise time has therefore been used. In all other cases, the rise time is derived from HXRBS data.

LENGTHS VS. RISE TIMES: THICK TARGET

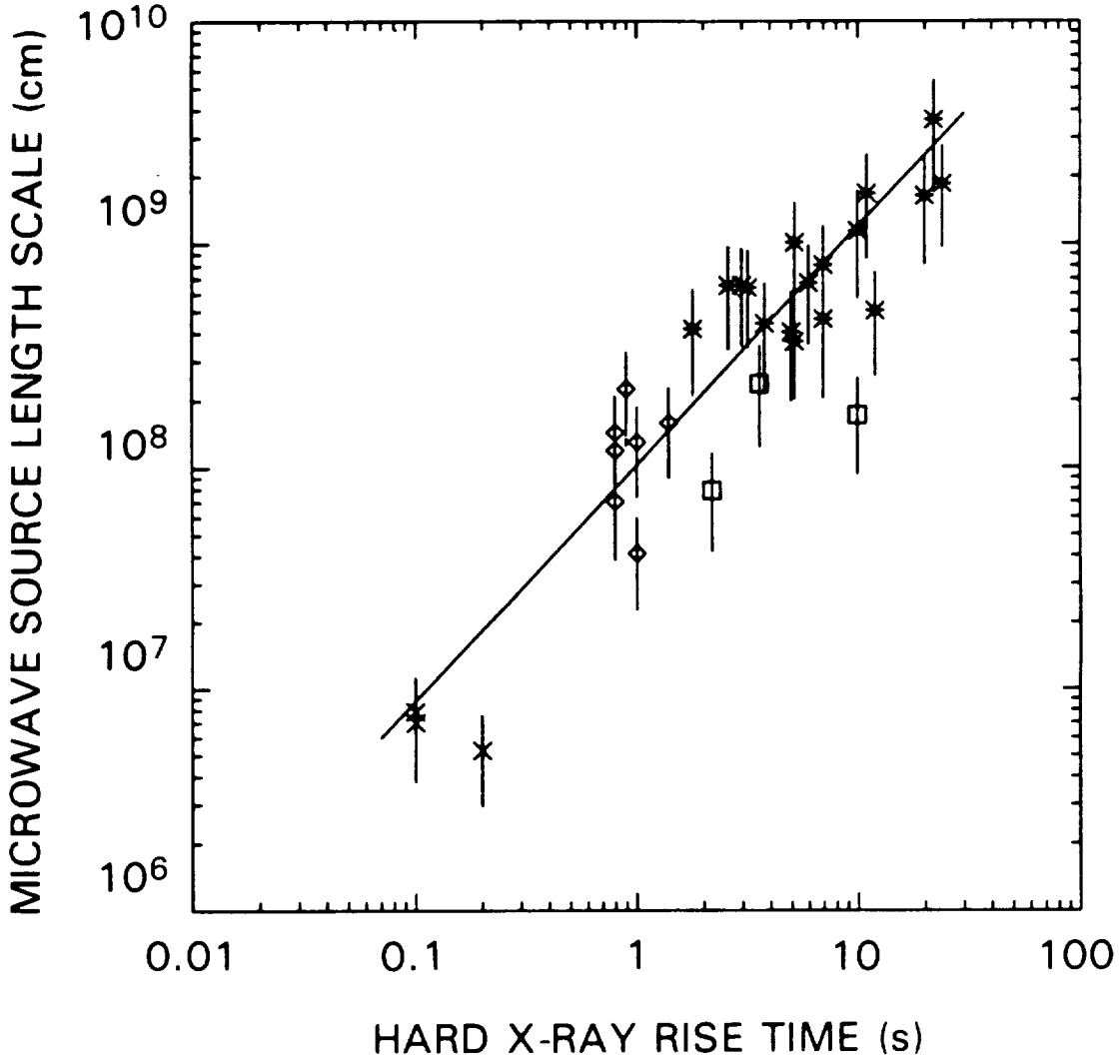

Figure 3. Plot of burst source length scales L vs. rise times t_r, assuming the TT model. Symbols: crosses label three bursts from the 1984 May 21 flare observed at Itapetinga; diamonds label seven bursts from the 1980 July 1 flare; all other symbols label bursts from other flares. Squares indicate limb events; because these bursts might have been partially occulted (reducing L), they were excluded from the least-squares fit. The fit, performed with the function $log\ L = log\ a\ +\ b\ log\ t_r$, yielded $a = 10^8$ cm s^{-1}, $b = 1.07$, $\sigma_{log\ a} = 0.08$, $\sigma_b = 0.05$, correlation coefficient $r = 0.95$. There are N = 27 points, so the probability that the quantities L and t_r are actually uncorrelated is $P_c(r, N) \ll 10^{-6}$.

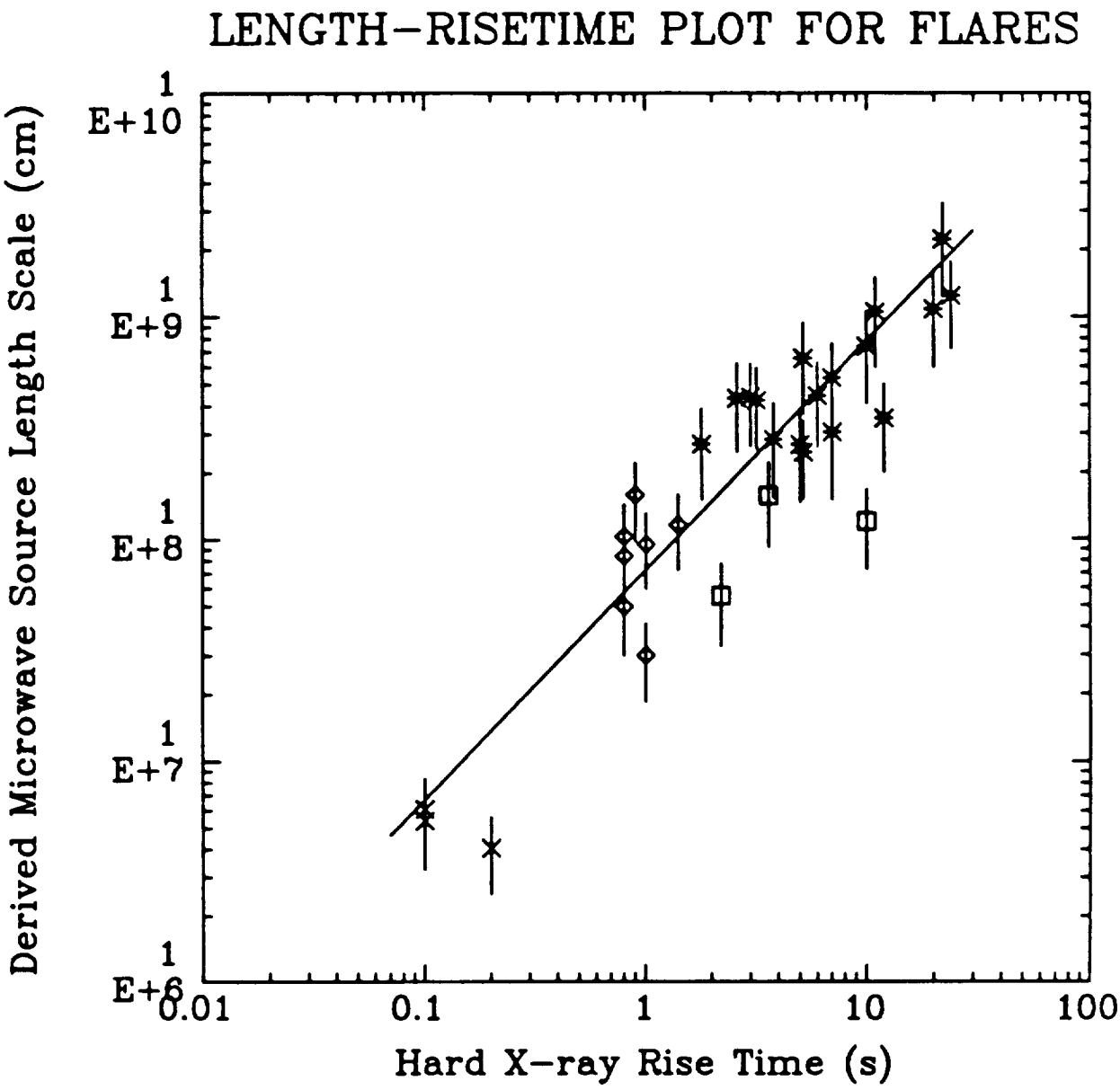

Figure 4. Same as Fig. 3 for the trap-plus-precipitation (TP) model. The fit parameters are similar: $a = 7.3 \times 10^7$ cm s^{-1}, $b = 1.03$, $\sigma_{log\ a} = 0.07$, $\sigma_b = 0.04$, correlation coefficient $r = 0.95$. Again with N = 27 points, the probability that the quantities L and t_r are actually uncorrelated is $P_c(r, N) \ll 10^{-6}$.

The nature of the causative agent and its characteristic velocity are specific to each model. The mean values are 10^8 cm s^{-1} for the TT model, 7 x 10^7 cm s^{-1} for the TP model, and 2 x 10^8 cm s^{-1} for the TCF model. In each model, the role of this agent is fundamental: it couples the energy release process to the geometrical scale of the burst source region and determines the duration of the most rapid impulsive energy release phase. Possible agents are shocks in the nonthermal models and TCFs. Any other processes of flare energy release that may be proposed also must include such an agent.

Perhaps it is no great surprise that a velocity of order 10^8 cm s^{-1} characterizes the growth of flare sources, but this has not been demonstrated heretofore by means of standard *nonthermal* models, nor has the dependence of the characteristic velocity on the chosen model been derived before. One can envision many ways that flare sources could grow with some characteristic speed, so the results described above do not permit us to discriminate between models. Nevertheless, the evidence for interpretation of the burst rise time as a phase of growing source area is an important departure from the long-standing interpretation that the time behavior of the injection of accelerated particles, convolved with particle propagation effects, determines burst rise times (*e.g.*, Emslie 1983; Lu and Petrosian 1988).

The results of this work suggest other new lines of investigation. First, the correlation $L \propto t_r$ supports the future use of A and L measurements as meaningful tools of source analysis, whereas they were more questionable before. Future studies may benefit from tests for correlations between L or A and other available flare parameters. Second, the causal agent responsible for the correlation must be thought of as a physical process that can operate in a similar manner on size scales that vary by three orders of magnitude, a useful datum for investigations of simulated flare energy release via magnetic reconnection. Conversely, something must serve to terminate the process on equally wide-ranging size scales. Third, these results give information about a few sources that are less than one arc second in angular size. Even the most advanced microwave imaging system for flares, the Very Large Array, can't provide such information with its images.

The clear evidence herein for source growth with a characteristic velocity during burst rises should be tested with spatially-resolved observations. Most of the bursts in this study had rise times too short for observations of their progressive growth with the VLA, given its 10-s time resolution. Comparisons of the source areas from the VLA with burst rise times are possible and would provide an important test of these results.

CONCLUSION

- Max '91 study of impulsive hard X-ray/microwave bursts should focus on identifying the causative agent suggested herein
- Combined images in hard X rays and microwaves (*e.g.* GRID/VLA) should be used to search for the following phenomena:
  * Shock acceleration
  * Thermal conduction fronts
  * Traveling magnetic reconnection instabilities
- These possible causative agents should reveal themselves via their distinctive relationships with coronal magnetic structures
  * Quasi-perpendicular orientation of field lines relative to a radially expanding disturbance
  * Conductive growth of hot sources longitudinally along field lines
  * Longitudinal source expansion at speed near Alfvén velocity

ACKNOWLEDGEMENTS

The author is very grateful to the HXRBS team and to the solar observers at Bern Radio Observatory, Toyokawa Observatory and Itapetinga Observatory for permission to use their data and for advice in the analysis. Critical reading of the manuscript by C.J. Crannell and B.R. Dennis is also appreciated.

REFERENCES

Batchelor, D.A., Crannell, C.J., Wiehl, H.J., and Magun, A. 1985, *Ap. J.*, **295**, 258.

Batchelor, D.A. 1987, in *Rapid Fluctuations in Solar Flares, NASA Conference Publication 2449*, eds. Dennis, B.R., Orwig, L.E., and Kiplinger, A.L., (NASA, Washington, 1987), p. 35.

Batchelor, D.A. 1989, *Ap. J.*, **340**, 607.

Bevington, P.R. 1969, *Data Reduction and Error Analysis for the Physical Sciences*, (McGraw-Hill, New York), Chap. 6.

Brown, J.C. 1971, *Solar Phys.*, **18**, 489.

Brown, J.C., Melrose, D.B., and Spicer, D.S. 1979, *Ap. J.*, **228**, 592.

Brown, J.C., Smith, D.F., and Spicer, D.S., 1981, in *The Sun as a Star, NASA Special Pub. 450*, ed. Jordan, S. (NASA, Washington), p. 181.

Crannell, C.J., Frost, K.J., Mätzler, C., Ohki, K., and Saba, J.L. 1978, *Ap. J.*, **223**, 620.

Dulk, G.A., and Marsh, K.A. 1982, *Ap. J.*, **259**, 350.

Emslie, A.G. 1983, *Ap. J.*, **271**, 367.

Gary, D.E. 1985, *Ap. J.*, **297**, 799.

Guidice, D.A., and Castelli, J.P. 1975, *Solar Phys.*, **44**, 155.

Kahler, S.W. 1982, *J. Geophys. Res.*, **87** (A5), 3439.

Kai, K. 1986, *Solar Phys.*, **104**, 235.

Kaufmann, P., Strauss, F.M., Schaal, R.E., and Laporte, C. 1982, *Solar Phys.*, **78**, 389.

Lu, E.T., and Petrosian, V. 1988, *Ap. J.*, **327**, 405.

Magun, A., Fuhrer, M., Kaempfer, N., Staeli, M., Schöchlin, W., and Wiehl, H. 1981, *Institute for Applied Physics Rept. 46* (University of Bern, Switzerland).

Mätzler, C. 1978, *Astron. Astrophys.*, **70**, 181.

Melrose, D.B., and Brown, J.C. 1976, *Mon. Not. R. Astron. Soc.*, **176**, 15.

Orwig, L.E., Frost, K.J., and Dennis, B.R. 1980, *Solar Phys.*, **65**, 25.

Ramaty, R. 1969, *Ap. J.*, **158**, 753.

Schmahl, E.J., Kundu, M.R., and Dennis, B.R. 1985, *Ap. J.*, **299**, 1017.

Švestka, Z. 1976, *Solar Flares* (Reidel, Dordrecht), pp. 176-180.

Takakura, T., and Kai, K. 1966, *Publ. Astron. Soc. Japan* **18**, 57.

Torii, C. 1979, *et al. Proc. Res. Inst. Atmos. Nagoya Univ.*, **26**, 129.

Solar Flare Gamma-Ray and Hard X-Ray Imaging with the GRID-on-a-Balloon

L. E. Orwig, C. J. Crannell, B. R. Dennis (LASP NASA/GSFC), R. Starr (LASP NASA/GSFC & The Catholic U. of America), G. J. Hurford, T. A. Prince (Caltech), H. S. Hudson (UCSD), F. van Beek (Delft U. of the Netherlands), M. E. Greene (Auburn U.), W. N. Johnson, J. P. Norris, K. S. Wood (NRL), J. M. Davis (NASA/MSFC).

ABSTRACT

A primary scientific objective for solar flare research during the rapidly approaching maximum in solar activity is the imaging of gamma-ray and hard X-ray sources of solar flare emissions. These goals will be pursued by the Gamma Ray Imaging Device (GRID) instrument, one of three instruments recently selected for NASA's Max '91 Solar Balloon Program. GRID is based on the technique of Fourier transform imaging and utilizes scanning modulation grid collimator optics to provide full-Sun imaging with 1.9-arcsecond resolution over the energy range from 20 to 700 keV at time resolutions from 0.1 to 2 s. GRID will employ 32 subcollimators, each composed of a matched pair of high-Z collimator grids separated by 5.2 meters and a phoswich scintillation spectrometer detector having no spatial resolution. The subcollimators and integrally-mounted fine aspect system are contained within a telescope canister which will be pointed to 0.1 degree accuracy and cyclically scanned to produce source modulation. The 32 subcollimators provide a uniform distribution of grid slit orientations and a logarithmic distribution of slit spacings corresponding to angular dimensions of 1.9 arcseconds to several arcminutes. The instrument is several orders of magnitude more sensitive than the HXIS instrument on SMM and nearly 10 times more sensitive than any similar instrument scheduled to fly during the next solar maximum. The payload, designed for long-duration high-altitude balloon capabilty, is scheduled for its first science flight (8 to 14 days duration) from the Antarctic in January of 1992.

SCIENTIFIC OBJECTIVES

- Image Dynamic Flare Geometries (where do the hard X-ray and gamma-ray emissions come from?)
- Investigate Energy Release (what processes liberate the energy stored in unstable magnetic fields?)
- Study Particle Acceleration (what mechanisms are at work?)
- Study Energy Transport (what mechanisms transport particles and energy away from the release site?)
- Investigate Magnetic Field Structures (how do simultaneous microwave and hard X-ray/gamma-ray images compare?)
- Provide Definitive Tests for Solar Flare Models
- Study Microflares

OBSERVATIONAL GOALS

- Obtain arc-second imaging of solar flare hard X-rays and gamma-rays with sub-second temporal resolution
- Compare spatially-resolved high energy emissions with simultaneous microwave observations
- Obtain significantly improved spatial resolution over previous measurements
- Extend imaging capability to photon energies not previously attainable (700 keV)
- Develop hard X-ray and gamma-ray imaging technology as a precursor to future instruments such as the Pinhole/Occulter Facility on Space Station

INSTRUMENTAL APPROACH

GRID is based on the concept of Fourier transform imaging using bi-grid collimators - an exact analog to the technique used in the microwave domain at facilities such as the VLA. The measurement of a single Fourier component is performed by a single subcollimator consisting of a pair of widely-spaced identical top and bottom grids. If the slit spacings and orientation of the top and bottom grids are identical, and the subcollimator structure is scanned across a source, rapid modulation in the X-ray transmission of the grid pair is produced. This modulated X-ray flux is measured by a detector which requires no spatial resolution, in this case a phoswich scintillation spectrometer. The amplitude and phase of the fundamental period of this temporally modulated X-ray signal provides a direct measure of the amplitude and phase of the corresponding spatial Fourier component of the source.

The GRID telescope contains 32 such subcollimators, each with grid pairs having different slit spacings and/or orientations. The slit spacings and orientations have been chosen to provide optimal coverage of the (u-v) spatial frequency plane.The modulation of the source is provided by cyclically scanning the telescope over a 3 arcminute radius at a 4 sec period using the main pointing system.

The primary science data consists of the energy and arrival time of each valid photon, along with precise aspect information provided once very 4 ms, all of which is recorded with on-board tape recorders. No significant on-board data processing is performed, greatly simplifying the tasks of the flight data handling electronics. Image reconstruction is then performed in the post-flight data analysis phase where the aspect information is used to "phase bin" each time-tagged photon. Over a chosen time interval the vector summation of the photons (by phase) in any chosen energy interval provides a measured amplitude and phase for that time interval, energy interval and subcollimator. The resulting set of amplitudes and phases can then be processed by standard interferometric image processing software to produce high-resolution images of the X-ray source.

PAYLOAD SUBSYSTEMS

The GRID consists of the following major payload subsystems:

- a set of 32 subcollimator grids each of which has a large number of parallel slits
- a pair of 1-m diameter trays on which the grids are mounted
- a 5.2-m long tube with the grid trays mounted at the ends
- an aspect system which provides a posterior knowledge of the angle between the optical axis of the X-ray grids and the source direction
- a set of phoswich scintillation spectrometers located beneath the lower grid tray
- a digital data system that tags each detected photon with it arrival-time, subcollimator ID, energy, and current aspect information
- an on-board data recording system with sufficient capacity for a 15-day flight and data-rate capability sufficient to handle the largest expected flare
- an on-board power subsystem providing 1000 Watts continuous power through the use of solar cells and rechargeable batteries
- a gondola with pointer used to solar point the telescope to 0.1 deg. accuracy and provide the cyclic scanning motion for the telescope

The first science flight of the GRID is baselined for a long-duration (8-15 day) balloon mission at a float altitude of 130,000 feet in December 1991 in Antarctica where optimum solar observations can be obtained for ~ 12 hours each day at Solar elevation angles between 24° and 36°. Although an Antarctic flight is the baseline the payload can easily be adapted for long-duration flights from mid-latitude launch sites such as Australia.

FOURIER TRANSFORM TELESCOPE

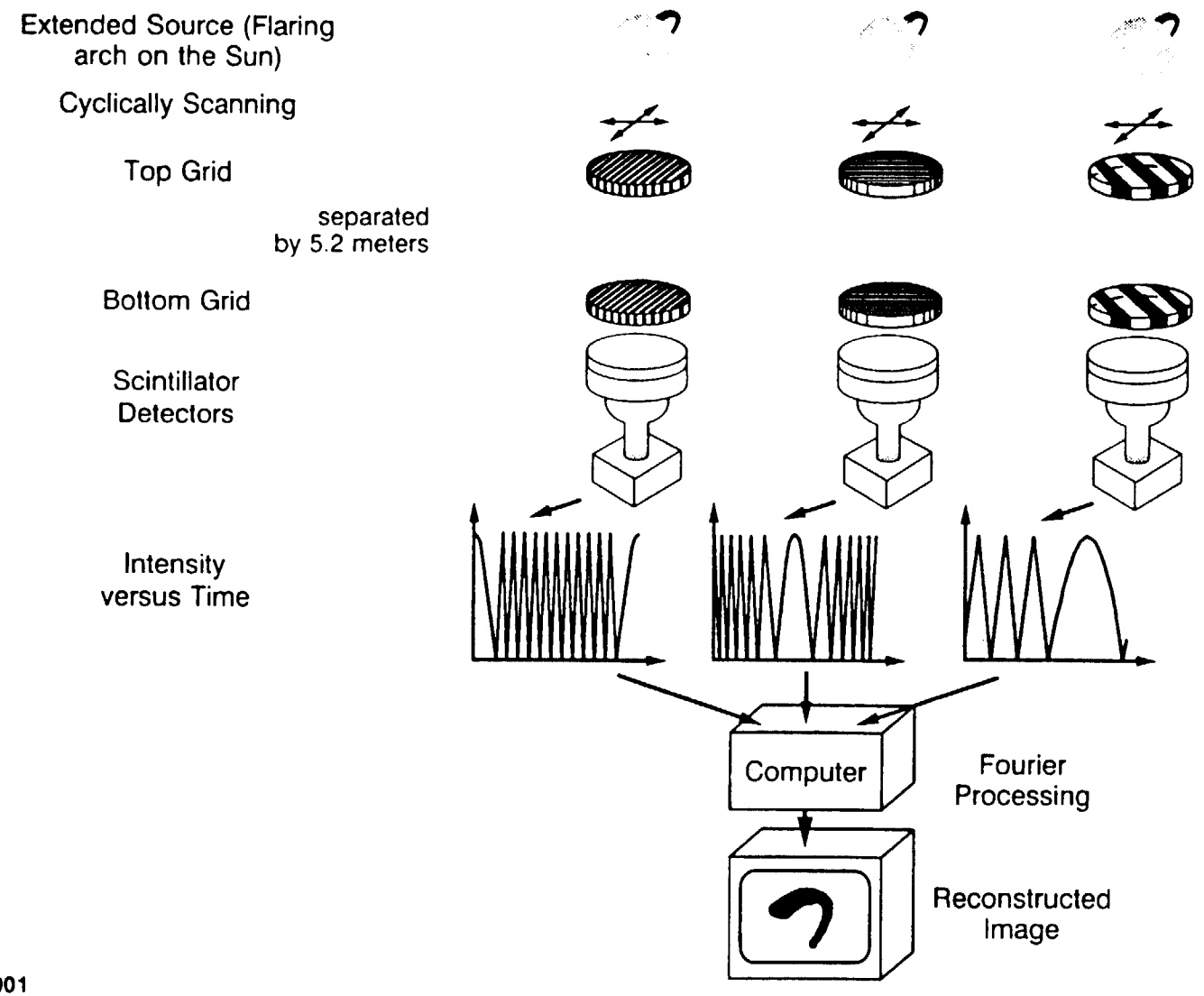

A194.001

EXPLODED VIEW OF TELESCOPE

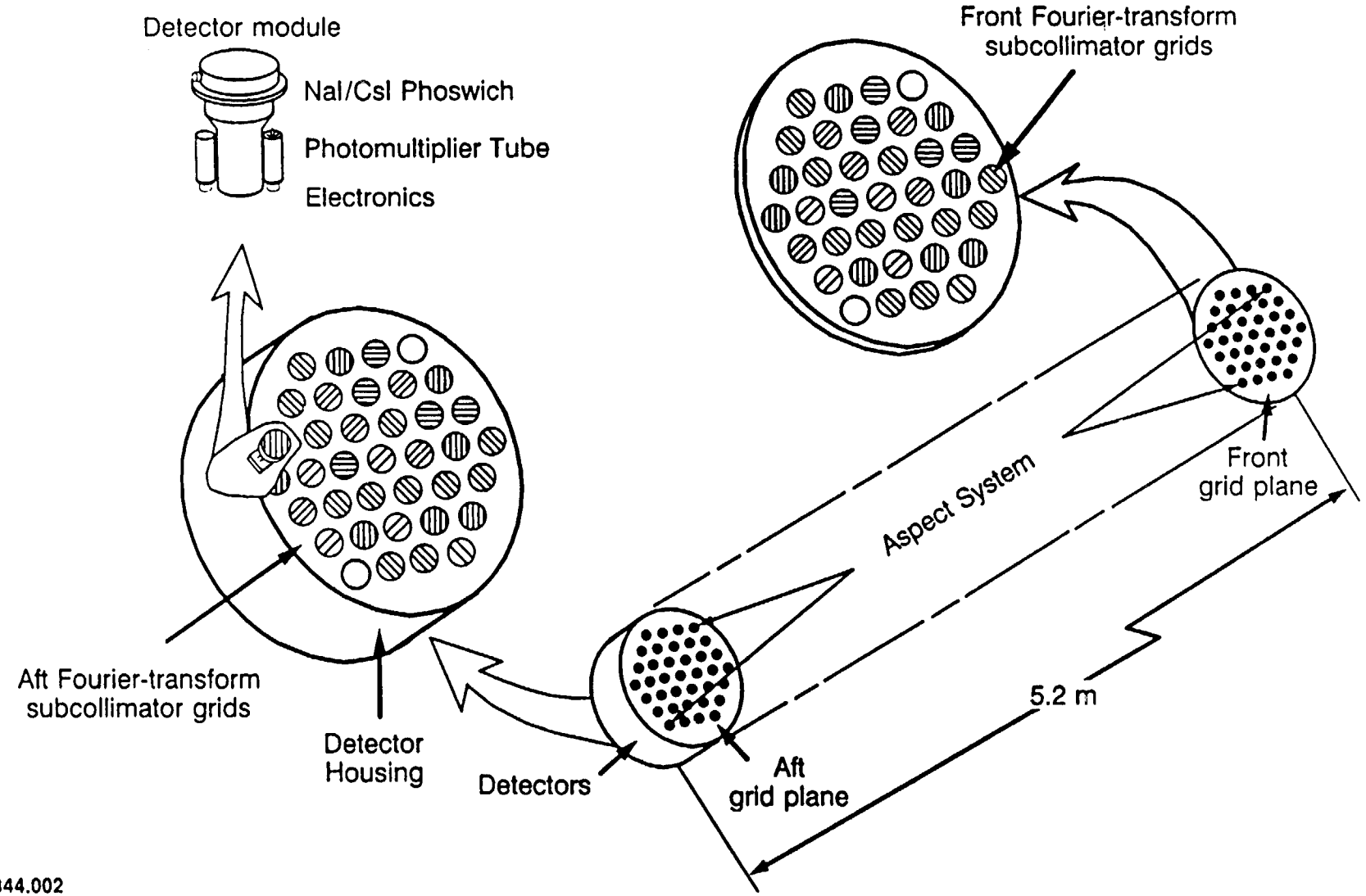

A344.002

GRID INSTRUMENT CHARACTERISTICS	
Detector type (number)	NaI/CsI phoswich scintillation spectrometers (32)
Detector area	2036 cm**2
Effective area	500 cm**2
Image formation	Fourier imaging using cyclically scanning modulation collimators
Energy range	20 keV - 700 keV
Subcollimator material	Tungsten (3 mm to 10 mm thick)
Number of Fourier components	32
Sensitivity	detect and locate about 140 flares per week
Maximum angular resolution	1.9 arc seconds
Field of view	1 degree FWHM (whole Sun)
Pointing accuracy requirement	0.1 degree (rms)
Pointing stability requirement	0.2 arc second per 4 ms (rms)
Expected flight duration	8 to 15 days

GRID DETECTOR MODULE
(ONE OF 32)

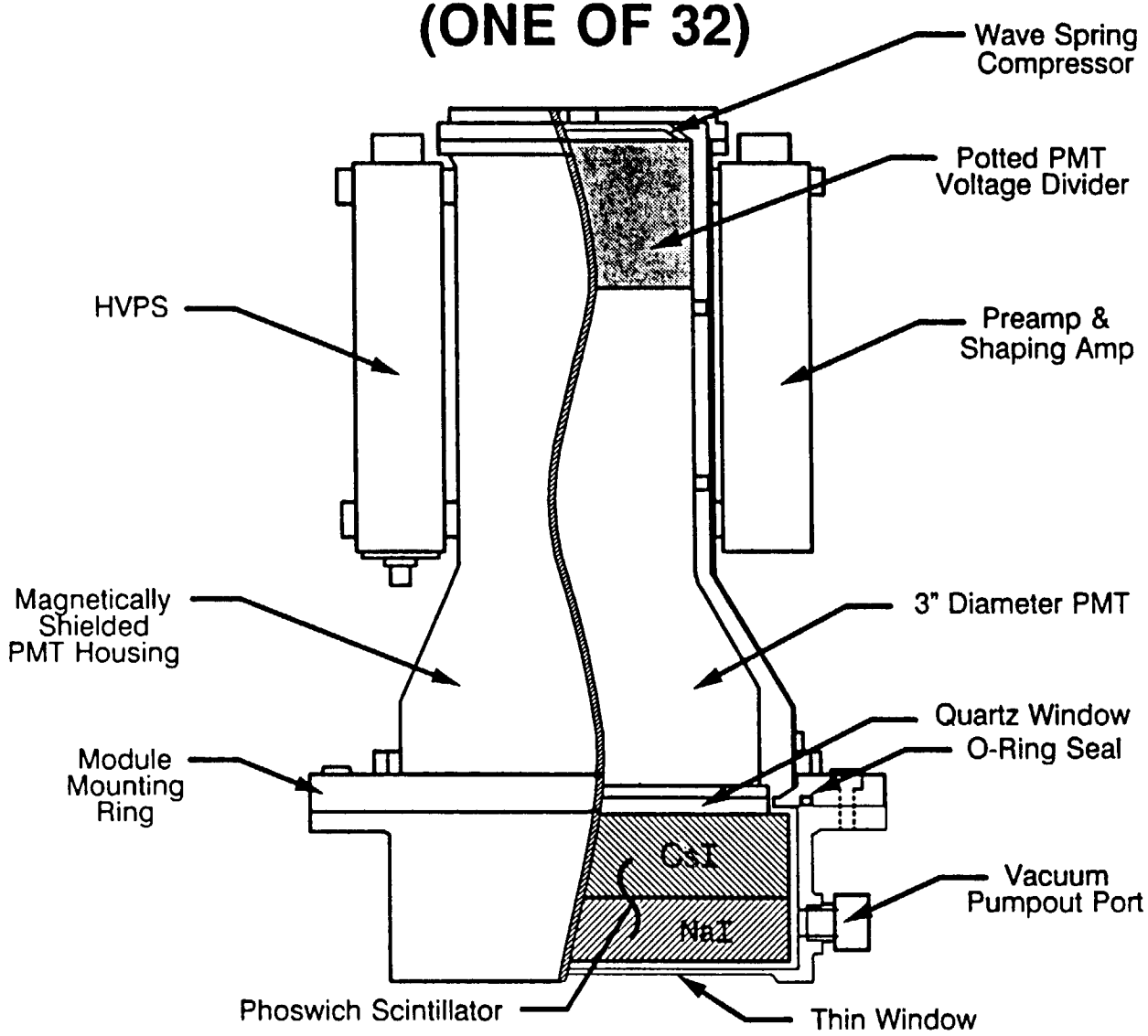

A344.001

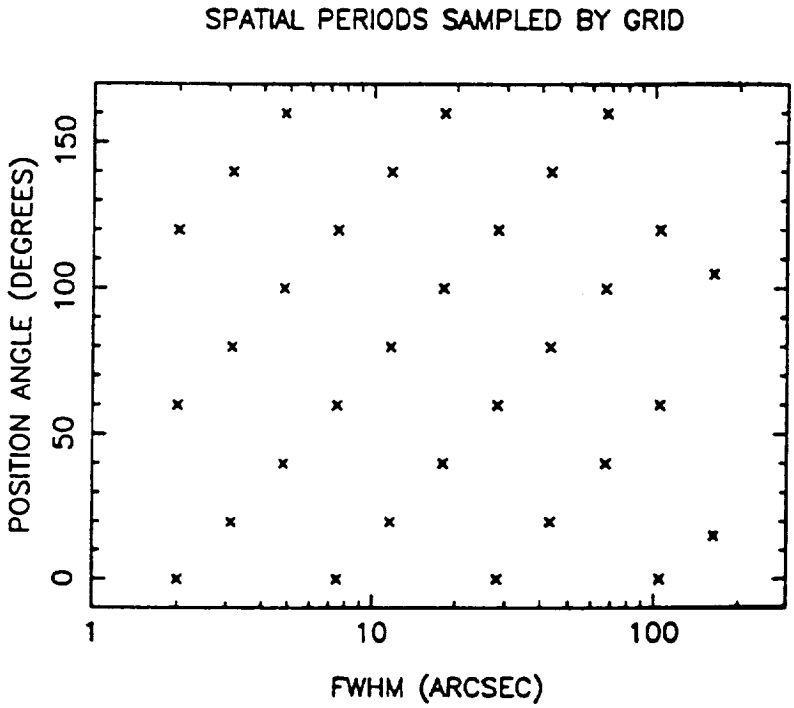
SPATIAL PERIODS SAMPLED BY GRID
POSITION ANGLE (DEGREES)
0
50
100
150
1
10
100
FWHM (ARCSEC)

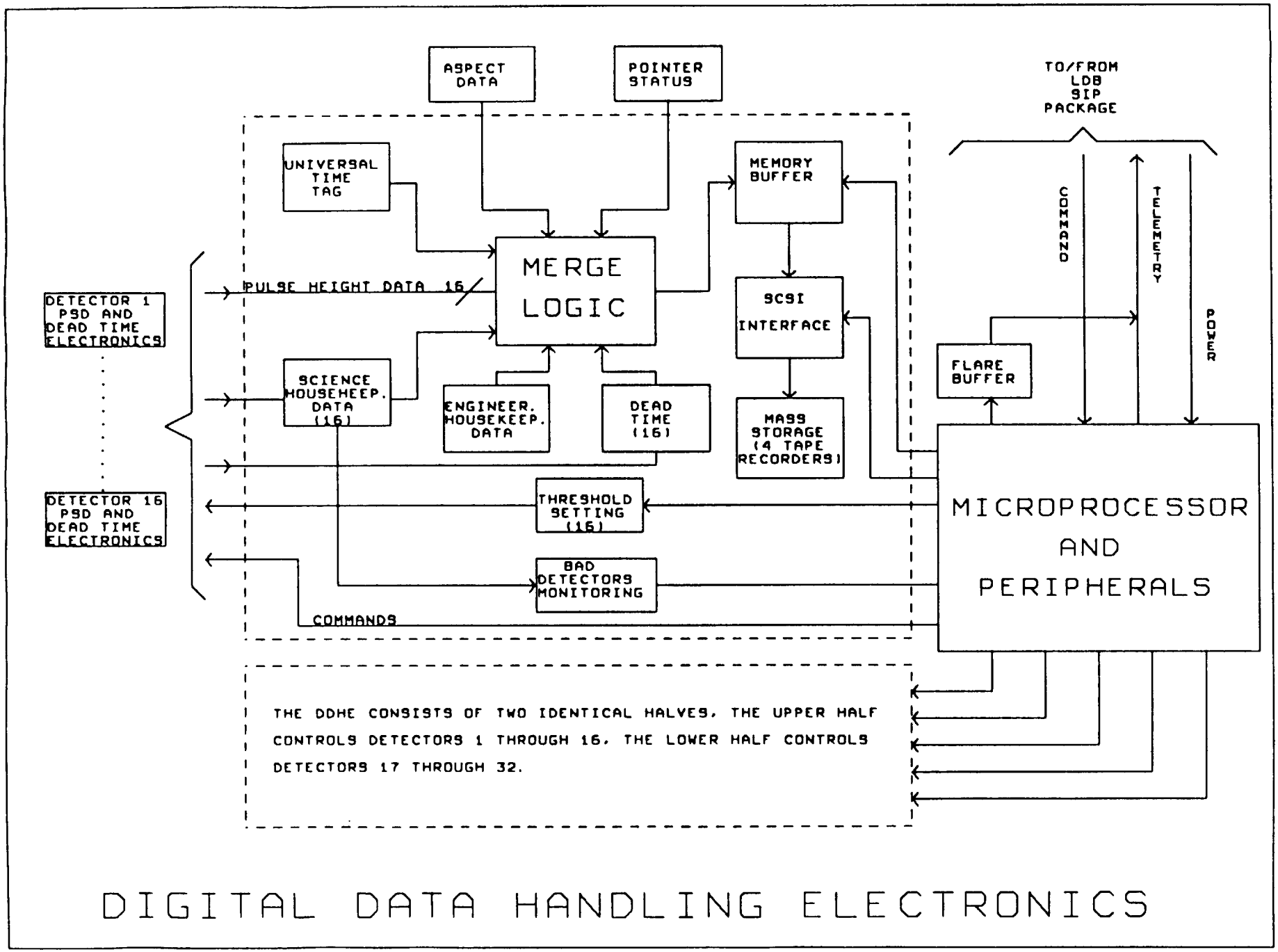

DIGITAL DATA HANDLING ELECTRONICS

GRID PAYLOAD

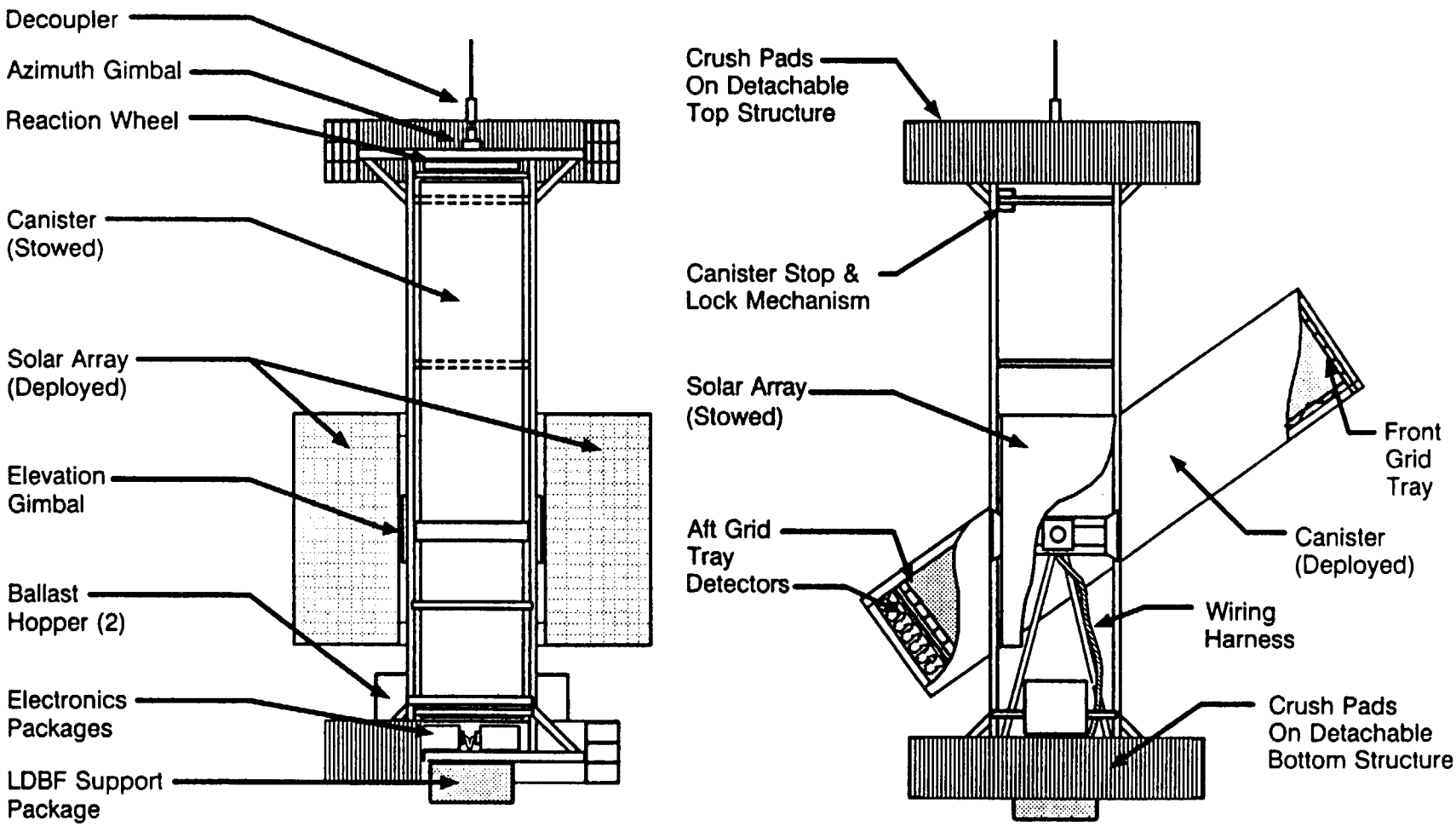

A344.003

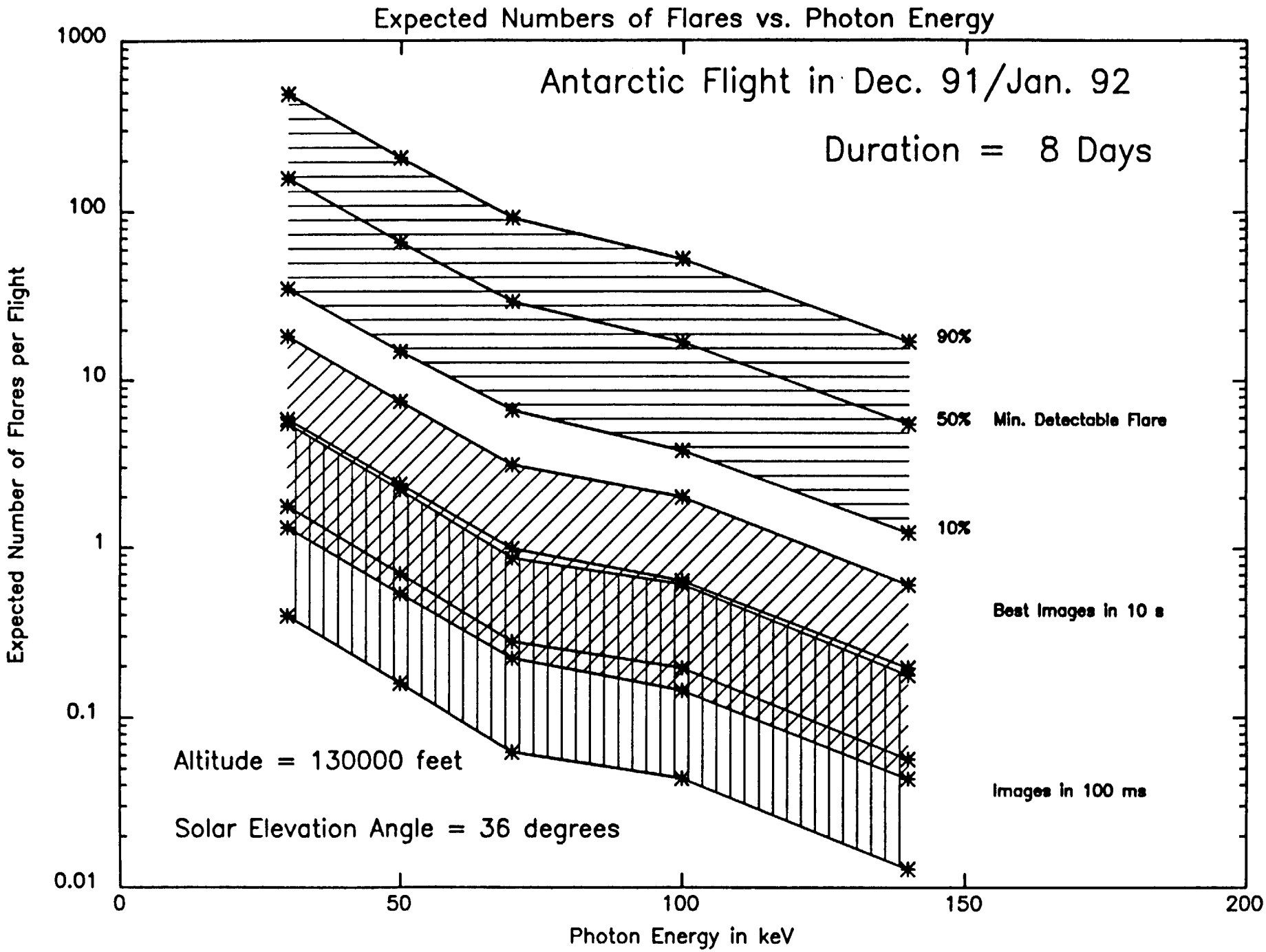
Expected Numbers of Flares vs. Photon Energy
Antarctic Flight in Dec. 91/Jan. 92
Duration = 8 Days
Expected Number of Flares per Flight
1000
100
10
1
0.1
0.01
0
50
100
150
200
Photon Energy in keV
90%
50%
10%
Min. Detectable Flare
Best Images in 10 s
Images in 100 ms
Altitude = 130000 feet
Solar Elevation Angle = 36 degrees

N90-12475

THE SOFT X-RAY TELESCOPE FOR SOLAR-A

W.A. Brown, L.W. Acton, M.E. Bruner, J.R. Lemen, K.T. Strong (Lockheed Palo Alto Research Lab.)

ABSTRACT

The *Solar-A* satellite being prepared by the Institute for Space and Astronautical Sciences (ISAS) in Japan is dedicated to high energy observations of solar flares. In collaboration with investigators at the National Astronomical Observatory of Japan (NAOJ) and the Institute for Astronomy of the University of Tokyo, we are preparing the Soft X-Ray Telescope (SXT) to provide filtered images in the 2 to 60Å interval. Prof. T. Hirayama of NAOJ is the SXT principal investigator.

The flight model is now undergoing tests in the 1000 foot tunnel at MSFC. Launch will be in September 1991. Earlier resolution and efficiency tests on the grazing incidence mirror have established its performance in soft x-rays. The unique one-piece, two mirror grazing incidence telescope is supported in a strain free mount separated from the focal plane assembly by a carbon-epoxy metering tube whose windings and filler are chosen to minimize thermal and hygroscopic effects. The CCD detector images both the x-ray and the concentric visible light aspect telescope. Optical filters provide images at 4308(fwhm30)Å and 4700(fwhm200)Å.

The SXT will be capable of producing over 8000 of the smallest partial frame images per day (64×64 pixels or 2.5×2.5 arcmin), or fewer but larger images, up to 1024×1024 pixel images. Image sequences with two or more of the five x-ray analysis filters, with automatic exposure compensation to optimize the charge collection by the CCD detector, will be used to provide plasma diagnostics. Calculations using a differential emission measure code were used to optimize filter selection over the range of emission measure variations and to avoid redundancy, but the filters were chosen primarily to give ratios that are monotonic in plasma temperature. Practical exposure times and counting statistics were included in the selection process.

Science planning in collaboration with NOAJ, U.Tokyo, ISAS,and US co-investigators at UC Berkeley, Stanford, and U of Hawaii has been underway for two years, and detailed plans for organization of data acquisition and eventual archiving are being developed. The LPARL work is supported by NASA under contract NAS8-37334.

Objectives of SXT Science

- Magnetic Structures and energy release
- Location of Particle acceleration and precipitation regions
- Electron Beams and heating of low atmosphere by energetic particles
- Superhot thermal plasma
- Plasma and magnetic parameters during flare energy build up
- Waves and moving fronts in the corona
- Flare periodicity and hot spots
- Electrical current systems and flaring
- Explosive chromospheric evaporation
- Coronal holes, x-ray bright points and global magnetic evolution
- Helioseismology

INSTITUTIONS AND NAMES OF SXT AND SOLAR-A PARTICIPANTS

INSTRUMENT	ACRONYM	PRINCIPAL INVESTIGATOR
Hard X-Ray Imager	HXT	K. Kai NOAJ
Soft X-Ray Telescope	SXT	T. Hirayama, NOAJ L. Acton , LPARL
Wide Band Spectrometer	WBS	J. Nishimura NOAJ
Bragg x-tal Spectrometer	BCS	E. Hiei NOAJ L. Culhane, MSSL

SOFT X-RAY TELESCOPE TEAM

T. Hirayama, T. Sakurai, T. Watanabe, NAOJ, S. Tsuneta, U. of Tokyo
Y. Ogawara, ISAS

L.W. Acton, US Principal Investigator, Lockheed Palo Alto Research Lab.

M.E. Bruner, J.W.Lemen LPARL Coinvestigators

R. Canfield, U.Haw., P. Sturrock, Stanford, S. Kane, UC, Coinvestigators

Relation of Solar-A to Max-91

The Solar-A spacecraft will be operated by scientists at the Institute of Space and Astronautical Science at Sagamihara, near Tokyo, Japan. As a mission primarily devoted to the the study of high energy solar physics it is expected that the Solar-A team will choose to participate in most Max '91 and FLARES 22 campaigns. A scientist at ISAS will be designated to facilitate this coordination and it is anticipated that Solar-A x-ray images will be made available to the Boulder forecast center in support of coordinated observing.

The Solar-A Soft X-Ray Telescope Program (SXT)

Launch Date August 1991

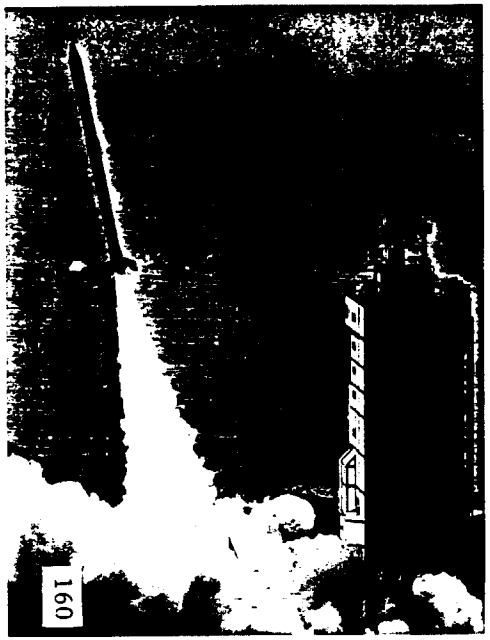

Overview

The SOLAR-A Mission is a program of the Institute of Space and Astronautical Science (ISAS), the Japanese agency for scientific space activity. The SOLAR-A satellite will be launched in August 1991 from Kagoshima Space Center (KSC) in Japan. It will be on board an M-3S three stage solid fuel vehicle. The purpose of this mission is to study high energy phenomena in solar flares. Under an international cooperative agreement between ISAS and NASA, Lockheed will provide a scientific investigation including manufacture of a Soft X-Ray Telescope (SXT), one of the primary experiments of the mission.

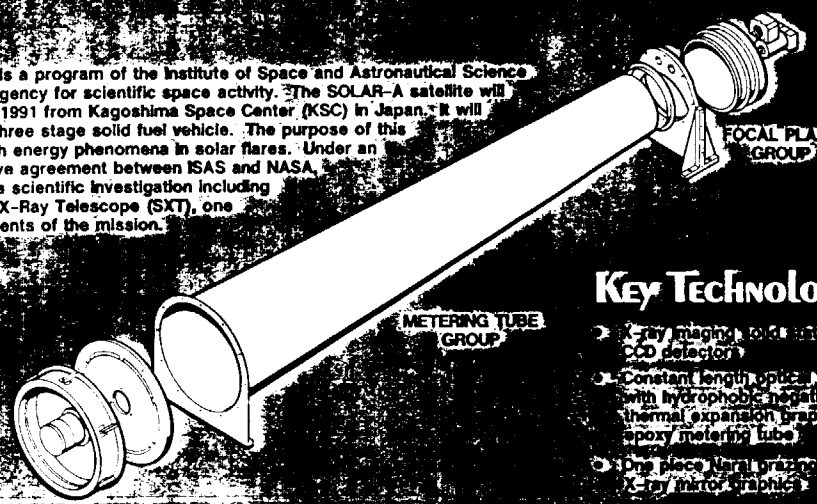

Key Technologies

- X-ray imaging, solid state CCD detector
- Constant length optical bench with hydrophobic, negative thermal expansion graphite epoxy metering tube
- One piece, Kirkpatrick-Baez grazing X-ray mirror module

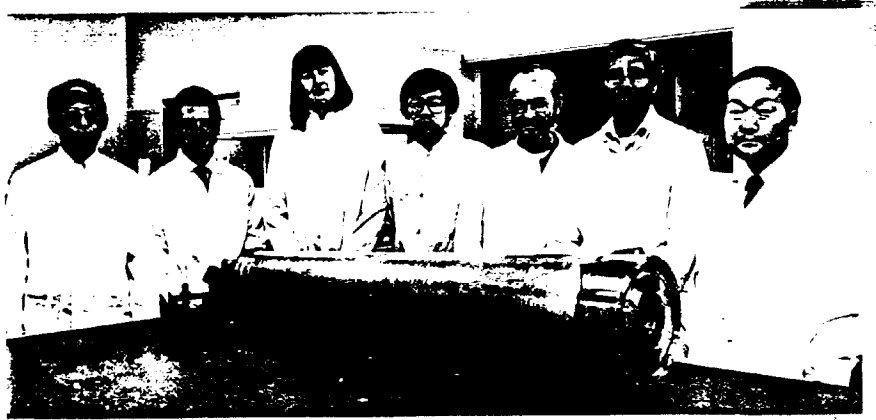

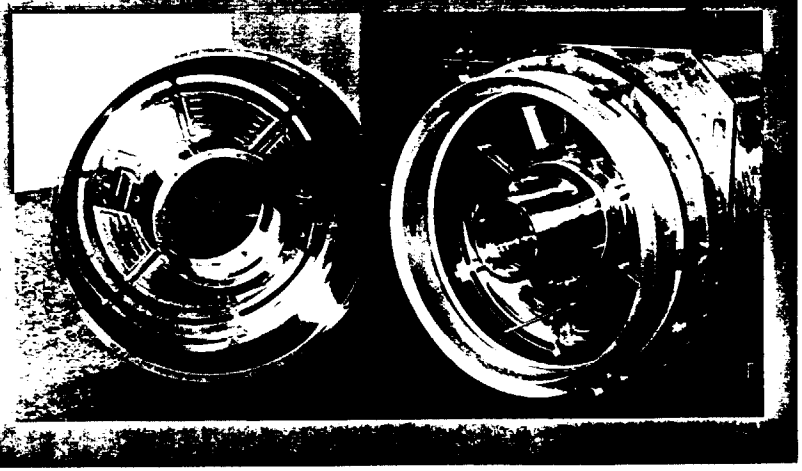

NASA

Lockheed Research & Development Divisions

SXT

National Astronomical Observatory of Japan

ISAS

SOLAR IMAGE ON SXT CCD

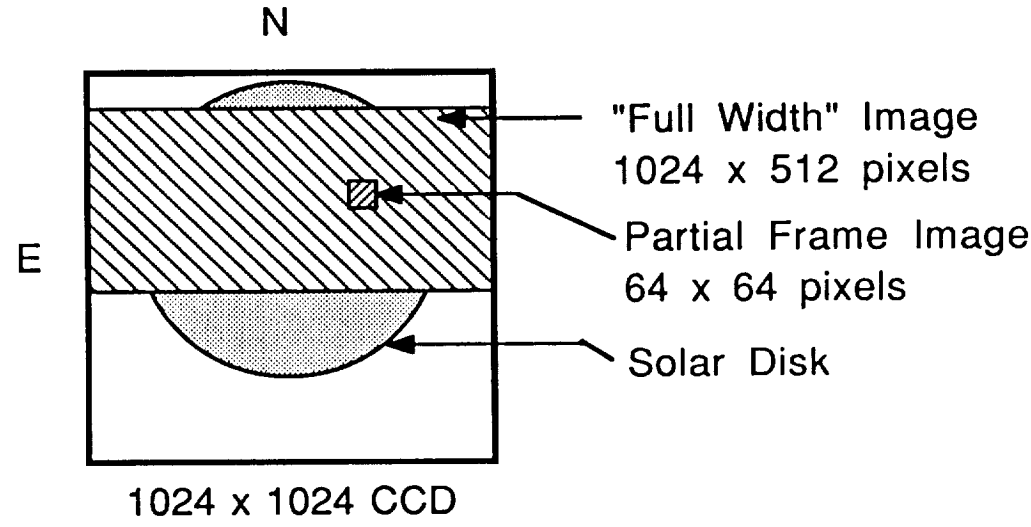

Arrangement of the solar image on the CCD. The partial frame image (64 x 64) pixels may be taken anywhere in the 1024 x 1024 pixel area while the full width image (1024 x 512 pixels) may be placed anywhere in the N-S direction.

SXT Image Parameters

Type	No. Pixels	Pixel Sum	Field-of-View	Time resol.
FWI	1024 x 512	1 x 1	41.6' x 20.8'	256 s
	512 x 512	2 x 2	41.6' x 41.6'	128 s
	256 x 256	4 x 4	41.6' x 41.6'	32 s
PFI	64 x 64	1 x 1	2.6' x 2.6'	2 s
	64 x 64	2 x 2	5.2' x 5.2'	2 s
	64 x 64	4 x 4	10.4 ' x 10.4'	2 s

SXT IMAGE CADENCE

Valid Partial Frame Image Mosiacs:

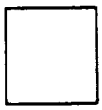

64 × 64 pixels

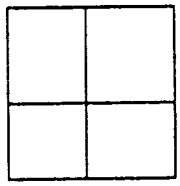

128 × 128 pixels

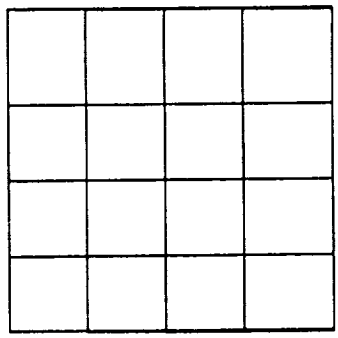

256 × 256 pixels

Time (secs) to complete Partial Frame Images (64 × 64) and Mosaics

Image Size (arcmin)	Pixel Size (arcsec) 2.5	5	10
2.5 × 2.5	2/ 8/16	–	–
5 × 5	8/32/64	2/ 8/16	–
10 × 10	32/128/256	8/32/64	2/ 8/16

Time (secs) to complete Full Width Images (1024 × 512)

Image Size (arcmin)	Pixel Size (arcsec) 2.5	5	10
40 × 20	256/1024/2048	–	–
40 × 40	–	128/512/1024	32/128/256

(3 TELEMETRY RATES: 2048/512/256 PIXELS/SEC)

SOLAR-A TELEMETRY AND DATA RATES

Telemetary Data Rate	32 Kbytes/s
Orbits per day	5*
Recorder Data Capacity	10.5 Mbytes
Total Daily Accumulated Data	52.5 Mbytes*
SXT partial frame images per day (64 × 64 pixels)	≥ 8000*
SXT full width images per day (1028 × 512 pixels)	≥ 5*

Quiet Mode Telemetry (60% SXT)

Basic Data	WBS	BCS	SXT 1	SXT 2

Flare Mode Telemetry (50% SXT)

Basic Data	WBS	BCS	HXT	SXT

* If Deep Space Network available increase by factor of about 2

ORIGINAL PAGE
BLACK AND WHITE PHOTOGRAPH

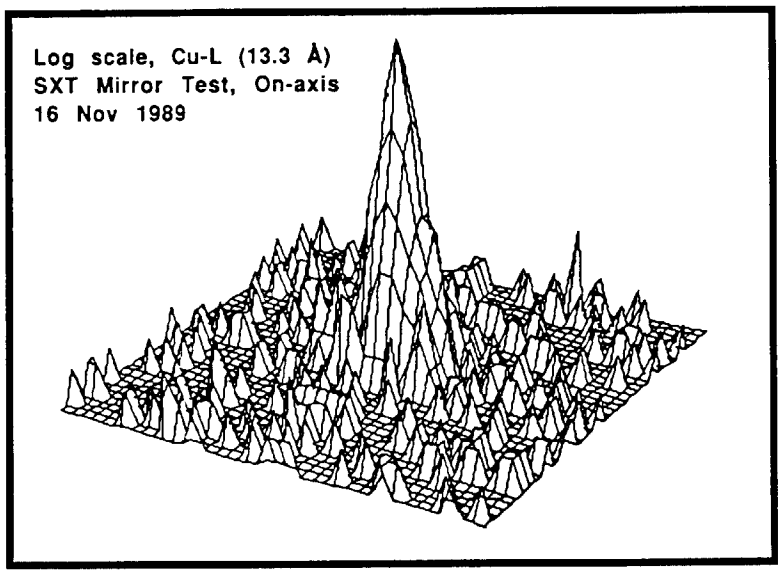

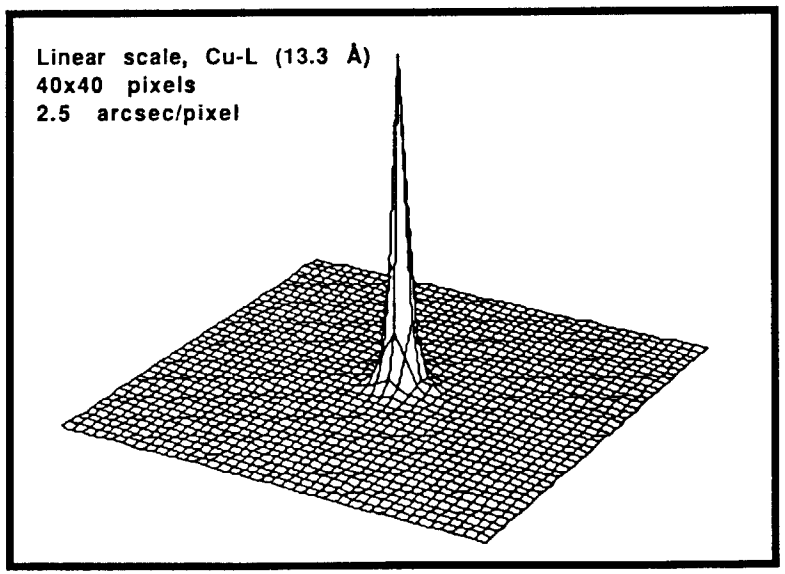

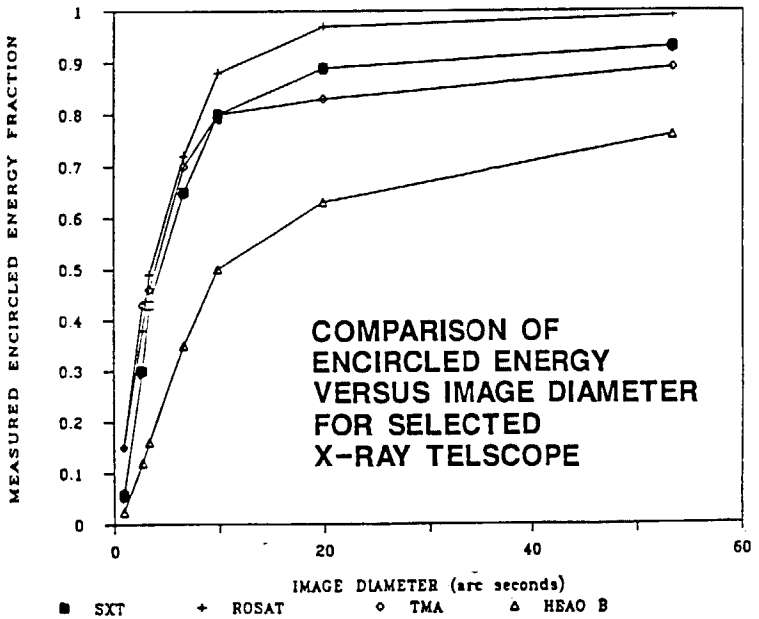

TEST OF POINT SPREAD FUNCTION OF THE X-RAY TELESCOPE. THE PLOTS SHOW LOG AND LINEAR SIGNALS COLLECTED ON THE CCD PIXEL ARRAY AND THE ENCIRCLED ENERGY. THIS DATA TAKEN AT THE BEST FOCUS OBTAINED IN MSFC TUNNEL.

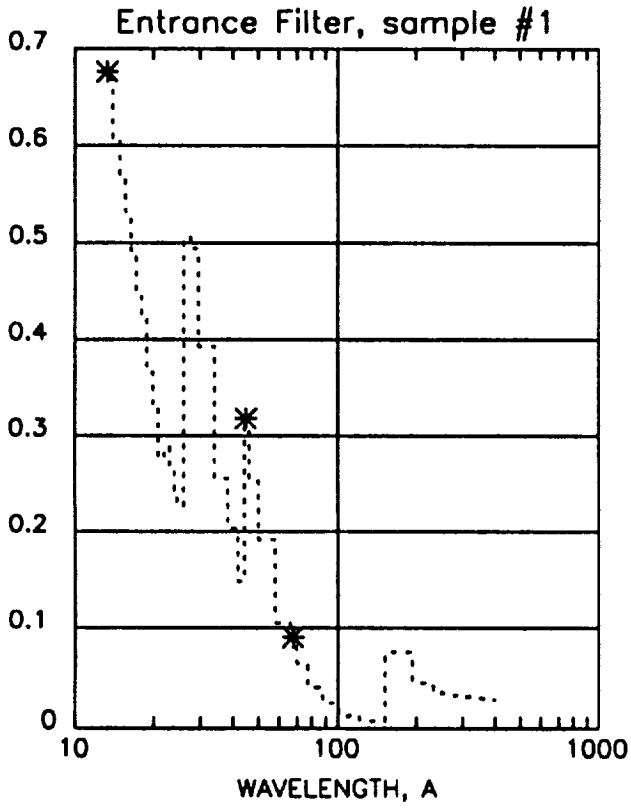

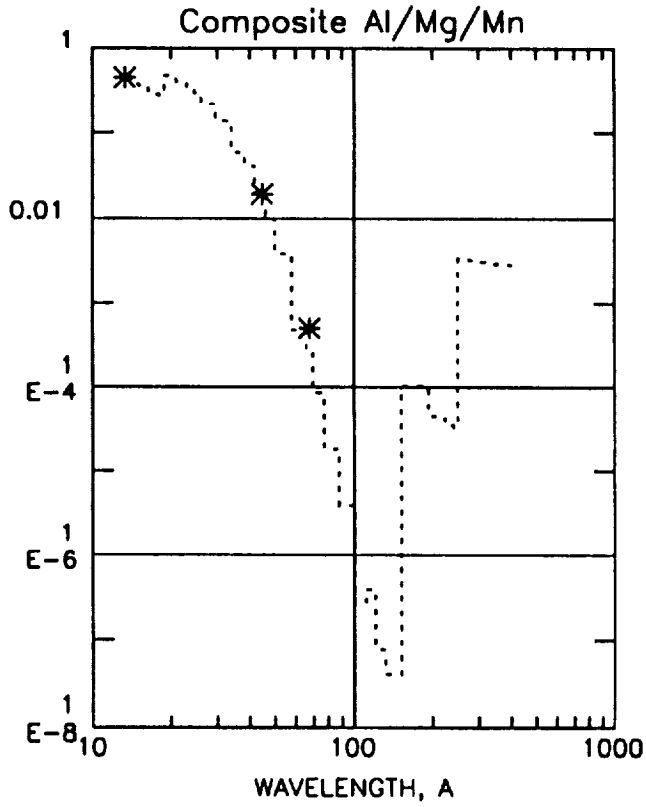

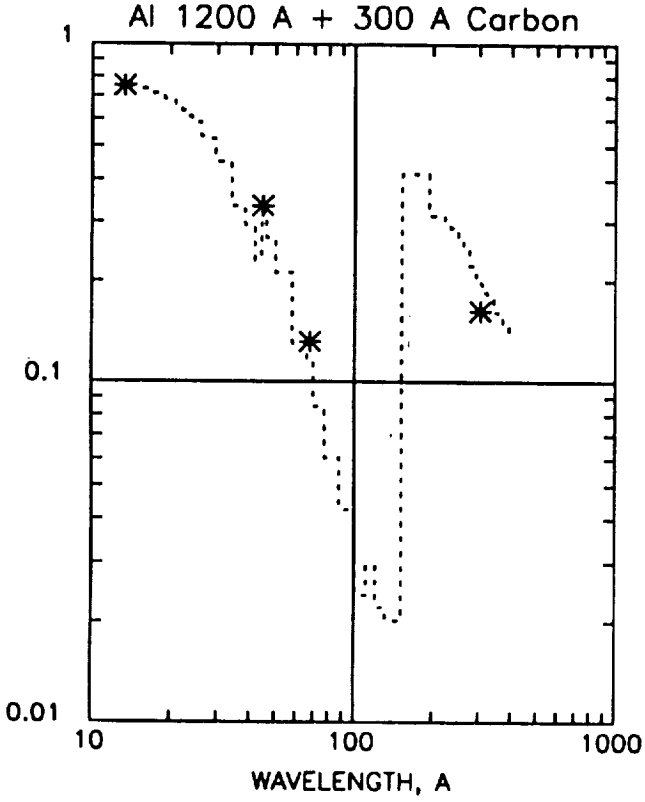

OBSERVED AND CALCULATED TRANSMISSIONS OF 3 SXT FILTERS

SXT Characteristics

X-RAY TELESCOPE:

Mirror	Nariai-Werner Double Hyperboloid, Gold on Fused Quartz
Focal Length	154 cm
Thermal Filter	1800 A Lexan + 800 A Al + 900 A Titanium (Doubled)
Metering Tube	Tapered epoxy-carbon fiber
Filter Wheels	Two 6 position wheels in tandem

X-Ray Analysis Filters
- 1200 Angstrom Aluminum (2 each, one in each wheel)
- 3 micron Magnesium
- Al/Mg/Mn 3000/2000/600 Angstrom DS
- 12 micron Aluminum
- 100 micron Beryllium

Detector CCD 1024x1024 18.3 micron pixels
- Front illuminated virtual phase

Resolution< 4 arcseconds over sun's diameter
- from geometric,diffraction, and mirror surface

ASPECT TELESCOPE:

Lens	achromatic doublet with .008" spacing, consisting of radiation-resistant crown and flint spherical elements
Clear Aperture	50 mm
Focal Length	Matched to X-ray mirror effec foc len to 0.2%

Filters

Entrance filter	4250-4800 A fwhm Al attenuator layer, IR blocking substrate, dielectric films for out-of-band reflection, + dielectric passband filter 0.001 peak transmission to match X-ray responsivity
Narrow band filter	Interference filter 30 A fwhm bandpass centered at 4308 A CH bandhead, plage and active region sensitive 0.1 +/- 0.05 peak transmission
Wide band filter	200 A fwhm bandpass centered at 4700 A
Opal glass,	flat field diffuser for radiometric calibrati

Detector	Shares the same CCD as x-ray telescope

ACCOMODATION:

Weight	29 kg
Power	18 watt average 29 watts peak
Envelope	30 x 30 x 200 cm + Electronics Boxes

The finished SXT x-ray mirror mounted in its flight support fixture. The two hyperboloids of revolution are polished into a single piece of Zerodur. (Mirror made by UTOS)

In the center is the support for the Aspect telescope.

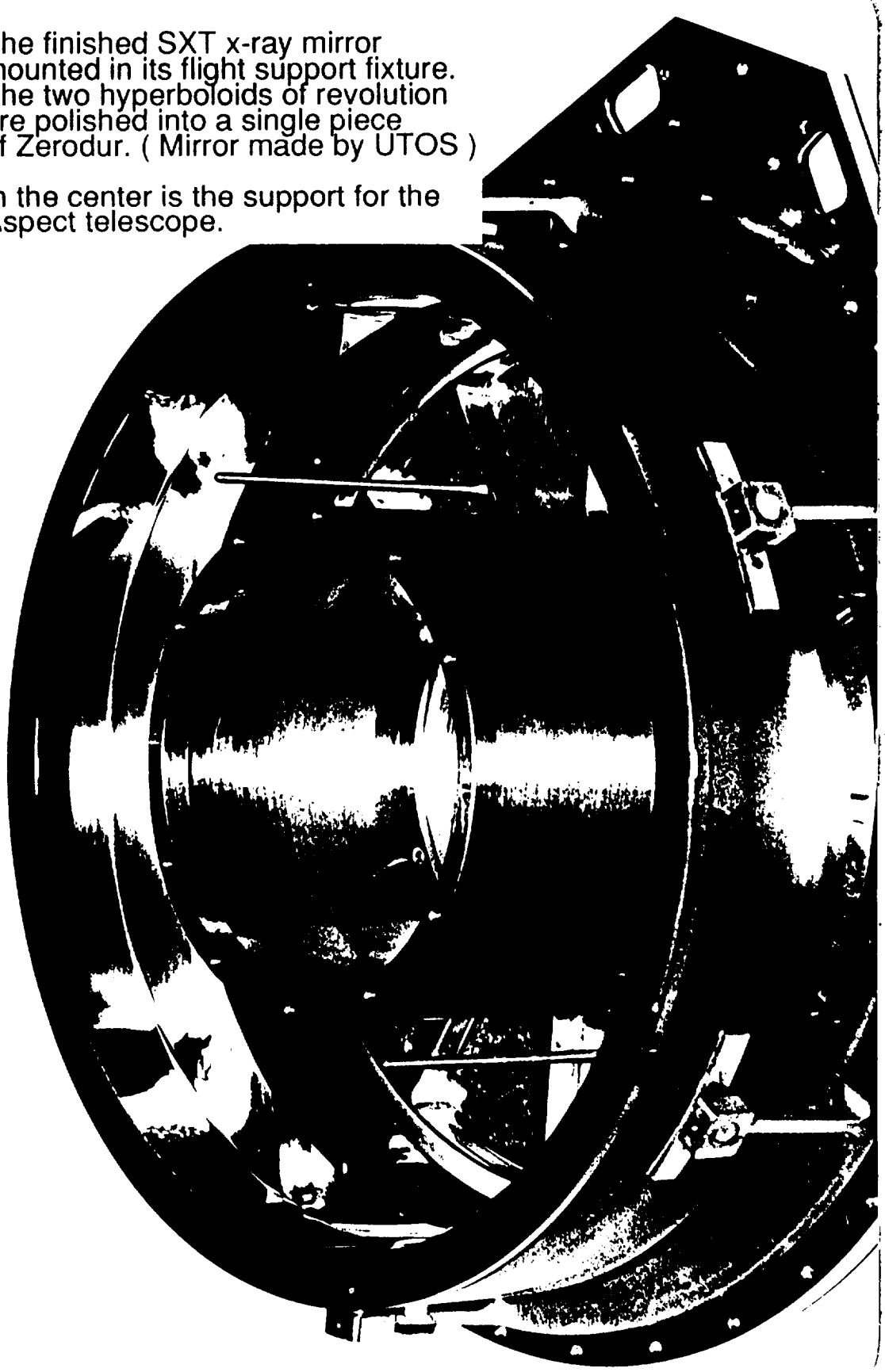

ORIGINAL PAGE
BLACK AND WHITE PHOTOGRAPH

C-3

ORIGINAL PAGE
BLACK AND WHITE PHOTOGRAPH

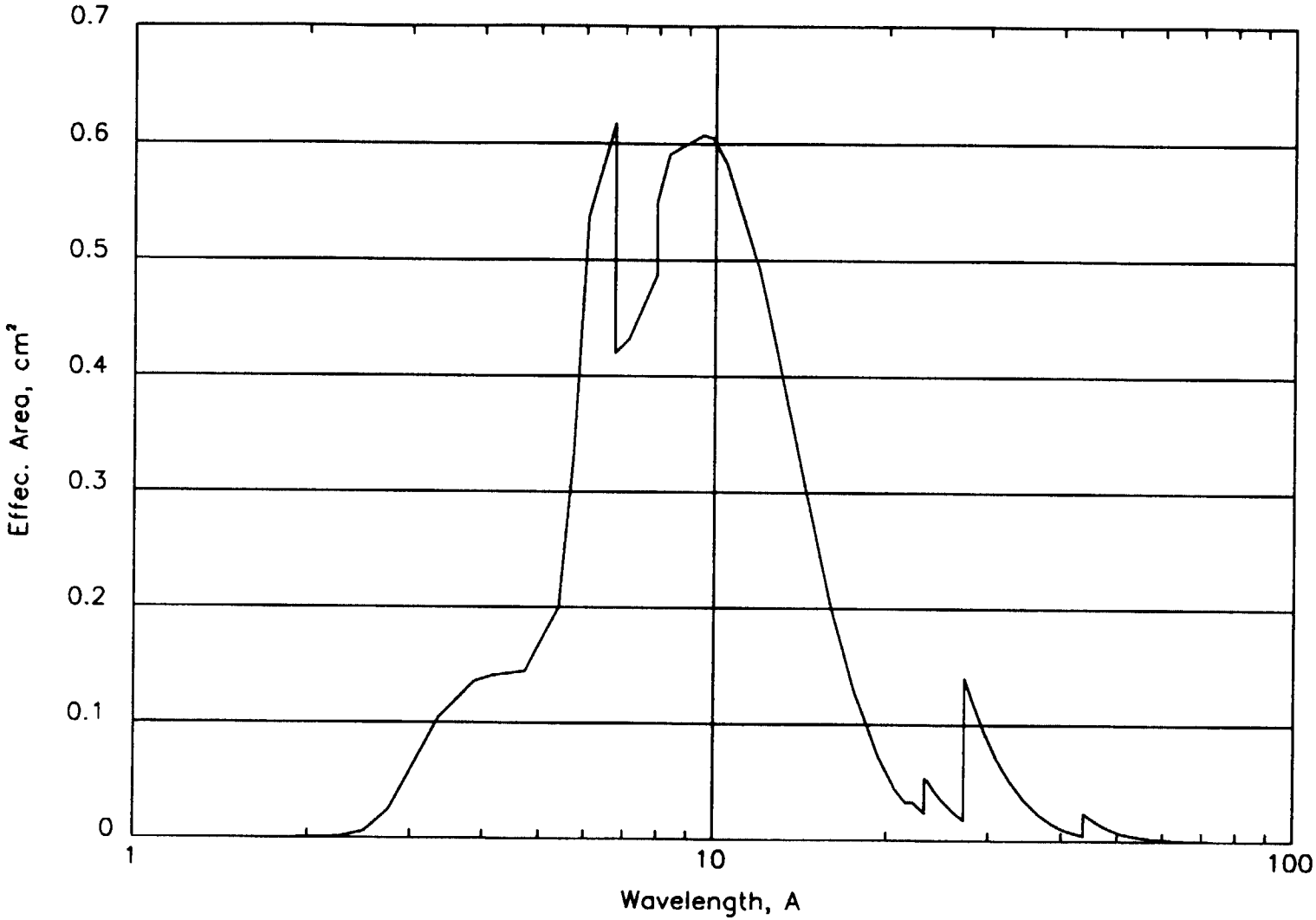

SXT Response Function including Mirror, Detector, and Entrance Filters

SXT SIGNALS FOR CONSTANT EMISSION MEASURE.

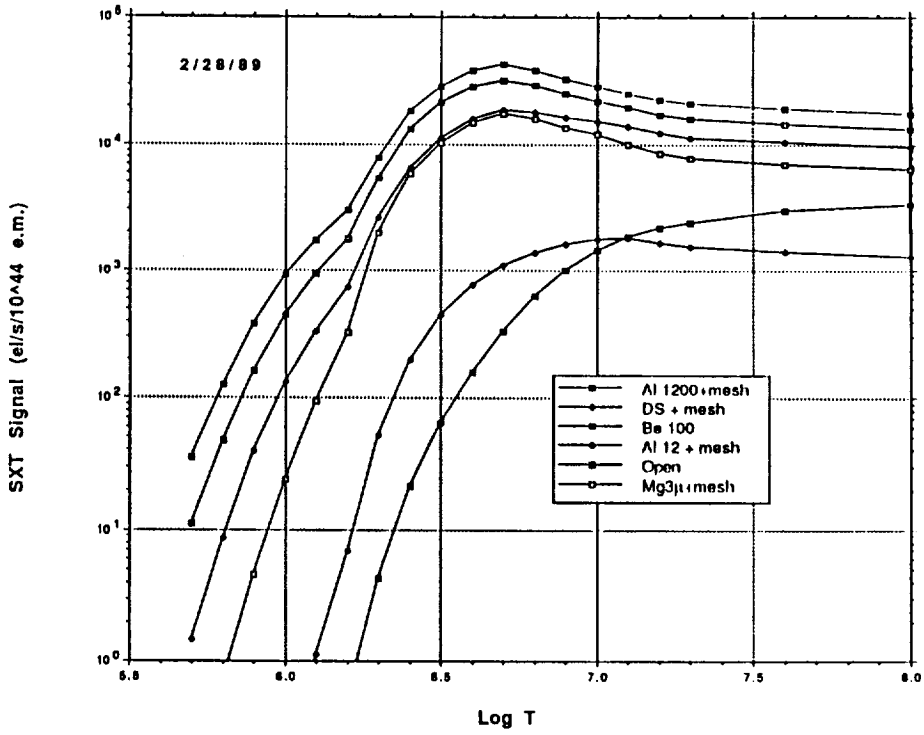

RATIOS OF SIGNALS ILLUSTRATING THE TEMPERATURE SENSITIVITY WITH FOUR PAIRS OF FILTERS

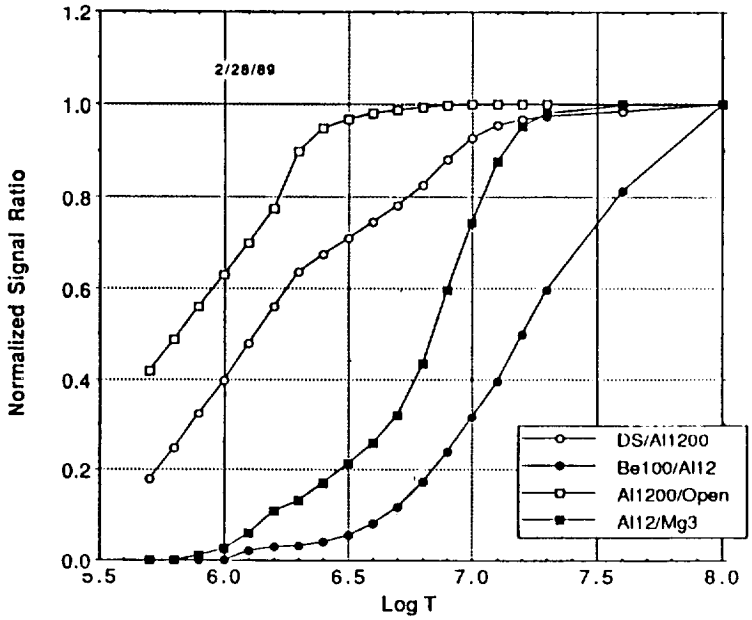

SIMULATIONS OF THE ABILITY OF THE SXT TO REPRODUCE A DIFFERENTIAL EMISSION MEASURE CURVE.

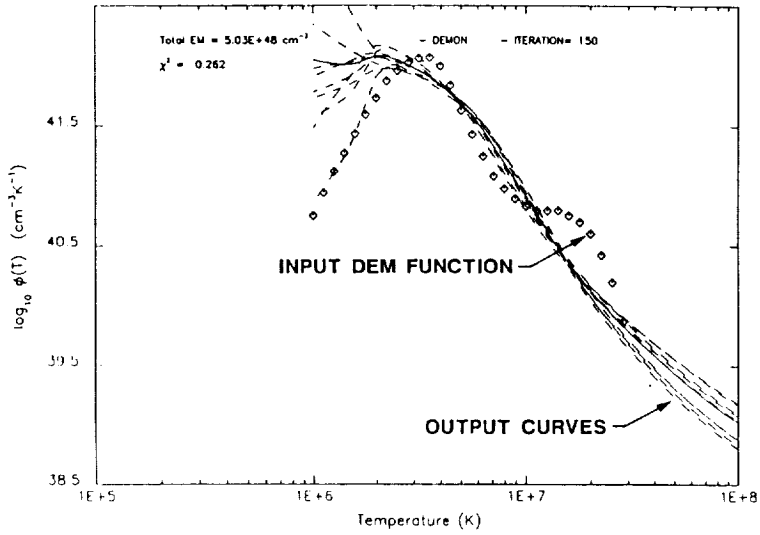

a. INPUT DEM CURVE INFERRED FROM SMM XRP DATA. VARYING PHOTON NOISE ADDED TO EACH DEMON RUN. NOTE THAT IN PRACTICE BCS DATA WILL BE USED TO IMPROVE HIGH ENERGY FIT.

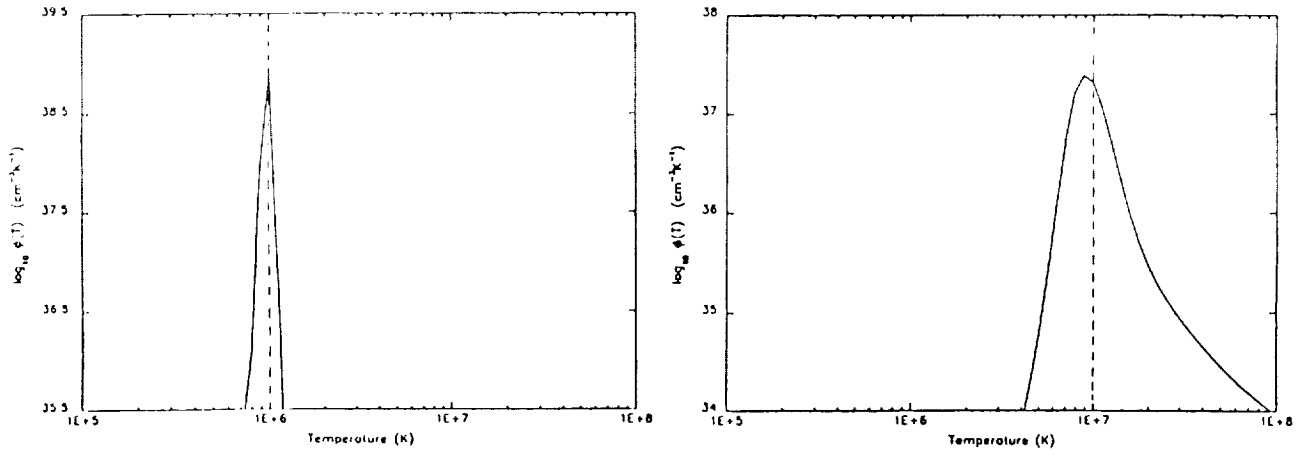

b. INPUT ISOTHERMAL SPECTRA AT 1 AND 10 MILLION DEGREES. NO NOISE ADDED.

Pre-pulses: Signature of a Trigger Process in Short (<60 secs) Solar Hard X-Ray Flares

U. Desai and L. E. Orwig (NASA/GSFC)

ABSTRACT

Our continuing study of short solar hard X-ray events (<60 sec duration) from the SMM HXRBS instrument has revealed a unique feature. A well-separated distinctly identifiable, narrow (2-6 sec wide) pulse occurs prior to the start of the longer-flare lasting emission activity. We present light curves of eight events showing this feature. These pre-pulses show symmetrical rise and fall times. We present spectral evolution of the pre-pulses and compare their evolution to that of the main event spectra. We argue for this feature to be the elementary flare burst (de Jager, 1978). These pre-pulses could be a signature of the magnetic reconnection phenomenon discussed by Sturrock et al. (1984).

INTRODUCTION:

The light curves of the hard X-ray emission (20-500 keV) associated with solar flare activity have very complex and diverse characteristics. Their durations extend from a few seconds to tens of minutes. Attempts to classify flares using their light curves to understand the physical processes involved in flare phenomena has been very difficult. Various schemes have been proposed (Heyvaert et al. 1977, Priest 1981, Tanaka 1983, Tsuneta and Tanaka 1987).

Broad classification on the basis of their duration, i.e. short (<few minutes) and long lasting (few minutes to tens of minutes), offers some opportunity to understand flare phenomena - their dynamics and energetics. The short events could be associated with compact flaring active regions while the long-lasting events could be associated with extended active regions. We are studying a subset of short events (< 60 sec) from the SMM/HXRBS data set to evaluate their fine time structure and their spectral evolution. The fine time structure studies involves the search for periodicities or quasiperiodicities and a search for homology in these events (Wiehl & Desai 1983, Desai et al. 1987).

We present in this paper evidence showing a well separated, distinctly identifiable narrow pulse feature prior to the start of longer-lasting hard X-ray flare activity. We have observed a symmetrical nature in the rise and fall times of their light curves and have compared their spectral evolution with that of the later flare activity. We argue that this pre-pulse feature is the true "elementary flare burst" (van Beek, de Feitor and de Jager 1974; de Jager and de Jonge 1978) and is the signature of the magnetic reconnection phenomenon discussed by Sturrock 1984.

DATA:

The SMM Hard X-ray Burst Spectrometer (HXRBS) has recorded about 8000 hard X-ray events over a period of eight years from 1980 to 1988. About 200 of these events have a duration of less than 60 secs and a peak counting rate of >100 counts per second. We present the analysis of ten of these events which show a narrow pulse feature at the beginning of the hard X-ray activity. Table 1 gives the date, time of occurrence, and some parameters of the events.

Table 1

	Date	Time (UT)	Duration (s)	Pre-pulse Peak rate (counts/s)	FWHM of Pre-pulse (s)
1	80/6/9	0251:20	27	800	4.0
2	80/7/5	1010:00	34	200	3.5
3	80/7/9	0145:36	30	400	3.5
4	81/2/7	1505:43	12	340	2.5
5	81/4/25	0046:50	18	600	5.0
6	81/7/10	0655:02	13	550	3.5
7	82/2/11	2351:48	30	420	3.0
8	82/6/12	2015:50	20	300	5.0
9	84/4/29	1736:58	10	800	4.0
10	87/5/26	1701:31	20	200	2.5

Figure 1 shows light curves of the events on June 9, 1980, and July 9, 1980. In both of these events the pre-pulse is clearly identifiable. The June 9 event, with a peak counting rate of 800 counts/s in the pre-pulse, exhibits some fine time structure. The rise at 0251:24 UT is statistically significant. The peak counting rate in the pre-pulse is the same as the peak counting-rate in the later activity. For all but one event this observed feature that the pre-pulse is as intense as the later flare activity is true. In the July 9th event the pre-pulse has a symmetrical structure with equal rise and fall times and shows no indication of any fine time structure. The later activity is more extended in time as compared to the event of June 9.

In Figure 2 we show three events on July 5, 1980, July 17, 1980 and May 26, 1987. These three events are not as intense as the previous two shown in Figure 1. The pre-pulses are also narrower. The pre-pulse to main phase delays in these three events are of the order of half a second. The total duration of flare activity are also very similar, indicating homology for the total flare emission. The event on May 26th, 1987 shows activity with a 12-second delay. For each of these three events the peak counting rate in the pre-pulse in the same as that in the main phase of flare activity.
Figure 3 shows light curves of the events of February 11, 1982 and June 12, 1982. The pre-pulse for the June 12th event is not as intense as the later main phase activity. The main phase activity of the February 11th event is delayed by about 12 seconds. In Figure 4 we show three events where there is only pre-pulse activity.

We have examined the spectral characteristic for the pre-pulse and main phase flare activity and do not find any significant difference between them. Figure 5 shows a light curve of the most intense event, that of June 9, 1980. The spectral index, ν, which results from a power-law fit to the flare data is the same during the pre-pulse and the later main phase activity and has a value of $\nu = 3$.

CONCLUSIONS:

In the events studied here the width of the pre-pulse varies from a couple of seconds to 5 seconds. This feature is quite unique with respect to its location in time, width, and symmetrical rise and fall characteristics. Earlier attempts to identify an "elementary event burst" from entire light curves of extended events could not establish its true characteristics. Our results show that the total energy in the pre-pulse, the "elementary event burst", lies in the range 10^{27} - 10^{28} ergs. This value is consistent with the value derived by Sturrock (1984), cf. 10^{27} -10^{28} ergs, or that of 10^{27} - 10^{29} ergs derived by van Beek et al. (1974).

REFERENCES:

de Jager, C. and de Jong, G., Solar Physics, 58, 127-137, 1978.

Desai, U. D., et al., Ap. J., 319, 567-573, 1987.

Heyvaerts, J., Priest, E. R., and Rust, D. M., Ap. J., 216, 123-137, 1977.

Sturrock, P. A., et al., Solar Physics, 94, 341-357, 1984.

Tanaka, K., IAU Colloquium, 71, 307, 1983.

Tanaka, K., Publ. Astron. Soc. Japan, 39, 1, 1987.

Tsuneta, S., et al., in Proc. of Japan-France Seminar on Active Phenomena in the Outer Atmosphere of the Sun and Stars, 243-260, 1983.

Wiehl, H. J. and Desai, U., Ap. J., 270, 256-264, 1983.

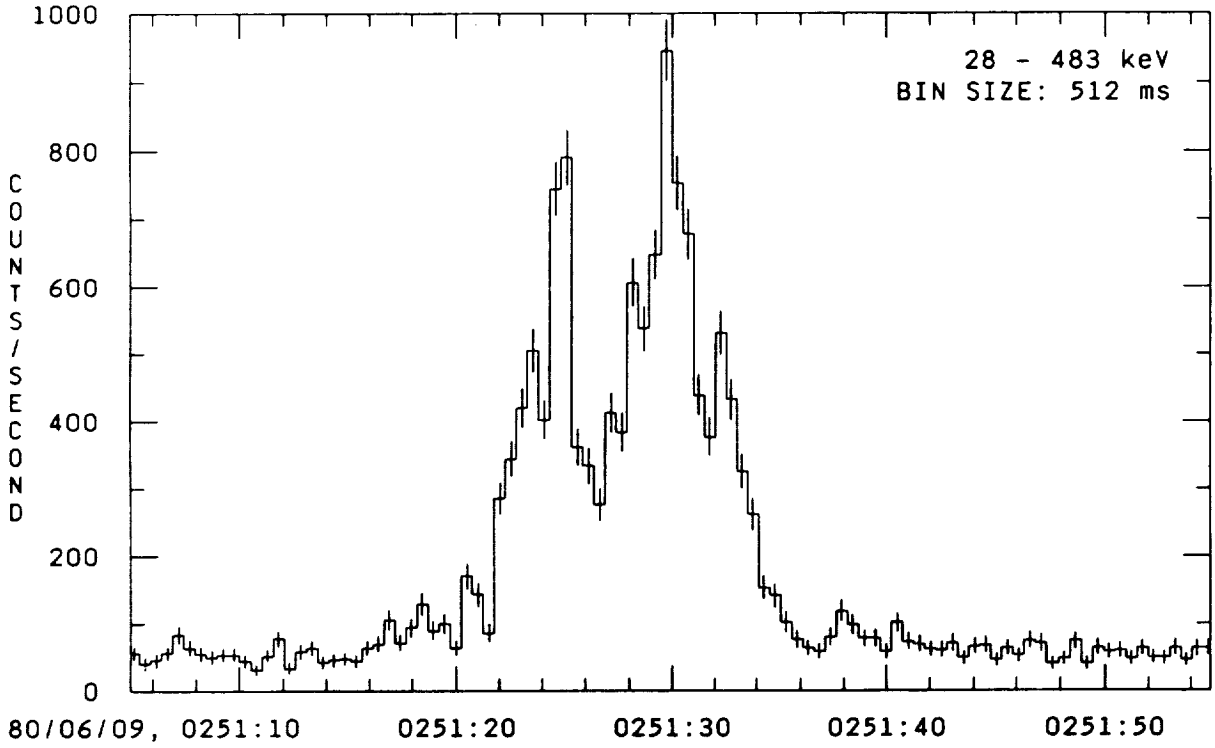
28 - 483 keV
BIN SIZE: 512 ms
COUNTS/SECOND
1000
800
600
400
200
0
80/06/09, 0251:10
0251:20
0251:30
0251:40
0251:50

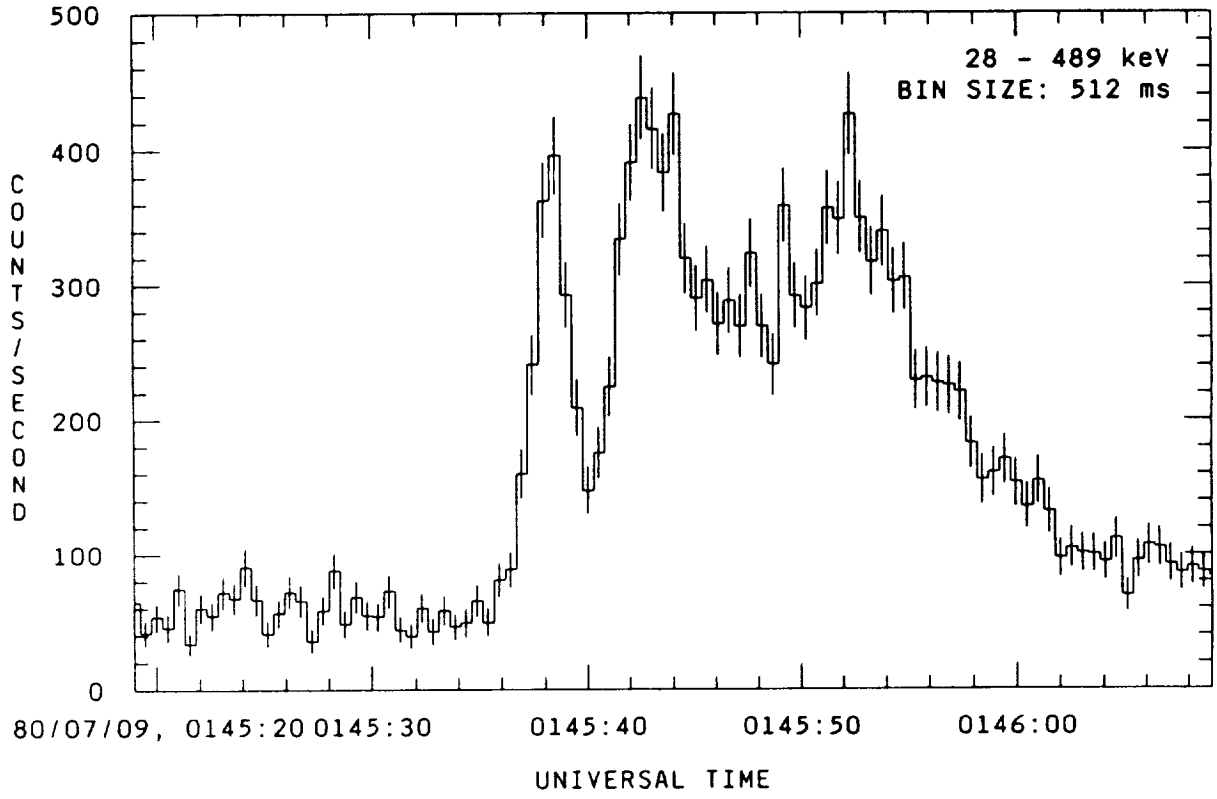
28 - 489 keV
BIN SIZE: 512 ms
COUNTS/SECOND
500
400
300
200
100
0
80/07/09, 0145:20
0145:30
0145:40
0145:50
0146:00
UNIVERSAL TIME

Fig. 1

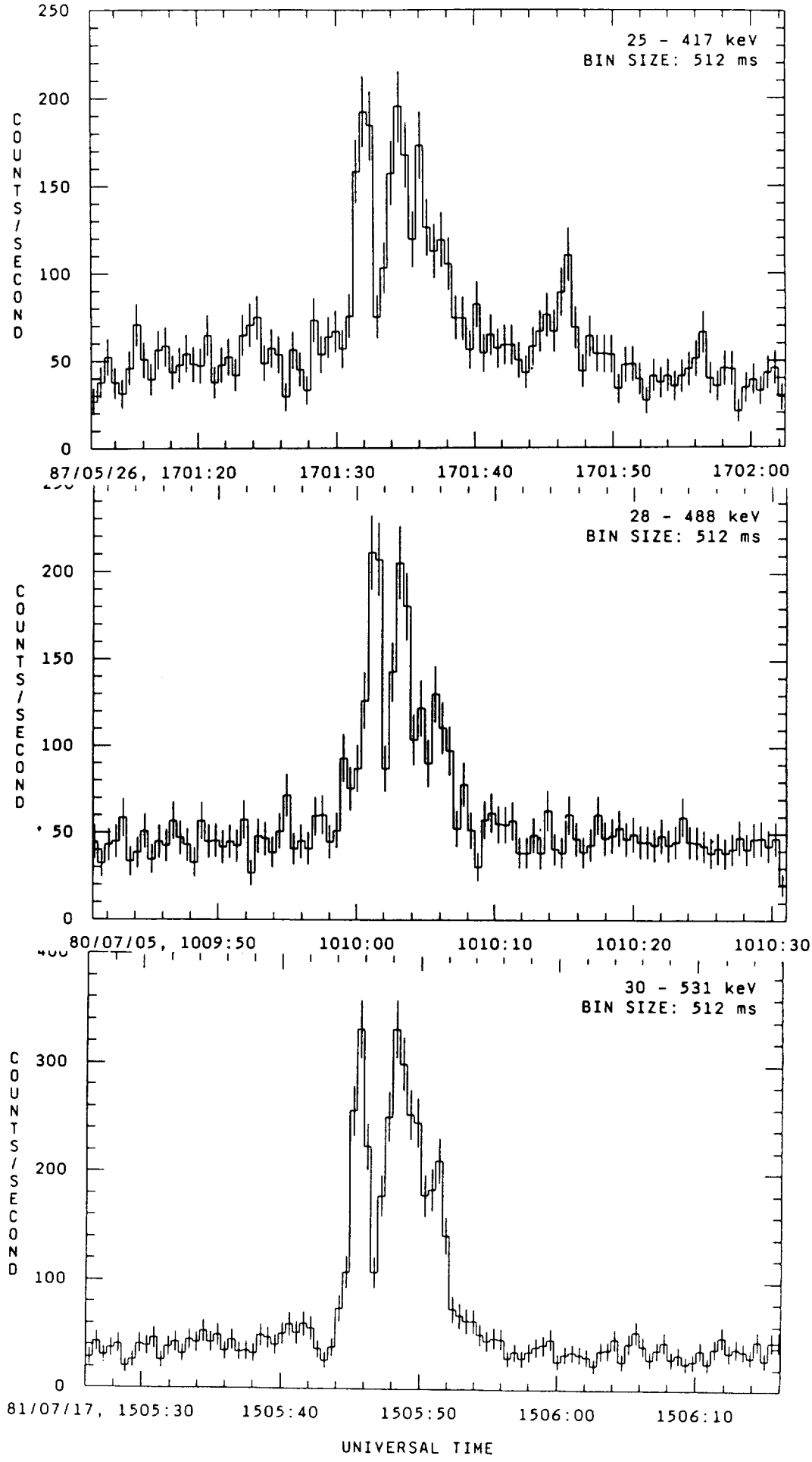
25 - 417 keV
BIN SIZE: 512 ms
COUNTS/SECOND
250
200
150
100
50
0
87/05/26, 1701:20
1701:30
1701:40
1701:50
1702:00
28 - 488 keV
BIN SIZE: 512 ms
COUNTS/SECOND
200
150
100
50
0
80/07/05, 1009:50
1010:00
1010:10
1010:20
1010:30
30 - 531 keV
BIN SIZE: 512 ms
COUNTS/SECOND
300
200
100
0
81/07/17, 1505:30
1505:40
1505:50
1506:00
1506:10
UNIVERSAL TIME

Fig. 2

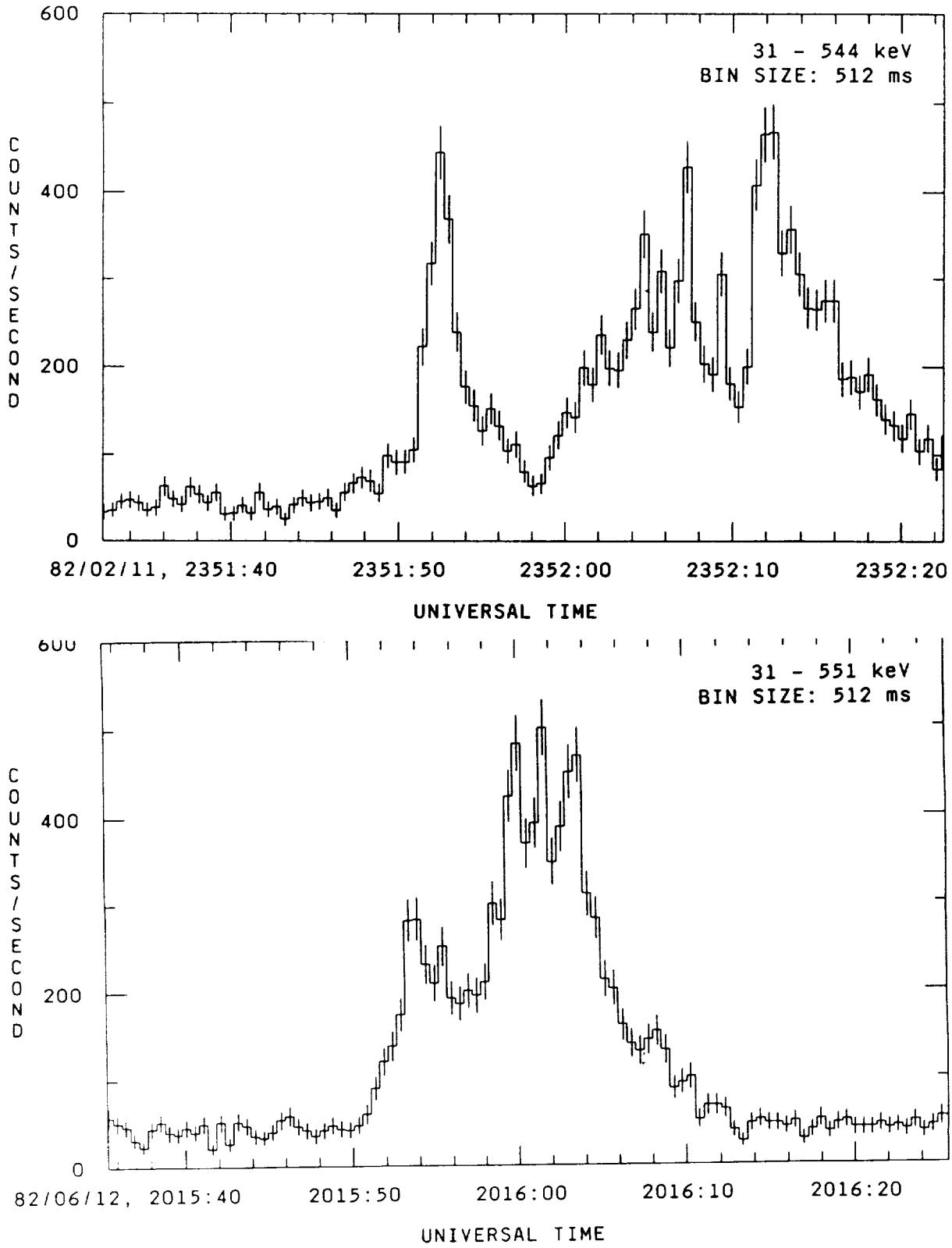
600
400
200
0
COUNTS/SECOND
31 - 544 keV
BIN SIZE: 512 ms
82/02/11, 2351:40
2351:50
2352:00
2352:10
2352:20
UNIVERSAL TIME
600
400
200
0
COUNTS/SECOND
31 - 551 keV
BIN SIZE: 512 ms
82/06/12, 2015:40
2015:50
2016:00
2016:10
2016:20
UNIVERSAL TIME

Fig. 3

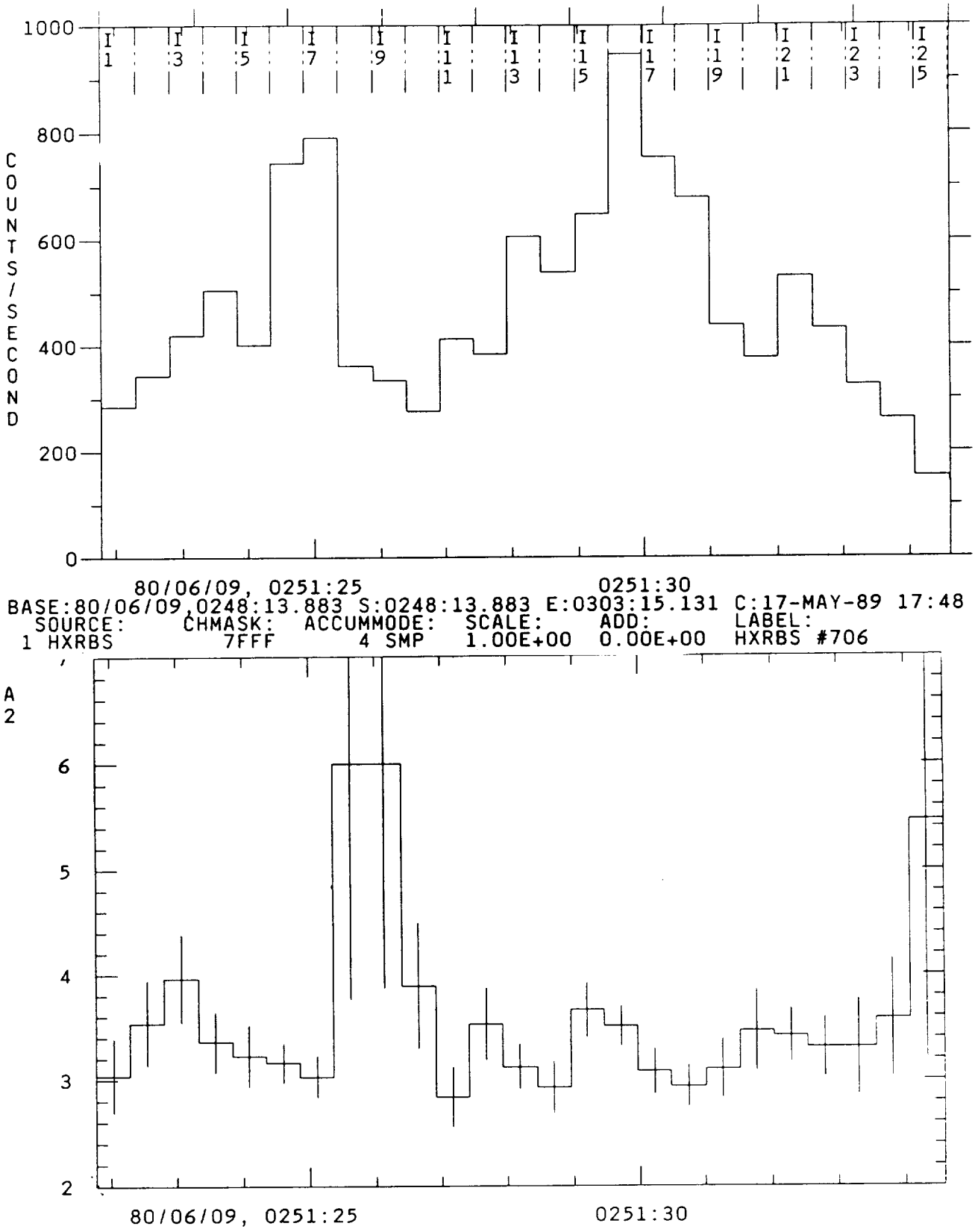
1000
800
600
400
200
0
COUNTS/SECOND
80/06/09, 0251:25
0251:30
BASE:80/06/09,0248:13.883 S:0248:13.883 E:0303:15.131 C:17-MAY-89 17:48
SOURCE: CHMASK: ACCUMMODE: SCALE: ADD: LABEL:
1 HXRBS 7FFF 4 SMP 1.00E+00 0.00E+00 HXRBS #706
A2
6
5
4
3
2
80/06/09, 0251:25
0251:30
1POWERL = A1*(E/EM)**(-A2)
80/06/09, 0251:21.787 17-MAY-8906:43:31
START INTERVAL= 1 TOTAL INTERVALS= 25

Fig. 5

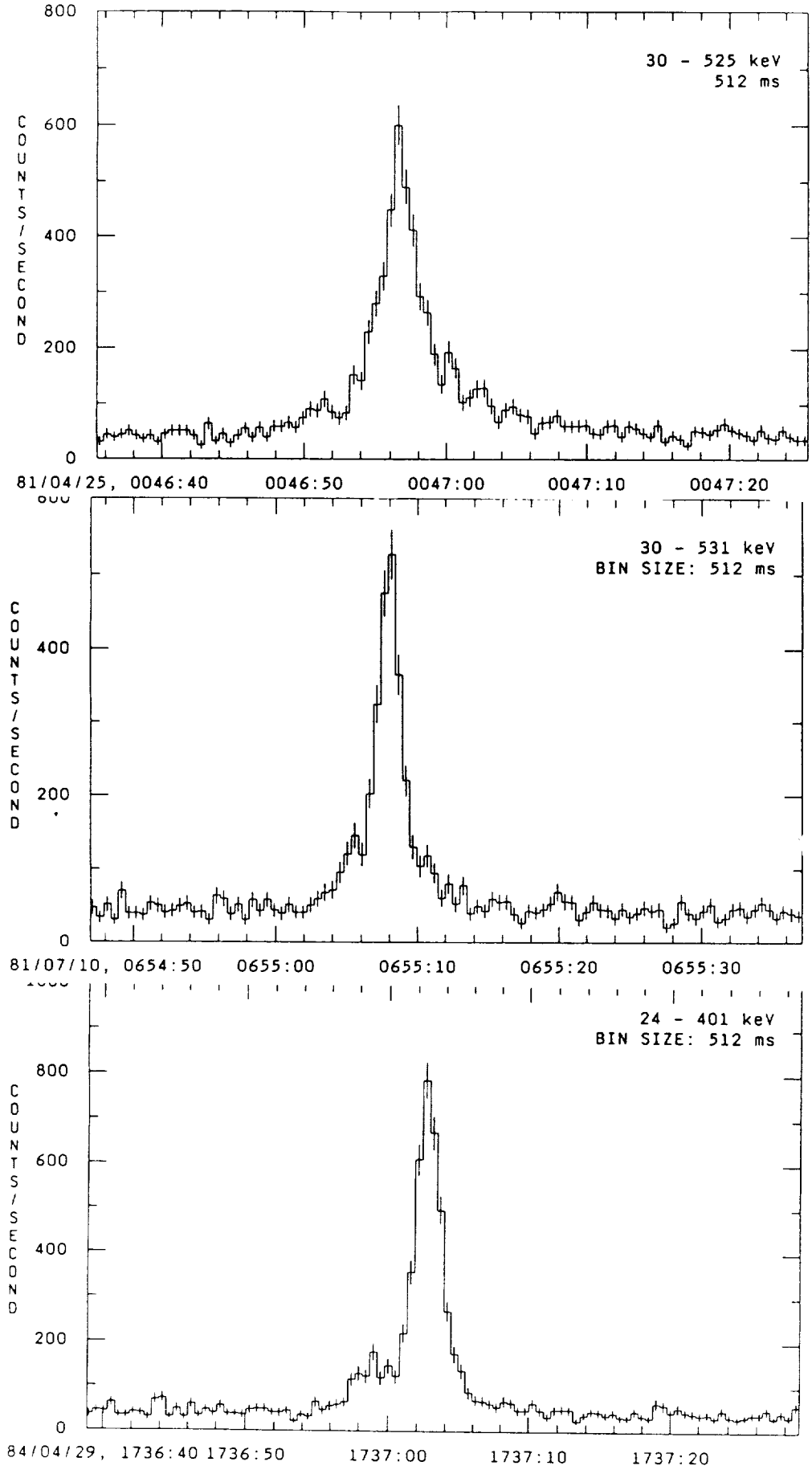
30 - 525 keV
512 ms
COUNTS/SECOND
800
600
400
200
0
81/04/25, 0046:40
0046:50
0047:00
0047:10
0047:20
30 - 531 keV
BIN SIZE: 512 ms
COUNTS/SECOND
400
200
0
81/07/10, 0654:50
0655:00
0655:10
0655:20
0655:30
24 - 401 keV
BIN SIZE: 512 ms
COUNTS/SECOND
800
600
400
200
0
84/04/29, 1736:40
1736:50
1737:00
1737:10
1737:20

Fig. 4

FLARE MODEL SENSITIVITY OF THE BALMER SPECTRUM

A. Falchi[1], R. Falciani[2], L.A. Smaldone[3] and G.P. Tozzi[1]

[1] Osservatorio Astrofisico di Arcetri
Largo E. Fermi 5 - 50125 Firenze (Italy)
[2] Dipartimento di Astronomia
Largo E. Fermi 5 - 50125 Firenze (Italy)
[3] Dipartimento di Scienze Fisiche
Pad. 19-20 Mostra d'Oltremare - 80125 Napoli (Italy)

Introduction.

Careful studies of various chromospheric spectral signatures are very important in order to explore their possible "sensitivity" to the modifications of the thermodynamic quantities produced by the flare occurrence.

Pioneer work of Canfield and co-workers (Canfield et al., 1984) have shown how the H_α behaviour is able to indicate different changes in the atmospheric parameters structure associated to the flare event.

We decided to study the behaviour of the highest Balmer lines and of the Balmer continuum in different solar flare model atmospheres. These spectral features, originating in the deep photosphere in a quiet area, may have a sensitivity different from H_α to the modification of a flare atmosphere.

The details of the method used to compute the Stark profile of the higher Balmer lines ($n \geq 6$) and their merging have been extensively given elsewhere (Donati-Falchi et al., 1985; Falchi et al.,1989).

We used the models developed by Ricchiazzi in his thesis (1982) who evaluated the chromospheric response to both the non-thermal electron flux, for energy $> 20Kev$, (F_{20}) and to the thermal conduction (F_c). The effect of the coronal pressure values (P_0) at the apex of the flare loop is also included.

Results

In order to compare our results to those obtained by Canfield et al. (1984) for the H_α profiles, we will separately explore the effects produced on the considered spectral features by the changes of the three input parameters of the considered flare atmospheres. The various models will be hereafter referred to as M:A:B:C in which $F_{20} = 10^A erg\ cm^{-2} sec^{-1}$, $F_c = 10^B erg\ cm^{-2} sec^{-1}$, and $P_0 = 10^C dyne\ cm^{-2}$.

Effects of non-thermal electron flux F_{20}

We considered two regimes of P_0:

$P_0 = 1 dyne\ cm^{-2}$ (low coronal pressure) and

$P_0 = 10^2 dyne\ cm^{-2}$ (nominal coronal pressure) in order to better understand the influences due to the F_{20} variations. The nominal value for F_c is assumed to be $10^7 erg\ cm^{-2} sec^{-1}$. The dependence on F_{20} of our spectral signatures is roughly the same for the two P_0 regimes: the Balmer continuum increases with F_{20} enhancements while the Balmer lines intensity seems to be rather insensitive. With the highest F_{20} values we only notice broader line profiles. The results obtained with the models M:9:7:2 and M:10:7:2 and M:11:7:2 are illustrated in Figures 1 and 2.

Effects of coronal pressure P_0

We considered three different values of P_0:
$P_0 = 1,\ 10^2,\ 10^3 dyne\ cm^{-2}$
with $F_{20} = 10^{10} erg\ cm^{-2} sec^{-1}$,
and $F_c = 10^7 erg\ cm^{-2} sec^{-1}$.

The Balmer continuum is quite sensitive ($\Delta I \simeq 2.$) to the value of the coronal pressure when P_0 is ranging from 1 to 10^2, while, in the interval $10^2 - 10^3$, the intensity remains practically the same but the slope. In fact all the highest Balmer lines are in absorption for $P_0 \leq 10^2$ and become in emission with very broad wings for $P_0 = 10^3$ and in this case the merging of the highest Balmer lines changes the slope of the continuum. These results are shown in Figures 3 and 4.

Effects of thermal conductive flux F_c

We considered 2 different regimes of P_0:
$P_0 = 1 dyne\ cm^{-2}$ with $F_c = 10^6, 10^7, 10^8 erg\ cm^{-2} sec^{-1}$
$P_0 = 10^2 dyne\ cm^{-2}$ with $F_c = 10^7, 10^8 erg\ cm^{-2} sec^{-1}$
For all these models a value of $F_{20} = 10^{10} erg\ cm^{-2} sec^{-1}$ is assumed. For P_0 ranging from 1 to 10^2 the Balmer continuum decreases as F_c increases The highest Balmer lines are in absorption with broad wings and a central narrow emission core. The Balmer line intensities seem to be quite insensitive to the F_c values increase. The results for models M:10:7:2 and M:10:8:2 are shown in Figures 5 and 6.

The $T_e(h)$ and $N_e(h)$ distributions for all the considered models are shown in Figures 7, 8 and 9.

CONCLUSIONS

Balmer Continuum

- its strong increase in intensity unambiguously reflects high values of F_{20}. This signature is equivalent to the H_α wings sensitivity found by Canfield et al. (1984);

- it decreases when F_c increases;

Balmer Lines

- broad and relevant wings in Balmer lines indicate a high F_{20} value as already found for H_α;

- strong variations in intensity can be due to a P_0 increase ($> 10^2$);

- they seem to be quite insensitive to F_c variations.

Calculations of the Na-D lines profiles are in progress. These spectral features may be used to disentangle the remaining ambiguities still present in H_α and Balmer continuum.

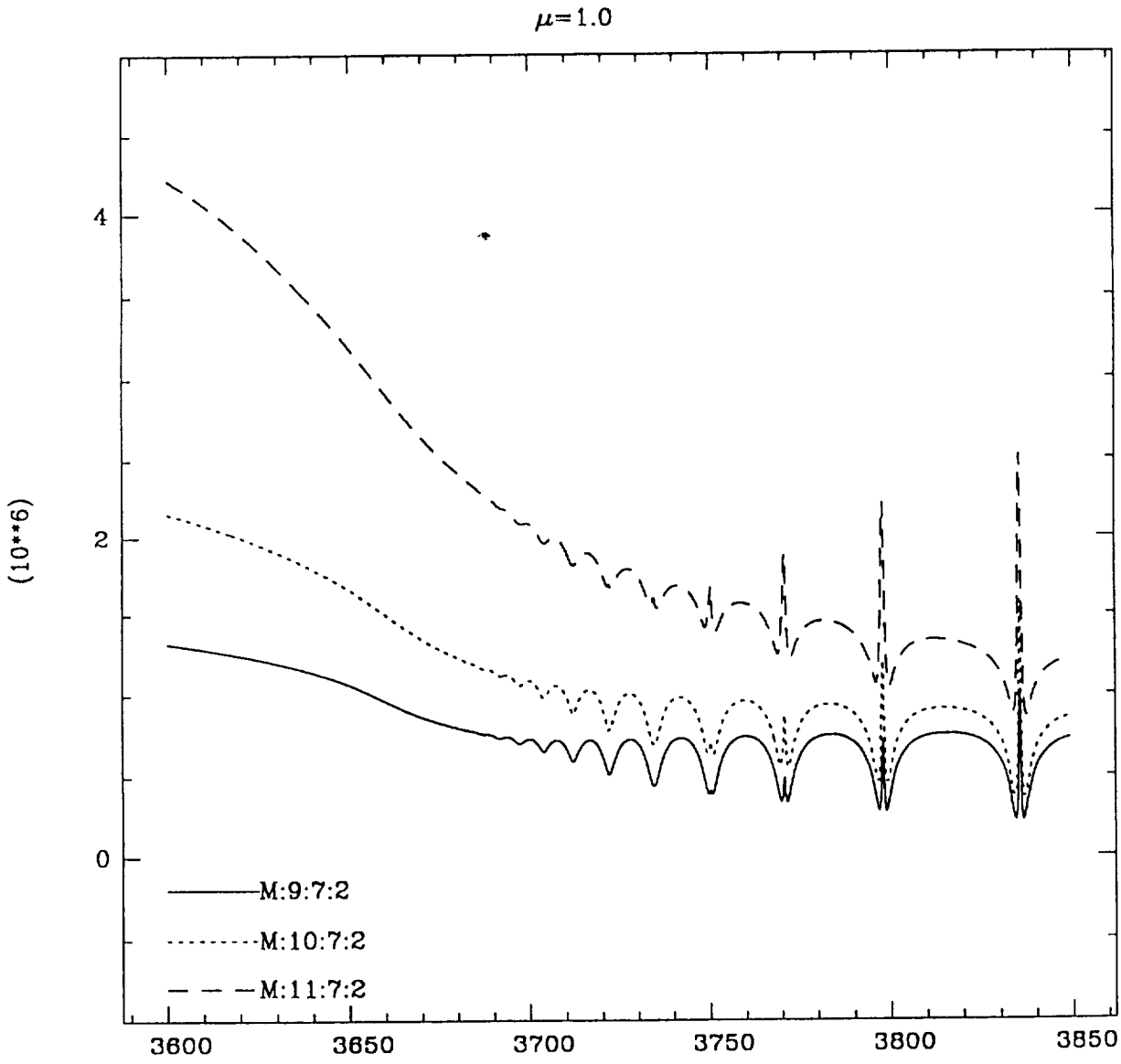

Fig. 1 - Flare net emission in the spectral range 3600 - 3850 Å computed for the labelled flare models (see the text for their meaning).

Units are $10^6 erg\ sec^{-1} cm^{-2} ster^{-1}$.

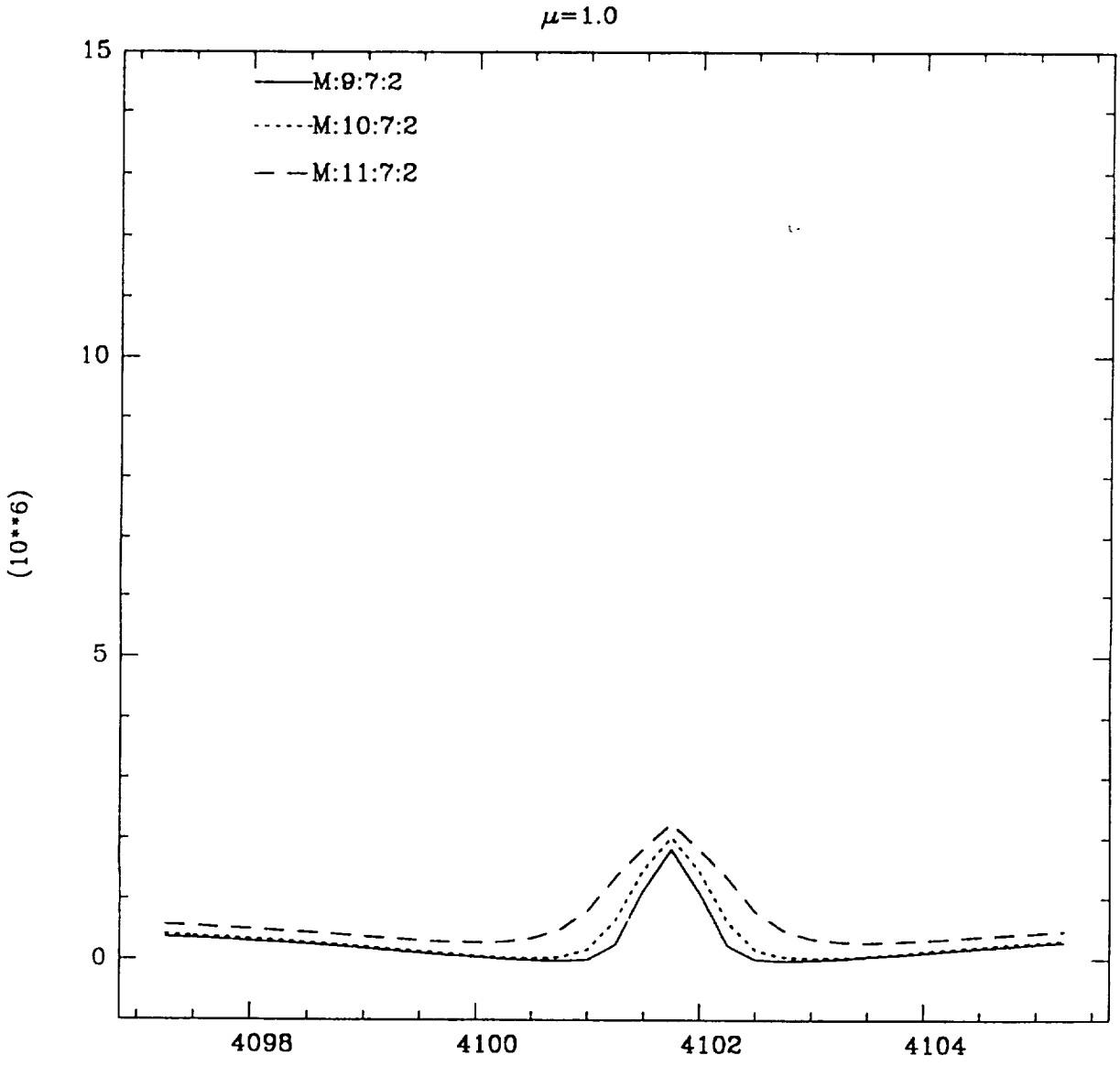

Fig. 2 - Flare net emission in H_δ line computed for the labelled flare models.

Units are $10^6 erg\ sec^{-1} cm^{-2} ster^{-1}$.

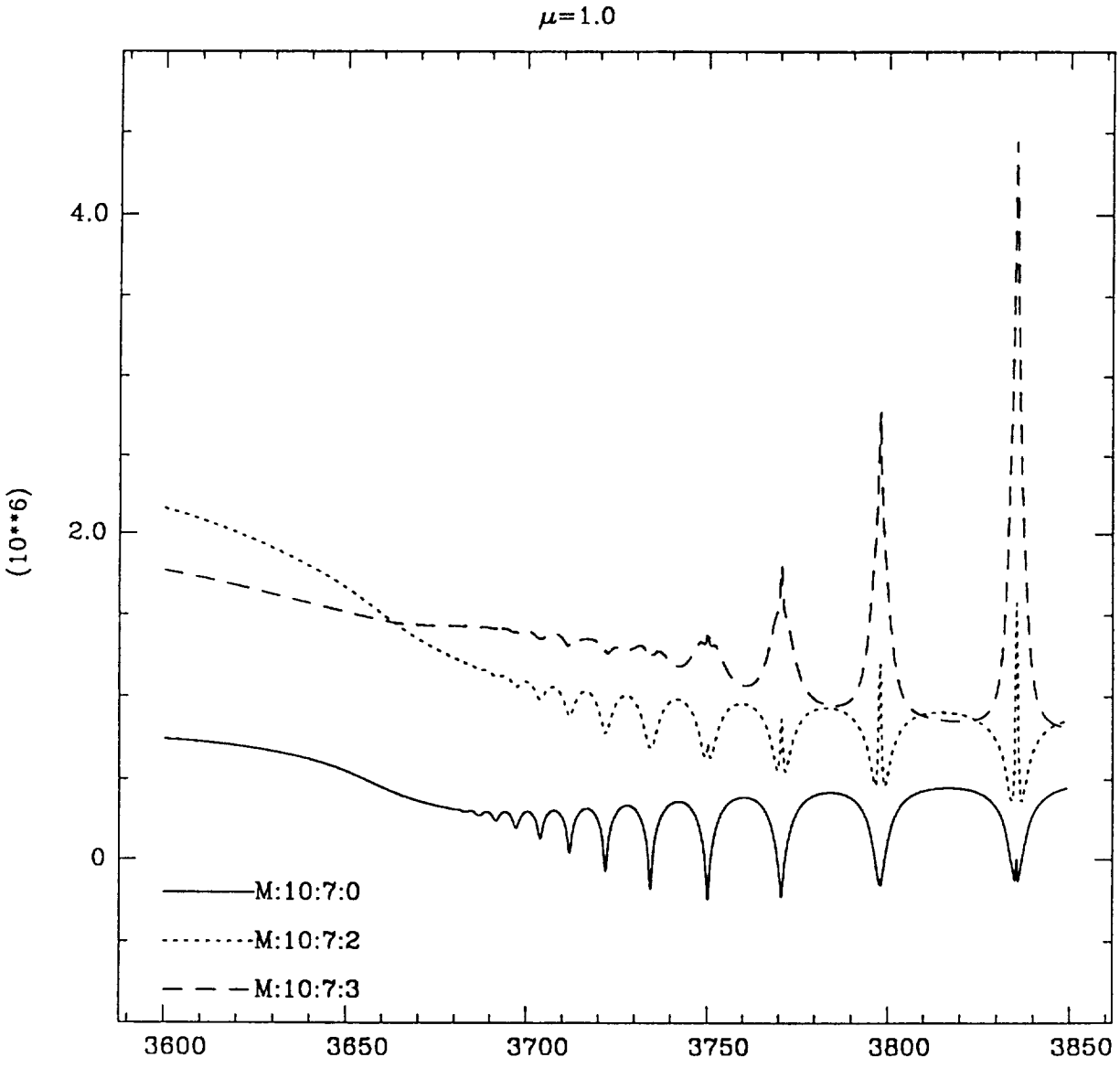

Fig. 3 - Flare net emission in the spectral range 3600 - 3850 Å computed for the labelled flare models (see the text for their meaning).

Units are $10^6 erg\ sec^{-1} cm^{-2} ster^{-1}$.

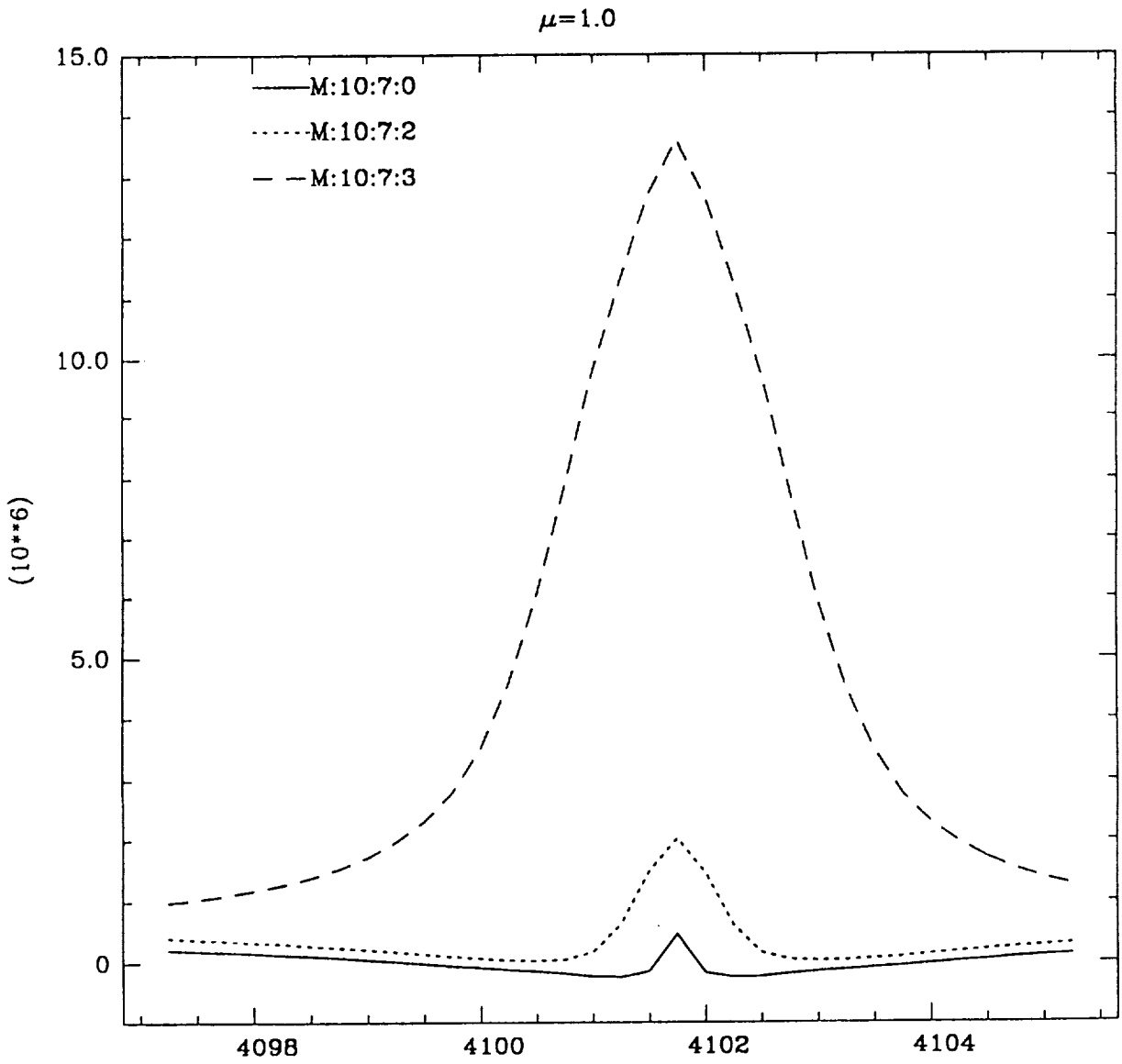

Fig. 4 - Flare net emission in H_δ line computed for the labelled flare models.

Units are $10^6 erg\ sec^{-1} cm^{-2} ster^{-1}$

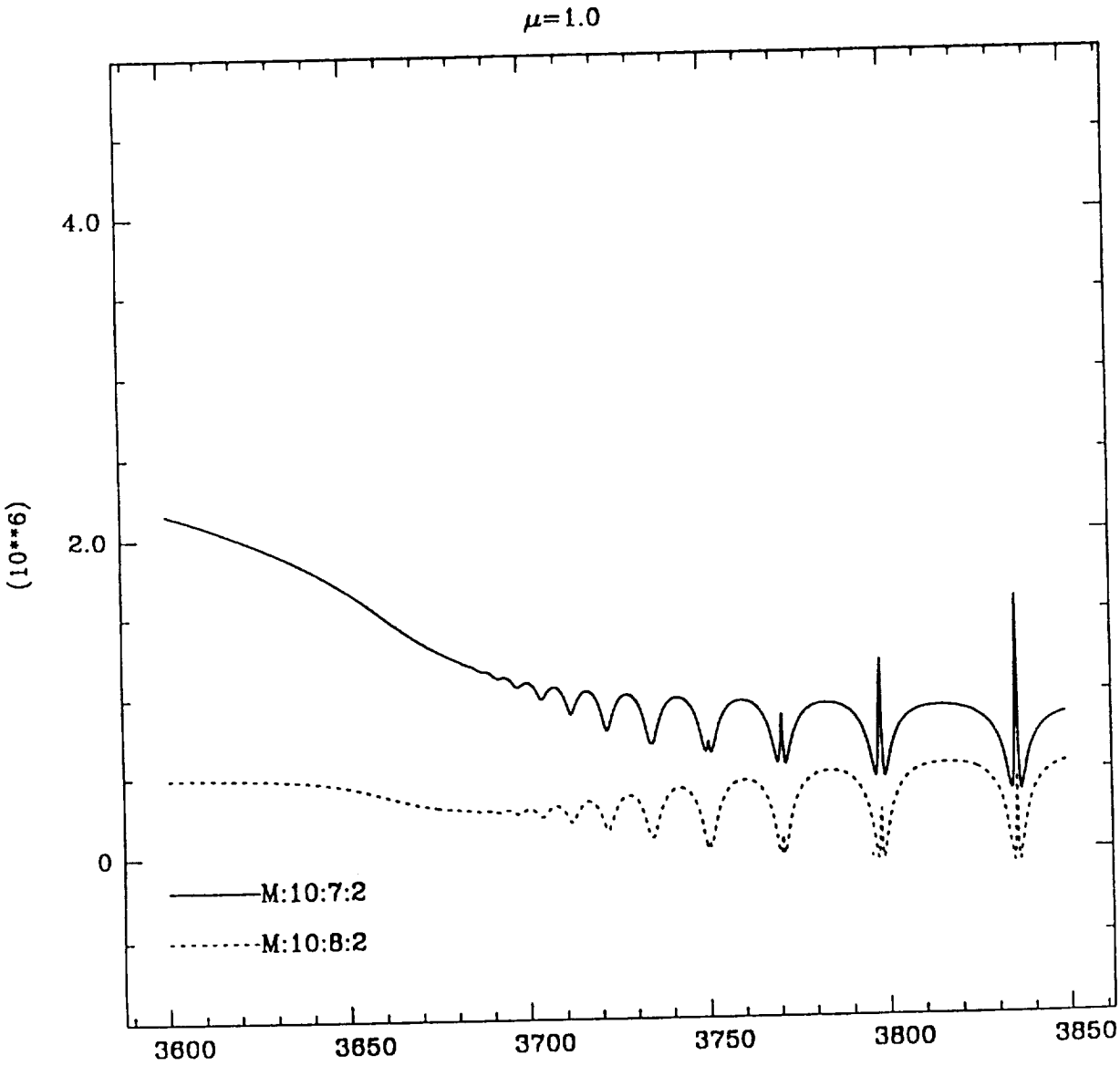

Fig. 5 - Flare net emission in the spectral range 3600 - 3850 Å computed for the labelled flare models (see the text for their meaning).

Units are $10^6 erg\ sec^{-1} cm^{-2} ster^{-1}$.

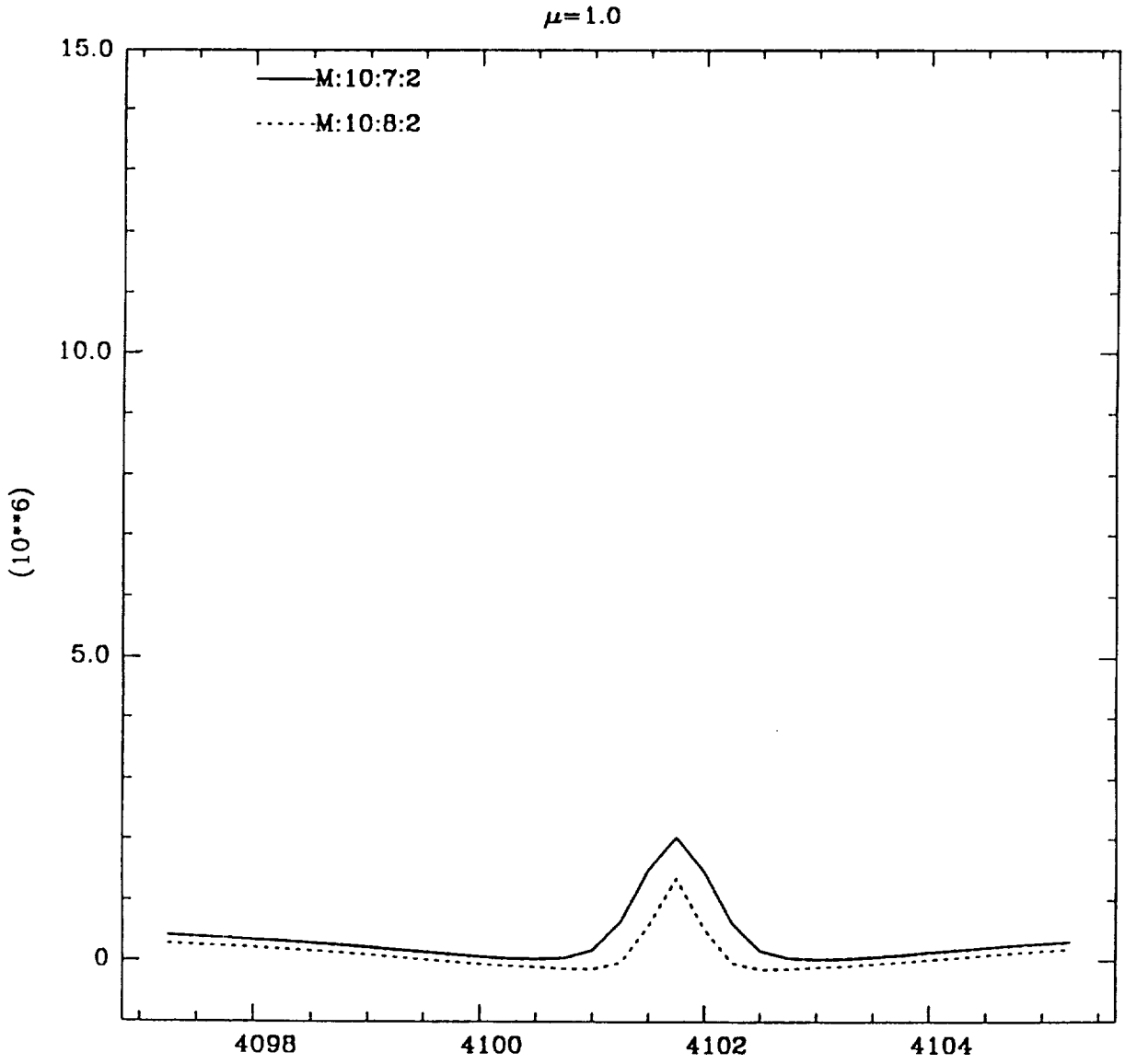

Fig. 6 - Flare net emission in H_δ line computed for the labelled flare models.

Units are $10^6 erg\ sec^{-1} cm^{-2} ster^{-1}$

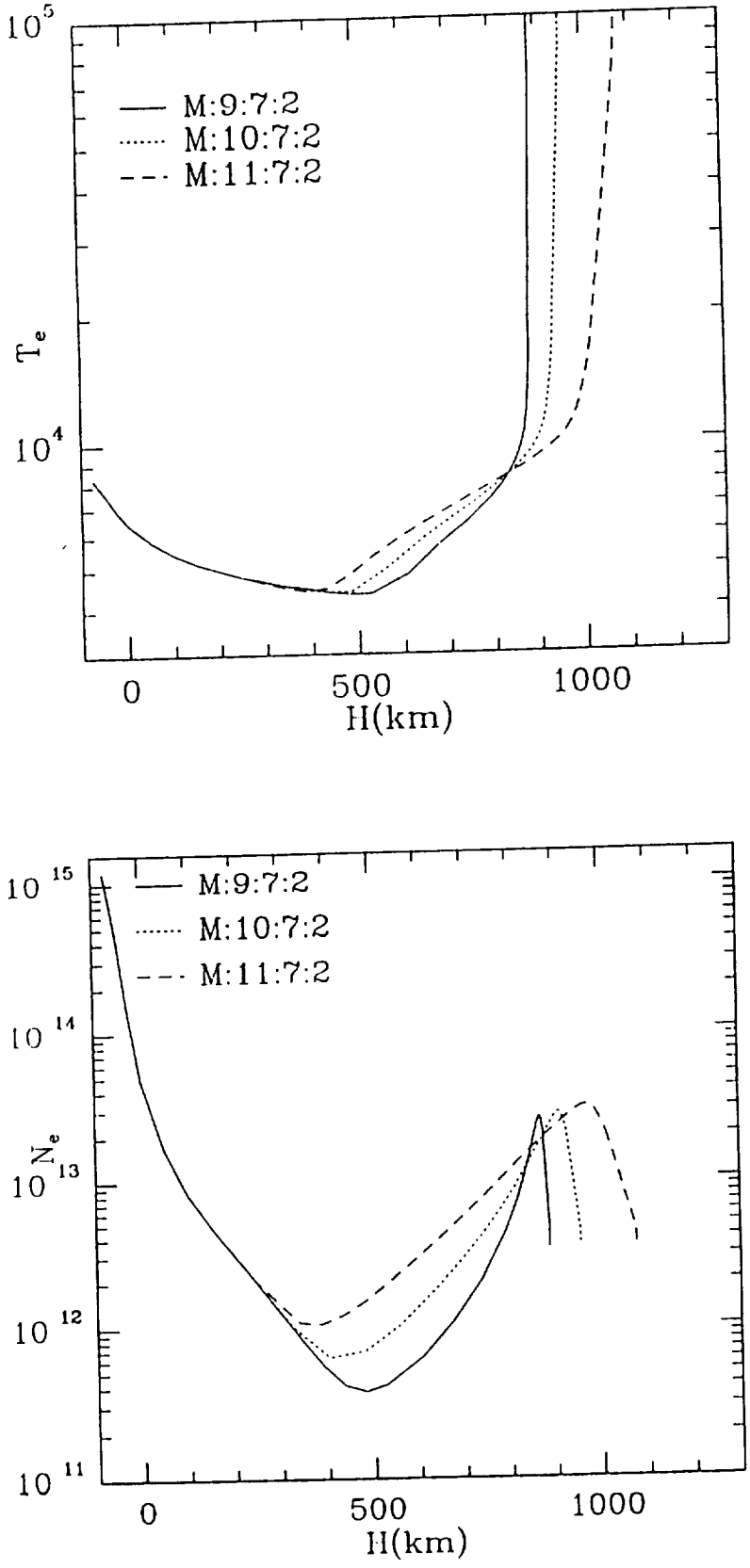

Fig. 7 - Log T_e and Log N_e distributions vs geometrical height.

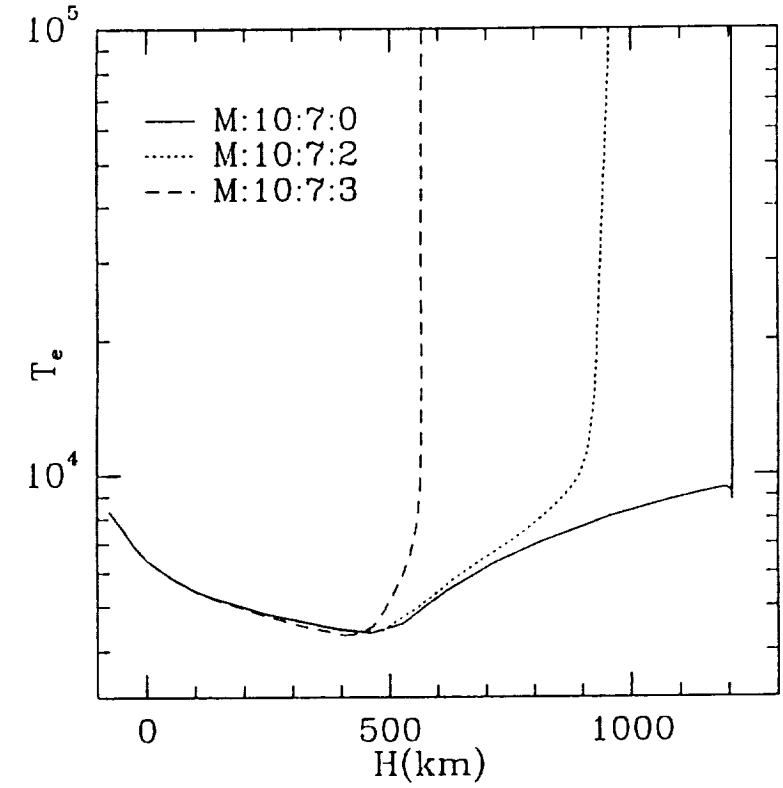

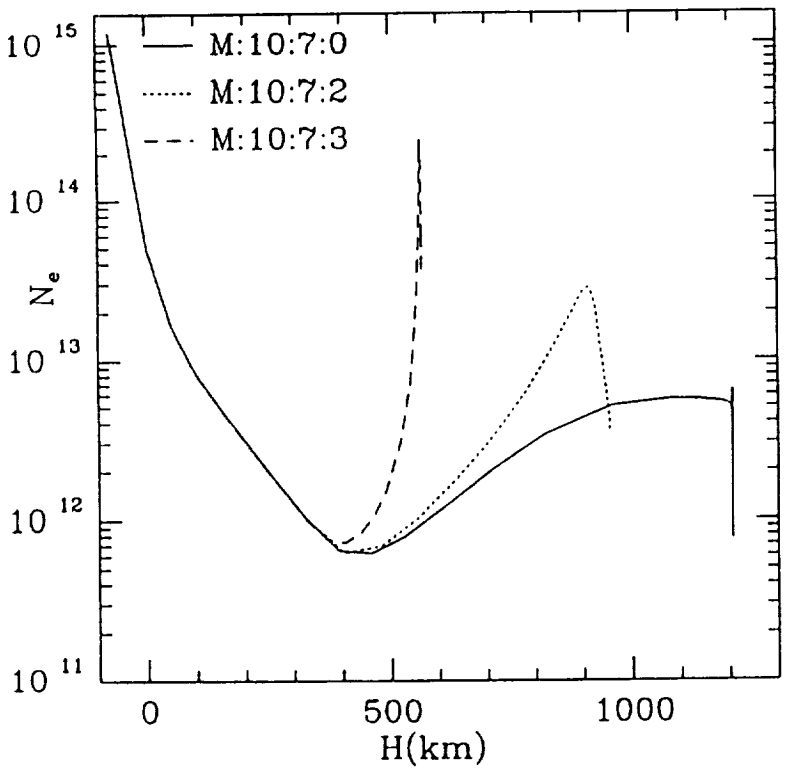

Fig. 8 - Log T_e and Log N_e distributions vs geometrical height.

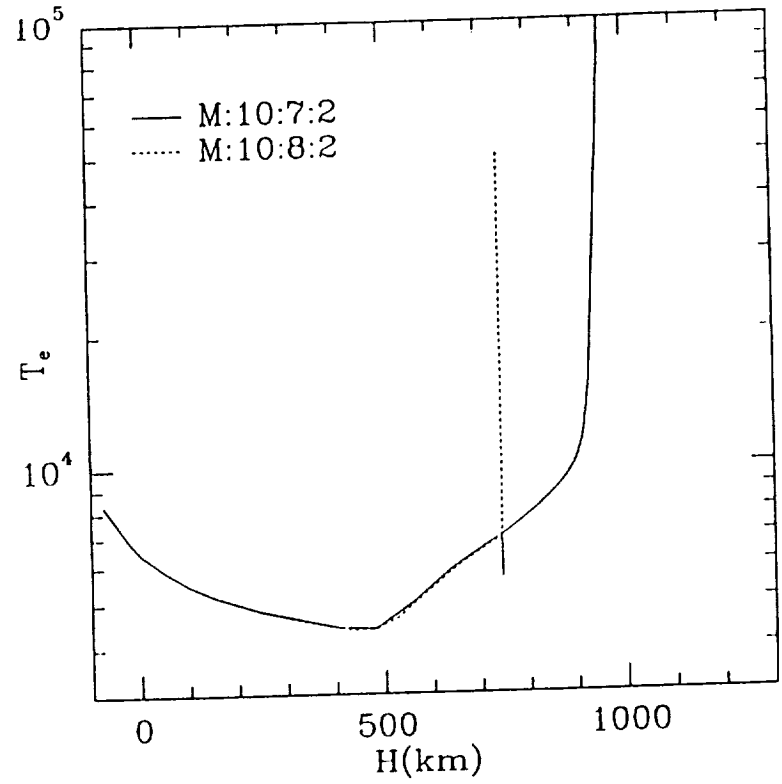

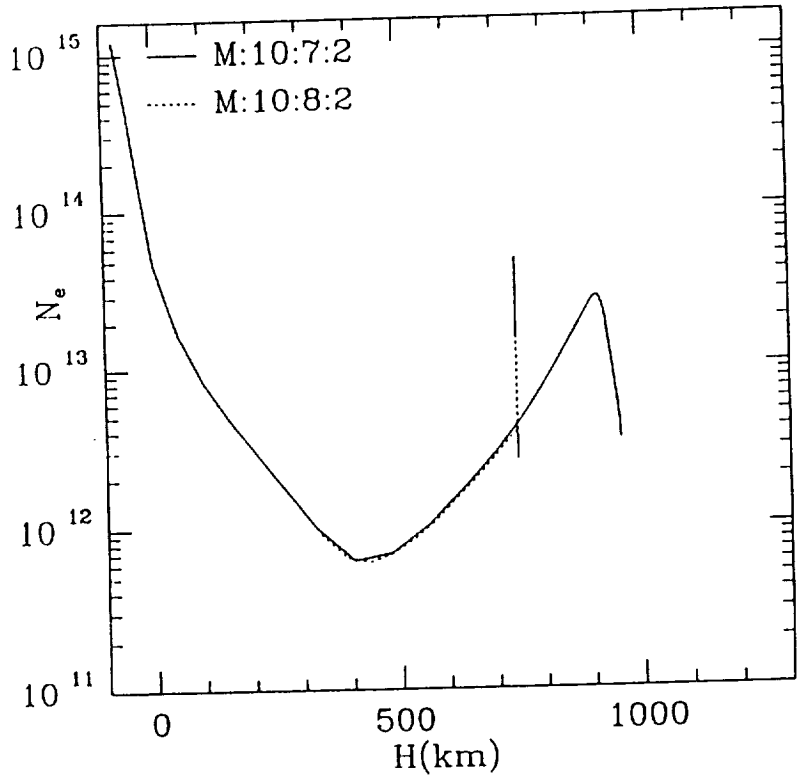

Fig. 9 - Log T_e and Log N_e distributions vs geometrical height.

Joule Heating and Runaway Electron Acceleration in a Solar Flare

Gordon D. Holman
(Lab. for Astronomy and Solar Physics, Code 682.1,
NASA/GSFC, Greenbelt, MD 20771)

Mukul R. Kundu
(Astronomy Program, U. of Maryland, College Park, MD 20742)

Sharad R. Kane
(U. of California, Berkeley, *and*
Code ES, NASA Headquarters, Washington, DC 20546)

Abstract

The hard and soft X-ray and microwave emissions from a solar flare (May 14, 1980) have been analyzed and interpreted in terms of Joule heating and runaway electron acceleration in one or more current sheets. It is found that all three emissions can be generated with sub-Dreicer electric fields. The soft X-ray emitting plasma can only be heated by a single current sheet if the resistivity in the sheet is well above the classical, collisional resistivity of a 10^7 K, 10^{11} cm^{-3} plasma. If the hard X-ray emission is from thermal electrons, anomalous resistivity or densities exceeding 3×10^{12} cm^{-3} are required. If the hard X-ray emission is from nonthermal electrons, the emissions can be produced with classical resistivity in the current sheets if the heating rate is $\sim$4 times greater than that deduced from the soft X-ray data (with a density of 10^{10} cm^{-3} in the soft X-ray emitting region), if there are at least 10^4 current sheets, and if the plasma properties in the sheets are characteristic of the "superhot" plasma observed in some flares by Lin *et al.* (1981, *Ap. J. Lett.* **251**, L109) and with *Hinotori*. Most of the released energy goes directly into bulk heating, rather than accelerated particles.

ELECTRON RUNAWAY "BASICS"

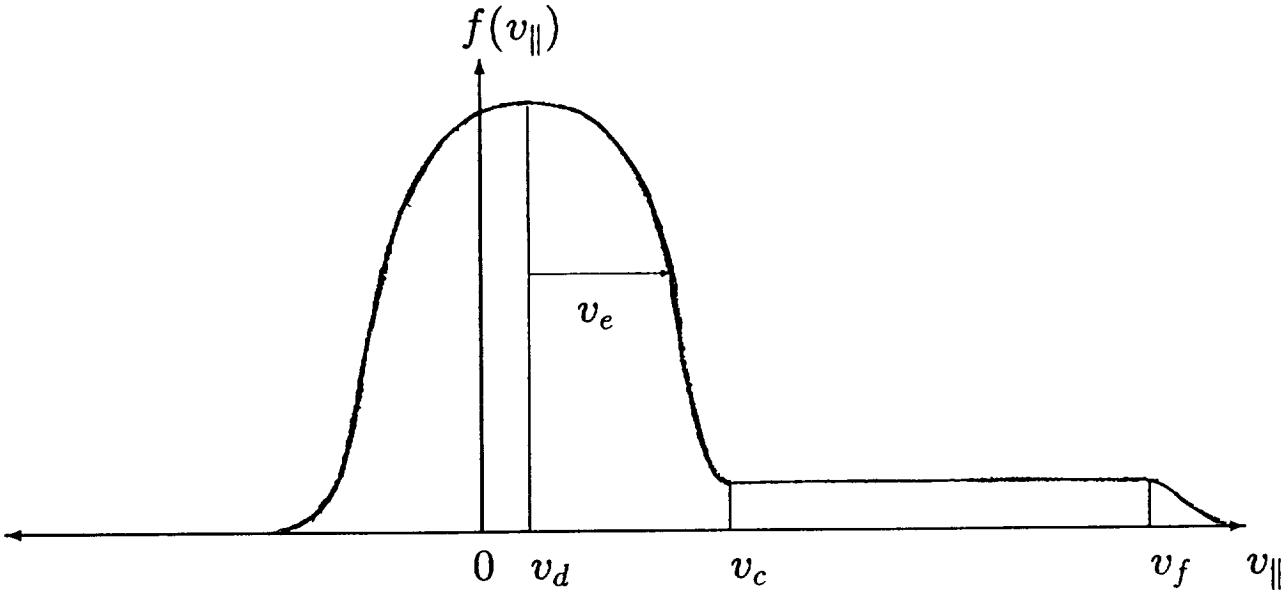

$$v_e = \sqrt{\frac{kT}{m}}$$

$$W_c = \frac{1}{2}mv_c^2$$

Dreicer Electric Field: $E_D = \frac{m}{e}v_e\nu_e$

$$\frac{E_D}{E} = \frac{v_e}{v_d} = (\frac{v_c}{v_e})^2 = \frac{2W_c}{kT}$$

Observable Quantities

$$W_f = (\gamma_f - 1)mc^2$$

HEATING AND ACCELERATION RATES

(see Holman 1985, *Ap. J.*, **293**, 584)

Joule Heating Rate $Q = sJEV_J$ (s = # of sheets)

Sheet Volume $V_J = A\delta r$, where δr is constrained by Ampere's Law.

$$E = \eta J$$

$$Q = 1.11 \times 10^{21} A_{18} B_2 T_7^{1/2} s (\frac{v_d}{v_e}) \nu_e \ \ erg\ s^{-1}$$

Runaway Acceleration Rate $\dot{N} = s\gamma n_s V_J$

$$\dot{N} = 2.83 \times 10^{29} A_{18} B_2 T_7^{-1/2} s \nu_e (\frac{v_e}{v_d})^{11/8} \exp\{-2^{1/2}(\frac{v_e}{v_d})^{1/2} - \frac{1}{4}(\frac{v_e}{v_d}) - (\frac{v_e}{c})^2[\frac{1}{8}(\frac{v_e}{v_d})^2 + (\frac{2^{3/2}}{3})(\frac{v_e}{v_d})^{3/2}]\} \ \ electrons\ s^{-1}$$

The Ratio $\frac{\dot{N}}{Q}$ depends only upon T and $\frac{E_D}{E}$.

Energy Gained by Direct Electric Field Acceleration:

$$W_f - W_c = eEL$$

PHYSICAL PARAMETERS FROM X-RAY SPECTRUM

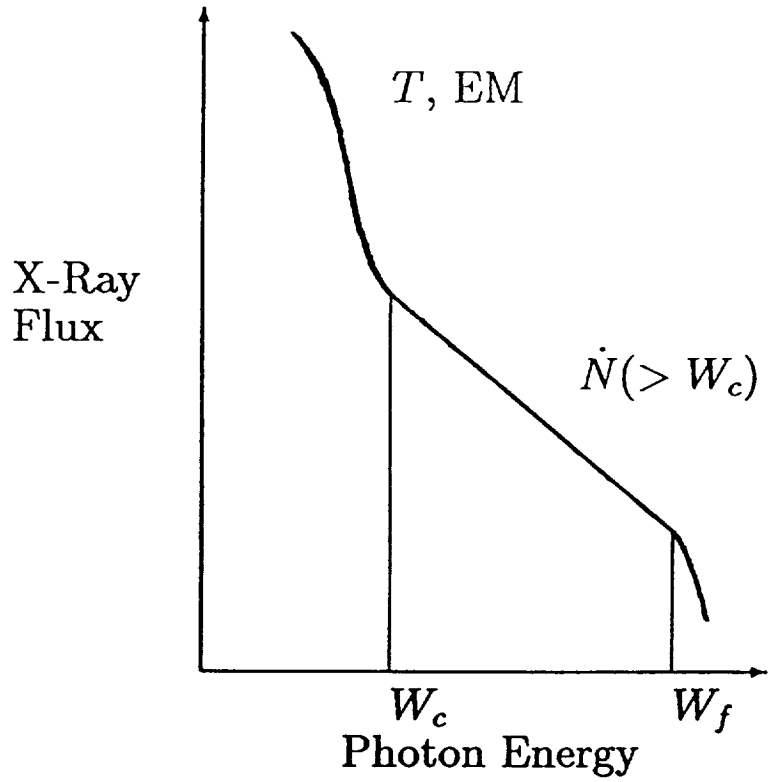

With a few basic assumptions, the following physical parameters can be deduced from a high-quality X-ray spectrum:

v_e	$\frac{E_D}{E}$ $(and\ \frac{\nu_e}{E})$	$E_D L$ $(and\ \nu_e L)$
v_d	$\dot{N}$	Q

If classical resistivity, $\nu_e \propto n_s/T^{3/2}$, giving

$$\frac{n_s}{E} \qquad and \qquad n_s L.$$

MINIMUM REQUIREMENTS FOR THE 1980 MAY 14 FLARE

If the hard X-ray emission is **thermal**, anomalous resistivity or densities exceeding $3 \times 10^{12}\, cm^{-3}$ are required.

If the hard X-ray emission is **nonthermal**

and $T_s \sim 10^7\ K$, for $E << E_D$ very high heating rates ($\sim 10^{30}\ erg\ s^{-1}$) are required.

and $T_s \sim 10^8\ K$, $E_D/E < 10$ and X-ray emission from the sheets is significant unless the resistivity is anomalous.

and $T_s \sim 4 \times 10^7\ K$, the emissions can be produced with classical resistivity if the heating rate is $\sim 4 \times 10^{28}\ erg\ s^{-1}$, $n_s \sim 4 \times 10^{11} cm^{-3}$, $E_D/E \sim 14$, and there are at least 10^4 current sheets.

Here T_s is the temperature in the current sheets.

(See Holman, Kundu, and Kane 1989, *Ap. J.*, in press, for details and other options.)

The soft and hard X-ray and microwave emissions can all be generated with sub-Dreicer electric fields and classical resistivity.

General Comments

- Electron acceleration/heating in current sheets provides a natural, determinable low-energy cutoff for the accelerated electrons.
- The energy input to direct heating will always exceed that to accelerated electrons as long as $E \ll E_D$.
- When the hard X-ray emission is predominantly nonthermal, a large number ($>10^4$) of oppositely directed current sheets is required. This is analogous to the fine-scale current/return current structures observed in the earth's auroral zone. The electrons can be accelerated in a "single" sheet if the resistivity in the sheet is highly anomalous and the particles escape the sheet on a length scale less than 10 km.

HEATING AND ACCELERATION OF CORONAL AND CHROMOSPHERIC IONS DURING SOLAR FLARES

M. E. McKean, R. M. Winglee, and G. A. Dulk

Department of Astrophysical, Planetary and Atmospheric Sciences, University of Colorado, Boulder, CO 80309-0391.

ABSTRACT

One-dimensional, electrostatic, particle-in-cell simulations are used to explore two mechanisms proposed to explain turbulent broadening of soft X-ray emission lines of heavy ions observed during solar flares and the presence of blue-shifted components. Results from the simulations are in qualitative agreement with the observations.

1. INTRODUCTION

Observations of soft X-ray emission lines of heavy ions during solar flares show the presence of energetic turbulent motions in the heavy ions and blue-shifted components (Antonucci et al. 1982; MacNeice et al. 1982; Tanaka 1987). The source of the energy for these phenomena is believed to be the energetic beam electrons produced in the impulsive phase of a flare. The exact mechanism (or mechanisms) that produces the emission line features is a subject of debate. Two such proposed mechanisms, similar in that both utilize superheated electron populations to drive the ion heating, are examined using electrostatic particle-in-cell simulations.

The first mechanism is *in-situ* coronal maser heating (Fig. 1), in which electron cyclotron maser radiation emitted by the energetic electrons is absorbed by ambient coronal electrons (Melrose and Dulk 1982, 1984; McKean, Winglee and Dulk 1989). The heated electrons expand up magnetic field lines in the presence of local density gradients, creating an ambipolar electric field due to the charge separartion between the electrons and the source region ions which then accelerates the ions. It is found that the ambipolar field produces differential ion motion between ion species; this differential motion is unstable to the ion-ion streaming instability, which then preferentially heats and accelerates the

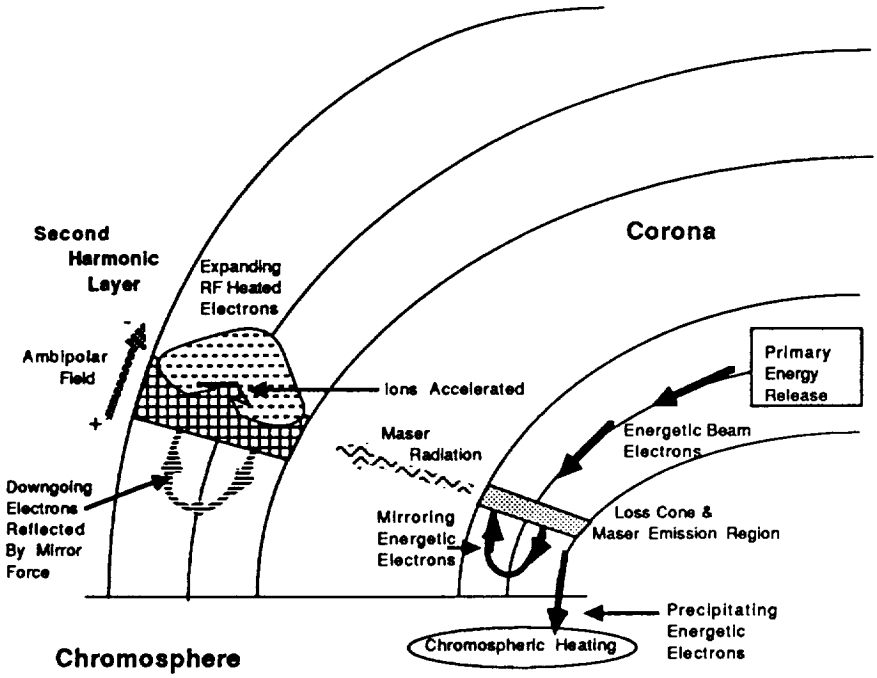

Fig 1: Schematic of coronal maser heating mechanism.

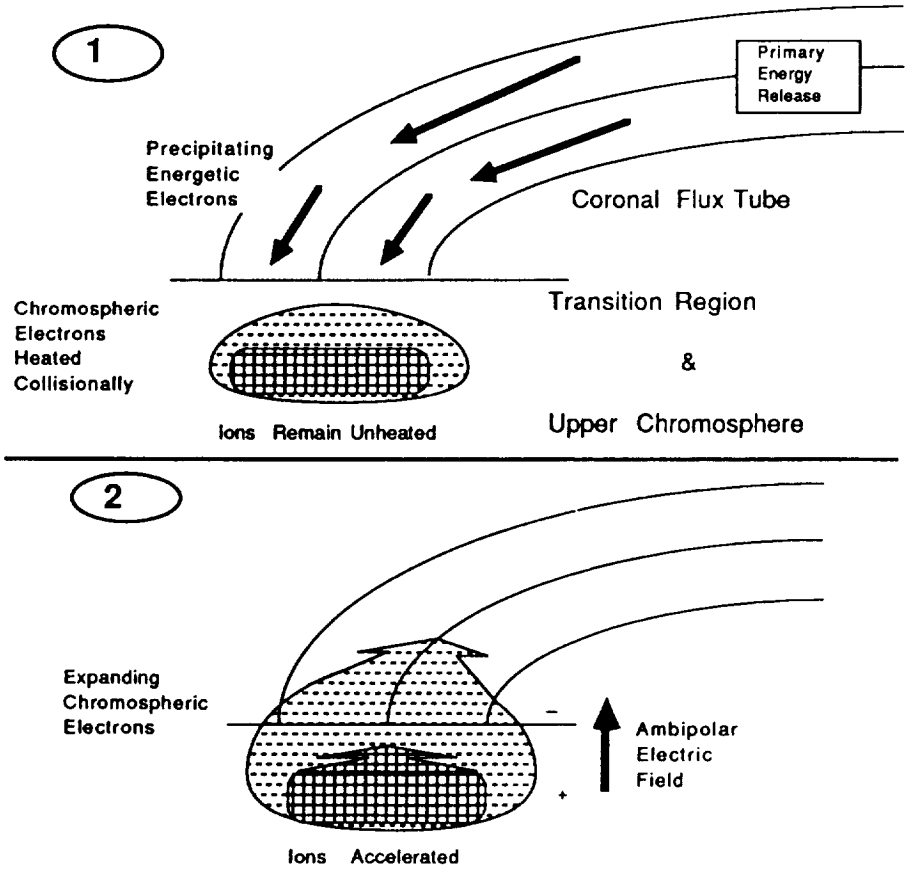

Fig. 2: Schematic of chromospheric heating mechanism.

heavier ion species. The resulting ion distribution functions bear similarities to observed soft X-ray line profiles.

The second mechanism is chromospheric heating (Fig. 2), in which chromospheric electrons are collisionally heated by energetic electrons (Winglee 1989). Under certain conditions, the collisional heating of the chromospheric electrons exceeds the collisional heating of the ions (Winglee 1989); the electrons then expand up field lines into the corona, which results in the formation of an ambipolar electric field and resultant ion acceleration. Heating due to the ion-ion instability is less important in this case, though turbulent-appearing spectra may still be produced due to spatially inhomogeneous ion velocity profiles.

2. SIMULATION MODEL

One-dimensional, electrostatic, particle-in-cell simulations are used in this paper to model the self-consistent evolution of plasma during the outward expansion of a superheated electron population into an ambient plasma at higher altitude and lower density, including the development of an ambipolar electric field and of wave-particle interactions.

The plasma is assumed to have two ion species. One species of ion with mass m_H corresponds to H^+, the dominant species in the solar atmosphere, and accounts for 90% of the total ion number in these simulations. The second ion has a mass $m_{He} = 4\ m_H$, so it is similar in behavior to He^+ or any other ion with $q/m = 1/4$. These heavier ions have a charge-to-mass ratio that roughly corresponds to an ion that has yet to be fully stripped of its electrons. The reason for simulating an ion species that has not yet been fully stripped is that, at the time the ions are being accelerated, they have not been in contact with a population of hot, energetic electrons long enough to have reached an equilibrium, fully stripped ionized state. In order to allow ions to react to electron motion on the time scale of the simulation, it is assumed that $m_H = 100 m_e$, where m_e is the electron mass.

The length of the simulation system (Figure 3) is 2048Δ, where Δ is the simulation cell size. The system is divided into three sections. Between $x = 0$ and $x/\Delta = 384$ lies Region A, which is a region of enhanced plasma density n_A. This region represents the lower corona in the coronal heating simulation and the chromosphere in the chromospheric heating simulation. Between $x/\Delta = 512$ and $x/\Delta = 2048$ lies Region C, which represents the ambient coronal plasma where the plasma density n_C is less than in Region A. Between $x/\Delta = 384$ and $x/\Delta = 512$ lies Region B, where there is a linear change in density between Regions A and C. The enhanced density in Regions A and B, with a hot electron population that has a temperature elevated significantly above the ion temperature, is the ultimate source of the free energy available for the formation of the ambipolar electric field and for the growth of the various instabilities seen in these simulations. Therefore, particles that begin the simulation in Regions A and B are referred to collectively "source region particles." In the chromospheric heating simulation, there is also an ion temperature gradient across Region B, with the ion temperature higher in the corona than in the chromosphere.

The plasma in these simulations is assumed to be collisionless. Particles are reflected after crossing either boundary of the system.

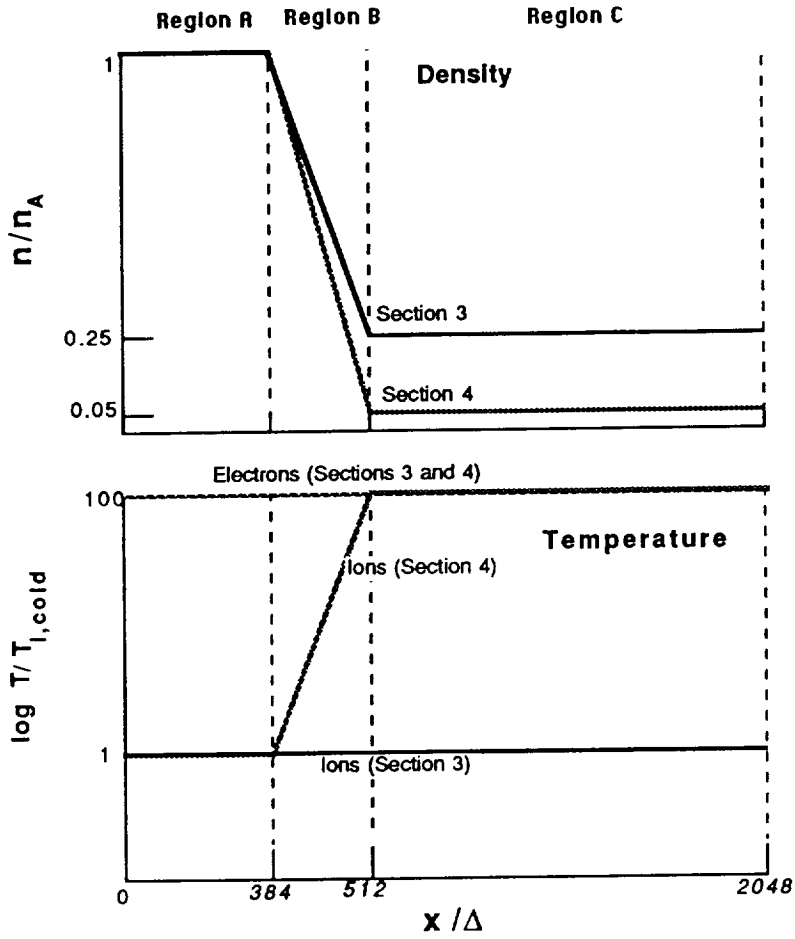

Fig. 3: Schematic model of simulation system showing where Regions A, B, and C lie and the initial ion and electron temperature and density profiles in the two simulations whose results are shown in this paper.

3. *IN-SITU* CORONAL HEATING

The effects of extended *in-situ* coronal heating are examined in this section. The electrons are assumed to be uniformly heated with the temperature uniform through the system and elevated above the ion temperature. Due to the assumed density gradient, there is a pressure excess in the dense region which drives an outward propagating conduction front and subsequent plasma heating. The plasma density changes by a factor of four across Region B, i.e., $n_A/n_C = 4$. The ratio of electron temperature to ion temperature

$T_e/T_i = 100$. The acoustic velocity $c_s = (T_e/m_H)^{1/2} = 1.18\ \omega_H \Delta$, where ω_H is the H^+ plasma frequency in Region A.

The electrons expanding out of the source region set up an ambipolar electric field due to the charge separation between the electrons and the source region ions. The potential drop across the ambipolar field can be inferred from the maxmimum velocity of the reflected electrons, which is about 2 v_{Te}, implying a potential drop of $\sim 4\ T_e$. This potential drop is strong enough to confine the bulk ($\sim 95\%$) of the source region electrons to the region within and behind the ambipolar field.

The ion dynamics is illustrated in Figure 4, which shows the development of the ion phase space, with the H^+ ions in the left column and the He^+ ions in the right column. The initial phase spaces are shown in Figs. 4a and 4b. Once formed, the ambipolar field accelerates both ion species outwards in bulk (Figs. 4c and d). The acceleration of the H^+ ions to high velocities occurs before the He^+ ions because of their higher charge-to-mass ratio; thus the average velocity of the accelerated H^+ is ~ 4 times higher than the same for the accelerated He^+ at $\omega_H t = 30$.

The ambipolar field, initially limited in spatial extent to Region B, expands beyond that region as the footpoints of the field (those points at which the H^+ bulk velocity equals zero) propagate away from Region B at about the local acoustic velocity c_s. By $\omega_H t = 30$, the ambipolar field extends from $x/\Delta \simeq 340$ to $x/\Delta \simeq 560$ (Fig. 4c).

The footpoints represent the movement of the two fronts of the ambipolar field, one of which (a compression front) propagates into and compresses the ambient ions, accelerating them forward; the other (an expansion front) moves into and expands the source region ions, drawing them outward. The two fronts initially overlap; when they separate, a velocity plateau forms in the H^+ phase space (Fig. 4e), and the electric field is zero or near zero in the region of the plateau.

After the fronts separate, the expansion front (marked by the right side dashed line in figures 4c-l) propagates to the left at $\sim 0.65\ c_s$. It constantly expands in size with time because its footpoint moves inward at a higher velocity ($\sim c_s$) than the entire front does. By contrast, the size of the compression front (which is marked by the left side dashed line in Figures 4c-l) front is monotonically reduced (Fig. 4g) until it becomes a narrow, shock-like structure (Fig. 4i, k), with the footpoint of the front moving to the left at $\sim c_s$ and the entire front at $\sim 1.3\ c_s$. The front does not break because, as it steepens, the dispersion of its energy increases and effectively counters the steepening.

By the times in in Figures 4i and k, the front can be described as a shock because there are sharp discontinuities in bulk plasma properties; in other words, large changes in plasma properties such as density and bulk velocity take place across a very narrow region (on the order of an ion acoustic wave wavelength wide). This shock is important because it marks the leading edge of a density wave associated with the expansion of the source region plasma. Its movement through a coronal loop may be seen in spatially resolved X-ray observations because the shock should leave an increased soft X-ray emission in its wake due to the sharply increased numbers of energetic electrons that are confined behind

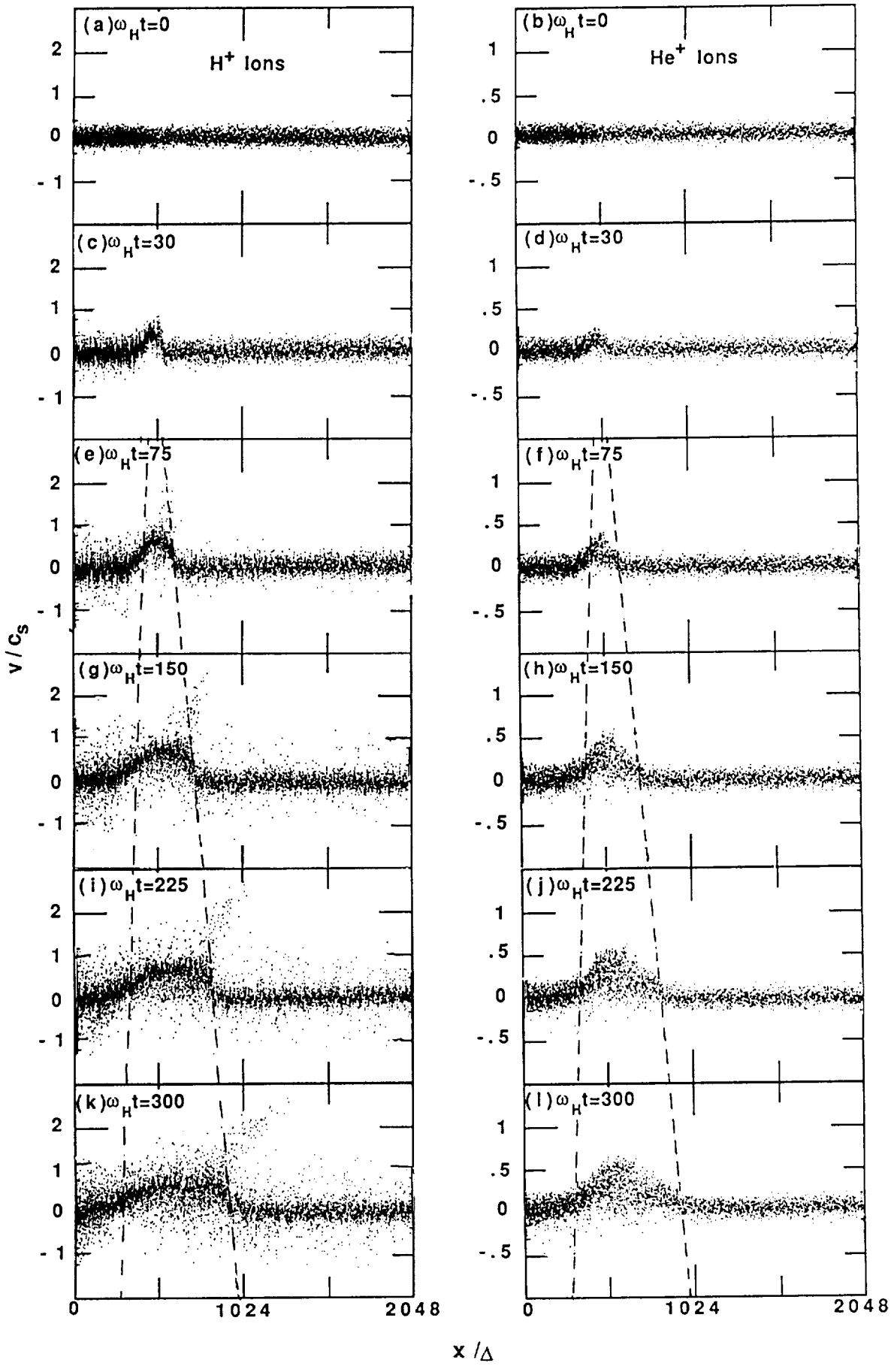

Fig. 4: Ion phase space for coronal heating simulation. Velocities are normalized to the initial acoustic velocity. The propagation of the expansion and conduction fronts are marked by dashed lines.

the shock. Moreover, since it is travelling only at $\sim c_s$, high time resolution is not required to resolve its propagation.

The compression front bears similarities to the ion sound conduction front of Brown, Melrose, and Spicer (1979) in that it confines energetic source region electrons to the region behind the front and reduces the heat flux outwards to a value determined by the velocity of the front, which is of order $\sim c_s$. This limitation of the heat flux is the principle function of a conduction front, which means that the compression front can be identified as a conduction front as well. Because of the different confinement mechanism, it is best described as an "ambipolar field conduction front" to differentiate it from the ion sound conduction front of Brown, Melrose, and Spicer (1979).

The passage of the two fronts through the plasma accelerates H^+ ions to a bulk velocity, hereafter the "beam" velocity, $v_b \simeq 0.65\, c_s$, which corresponds to a "beam" energy of $\sim 0.42\, T_e$. The H^+ ions clearly do not experience the potential drop of $\sim 4T_e$ that the electrons do. The explanation for this apparent discrepancy is that the ambipolar field fronts move through the ions in less time than it would take for an ion to experience the full potential drop if the fronts were stationary. Because of their smaller charge-to-mass ratio and hence mobility, He^+ ions gain less energy than H^+ ions in the potential drop of a front.

Ion acoustic waves excited by expanding heated and return current electrons are manifested as high energy tails in the H^+ ion phase space (Fig. 4e) but not the He^+ phase space (Fig. 4f). These tail ions can reach energies as high as T_e. The highest energy H^+ ions are produced in and close to the conduction front (Figs. 4e and g). This phenomena is a result both of the ambipolar field and of the rapid dissipation of ion waves in this region, which happens because the steep velocity gradient increases the effective temperature of the H^+ ions in the front, thereby reducing T_e/T_i. The dissipated wave energy goes into the production of a population of high energy ions, which are further accelerated through interaction with the ambipolar field. These ions, hereafter called "fast beam ions," can reach velocities as high as $\sim 2.6\, c_s$, or energies of $\sim 7\, T_e = 700\, T_i$ (Figs. 4g, i and k).

The differential motions between the H^+ ions and the He^+ ions can excite an ion-ion streaming instability which transfers energy from the faster to the slower ions. The requirements for this instability to appear in a one-dimensional plasma are (a) that the ratio $T_e/T_i \gg 1$ and (b) that $c_s \geq \Delta u_i > v_t$, where $\Delta u_i = u_H - u_{He}$ is the difference between the H^+ and He^+ bulk velocities and $v_t < c_s$ is the threshhold velocity for the instability (Dusenberry et al. 1988; Winglee 1989). Two important signatures of the ion-ion instability are: (i) nonthermal heating and acceleration of the heavy ions, which produces a distribution function with a broad plateau between the initial H^+ and He^+ bulk velocities and a corresponding increase in the He^+ bulk velocity (Winglee et al. 1989); and (ii) the formation of a large, nonthermal low-energy tail on the H^+ distribution and a corresponding decrease in the H^+ bulk velocity (Winglee et al. 1989; Winglee 1989).

These signatures of the ion-ion instability can be seen at later times in Figure 4. Heavy ions in the beam region and in the fronts have undergone some heating by $\omega_H t = 150$

(Fig. 4h); the velocity dispersion increases further over the remainder of the run (Figs. 4j and l). The heating causes an increase in the maximum velocities of the He^+ ions to the point where they are comparable to the H^+ beam velocity. In the H^+ phase space plots, a low energy tail develops between $v = 0$ and $v = v_b$ in the beam region (Fig. 4g). This low energy tail increases in density with time (Figs. 4i, k).

Figures 5a and b shows the variation of the density with x at $\omega_H t = 0$, 150 and 300 for the H^+ and He^+ ions. The bulk flow of H^+ ions outward reduces the density in the source region, though the simulation ends before any significant depletion occurs at the left boundary. The conduction front is characterized by a sharp jump in H^+ density, which reflects the shock formation at that front. Behind the front, the H^+ ions have a uniform density between $x/\Delta \simeq 450$ and 650 at $\omega_H t = 150$, and $x/\Delta \simeq 450$ and 900 at $\omega_H t = 300$. Thus, in this region, the ambipolar field has destroyed the density gradient, and, since this region corresponds to the velocity plateau in Figures 4g and k, its fronts have left the region.

The He^+ density profile (Fig. 5b) lags the H^+ profile because of the slower bulk movement of these ions. This lag results in an enhancement of He^+ with respect to H^+ in some places (such as at the left end of the H^+ beam region) and a deficiency in others (such as at the conduction front).

The profile of the electron temperature in the region behind the conduction front shows continuous electron cooling throughout the run (Figure 5c). The electrons cool through reflection in the conduction front, the energy loss arising from the rightward movement of the electric field. This energy loss (electron energy is almost all thermal; bulk kinetic energy is a negligible portion of the total) is the source of the free energy driving the ambipolar field and, indirectly, the instabilities. The total energy loss of electrons behind the shock front is $\sim$ 25% at the end of the run, with the minimum temperature being about 50% of the initial electron temperature.

The bulk velocity and effective temperature of the H^+ and He^+ ions is shown in Figure 6 for $\omega_H t = 75$, 150, and 300. The effect of the differential acceleration of the two ion species is evident in Fig. 6a, in which the heavy ions have a peak bulk velocity which is less than half the H^+ peak bulk velocity. The He^+ bulk velocity later increases at the expense of the H^+ bulk motion (Fig. 6b) due to the ion-ion instability. Indeed, by the end of the run (Fig. 6c), the He^+ peak kinetic energy is $\sim$ 1.8 times greater than the H^+ beam region kinetic energy, for the H^+ velocity in the beam region has fallen to $\sim 0.53\ c_s$ and the He^+ peak velocity has risen to $\sim 0.36\ c_s$.

The heating seen in Figures 6d-f is caused by several mechanisms. The H^+ temperature spikes are caused by the presence of fast beam ions, so they are due to an acceleration process which creates a secondary beam of ions rather than to a heating process. The He^+ temperature spikes are signatures of the heating caused by ion-ion turbulence. These spikes are twice as high as the local H^+ temperature in Figures 6e and f, and thus a clear signature of the preferential heating of the heavy ions. Ion acoustic turbulence is responsible for the steady rise in H^+ temperature to the left of the beam region as well as the

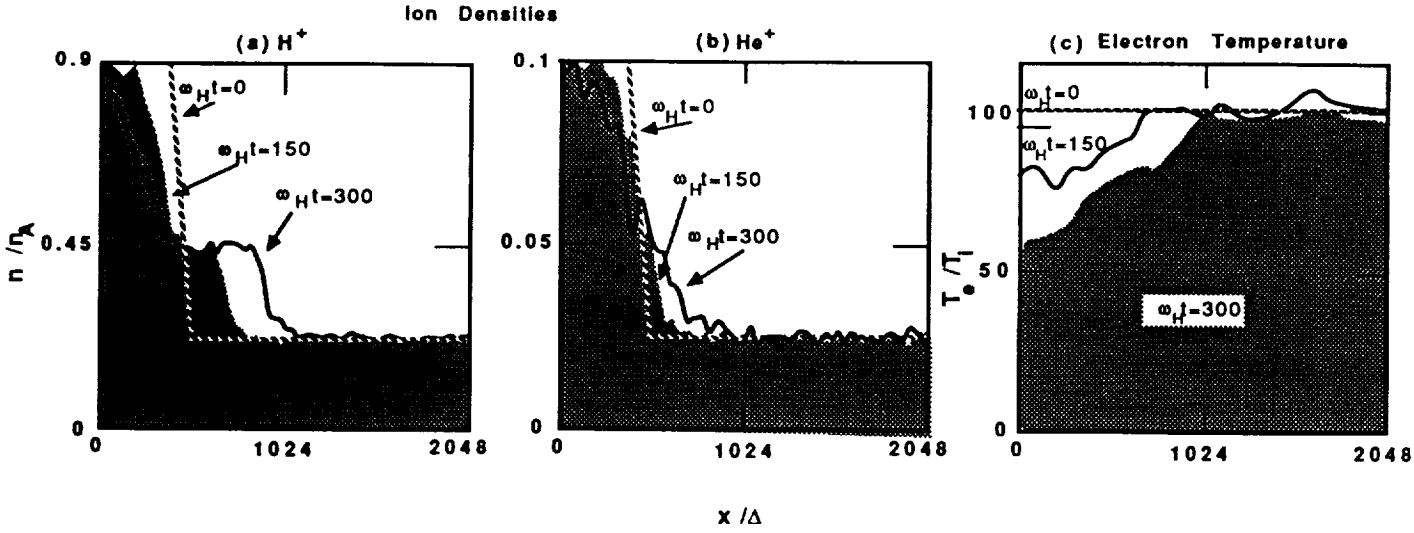

Fig. 5: Ion density profiles for (a) H^+ and (b) He^+ with the density normalized to the initial electron density in Region A. (c) Electron temperature profile with the electron temperature normalized to the initial ion temperature.

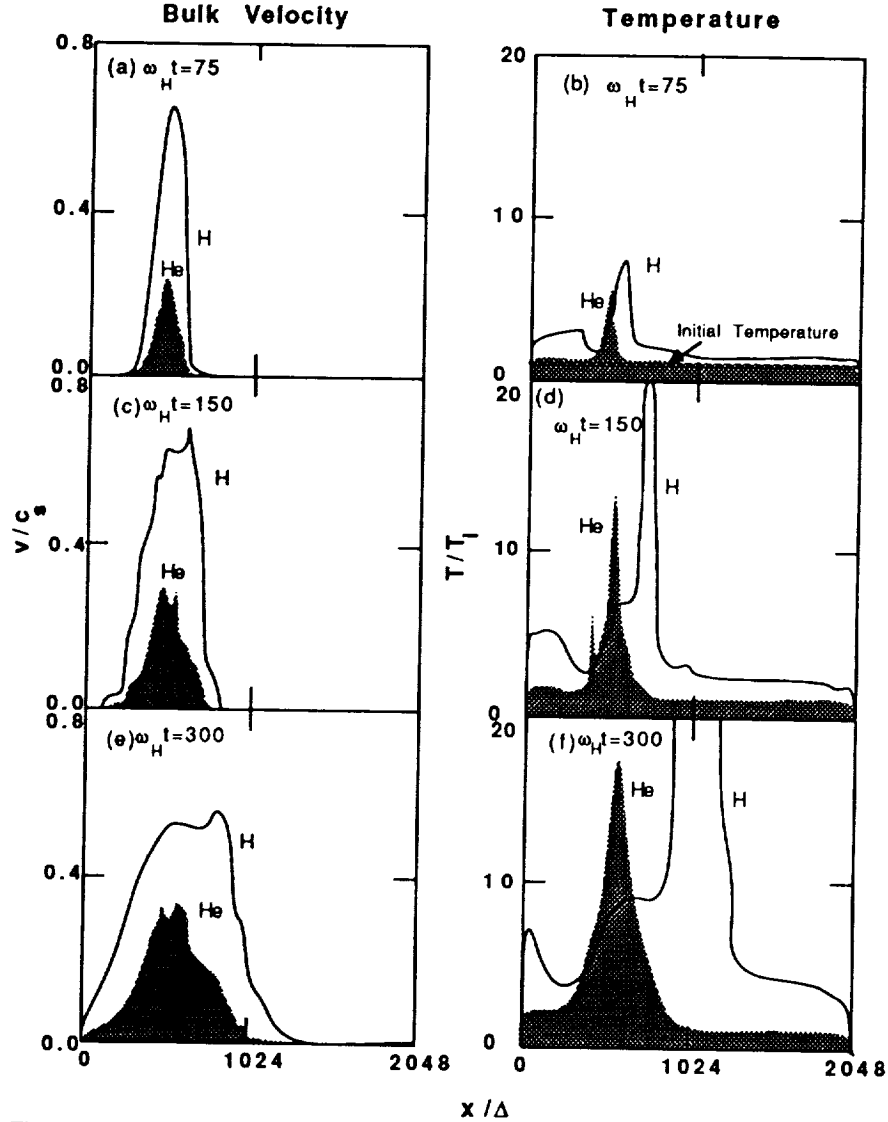

Fig. 6: Ion bulk velocity and temperature profiles. The bulk velocity is normalized to the initial value of the acoustic velocity; the temperature to the initial ion temperature.

rise in temperature in the ambient region to the right of the H^+ spikes. Both ion acoustic and ion-ion turbulence heat the H^+ ions in the beam region and in the fronts.

If the entire simulation system were to correspond to a soft X-ray source region, then distribution functions for the whole system should bear qualitative similarities to soft X-ray line profiles. Figures 7a and b shows such distribution functions for (a) H^+ and (b) He^+ for the beginning, middle and end of the run. Both species have a positive velocity (or blue-shifted) component halfway through the run which grows as a proportion of the total distribution function with time, though it never exceeds the stationary component in size. The H^+ moving component is more substantial; by contrast, the He^+ component is broader and, unlike the H^+ component, increases in velocity with time due to acceleration of H^+ ions by the ion-ion instability. For neither species does the portion of the stationary component for $v < 0$ broaden significantly during the run. For an electron temperature of 10 keV, the effective width of the of the He^+ distribution (about 200 km/s) and the velocity of its blue-shifted component (about 300 km/s), are in rough agreement with velocities inferred from soft X-ray observations. Thus, the ion distribution functions reproduce many, though not all, of the features seen in soft X-ray line profiles.

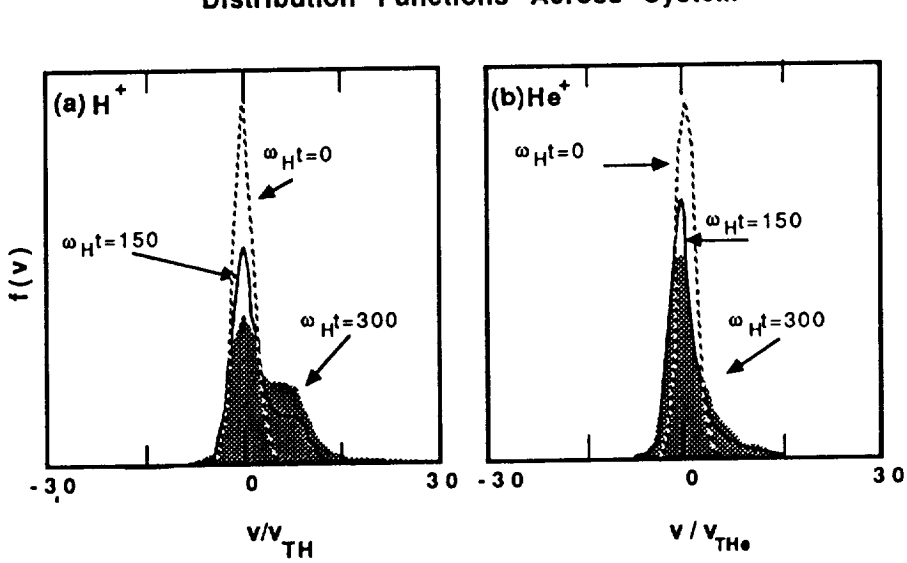

Fig. 7: Ion distribution functions for the entire simulation system. Velocities are normalized to the initial thermal velocities of the two species.

4. CHROMOSPHERIC HEATING

In this section, the acceleration and heating of ions is examined in a case analogous to chromospheric heating. Chromospheric electrons are assumed to be heated to coronal temperatures, so the electrom temperature is uniform through the system, as in Section 3. The electron temperature is elevated with respect to the ion temperature in the chromosphere, but not in the corona, so v_{Ti} is no longer much less than c_s throughout the system, as is true in Section 3. As a result, a pressure excess in the dense region still

drives an outward propagating ambipolar electric field, but no conduction front or density wave forms and little ion heating occurs. The density jump of 20 in this section is larger than in Section 3, a difference that is not examined in detail because simulations run with this density jump but no ion temperature gradient yield essentially the same qualitative features as seen in Section 3. The parameters of the simulation are the same as in Section 3, except $n_A/n_C = 20$, $T_e/T_{iA} = 100$, and $T_e/T_{iC} = 1$.

The ion phase space diagrams are shown in Figure 8. Figures 8a and b are the initial phase space plots of the H^+ and He^+ ions respectively. As in the coronal case, the source region ions are accelerated outwards by the ambipolar field created by the expansion of the heated source region electrons. A difference from the previous simulation is that the ambient, or coronal, ions are not swept outward by a conduction front. Instead, many of the coronal ions are able to penetrate the ambipolar field region (delimited by the dashed lines in Figures 8c-f) because, since the coronal ion thermal velocity $v_{TiC} \sim c_s$, they have sufficient kinetic energy to overcome the potential energy barrier the field region represents. As a result, no conduction front or shock front forms, and neither does a density wave (Figs. 8c, e, and g).

The region containing the ambipolar field initially confined to the transition region, penetrates deeply into both the chromosphere and corona during the run. The left edge of the field region propagates to $x/\Delta \simeq 128$ by the end of the run, with an average velocity of $\sim 0.7\ c_s$. The right edge (indicated by the right side arrows) propagates to $x/\Delta \simeq 1280$ by $\omega_H t = 300$ for an average velocity of $\sim 2.5\ (T_e/m_H)^{1/2}$, which is only slightly greater than the local sound speed once the ion temperature is taken into account. While the field region expands, the potential drop across it remains roughly constant ($\sim 4\ T_e$), so the average field strength in the region decreases monotonically with time.

The initial velocity of many transition region ions matches or exceeds that of the outgoing electric field, whose velocity averages $\sim 1.2 c_s$. As a result, these ions are accelerated more efficiently by the ambipolar field, i. e., they gain more energy in the potential drop of the field than slower ions, in a fashion similar to the mechanism that produced the fast beam ions of the last section. For example, transition region H^+ ions that begin with a velocity of $\sim c_s$ in Figure 8a, have been accelerated to a velocity of $> 2\ c_s$ in Figure 8e, an energy gain of $> 3T_e$. Initially fast He^+ ions are likewise accelerated efficiently; ions that begin with a velocity of $\sim 0.5\ c_s$ (Fig. 8b) are accelerated to velocities of $\sim 0.8\ c_s$, an energy gain of $\sim 2\ T_e$. These fast ions form the leading edges of the outfowing ion "beams."

The effects of the ion-ion streaming instability are visible in the phase space plots of both ion species. The velocity dispersion of source region He^+ ions to the right of $\sim x_1$ is increased between $\omega_H t = 75$ and 150 (Figs. 8d and f) due to the instability, and increases further between $\omega_H t = 150$ and 300 as ion-ion turbulence grows in strength. This heating is accompanied by a weak low energy tail in the H^+ beam (Fig. 8g). The heating of both species is weaker than in the coronal case due to the presence of hot coronal ions which effectively decrease the ratio of T_e/T_i and thereby suppress the ion-ion instability.

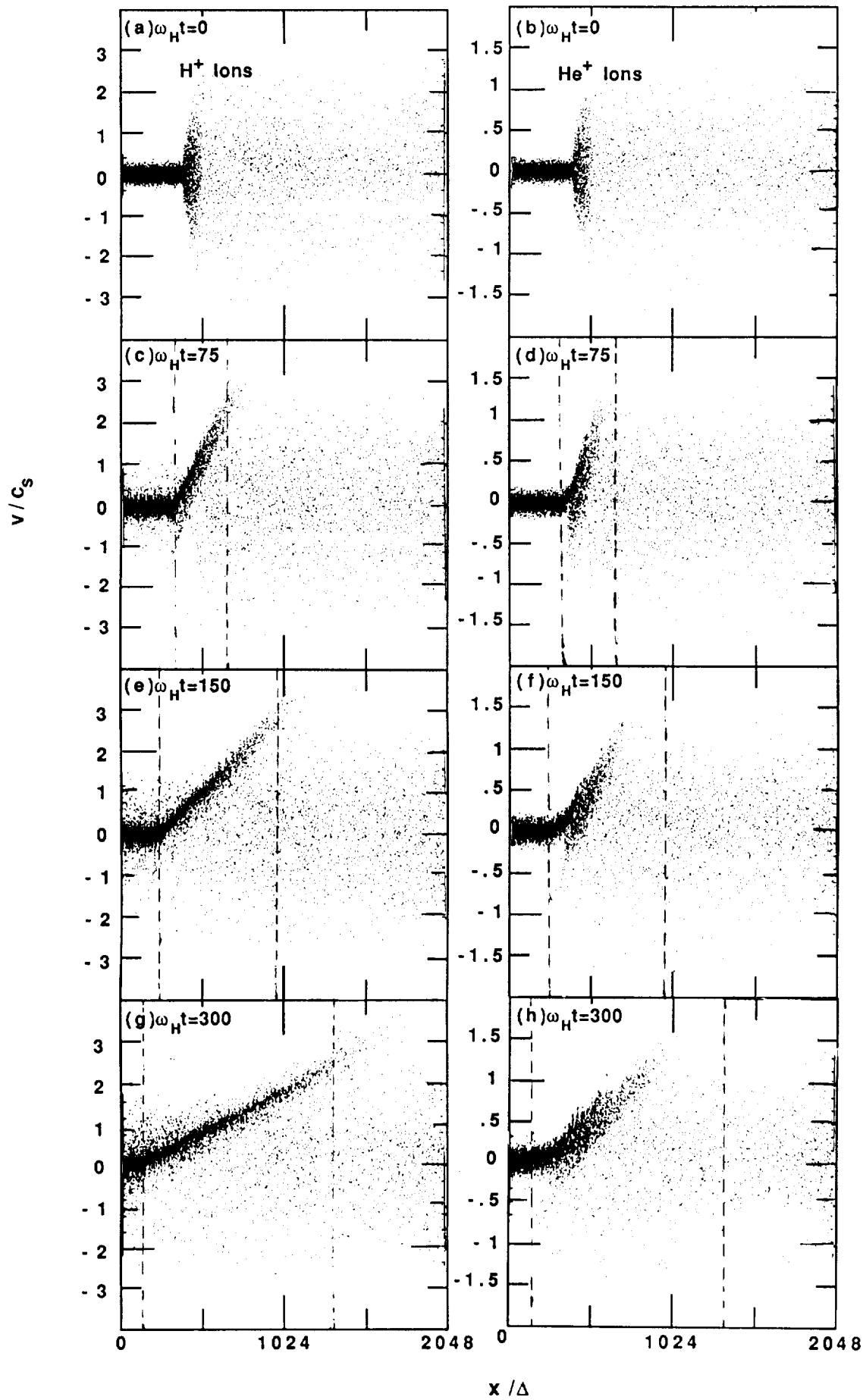

Fig. 8: Ion phase space for chromospheric heating simulation. Velocities are normalized to the initial chromospheric acoustic velocity. The region containing the ambipolar electric field is delimited by dashed lines.

Figure 9 shows the bulk velocity and temperature profiles of the chromospheric and transition region ions only, since these parameters for the coronal ions remain largely unchanged over the course of the run. The ambipolar field more readily accelerates the faster transition region ions to high velocitie than the slower transition region and chromospheric ions. Such an acceleration hierarchy results in outflowing particle beams with monotonically increasing bulk velocity profiles for both ion species (Fig. 9a). The H^+ beam is more extended than the He^+ beam because of the greater velocity of the H^+ ions. The peak kinetic energy of the He^+ ions initially is also smaller than the H^+ peak energy due to the more gradual acceleration of He^+ ions by the ambipolar field (Fig. 9a). As the leading edge of the He^+ ion beam undergoes further acceleration, its velocity becomes half that of, and represents the same kinetic energy as the peak H^+ velocity (Fig. 9c).

The heating caused by the ion-ion instability is evident in Figures 9c and d, in which the He^+ temperature exceeds the H^+ temperature between $x/\Delta \simeq 400$ and 700 in Figure 9c, and between $x/\Delta \simeq 300$ and 900 in Figure 9d (the H^+ heating actually is due more to ion acoustic turbulence than ion-ion turbulence). The extent of the heavy ion heating grows between $\omega_H t = 150$ and 300, indicating that ion-ion turbulence peaks in strength after $\omega_H t = 150$.

In order to compare these results to soft X-ray line emissions, we examine the distribution functions of the two ion species, which are shown in Figure 10 (H^+ in Fig. 10a, He^+ in Fig. 10b). As seen previously in the coronal case (Fig. 7), the blue-shifted component of both ion species increases in size as the run continues, with that of H^+ consisting of a greater proportion of the total distribution function than the blue-shifted component of He^+ at any time $t > 0$. The central difference is that the velocity of the peak of the blue-shifted component increase with time in both distributions rather than just the He^+ distribution due to the continuous acceleration over time of source region ions by the ambipolar field. The effective temperature, or velocity dispersion, of the blue shifted components of both species also appears to increase with time, to a value approaching T_e by the end of the run. The broadened distributions bear close qualitative similarities to the distribution functions for the coronal heating simulation (Fig. 7). However, if one assumes that the electron temperature is 100 eV, the effective thermal velocity of the He^+ distribution, as well as the velocity of the moving component, is only about 50 km/s, which is too low to explain the observations, however.

5. CONCLUSION

Ion heating associated with the expansion of hot electron populations in both coronal chromospheric applications during solar flares have been analyzed using particle simulations as methods of reproducing heavy ion soft X-ray line features observed during solar flares; specifically, nonthermal line broadening and the presence of blue-shifted components. In the simulations, the expansion of heated electrons across density gradients is

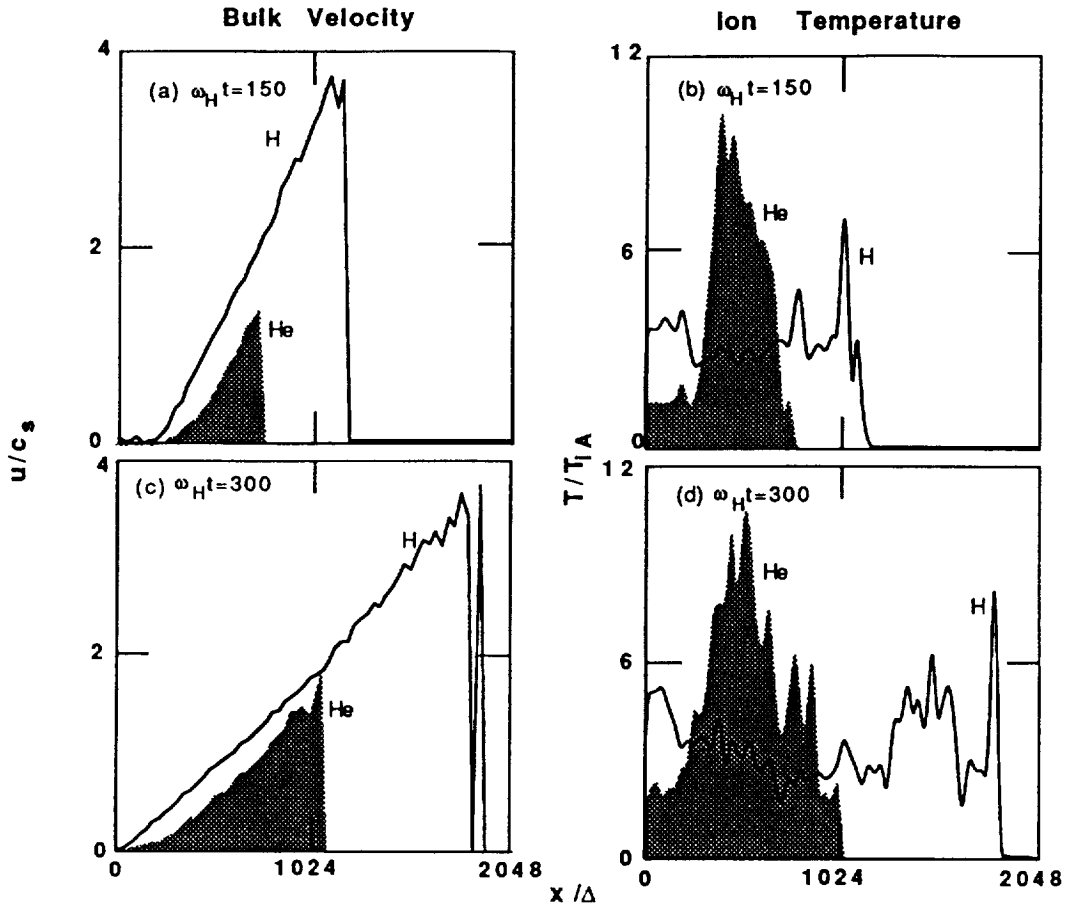

Fig. 9: Ion bulk velocity and temperature. The bulk velocity is normalized to the initial chromospheric acoustic velocity; temperature, to the initial chromospheric ion temperature.

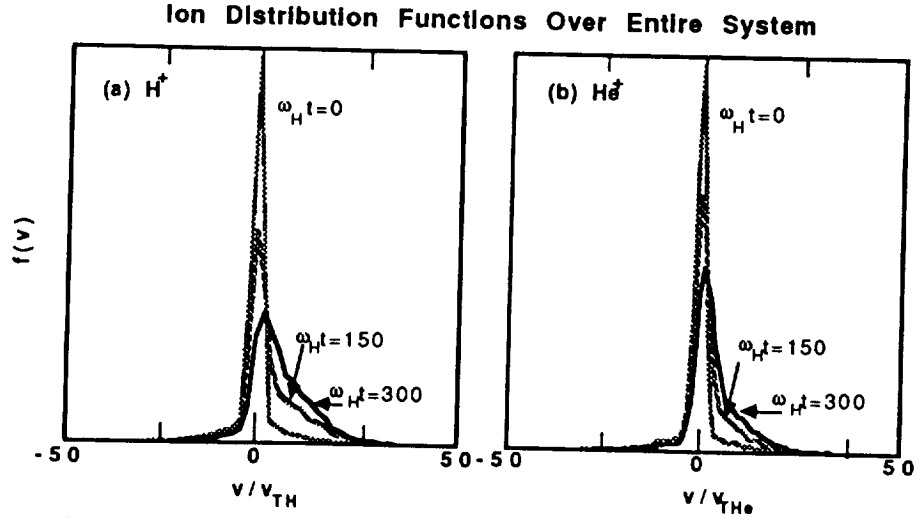

Fig. 10: Distribution functions for all the ions in the simulation system. Velocities are normalized to initial chromospheric thermal velocities.

found to create an ambipolar electric field which is capable of accelerating ions up to energies of order the lectron thermal energy. In the coronal case, the H^+ ions form a constant velocity and density beam region between forward and backward propagating fronts of the ambipolar field, the forward front eventually steepening into an electrostatic shock. The ions in the beam region are unstable to the ion-ion streaming instability, which then acts to preferentially heat and accelerate the He^+ jions by extracting the H^+ beam energy. This nonthermal heating as well as the acceleration is clear in the ion distribution functions, which bear some similarity to soft X-ray line profiles. In the chromospheric case, no similar beam region is formed, the ion-ion instability is weaker, and little preferential heavy ion heating occurs. However, substantial broadening is present in the ion distribution functions due to the nonuniform motion of the ions. Thus, these simulations have been able to reproduce some of the features, though not all, of soft X-ray line emissions. Only in the coronal heating simulation are the broadening and the speed of the blue-shifted component in agreement with soft X-ray line observations.

Future work on this project includes the addition of a heavy ion with a charge to mass ratio of about 2 to represent those ions actually emitting the soft X-rays, and the addition of a method to simulate the continuous heating of the system by energetic electrons.

This work was supported by National Science Foundation grant ATM-8719371 and by NASA's Solar Terrestrial Theory and Solar Heliospheric Physics Programs under grants NAGW-91 and NSG-7287 to the University of Colorado. The simulations were performed on the CRAY X-MP at the San Diego Supercomputer Center which is supported by the National Science Foundation.

REFERENCES

Antonucci, E. (and 8 others) 1982, *Solar Phys.*, **78**, 107.
Brown, J. C., Melrose, D. B., and Spicer, D. S. 1979, *Ap. J.*, **228**, 592.
Dusenberry, P. B., Martin, R. F., and Winglee, R. M. 1988, *J. Geophys. Res.*, **93**, 5655.
MacNeice, F. (and 8 others) 1985, *Solar Phys.*, **99**, 167.
McKean, M. E., Winglee, R. M., and Dulk, G. A. 1989, *Solar Phys.*, in press.
Melrose, D. B., and Dulk, G. A. 1982, *Ap. J. (Letters)*, **259**, L41.
Melrose, D. B., and Dulk, G. A. 1984, *Ap. J.*, **282**, 308.
Winglee, R. M. 1989, *Solar Phys.*, in press.

CHROMOSPHERIC-CORONAL COUPLING DURING SOLAR FLARES: CURRENT SYSTEMS AND PARTICLE ACCELERATION

R. M. Winglee, M. E. McKean and G. A. Dulk

Department of Astrophysical, Planetary and Atmospheric Sciences
University of Colorado, Boulder, CO 80309-0391

Abstract

Two-dimensional (three velocity) electrostatic particle simulations are used to investigate the particle heating and acceleration associated with the impulsive phase of a solar flare. A cross-field current in the high corona (which is presumably driven by reconnection processes) is used to initiate the flare. Due to the differential motion of the electrons and ions, currents and associated quasi-static electric fields are generated with the primary current and balancing return current being on adjacent field lines. These currents extend from the corona down into the chromosphere. Electrons can be accelerated to energies exceeding 100 keV on short time scales via the quasi-static fields and wave-particle interactions. The spectra of these electrons has a broken power-law distribution which hardens in time. The spatially separate primary and return currents are closed by the cross-field acceleration of the ambient ions into the primary current region. These ions are then accelerated upwards into the corona by the same quasi-static electric field accelerating the electrons downwards. This acceleration can account for the broadened stationary and weak blue shifted component seen in soft X-ray line emissions and enhancements in heavy ion abundances seen in the solar wind in association with solar flares.

1. Introduction

Energetic electrons produced in the impulsive phase of a solar flare are responsible for a wide range of phenomena, including intense radio, soft and hard X-ray emissions. These emissions can provide important information on the dynamics of the coronal and chromospheric plasma during a flare. Observations of the hard X-ray spectra show that impulsive flares can often be categorized by a hardening of the electron spectrum during the rise and peak of the X-ray emissions and a softening of the spectrum during the decay phase (Dennis, 1988 and references therein). The spectrum can also evolve from a single power to a broken power-law (Lin and Schwartz, 1987). Observations of soft X-ray line emissions from heavy ions, such as Ca XIX and Fe XXV, indicate bulk upward motions of plasma with speeds of the order of 100 – 500 km/s and turbulent velocities exceeding 100 km/s (e.g., Antonucci et al., 1985). In addition to this upflow, the relative abundances of certain heavy ions associated with the flare can change, as indicated by in-situ measurements in the solar wind (Reames et al., 1985; Mason, 1987) and by the relative intensities of certain X-ray line emissions (Doschek et al., 1980; Sylwester et al., 1984).

The above inferred particle acceleration can occur via a variety of processes. The spectrum of the energetic electrons is determined by the characteristics of the acceleration mechanism in the primary energy release site and by their interaction with the coronal and chromospheric plasmas. This interaction can, in turn, lead to the generation of intense waves which can produce

further plasma heating, including the generation of high energy tails. The ambient plasma can also experience strong acceleration and heating via both the quasi-static electric fields and induced wave-fields. In addition to these processes, the chromospheric plasma is subject to collisional heating via precipitating energetic electrons.

To date, models for the particle acceleration and heating have concentrated only on limited aspects of the above processes. Recently, collisionless particle simulations have been used by Winglee et al. (1988a,b) and McKean et al. (1989a,b) to model the propagation of energetic electrons and conduction fronts through the corona, self-consistently with the associated return currents and particle heating. Such simulations allow the inclusion of effects arising from both quasi-static electric fields and wave-particle interactions, thereby allowing more detailed modelling.

The purpose of this paper is to extend the above simulations by including (i) an acceleration mechanism or driver which will allows the dynamics of the primary energetic electrons to be determined self-consistently with the dynamics of the ambient plasma and (ii) a collisional plasma at low-altitudes representing the chromospheric plasma. The properties of the currents in the corona are coupled to the properties of chromospheric plasma since the latter component is important in closing the currents and provides a sink for the energy of precipitating energetic electrons. The present study seeks to determine the particle acceleration associated with both quasi-static electric fields and wave-particle interactions under realistic flare conditions in relation to the above observationally inferred properties including

(i) the electron energy spectrum
(ii) the characteristics of the acceleration and heating of the plasma ions, and
(iii) the change in apparent heavy ion abundances.

The outline of the paper is as follows. The simulation model is outlined in section 2. In section 3, the evolution of the electron distribution is described and compared with spectrum inferred from hard X-ray emissions. In section 4, the properties of the induced acceleration and heating of the plasma ions is described and compared with those inferred from the soft X-ray line emissions and observed changes in abundances. A summary of results is given in section 5.

2. Simulation Model

Because of the complexity, variety and nonlinearities of the processes involved, two-dimensional (three velocity) electrostatic particle simulations are utilized. Such simulations allow a self-consistent treatment of the particle dynamics and the associated electric fields, including the acceleration produced by quasi-static electric fields and heating produced by wave-particle interactions. Two-dimensions in the simulations are important since they allow cross-field transport to be evaluated. This cross-field transport is an important factor in the closure of the currents and the ion dynamics (Winglee et al., 1988).

The assumed plasma profile is shown schematically in Figure 1. The corona is represented by a collisionless plasma on the left half of the simulation system. The density is assumed to increase approximately linearly by a factor of four from the left hand edge (representing high altitudes) to the beginning of the transition region which is 3/5 down the simulation system. The transition region and chromosphere are represented by a collisional plasma where the ion collision frequency increases from 0.4 Ω_H at the beginning of the transition region to 8 Ω_H at the lowest altitudes. The density is assumed to increase by a factor of five across the transition region, giving a total

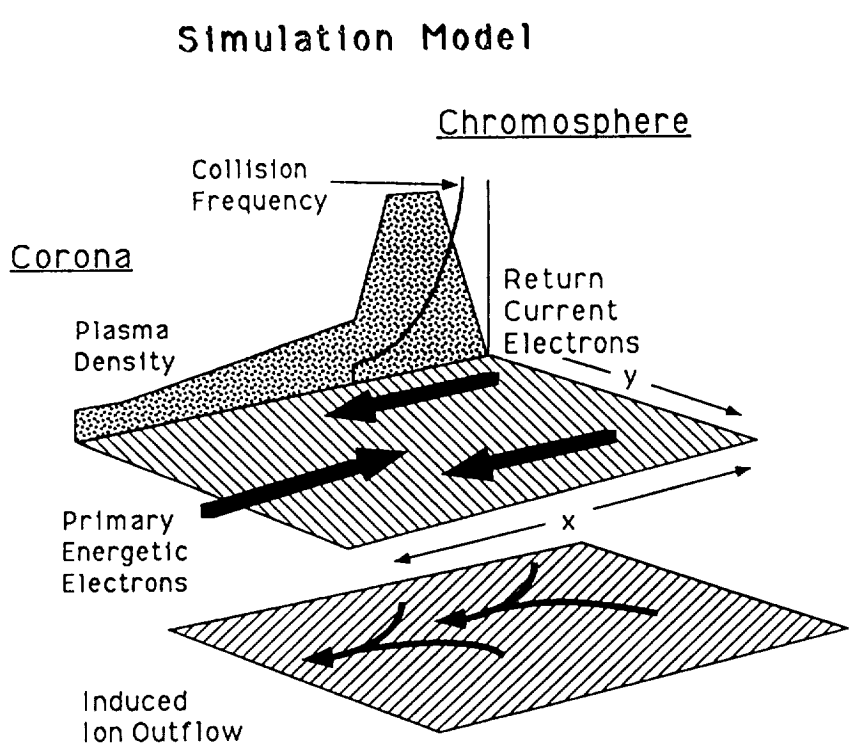

Figure 1. Schematic of the simulation model, including profiles of the density and collision frequency and the induced plasma flows.

increase density of a factor of twenty from the corona to the chromosphere. These changes in density are comparable to those expected in the flaring flux tube and provide a relatively smooth transition from the properties of the coronal plasma to the chromospheric plasma; the exact value of the density increases is not important.

Both plasmas are assumed to be initially in temperature equilibrium with the ion temperature equal to the electron temperature and the coronal temperature equal to 100 eV. The plasma ions are represented by two ion species: H^+ and He^+. The latter represents not only the He but also heavy ion species with charge-to-mass ratios similar to He^+. This heavy ion species is included so that their characteristics in both velocity and coordinate space can be compared with those inferred from observations. For simplicity, variations in the charge-to-mass ratio of an ion due to plasma heating are not considered here. The He ions are assumed to comprise 25% of the plasma. This ratio is higher by about a factor of 2.5 above cosmic abundances although the total charge density associated with the He is comparable to that when the He ions are fully ionized. It is assumed here so that there are sufficient particles for proper statistics for the velocity distribution and density profiles. The following results are not sensitive to the actual relative density provided that it is much less than that of H.

The induced current system and particle acceleration shown in the following are produced by applying a cross-field current at the top of the coronal plasma. Such a current may, for example, arise from reconnection processes in the primary energy release site and is modelled in the simulations by injecting both electrons and energetic ions from the central portion of the left hand boundary. The electrons with their small gyro-radius remain tied to the field lines and carry little perpendicular current. The energetic ions on the other hand have a much larger gyroradius and stream across the field lines to set up the cross-field current.

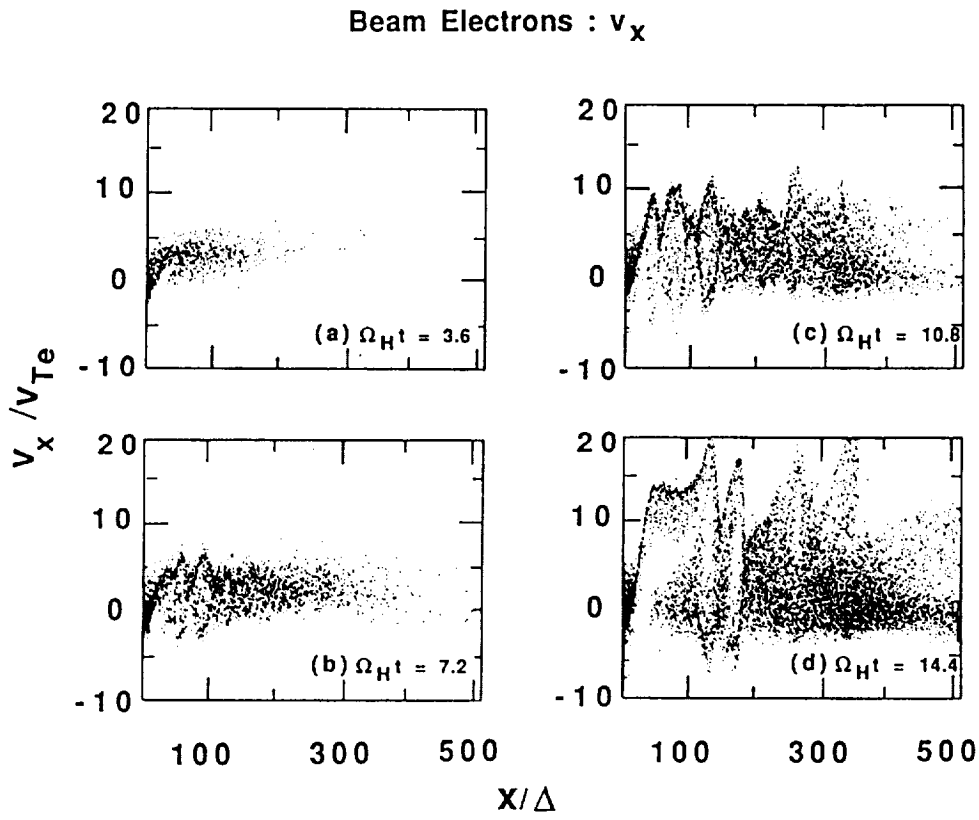

Figure 2. The $v_x - x$ phase space of the beam electrons showing the bulk acceleration and heating when the system is driven by the assumed cross-field current in the corona. Electrons with energies exceeding 40 keV are created on fast time scales.

Thus, in the center of the system (hereafter called the primary current region), there is an excess of electrons while on adjacent field lines (hereafter called the return current region) there is an excess of positive charge (cf. Winglee et al., 1988). This space-charge separation produces fields which accelerate electrons in the primary current regions downwards into the chromosphere and electrons in the return current region up into the corona. It is the formation of this current system and the associated particle acceleration which is addressed in the following.

3. Electron Properties

The downward acceleration of electrons in the primary current region is illustrated in Figure 2 which shows the evolution of the parallel velocity of the beam electrons (i.e., those injected with the energetic ions). The beam electrons which are injected near the left hand boundary with low velocity (i.e., $x/\Delta \simeq 0$ and $\mid v \mid \lesssim 3v_{Te}$) are seen to be accelerated by the quasi-static electric field to bulk velocities of the order of $10v_{Te}$. For a typical coronal temperature of 100 eV, this bulk velocity corresponds to an an energy exceeding 10 keV.

In addition to this bulk acceleration, intense wave are generated as evidence by the vortices in the particle phase spaces in Figure 2. These waves which arise through the beam-plasma interaction accelerates some of the electrons to energies exceeding 40 keV while some of the electrons are slowed

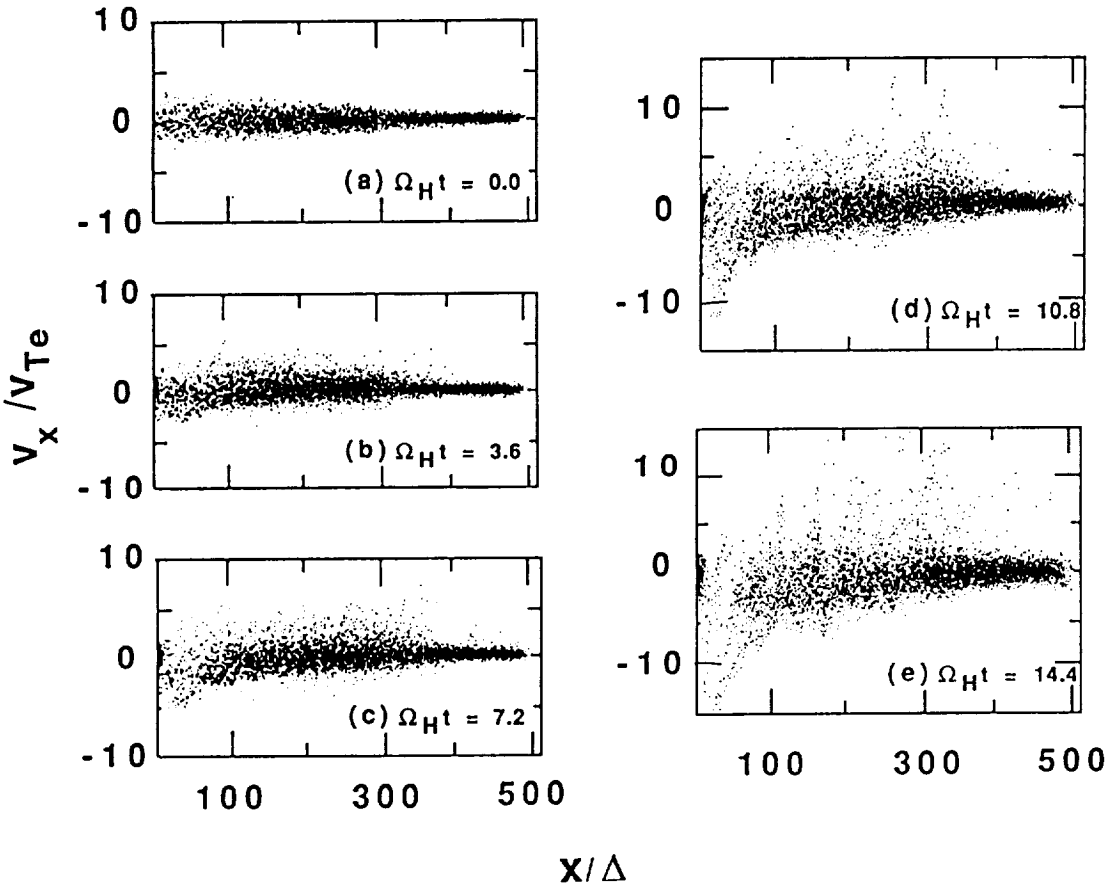

Figure 3. The $v_x - x$ phase space of the ambient plasma electrons. Electrons in the primary current region attain positive velocities of the order of 10 v_{Te} while the return current electrons attain negative velocities of about half the magnitude.

via the interaction, causing the electrons to become dispersed in phase-space, particularly at low altitudes.

The ambient plasma electrons also experience strong bulk acceleration and heating. This is illustrated in Figure 3 which shows the $v_x - x$ phase space of the ambient electrons for the same times as in Figure 2. Electrons in the primary current region are accelerated downwards, attaining positive velocities of the order of 10 v_{Te}, similar to the beam electrons. The return current electrons which are on adjacent field lines are seen in Figure 3 as electrons with negative velocities whose magnitude increases in time. At the end of the simulation their speed is of order of 5 v_{Te} in the corona. This speed is about half the bulk speed of the beam electrons and is sufficient to provide the balancing current since the return current region is twice as large as the primary current region.

Hard X-Ray Characteristics

The predicted spectrum of electrons precipitating into the chromosphere (i.e., $x/\Delta > 200$) is shown in Figure 4. This spectrum is categorized by a broken power law distribution which hardens in time, similar to that observed by Lin and Schwartz (1987). The energy where the break occurs is

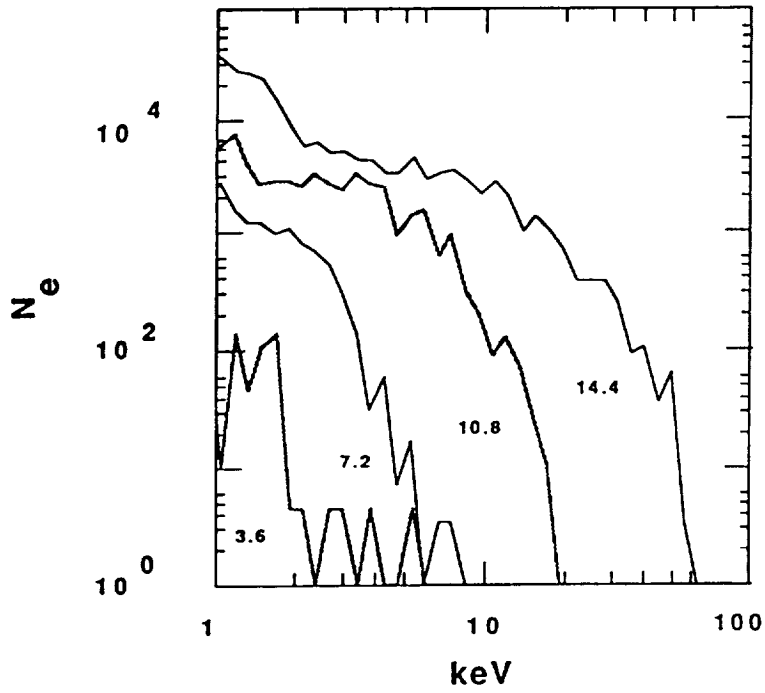

Figure 4. The evolution of the spectrum of electrons impacting on the chromosphere.

indicative of the potential drop associated with the quasi-static electric field in the primary current region.

A unique feature of the present model is that, since the acceleration is driven by quasi-static electric fields extending from the corona down to the chromosphere, the low energy (1 – 10 keV) electrons impact on the chromosphere before the 10 – 100 keV electrons. This prediction differs from acceleration models where the electron acceleration occurs in a limited region in the corona. In this case due to the difference in speeds, the fastest electrons are expected to impact on the chromosphere first.

Another important feature of the model is that the chromosphere is subject to heating before the arrival of the high energy electrons. This heating is seen in Figures 3 c–e as an increase in v_x of electrons at $x/\Delta \gtrsim 400$ and is due to the penetration of the quasi-static fields into the chromosphere on fast time scales. On comparing with Figure 4, the hard X-ray electrons do not arrive until nearly the end of the simulation. The situation is analogous to electrically pulsing a wire: the electric field propagates through at light speed while the actual electrons drift through the wire at much slower speeds. This initial heating of the chromosphere can create electrons exceeding 10 eV and thereby produce $H\alpha$ emissions preceding the rise of the hard X-ray emissions.

4. Ion Properties

The ambient ions are also accelerated by the quasi-static electric fields driving the current system. This acceleration is illustrated in Figure 5 which shows the phase spaces of the H ions as functions across the field in the coronal and transition regions. (The He ions have a similar phase space and are not shown.) In the primary current region, the ions are accelerated upwards reaching peak negative velocities of the order of 10 v_{TH} in the corona (Figure 5b) and about a

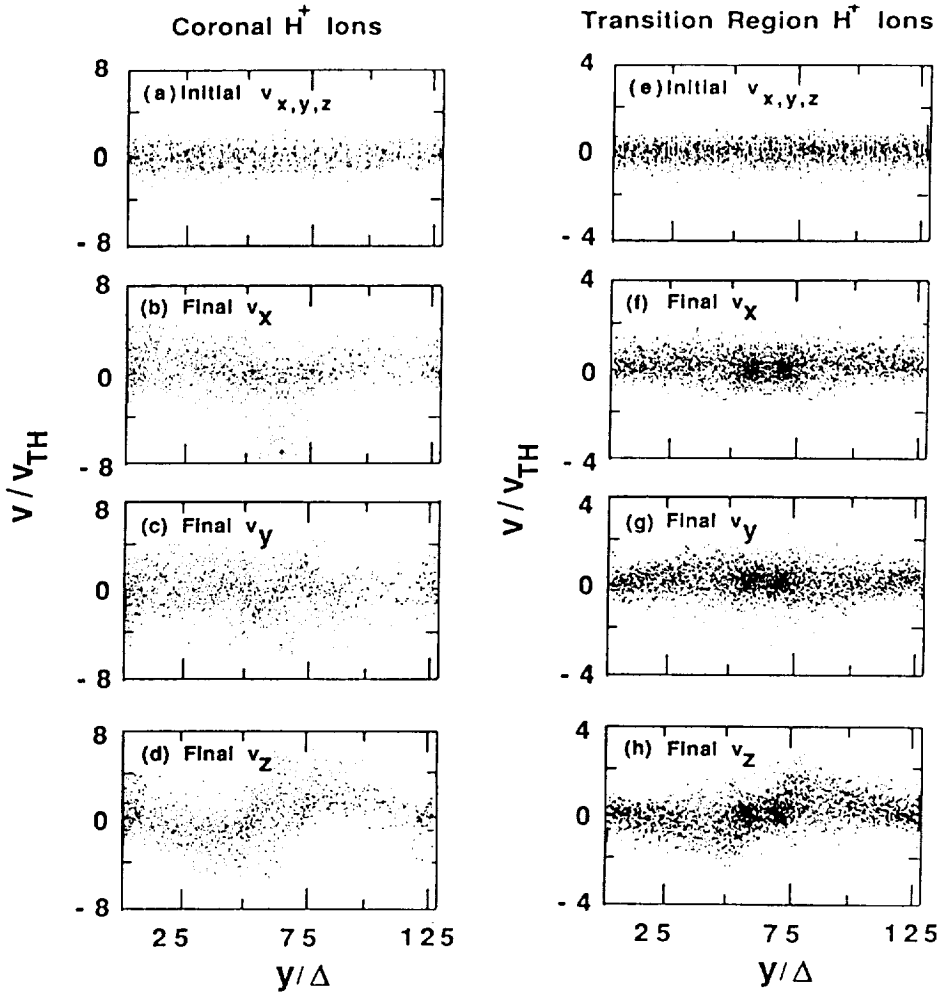

Figure 5. The phase spaces of the H^+ ions in the corona and transition region as functions of position across the field lines, i.e., y, and normalized to the initial thermal speed of the coronal ions v_{TH}.

quarter of this value in the transition region (Figure 5f). In the return current regions, there is some weak acceleration of ions down into the chromosphere.

In addition to this parallel acceleration, the ions experience strong perpendicular acceleration, as seen in the lower panels in Figure 5. This perpendicular acceleration is an integral part of the current system. In particular, since the primary and return currents are not cospatial, a perpendicular current must be drawn in order to close the system. This perpendicular current is most easily carried by the ions which have a larger gyro-radius and hence mobility across the field lines. This current is seen in Figures 5c and 5g as a net flow of ions into the primary current region with ions with $y/\Delta < 64$ having a net positive v_y and ions with $y/\Delta > 64$ having a net negative v_y.

However, even with their larger gyroradius, the ions are still not totally free to propagate across the fields lines and are also subject to strong $\boldsymbol{E} \times \boldsymbol{B}$ drifts in v_z, as seen in Figure 5d and 5h. These drifts can exceed the bulk velocity in y, particularly in the corona. In the chromosphere, the collisions tend to reduce the $\boldsymbol{E} \times \boldsymbol{B}$ drift and enhance the cross-field motion into the primary current region. It is this enhanced cross-field motion which allows the currents to be finally closed.

Soft X-Ray Line Profile Characteristics

The reduced-velocity distributions of the plasma ions convolve with the density of electrons with energies greater than 2 keV are shown in Figure 6. A convolution is taken since the profiles inferred from the soft X-ray line emissions involve a similar convolution. Two viewing angles are shown: a field-aligned viewing angle at 0° and one at 45°. The distributions in each case are integrated over velocities orthogonal to the viewing angle so that for the field-aligned viewing the speed has contributions from the parallel velocity whereas for the cross-field viewing angle which is the most probable, the speed has contributions from both parallel and perpendicular velocity components.

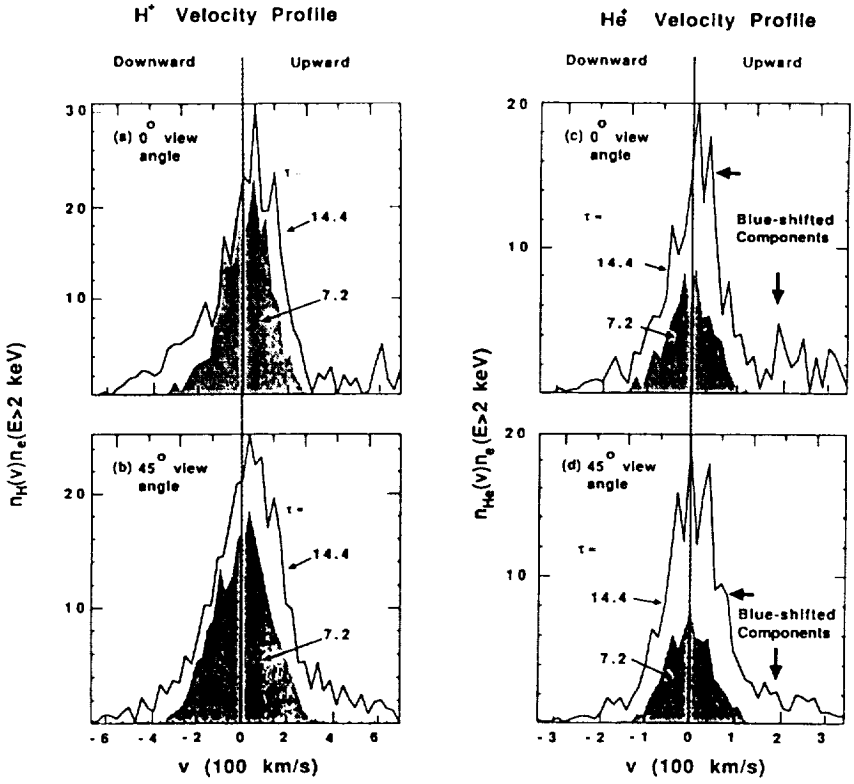

Figure 6. The predicted reduced distributions of the H and He ions for two different viewing angles.

For both viewing angles, the distribution has a stationary component and a blue-shifted (upward moving component) with the velocity range being comparable to those inferred from observations. Both components are seen to grow in time as the flare evolves, but the stationary component remains the dominant feature, similar to the observations. The stationary component appears broader for the 45° viewing angle due to the perpendicular acceleration and heating of the ions which produces velocity components both in the forward and backward directions, for viewing angles oblique to the magnetic field. As a result of this broadening arising from the perpendicular acceleration and heating, the stationary component appears relatively weak for the cross-field viewing angle.

An additional feature is that the distributions also show the presence of a weak red-shifted component. This component is strongest for the H ions and is associated with the downward acceleration of H ions in the return current regions. Like the blue-shifted component, this component appears strongest for field-aligned viewing angles.

Changes in Heavy Ion Abundances

Another important characteristic associated with the closing of the current by perpendicular ion acceleration is that changes in the relative abundances of different ion species can result. This change in abundances arises from the fact that the different ion species have different gyroradii, with the heavy ions in low ionization states having the largest gyroradius. Such heavy ions are able to propagate greater across distances from the return current region into the primary current region than the light ions so that a heavy ion concentrations develop in the primary current region and depletions in the return current regions.

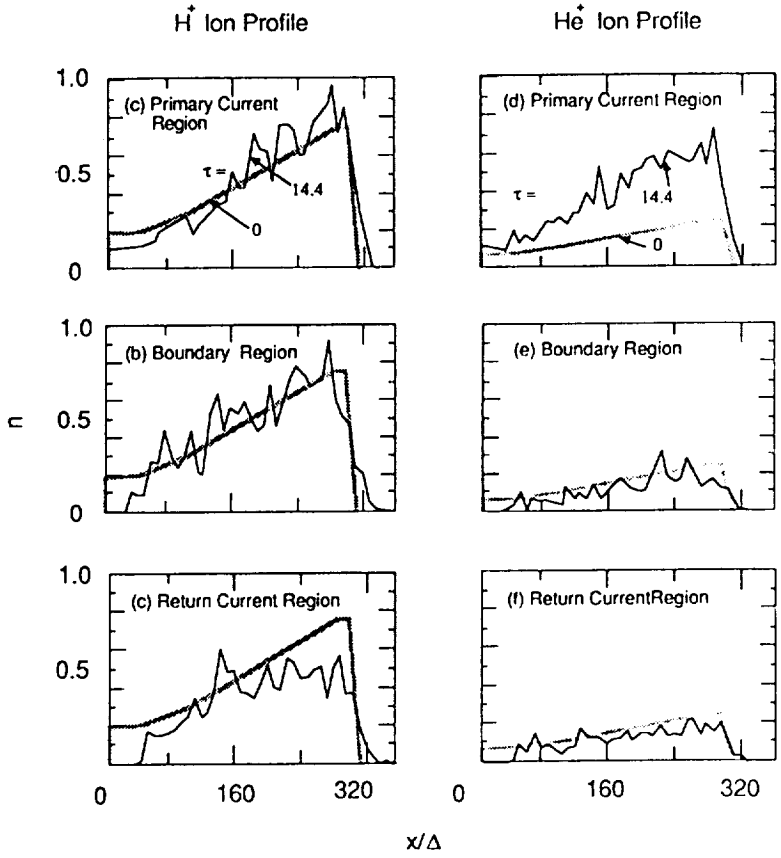

Figure 7. Profiles of the H^+ and He^+ ions at the beginning and end of the simulation at (i) the center of the primary current region, (ii) near the boundary between the primary and return current regions and (iii) in the return current region.

This change in relative abundance is illustrated in Figure 7. The H density in the primary current region changes by only a few tens of percent while the He density is nearly three times larger than its initial density. Since the X-ray emission is dominated by that in the primary current region, the plasma as view from X-ray diagnostics will appear enriched with heavy ions. Moreover, since the outward ion acceleration is dominated by that in the primary current region, the plasma escaping into the solar wind will also appear enriched in heavy ions.

5. Summary

Two dimensional (three velocity) electrostatic particle simulations have been used to investigate the characteristics of the particle acceleration and associated current systems during solar

flares. In the simulations a cross-field current in the high corona (which presumably is driven by reconnective processes) is used to initiate the flare. The results show

(i) the presence of hot electron current channels or primary current regions where the electrons can be accelerated to energies of the order of 100 keV by quasi-static electric fields and wave-particle interactions on short time scales;

(ii) these electrons have a hardening broken power law distribution with the energy at the break indicating the potential associated with the quasi-static electric field;

(iii) return currents are generated on adjacent field lines with the total current matching that of the primary current – this latter requirement implies that the return current electrons are in general less energetic than the beam electrons assuming that the primary current region is narrower than the return current region;

(iv) ions are accelerated across the field lines from the return current regions into the primary current regions to produce current closure - collisions in the chromosphere are particularly important in providing enhanced cross-field transport;

(v) heavy ions in initially low ionization states with their relatively large gyro-radius are preferentially accelerated into the primary current regions which results in enhancements in the abundances of the heavy ions in the X-ray emitting plasma;

(vi) as the ions enter the primary current region they are accelerated upwards by the quasi-static electric field and this field-aligned acceleration results in the blue-shifted component seen in soft X-ray line emissions; broadening of the stationary component is attributed to the perpendicular acceleration of the ions.

Acknowledgements. This work was supported by National Science Foundation grant ATM - 8719371 and by NASA's Solar Terrestrial Theory, Solar Heliospheric and Ionospheric Physics Programs under grants, NAGW-91, NSG-7287 and NAGW-1587 to the University of Colorado. The simulations were performed on the CRAY X-MP at the San Diego Supercomputer Center which is supported by the National Science Foundation.

References

Antonucci, E., Dennis, B. R., Gabriel, A. H., and Simnett, G. M. 1985, *Solar Phys.*, **96**, 129.

Dennis, B. R. 1988, *Solar Phys.*, **118**, 49.

Doschek, G. A., Feldman, U., Kreplin, R. W., and Cohen, L. 1980, *Ap. J.*, **239**, 725.

Lin, R. P., and Schwartz, R. A. 1987, *Ap. J.*, **312**, 462.

Mason, G. M. 1987, *Rev. Geophys.*, **25**, 676.

McKean, M. E., Winglee, R. M., and Dulk, G. A. 1989a, *Proc. Second MAX'91 Workshop*, edited by R. M. Winglee, submitted.

McKean, M. E., Winglee, R. M., and Dulk, G. A. 1989b, *Ap. J.*, submitted.

Reames, D. V., von Rosenvinge, T. T., and Lin, R. P. 1985, *Ap. J.*, **292**, 716.

Sylwester, J., Lemen, J. R., and Mewe, R. 1984, *Nature*, **310**, 665.

Winglee, R. M., Pritchett, P. L., and Dulk, G. A. 1988a, *Ap. J.*, **327**, 968.

Winglee, R. M., Pritchett, P. L., and Dulk, G. A. 1988a, *Ap. J.*, **329**, 440.

Development of a Numerical Solution to the Time Dependent Kinetic Equation

Russell J. Hamilton Edward T. Lu Vahé Petrosian
Center for Space Science and Astrophysics
Stanford University
Stanford, CA 94305

Abstract

We have developed a numerical solution for the time dependent Fokker-Planck equation for arbritrary distributions of electrons injected into a magnetized plasma. We have calibrated and tested our code which includes energy loss and pitch angle scattering due to Coulomb collisions and changes in pitch angle due to inhomogeneous magnetic fields. The numerical method is versatile so that other scattering or radiation terms can be easily included. Using this code we will investigate many processes associated with the impulsive phase of solar flares.

Introduction

The evolution of a distribution of electrons in magnetized plasma is given by the equation

$$\frac{\partial f}{\partial t} = -\mu c\beta\frac{\partial f}{\partial s} - \frac{\partial}{\partial \mu}(\dot{\mu} f) - \frac{\partial}{\partial E}(\dot{E} f) + \frac{\partial}{\partial \mu}(D_{\mu\mu}\frac{\partial f}{\partial \mu}) + \frac{\partial}{\partial E}(D_{EE}\frac{\partial f}{\partial E}) + \frac{\partial}{\partial E}(D_{E\mu}\frac{\partial f}{\partial \mu}) + \frac{\partial}{\partial \mu}(D_{E\mu}\frac{\partial f}{\partial E}) + S(E,\mu,s,t), \quad (1)$$

where E, βc, μ, and s are the electron, energy, velocity, pitch angle cosine, and postion respectively. The coefficients $\dot{E}$ and $\dot{\mu}$ are the systematic changes in energy and pitch angle cosine due to external forces, radiation, and scattering, while the diffusion coefficients D_{ij} are due only to scattering processes. The term $S(E,\mu,s,t)$ is the source (or sink) of electrons which accounts for those acceleration (or loss) processes with timescales which are much faster than the processes giving rise to the coefficients $\dot{E}$, $\dot{\mu}$, and D_{ij}.

For electrons of energy 10 keV to 1 MeV and an ambient plasma with magnetic field strength 10^2 to 10^3 Gauss and plasma density 10^9 to 10^{14} cm^{-3} the dominant processes are Coulomb collisions and magnetic mirroring. Therefore, we need only to determine the coefficients which arise from Coulomb collisions and magnetic mirroring in equation (1) and solve the resulting equation to determine the time evolution of electrons of the above energies for typical solar flare conditions. We obtain

$$\frac{\partial f}{\partial t} = -\mu c\beta\frac{\partial f}{\partial s} + \beta c\frac{d\ln B}{ds}\frac{\partial}{\partial \mu}\left(\frac{(1-\mu^2)}{2}f\right) + \frac{c}{\lambda_0}\frac{\partial}{\partial E}\left(\frac{f}{\beta}\right) + \frac{c}{\lambda_0\beta^3\gamma^2}\frac{\partial}{\partial \mu}\left[(1-\mu^2)\frac{\partial f}{\partial \mu}\right] + S(E,\mu,s,t), \tag{2}$$

where $\lambda_0 = 10^{24}\mathrm{cm}/n(s)\ln\Lambda$ is the mean free path of an electron with energy equal to its rest mass, $n(s)$ is the background plamsa number density (in cm^{-3}), and $\ln\Lambda \approx 20$ is the Coulomb logarithm (see Lu and Petrosian 1988).

Numerical Solution

Our numerical solution ultilizes a finite difference scheme along with the powerful method of operator splitting. Operator splitting (or time split method) is a method of solving partial differential equations which contain a number of differential operators such as equation (1) or (2). The complete numerical solution is obtained by finding the finite difference solution for each individual operator and then applying these cyclically (see Centrella and Wilson 1984, Hawley, Smarr, and Wilson 1984).

An important aspect of the development of a numerical code for the study of a physical system is code calibration. In order to check the accuracy of our numerical solution, we compare the numerical solution with known analytic solutions for simplified physical conditions. In addition to demonstrating the accuracy of the numercial solution, the calibration also provides us with the limitations of the numerical code as well as the number of grid points necessary to resolve features in the electron distribution.

Applications

The numerical code that we have developed to solve equation (2) can be used to study the evolution of a distribution of electrons during the impulsive phase of a solar flare under conditions for which an analytic solution is impossible. Therefore, we will be able to compute the expected time evolution of the radiation spectrum and of the spatial variation of the radiation for arbitrary density and magnetic field structures for arbitrary sources of electrons.

We have already begun to utilize the numerical code for study of the impulsive phase of solar flares. In a completed study, we used our solution to investigate the relative timing of microwaves and hard X-rays (Lu and Petrosian 1989). We are also using this code to study the onset of kinetic plasma instabilities which result from the propagation and mirroring of electrons such as the cyclotron instability. In a previous investigation, the correlation of type III bursts and hard X-rays was studied (Hamilton and Petrosian 1989). We will use our numerical solution to analyze the type III burst hard X-ray association. As the ability to resolve temporal and spatial variations in X-rays improves, comparison of the new data with our models will allow us to place more stringent limits on the coronal conditions and specifically the characteristics of the accelerated electrons during the impulsive phase.

Modification of the code to include other processes such as a direct electric field, scattering from Langmuir or Alfvén wave turbulence (Hamilton and Petrosian 1987), or synchrotron radiation losses is straightforward. Therefore, other applications of our code include the study of the acceleration of electrons by parallel electric fields, the scattering and/or the acceleration of electrons by turbulence, and the evolution of continuum gamma-ray emission.

Acknowledgments

We enjoyed many useful discussions with Jim McTiernan while developing this code and we acknowledge the support of this work by National Aeronautics and Space Admin-

istration grant NSG-7092 and National Science Foundation grant ATM 8705084.

References

Centrella, J., and Wilson, J.R. 1984, *Ap. J. Suppl.*, **54**, 229.

Hamilton, R.J., and Petrosian, V. 1987, *Ap. J.*, **321**, 721.

Hamilton, R.J., and Petrosian, V. 1989, *Submitted for publication.*

Hawley, J.F., Smarr, L.L., and Wilson, J.R. 1984, *Ap. J. Suppl.*, **55**, 211.

Lu, E.T., and Petrosian, V. 1988, *Ap. J.*, **327**, 405.

Lu, E.T., and Petrosian, V. 1989, *Submitted for publication.*

Some of the Terrestrial Effects of AR 5395

D. Speich
Space Environment Laboratory/NOAA

Overview of AR 5395

Active Region 5395 was extraordinary for both its flare production for a complete disk transit and for one of the largest geomagnetic storms on record.

By any measure, Active Region 5395 was a spectacular flare producer. The Space Environment Services Center classifies peak flare intensity by both the peak flux in the 1-8A X-ray band and optically by peak Hα intensity and area. Routine measurement of full disk X-ray fluxes began in 1974. A simple measure of the flare productivity of an active region is to sum the peak X-ray intensities of the flares observed from that region. Using that measure, figure 1 illustrates the "top ten" flare producing regions since 1974 and the smoothed sunspot number during that period. Active Region 5395 was by far the most prolific X-ray flare producer during the last 15 years. Additionally, two of the larger flares (06 and 10 March) were remarkable in that their complete X-ray durations approached 24 hours. Figure 2 illustrates the X-ray flare activity during the disk transit of Active Region 5395. A total of 11 class X and 48 class M flares were observed.

A moderate intensity solar proton event (at particle energies greater than 10 MeV) was detected by NOAA geosynchronous sensors beginning at 08/1735UT. It decayed below event threshold near 14/1135UT and began again at 17/1855UT due to a large flare from Active Region 5395 while in the western hemisphere. This final near earth proton event finally ended near 20/1200UT.

The great geomagnetic storm of 13-14 March is attributed to a long duration X4/3B flare from Active Region 5395 which occurred at 10/1922UT from N31E22. Geomagnetic disturbances are measured and defined by several methods.

One classical measure of storm conditions is the three hourly K index. The K index is a measure of the maximum deflection of the intensity or direction of the geomagnetic field minus the normal quiet day variations. K indices are quasi-logarithmic and range in value from 0-9 with a K of nine denoting the most severe geomagnetic storm conditions. The eight daily K indices form the basis for the daily A index or other time scale indices.

The Institut fuer Geophysik in Gottingen, Germany calculates a daily A "planetary" index of geomagnetic conditions from 13 magnetic observatories located near the 50th geomagnetic latitude. This A index for 13 March was 246 - the second largest on record

since 1932 when the data series began. The largest daily value in this record occurred on 13 November 1960 at an A index of 280.

A longer measure of geomagnetic disturbances is the aa index. The Institut de Physique du Globe de Paris derives this 12 hour index from the K indices of two antipodal magnetic observatories, and has done so since 1868. In that record, the 13 March storm ties with the 13 November 1960 storm at a value of 462. This value is the third largest in that record. The highest aa values were 546 on 25 September 1909 and 477 on 18 September 1941. By these and the other various measures of geomagnetic activity, the storm of 13 March 1989 from Active Region 5395 was extraordinary - easily the most severe in almost 30 years.

Some Specific Terrestrial System Effects from AR 5395

Radio propagation suffered severely during the transit of Active Region 5395 from 06-20 March 1989. During X-ray flares of class M or X peak flux, short wave (3-30 MHz) transmissions in or through the daylit hemisphere can experience complete fadeout due to increased ionization in the Earth's ionosphere. This occurred almost 60 times due to flare activity from Active Region 5395. Complete outages in excess of 12 hours were experienced during the great flares of 06 and 10 March.

During the geomagnetic storm of 13-14 March, high frequency communications were all but absent. This is due to signal penetration through the ionosphere due to auroral electron precipitation and dynamic compositional storm effects (Figure 3). Inversely, VHF (30-300MHz) signals were enhanced by "auroral E" propagation where auroral charged particle precipitation increases the electron content at low altitudes.

The disk transit of Active Region 5395 occurred near the vernal equinox. This resulted in severe radio noise interference between geosynchronous satellites and ground stations when the sun was within the field of view of the antenna and a flare was in progress. This noise interfered with transmissions from some communications satellites and for a time interrupted cloud image transmissions from the nation's weather satellites.

Satellite operators experienced other system effects during the great magnetic storm of 13-14 March. During geomagnetic storms, the neutral atmosphere is heated increasing the drag on orbiting spacecraft below approximately 1000 km altitude. The result is in track and cross track errors in spacecraft location from that modeled and used by spacecraft operators. Since nearly every orbital object has a unique shape, composition, and cross section, the drag effect is unique for each. Figure 4 illustrates the in and cross track errors experienced by the OSCAR series of navigational satellites during the 13-14 March storm. Accurate satellite location to less than 30 meters is required to derive accurate terrestrial

locations from navigation satellites. During the storm, all OSCAR satellites were taken out of service for between a few days to a week for the lowest altitude spacecraft.

The U. S. Air Force and U. S. Navy routinely monitor the position of orbiting objects. Figure 5 illustrates the number of uncorrelated targets tracked by the Navy (over 5000) resulting from tracking errors due to the March geomagnetic storm. Each of these objects had to be reidentified.

The NOAA TIROS weather satellites experienced another problem related to increased atmospheric drag. Momentum wheels are the primary method used to orient these spacecraft. During the severe geomagnetic storm, the wheels spun up to design tolerance in an attempt to maintain attitude control (figure 5). Emergency backup systems engaged and control was maintained. If the storm had continued another 24 hours, control could have been lost.

The Space Shuttle was aloft during the March storm. The primary mission was the deployment of a TDRS communications satellite. The TDRS traverse to geosynchronous altitude was difficult with attitude control a serious problem. Ground rules for the subsequent launch of the Magellan spacecraft were developed to not begin its interplanetary flight during such conditions. The Shuttle itself experienced drag approximately 15% greater than on previous flights. Continual updates were required to ensure uninterrupted communications and accurate tracking.

Probably the most severe and publicly known effect of the 13-14 March storm was the Quebec power failure. During storm conditions, the fluctuating magnetic field induces currents in long conductors such and pipe lines and power lines. The fundamental period of geomagnetically induced currents (GIC) is on the order of several minutes and quasi dc compared to the normal 60 Hz or 50 Hz power grid frequency. This leads to half- cycle saturation of power transformers due to simultaneous ac and dc excitation, system voltage and frequency excursions, and tripping of protective relays. At 2:45 am local time on 13 March, Hydro-Quebec, Montreal, Canada suffered a system wide blackout and more than nine hours were required to restore service. At nearly the same moment there was also a voltage loss on half a dozen power distribution lines in middle and southern Sweden. Many other power systems experienced significant transmission anomalies but maintained service.

This brief overview, with some specific examples, is intended to illustrate only some of the more dramatic terrestrial effects resulting from flare activity in Active Region 5395. Material was gathered from several sources, especially from a presentation to the AGU in May, 1989 by J. A. Joselyn.

NOAA DATA AVAILABLE FROM THE NATIONAL GEOPHYSICAL DATA CENTER ON THE DISK TRANSIT OF ACTIVE REGION 5395

1. Continuous (3 second resolution) full disk X-ray fluxes in the 1-8A and .5-4A bands.
2. Continuous (5 minute resolution) energetic particle fluxes.
3. Selected imagery of Active Region 5395 in H-alpha and white light from the Holloman, New Mexico and Learmonth, Australia SOON observatories. Spatial resolution approximately .5 arcsec/pixel in 512 x 512 format.
4. Continuous (to one minute resolution) geomagnetic field measurements and indices.

USAF DATA AVAILABLE FROM THE NATIONAL GEOPHYSICAL DATA CENTER ON THE DISK TRANSIT OF ACTIVE REGION 5395

1. 35mm film patrol imagery from 5 SOON sites.
2. Regional magnetograms (5 arcsec resolution - several/day).
3. Radio burst (discrete and swept frequency) profiles.
4. Video of selected flares observed by the Holloman Observatory.

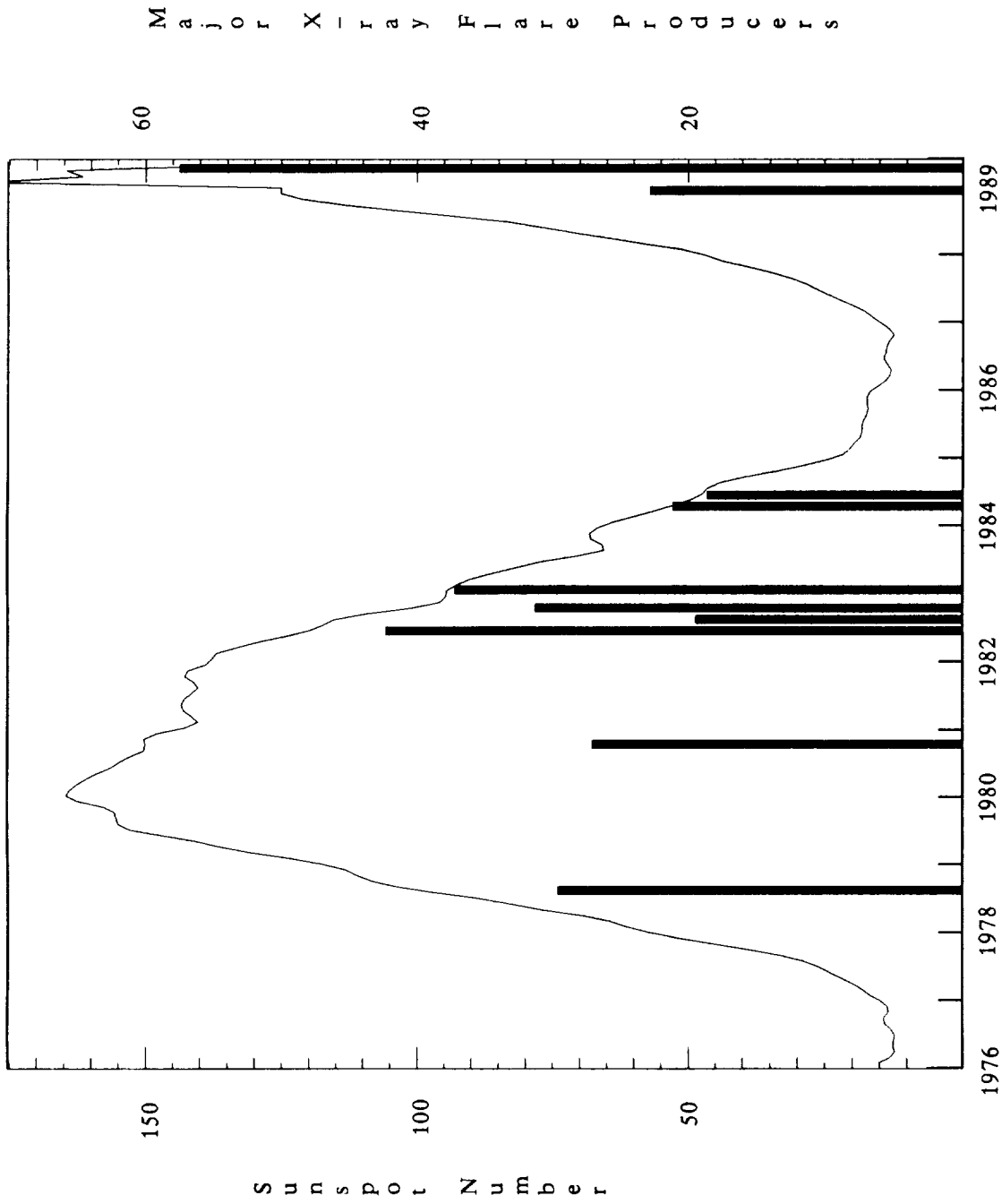

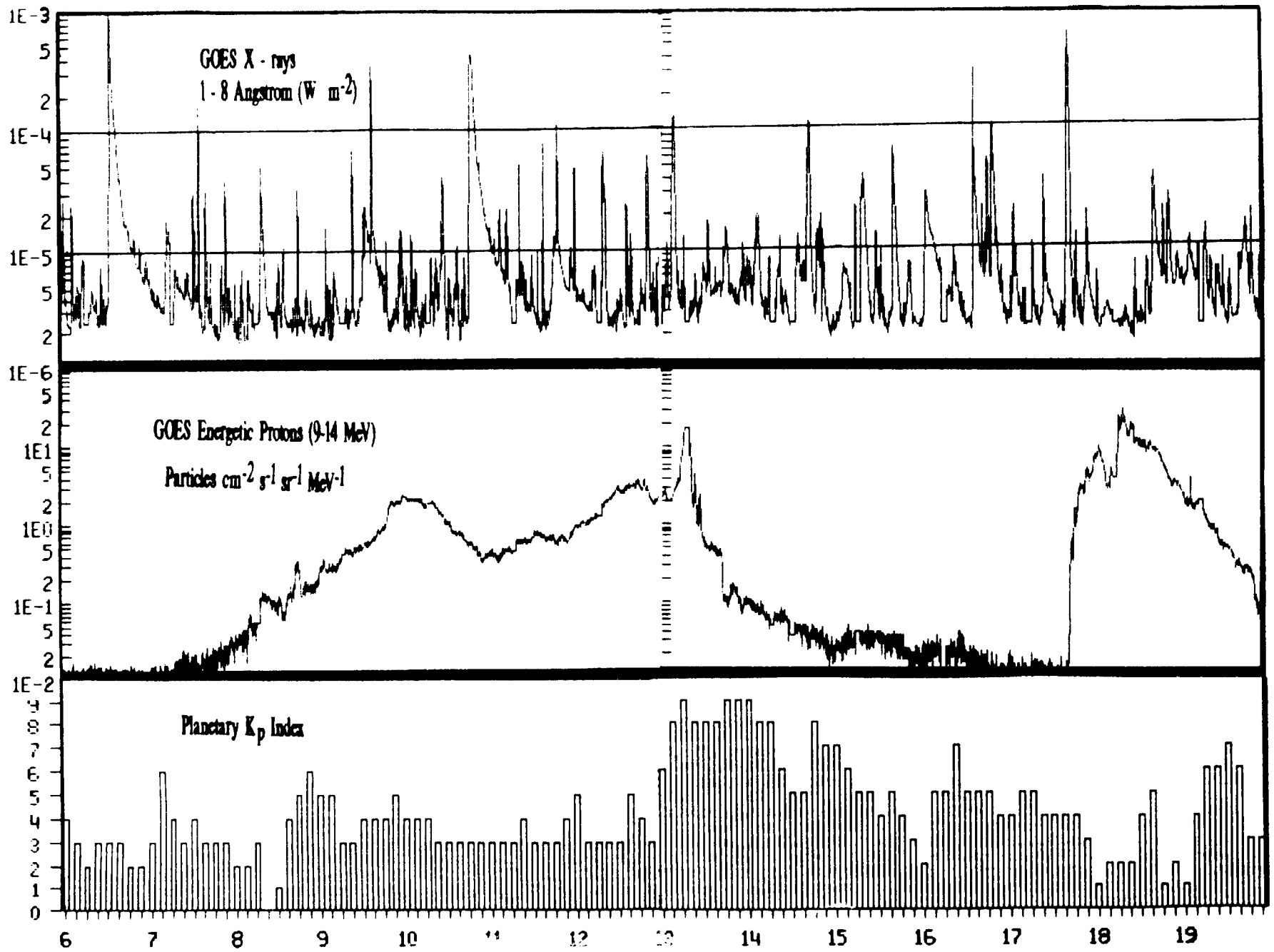

March 1989

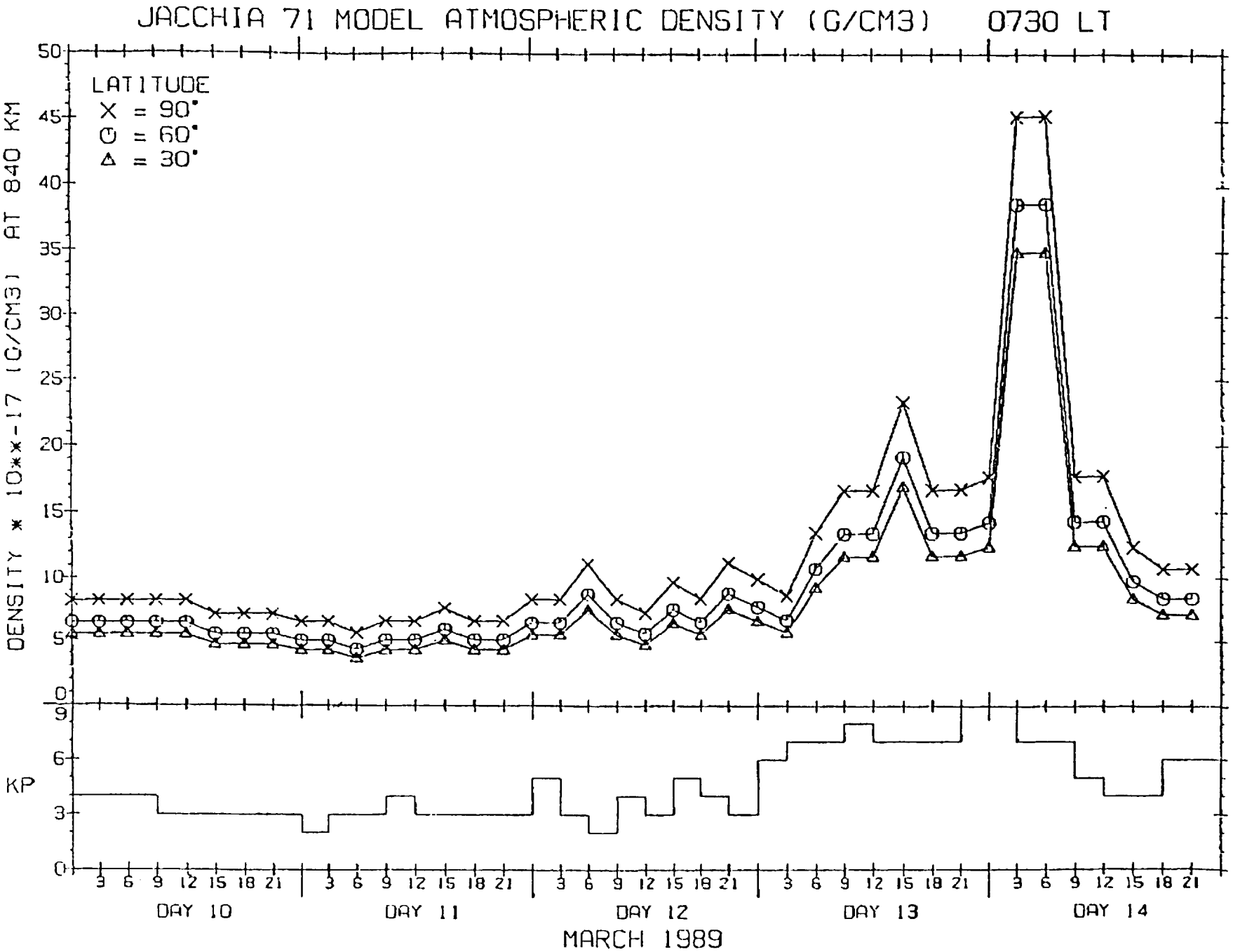
JACCHIA 71 MODEL ATMOSPHERIC DENSITY (G/CM3) 0730 LT
LATITUDE
X = 90°
O = 60°
Δ = 30°
DENSITY * 10**-17 (G/CM3) AT 840 KM
KP
DAY 10
DAY 11
DAY 12
DAY 13
DAY 14
MARCH 1989

13 MAR89 SOLAR FLARE – RMS POSITION ERROR

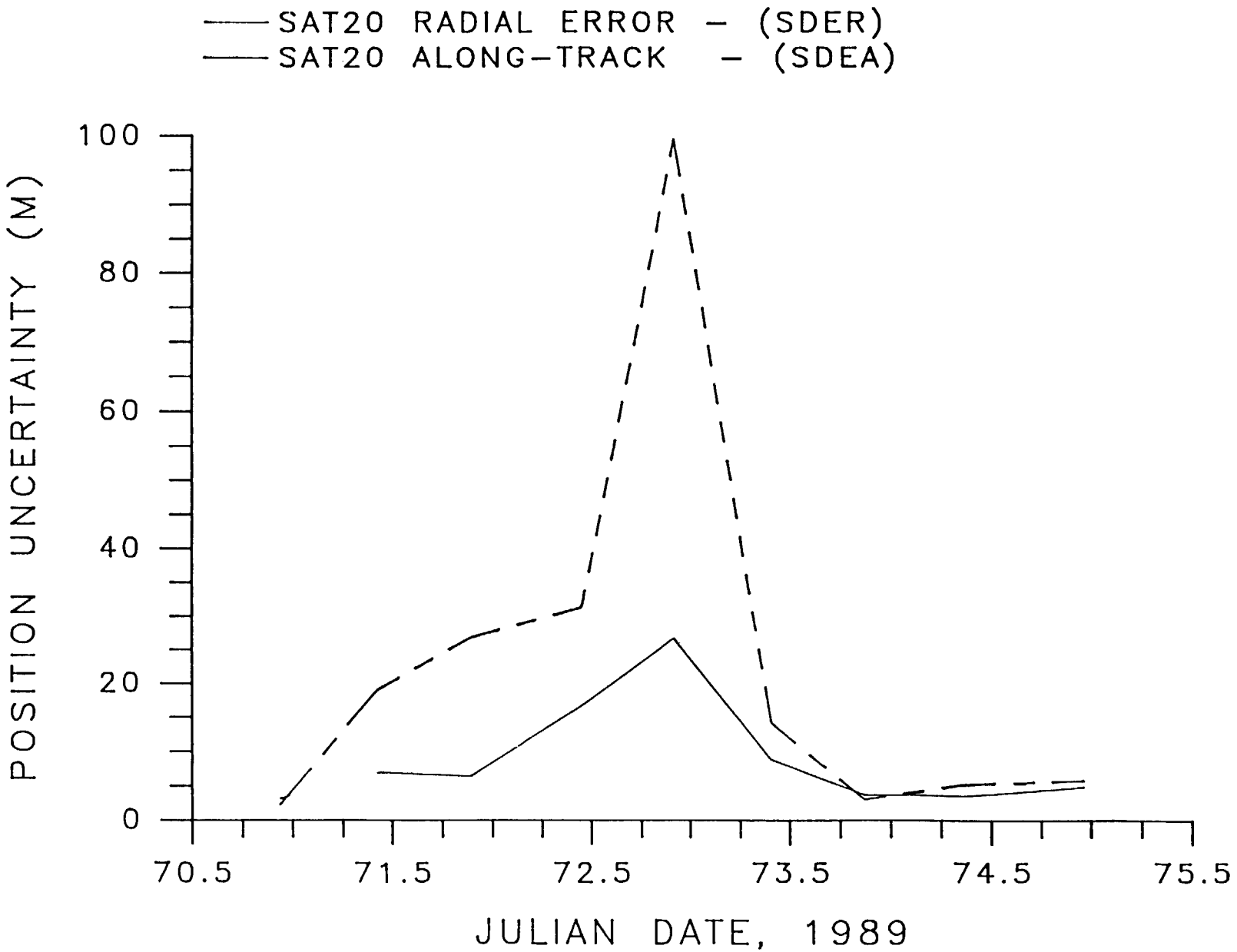

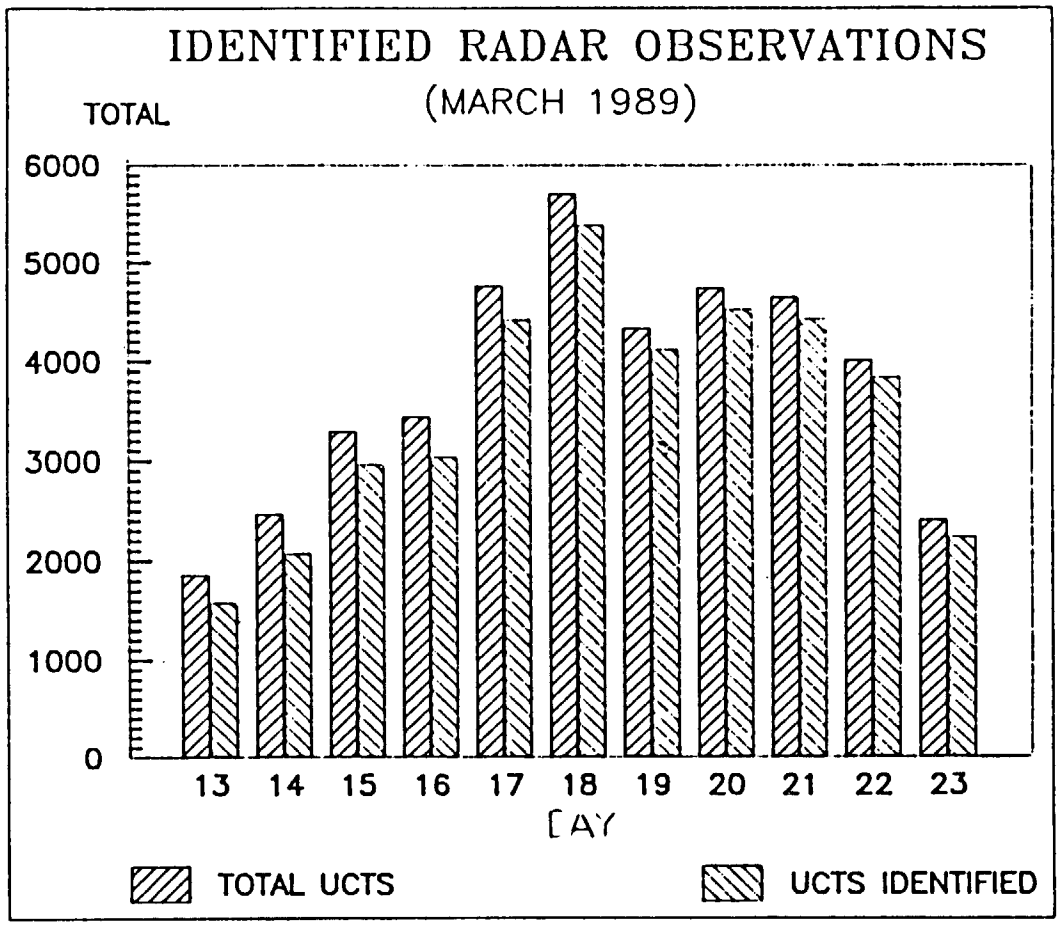
IDENTIFIED RADAR OBSERVATIONS
(MARCH 1989)
TOTAL
6000
5000
4000
3000
2000
1000
0
13
14
15
16
17
18
19
20
21
22
23
DAY
TOTAL UCTS
UCTS IDENTIFIED

10.7-cm Microwave Observations of AR 5395 and Related Terrestrial Effects

V. Gaizauskas, T.J. Hughes, and K.F. Tapping

Herzberg Institute of Astrophysics,
National Research Council of Canada, Ottawa, Canada K1A 0R6

The 10.7-cm flux patrols in Canada recorded 4 Great Bursts (peaks > 500 sfu) during the disk passage of AR 5395 in March l989 (Figures 1 and 2). The Great Bursts of 16 and 17 March were simple events of great amplitude and with half-life durations of only several minutes (Figure 2). Earlier Great Bursts, originating on 6 March towards the NE limb and on 10 March closer to the central meridian, belong to an entirely different category of event. Each started with a very strong impulsive event lasting just minutes (Figure 1). After an initial recovery, however, the emission climbed back to levels as great or greater than the initial impulsive burst. The events of 6 and 10 March stayed above the Great Burst threshold for at least 100 minutes. The second component of long duration in these two cases is associated with Type IV continuum emission and thus very likely with CME's.

Major geomagnetic disturbances did not occur as a result of the massive complex event of 6 March or the two simple but strong events of 16 and 17 March. But some 55 hours after the peak in the long-enduring burst of 10 March , a storm began which qualifies as the fourth strongest geomagnetic storm in Canada since 1932 (preceded by 18 Sept. 1941, 12 Nov. 1960, and 24 March 1940). Figure 3 depicts the vertical component of the earth's field measured during the storm by a fluxgate magnetometer at a station in Manitoba, one of several in the CANOPUS Network, Canada's contribution to the OPEN study of the magnetosphere. Within a minute of the sudden commencement of this storm, a series of breakdowns began in the transmission system of Hydro-Quebec which resulted in a total loss of power, on a bitterly cold winter's day, for at least 10 hours. Some remote parts of Quebec were without power for most of 13 March. The loss of power provoked an enormous outcry from a public frustrated by innumerable local outages during recent years. In view of that poor performance record, it proved difficult to convince the general public that there was an explanation rooted in Nature - a combination of geography and solar-terrestrial physics! Or that the results might have been much more severe had the event of 6 March occurred when AR 5395 was much closer to central meridian. On the other hand, large power utilities are now much more receptive to the need for monitoring solar as well as geomagnetic activity.

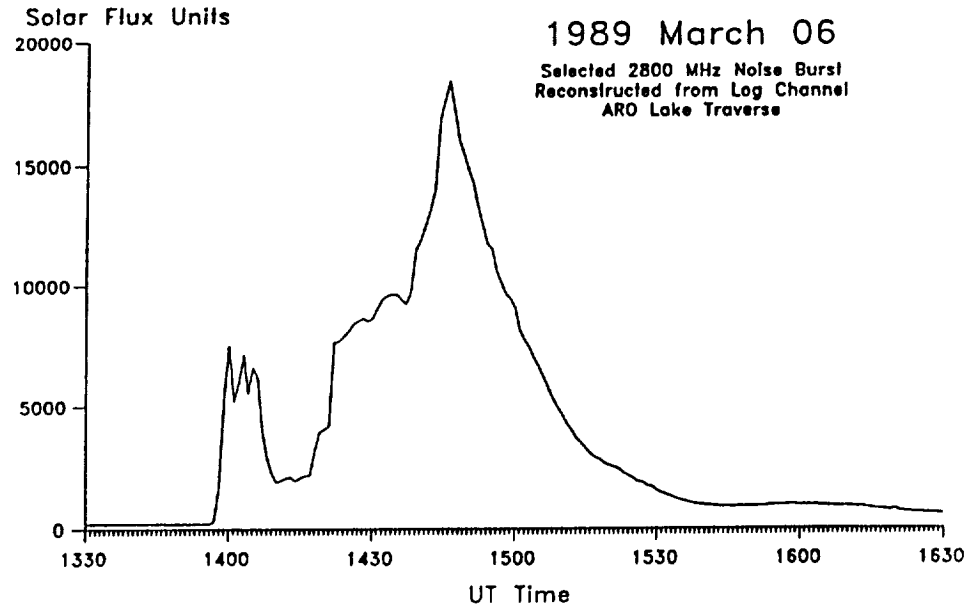

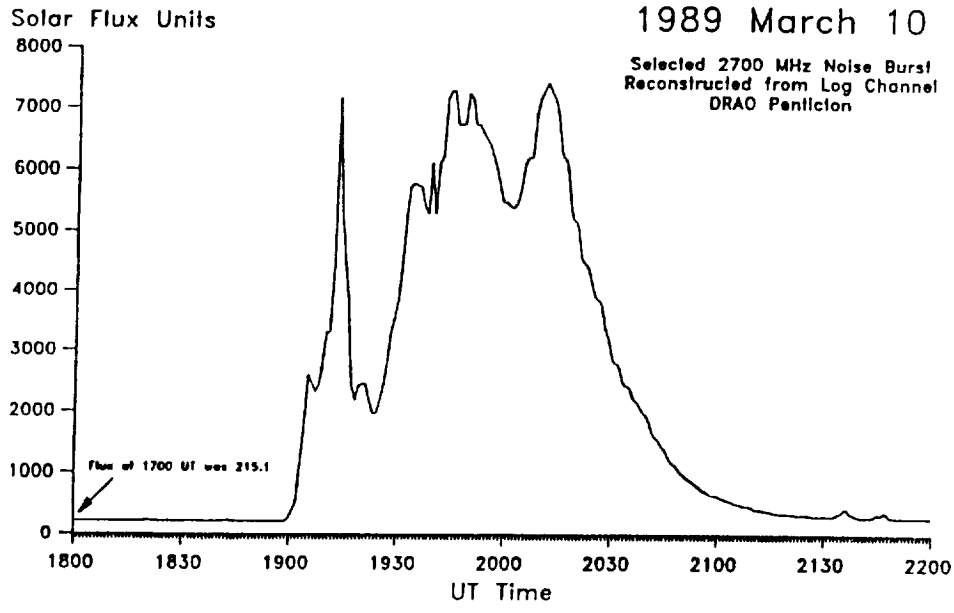

Figure 1. Great Bursts at 10.7-cm wavelength with long-enduring emission associated with Type IV bursts.

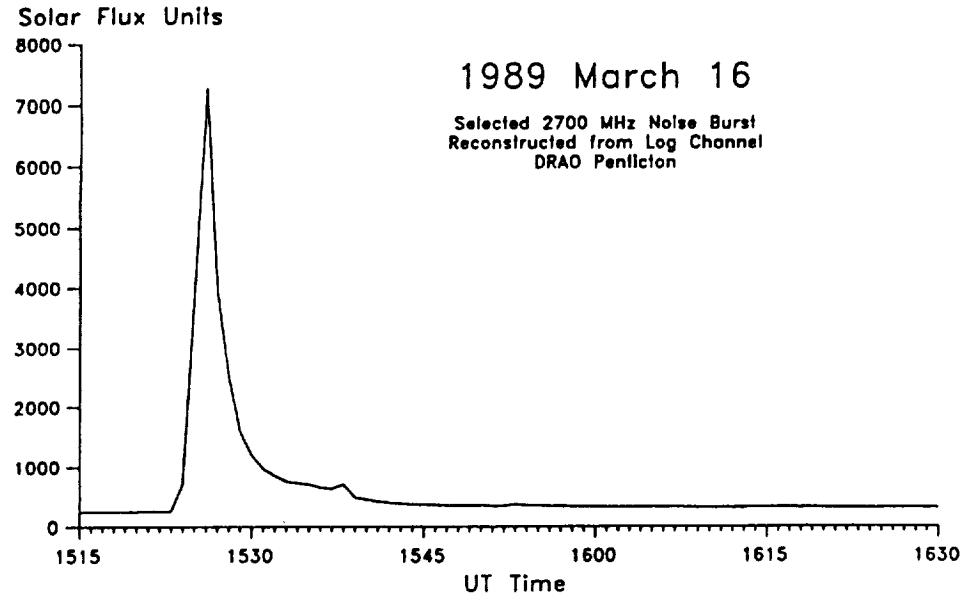

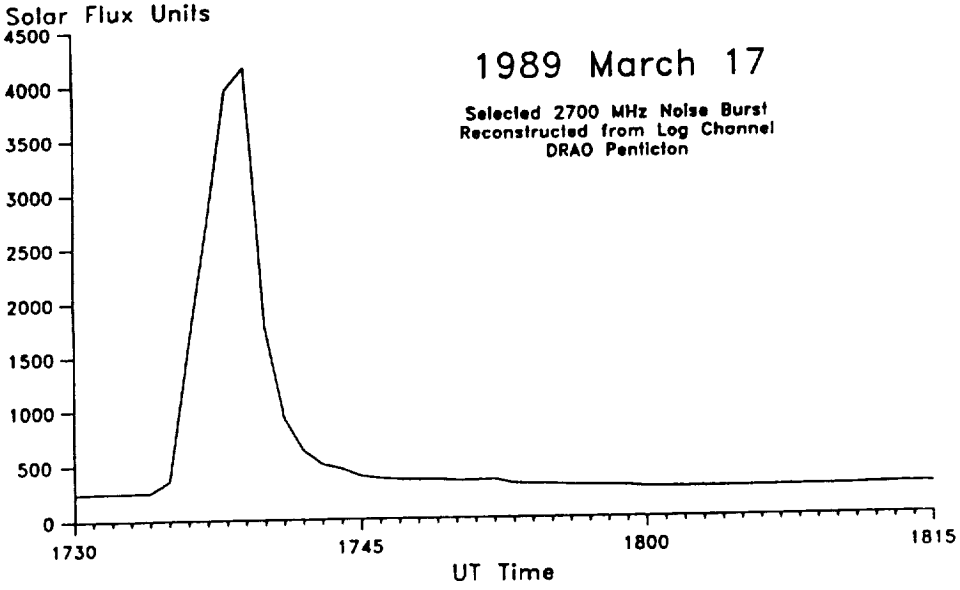

Figure 2. Great Bursts of short duration at 10.7-cm wavelength.

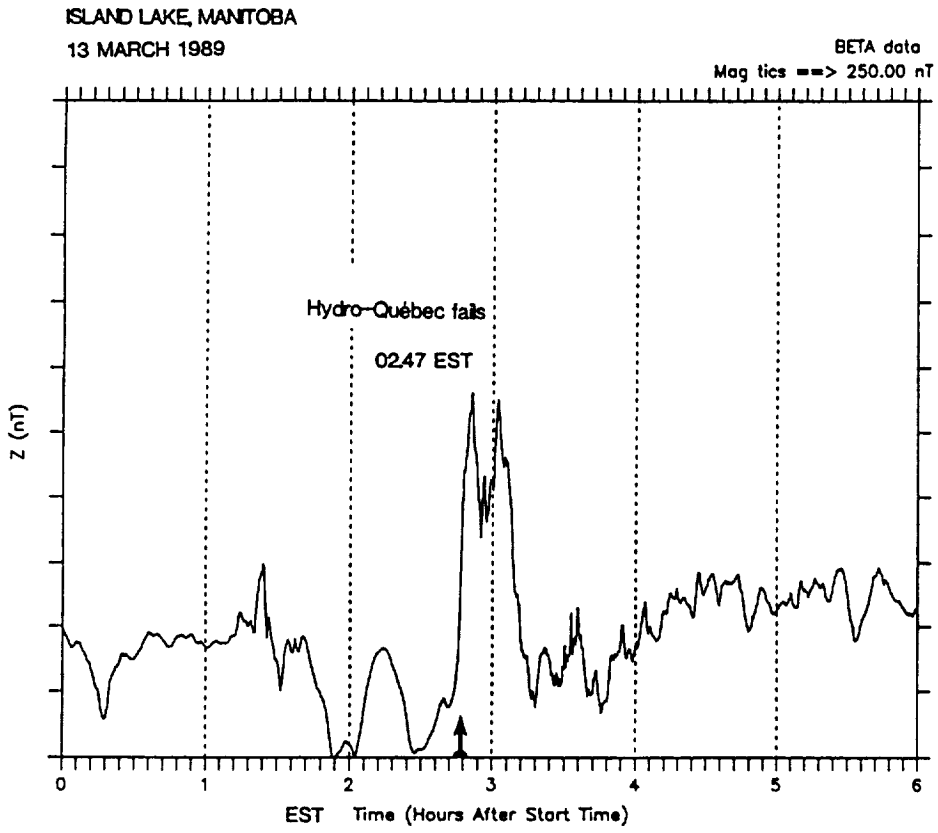

Figure 3. Vertical component of the Earth's magnetic field in Northern Manitoba.

N90-12484

Interplanetary Energetic Particle Observations of the March 1989 Events

E. T. Sarris[1 2] *and S. M. Krimigis*[1]

[1] Applied Physics Laboratory, the Johns Hopkins University, Laurel, Maryland, 20707

[2] Demokritos University of Thrace, Xanthi, Greece

The IMP-8 spacecraft placed in an elongated $\sim 25\ R_E \times R_E$ orbit around the Earth was the only monitor of the energetic particle environment of the near interplanetary space during the period of the solar particle events associated with the Active Region 5395 in March 1989.

Measurements of energetic ion and electron intensities were obtained by the CPME experiment of the Applied Physics Laboratory, the Johns Hopkins University in a series of channels within the energy ranges: 0.3–440 MeV for protons, 0.6–52 MeV/nuc for alpha particles, 0.7–3.3 MeV/nuc for nuclei with $Z \geq 3$, 3–9 MeV/nuc for nuclei with $Z \geq 20$ and 0.2–2.5 MeV for electrons.

Figure 1 displays the responses of selected energy channels during the period 5–23 March 1989. It is clearly noted that the most prominent energetic ion intensity enhancements in that time interval were associated with the interplanetary shock wave of March 13 (07:43 UT) as well as that of March 8 (17:56 UT), which have distinct particle acceleration signatures. These shock waves play a major role in determining the near Earth energetic ion intensities during the above period by accelerating and modulating the ambient solar energetic particle population, which was already present in high intensities in the interplanetary medium due to the superposition of a series of solar flare particle events originating in AR 5395.

The differential ion intensities at the lowest energy channel (0.3–0.5 MeV) of the CPME experiment, which were associated with the March 13 shock wave, reached the highest level ($j \sim 10^5$ p/cm^2·sec·sr·MeV) in the life of the IMP-8 spacecraft at this energy. At high energies, i.e., in the energy range 190–440 MeV, the shock associated intensity peak was smaller by less than a factor of 3 than the maxima of solar flare particle intensities from some other major flares, in particular from those with sites well connected to the Earth's magnetic flux tube.

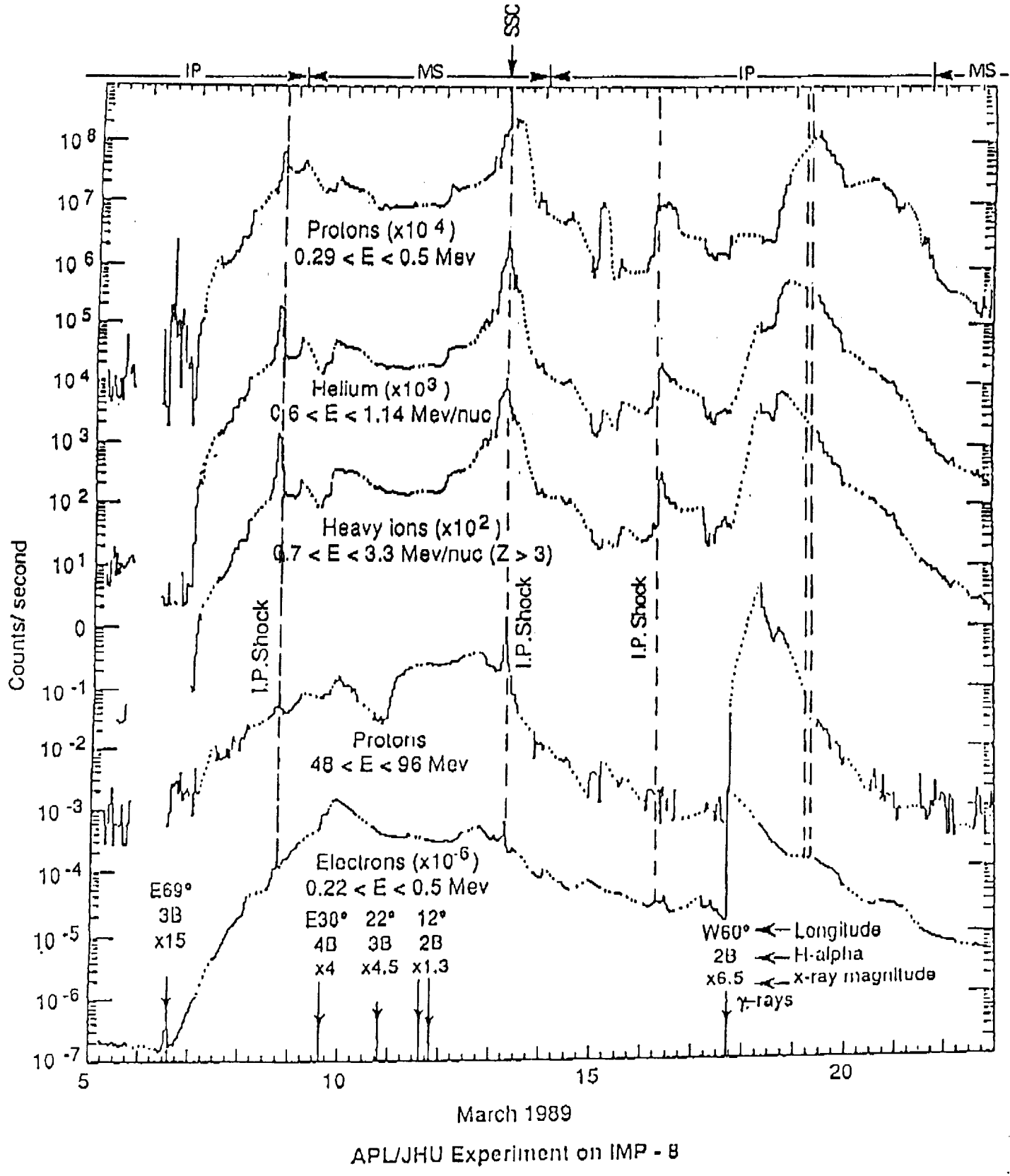

APL/JHU Experiment on IMP - 8

SMM UV OBSERVATIONS OF ACTIVE REGION 5395

Stephen A. Drake[1,2], Joseph. B. Gurman[2]

[1] ST Systems Corp. [2] NASA/Goddard Space Flight Center.

ABSTRACT

The Ultraviolet Spectrometer and Polarimeter (UVSP) on the *Solar Maximum Mission* (*SMM*) spacecraft has been used extensively to study the spatial morphology and time variability of solar active regions in the far UV (at $\sim \lambda 1370$ Å) since July 1985. The normal spatial resolution of UVSP observations in this 2nd-order mode is 10″, and the highest temporal resolution is 64 milliseconds. To make a full-field, $4' \times 4'$ image this wavelength using 5″ raster steps takes about 3 minutes. UVSP can also make observations of the Sun at $\sim \lambda 2790$ with 3″ spatial resolution when operated in its 1st-order mode; a full-field image at this wavelength (a so-called SNEW image) takes about 8 minutes.

UVSP made thousands of observations (mostly in 2nd-order) of AR 5395 during its transit across the visible solar hemisphere (from 7 to 19 March, inclusive). During this period, UVSP's duty cycle for observing AR 5395 was roughly 40%, with the remaining 60% of the time being fairly evenly divided between aeronomy studies of the Earth's atmosphere and dead time due to Earth occultation of the Sun. UVSP observed many of the flares tagged to AR 5395, including 26 GOES M-level flares and 3 X-level flares, one of which produced so much UV emission that the safety software of UVSP turned off the detector to avoid damage due to saturation. (See Table 1 for list of the UVSP experiments corresponding to these strong X-ray flares.) We present images and light curves of some of the more spectacular of the AR 5395 events (See Table 2 and Figures).

All of the UVSP AR 5395 data are available from the authors upon request.

Table 1

M and X-class GOES flares from AR 5395 observed by UVSP

Date	GOES level	GOES t_{max} (UT)	UVSP Max. Counts $(0.056\ s)^{-1}$	UVSP t_{max}(UT)
07 March	M2.0	06:00	6762	05:58
	M4.1	13:26	10855	<13:25
	M2.4	13:44	3620	<13:42
	X1.8	14:58	43775	<14:58
	M3.8	16:56	10961	17:00
	M4.2	22:38	12745	<22:45
08 March	M2.1	08:33	2271	08:30
	M4.6	18:57	6681	<18:57
09 March	M1.8	02:46	11276	<02:44
	M1.3	23:20	4177	23:19
10 March	X4.5	19:22	>59310*	>19:12
11 March	M1.6	01:56	4538	<01:46
	M2.0	03:34	13056	03:42
	M1.2	06:50	2700	<06:45
	M1.2	18:36	4129	18:35
	M1.1	23:18	4396	<23:11
12 March	M2.5	15:10	4587	15:11
	M1.8	16:24	10276	16:22
	M6.3	21:03	4964	21:01
13 March	M1.4	01:37	2686	<01:38
	X1.2	03:26	5935	<03:25
14 March	M2.0	03:05	2094	03:01
15 March	M4.8	06:52	13673	06:47
	M4.2	08:39	2541	08:27
16 March	M1.4	19:01	7510	18:54
17 March	M2.5	02:47	14359	02:45
18 March	M3.3	20:35	893	20:31
	M3.1	22:05	1380	21:57
19 March	M1.3	07:49	1118	07:38

* Detectors shut down when count rate exceeded $10^6\ s^{-1}$

Table 2

Highlights of UVSP-*SMM* Observations of AR 5395
6 - 20 March 1989

Date	Time (UT)	Expt. No.	Type	Max.*	Comments
6 March	0921 - 1002	85125	SNEW	1st order	Spot group
7 March	1325 - 1338	85209	BPFIND	10855	M4.1 at 1326
7 March	1455 - 1458	85216	raster	43775	X1.8 at 1458
8 March	1853 - 1857	85302	raster	24057	M4.0 at 1857
10 March	1907 - 1910 1911 - 1913	85489 85491	raster TINYRAST	35413 59310	X4.5 at 1922
11 March	0915 - 0951	85557	SNEW	1st order	1st order flare
19 March	0733 - 0747	86230	BPFINDWL	1118	Post-flare loops

* Counts per 0.056 s

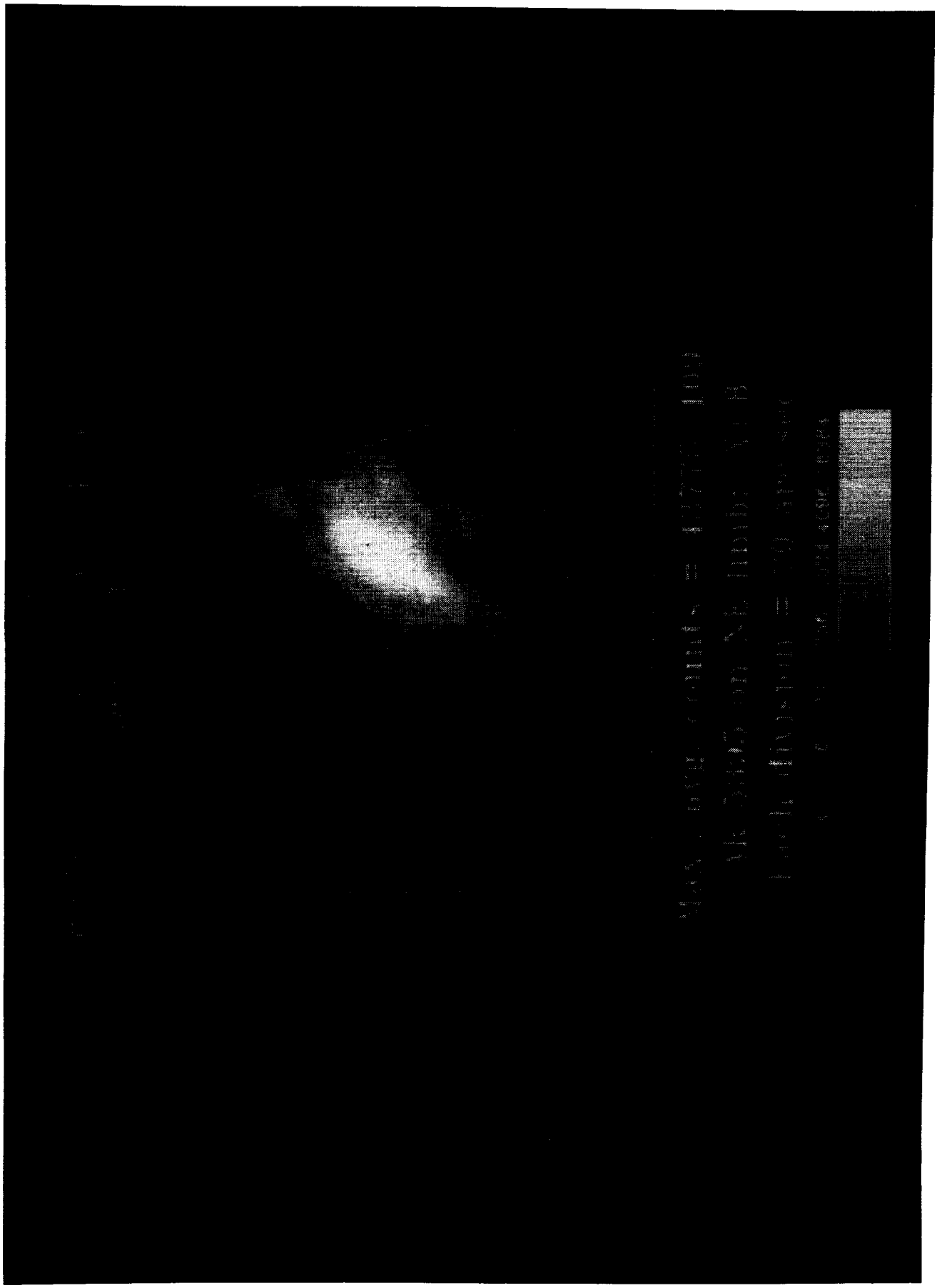

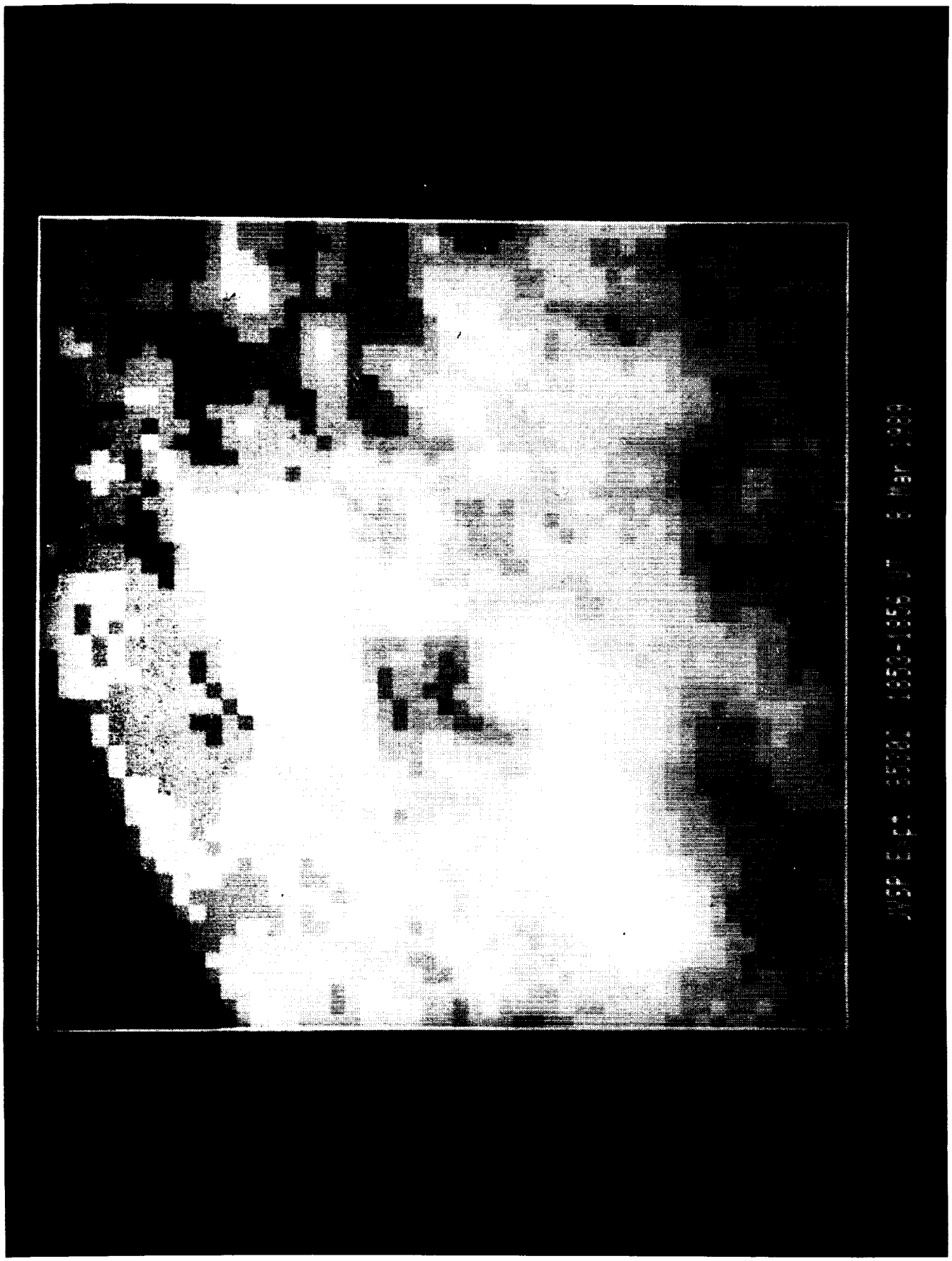

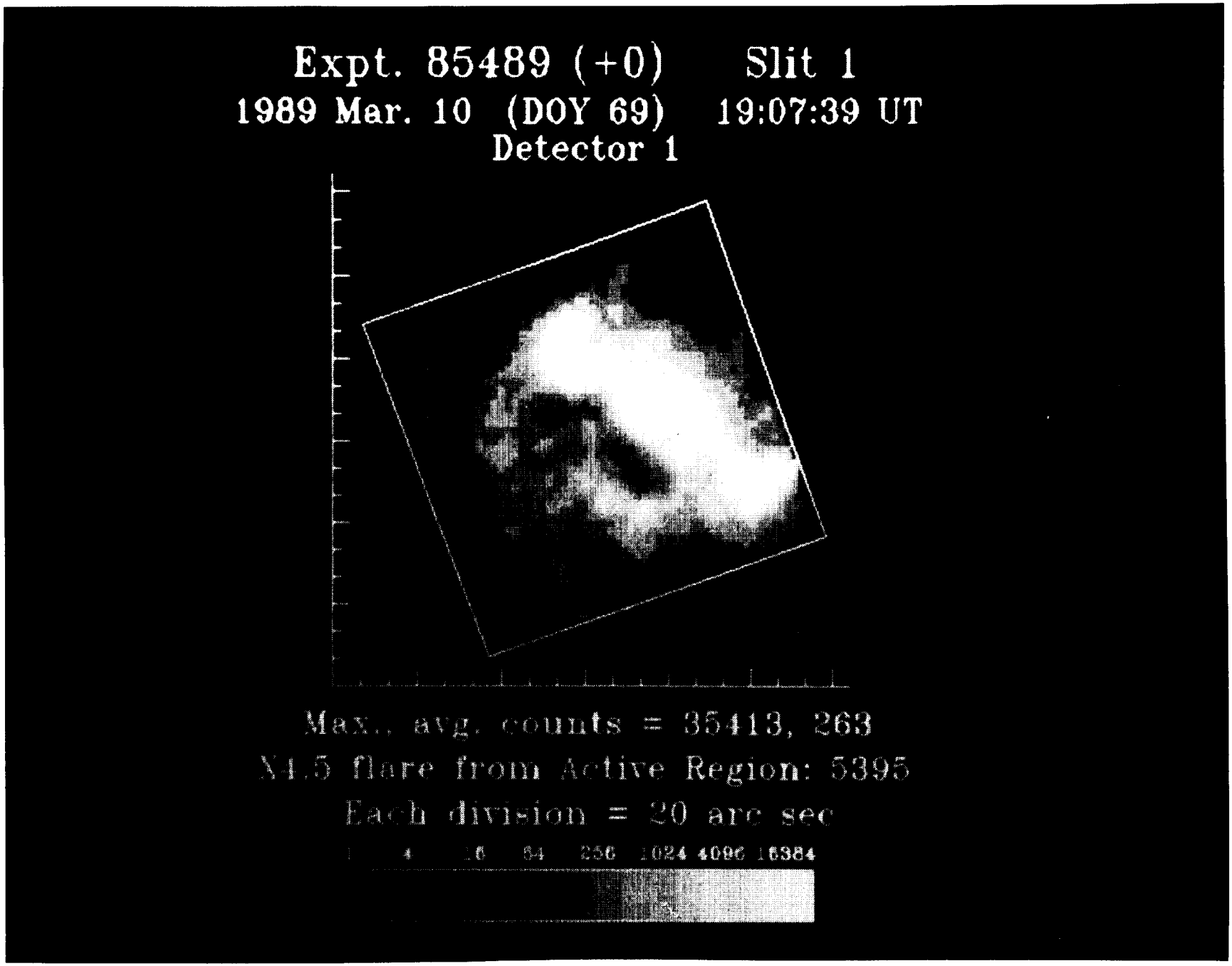

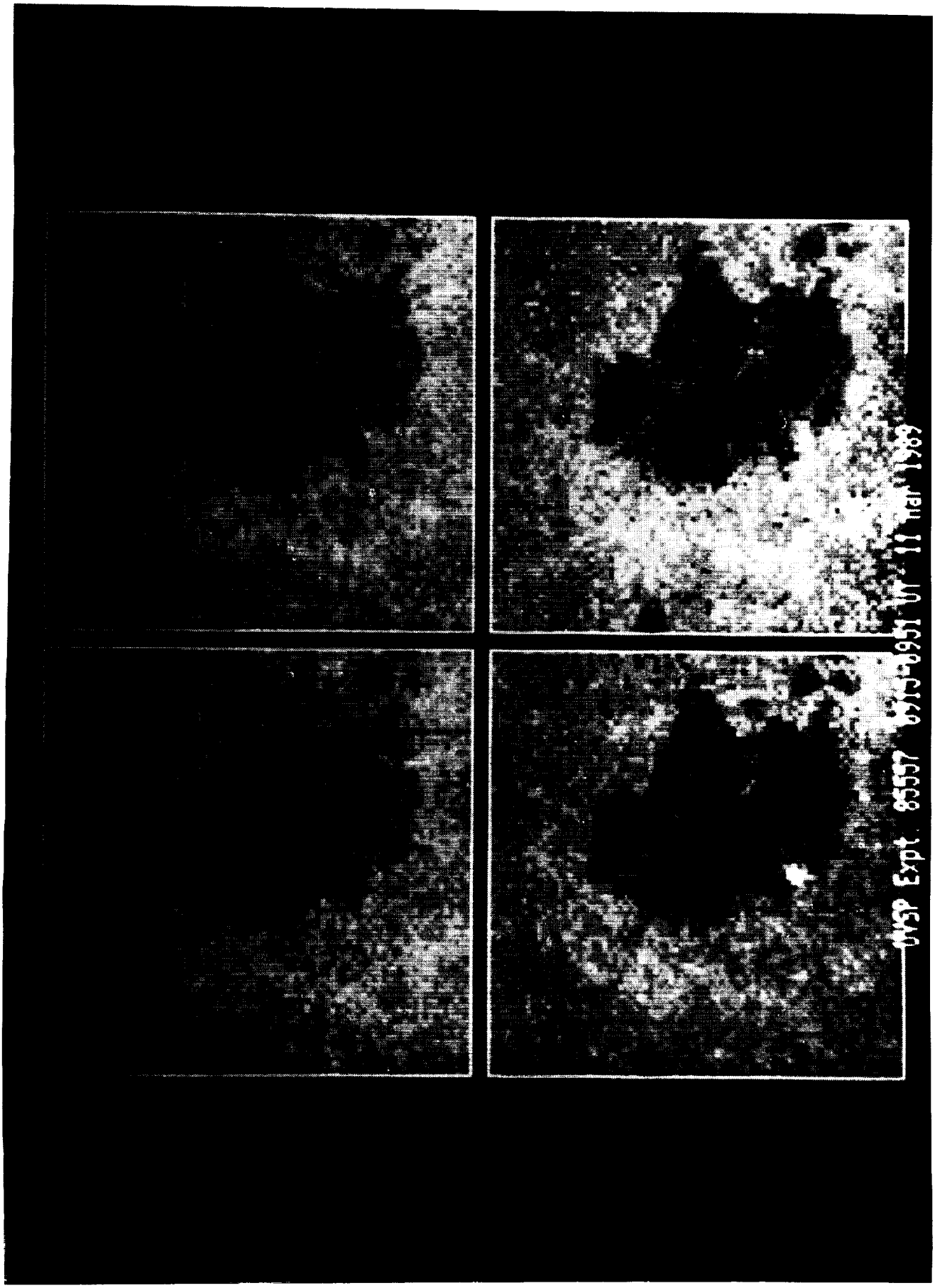

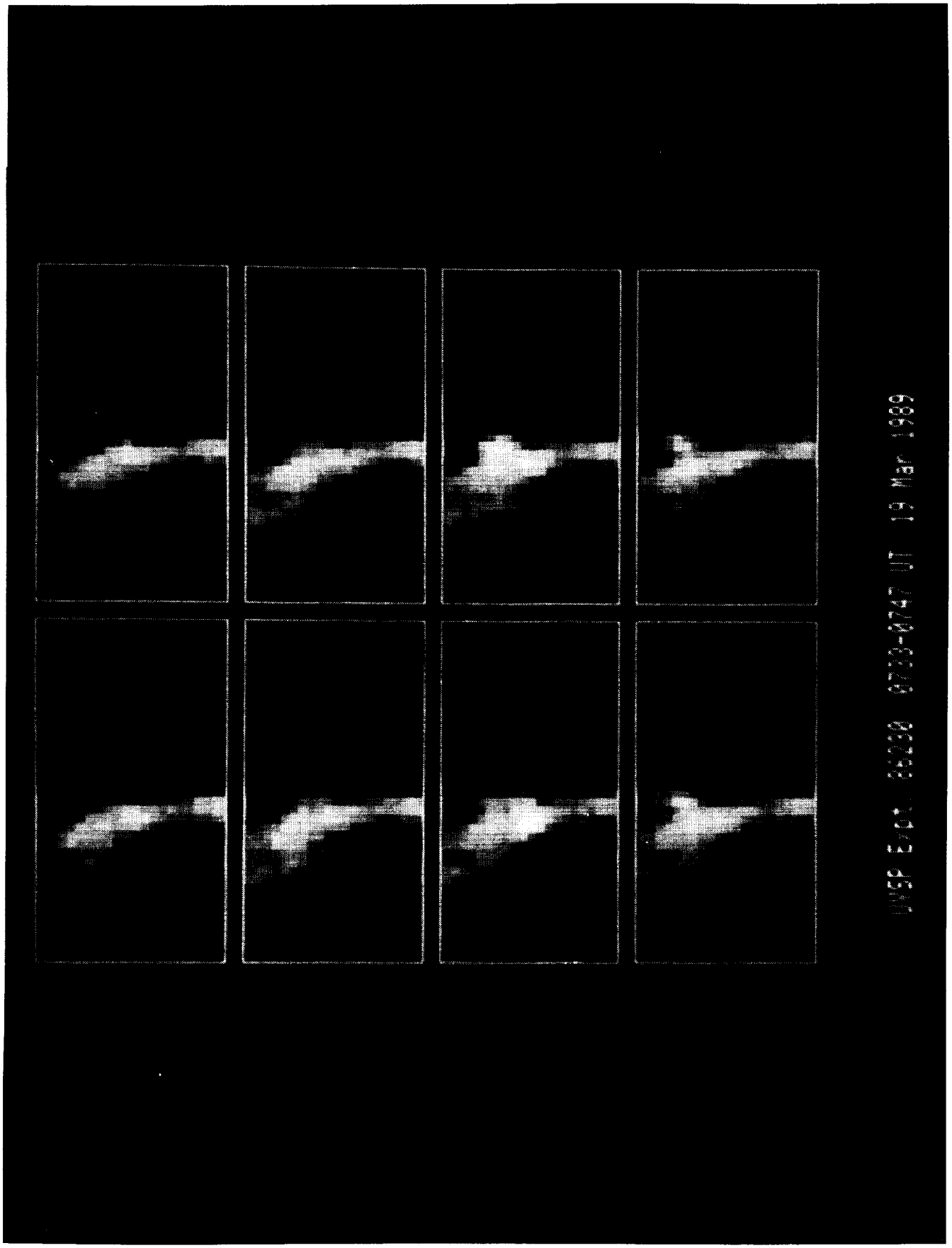

C 4/

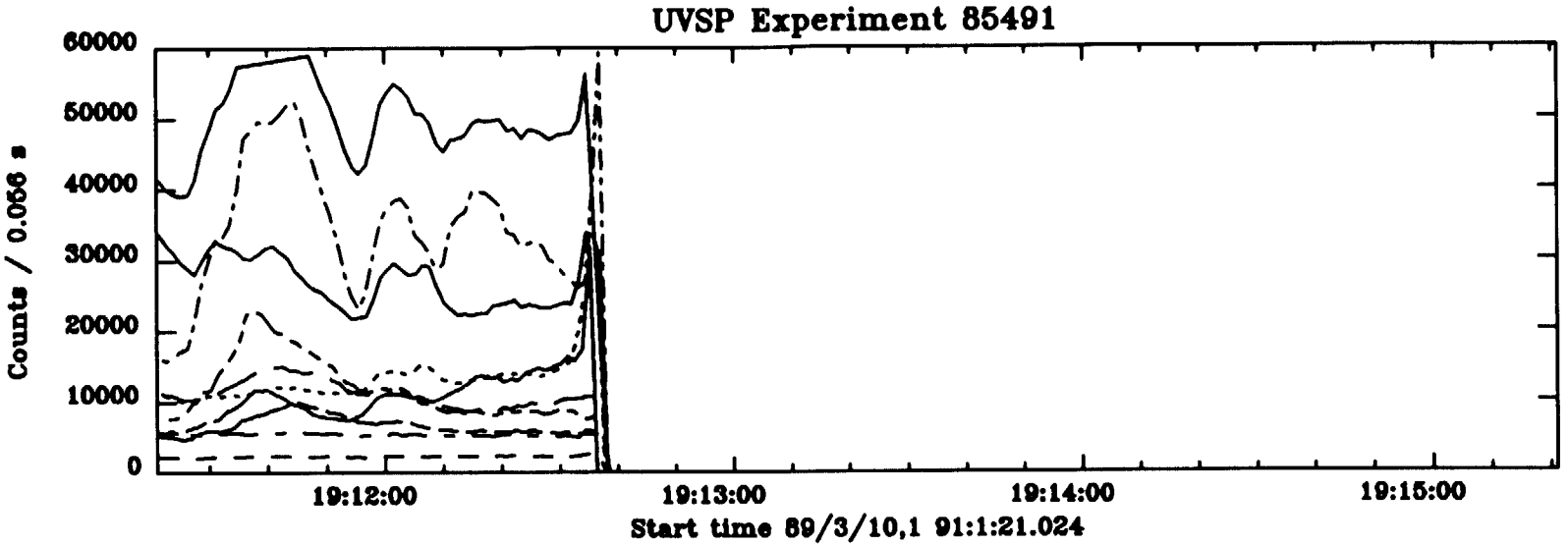

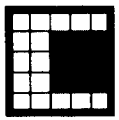

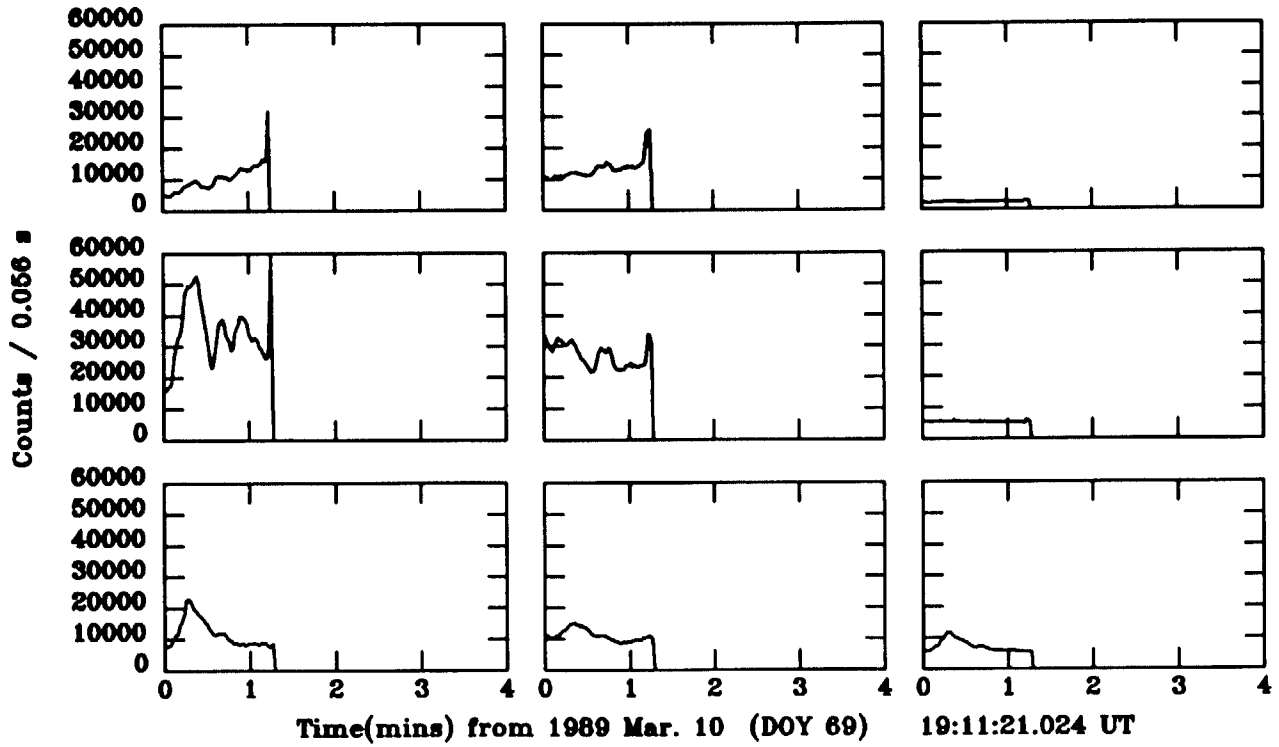

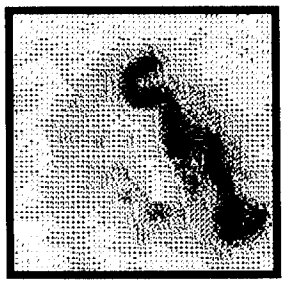

V85489 (52 x 52)

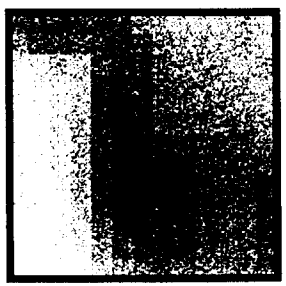

V85490 (13 x 13)

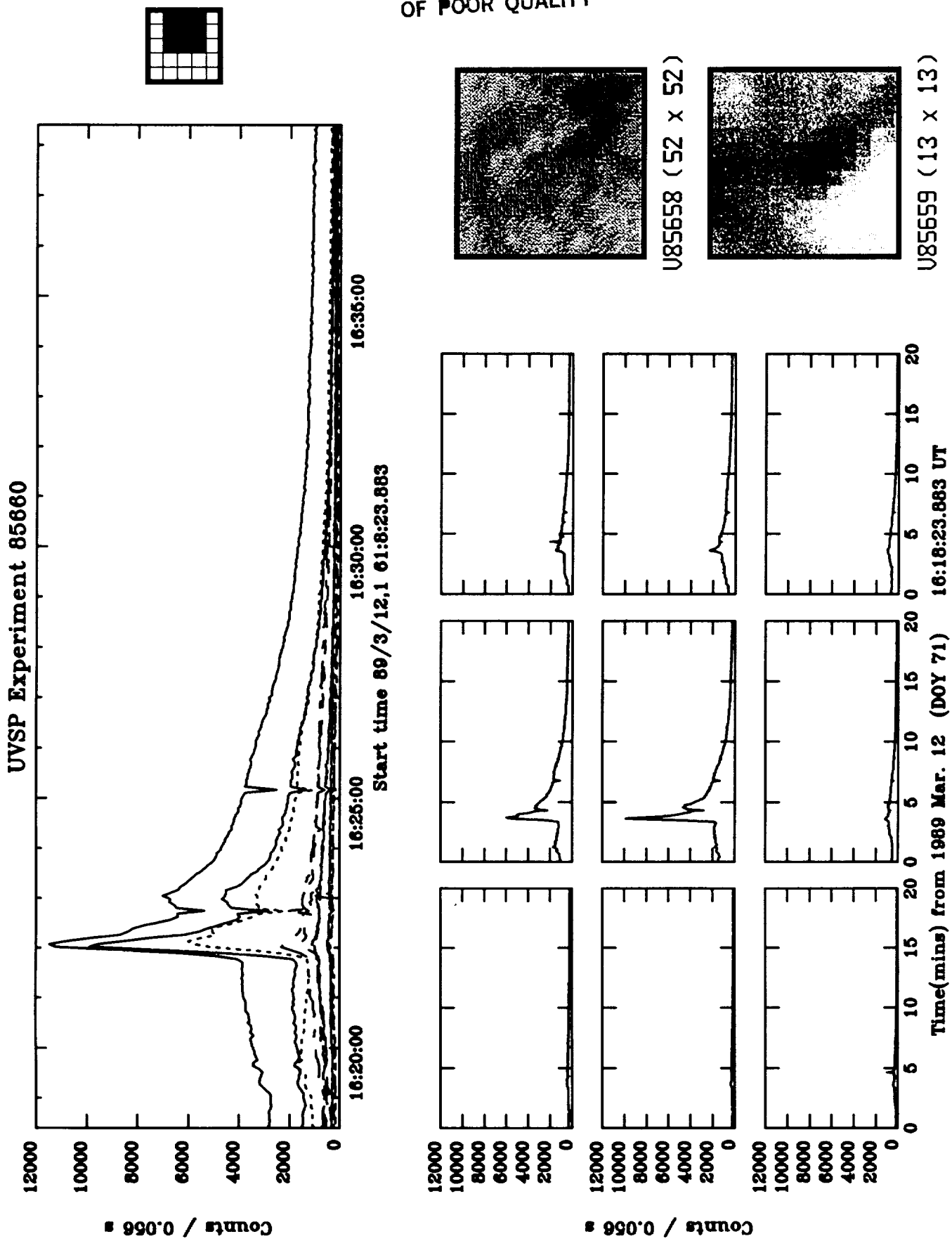

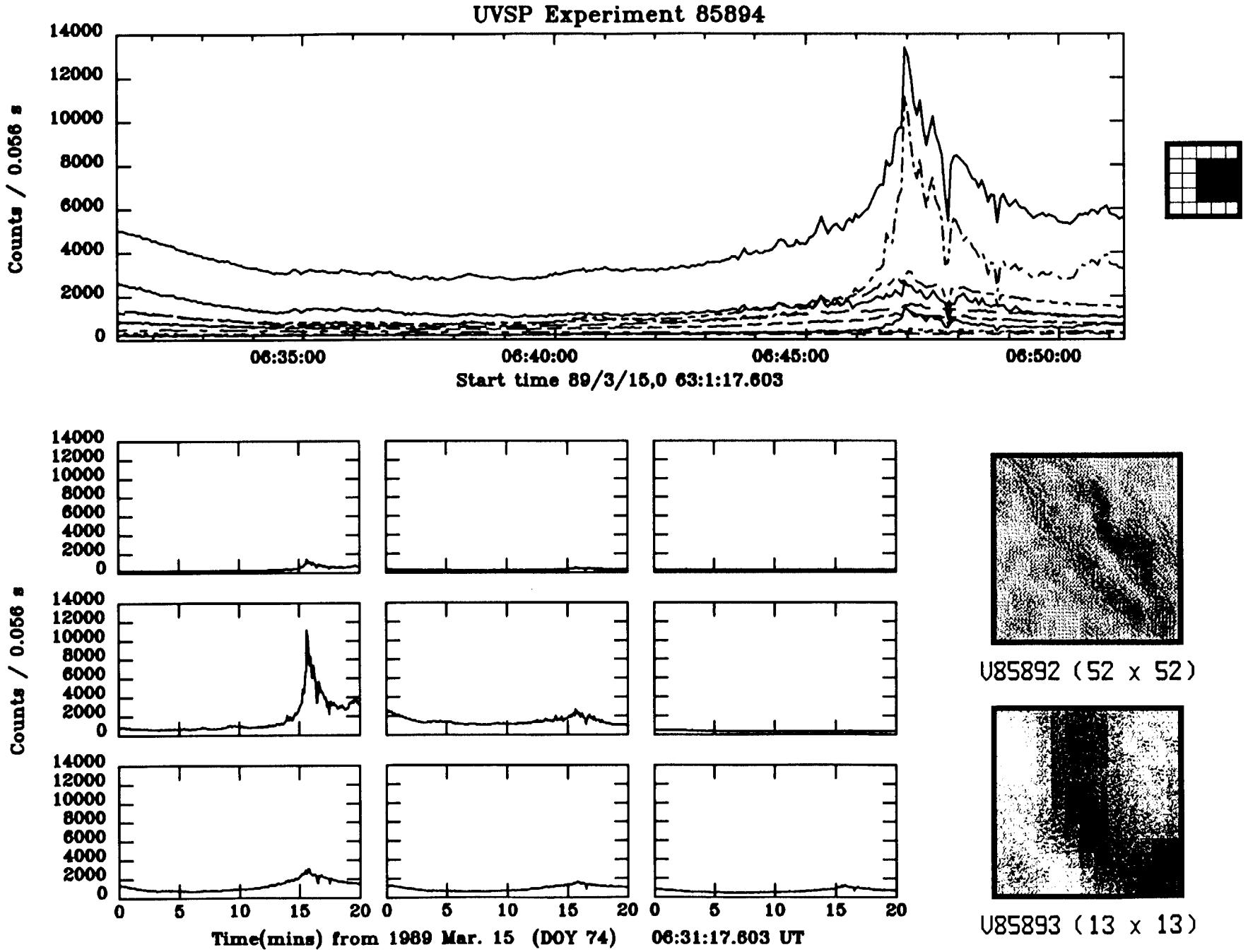

XRP Observations of AR 5395

Greg Slater

Applied Research Corporation/Lockheed PARL

SPECTRA

BCS -	Ca XIX	3.17 - 3.22Å
	Fe XXV	1.84 - 1.89Å
	Fe Kα	1.89 0 1.95Å

- Integrated over 6 arc minute fov
- 3-11 sec time resolution throughout March 6-20.

IMAGES

FCS -	O VII	18.97Å
	Mg XI	9.17Å
	S XV	5.04Å
	Fe XXV	1.85Å
	Fe Kα	1.935Å

- O VII, Mg XI observations consisted of large scale 3-4 arc minute maps of ~ 4 minute cadence during March 6-8.
- S XV, Fe XXV observations consisted of large scale 3-4 minute maps during March 6-11, 16-20.
- Fe Kα observations consisted of 20 arc second high cadence maps, March 11-16.

GOES X-Ray History of AR 5395

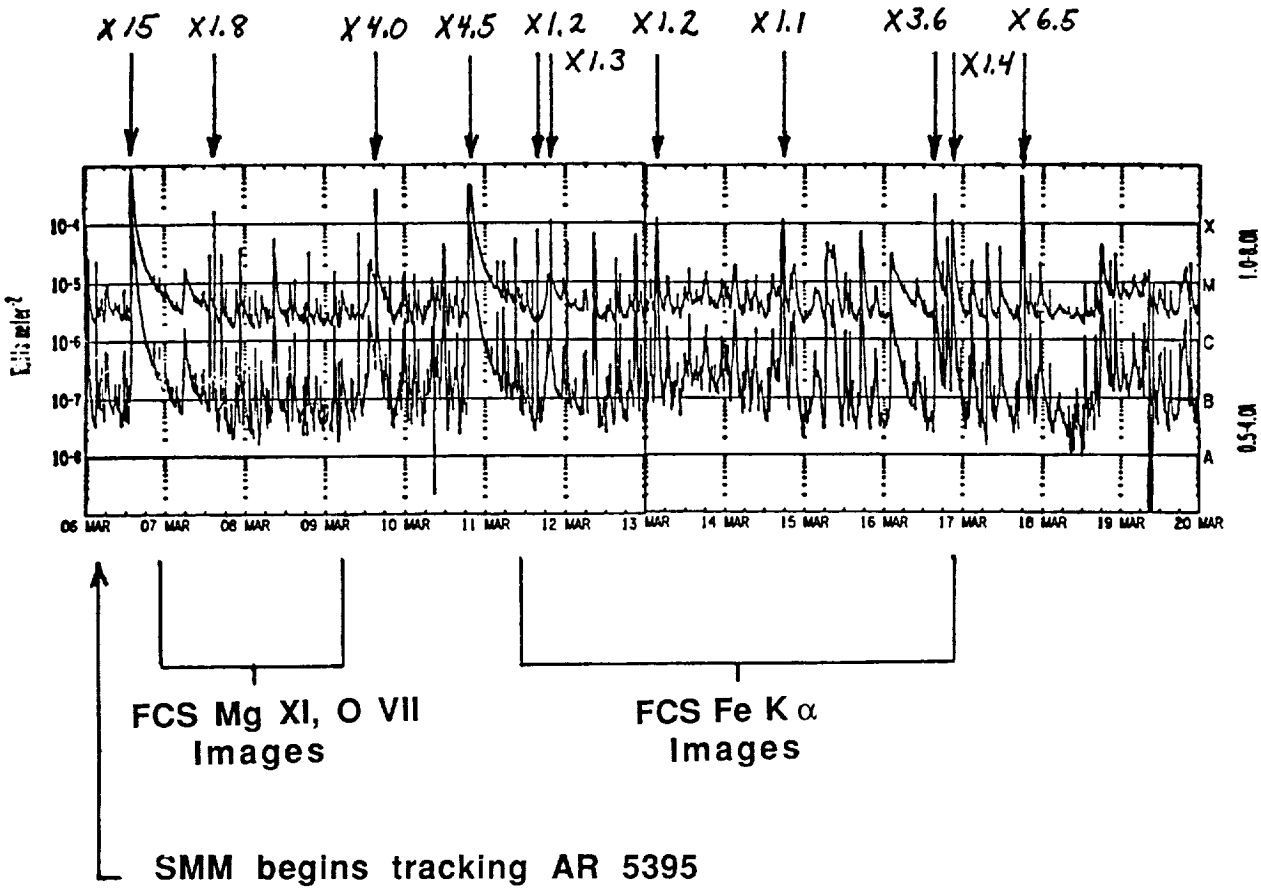

X15 Flare FCS S XV

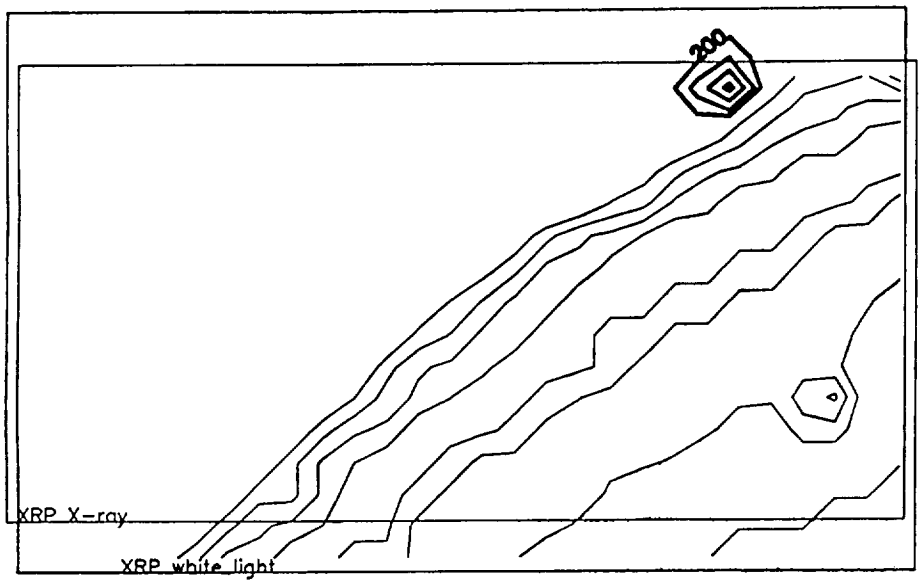

XRP IMAGE

FCS Ch 5: S XV
T: 89/ 65 13:56:23
Max cps = 1688
Size = 7.0 min x 4.0 min
Pixel = 15 sec
Smooth = 1

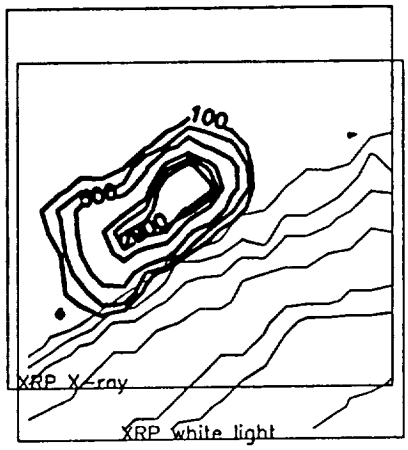

XRP IMAGE

FCS Ch 5: S XV
T: 89/ 65 14: 4: 3
Max cps = 5541
Size = 3.0 min x 3.0 min
Pixel = 10 sec
Smooth = 1

X15 Flare FCS Fe XXV

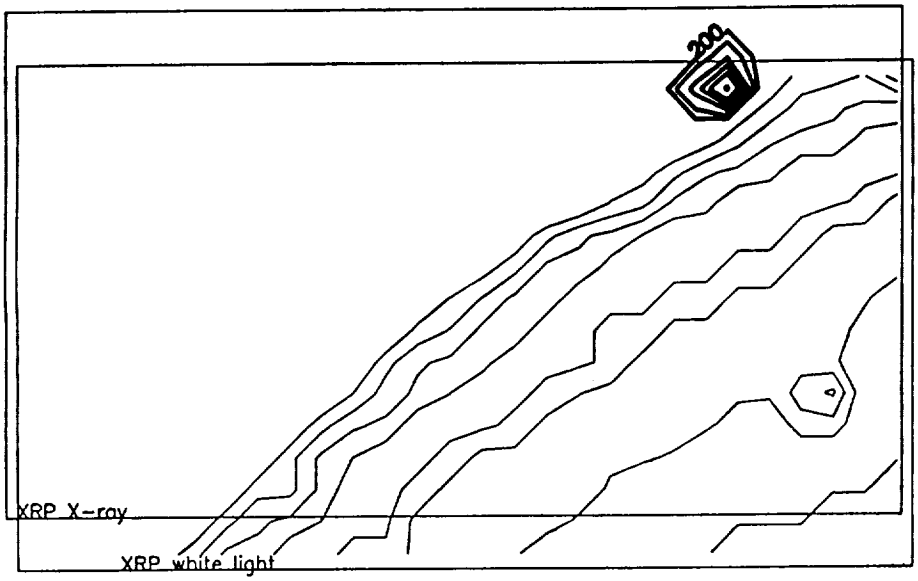

XRP IMAGE

FCS Ch 7: Fe XXV
T: 89/ 65 13:56:23
Max cps = 2993
Size = 7.0 min x 4.0 min
Pixel = 15 sec

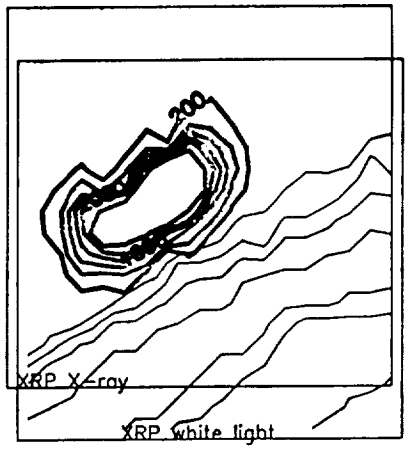

XRP IMAGE

FCS Ch 7: Fe XXV
T: 89/ 65 14: 4: 3
Max cps = 7539
Size = 3.0 min x 3.0 min
Pixel = 10 sec
Smooth = 1

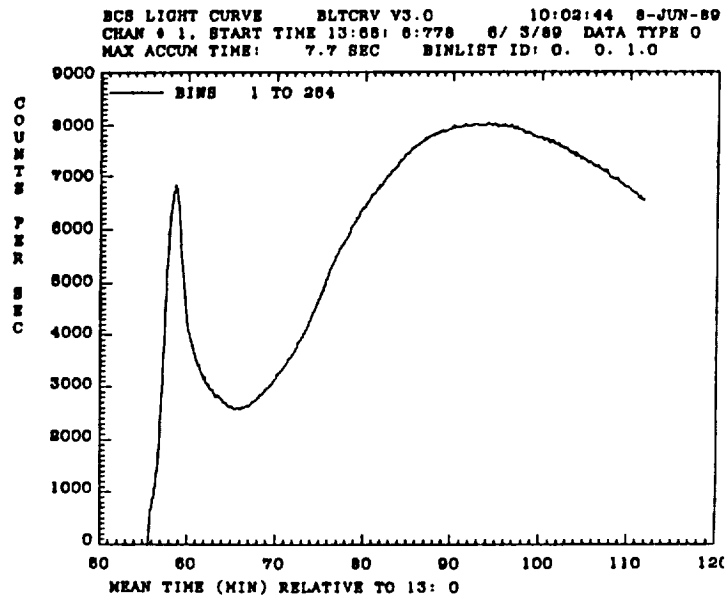

Ca XIX

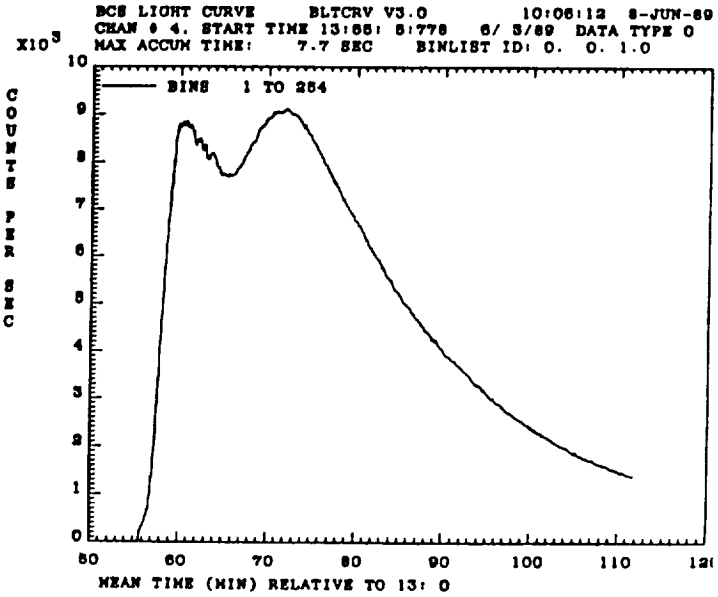

Fe XXV

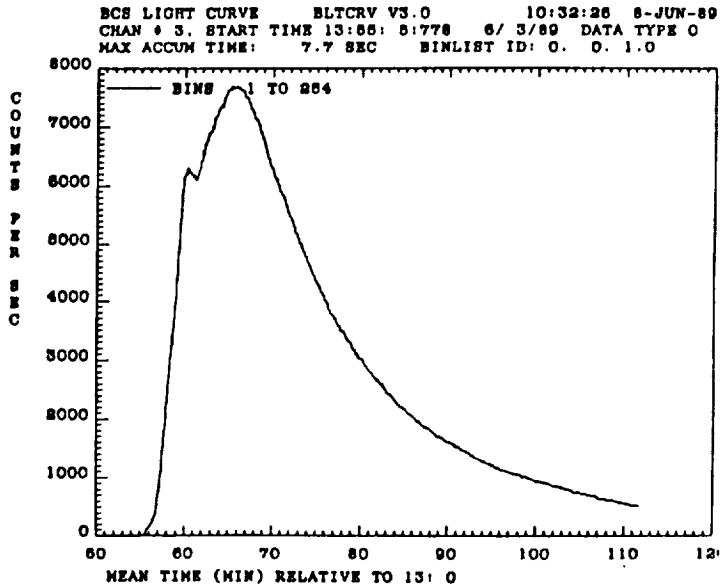

Fe Kα

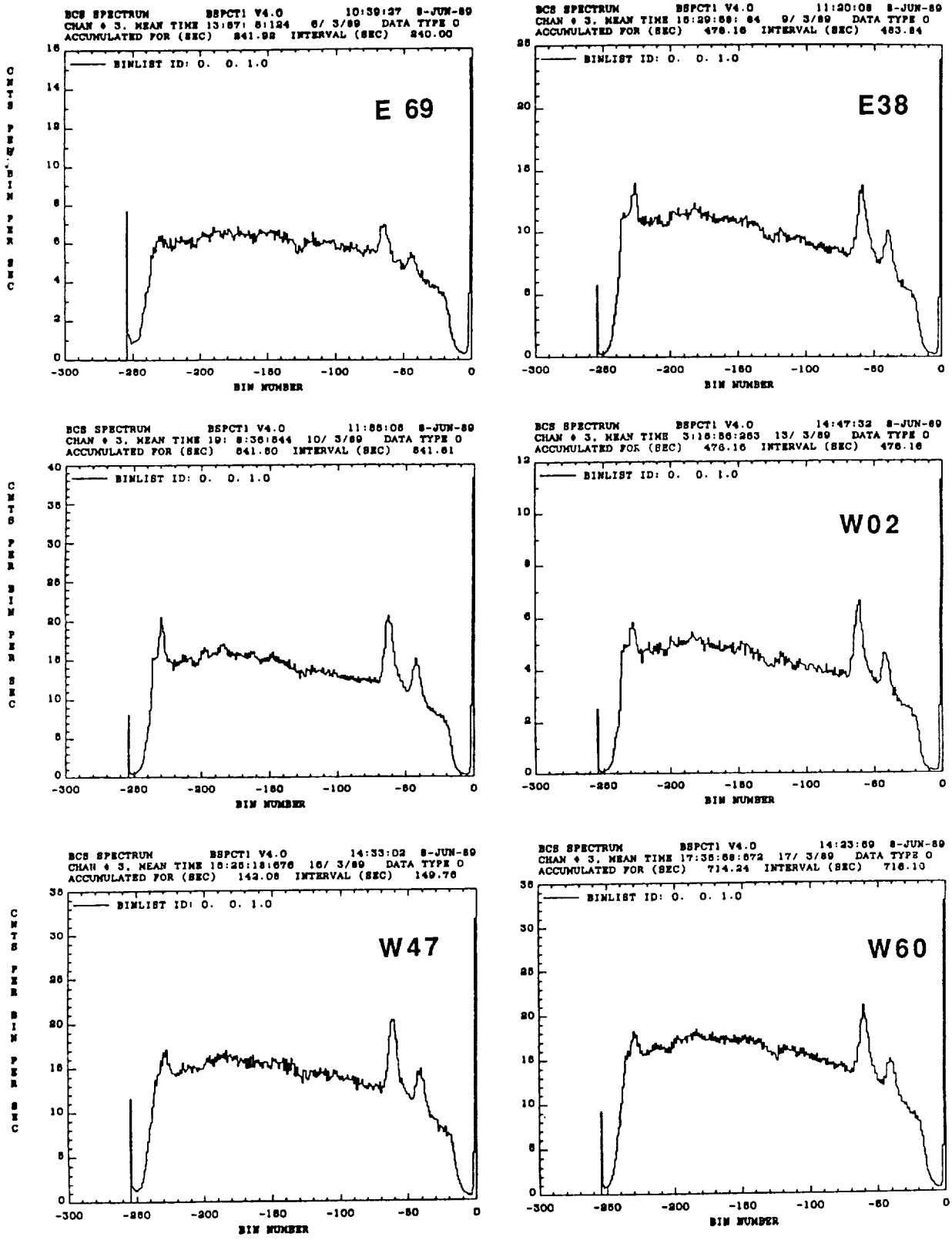

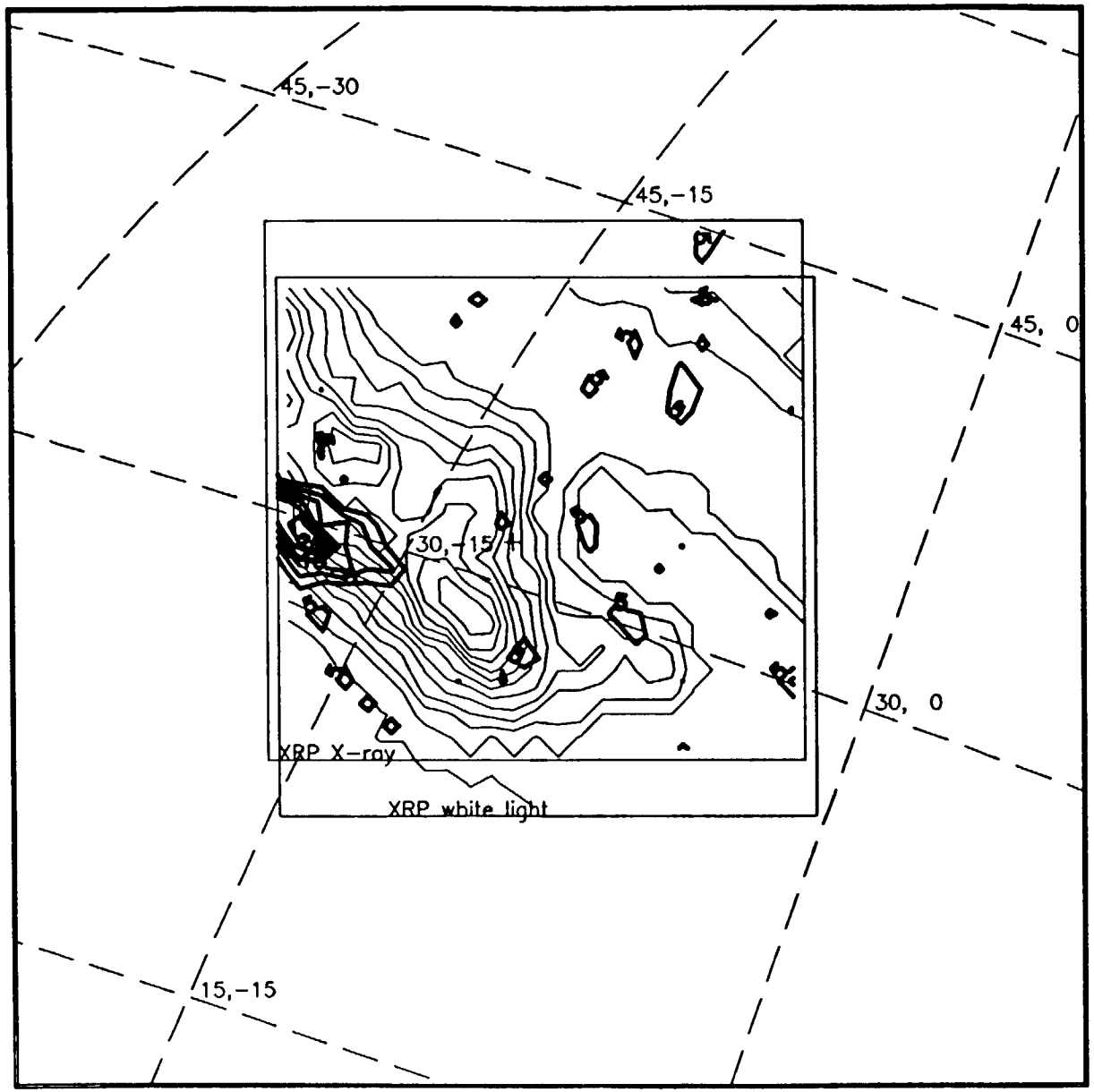

Levels: 5, 10, 15, 20, 25, 30, 35, 50, 75, 100, 150, 200, 250, 300

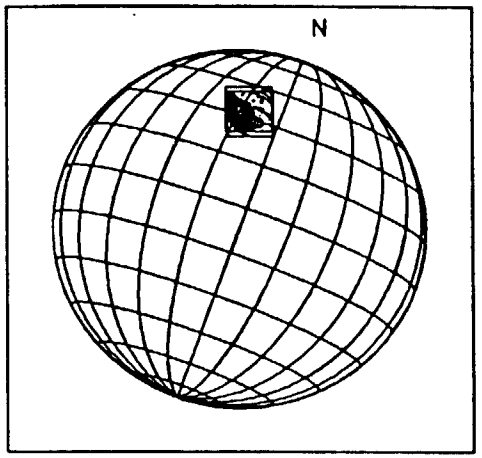

XRP IMAGE

FCS Ch 7: Fe XXV
T: 89/ 72 3:29:22
Max cps = 35
Size = 4.0 min x 4.0 min
Pixel = 10 sec
Smooth = 1
Yaw : -53.
Pitch: -646.
Roll : -20.0

Latitude : 33.37
Longitude: -12.24

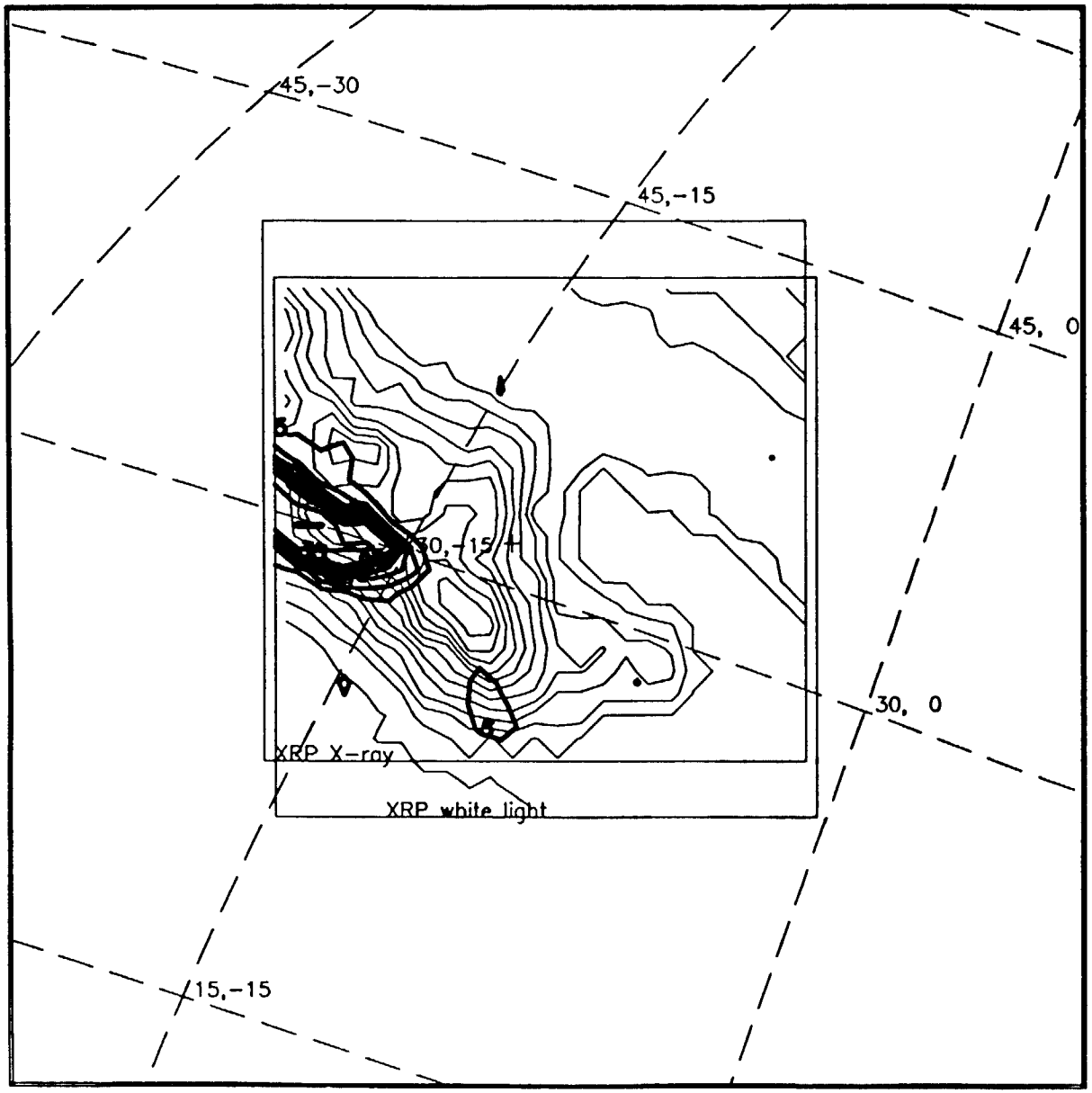

Levels: 5, 10, 15, 20, 25, 30, 35, 50, 75, 100, 150, 200, 250, 300

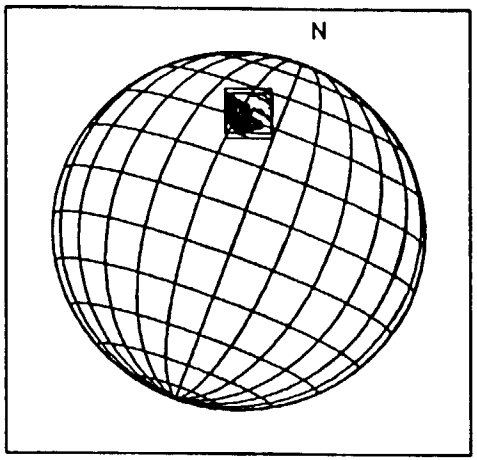

XRP IMAGE

FCS Ch 5: S XV
T: 89/ 72 3:29:22
Max cps = 77
Size = 4.0 min x 4.0 min
Pixel = 10 sec
Smooth = 1
Yaw : -53.
Pitch: -646.
Roll : -20.0

Latitude : 33.37
Longitude: -12.24

Hard X-Ray Highlights of AR 5395

R.A. Schwartz (S.T. Systems), B.R. Dennis (NASA/GSFC)

Active Region 5395 produced an exceptional series of hard X-ray bursts notable for their frequency, intensity, and impulsivity. Over the two weeks from March 6-19, 447 hard X-ray flares were observed by the Hard X-Ray Burst Spectrometer on Solar Maximum Mission (HXRBS/SMM), a rate of ~35 per day which exceeded the previous high by more than 50% (figure 1). During one 5 day stretch, more than 250 flares were detected, also a new high. The three largest GOES X-flares were observed by HXRBS and had hard X-ray rates over 100,000 s^{-1} (figure 2) compared with only ten flares above 100,000 s^{-1} during the previous nine years of the mission.

Throughout the entire two weeks many of the flares showed extreme impulsivity, some events with a collection of fast spikes and others showing a single rapid intense spike. One form of impulsivity was exhibited by the M2 flare of 1989 March 7 (figure 3), which is the most intense single spike event measured by HXRBS. The flare starts in hard X-rays close to 557 UT and begins a steady exponential rise (e-folding time ~3.7 s) to a peak above 40,000 s^{-1} at 557:45 UT. Subsequently, the event decays rapidly to a small fraction of its peak within 30 s. Such events are usually thought to show the rapid acceleration of particles, fast release of flare energy, and the probable injection of energetic electrons into a dense cooler medium where the X-rays are produced. Another variety of impulsive flare is illustrated by the fast event on 1989 March 13 starting close to 1225 UT (figure 4). After 10-20 s of weak activity there are two consecutive hard X-ray spikes which each rise and fall within a second. Fast spikes have been seen before but these are more intense than most such events.

An ongoing effort for the HXRBS group has been the correlated analysis of hard X-ray data with flare data at other wavelengths with the most recent emphasis on those measurements with spatial information. During a series of bursts from AR5395 at 1644-1648 UT on 12 March 1989, simultaneous observations were made by HXRBS and UVSP (Ultra Violet Spectrometer Polarimeter) on SMM, the two-element Owens Valley Radio Observatory (OVRO) interferometric array, and R. Canfield's Hα Echelle spectrograph at the National Solar Observatory at Sacramento Peak. The data in figures (5) and (6) show strong correlations in the hard X-ray, microwave, and uv lightcurves. This event will be the subject of a combined analysis.

The UVSP data (figure 6) from this same flare are an example from a continuing study with HXRBS. Previous studies by SMM of bursts in hard X-rays and ultraviolet (UV) have shown a close temporal and spatial relationship between the fast spikes in both wavebands (Orwig and Woodgate 1986, Poland et al. 1982). In fact, to within instrumental resolution of ~.1 s, there is frequently no discernible delay between peaks in the hard X-rays and the UV. Within the context of thick-target X-ray emission, this near simultaneity suggests that the UV is produced very close to the fast-electron energy loss region. The emitting regions would be virtually cospatial assuming that the UV is produced within the transition zone or separated by no more than a couple of arcseconds assuming fluorescence from the temperature minimum immediately below.

The UVSP data (figure 6) are obtained at a wavelength of ~λ1375 A and consist of the time histories from a 3 x 3 array of 10 arcsecond pixels, sampled every 1.2 s (56 ms dwell time per pixel), centered on a previously identified UV bright point. Four (bottom right and the three on the left) of the nine pixels show common fast structures clearly identifiable within the hard X-ray light curve. These fast structures are simultaneous within the 1.2 s cycle implying a minimum propagation velocity of at least 8000 km/sec between the corner pixels (14"x750 km/ 1.2 s). In figure (7) the HXRBS data and the UVSP data from pixel 02 (lower left in figure (6)) reveal several simultaneous temporal features. Depending on the spatial structure revealed at other wavelengths, these data could provide strong evidence of foot-point electron energy loss.

Orwig, L.E. and Woodgate, B.E.: 1986, in "The Lower Atmosphere in Solar Flares", 306-317.
Poland, A.I. et al.: 1982, Solar Phys. 78, 201.

Figure Captions

1. HXRBS event rate for two week intervals over the entire mission. The peak at 27 events/day was during the passage of AR5395 across the disk.

2. All of the HXRBS events with-a peak rate greater than 10,000 counts/s with the events over 100,000 counts/s specially noted. The three largest GOES-class X flares from AR5395 all occurred during spacecraft day and each produced in excess of 100,000 counts/s.

3. The most intense single spike event seen by HXRBS during the mission rising two orders of magnitude in 15 seconds to a peak of over 40,000 counts/sec.

4. Two fast consecutive spikes seen by HXRBS from AR5395. Both spikes rise and fall in about 1s and are unusually intense to have such fast time constants.

5. The integrated hard X-ray flux and multiband microwave data from the flare on 12 March 1989 at 1646 UT from AR5395 seen by HXRBS and the OVRO 2-element array.

6. The light curves from the UVSP 3x3 raster. (10x10 arcsecond pixels spaced by 10 arcsecond with a 1.2 s cycle time) Four (bottom right and the three on the left) of the nine pixels show fast structure clearly identifiable with the hard X-ray light curve and amongst themselves.

7. The same flare as in figures (5) and (6) illustrating the correspondence between the UV and hard X-ray structures for a single pixel from the raster. Here we have identified at least 5 common features simultaneous between the two within the cycle time limitation imposed by the raster.

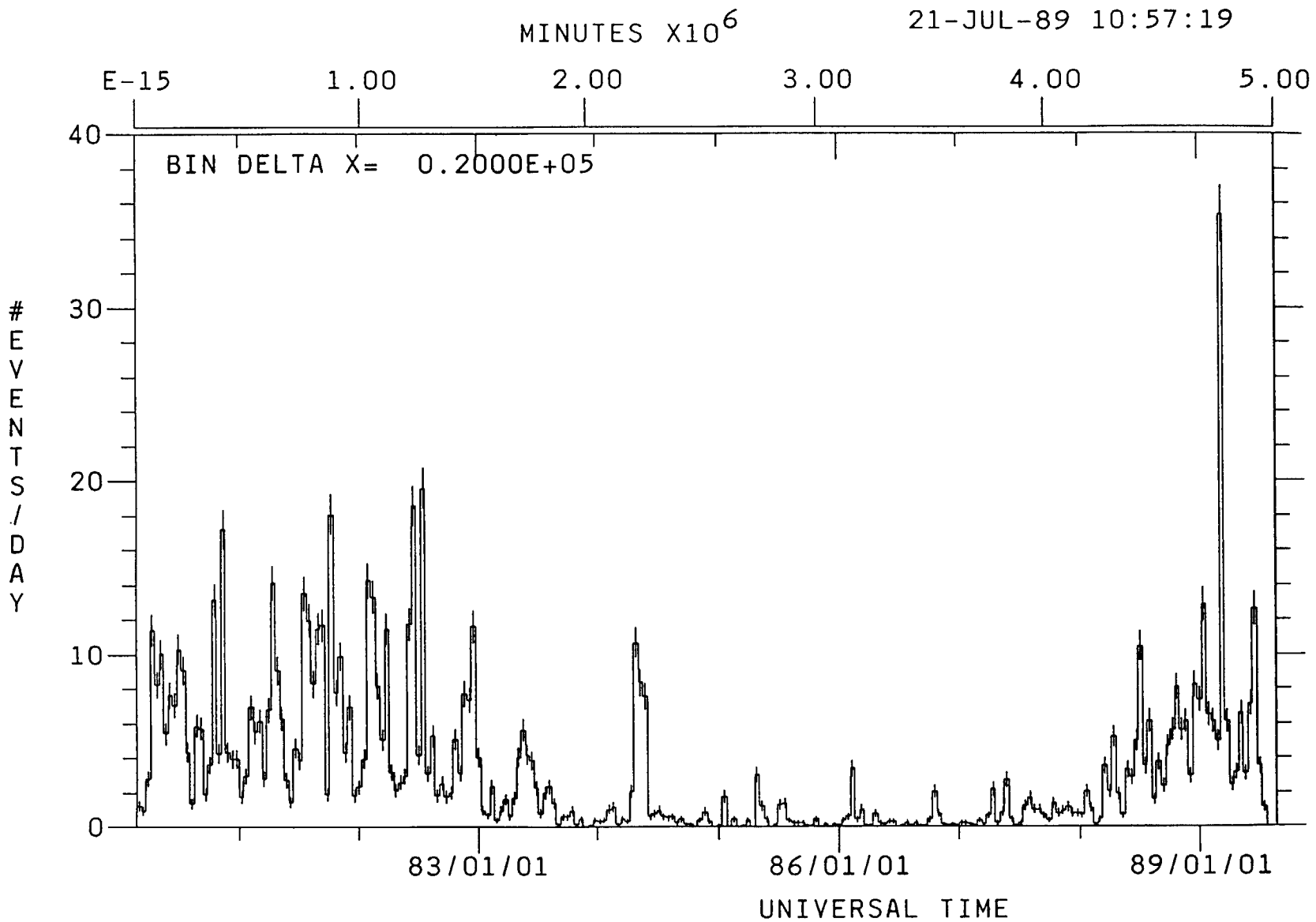

FLARES 1-11694
X: HXRBS PEAK TIME
Y: DOWN TIME INCLUDED

BASE TIME: 80/02/15, 0000:00.000

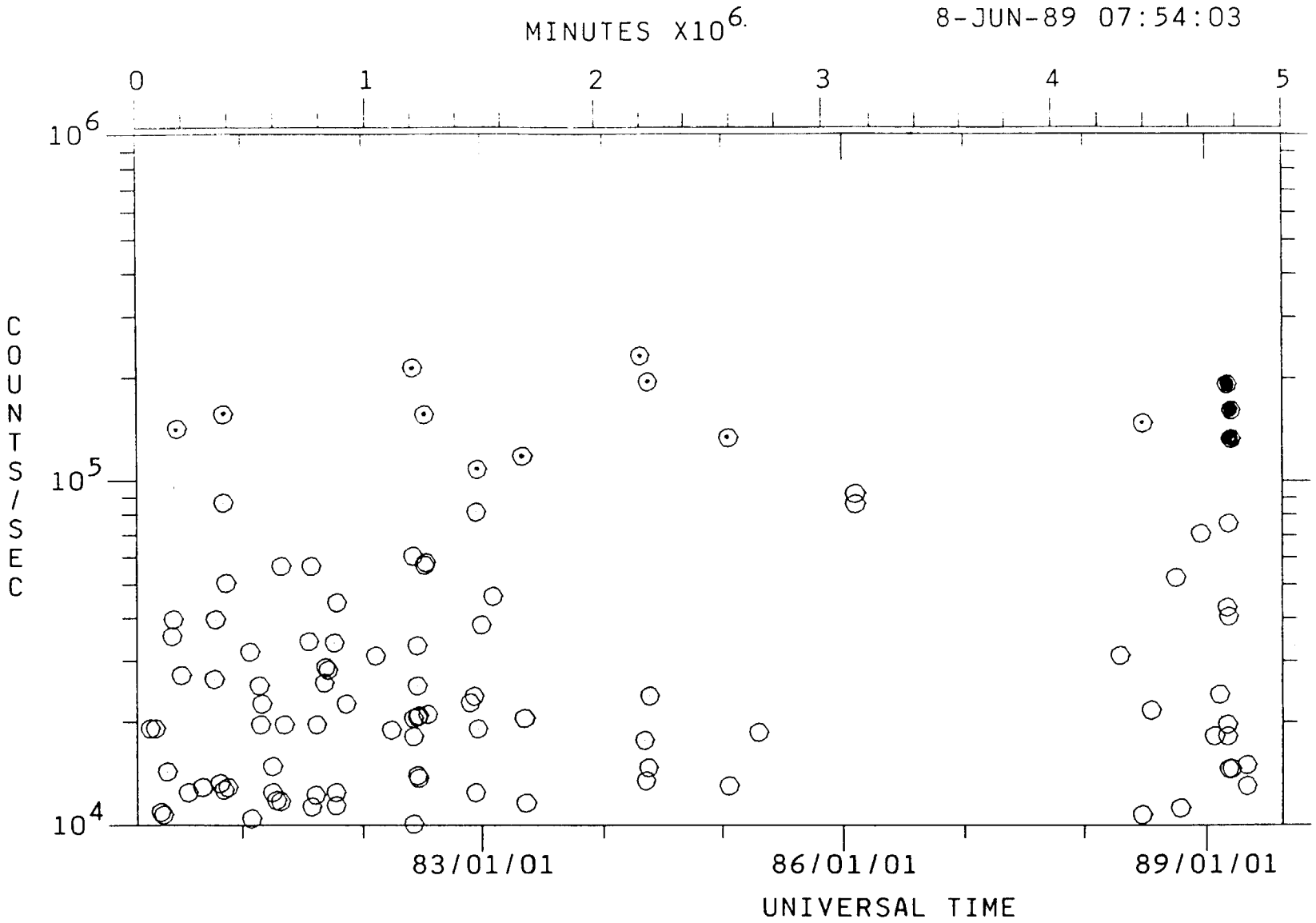

FLARES 1-11384

Y: HXRBS PEAK TIME BASE TIME: 80/02/19 0749:35.000

Y: HXRBS PEAK RATE

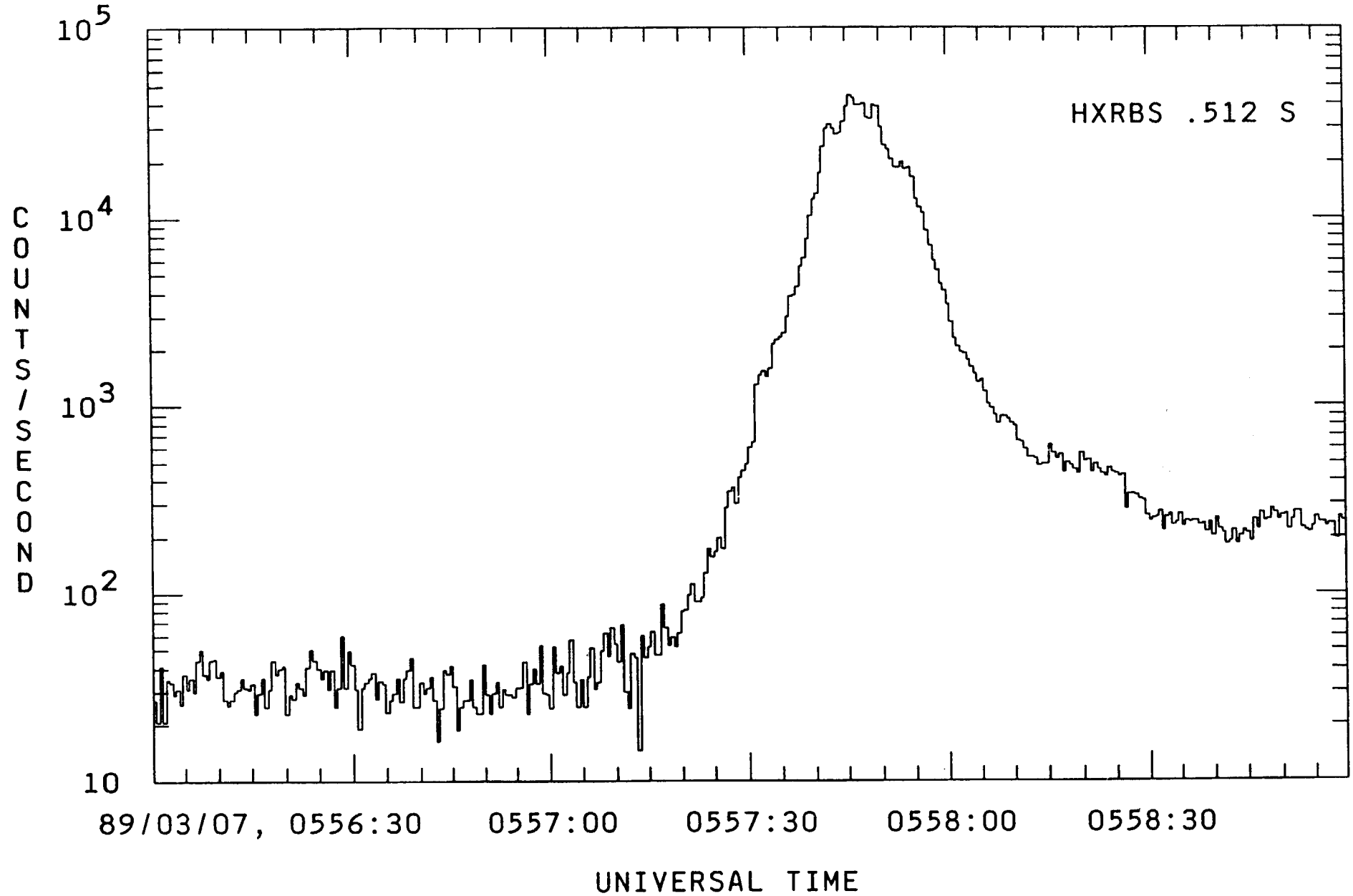
HXRBS .512 S
COUNTS/SECOND
10^5
10^4
10^3
10^2
10
89/03/07, 0556:30
0557:00
0557:30
0558:00
0558:30
UNIVERSAL TIME

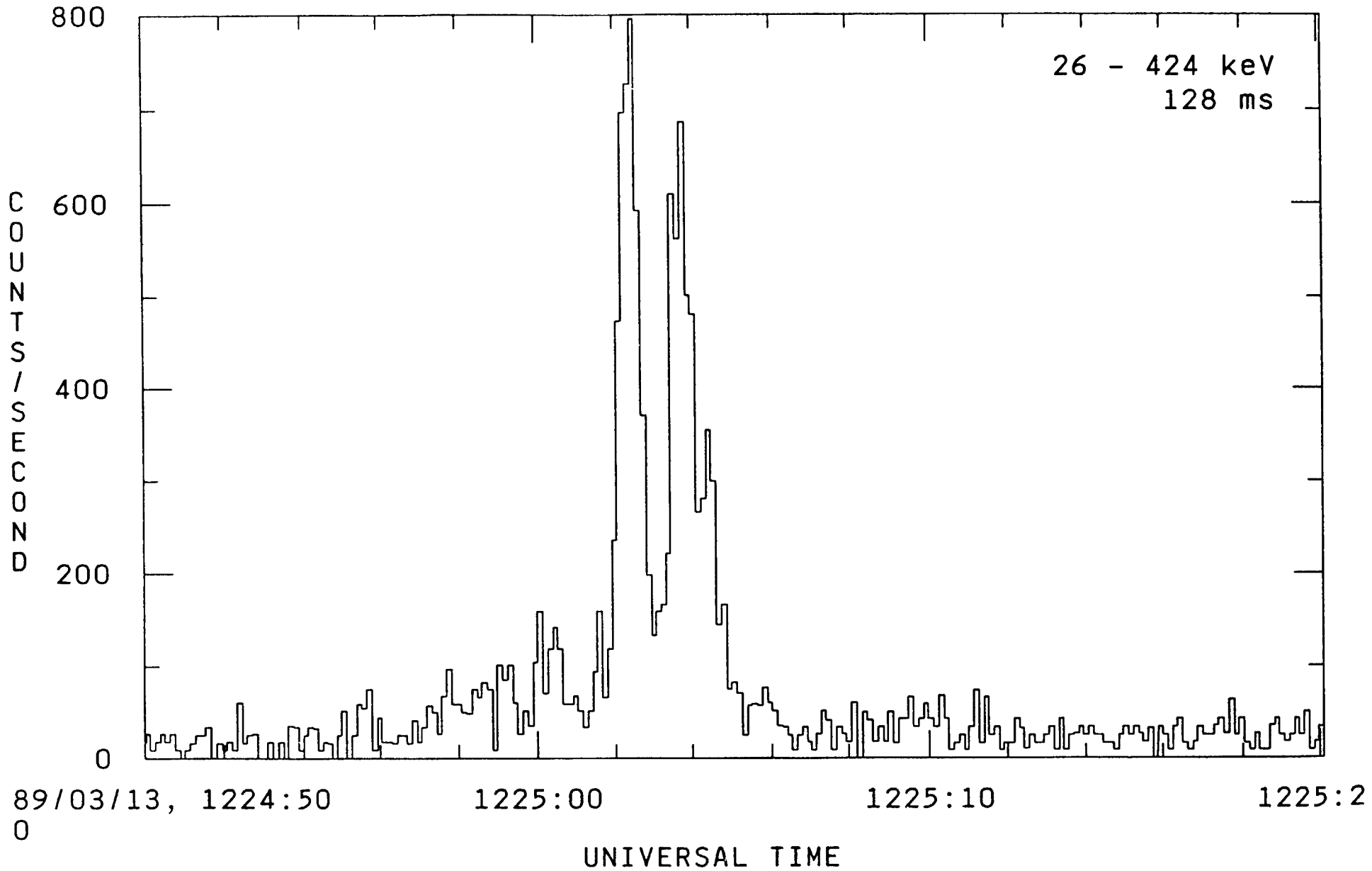
800
600
400
200
0
COUNTS/SECOND
26 - 424 keV
128 ms
89/03/13, 1224:50
1225:00
1225:10
1225:20
UNIVERSAL TIME

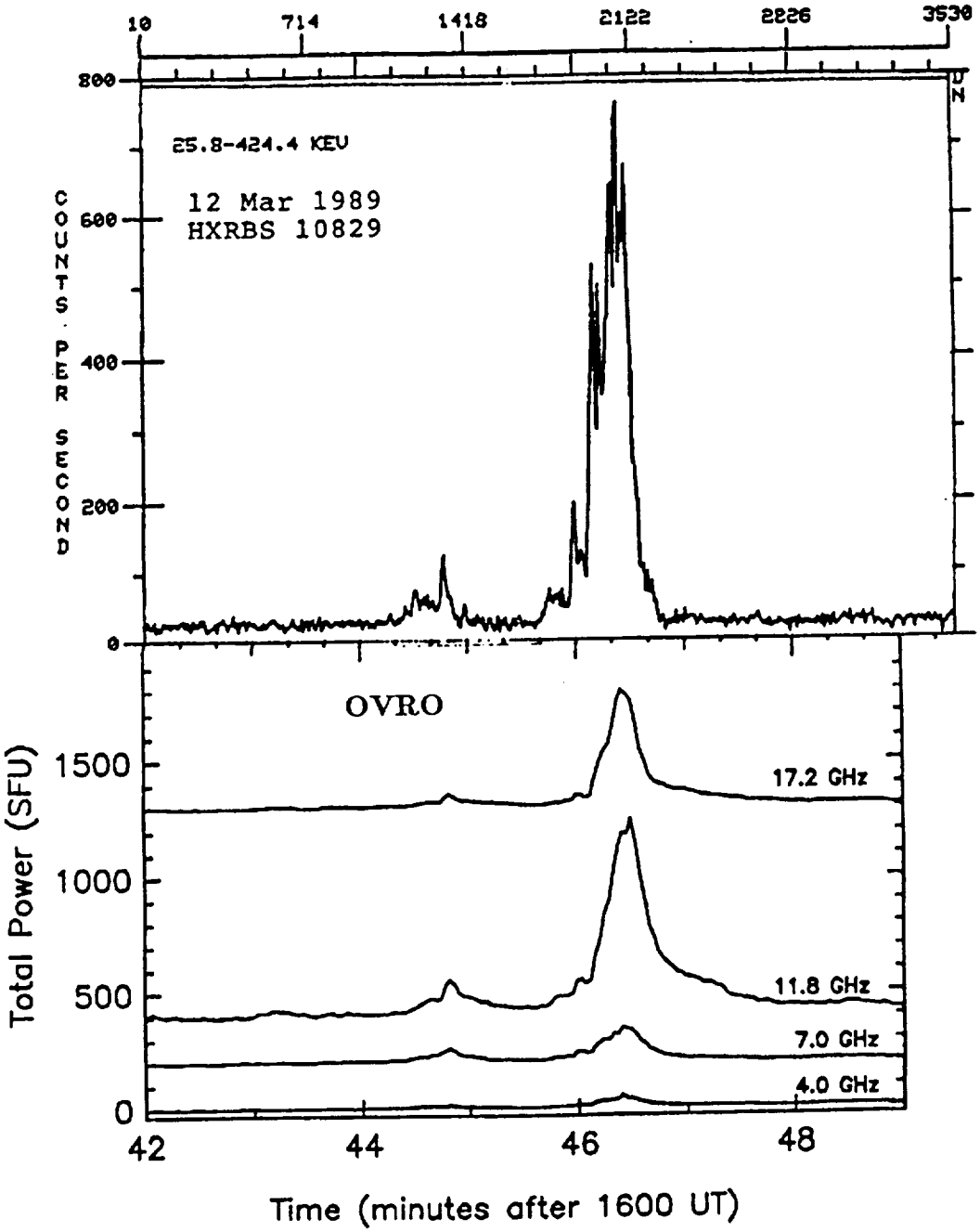
10
714
1418
2122
2826
3530
800
600
400
200
0
25.8-424.4 KEU
12 Mar 1989
HXRBS 10829
COUNTS PER SECOND
OVRO
17.2 GHz
11.8 GHz
7.0 GHz
4.0 GHz
Total Power (SFU)
1500
1000
500
0
42
44
46
48
Time (minutes after 1600 UT)

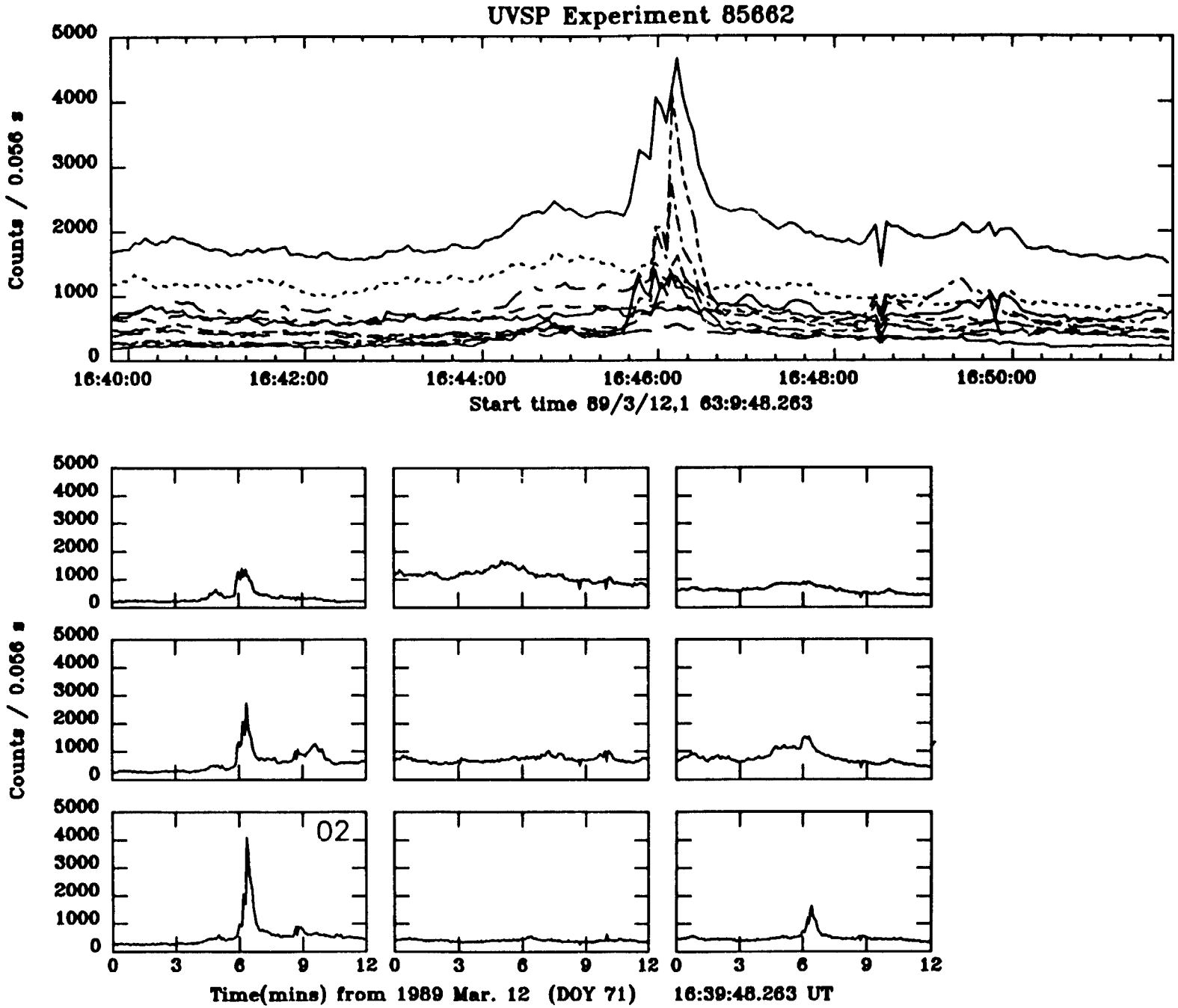
UVSP Experiment 85662
Counts / 0.056 s
5000
4000
3000
2000
1000
0
16:40:00
16:42:00
16:44:00
16:46:00
16:48:00
16:50:00
Start time 89/3/12,1 63:9:48.263
02
0
3
6
9
12
Time(mins) from 1989 Mar. 12 (DOY 71) 16:39:48.263 UT

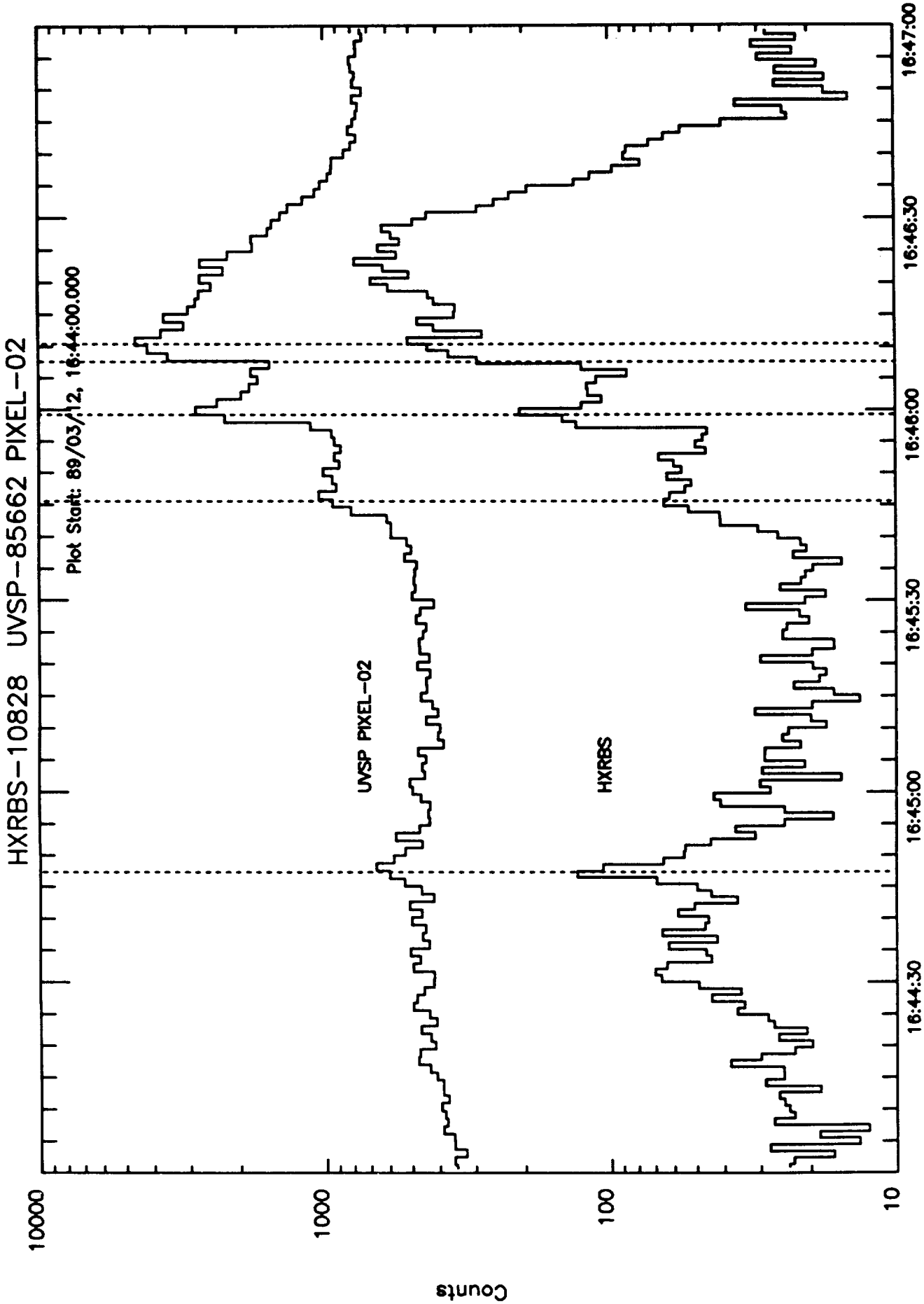
HXRBS-10828 UVSP-85662 PIXEL-02
Plot Start: 89/03/12, 16:44:00.000
UVSP PIXEL-02
HXRBS
Counts
10000
1000
100
10
16:44:30
16:45:00
16:45:30
16:46:00
16:46:30
16:47:00

omit
to P310

SMM-GRS Observations of AR 5395

David J. Forrest

University of New Hampshire

A list of flares observed by SMM-GRS at energies > 200 keV in March 1989 is presented in the following table. A sample of time histories from some of the flares observed at energies > 10 MeV are shown in Figures 1 – 3. All of these figures were prepared by Erich Rieger at MPI.

These flares are different from most of our earlier flare observation because of;

The large number of flares observed from one Active Region

The presence of very impulsive "bursts" extending to energies well above 10 MeV

The impulsive burst are most interesting and difficult to understand. An extreme example is the 10 March flare at 19:20 UT. The duration of the data points in the 10-25 MeV is 2 sec. The initial thought was that this was a chance coincidence of a Cosmic Gamma-Ray Burst detection during a flare and this has not been completely ruled out. However the presence of similar bursts in other flares makes this unlikely. Comparison with HXRBS data, with it narrower FOV, will settle this point.

The spectra of these bursts are quite hard, PL index ~2.5. The lack of a spectral break near 7 MeV and the extension of the spectrum to energies > 10 MeV suggests the emission is electron bremsstrahlung. However the electron spectrum must be extremely hard and the observations may require that it be actually peaked at MeV energies.

Day	Date	Time Interv. U.T.	Flare	AR/Loc.	E_{max}
10	1.10.89	2024-2031	X1.4/1B	5312/S31E30	MCW?
15	1.15.89	1549-1552	M4.5/1B	5312/S31W36	<0.7 MeV
16	1.16.89	2216-2221	M7.2/1B	5312/S30W51	<0.6 MeV
26	1.26.89	1411-1412	M1.2/SM	5329/N15W03	<0.6 MeV
26	1.26.89	2350-2352	M3.2/1N	5334/S22E74	<0.6 MeV
40	2.9.89	1300(Occ)-1304	M3.2/1N	5355/N22E29	< 1 MeV
65	3.6.89	1356/1543	X15/3B	5395/N35E69	MCW, Heat
66	3.6.89	0557-0558	M2.0/1F	5395/N29E69	MCW
66	3.7.89	1318-1321	M4.1/1B	5395/N31E65	MCW
66	3.7.89	1343-1344	M2.4/-	? ?	<0.6 MeV
66	3.7.89	1452-1456	X1.8/2B	5395/N32E65	MCW
66	3.7.89	1651-1655	M3.8/2B	5395/N29E63	<0.6 MeV
66	3.7.89	2105-2106	?	?	<1.7 MeV
67	3.8.89	1447-1448	,1/22B	5395N28E48	<0.8 MeV
67	3.8.89	1852-1857	M4.6/-	?	<1.0 MeV
69	3.10.89	1903(Occ)-1949(Occ)	X4.5/3B	5395/N31E22	MCW,HE1
70	3.11.89	1535-1539	X1.2/2B	5395/N28E13	<0.6 MeV
71	3.12.89	0839-0842	M6.7/1N	5395/N29E04	<0.6 MeV
74	3.15.89	0647-0650	M4.8/1F	5395/N34W35	<0.8 MeV
75	2.16.89	1523-1532	X3.6/2B	5395/N36W47	MCW,HE1
76	3.17.89	0331-0332	"?	?	<0.8 MeV
76	3.17.89	0716-0718	M6.8/2B	5395/N32W59	MCW
76	3.17.89	1731-1744	X6.5/2B	5395/N33W60	NCW,HE1
77	3.18.89	1242-1244	C9.2/SF	5395/N36@85	<0.8 MeV
77	3.18.89	2156-2159	M3.1/-	?	<0.6 MeV
82	3.23.89	1936-1948	X1.5/3B	5409/N18E28	<0.8 MeV
83	3.24.89	2027-2031	M1.2/2B	5409/N17W44	<0.6 MeV

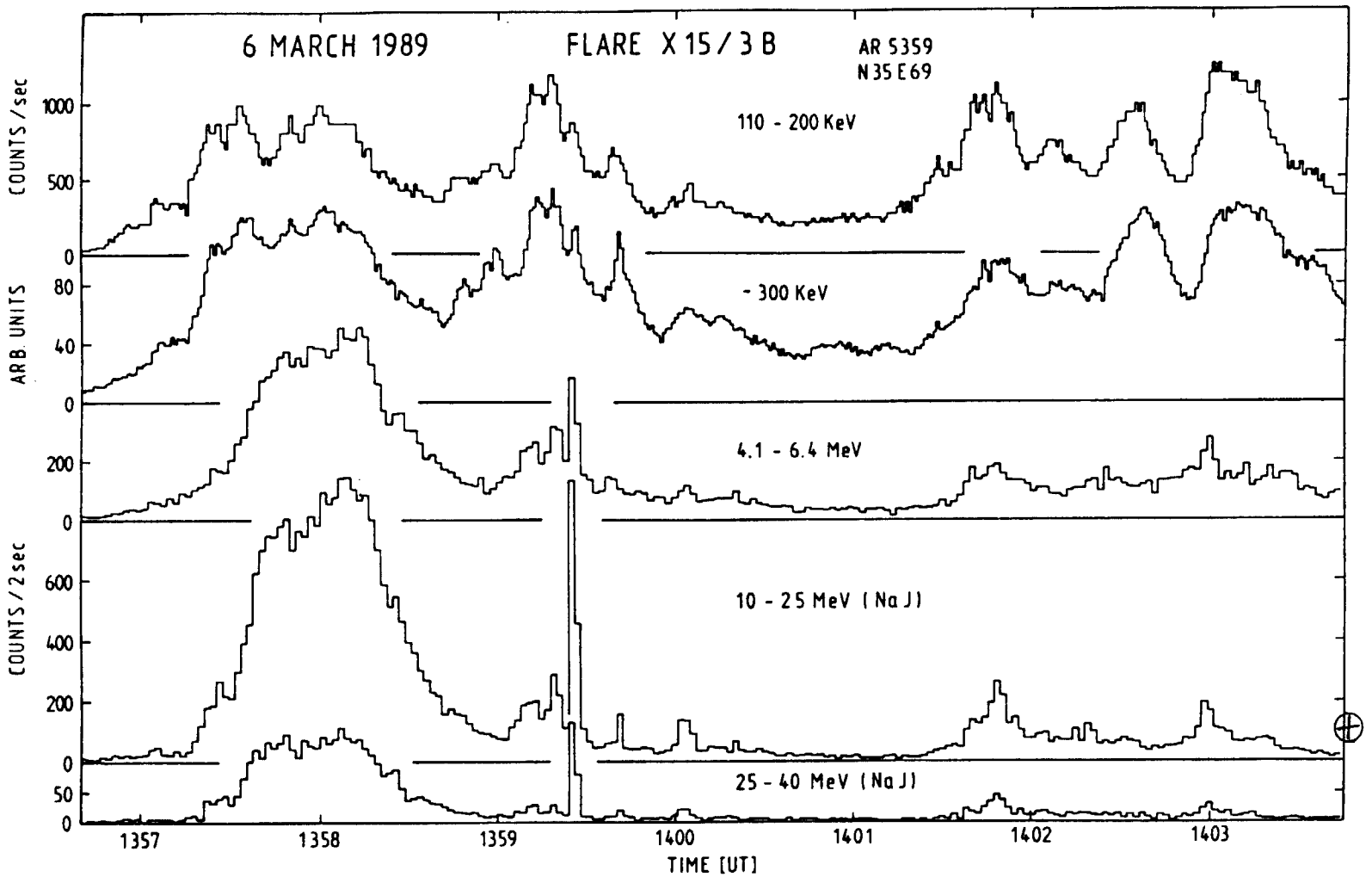
6 MARCH 1989
FLARE X 15 / 3 B
AR 5359
N35 E69
110 - 200 KeV
- 300 KeV
4.1 - 6.4 MeV
10 - 25 MeV (Na J)
25 - 40 MeV (Na J)
COUNTS / sec
ARB UNITS
COUNTS / 2 sec
1000
500
0
80
40
0
200
0
600
400
200
0
50
0
1357
1358
1359
1400
1401
1402
1403
TIME [UT]

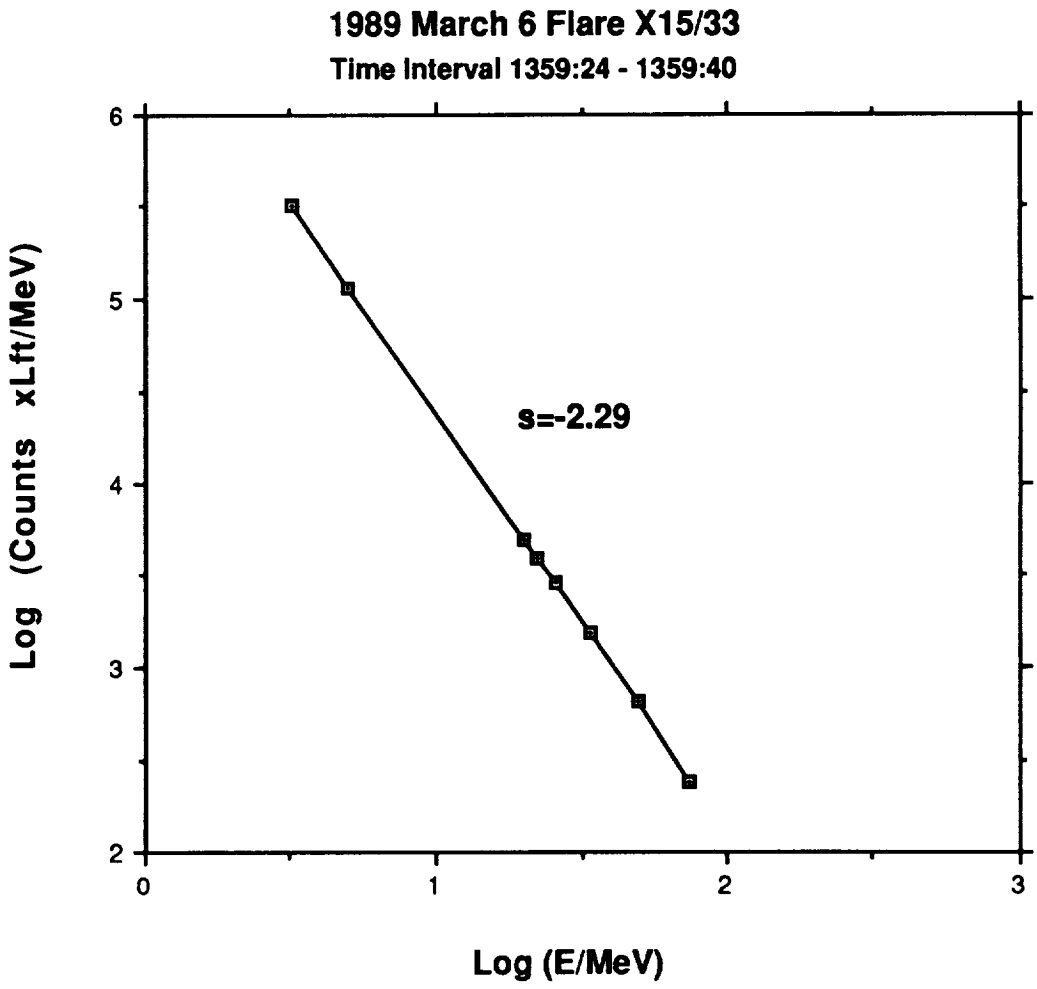
1989 March 6 Flare X15/33
Time Interval 1359:24 - 1359:40
Log (Counts xLft/MeV)
Log (E/MeV)
s=-2.29
6
5
4
3
2
0
1
2
3

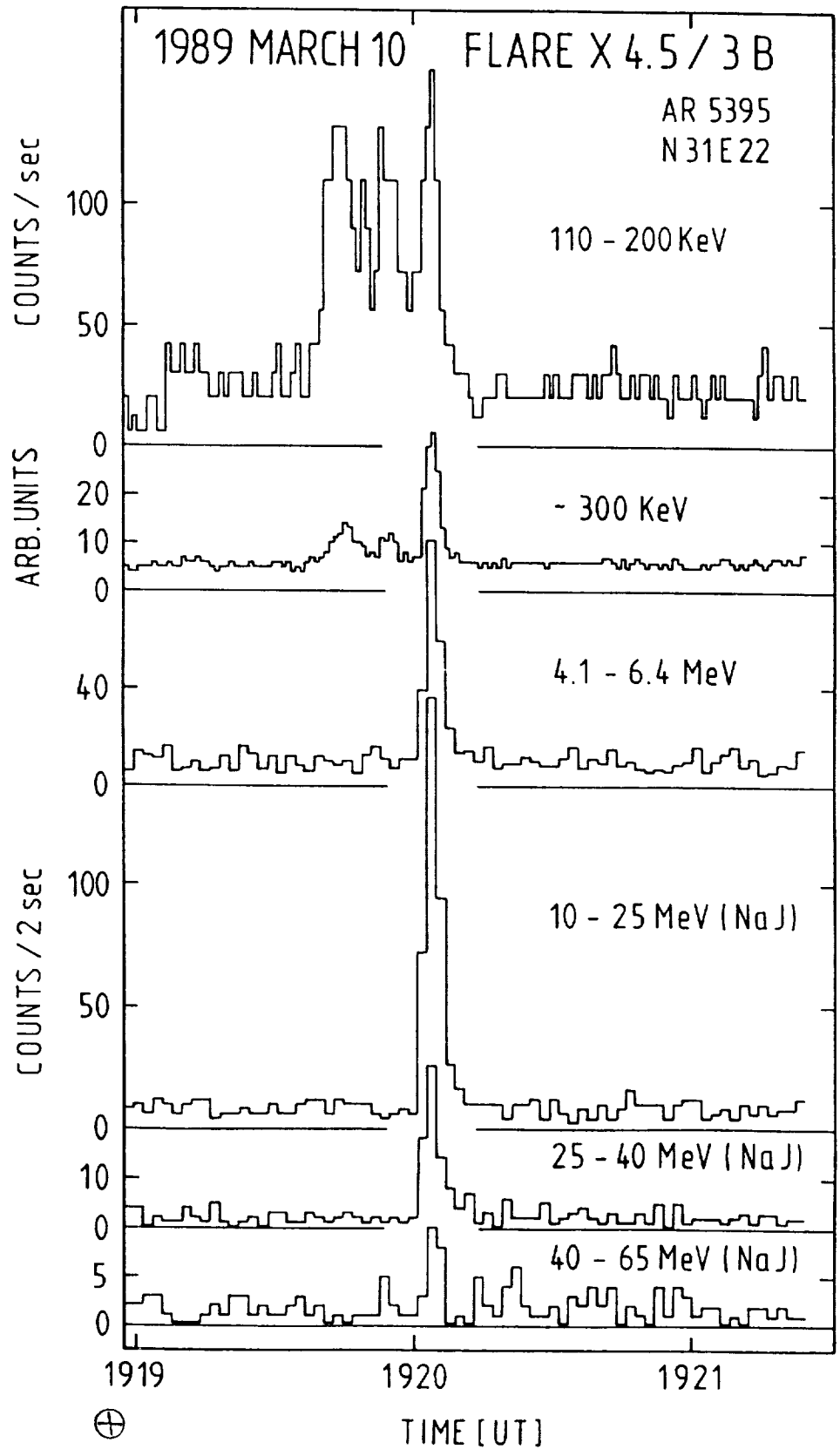
1989 MARCH 10 FLARE X 4.5 / 3 B
AR 5395
N 31 E 22
COUNTS / sec
110 - 200 KeV
ARB. UNITS
~ 300 KeV
4.1 - 6.4 MeV
COUNTS / 2 sec
10 - 25 MeV (NaJ)
25 - 40 MeV (NaJ)
40 - 65 MeV (NaJ)
1919
1920
1921
TIME [UT]

OBSERVATIONS OF AR 5395 IN CORONAL EMISSION LINES

Richard C. Altrock
Geophysics Laboratory (AFSC)
National Solar Observatory/Sacramento Peak
Sunspot, NM 88349

Observations of AR 5395 and subsequent rotations were obtained with the NSO/SP Emission-Line Coronal Photometer. Observations in Fe XIV 5303A (~2MK), Ca XV 5694A (>~3MK), and Fe X 6374A (~1MK) were obtained at radii between 1.13 and 1.15. The data are corrected in real time for the sky background and reduced to absolute intensities in millionths of the brightness of the center of the disk at the local wavelength.

1. Figure 1 is a polar plot of the intensity in Fe XIV at 1.15Ro on 5 Mar. The zero level is at the outer circle. Only moderate intensities (30 millionths) were observed on the limb above the approaching active region in the NE.
2. Figure 2 shows the earliest observations of the region the next day (6 Mar) in all three lines. Note the times in the lower right. Intensities near 30 degrees NE in Fe XIV have radically decreased, probably implying the occurrence of a mass ejection (possible streamer blowout) since the observations on 5 Mar. Ca XV emission, implying unusual heating, is occurring just south of the AR. All three lines are present in this southerly area, indicating a complex temperature structure along the line of sight (these lines are all optically thin).
3. Figure 3. Later on 6 Mar (>1700 UT) one or more transients occurred, producing highly variable Fe XIV emission in a small region near 40N, which continued for the rest of our observing day until ~2200 UT. This event is being studied.
4. Figure 4 shows that early the next day (7 Mar) emission in all three lines had returned to the "zone of avoidance" of early 6 Mar, probably indicating that coronal magnetic fields had relaxed back to an equilibrium configuration.
5. Figure 5. Five minutes after the Ca XV observations of Figure 4, during an X1.8/1B flare, the Ca XV emission doubled to 1.5 millionths directly over the flare site at 31N. Evidence for a possible streamer blowout later on 7 Mar near the north pole is being investigated.

   With the exception of a possible overnight transient near 40N between 7 and 8 Mar, the corona in the NE was quiescent on 8 Mar. No transients occurred on the 8th, and no Ca XV emission was observed. The limb passage of AR 5395 was over.
6. No unusually bright Fe XIV emission was seen during the first limb passage of AR 5395. However, on the return of its coordinates in April, strong emission was seen over the "spotless plage" (AR 5440) seen in the chromosphere. Figure 6 is a spherical projection of a synoptic map centered on the 9 Apr central meridian passage (CMP) of East limb observations (observations on the central meridian are from 2 Apr). It is a pseudo-full-disk picture of the Fe XIV corona on 9 Apr. It shows that a large area of Fe XIV emission over 48 millionths, with some regions over 64 millionths (note annotations on the contours), was found near CMP 27 days after the first CMP passage of AR 5395, although some of this emission may have come from AR 5441 further to the East. No transients were observed during this limb passage.

7. Figure 7, also centered on 9 Apr CMP, shows that strong (>1 millionth) Ca XV emission still existed over the region. This fact, combined with the strong Fe XIV emission seen in Figure 6, indicates that the corona had become denser over AR 5395 than during the first apparition. An alternative explanation, that the region had cooled sufficiently to allow Fe XIV emission, is belied by the continued presence of Ca XV emission. No further Ca XV emission was seen on subsequent CMPs.

8. Figure 8, centered on 6 May CMP, shows that some strong emission above 48 millionths still occurred in Fe XIV during the May apparition, although by this time AR 5470 had erupted over the previous site of AR 5395. A dense spotless area to the East had now developed near the previous site of AR 5441, again indicating that activity in the corona may continue long after the disappearance of chromospheric and photospheric tracers.

In summary, coronal observations of AR 5395 showed some interesting properties. Fe XIV emission was only moderate during its first limb passage, but it increased during subsequent rotations. This, combined with Ca XV observations, implies that the density over the coordinates of AR 5395 increased during its second apparition, even though chromospheric activity dramatically decreased. Several transients occurred, some of which were well-observed in the lower corona by the Sacramento Peak instrumentation. Finally, several instances of complex temperature structure along the line of sight were observed. These and the transients should prove interesting to study in conjunction with other coronal observations.

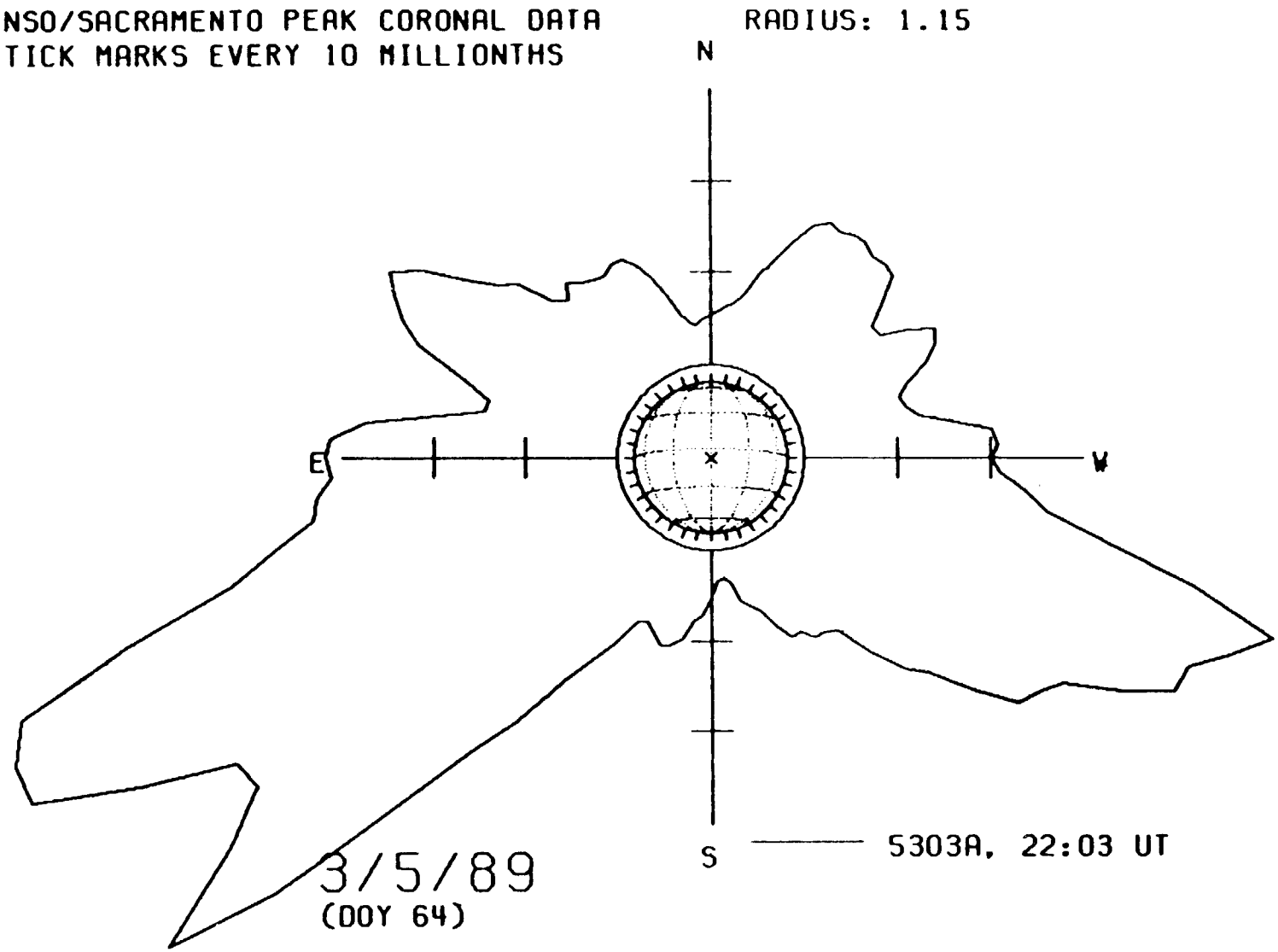
NSO/SACRAMENTO PEAK CORONAL DATA
TICK MARKS EVERY 10 MILLIONTHS
RADIUS: 1.15
N
E
W
S
5303A, 22:03 UT
3/5/89
(DOY 64)

Figure 1

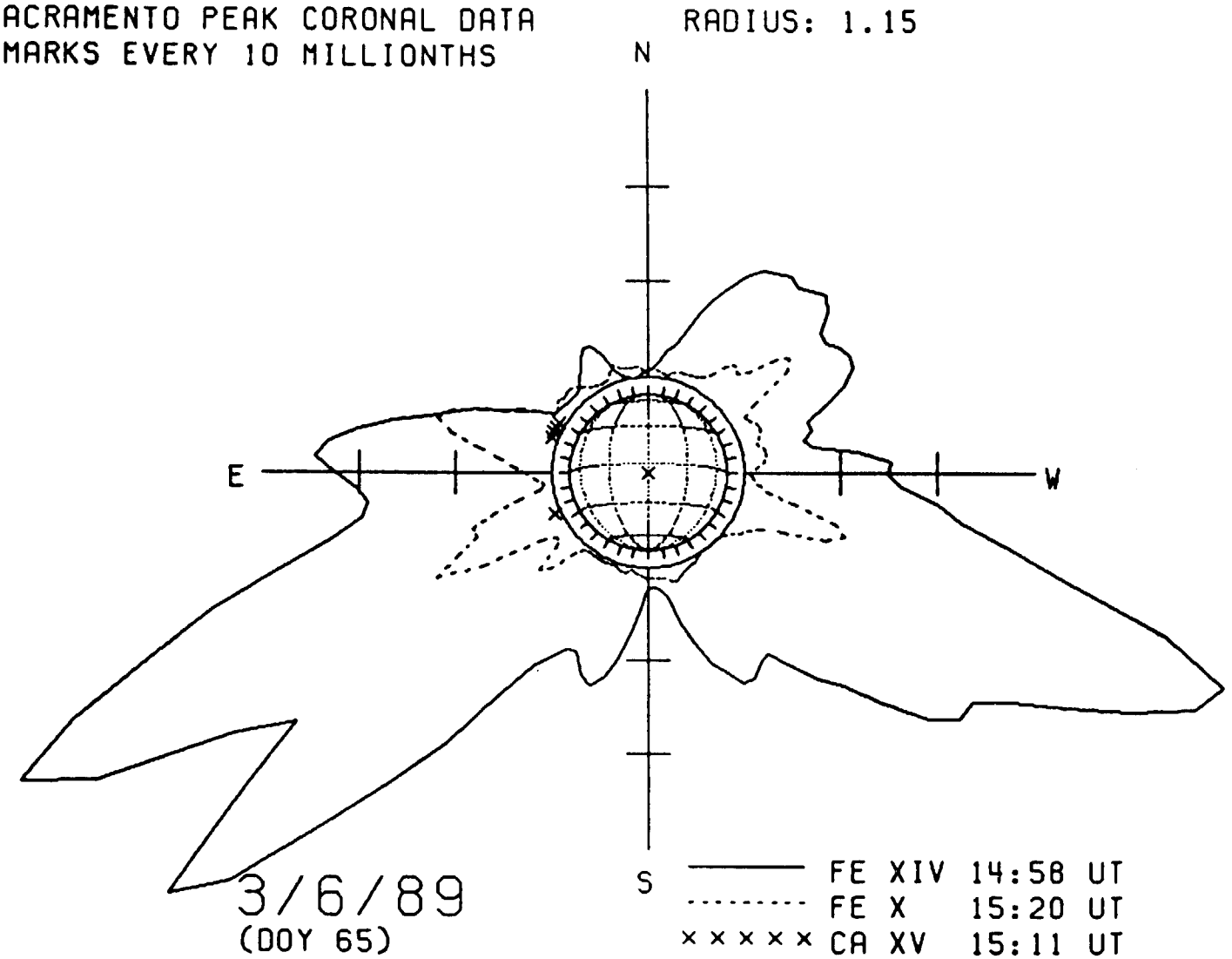
NSO/SACRAMENTO PEAK CORONAL DATA
TICK MARKS EVERY 10 MILLIONTHS
RADIUS: 1.15
N
E
W
S
3/6/89
(DOY 65)
FE XIV 14:58 UT
FE X 15:20 UT
CA XV 15:11 UT

Figure 2

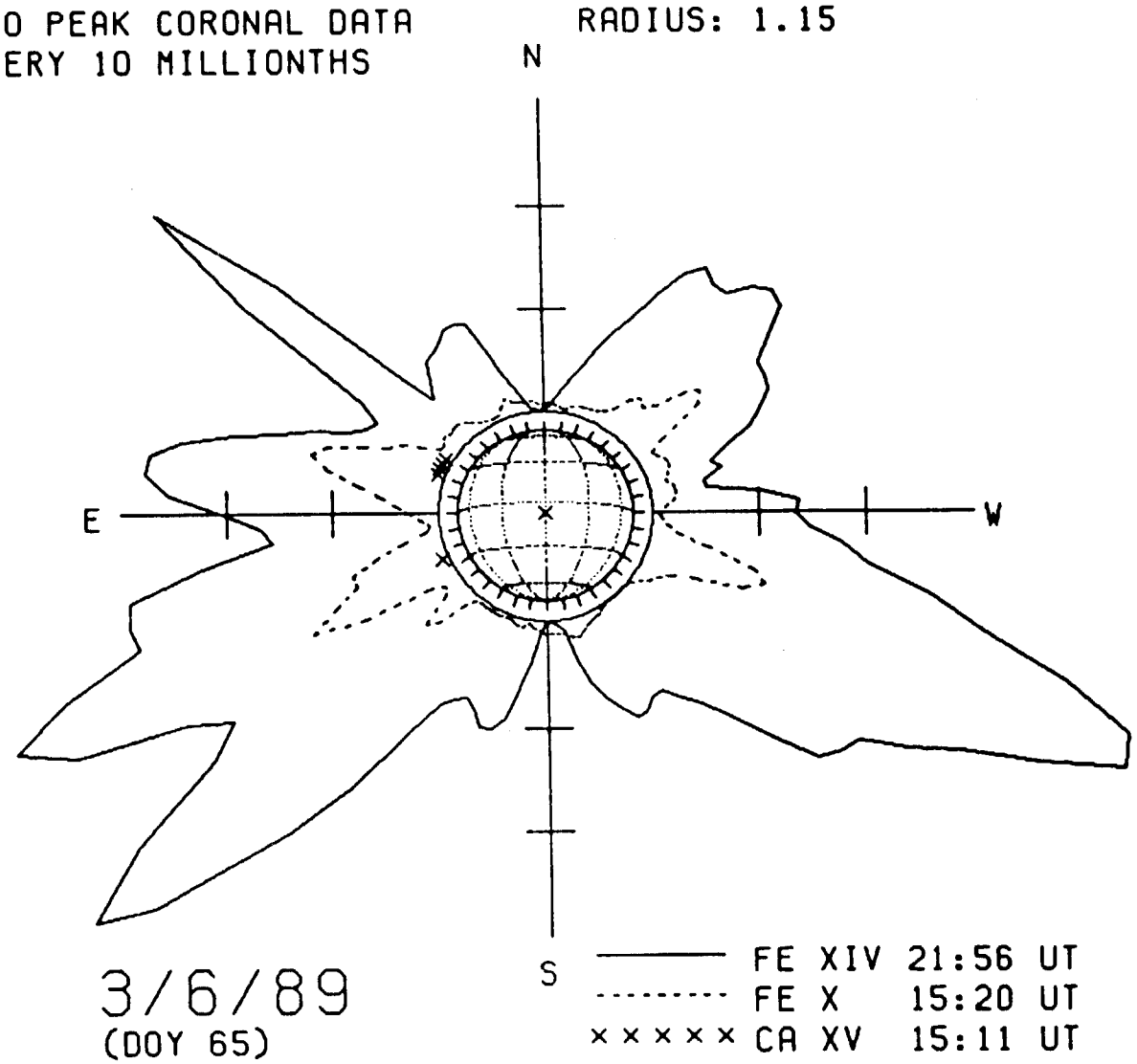
NSO/SACRAMENTO PEAK CORONAL DATA
TICK MARKS EVERY 10 MILLIONTHS
RADIUS: 1.15
N
E
W
S
3/6/89
(DOY 65)
FE XIV 21:56 UT
FE X 15:20 UT
CA XV 15:11 UT

Figure 3

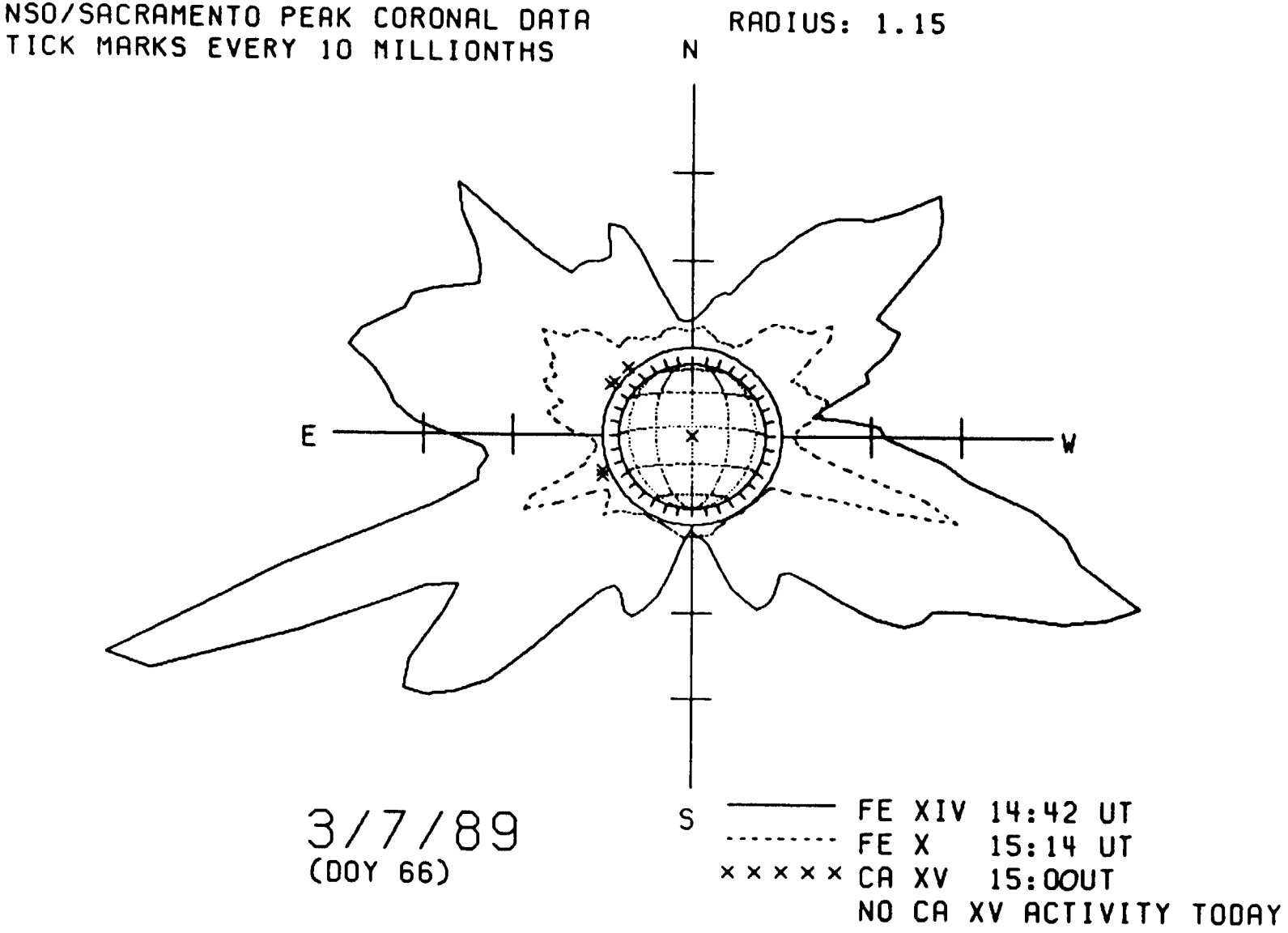
NSO/SACRAMENTO PEAK CORONAL DATA
TICK MARKS EVERY 10 MILLIONTHS
RADIUS: 1.15
N
E
W
S
3/7/89
(DOY 66)
FE XIV 14:42 UT
FE X 15:14 UT
CA XV 15:00UT
NO CA XV ACTIVITY TODAY

Figure 4

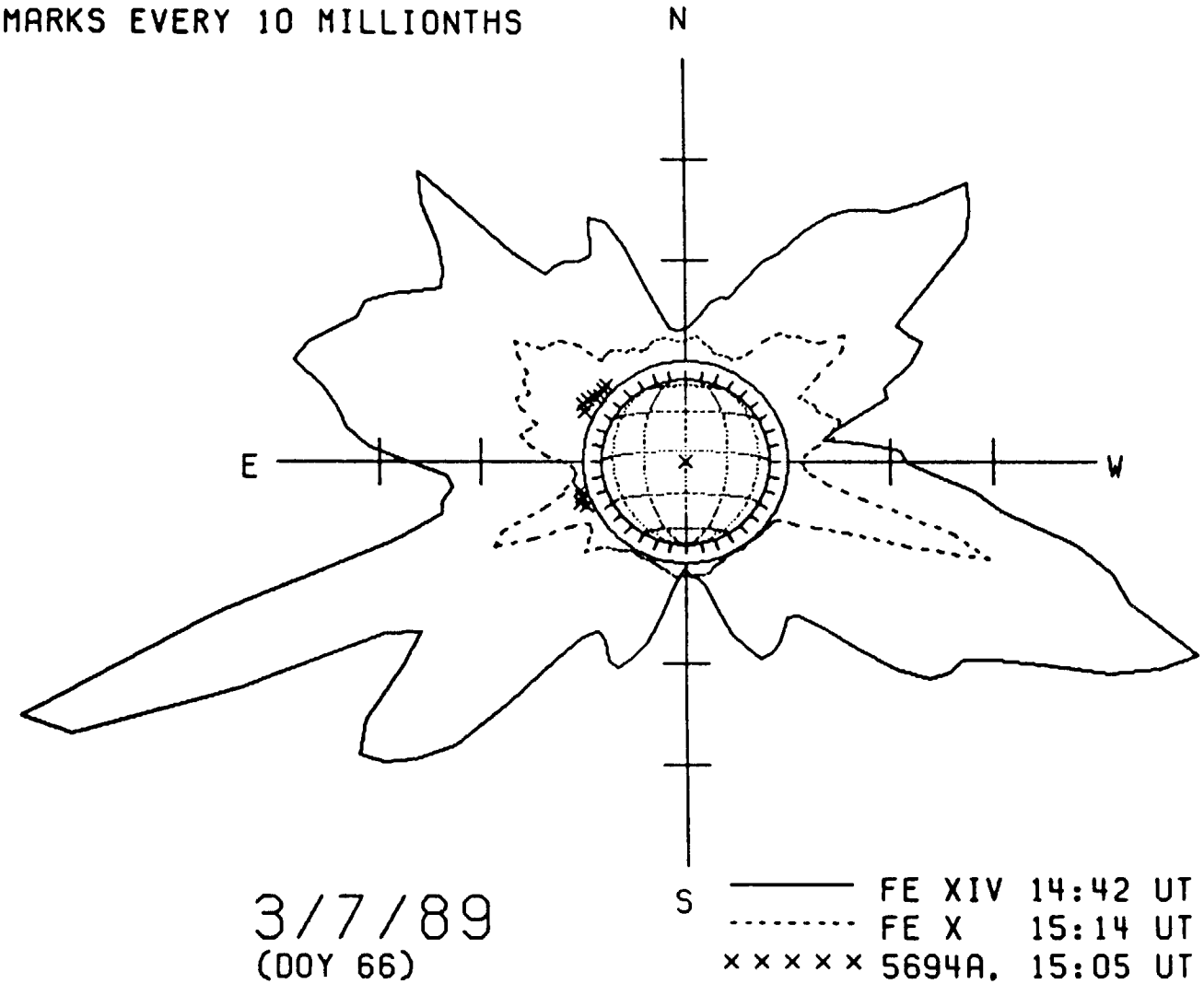
NSO/SACRAMENTO PEAK CORONAL DATA
TICK MARKS EVERY 10 MILLIONTHS
RADIUS: 1.15
N
E
W
S
3/7/89
(DOY 66)
FE XIV 14:42 UT
FE X 15:14 UT
5694A. 15:05 UT

Figure 5

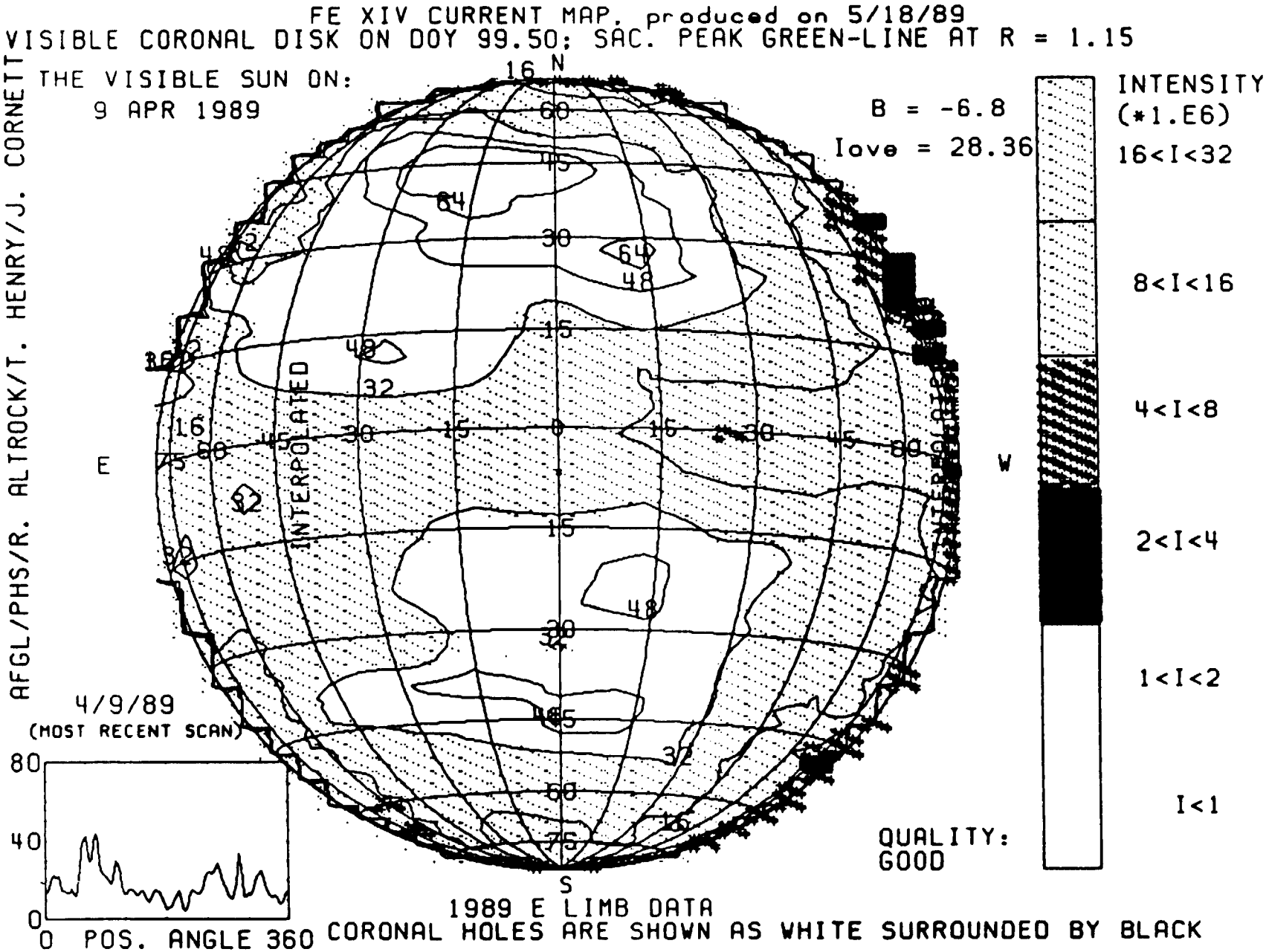

Figure 6

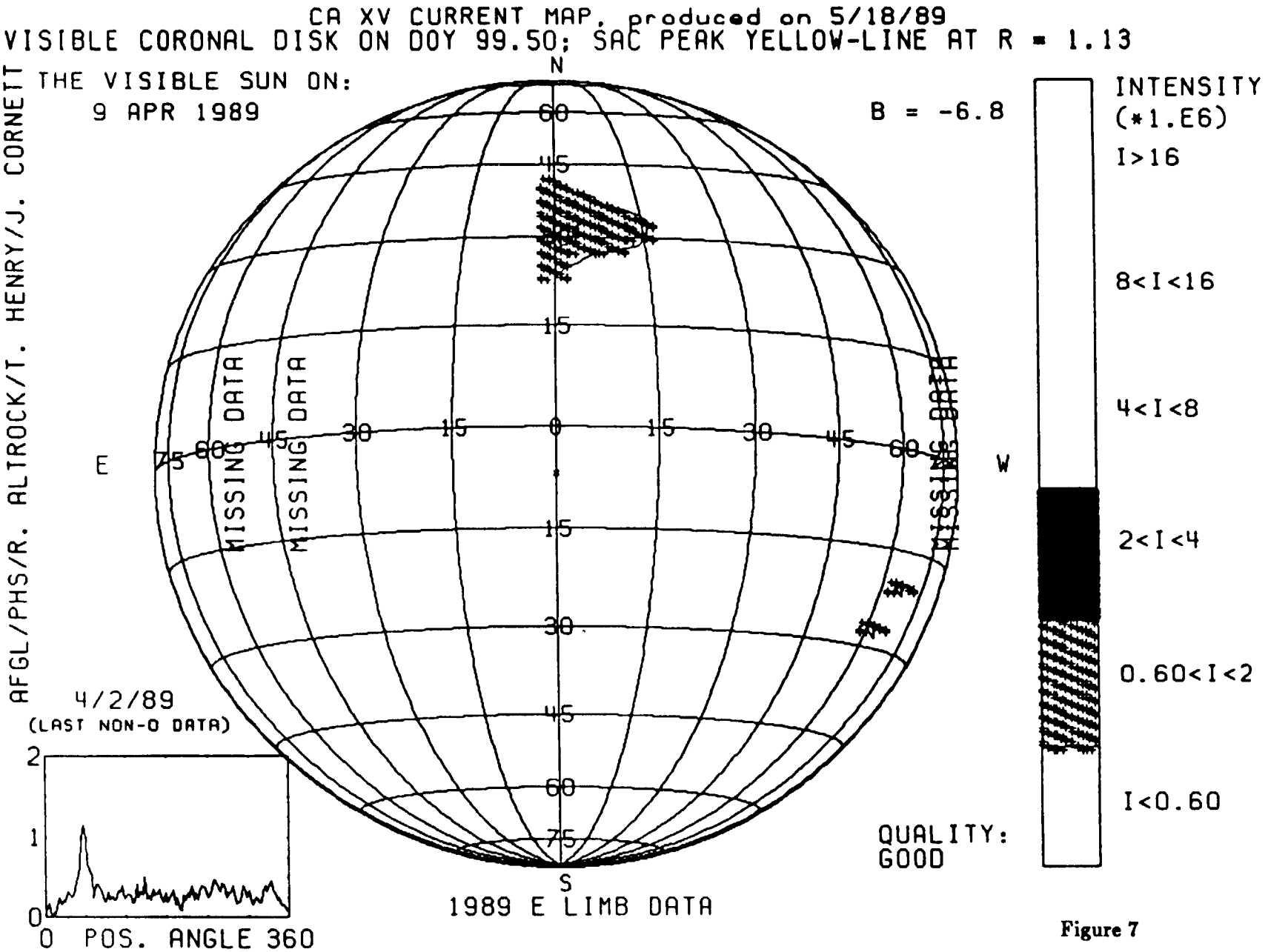
CA XV CURRENT MAP, produced on 5/18/89
VISIBLE CORONAL DISK ON DOY 99.50; SAC PEAK YELLOW-LINE AT R = 1.13
AFGL/PHS/R. ALTROCK/T. HENRY/J. CORNETT
THE VISIBLE SUN ON:
9 APR 1989
B = -6.8
N
S
E
W
MISSING DATA
MISSING DATA
MISSING DATA
INTENSITY
(*1.E6)
I>16
8<I<16
4<I<8
2<I<4
0.60<I<2
I<0.60
QUALITY:
GOOD
4/2/89
(LAST NON-0 DATA)
0 POS. ANGLE 360
1989 E LIMB DATA

Figure 7

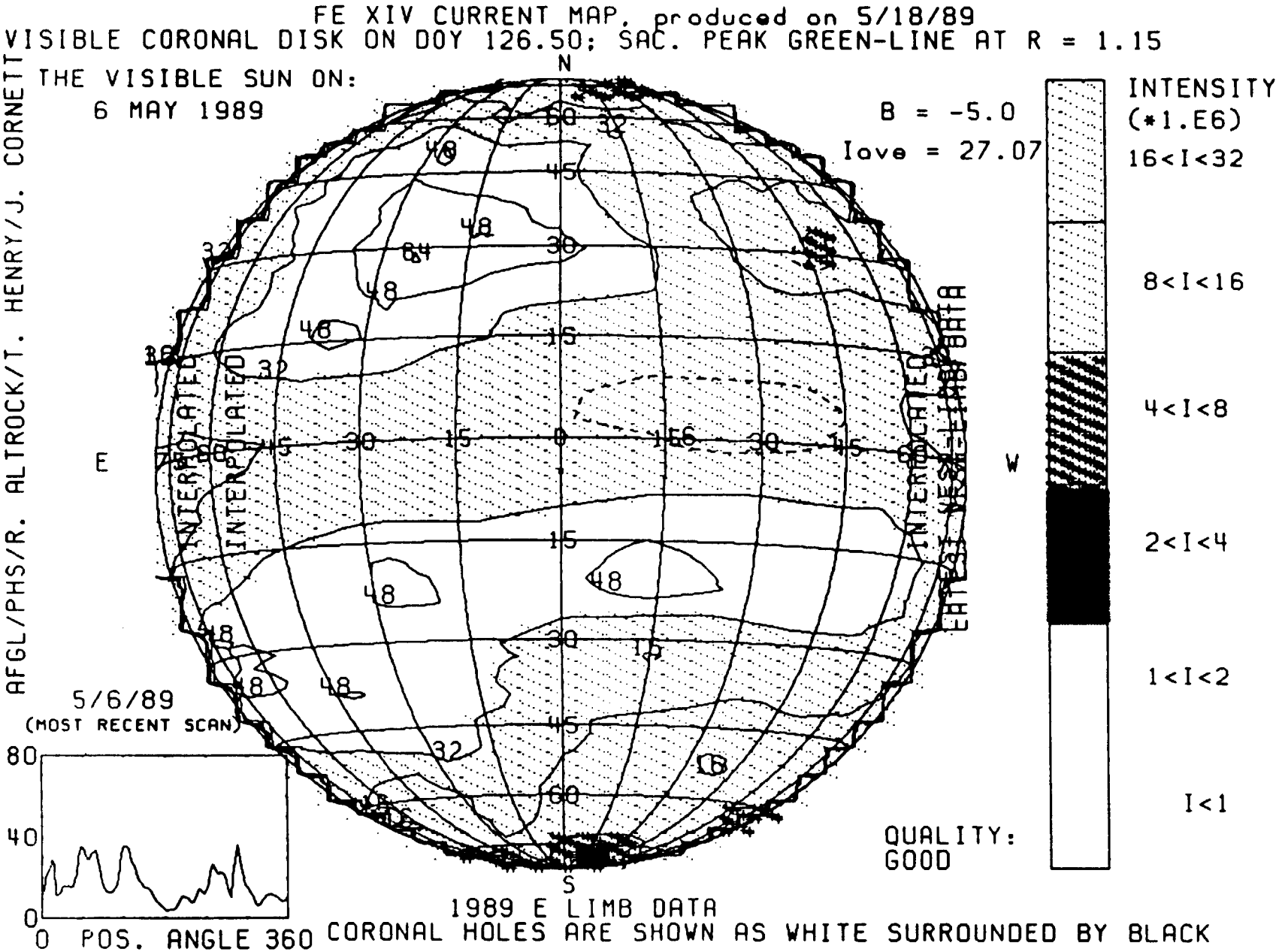

Figure 8

Hα Imaging Spectroscopy of March 1989 Flares

J.-P. Wülser and R.C. Canfield

University of Hawaii

We made Hα line profile observations of Active Region 5395 from March 9 until March 13, 1989 with the CCD camera at the Vacuum Tower Telescope of Sacramento Peak Observatory. We obtained digital Hα line profiles and spectroheliograms of a 3' by 3' field of view every 11 s at a spatial resolution of 2.6".

The region produced a large number of flares, and many of them were successfully observed (see flare list). The largest was a X4.6/3B two ribbon flare which started around 19:00 UT on March 10. Two other class X flares were observed on March 11 around 15:35 UT, and 19:33 UT, respectively. These flares are the largest ever observed with Hα imaging spectroscopy. Figures 1 and 2 illustrate our observations of the large flare on March 10.

Hα Imaging Spectroscopy
Flare List March 1989

March 9

(data: 22:21 UT - 24:07 UT)

start ~23:10 UT	M 1.3	SMM day: 22:50 UT - 23:46 UT
start ~23:34 UT	M 1.5	SMM day: 22:50 UT - 23:46 UT

March 10

(data: 13:41 UT - 15:44 UT, 16:02 UT - 20:26 UT, 20:43 UT - 24:44 UT)

start ~15:20 UT	M 1.2	SMM day: 14:24 UT - 15:23 UT
start ~17:30 UT	C 8.9	SMM day: 17:30 UT - 18:29 UT
start ~19:00 UT	X 4.6	SMM day: 19:04 UT - 19:53 UT

March 11

(data: 14:01 UT - 14:17 UT, 14:44 UT - 20:45 UT, 20:56 UT - 24:48 UT)

start ~14:03 UT	M 1.0	SMM day: 13:44 UT - 14:43 UT
start ~15:35 UT	X 1.2	SMM day: 15:17 UT - 16:16 UT
start ~18:30 UT	M 1.3	SMM day: 18:24 UT - 19:11 UT
start ~19:33 UT	X 1.3	SMM night
start ~24:18 UT	M 7	SMM night

March 12

(data: 14:34 UT - 16:00 UT, 16:20 UT - 16:59 UT, 18:20 UT - 21:33 UT; often cloudy)

start ~14:58 UT	M 2.5	SMM day: 14:37 UT - 15:36 UT
start ~16:33 UT	M 1.3	SMM day: 16:11 UT - 17:10 UT
start ~20:35 UT	M 6	SMM night

March 13

(data: 17:10 UT - 18:27 UT)

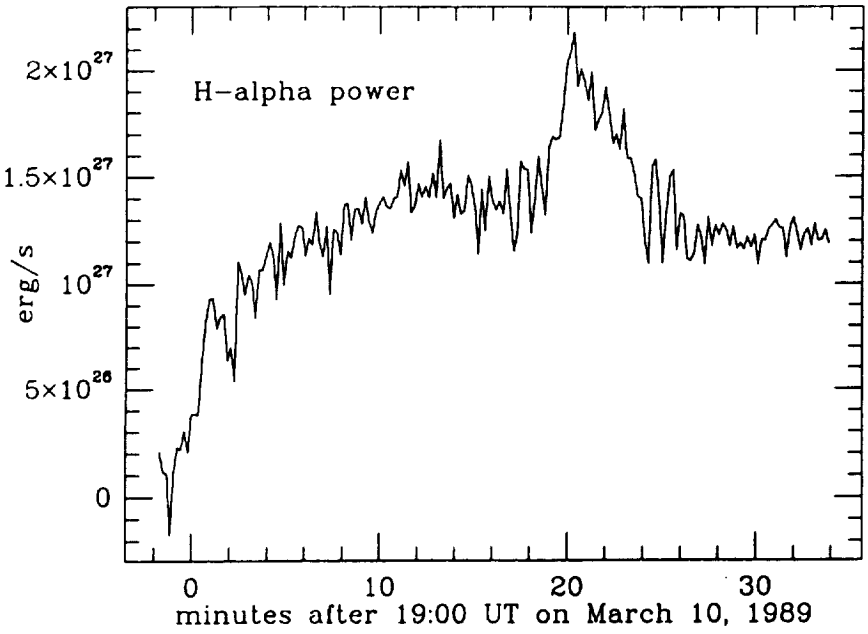

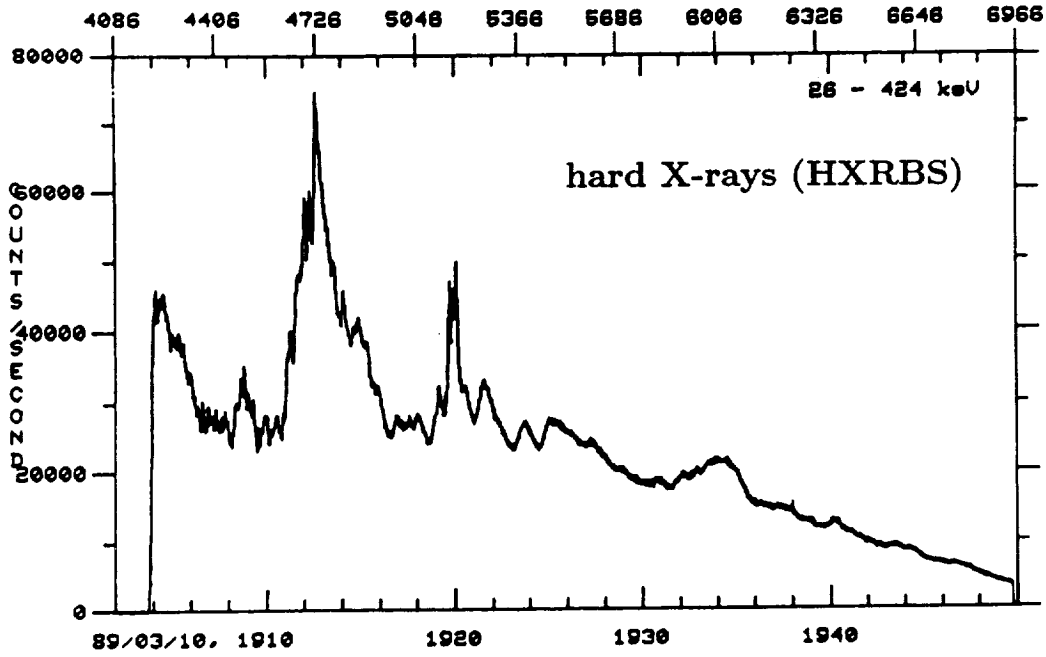

Fig. 1. - Temporal evolution of the flare on March 10, 1989 in Hα, and in the hard X-rays. The hard X-ray data are from HXRBS aboard the Solar Maximum Mission which had sunrise at 19:04, and therefore missed the very beginning of the flare. The total Hα power does not show a significant peak at the time of maximum hard X-ray emission at 19:12:30. However, the bright Hα flare kernels are most dominant at this time, and exhibit the broadest line profiles. The Hα and hard X-ray peaks at 19:20 are associated with another flare occurring in the same active region.

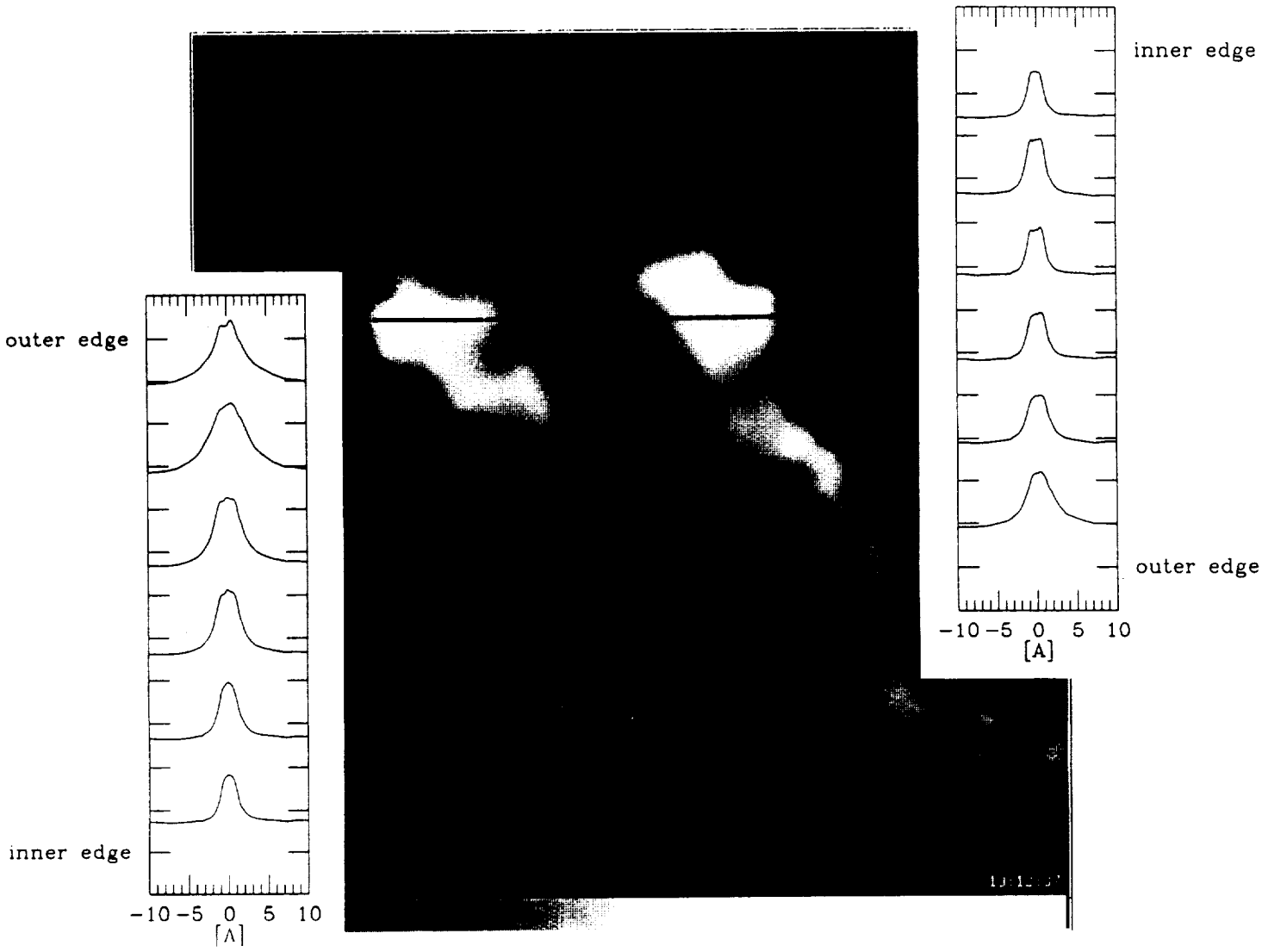

Fig. 2. - A line-center Hα spectroheliogram of the flare on March 10, at the time of hard X-ray maximum. The insets show the variation of the Hα line profile across the flare ribbons. The emission profile is broadest at the outer edge of the ribbons. Theoretical line profile calculations indicate that broad emission wings are a signature for nonthermal electron heating.

Omit

OPTICAL OBSERVATIONS OF AR 5395

DONALD F. NEIDIG

Geophysics Laboratory (AFSC), National Solar Observatory/Sacramento Peak, Sunspot NM 88349

Coverage:

(a) High time (0.5 sec) and spatial (1 arcsec) resolution CCD-array observations in Hα+3 and -3 Å and 5000 Å continuum, using the Vacuum Tower Telescope: 6 and 7 March (see example in Figure below).

(b) Low time (15 sec) resolution photographic observations at 3610 and 4275 Å, using Multiband Patrol: coverage for 6-19 March.

(c) Hα full disk photographic patrol: coverage for 6-19 March.

Work in Progress: Data types (a) and (b) are being used to measure optical radiative losses from the chromosphere; comparison is made with SMM/HXRBS data in order to study energy transport mechanisms in flares. Specific approach is to look for evidences of Doppler shifted Hα emission and temporal response of optical relative to hard x-ray burst structures.

Figure Caption

Comparison of hard x-ray burst with time variation of optical emissions in three wavelengths, for flare kernel showing white-light emission. Note red asymmetry in first impulsive peak of the Hα curves (see arrows in Figure). The photometry represents the sum of six pixels (2x3 arcsec) at 0.5 sec time resolution; the individual images are software corrected for both image motion and distortion due to atmospheric seeing.

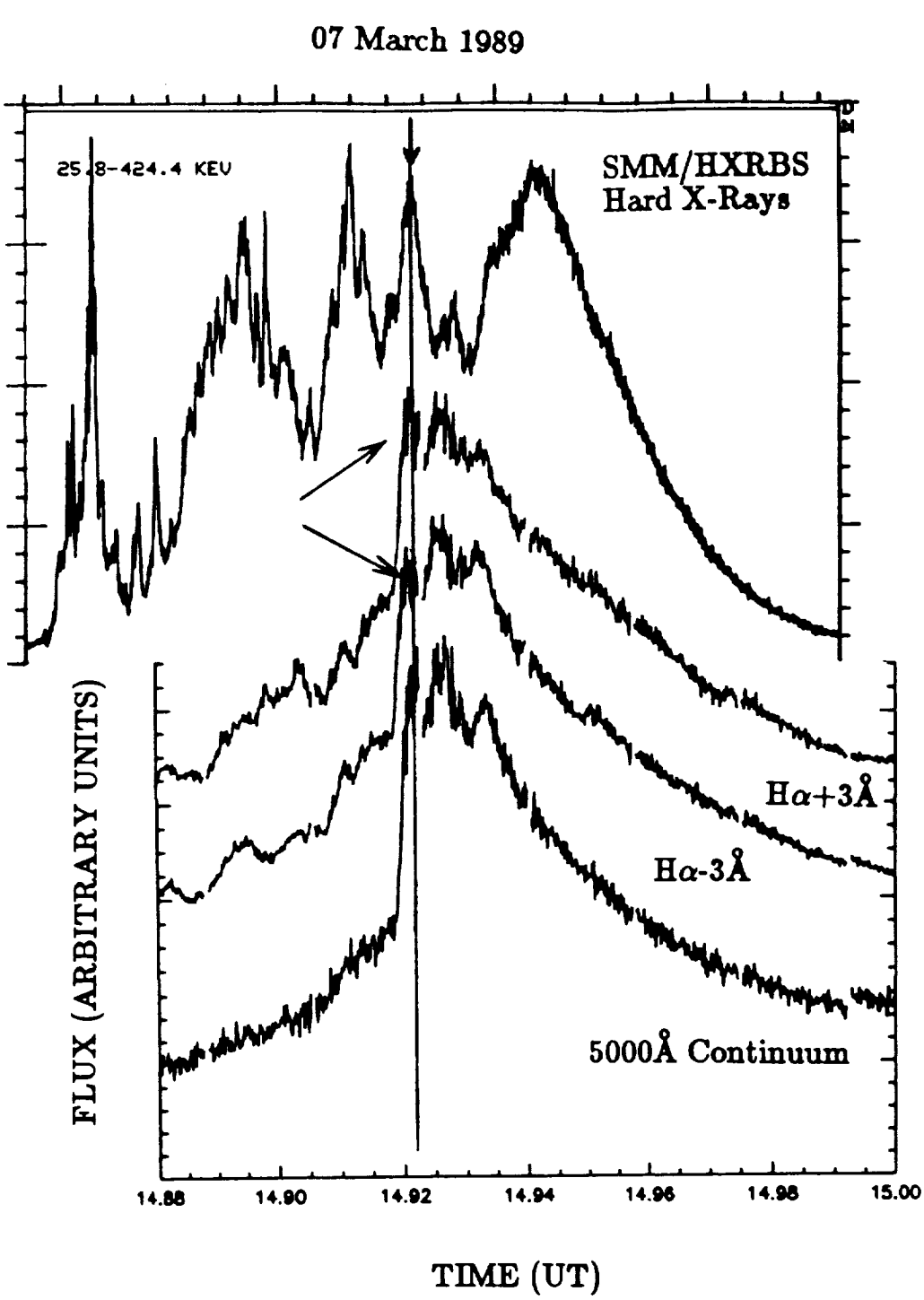
07 March 1989
25.8-424.4 KEV
SMM/HXRBS
Hard X-Rays
Hα+3Å
Hα-3Å
5000Å Continuum
FLUX (ARBITRARY UNITS)
14.88
14.90
14.92
14.94
14.96
14.98
15.00
TIME (UT)

Magnetograph Observations of AR5395 from NSO/Kitt Peak

Harrison P. Jones

NASA/GSFC, Laboratory for Astronomy and Solar Physics
Southwest Solar Station/NSO

Full disk magnetograms containing all or portions of AR5395 were observed daily (except March 6) from March 4 - March 19. A sequence of magnetograms of the active region is shown in the following figure. Time sequences of area-scan magnetograms of AR5395 were obtained on March 9,10,12,15, and 17. Although interesting phenomena may sometimes be seen on magnetograms in apparent association with flares, they are not distinct signatures of flare activity and cannot be used to derive a useful event list. However, one sequence obtained by Braun and Duvall on March 10th (approx 19:00UT) shows a rare record of a flare which appears in magnetic, velocity, and intensity data, presumably as a result of the FeI 8688 line going into emission. This data is undergoing further analysis.

ORIGINAL PAGE
BLACK AND WHITE PHOTOGRAPH

BBSO Coverage of AR5395

H. Zirin

Big Bear Solar Observatory/Caltech

BBSO observed AR 5395 every day during its disk passage March 6 to March 17.

* Flares observations were made in: Centerline H alpha
  H alpha - 0.6A
  He D3

* The following major flares of the region were observed at BBSO

Date	Time(max)	Class(From PSGD)	Remarks
March 6	1410	X15/3	after 1550UT
7	0002	/1	
	2232	M4/2	from 2233UT
9	1532	X4/4	
	1925	M1/1	
	2324	M1/1	
	2354	M2	
10	1736	M1/S	
	1912	X5/3	
11	1837	M1/1	
	1940	X1/2	
12	0029	M7/2	
	2040	M6/2	
14	1726	X1/2	
	2036	M1/S	
15	1653	M8/2	
16	1526	X4/2	
	1915	M7/1	
	2040	X1/1	
17	1737	X7/2	

Other data include:

* Longitudinal magnetograph observation of the region Mar.7 - 16
* Transeverse magnetic field observation of the region Mar.8 - 15
* Daily Dopplergram observation of the region
* Full disk observation in H alpha

Owens Valley Observations of AR 5395

G. Hurford

Caltech/OVRO

COVERAGE:	1989 March 6-10,12-16	2-element	365 m	EW baseline
	1989 March 17-20	3-element	365, 577, 942 m	EW baselines

HOURS: 1600-2400 UT

DATA TYPE: Frequency-agile interferometry (fully calibrated)
25 frequencies from 1-18 GHz, Stokes I
2.5 second time resolution

APPLICATIONS:
- Diagnostics of impulsive phase electron and field parameters
- Diagnostics of thermal flare plasma and field parameters
- 1-dimensional spatial structure of microwave bursts
- Evolution and configuration of coronal magnetic fields

DATA CUBE:

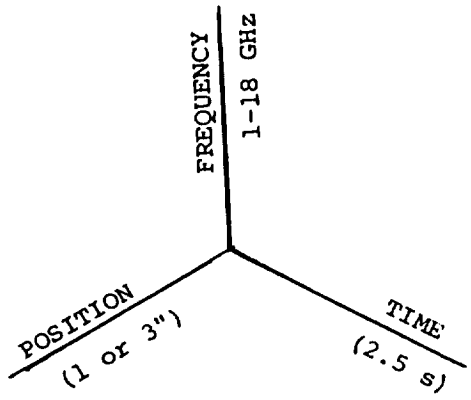

Contact: Gordon Hurford (818)356-3866 SUNDOG::GH (SPAN)
OR Dale Gary (818)356-3863 DG@SUNDOG.EDU

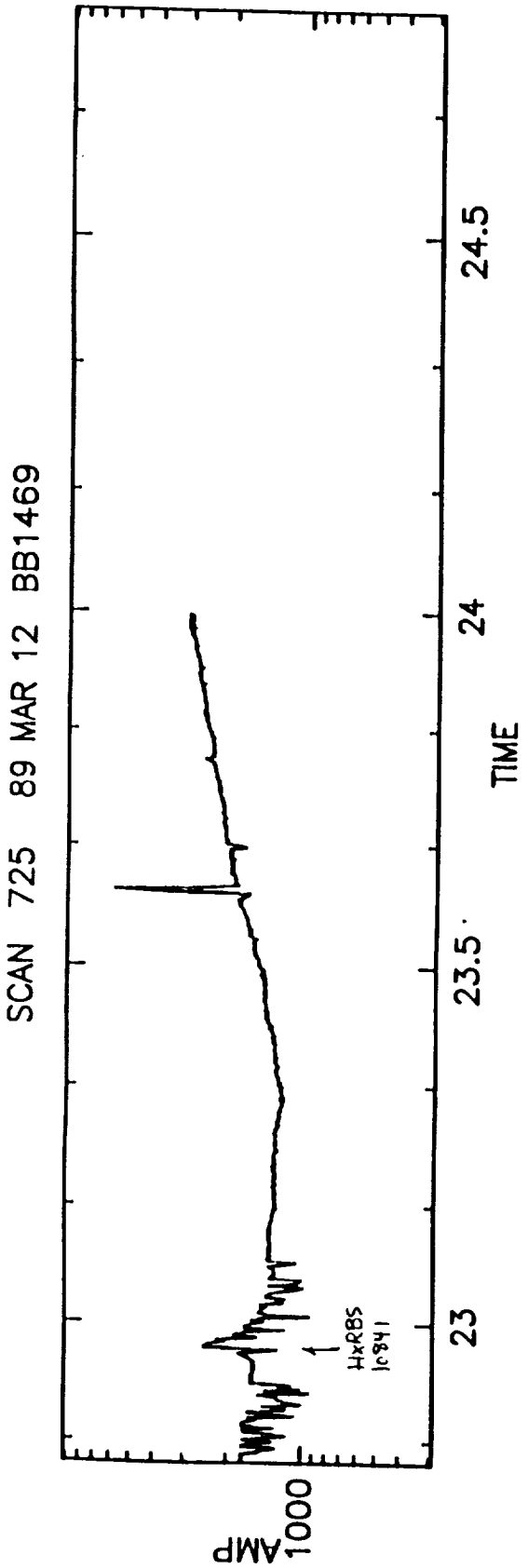
SCAN 725 89 MAR 12 BB1469
AMP
1000
23
23.5
24
24.5
TIME
1
HxRBS
Ic841

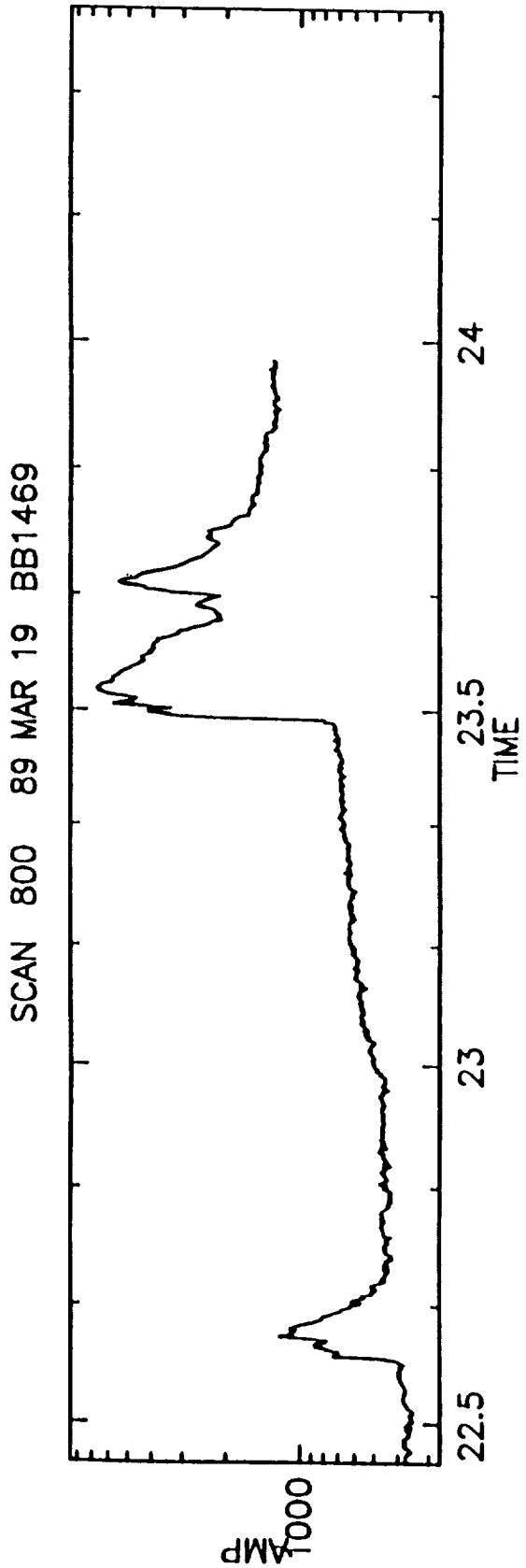
SCAN 800 89 MAR 19 BB1469
AMP
1000
22.5
23
23.5
24
TIME

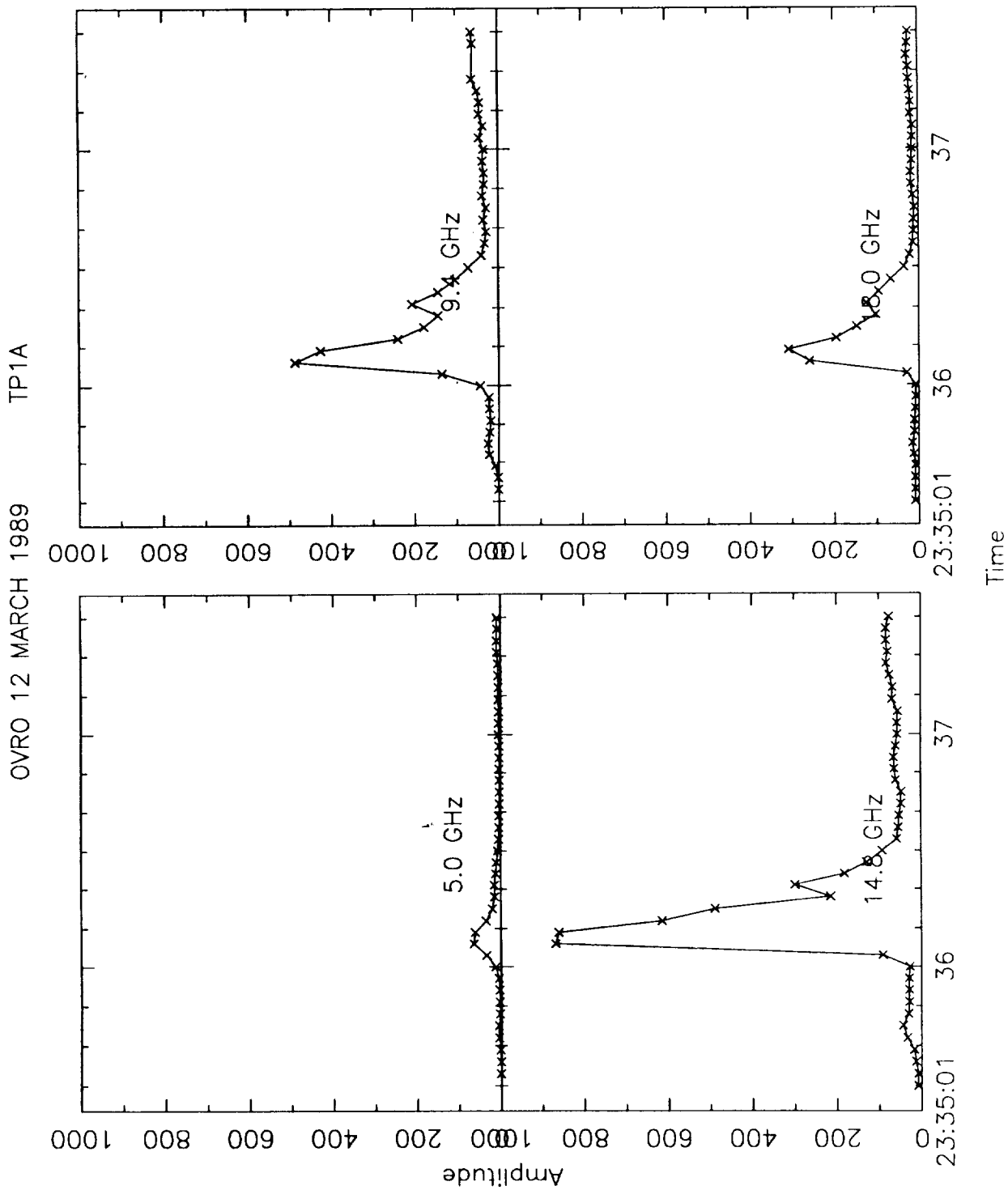
OVRO 12 MARCH 1989
TP1A
Amplitude
Time
5.0 GHz
9.4 GHz
14.8 GHz
18.0 GHz
0
200
400
600
800
1000
23:35:01
36
37

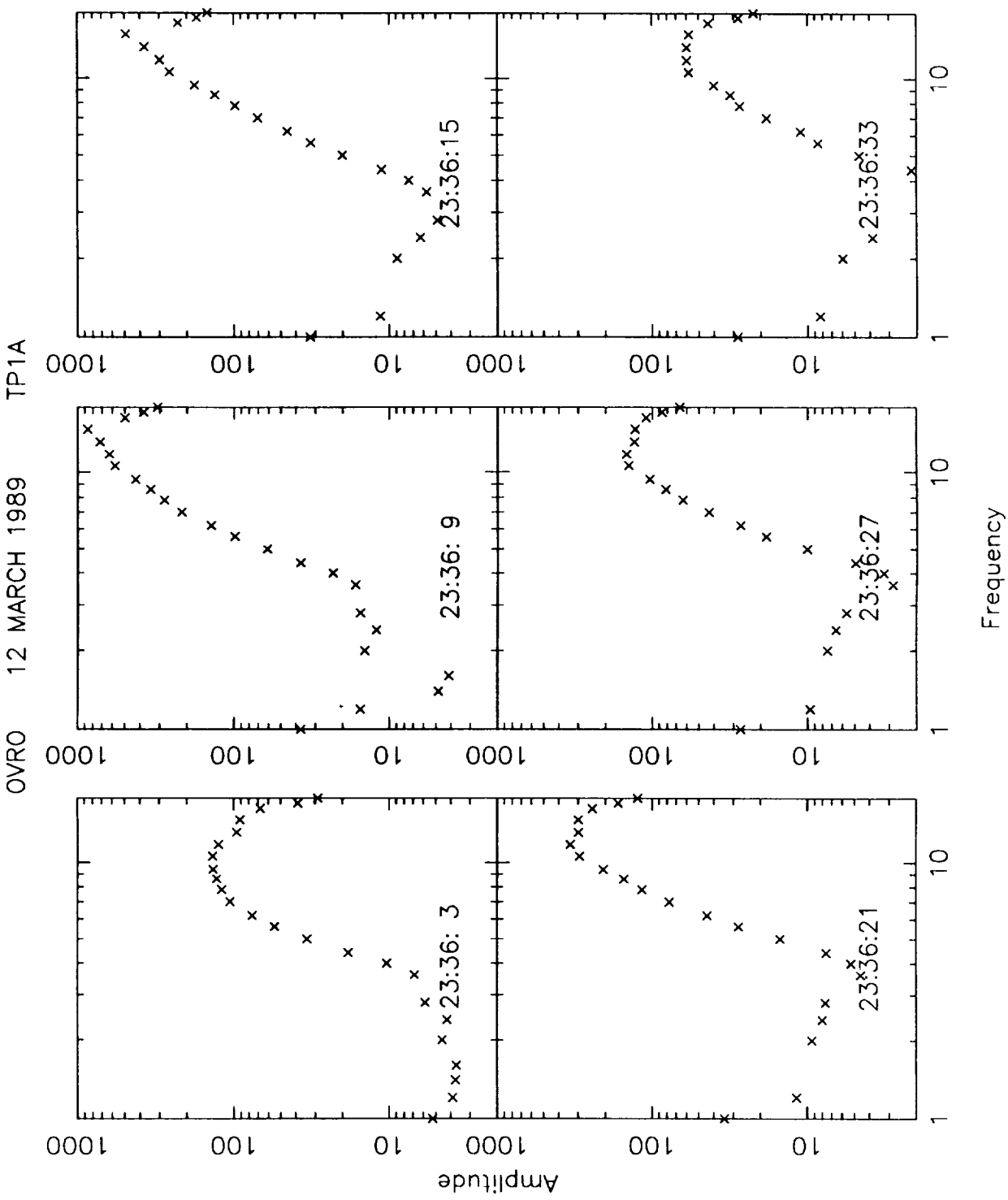
OVRO 12 MARCH 1989 TP1A
Amplitude
Frequency
23:36: 3
23:36:21
23:36: 9
23:36:27
23:36:15
23:36:33

Flare list from Active Region 5395 (BB1469)

Legend: NR = flare not reported
--- = flare reported, but no X-ray class given

Date	Time	OVRO pk*	X-ray Class	Comments
Mar 7	2004	400	C2.5	Region?
	2106	12000	C3.6	Other region
	2120	800	C9.2	
	2144	900	NR	
	2223	10000	M4.2	
Mar 8	1653	700	NR	
	1858	18000	M4.6	Nice multi-spike
	2050	1000	---	SF in H-alpha
	2126	1600	---	SF/other region
	2143	700	---	SF/other region
Mar 9	-- extremely windy. No good data --			
Mar 10	1648	8000	NR	Good, but unreported?
	1736	2500	M1.1	Windy?
	1900	200000	X4.5	Grand-daddy event
Mar 11	-- no observations (wind) --			
Mar 12	1619	7000	M1.8	
	1647	10000	NR	Spikes. Not real?
	1907	3300	C6.0	Very gradual event
	1936	3300	NR	Spike. Not real?
	2037	80000	M6.3	Long duration, many spikes
	2219	11000	---	SF/lots of radio
	2337	6000	M1.4	VERY narrow spike!
Mar 13	1737	3300	M1.5	
	1842	6000	---	SF/other region
	2117	3000	---	SF, three peaks
	2304	20000	M1.2	Lists one event, but many spikes
Mar 14	1724	300000	X1.1	Broad, interesting event
	1855	2100	NR	Little spikes
	2035	3000	M1.4	Very broad, broken by cal scan
	2221	1800	---	SF/Single spike
Mar 15	1623	3000	NR	Tiny spike
	1652	160000	M8.4	Beautiful spike and decay
	1924	1400	---	SF/other region
	2002	4000	C3.7	Nice, but other region
	2053	2000	NR	Chaotic, real?
Mar 16	1613	5000	NR	Real?
	1752	4200	M2.4	Radio delayed from H-alpha pk.
	1915	2600	M6.5	Small, gradual event
	2040	5000	X1.4	Small, gradual, but nice
	2207	1500	M1.6	Little spikes
	2247	1800	NR	Decay of something
	2317	4500	C8.2	
---------- Start 3-element observations ----------				
Mar 17	2337	3100	M2.4	Caught last part?
Mar 18	1732	17000	M4.4	Nice, 3-element + other region?
	1921	500	NR	Gradual increase
	2030	900	M3.3	Small event
	2157	11000	M3.1	Nice, 3-element event
	2302	2300	---	SF/other region
Mar 19	1804	800	NR	
	1917	530	NR	
	2237	1200	M3.1	Region?
	2331	6800	NR	Big event, but no report?
Mar 20	1749	320	NR	
	1856	700	---	SF/other region?

* Arbitrary units

RSTN Observations of the 06 and 10 March 1989 Solar Flares

E. W. Cliver
Geophysics Laboratory
Hanscom AFB, Massachusetts 01731 USA

L. C. Gentile
Emmanuel College Physics Research Division
400 The Fenway
Boston, Massachusetts 02115 USA

Radio Solar Telescope Network

The Radio Solar Telescope Network (RSTN) is operated by the Air Weather Service of the U.S. Air Force. RSTN stations are located at Sagamore Hill (Massachusetts), Palehua (Hawaii), Learmonth (Australia), and San Vito (Italy). The RSTN stations monitor the quiet and disturbed Sun at eight fixed frequencies logarithmically spaced from 245 - 15,400 MHz. The radiometer patrols are operated from sunrise to sunset. Data are stored on magnetic tape with one second time resolution and archived at the World Data Center A for Solar-Terrestrial Physics in Boulder, Colorado, for dissemination to the scientific community. The Palehua site became operational in July 1980, followed by Learmonth in August 1980, Sagamore Hill in October 1981, and San Vito in September 1986.

Time-Intensity Profiles

RSTN observations from Sagamore Hill Observatory for the 06 and 10 March 1989 solar flares are presented in Figures 1 and 2, respectively. For both events, the pre-event background (quiet-sun-flux) value was subtracted from the radiometer output at each frequency and every tenth second of the resulting burst was plotted. For the 06 March event, the background was determined from a 60 second average from 1310 to 1311 UT; for the 10 March event, the corresponding time was 1830 to 1831 UT.

Discussion

The 06 and 10 March 1989 microwave bursts are notable for their high peak flux densities (Sp). Inspection of lists of large microwave bursts from visible disk flares for the period 1965-1979 (Cliver, McNamara, and Gentile 1985) and gamma-ray-line/proton flares for the years 1980-1984 (Cliver et al. 1989) reveals only a handful of events with averaged reported values of Sp(10 GHz) > 15,000 solar flux units (sfu). Such events occurred on 23 May 1967 (27,000 sfu), 04 August 1972 (18,000 sfu), 07 August 1972 (16,000 sfu), 12 October 1981 (19,500 sfu), 07 December 1982 (24,500 sfu), and 25 April 1984 (20,500 sfu). An additional large burst with Sp(10 GHz) > 25,000 sfu occurred in association with the well-known limb flare of 30 March 1969 (Badillo and Salcedo 1969; Frost and Dennis 1971).

Comparison of the time-intensity profiles at frequencies $\geq$ 1,415 MHz in Figures 1 and 2 shows a similar temporal evolution, suggesting homology. For both events, an impulsive phase is followed by an extended gradual phase. The smooth profiles during the gradual phase of these events probably

result from electron trapping (Cliver et al. 1986; Kosugi, Dennis, and Kai 1988) and the details of the acceleration process are lost. Hard X-ray profiles are ostensibly less affected by electron trapping and thus comparison of the > 20 keV histories for these events should give a better indication of the degree of similarity in flare development.

We thank Kurt Lutz of World Data Center A for providing the Sagamore Hill data for these events.

References

Badillo, V. L., and Salcedo, J. E.: 1969, Nature, 224, 503.
Cliver, E. W., McNamara, L. F., and Gentile, L. C.: 1985, AFGL-TR-85-0180.
Cliver, E. W., Dennis, B. R., Kiplinger, A. L., Kane, S. R., Neidig, D. F., Sheeley, N. R., Jr., and Koomen, M. J.: 1986, Ap. J., 305, 920.
Cliver, E. W., Forrest, D. J., Cane, H. V., Reames, D. V., McGuire, R. E., von Rosenvinge, T. T., Kane, S. R., and MacDowall, R. J.: 1989, Ap. J. (in press).
Frost, K. J., and Dennis, B. R.: 1971, Ap. J., 165, 655.
Kosugi, T., Dennis, B. R., and Kai, K.: 1988, Ap. J., 324, 1118.

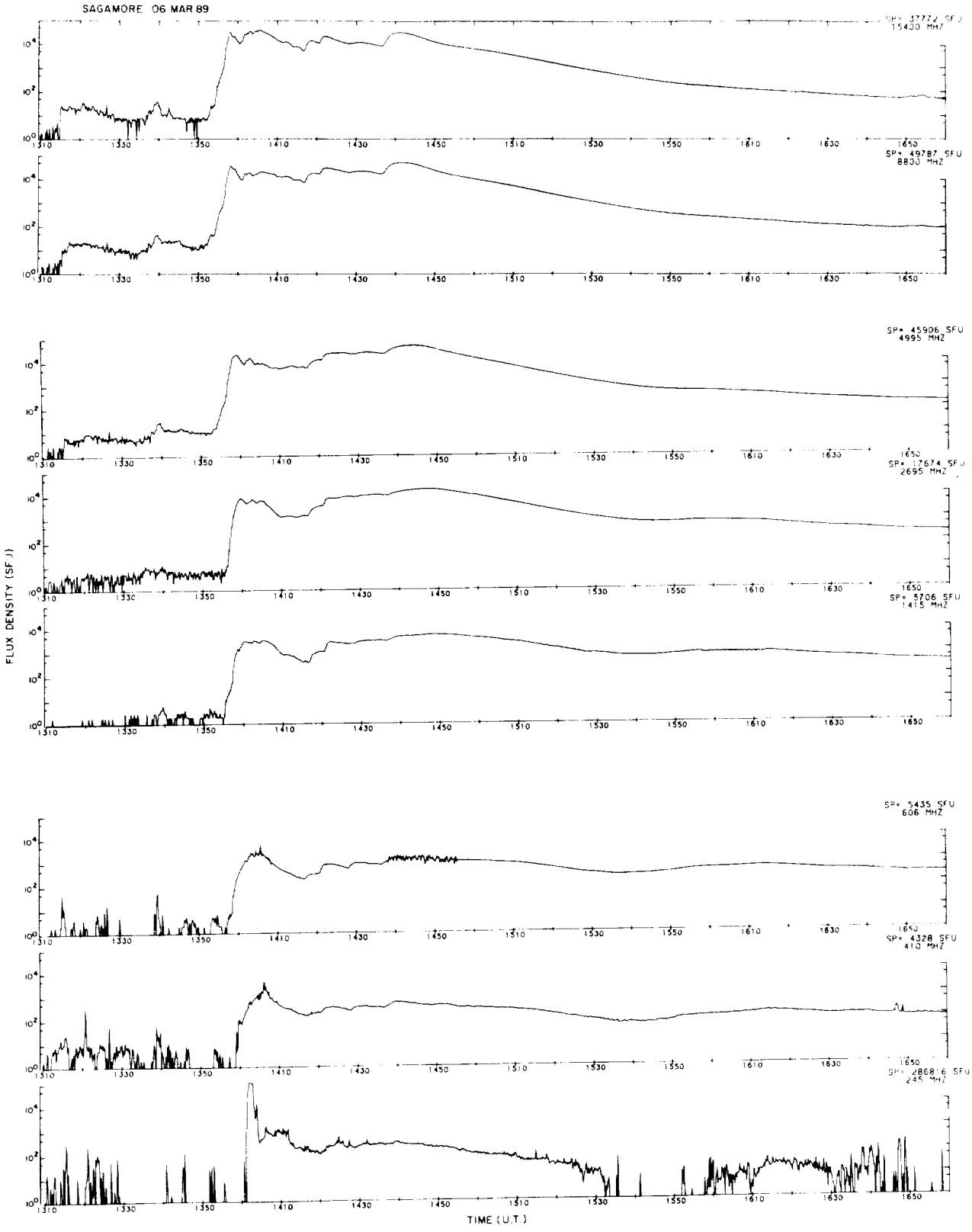

Fig. 1 Sagamore Hill observations of the large microwave burst on 06 March 1989.

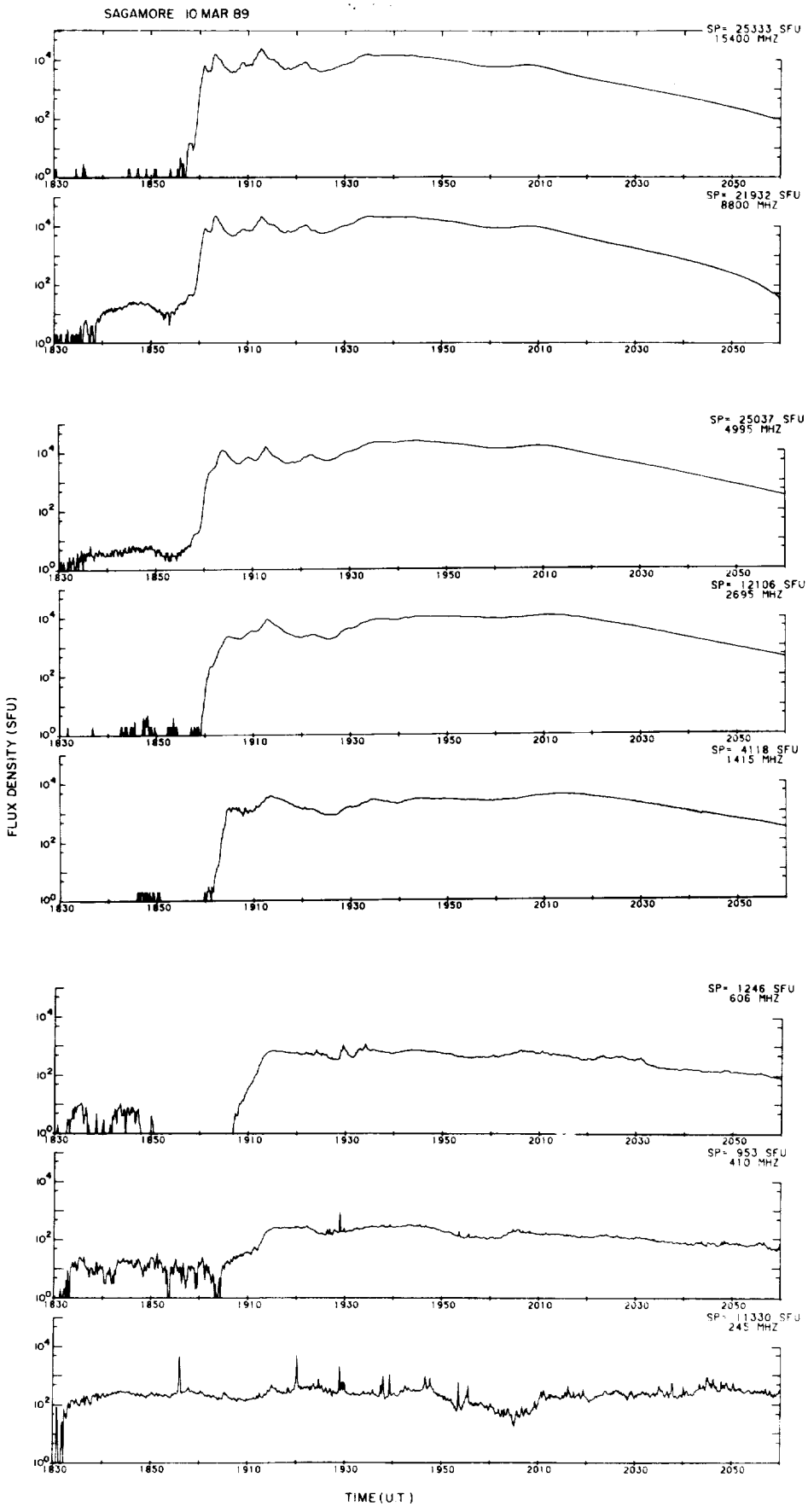

Fig. 2 Sagamore Hill observations of the large microwave burst on 10 March 1989.

Investigation of Active Regions at High Resolution by Balloon Flights of the Solar Optical Universal Polarimeter (SOUP)

T. Tarbell, Z. Frank, C. Gilbreth, R. Shine, A. Title,
K. Topka, J. Wolfson (Lockheed Palo Alto Research Labs)

SOUP is a versatile, visible-light solar observatory, built for space or balloon flight. It is designed to study magnetic and velocity fields in the solar atmosphere with high spatial resolution and temporal uniformity, which cannot be achieved from the surface of the earth. The SOUP investigation is carried out by the Lockheed Palo Alto Research Laboratory, under contract to NASA's Marshall Space Flight Center. Co-investigators include staff members at a dozen observatories and universities in the US and Europe.

The primary objectives of the SOUP experiment are:

(1) To measure vector magnetic and velocity fields in the solar atmosphere with much better spatial resolution than can be achieved from the ground;

(2) To study the physical processes that store magnetic energy in active regions and the conditions that trigger its release;

(3) To understand how magnetic flux emerges, evolves, combines, and disappears on spatial scales of 400 to 100,000 km.

SOUP is designed to study intensity, magnetic, and velocity fields in the photosphere and low chromosphere with 0.5 arcsec resolution, free of atmospheric disturbances. The instrument includes: a 30 cm Cassegrain telescope; an active mirror for image stabilization; broadband film and TV cameras; a birefringent filter, tunable over 5100–6600 Å with 0.05 Å bandpass; a 35 mm film camera and a digital CCD camera behind the filter; and a high-speed digital image processor. The filter bandpass is narrow enough to resolve the absorption lines in the solar spectrum, and therefore measurements of line profiles can be made over the entire field-of-view from sets of filter images. The lines available using the tunable filter include Hα, He D3, Na D1, Mg b, and several Fe I lines for magnetic and Doppler measurements. An analyzer allows precise measurement of circular and linear polarization for making longitudinal and transverse magnetograms. In addition, images spaced at intervals across the Hα line show the paths of chromospheric fibrils, allowing the connectivity of magnetic field lines to be inferred. The broadband frames are used to measure transverse velocities; thus

the flow patterns which shear the magnetic fields of an active region can be measured independently of the fields themselves.

SOUP flew on the shuttle Spacelab 2 mission in August, 1985, and one day of observing time was available for SOUP during the flight, during which 6000 frames of diffraction-limited white light data were collected. A second shuttle flight on the Sunlab mission was planned, but this has been cancelled following the "Challenger" disaster. High-resolution imaging on balloon flights was achieved by Project Stratoscope in the late 1950's, and has been exploited since then by German, Russian, and Japanese groups for additional white light studies. Balloon flights of SOUP will produce our first views of active region magnetic fields at resolution approaching the size of the basic flux tubes themselves.

As of July, 1989, the project has just begun a four-month definition phase. The gondola and solar pointing system will be provided by NASA and their specification is under way. If NASA approval and funding for flight are forthcoming at the end of this phase, then the first flight could still take place in 1991.

This project is supported by NASA Contract NAS8-32805 (SOUP). Development of the CCD camera has been supported by NASA Contract NAS5-26813 (CIP for OSL). Data analysis is also supported by the Lockheed Independent Research Fund.

INSTRUMENT SUMMARY

TELESCOPE

Aperture	30 cm
Type	f/15 Cassegrain
Wavefront Quality	0.06 waves rms at 6328 Å
Spatial Resolution	0.5 arcsec

COARSE POINTER (offset pointing and drift compensation)

Range	±40 arcmin
Slew Rate	30 arcsec/s
Drift Compensation Rate (peak)	1 arcsec/s

FINE GUIDER (jitter compensation)

Range	±15 arcsec
Servo Sensor	4 photodiode limb sensors on movable mounts
Servo Actuators	Secondary mirror on PZT mounts
Residual Jitter	< 0.01 arcsec rms

BROADBAND IMAGING SYSTEM

Focal Length	1800 cm (f/60)
Field of view: film	168 × 260 arcsec
video	103 × 138 arcsec
Wavelength Band	5000 – 5500 Å
Typical exposure time	0.10 sec

TUNABLE FILTER IMAGING SYSTEM

Focal Length	2700 cm (f/90)
Field of view: CCD	72 × 72 or 143 × 143 arcsec (selectable)
film	138 × 183 arcsec
video	same as CCD
Wavelength Band	5100 – 6600 Å
Typical exposure time	0.5 – 2 sec

TUNABLE FILTER

Universal birefringent filter, alternate partial polarizer design

Bandpass: 5200 Angstroms	50 or 80 mÅ (selectable)
6500 Angstroms	78 or 128 mÅ
Wavelength Reference	HeNe Laser (6328 Å)
Polarization analyzers	RCP, LCP, 4 linear orientations
Spectral prefilters	8 regions, 7 – 10 Å wide

TUNABLE FILTER CCD CAMERA

Sensor Type	1024 × 1024 18 micron pixel CCD
Image Format	512 × 512 pixels, 12 bits/pixel
Readout Time	0.6 sec
Full Well	200,000 electrons
Photometric Accuracy (1 read)	300:1 or 600:1

TUNABLE FILTER SPECTRAL LINES

Continuum	Temperature, Horizontal Flows
Fe I 5250 Å	Magnetic Field Strength
Fe I 5247 Å	Magnetic Field Strength
Fe I 5576 Å	Doppler Shifts (g=0)
Fe I 6302 Å	Vector Magnetograms
Ni I 6768 Å	Doppler Shifts (GONG & SOI Line)
Mg I 5173 Å	Magnetograms, Dopplergrams
Na I 5896 Å	Magnetograms, Dopplergrams
Hα 6563 Å	Chromospheric Morphology, Flows, Flares
He I 5876 Å	Chromospheric & Coronal Morphology, Flares

FIGURE CAPTIONS

Figure 1. SOUP instrument: telescope, focal plane package, and flight computer.

Figure 2. SOUP telescope and focal plane package optical/mechanical schematic.

Figure 3. SOUP tunable birefringent filter.

Figure 4. 1024 $\times$ 1024 pixel brassboard CCD camera.

Figure 5. Broadband and tunable filter system schematics.

Figure 6. Data flow diagram for SOUP CCD and film observations.

ORIGINAL PAGE
BLACK AND WHITE PHOTOGRAPH

SOLAR OPTICAL UNIVERSAL POLARIMETER
OPTICAL/MECHANICAL SCHEMATIC

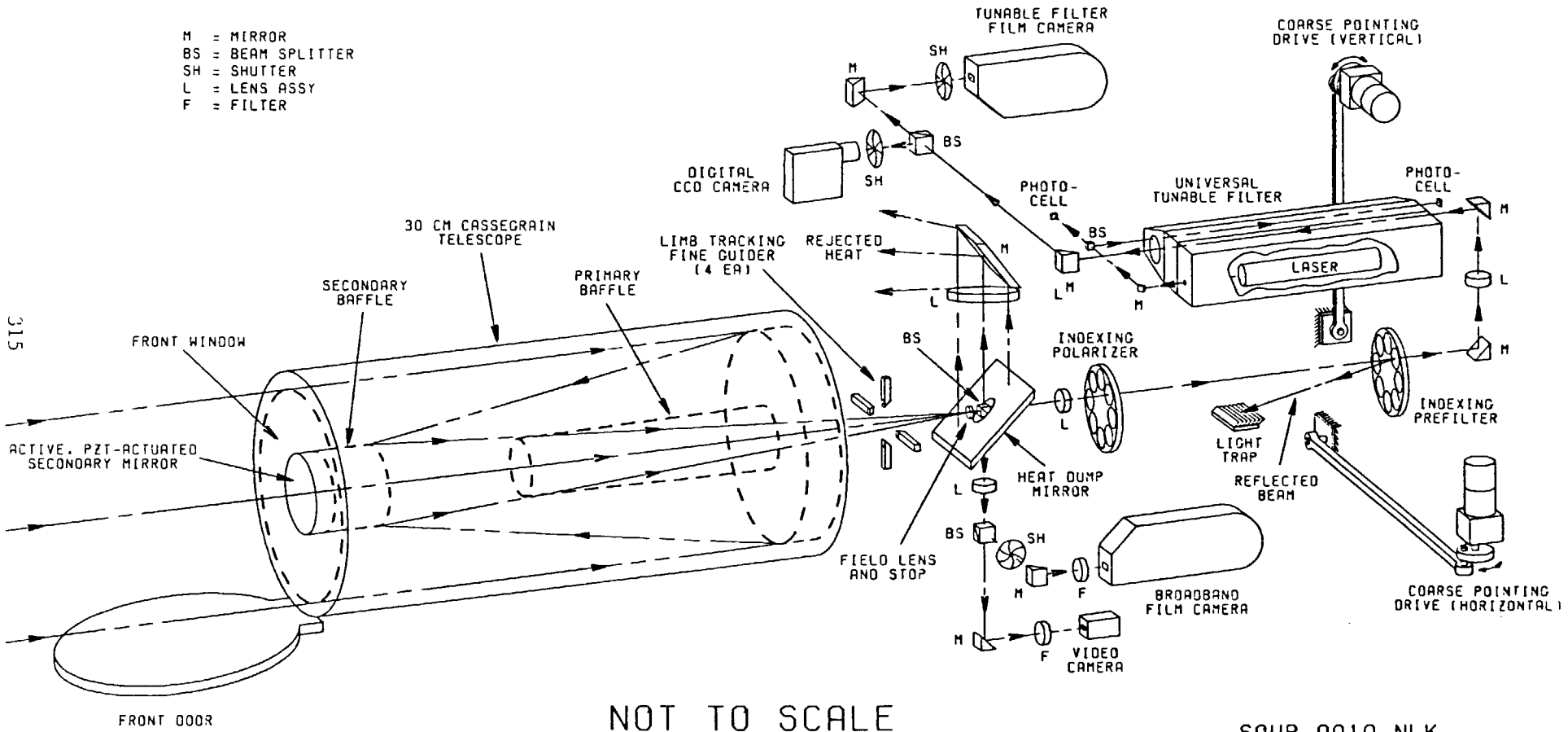

NOT TO SCALE

SOUP 0010 NLK
NOAH KATZ 20 JUL 88
REV DATE 21 JUL 88

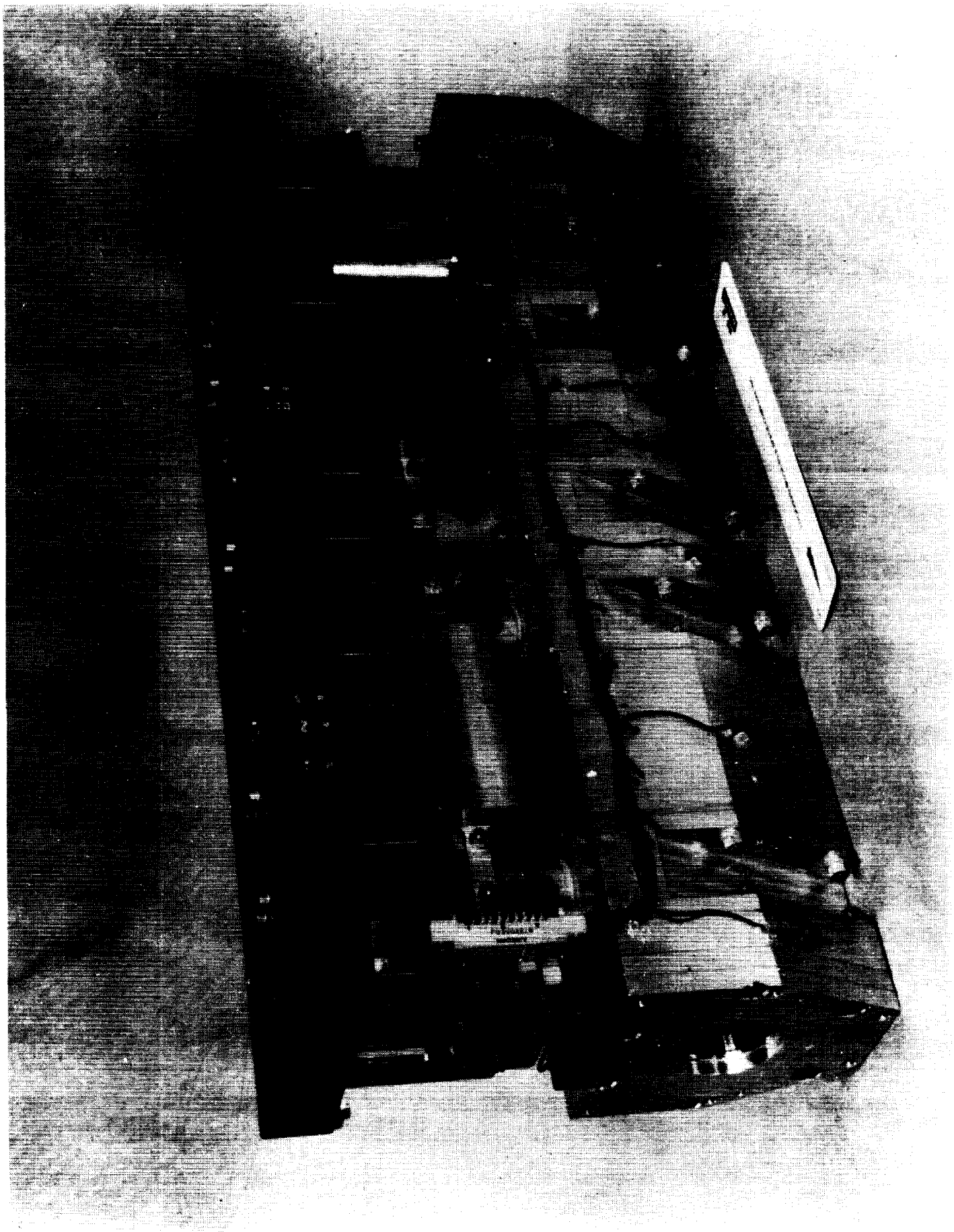

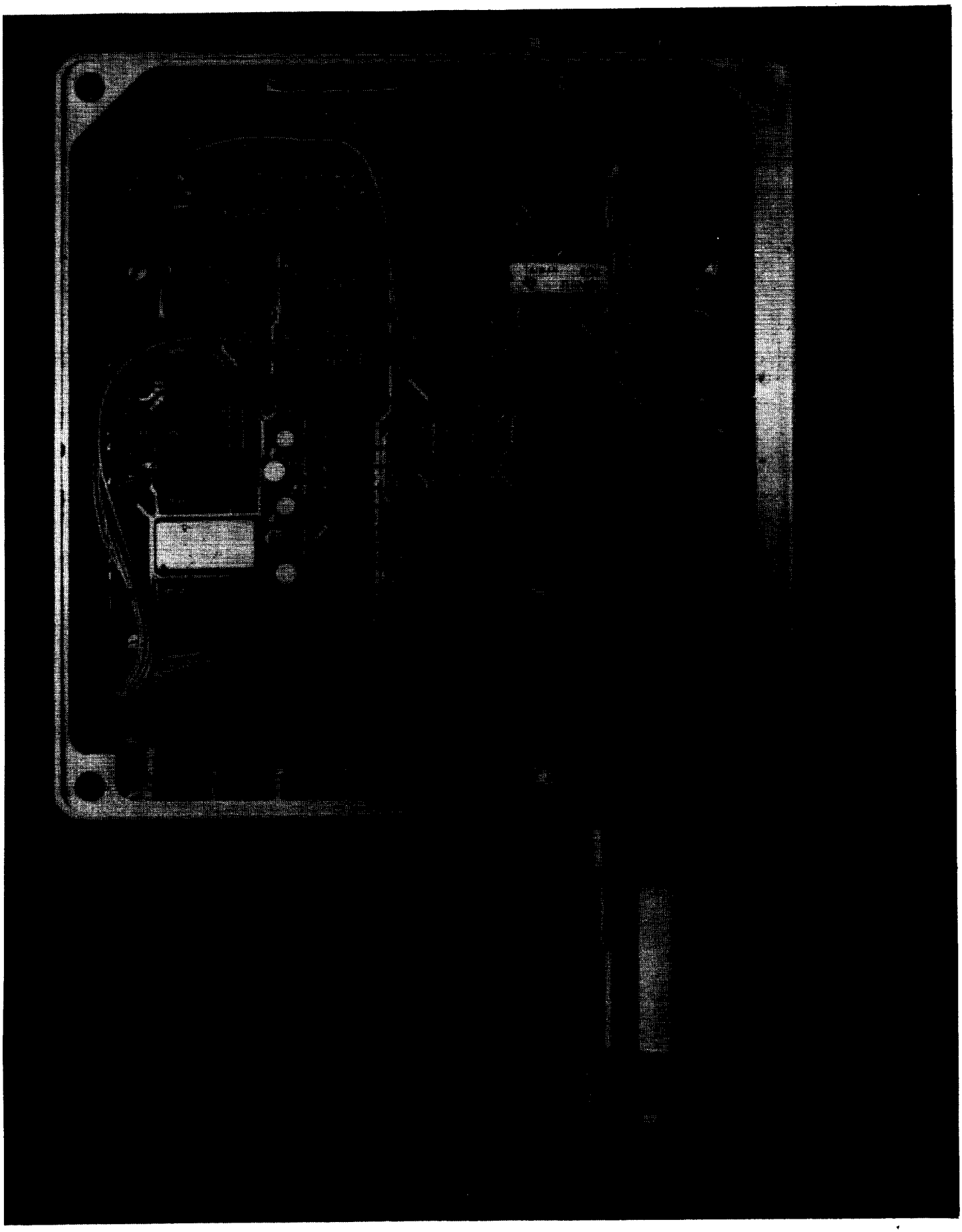

SOUP OPTICAL/MECHANICAL SCHEMATICS

BROADBAND

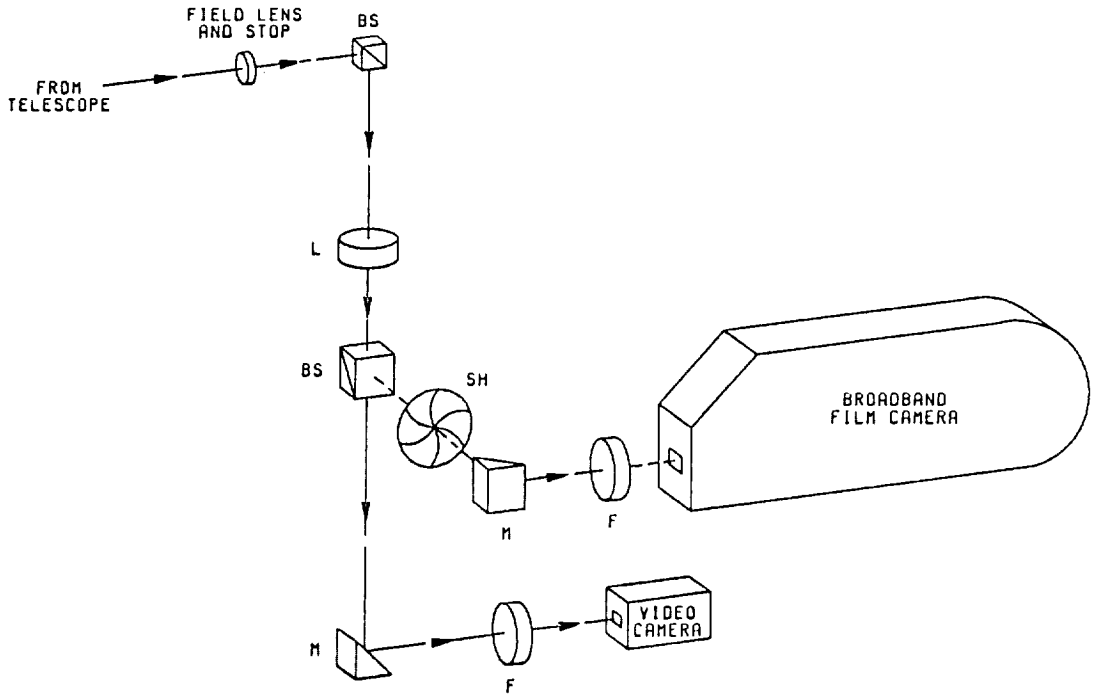

TUNABLE FILTER

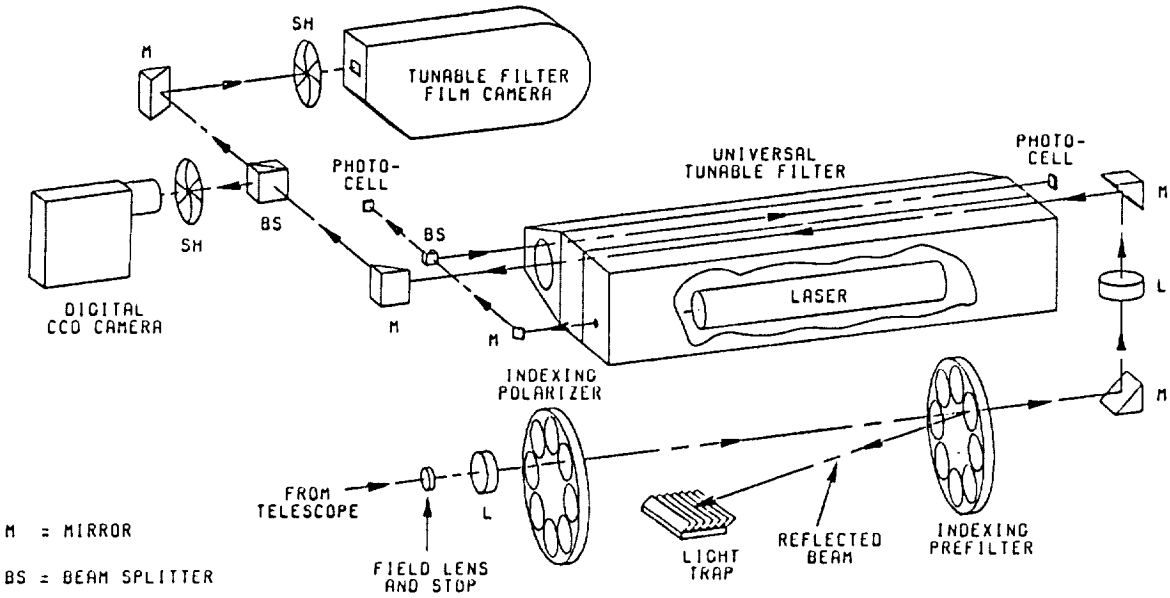

M = MIRROR

BS = BEAM SPLITTER

SH = SHUTTER

L = LENS ASSY

F = FILTER

NOT TO SCALE

SOUP 0013 NLK
NOAH KATZ 25 JUL 88
REV DATE 26 JUL 88

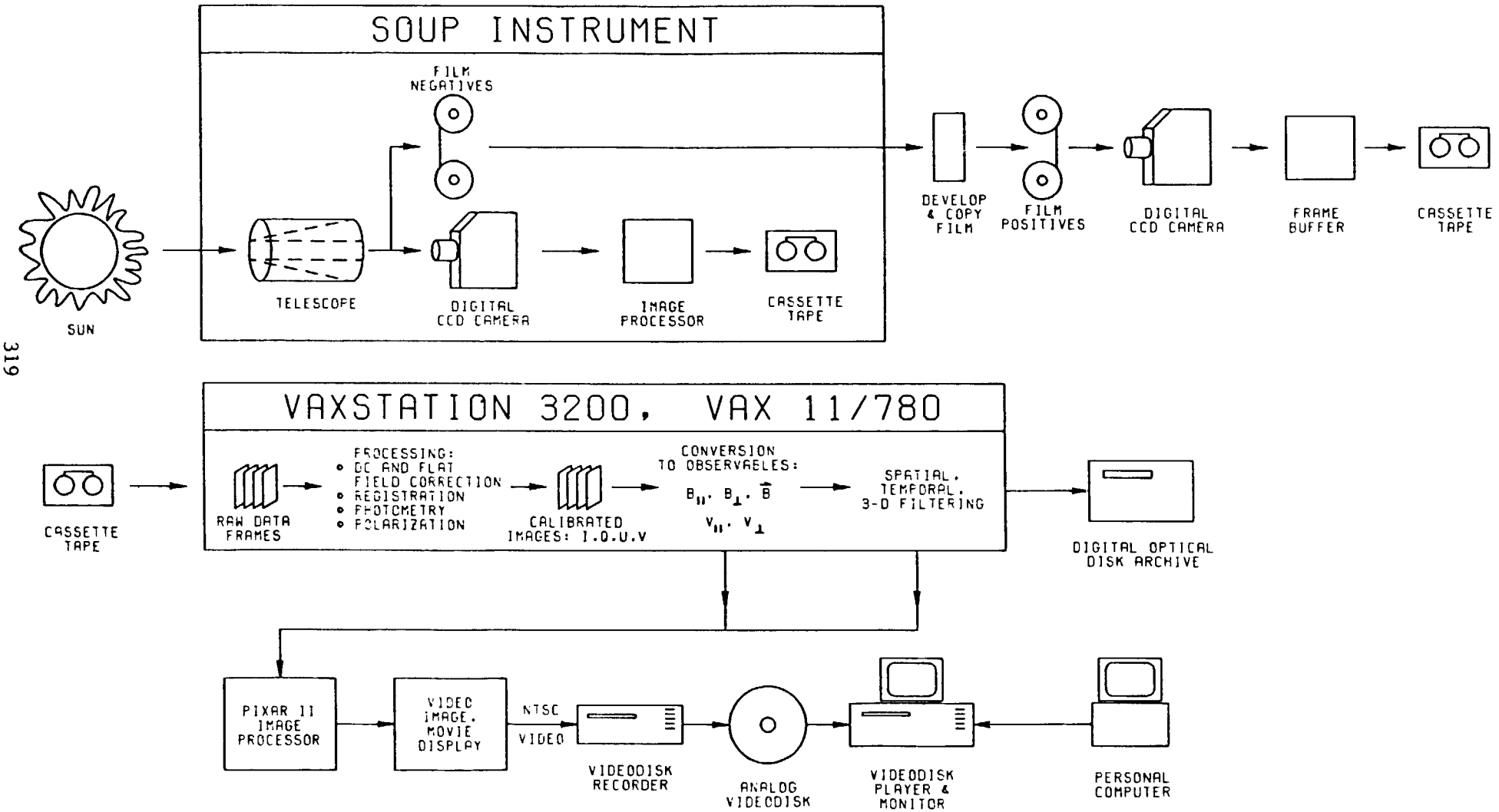
SOUP INSTRUMENT
FILM NEGATIVES
SUN
TELESCOPE
DIGITAL CCD CAMERA
IMAGE PROCESSOR
CASSETTE TAPE
DEVELOP & COPY FILM
FILM POSITIVES
DIGITAL CCD CAMERA
FRAME BUFFER
CASSETTE TAPE
VAXSTATION 3200, VAX 11/780
CASSETTE TAPE
RAW DATA FRAMES
PROCESSING:
• DC AND FLAT FIELD CORRECTION
• REGISTRATION
• PHOTOMETRY
• POLARIZATION
CALIBRATED IMAGES: I,Q,U,V
CONVERSION TO OBSERVABLES:
$B_{\parallel}$, $B_{\perp}$, $\vec{B}$
$V_{\parallel}$, $V_{\perp}$
SPATIAL, TEMPORAL, 3-D FILTERING
DIGITAL OPTICAL DISK ARCHIVE
PIXAR II IMAGE PROCESSOR
VIDEO IMAGE, MOVIE DISPLAY
NTSC
VIDEO
VIDEODISK RECORDER
ANALOG VIDEODISK
VIDEODISK PLAYER & MONITOR
PERSONAL COMPUTER

THE ONSET OF THE SOLAR ACTIVITY CYCLE 22

H.S. Ahluwalia
Department of Physics and Astronomy
The University of New Mexico
Albuquerque, New Mexico 87131

INTRODUCTION

There is a great deal of interest in being able to predict the main characteristics of a solar activity cycle (SAC). One would like to know, for instance, how large the amplitude (R_m) of a cycle is likely to be, i.e., the annual mean of the sunspot numbers at the maximum of SAC. Also, how long a cycle is likely to last, i.e., its period. It would also be interesting to be able to predict the details,like how steep the ascending phase of a cycle is like to be. Questions like these are of practical importance to NASA in planning the launch schedule for the low altitude, expensive spacecrafts like the Hubble Space Telescope, the Space Station, etc. Also, one has to choose a proper orbit, so that once launched the threat of an atmospheric drag on the spacecraft is properly taken into account. A reboost schedule may also have to be planned for an existing spacecraft threatened by an enhanced atmospheric drag which increases as the solar activity rises. The frequency of reboosts, and the corresponding high accompanying costs, depends upon the amount of drag expected with the rise in the solar activity. For the purpose of proper planning, one would like to have an advance warning of two to three years.

Waldmeier (1935) probably made the first attempt at understanding the behavior of the SAC when he discovered that the steepness of the ascending phase (rise time) of the SAC appears to correlate well with its amplitude, R_m. The steeper the rise, the larger the R_m and vice versa. He also found that even cycles seem to have less steep rise and therefore smaller R_m, whereas odd cycles have a steeper rise and therefore a larger value of R_m. Waldmeier even derived mathematical relations between R_m and the rise time of the odd and even cycles. Attempts have been made to improve Waldmeier's approach (Xanthakis, 1967; Wilson, 1988 and references therein).

In recent times prediction models have been developed based on quasi-physical plausibility arguments. These models rely on a precursor physical signature at the minimum in the previous SAC, such as the geomagnetic and the auroral activity (Kane, 1978) and the solar polar field (Schatten et al., 1978). The methods in this class tend to give a higher value for R_m (Brown and Simon, 1986).

In this paper we explore the possibility of using cosmic ray data for making general predictions about the characteristics of the SAC 22.

DATA AND DISCUSSION

It has been known for many years that an inverse correlation exists between the cosmic ray intensity, at a given site, and the solar activity cycle (Forbush, 1966). The precise physical cause for this long-term modulation of the cosmic ray intensity is not known yet. In recent times, arguments have been advanced that observed 11-year variation may be produced by interacting regions in solar wind (Burlaga et al., 1985), charged particle drifts (Kota and Jokipii, 1983 and references therein), tilt of the heliospheric neutral current sheet (Smith and Thomas, 1986), magnetic helicity (Bieber et al., 1987) and quite possibly by all the processes listed above and some not yet discovered. The reader is referred to an

excellent review on this subject by McKibben (1988). Solar polar fields also appear to play a role in influencing the observed features of the modulation (Ahluwalia, 1980; Jokipii and Kota, 1989).

In Figure 1 we have plotted monthly mean hourly counting rates obtained with a neutron monitor (NM) at Huancayo (Peru) and Deep River (Canada). The median primary rigidities of response for the two detectors are 30 GV and 15 GV respectively. Monthly mean international sunspot numbers (R_i) are also plotted. Data for R_i and Deep River NM cover a period of 30 months from January 1987 to June 1989. Data for Huancayo NM are not yet available for the period March to June 1989. The scale for NM data gives the percent decrease in intensity from maximum intensity observed in March 1987. The following features may be noted.

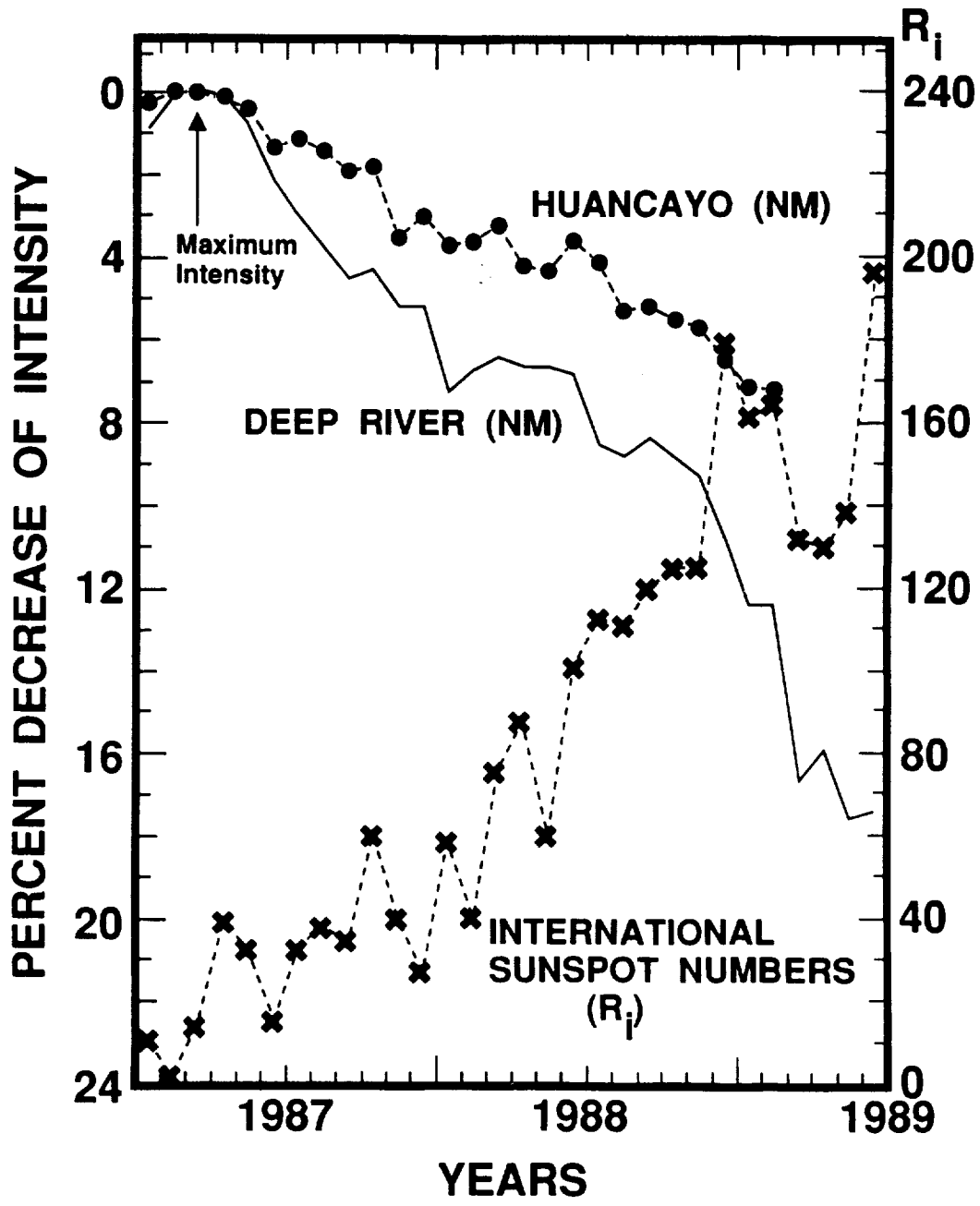

Figure 1.

1) The counting rate for the two neutron monitors decreases continuously after March 1987, as the monthly mean value of the sunspot numbers increases. So an inverse correlation exists between R_i and cosmic ray data. Note that the overall value of R_i increases in a zig-zag manner. The most prominent pulse-like increases in R_i occur in December 1988 and June 1989. However, the counting rate for the Deep River NM keeps going down continuously during this period. For example, the value of R_i in April 1989 is not much different from that in November 1988 but the Deep River NM counting rate has decreased by 6.7%!

2) The counting rates for both monitors begin to decrease simultaneously but the decrease for Deep River NM is steeper. One should also note that the maximum intensity level is attained more rapidly by Huancayo NM. Moreover, the minimum in R_i is reached in June 1986 (not shown) while the counting rates do not recover completely until eight to nine months later. This behavior is typical of cosmic ray modulation (Simpson, 1962).

3) The monthly mean hourly counting rate for June 1989 for the Deep River NM has decreased to a level 17.5% below its level in March 1987. Also note that the value of R_i for June 1989 is 196, the highest observed so far in SAC 22. We may compare this situation with that available in previous activity cycles 21 and 20. For SAC 21, the largest decrease observed at Deep River was 17.9% in September 1982 with respect to the level in September 1976, i.e., the decrease took place over a period of six years. The largest monthly mean value for R_i of 224.3 was observed in October 1981. Similarly during SAC 20, the largest observed decrease of 13.7% at Deep River occurred in June 1969 below the level in April 1965. The largest value for R_i was 135.8 in March 1969. It is clear therefore that activity observed in SAC 22 so far has already exceeded that in SAC 20 and is very close to that observed in SAC 21. Note that the maximum value of R_i has not yet been reached in the present SAC. From cosmic ray data it is clear that SAC 22 is likely to be even more active than SAC 21, although we can't predict yet what the value of R_m will be. This is because quantitative relationships have not yet been established between the cosmic ray data and R_i. But the approach of using cosmic ray data for prediction purposes looks very encouraging. In particular it should be pointed out that after June 1987 it was clear to me that solar activity minimum had already occurred in 1986. It should be emphasized that the observed decrease in Deep River NM counting rate is already close to maximum decrease observed in SAC 21. This decrease has taken place in a very short interval of time (30 months).

We agree with George Withbroe (private communication at this meeting) that SAC 22 is likely to be more like SAC 19. We also agree with Schatten et al. (1987) that SAC 22 will be an exception to Waldmeier (1935) prediction that even activity cycles tend to be less active. However, his basic result is still valid; the rise time of SAC 22 seems to be as steep as that of SAC 19 (private communication from George Withbroe at this meeting). Dicke (1978) suggested that strong sunspot cycles are advanced in phase with respect to the regular ticks of an internal solar clock. It would be nice to explore the implications of this suggestion.

CONCLUSIONS

Cosmic ray data seem to indicate that solar activity cycle 22 will surpass SAC 21 in activity. The value of R_m for SAC 22 may approach that of SAC 19. It would be interesting to see whether this prediction is borne out. We are greatly encouraged to proceed with the development of a comprehensive prediction model which includes information provided by cosmic ray data.

Acknowledgement

I am very grateful to the staff of the World Data Center at Boulder for making available to me the recent data on sunspot numbers and monthly mean hourly counting rates for Deep River NM. In particular, I wish to thank Helen Coffey and Bruce Bauer for this service. This research is supported by NASA Grant NAGW-1468.

References

Ahluwalia, H.S. Solar and Interplanetary Dynamics, D. Reidel Publ. Co., Boston. Eds. M. Dryer and E. Tandberg-Hansen. p. 79, 1980.

Bieber, J.W., Evenson, P., and Mathaeus, W. H., Geophys. Res. Lett., 14, 864, 1987.

Brown, G.M., and Simon, P.A., Solar-Terrestrial Predictions: Proc. Workshop at Meudon, France. NOAA-AFGL Publ., Eds. P.A. Simon, G. Heckman, and M.A. Shea. p. 1, 1986.

Burlaga, L.F., McDonald, F.B., Goldstein, M.L., and Lazarus, A.J., J. Geophys. Res., 90, 12027, 1985.

Dicke, R.H. Nature, 276, 676, 1978.

Forbush, S.E. Handbuch der Physik, Springer Verlag, Ed. S. Flugge. New York, 49(1), p. 159, 1966.

Jokipii, J.R. and Kota, J. Geophys. Res. Lett., 16, 1, 1989.

Kane, R.P. Nature, 274, 139, 1978.

Kota, J., and Jokipii, J.R., Astrophys. J., 265, 573, 1983.

McKibben, R.B., Proc. 6th Intern. Solar Wind Conf., NCAR Tech Note, 306 Eds. V.J. Pizzo, T.E. Holzer, D. G. Sime. 2, 615, 1987.

Schatten, K.H., Scherrer, P.H., Svalgaard, L., and Wilcox, J.M. Geophys. Res. Lett., 5, 411, 1978.

Simpson, J.A. Proc. Pontificiae Acad. Sci. Seminar on: The Problem of Cosmic Radiation in Interplanetary Space at Vatican, Italy, 1-6 October, 1962.

Smith, E.J., and Thomas, B., J. Geophys. Res., 91, 2933, 1986.

Waldmeier, M., Astron. Mitt. Zurich, 14, 105, 1935.

Wilson, R.M., J. Geophys. Res., 93, 10011, 1988.

Xanthakis, J. Solar Physics, John Wiley & Sons, New York. Ed. J. N. Xanthakis. p. 157, 1967.

AN IMAGING VECTOR MAGNETOGRAPH FOR THE NEXT SOLAR MAXIMUM

A Progress Report

D. L. Mickey, B. J. LaBonte, and R. C. Canfield
Institute for Astronomy, University of Hawaii

We describe the conceptual design of a new imaging vector magnetograph currently being constructed at the University of Hawaii. The instrument combines a modest solar telescope with a rotating quarter-wave plate, an acousto-optical tunable prefilter as a blocker for a servo-controlled Fabry-Perot etalon, CCD cameras, and on-line digital image processing. Its high spatial resolution (1/2 arcsec pixel size) over a large field of view (5 by 5 arcmin) will be sufficient to significantly measure, for the first time, the magnetic energy dissipated in major solar flares. Its millisecond tunability and wide spectral range (5000 - 7000 A) enable nearly simultaneous vector magnetic field measurements in the gas-pressure-dominated photosphere and magnetically-dominated chromosphere, as well as effective co-alignment with Solar-A's X-ray images. We expect to have the instrument in operation at Mees Solar Observatory (Haleakala) in early 1991.

We have chosen to use tunable filters as wavelength-selection elements in order to emphasize the spatial relationships between magnetic field elements, and to permit construction of a compact, efficient instrument. This means that spectral information must be obtained from sequences of images, which can cause line profile distortions due to effects of atmospheric seeing. To ensure that sequential images sample the same solar features, we plan to use two techniques for seeing compensation. First, a tip-tilt mirror will correct for average image motion, using a sunspot in the field for guiding. Second, we will use two identical CCD cameras coaligned to high precision. The first camera will measure polarimetrically modulated images to derive monochromatic Stokes images; the second will observe unmodulated, broad-band images at the same time, to determine the instantaneous distortion due to seeing. The latter set will be used to separate atmospheric effects from modulation due to polarization.

1. INTRODUCTION

Solar high energy phenomena cannot be understood without accompanying vector magnetic field measurements. To ensure adequate continuity, frequency, and reliability of vector magnetic field measurements for interpretation of coordinated solar X-ray and γ-ray data obtained with Solar A, Gamma-Ray Observatory (GRO), balloon and rocket payloads during the Max '91 time period (1991-1994), and to compensate in part for the lack of space-borne vector magnetographs, the National Aeronautics and Space Administration, the National Science Foundation, and the University of Hawaii funded the development of a ground-based vector magnetograph, called the Imaging Vector Magnetograph (IVM). This instrument is now under development at the University. Work was begun in August, 1988, and is expected to be completed by the end of 1990, in time for the August 1991 launch of the Solar-A spacecraft. The IVM will be put into operation at Mees Solar Observatory of the University of Hawaii, Haleakala, Maui.

2. PROGRESS TO DATE

2.1. Conceptual design

The design includes a Cassegrain reflector telescope, an acousto-optic tunable prefilter (AOTF), a single Fabry-Perot interferometer, and a two CCD cameras (for white-light and magnetic images). White-light reference images will be used for real-time image motion compensation and post-observation separation of solar and atmospheric components of the magnetic-field images. Using array processors for on-line post-processing, we expect to do flat-fielding, remove intensity fluctuations due to five-minute oscillations, and apply subsonic filtering. Available array processors can complete these tasks within about ten minutes of the polarimetric data acquisition.

3. Performance Specifications

Performance specifications for the final IVM design and hardware are as follows: 1.84 x 10^7 electrons per second per square arcsecond flux, 0.6 arcsecond pixel size, 0.04 second waveplate time , 16 waveplate angles, 8 wavelengths, 48 useful frames per rotation. For the CCD of choice the instrument will have a 5.1 x 5.1 arcminute field of view, and will achieve a signal-to-noise ratio of 10^4 in the quiet sun in 310 seconds or 10^3 in a sunspot in 77 sec, including all processing to produce a magnetogram corrected for supersonic image distortions. Roughly speaking, a signal to noise ratio of 10^4 corresponds to a longitudinal field of 10 Gauss and a transverse field of 100 Gauss.

3.1. Current Activities

At the present time the major mechanical and optical work is taking place on the Cassegrain telescope, rather than the polarimeter (an engineering drawing is shown in this paper). The top-level data flow scheme has been worked out. We have received most of the IVM computer hardware and software. We have the Bitbus approach to control iterfacing worked out and the initial equipment purchases started. On the hardware side, within the next ten months we expect to complete the procurement of the analysis hardware, the CCD camera, the Fabry-Perot filter, the AOTF, and the imager stabilizer. We expect to complete the design and fabrication of the calibrator, modulator, and blocking filter. On the softare side we expect to complete the codes for data proccessing, camera control, filter control, pointing and image stabilization, calibration, modulator control, and the operator interface.

PERFORMANCE SPECIFICATIONS

- **Spatial resolution: 1.2 arcsec.** Detector pixel spacing 0.6 arcsec over a 5.1 x 5.1 arcmin field of view.
- **Spectral resolution: 70 mÅ at 6000Å.**
- **Flux: 1.9×10^7 electrons per second per square arcsec** in the continuum at 6000Å.
- **Spectral range: 5000 - 6500 Å.** We expect to observe a three-line set: one photospheric magnetic line (Fe I λ6302), one chromospheric magnetic line (Mg I λ5173), and Hα (line center only).
- **Temporal cadence: typically one minute for strong fields.** Signal-to-noise ratio of 10^4 in the quiet sun in 310 seconds, 10^3 in a sunspot in 77 seconds, including all magnetogram processing.
- **Sensitivity: 10 Gauss longitudinal fields and 100 Gauss transverse fields.** Simultaneous velocity measurements to 10 m/s. Temporal cadence can be traded for sensitivity.
- **Co-alignment: A simultaneous photospheric white-light image of the full field of view,** for precise co-alignment with Solar-A images and Max'91 ground and balloon-borne experiments.

DESIGN FEATURES

- **Telescope: 30-cm Cassegrain reflector.**
- **Monochromator: Air-spaced tunable Fabry-Perot, 70mÅ bandpass.** Order-sorting using an acousto-optic tunable filter (AOTF) with bandpass of 2 Å, a contrast of 1000:1, a large field of view, rapidly tunable over the full wavelength range.
- **Polarization Modulator: Rotating quarter-wave plate.** The AOTF will double as a beam-splitting analyzer.
- **Detectors: High-resolution commercial CCD cameras.** No mechanical shutter is necessary; turning off the radio-frequency signal to the AOTF turns off the diffracted beams imaged on the cameras. 512 x 512 pixel detector arrays.
- **Data Acquisition: 68020-based computer in a VME-bus chassis.** A minimum modulation sequence consists of a half-rotation of the wave plate, i.e. eight camera reads, which are combined to derive Stokes parameters. Recording on 8mm digital video cassettes.
- **Analysis and Archiving:** Off-line analysis on a Sun workstation. Archival medium is the original 8mm video cassette. Digital optical disk for archiving working datasets. Video disk recorder for time-dependence studies.

THE OWENS VALLEY SOLAR ARRAY

G. J. Hurford and D. E. Gary

Solar Astronomy, Caltech

INTRODUCTION

* Solar microwave emission contains essential information for the study of the coronal magnetic structure of active regions and of thermal and nonthermal flare electrons.

* To exploit this potential requires BOTH imaging and spectroscopy with sufficient resolution to resolve spatial and spectral features.

* The VLA provides excellent solar imaging (when in the C and D configurations) but inadequate spectral coverage. The existing Owens Valley system has excellent spectral coverage but imaging that is adequate only for very simple sources.

* The Owens Valley system is currently undergoing an expansion, which when completed in October 1990 will provide a SOLAR-DEDICATED 5 antenna array (10 baselines). By using frequency-synthesis, this will provide a significant imaging capability in addition to its current spectral coverage.

* At present, the application of microwave diagnostics is limited to spatially simple sources. The expanded array will permit their application to most flares and active regions.

SCIENTIFIC MOTIVATION

* Microwave imaging and spectroscopy have two primary roles to play in the study of solar activity:

    * In active regions, gyroresonance opacity provides a unique sensitivity to the strength of coronal magnetic fields. The combination of imaging and spectroscopy provides the capability for quantitative magnetograms at the base of the corona.

* For flares, the shape of the microwave spectrum indicates whether the electron spectrum is thermal or nonthermal. while the peak flux/frequency provides plasma/field and/or energetic electron parameters. Theoretical spectra and examples of observed thermal and nonthermal spectra are illustrated below.

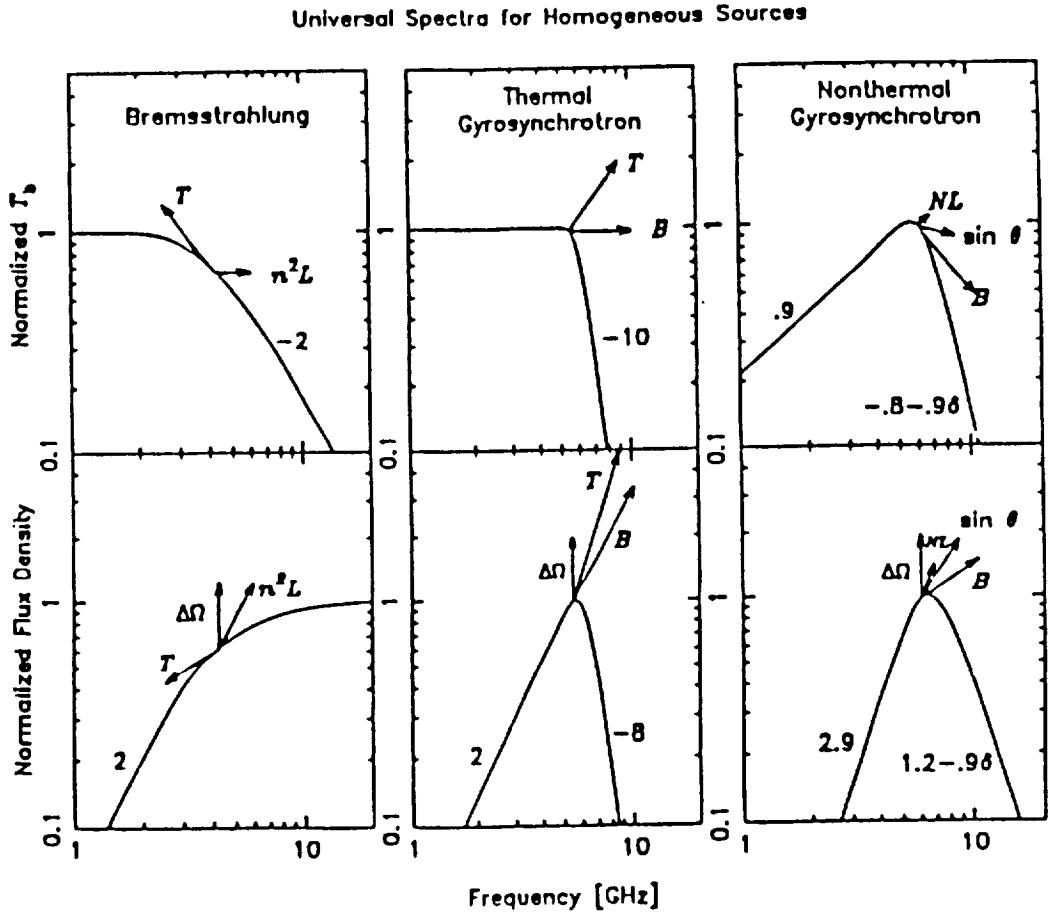

Theoretical spectra for emission from a homogeneous source by the mechanisms indicated. Note that each mechanism is characterized by a distinct shape that remains invariant over a wide range of parameter space. The arrows indicate the direction and magnitude that the spectrum would shift for a factor of 2 increase in the indicated parameter.

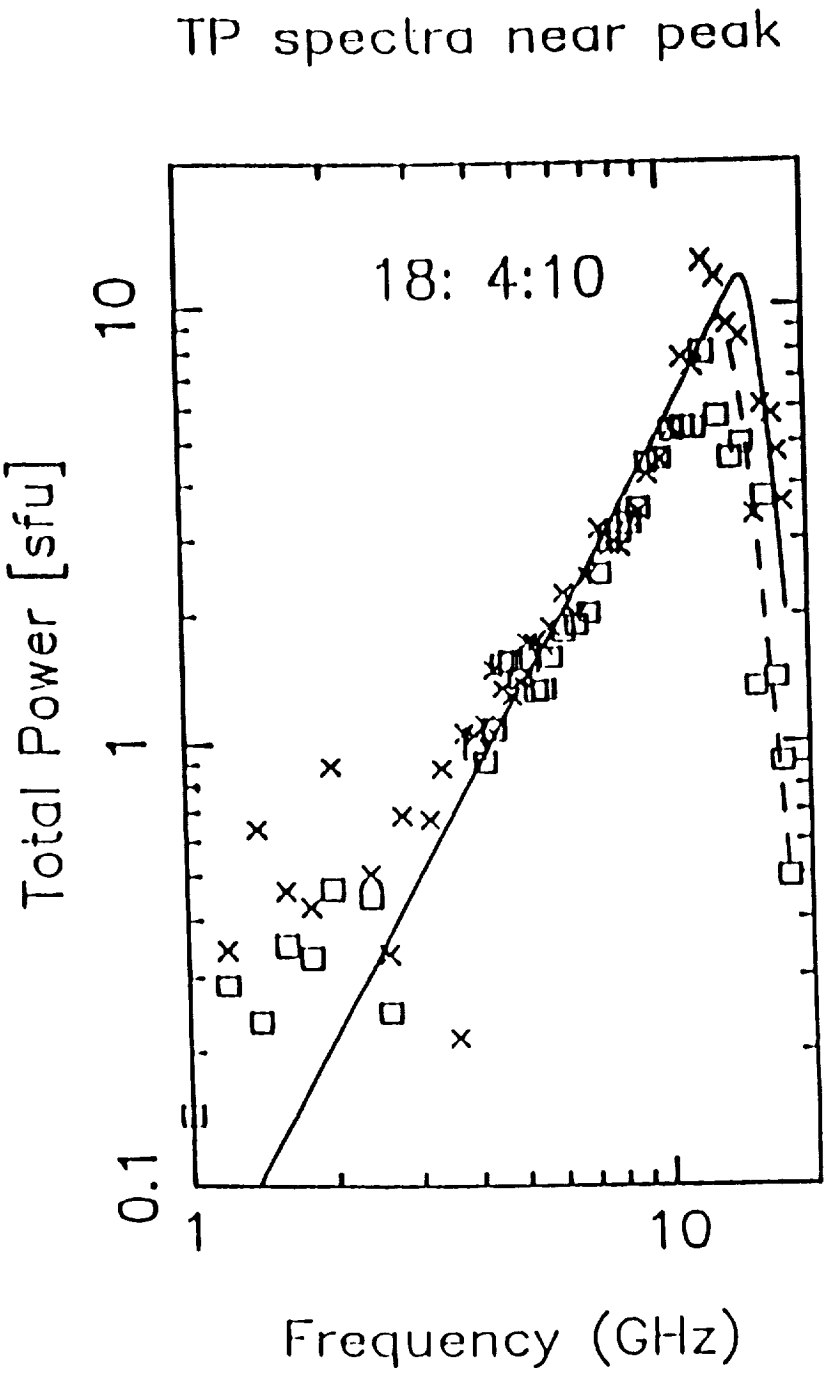

Microwave spectra in right- and left-circular polarization for a demonstrably simple burst. The overlaid curves are for THERMAL gyrosynchrotron spectra of the form illustrated above.

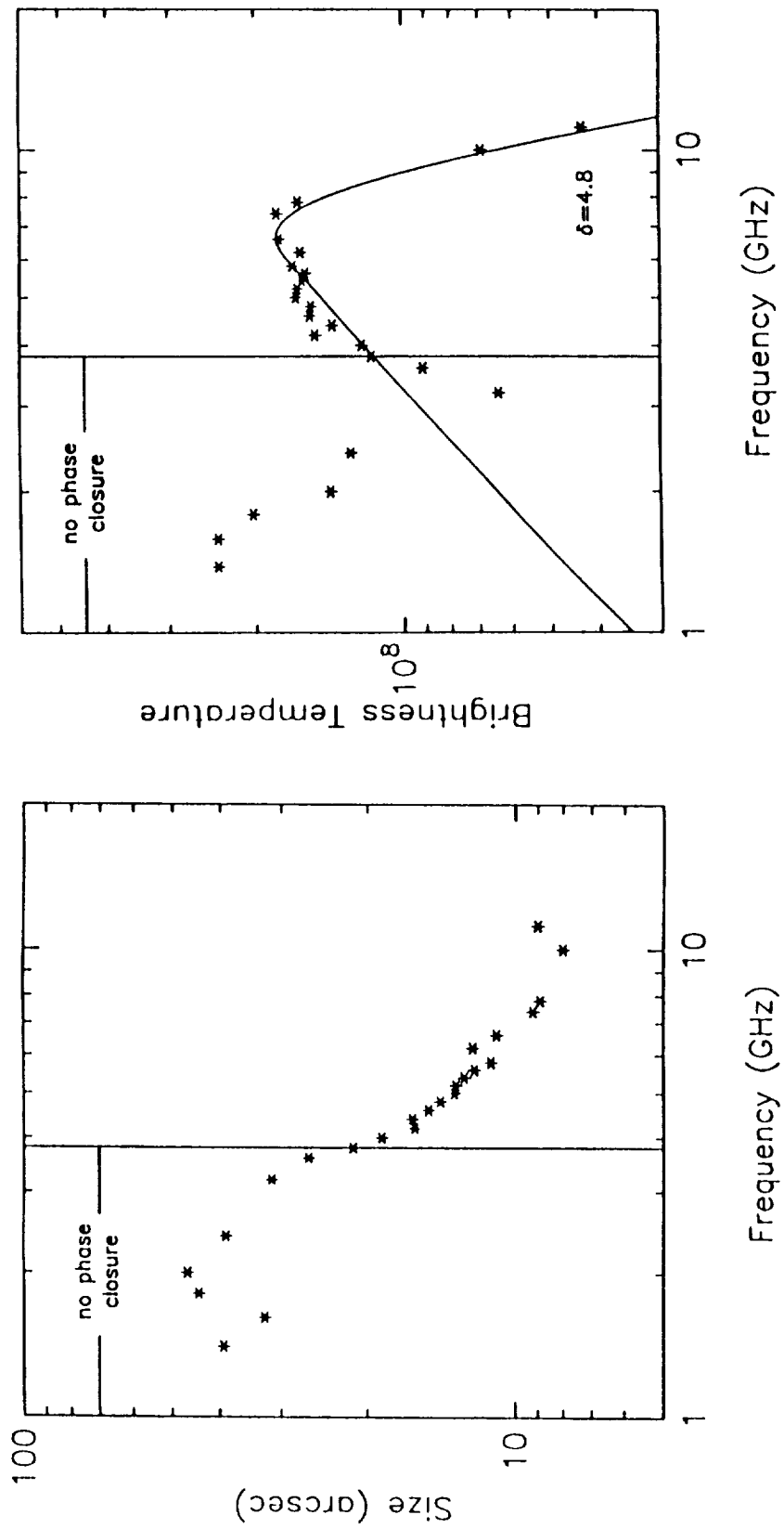

Impulsive-phase spectra for an event observed with three antennas on August 2, 1988. Closure phase data indicates that above 3.8 GHz, the emission was dominated by a single source whose size and brightness temperature is shown. The shape of the brightness temperature spectrum unambiguously implies a NONTHERMAL electron distribution.

FREQUENCY-SYNTHESIS IMAGING

* An interferometric observation at a single frequency with a single antenna pair measures one Fourier component of the source distribution. The relevant parameter is the antenna separation in units of wavelength.

* Conventional aperture synthesis at a single frequency uses many antenna pairs (36 to 351 at VLA, depending on the number of subarrays) to measure many Fourier components from which a map is derived.

* Alternatively, a single antenna pair observing at many wavelengths (eg 45 at OVRO) can measure many Fourier components. In this case the derived "frequency-synthesis" map represents an average over a frequency band.

* The observed spectral shape provides a reliable guide as to what frequency range is reasonable so that the resultant image does not represent an unwelcome average of diverse sources.

* In practice, the images are not sensitive to spectral assumptions or weighting.

* The expanded array typically will observe at 450 baseline/frequency combinations, which can be divided a posteriori among an appropriate number of maps in different spectral bands.

* Examples of frequency-synthsis imaging are given below.

ORIGINAL PAGE
BLACK AND WHITE PHOTOGRAPH

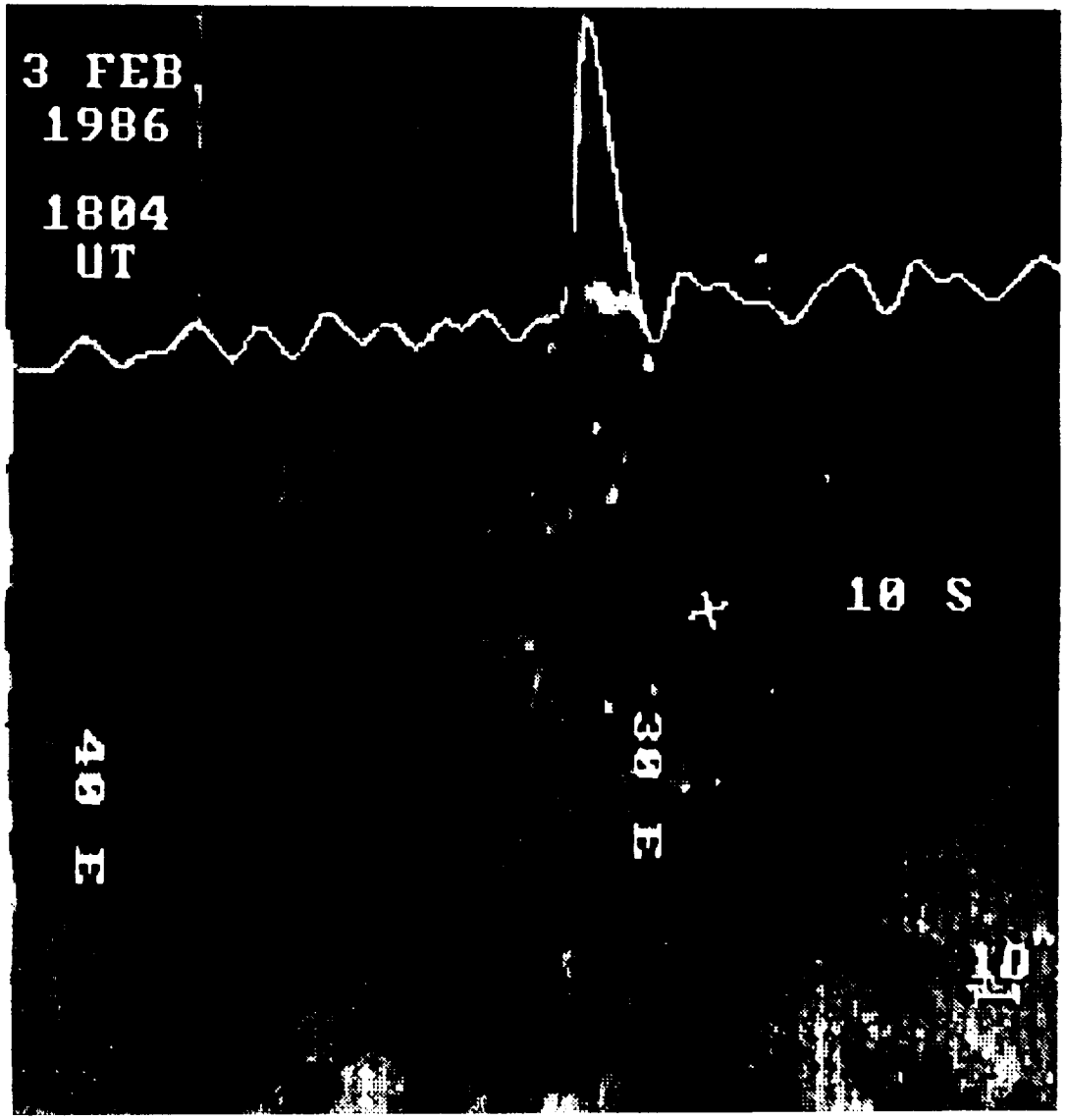

One antenna pair was used to make a 1-dimensional frequency-synthesis map of a flare. The microwave emission is dominated by a single source coincident with the H-alpha emission.

ORIGINAL PAGE
BLACK AND WHITE PHOTOGRAPH

Frequency synthesis maps

Two baselines were used to make two 1-D frequency-synthesis maps with different orientations from which the 2-D flare source locations (crosses) could be determined. This was done in both right-circular polarization (black) and left-circular polarization (blue). Note that the LCP emission came from two widely separated locations while the RCP emission was found to be restricted to the position near the H-alpha kernel.

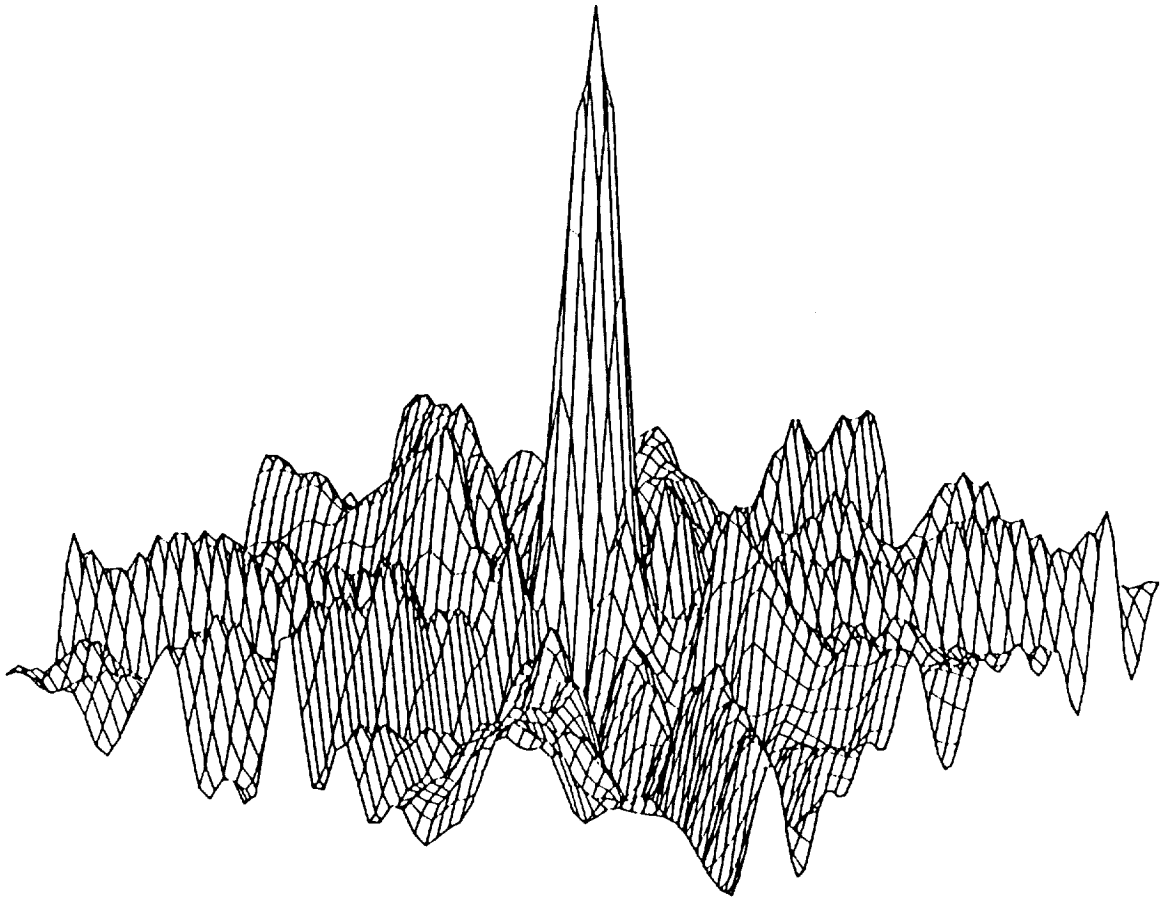

The ten baselines in the completed array will provide a substantial improvement in imaging capability. Shown above is a snapshot beam (applicable to flares) using 20 frequencies from 4 to 12 GHz. The highest sidelobe is at the 24% level. Extrapolating from our current experience, we expect that in the cleaned maps, sidelobe levels will be below 5% in most cases. The spatial grid is 2 x 2 arcseconds.

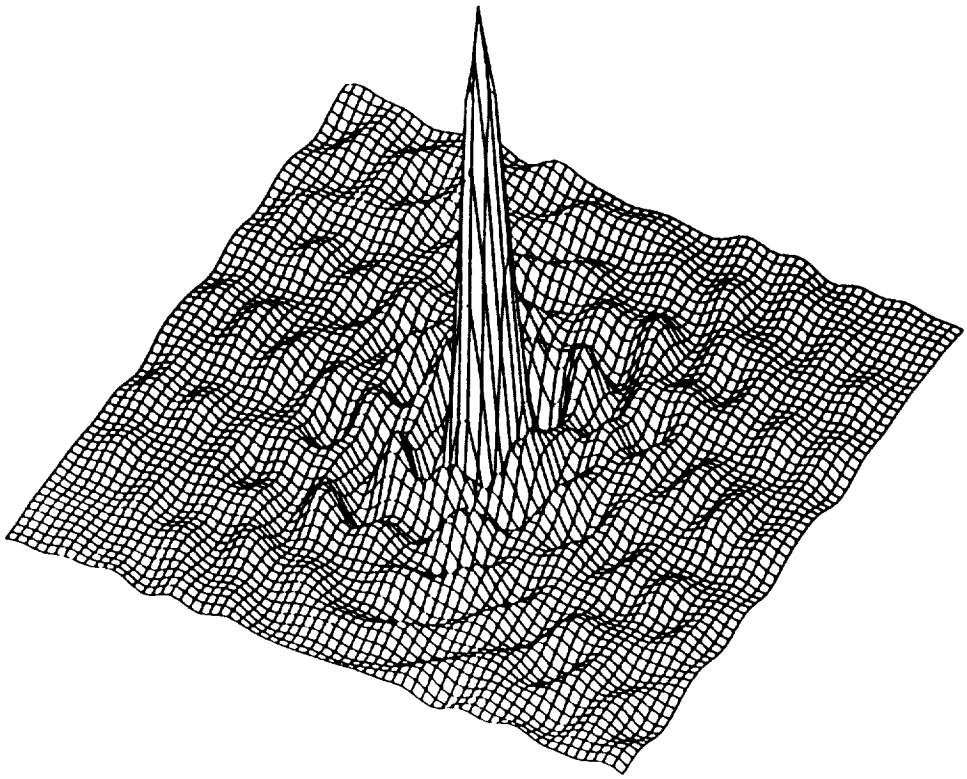

Illustrated above is the synthesised beam for an 8-hour synthesis map using 12 frequencies from 5 to 10 GHz. Using such beams at different frequency bands, it will be possible to produce sets of high-quality active region maps on a daily basis in support of SOLAR-A.

IMPLEMENTATION

* The present Owens Valley interferometer is based on two 27-m parabolic antennas, occasionally supplemented by the use of a third 40-m antenna. All antennas are equipped with frequency-agile receivers which can observe at up to 86 frequencies from 1 to 18 GHz in rapid succession (10-30 frequencies/second).

* The array expansion consists of adding three small 2-m antennas (also equipped with frequency-agile receivers) to work with the two 27-m antennas.

* Note that for solar work, large antennas are needed for calibration on cosmic sources and to restrict the field of view to a single active region. Large collecting areas are NOT needed for solar sensitivity. The combination of large and small antennas will still permit calibration on cosmic sources and the restricted field of view.

* The expanded array will NOT require additional delay lines, correlators, etc. Instead, provision has been made to rapidly time-multiplex existing systems which can handle 3 baselines simultaneously. In typical operation, the system will spend 100 milliseconds at a single frequency. This time will be divided into 5 successive 20 millisecond intervals as follows:
    1. Changing to the new frequency and reacquiring phaselock.
    2. Correlating antennas A, B and C.
    3. Correlating antennas A, B and D.
    4. Correlating antennas A, B and E.
    5. Correlating antennas C, D and E.

  Successive 100 millisecond periods would be devoted to different frequencies, so that 10 different frequencies per second would be sampled with all baselines. As at present, 45 frequencies in both right- and left-circular polarization could be measured every 10 seconds.

* Note that the critical design simplifications (and cost savings afforded by) the use of small antennas and time-multiplexing are made possible by the high signal levels provided by the sun.

* The first 2-m antenna is currently being assembled, and will see see first light this summer. Test observations in a 4-element configuration with the 40 m telescope are planned for the 4th quarter of this year. The 5 element array is expected to be complete by October 1990.

* A SIGNIFICANT EFFORT IS BEING MOUNTED TO ENSURE THAT BOTH OPERATIONS AND ANALYSIS ARE HIGHLY AUTOMATED AND USER FRIENDLY.

* OUTSIDE USERS OF THE ARRAY AND ITS DATA ARE WARMLY WELCOMED.

Solar observations at Owens Valley are supported by the NSF under grants ATM-8610330 and AST-8702682. Expansion of the array is supported by NASA under grant NAGW-1706.

THE HAO/NSO ADVANCED STOKES POLARIMETER

B. W. Lites, D. F. Elmore

High Altitude Observatory
National Center for Atmospheric Research[1]

ABSTRACT

The Advanced Stokes Polarimeter (ASP), now under development at the High Altitude Observatory (HAO) of the National Center for Atmospheric Research (NCAR) and the National Solar Observatory (NSO), will simultaneously measure full Stokes profiles at two widely separated wavelengths. The data from this instrument are intended to permit quantitative analysis of vector magnetic fields in both the photosphere and chromosphere. We expect to produce maps of active region vector magnetic fields with an angular resolution of 1" or better, beginning in mid-1991. The conceptual design of the instrument is discussed in light of scientific requirements and technical constraints.

[1]The National Center for Atmospheric Research is sponsored by the National Science Foundation

SCIENCE OBJECTIVES

* **Sunspots:** Magnetostatic Structure, Fine Scale Structure

* **Magneto-Convection:** Understanding Processes in Relationship to Observed Fine-Structure

* **Magnetic Canopy:** Evaluation of Magnetic Field Structure Above the Photosphere

* **Solar Flares:** Evolution of Vector Magnetic Field in Photosphere and Chromosphere

* **Active Regions:** Processes of Emergence and Decay (submergence, annihilation, diffusion, etc.)

* **Flux Tubes:** Observed Properties of Isolated Flux Tubes

INSTRUMENTAL REQUIREMENTS SET BY SCIENCE OBJECTIVES, ANALYSIS TECHNIQUES

* **Spatial Resolution:** <1" (Set by seeing, Available Telescopes)

* **Polarization Sensitivity:** 10^{-3} I_{cont}

* **Spectral Resolution:** 20 m Å (Resolve Doppler Width of Fe I lines in Sunspot Umbrae)

* **Spectral Coverage:** Simultaneous Measurement of Profiles of Two Members of a Multiplet

* **Height Sampling:** Simultaneous Measurement of Photospheric, Chromospheric Lines

* **Time Resolution:** Coverage of Active Region in ~30 Minutes

FEATURES OF THE SYSTEM

* NSO/Sunspot Vacuum Tower Telescope

* Rotating Waveplate Modulator (3.75 Hz, ~3/8 λ)

* Image Motion Compensation

* Spectrograph Optimized for Array Detectors

* Universal Birefringent Filter For Slit-Jaw Monitor

* Simultaneous Detection of Stokes Parameters Coded into Orthogonal States of Linear Polarization (High System Efficiency, Low Crosstalk Due to Seeing)

* Detection/Readout of Spectral Images at Twice-Video Rate (60Hz)

* Real-Time Demodulation

* Quick-Look User Displays

ANTICIPATED INSTRUMENT PERFORMANCE

* **Angular Resolution:**	0.8"
* **Polarization Systematic Errors:**	$\sim 10^{-3}$
* **Signal-to-Noise:**	~1000
* **Spectral Resolution:**	180,000
* **Simultaneous Spectral Coverage:**	630.1, 630.2 + 517.3, 518.4 nm
* **Time for Active Region Map:**	10 min.
* **Map Size:**	96" × 96"

OPPORTUNITY FOR MAX'91 PROGRAM

Many of the scientific goals of the ASP overlap with those of the MAX'91 program. The ASP will be unique in its capability to provide quantitative measures of the vector magnetic field with high angular resolution, both in the photosphere and in the low chromosphere. The ASP will not produce synoptic measurements, but observational programs may be designed in collaboration with MAX'91 investigators. The present timeline has the ASP system operational by mid-1991. The ASP science team may design collaborative studies with MAX'91 participants during the first year of operation. Following the first year of operation, the facility will be opened to general use by the outside community, and proposals for use of this facility will be accepted by the National Solar Observatory.

Observing Facilities for Max '91 at NSO/Kitt Peak

Harrison P. Jones

NASA/GSFC Laboratory for Astronomy and Solar Physics
Southwest Solar Station/NSO

Synoptic Facilities

A. *Vacuum Telescope/Diode Array Magnetograph.*

1. Daily Full-Disk Magnetograms (1 arcsec pixels).
2. Daily Full-Disk He I 10830 Spectroheliograms.
3. Area Scan Magnetograms: intensity, velocity, magnetic field – 1 arcsec pixels; variable FOV; typical cadence 2.5 minutes; can be formatted as a digital movie.
4. Area Scan He 10830 Spectroheliograms – same specifications as Item 3 above.
5. Semi-dedicated operation to support NASA flight missions (e.g. MAX '91).

B. *Vacuum Telescope/Spectromagnetograph* (nearing completion).

1. Same imaging/operational capabilities as above.
2. Magnetic, velocity, intensity data derived in "real time" from line profiles – well calibrated and free from crosstalk.
3. Possible additional data products – line widths, continuum intensity, differential continuum, line wing intensities; interactions of magnetic fields, flows and thermodynamic state of plasma.
4. Video-rate spectral polarimetry for flare observ- ing.

C. *Razdow H-Alpha Telescope:* Visual reference; patrol mode data recording on film or video tape.

D. *Digitial Movie Processing:* Automatic registration software, optical disk.

General Facilities

A. McMath/Main Spectrograph

B. McMath/FTS

C. Image Stabilizer

D. IR Spectrograph (being refurbished)

E. IR Detector Packages (under development)

More complete description of NSO instrumentation is in the Facilities Manual, available on request from the NSO director's office.

NEW INSTRUMENTATION AT NSO/SAC PEAK

RAYMOND N. SMARTT

National Solar Observatory/Sacramento Peak, Sunspot, NM 88349

The instrumentation listed here is new since 1980, and covers existing systems, others under development, and two that rely on pending support for completion. It is anticipated, however, that much of this instrumentation, together with the other standard equipment, will be available for Max '91.

Sac Peak Vacuum Tower Telescope

Advanced Stokes Polarimeter (ASP) (Not available before 1991): Polarimetric measurements of line profiles for vector magnetic field measurements; ASP is a joint project between HAO and NSO/SP.

Thin Window: Fused-silica, high-optical-quality entrance window for improved polarimetric capability.

Universal Birefringent Filter (UBF) Upgrade: Provides high-precision wavelength settings over the range 4000 to 7000 Å; computer controlled, programmable.

Fabry-Perot Filter (Available in 1990): 0.020 Å bandpass, tunable; used in conjunction with UBF.

Multiple CCD Arrays (MDA): Offers simultaneous imaging on up to four arrays; can be used simultaneously in different wavelengths using the UBF with branch feed, or Echelle spectrograph for imaging spectroscopy.

Auto-Correlation Tracker (Under development): Provides auxiliary guiding on scenes of low contrast and arbitrary structure which are variable in time.

Adaptive Optics: R&D program to develop a wavefront-correcting mirror system that is integrated with the spectrographs, UBF, and other filter systems. A non-optimized system could be available in two years. This program also involves the construction of a new horizontal spectrograph.

Universal Spectrograph (USG): Medium spectral resolution over 3500 to 10,000 Å (entire telescope-spectrograph system is free of chromatic aberration); data recorded on film.

High Precision Time Standard: Signal accurate, in practice, to one millisecond, and is recorded on each CCD image or record.

John W. Evans Facility

Three-Line Photoelectric Coronal Photometer: Photoelectric limb scans with sky background removed, in red, green, and yellow coronal emission lines.

Photoelectric Coronagraph Upgrade (Pending outcome of proposal to NSF): CCD array detector used in focal plane of the Coronal Photometer (above).

Universal Spectrograph Upgrade: Instrument is similar to USG described above, now computer controlled.

Reflection Coronagraph (under development, due for completion in 1991): 35-cm aperture, records images of active region coronal structure in the primary coronal lines, including I.R., with video capability.

Hilltop Dome

Multi-Band Patrol (MBP) Upgrade (Available in 1991): Simultaneous recording in four wavelength/bandpasses at 3618/50, 4264/50, 4969/50, and 7005/50 Å, over active region field-of-view; data recorded on film.

JHU/APL Vector Magnetograph (Available in 1990): Uses CCD array and Fabry-Perot filter; instrument features high polarization sensitivity, correlation-tracked image stabilization, and active region field-of-view.

Full-Limb Emission Line Coronagraph (One-Shot) Upgrade (Pending outcome of NSF proposal): Replacement of 70-mm film with CCD array; coverage in red and green coronal lines plus Hα.

Reflecting Coronagraph Prominence Monitor: Video camera detection; records faint Hα emission at large distances above the limb.

N90-12491

A High-Speed Digital Camera System for the Observation of Rapid Hα Fluctuations in Solar Flares

Alan L. Kiplinger[1,2]

[1]Department of Atmospheric, Planetary and Astrophysical Sciences
University of Colorado, Boulder, CO 80309-0391

[2]NOAA/Space Environment Laboratory, Boulder, CO 80303

and

Brian R. Dennis and Larry E. Orwig

Laboratory for Astronomy and Solar Physics
NASA/Goddard Space Flight Center, Code 682
Greenbelt, Maryland 20771

Abstract

We have developed a prototype digital camera system for obtaining H-alpha images of solar flares with 0.1 s time resolution. We intend to operate this system in conjunction with SMM's Hard X-Ray Burst Spectrometer, with X-ray instruments which will be available on the Gamma Ray Observatory and eventually with the the Gamma Ray Imaging Device (GRID), and with the High Resolution Gamma-Ray and Hard X-Ray Spectrometer (HIREGS) which are being developed for the Max '91 program. The digital camera has recently proven to be successful as a one camera system operating in the blue wing of H-alpha during the first Max '91 campaign. Construction and procurement of a second and possibly a third camera for simultaneous observations at other wavelengths are underway as are analyses of the campaign data.

I. Instrument Development

Considerable progress has been made in the first half of 1989 with regard to the development of the High-Speed H-alpha Camera system. The system became electronically operational at Goddard in April and a decision to ship the system to Boulder for support of SMM and the first Max '91 campaign was made in Mid-may. With the Max '91 campaign beginning on June 16, the system arrived in Boulder on June 9 and was operating electronically by June 10.

The High Speed H-alpha camera system was integrated to 18-inch cassegrain telescope of the Sommers Bausch Observatory and began observations on June 15. The

weather was sufficiently good for camera operation on 14 of the 16 days of the campaign. During the campaign, the camera recorded approximately 60 gigabytes of data which translates to more than three million digital images. The absolute timing accuracy of each image is 1 millisecond.

The High-Speed Camera's coverage of the campaign activity was excellent. Obtaining observations in the blue wing of H-alpha, the camera recorded the largest flare of the campaign, an X-1.9 as measured in the 1-8 Angstrom band, as well as six M class flares and numerous C class flares. Several events were observed simultaneously with the VLA and the Owens Valley interferometers. Two flares were recorded which displayed dramatic coronal mass ejections, one of which showed prominence material beyond 1 solar radius from the limb. Additional flares exhibited rapid fluctuations in hard x-rays and point brightenings. During one M flare, we believe the camera accurately recorded the ascent of mass and the redistribution of this mass into a classic post flare loop system.

II. Planned Analyses

Although the camera was developed to study rapid fluctuations in solar flares, many of its observations during the campaign were of major flares with mass motions with high velocities. We first intend to study the tapes which recorded flares that exhibit rapid fluctuations in hard X-rays. We intend to produce optical light curves from various parts of the flare with which to compare the X-ray and microwave data. A primary objective is to discern electron time-of-flight effects. We also intend to study the impulsive phases of the larger two ribbon flares with emphasis upon the liftoff of the coronal mass ejections. Supporting radio observations from the VLA, Owens Valley, Nancay, Zurich, Berne and Brazil should be especially helpful.

III. Future Development and Observations

Goals of the next year include:

* To operate the high speed camera as a one camera system during periods of solar flare activity until SMM falls to earth.

* To complete and operate the camera as a two camera system with the Gamma Ray Observatory during periods of solar flare activity. The hardware for synchronizing two additional cameras is already in place. The fundamental clock for the current camera and ultimately all cameras is an oscillator that is precisely phase locked to the atomic clock in Fort Collins Colorado; thus, it is possible to synchronize the cameras so that the images obtained are precisely simultaneous.

IV. Bibliograpy

"Development of a High Speed H-Alpha Camera System for the Observation of Rapid Fluctuations in Solar Flares", Kiplinger, Dennis, Orwig and Chen, Proceedings, of the First Max '91 Workshop, Kansas City, June 1988, p. 214.

Rapid Fluctuations in Solar Flares, NASA Conference Publication 2449, Dennis, Orwig and Kiplinger eds. (Washington D. C., NASA), 1986.

"The Relative Timing of Microwaves and Hard X-Rays in Solar Flares", Cornell, Hurford, Kiplinger and Dennis, Ap. J. Lett., 265, L99, 1984.

"Fast Variations in High Energy X-Rays from Solar Flares and Their Constraints on Non-thermal Models.", Kiplinger, Dennis, Frost and Orwig, Ap. J. Lett., 287, L105, 1984.

Analysis of Video Spectra-Spectroheliograms From the San Fernando Observatory

by

G. A. Chapman and S. R. Walton
San Fernando Observatory, and
Department of Physics and Astronomy
California State University, Northridge

ABSTRACT

For the past several years, the San Fernando Observatory, SFO, has recorded two-dimensional spectra of active regions using a magnetically sensitive line. Beginning in 1988, these spectra were recorded with a COHU CCD camera and a 3/4-inch width, U-matic VCR. These video spectra-spectroheliograms, VSSHG, typically are recorded with a spatial scale of 1 arc-sec per pixel and a spectral resolution of about 16 mA. Observations of active regions have typically 300 x 480 arc-sec. Observations are usually obtained around the 6302.5 A line. This line has a telluric O-2 line on either side for wavelength comparison. Analysis of these spectra should result in maps of magnetic, line-of-sight velocity, and relative intensity information. So far, preliminary analysis has given magnetic field strength in sunspots of about 2400 gauss. The analysis of non-spot fields is continuing, but shows line-of-sight field strengths that are typically seen by standard magnetographs (several hundred gauss).

1. Introduction

At the San Fernando Observatory, we have been embarked on a study of solar irradiance variations associated with sunspots and other magnetic phenomena, notably, faculae. These observations have not measured the magnetic field strength nor the motions associated with these field elements. By recording the entire line profile and continuum, using two-dimensional video, we can measure all of these parameters from the same data set. Using commercially available video equipment, controlled by a computer, we can produce two-dimensional maps of irradiance fluctuation and magnetic field strength, obtained simultaneously. Furthermore, we can estimate the irradiance contributions due to lines, separately from the continuum, something that is not possible with our present fixed bandpass photoelectric system based on linear diode arrays.

2. Recent Results

Figure 1 shows a photoelectric spectroheliogram (SHG) from 6 Aug 1988 obtained at 6303A. Figure 2 shows a continuum SHG obtained from VSSHG data at a wavelength of 6302.2A. The variations in the diode response have not yet been removed in

the VSSHG presentation. The VSSHG was scanned at a somewhat higher speed than planned resulting in some north-south distortion. This has now been remedied. Furthermore, the VSSHG image has been inverted, east for west.

Since the data all have wavelengths around the 6302.5A line, we can examine the splitting and central position of the line, extracting the magnetic field strength, the Doppler shift, proportional to the line-of-sight velocity, and the continuum intensity, from the nearby continuum. The SHG of Fig. 1 was obtained from the continuum using linear diode arrays.

A prime advantage of the VSSHG is that it does not saturate in a sunspot, as does a Babcock-type magnetograph, and it can obtain a Doppler shift for each line of the image that is separated from magnetic field effects. Furthermore, the magnetic and velocity shifts can be determined without strong systematic effects caused by changes in the shape of the spectrum line. Changes in line shape are a major cause of systematic error in most magnetographs that measure magnetic and velocity fields on the sun.

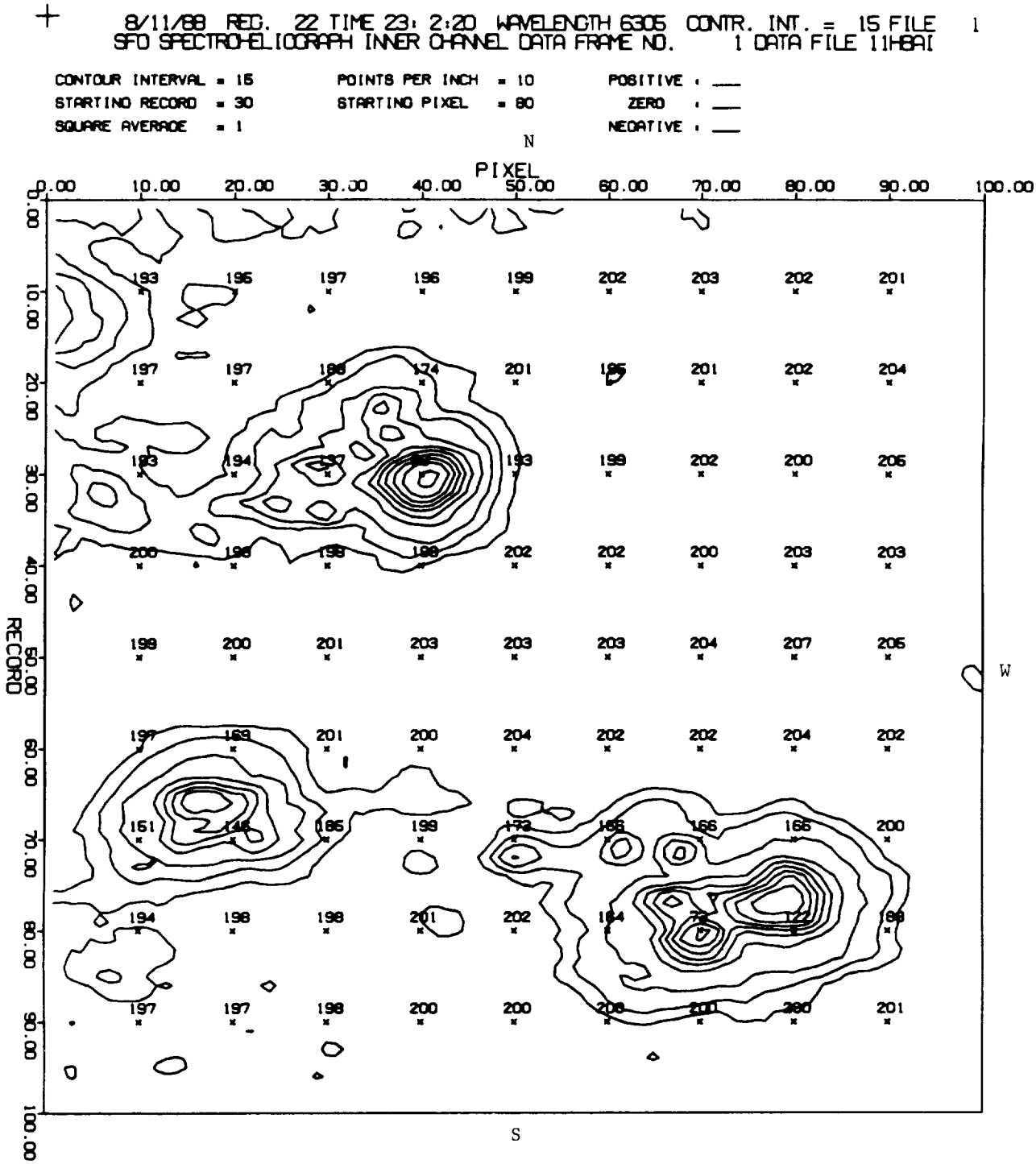
8/11/88 REC. 22 TIME 23: 2:20 WAVELENGTH 6305 CONTR. INT. = 15 FILE 1
SFO SPECTROHELIOGRAPH INNER CHANNEL DATA FRAME NO. 1 DATA FILE 11HBAI
CONTOUR INTERVAL = 15
STARTING RECORD = 30
SQUARE AVERAGE = 1
POINTS PER INCH = 10
STARTING PIXEL = 80
POSITIVE : ___
ZERO : ___
NEGATIVE : ___
N
PIXEL
0.00
10.00
20.00
30.00
40.00
50.00
60.00
70.00
80.00
90.00
100.00
RECORD
W
S

Fig. 1

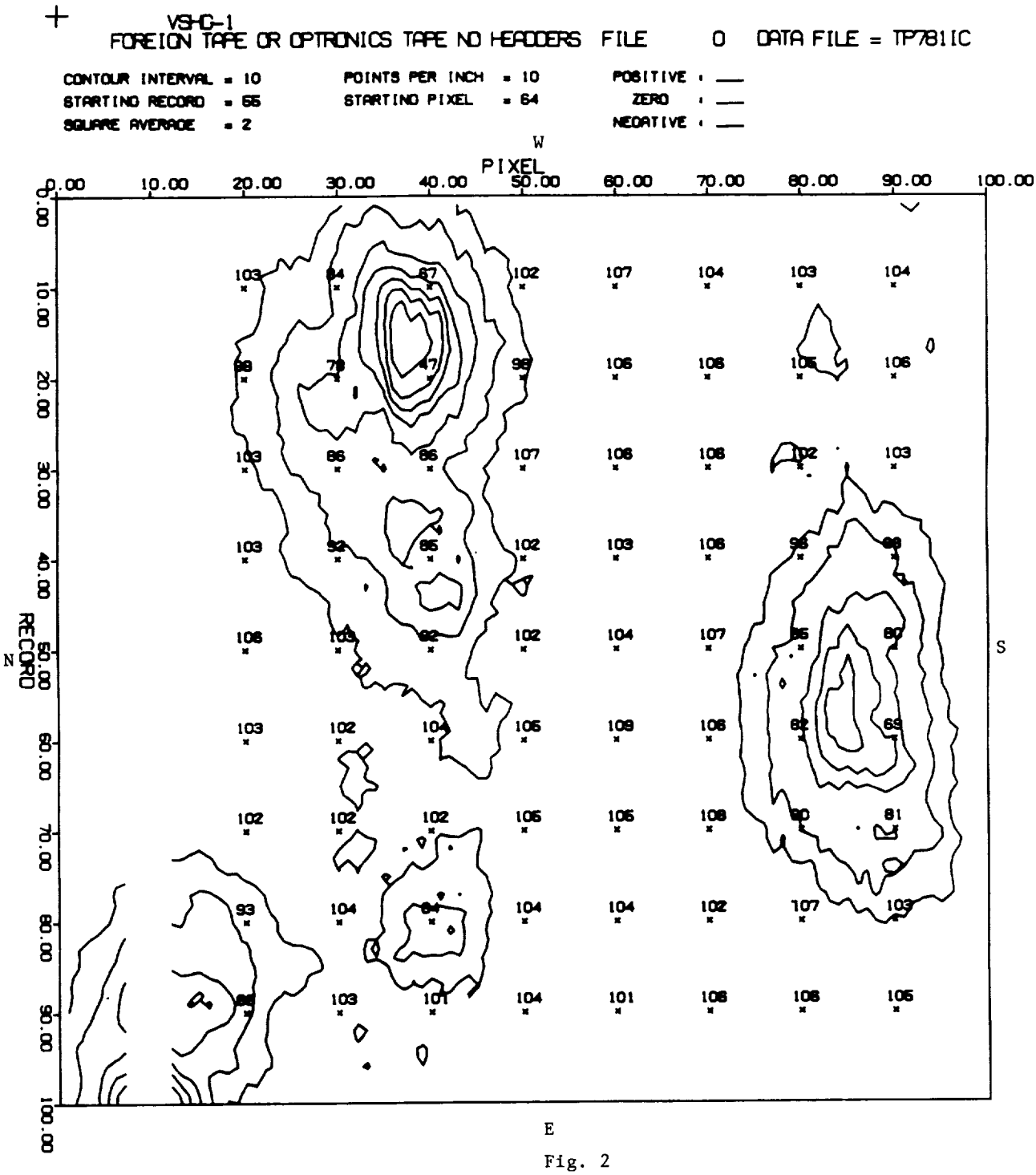
VSHC-1
FOREIGN TAPE OR OPTRONICS TAPE NO HEADERS FILE 0 DATA FILE = TP781IC
CONTOUR INTERVAL = 10
STARTING RECORD = 65
SQUARE AVERAGE = 2
POINTS PER INCH = 10
STARTING PIXEL = 64
POSITIVE : —
ZERO : —
NEGATIVE : —
W
PIXEL
0.00
10.00
20.00
30.00
40.00
50.00
60.00
70.00
80.00
90.00
100.00
RECORD
N
S
E

Fig. 2

Limb-Occulted Microwave and X-ray Flares

E. J. Schmahl[1], *M.R. Kundu*[1], *James Tappin*[2] *and George Simnett*[2]

[1] Astronomy Program, University of Maryland, College Park, MD 20742

[2] Space Research Department University of Birmingham Birmingham B15 2TT, England

Using the VLA at 6 cm, the HXIS instrument in soft x-rays, and the HXRBS and ISEE-3 hard X-ray spectrometers, we have observed a sequence of limb flares on November 18, 1980. The initial burst of these events occurred at 14:52 UT and has been discussed in detail by Schmahl et al (1985) and Simnett and Strong (1984). This flare was followed by some smaller, gradual bursts in microwaves and soft x-rays at limb locations a few arc sec away from the initial impulsive burst.

These events may be part of the decay phase of the 14:52 flare, but it appears more likely that they are independent bursts in nearby parts of the active region. Only one of the events is associated with an impulsive burst in hard (> 25 keV) X-rays. The X-ray spectrum of this event is similar to that observed in stereoscopic behind-the-limb flares (e.g. Kane et al, 1982), in that the ratio of impulsive hard X-rays to the softer, gradual x-rays is small compared to the same ratio for our first (non-occulted) burst. Thus the observed characteristics of the burst are as expected if the impulsive radiation occurs at lower altitudes than the gradual radiation. In another of the gradual soft x-ray events in this sequence, the impulsive phase was absent at all energies, suggesting that the burst occurred further behind the limb, causing more occulting.

In general, maps of microwave bursts show that the primary electrons are located at the apex or in the legs of the flare loop, while thick target models show that the sources of impulsive hard X-rays emission occur well below the sources of microwave emission, so that a burst partially occulted by the limb should hide more of the hard X-rays than microwaves. However, the 6 cm emission in all the "aftermath" events we have studied is very gradual: i.e. impulsive microwave bursts are absent. For the event in which impulsive hard X-rays were observed, this raises the question: what happened to the impulsive microwaves? One possibility is that thermal cyclotron absorption at low harmonics of the gyrofrequency hid the impulsive emission. Such absorption is more likely near the limb, and this phenomenon may not may not often occur in disk flares. Our 6 cm maps show that microwave emission appeared above and to either side of the pixel of maximum emission in the HXIS band 1 and 2 maps. Therefore it seems likely that after the "post-flare" loops expanded somewhat the emission appeared above or around the absorbing site.

Other possibilities that might explain the discordance between microwaves and X-rays are that the beams were highly anisotropic or involve primarily ions, so that gyrosynchrotron emission was weak. Future observations of limb flares in microwaves and X-rays may be able todetermine which of these hypotheses is correct.

REFERENCES

Kane, S.R., Fenimore, E.E., Klebesadel, R.W., and Laros, J., 1982, Ap. J. Lett., **254**, L53.

Schmahl, E.J., Kundu, M.R., and Dennis, B.R., 1985, Ap. J., **299**, 1017.

Simnett, G.M. and Strong, K.T., 1984, Ap. J. **284**, 839.

VLA CAPABILITIES FOR MAX 91

Kenneth R. Lang

Department of Physics and Astronomy
Tufts University, Medford, MA 02155

Abstract

We discuss the capabilities for VLA observations of solar activity that were not available during the last maximum in activity. New capabilities include: observations of coronal loops on the small -scale within individual active regions at 20 cm wavelength, observations of the 92 cm coronal emission from filaments and other large-scale magnetic loops, and VLA snapshot maps of brightness temperature and polarization during solar flares at times as short as 1.67 seconds. These new capabilities are illustrated by unpublished data that will appear in the two papers referenced at the end of this article. The scientific potential of the VLA during the coming solar maximum is illustrated by the June 1989 Max 91 campaign for simultaneous SMM-VLA observations. Future campaigns can include VLA-GRID and VLA-GRO observations during specific two-week sequences. Some of the scientific returns expected from these campaigns were illustrated in another part of these workshop proceedings in the paper entitled "VLA-MAX 91 Tests of High Energy Flare Physics". He , for example, we showed how the VLA can be used to spatially resolve the pre-burst, impulsive and decay phases of solar flares. These results indicaye that the large collecting area and 356 interferometer baselines of the VLA result in a strong scientific return whenever the VLA is used, and that a solar-dedicated radio instrument is not necessarily required to support future NASA space flights.

What's New at the VLA Since the Last Solar Maximum?

New capabilities for the VLA during MAX 91 include:

1. All 27 antennas now operate at 2, 3.5, 6. 20, and 92 cm 2 wavelength. During the previous solar maximum the full VLA was not working at 20 cm, and there were no receivers at 3.5 and 92 cm.

2. It is now possible to observe total intensity, I, and circular polarization, V, at any band simultaneously with 92 cm. For example, I and V can be recorded every 1.67 seconds simul- taneously at 20 cm and 92 cm wavelength.

3. A higher time resolution of 1.67 seconds is now possible; the previous limit to integration time was 3.3 seconds.

4. The solar calibration procedures are now better understood, and the new 3.5 cm system has solar calibration noise diodes on all 27 antennas.

5. Solar observations by a variety of outside users has been made easier by an improved VLA program which provides a greater flexibility for creating observing files.

These new capabilities are illustrated in Figures 1,2,and 3 that come from the unpublished data of Lang and Willson (1989a,b) Figure 1 shows that the visible solar disk can now be imaged with high angular resolution at both 20 cm and 92 cm. The 20 cm syn- thesis maps delineate the million-degree plasma trapped within coronal loops in individual active regions. The 92 cm synthesis maps reveal large-scale (angular size 3'), hot (brightness temperatures Tb 3 x 10**5 K) structures that overlie dark H-alpha filaments. The similarity between the shape, position, elongation and orientation of the radio and optical features suggests their close association. We have interpreted the 91.6 cm emission in terms of the thermal bremsstrahlung of a hot sheath that envelops the cooler H-alpha filament.

Figures 2 and 3 describe time-correlated bursts that occur in active regions on opposite sides of the solar equator. These regions are apparently linked by large-scale trans-equatorial magnetic loops that are at least 2.6 x 10**5 km (or 6') long. Energetic electrons accelerated during a radio burst in one active region probably move along this magnetic conduit at velocities of about a third the velocity of light, thereby triggering radio bursts in the other active region.

Scientific Potential for VLA Investigations During MAX 91

The scientific potential of the proposed VLA observations was illustrated by the SMM-VLA MAX 91 campaign. Altogether, thirteen days of VLA solar observing were allocated to several solar radio astronomers between June 16 and July 1, 1989 thereby demonstrating the future capability of obtaining two-week VLA intervals during balloon flights or satellite-targeted sequences. The rich variety of scientific return expected from the MAX 91 campaign includes studies of filament cavities, examination of coronal bright points, the thermal and non-thermal components of the coronal plasma, the spatial and temporal fine structure of solar flares, and the physical parameters, energetics and radiation mechanisms during the pre-flare, impulsive and post-flare stages.

NASA's Solar Physics program can be supported during MAX 91 by obtaining VLA images with high spatial and temporal resolution during the flights of solar spacecraft such as GRID, GRO, ULYSSES and SOLAR A. Specific two-week VLA campaigns can be organized for the GRID and GRO telescopes, thereby comparing hogh-resolution radio and hard X-ray images and detecting numerous weak flares at both radio and gamma rays with high spatial and spectral reso- lution. These VLA supporting observations

can be coordinated with ground-based microwave spectroscopy (Nancay Radioheliograph and Phoenix), vector magnetographs, coronagraphs and H-alpha images as part of the MAX 91 program. This will enable us to fully exploit the sensitivity of the VLA, as well as the unique spatial and spectral information of NASA's space-bourne telescopes. Such combined observations will enhance the scientific return of any of these instruments beyond that occurring by using them alone.

References

Lang, K.R., and Willson, R.F. 19898a, "Radio Emission From Quiescent Solar Filaments at 91.6 cm Wavelength," to be published in the Astrophysical Journal Letters.

Lang, K.R., and Willson, R.F. 1989b, "Time-Correlated Bursts From Widely-Separated Solar Active Regions", to be published in the Astrophysical Journal Letters.

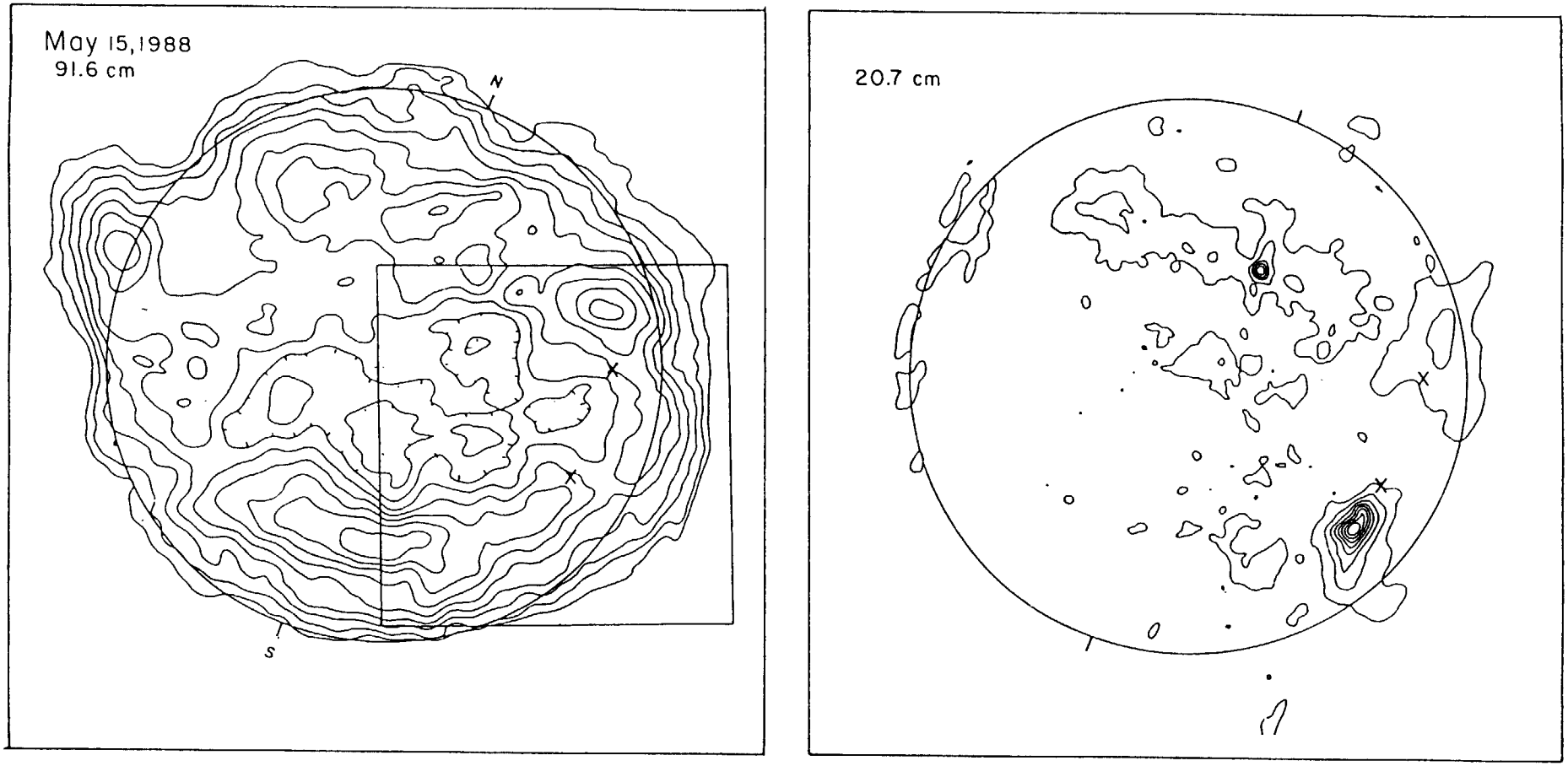

Fig. 1. A 91.6 cm map (left) exhibits large-scale coronal loops associated with the emission of filaments while the 20.7 cm VLA map (right) shows smaller-scale coronal loops within individual active regions. The peak brightness temperatures of the filament transition sheaths are $T_B = 2.5 \times 10^5$ K, while those of the active-region coronal loops are $T_B = 2.5 \times 10^6$ K. The box in the 91.6 cm map shows the sites of the time-correlated flares (Figure 8).

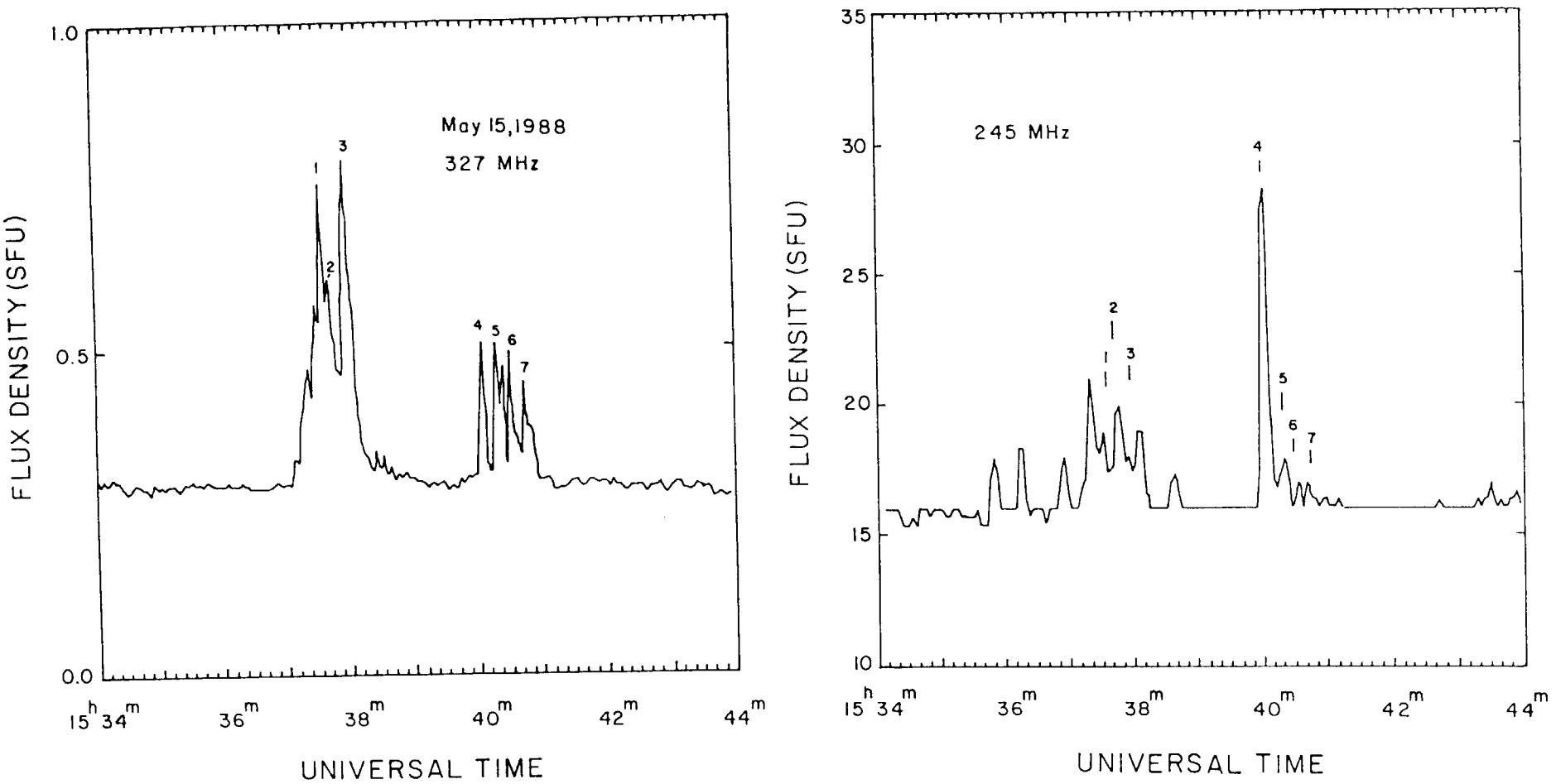

Fig. 2. Time profiles of nonthermal radio bursts that are most intense at the lower frequencies (245 MHz- Sagamore Hill data). VLA snapshot maps at 327 MHz (Figure 3) show that successive bursts appear on opposite sides of the equator.

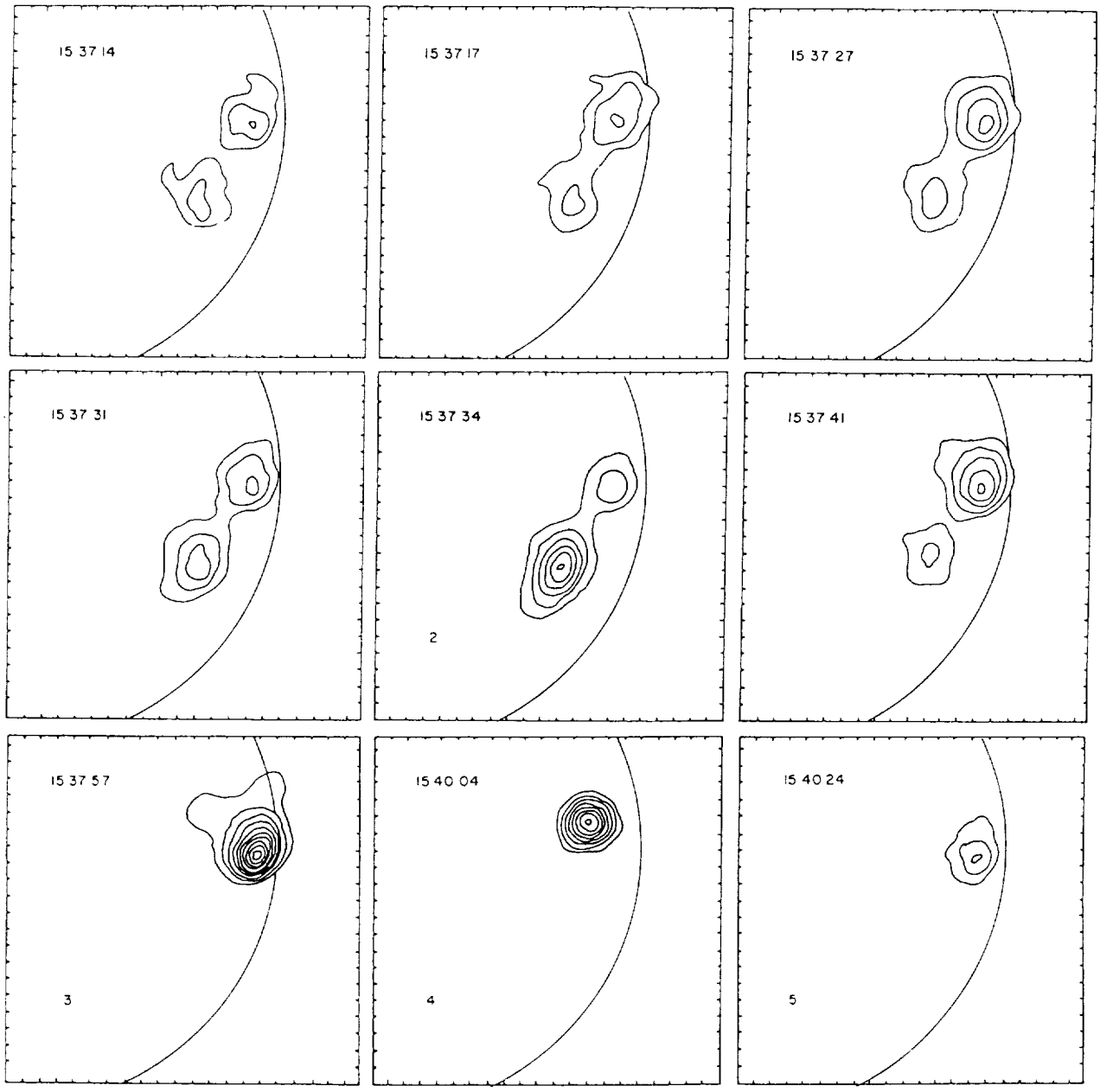

Fig. 3 Successive three-second VLA snapshot maps show time-correlated bursts over separations of L 1 x 10^5 km. They are attributed to energetic electrons travelling at 0.3 times the velocity of light along vast trans-equatorial magnetic loops. The highest peak brightness temperature is $T_{B_{max}}$ = 1 x 10^7 K.

Status Report for the MAX'91 Campaign from the Ottawa River Solar Observatory

V. Gaizauskas

Herzberg Institute of Astrophysics
National Research Council of Canada

Observing Window: 12:00 - 22:00 UT

Primary Instrument: 25 cm aperture photoheliograph equipped with a tunable quarter-Angstrom Zeiss filter for scanning across the H-alpha line. The image scale in the focal plane is about 15 arc-sec/mm. The recording medium is 35 mm fine-grain film (Kodak TP2415). There are 4 pre-programmed modes of operation:

I. Fixed Field of View (FOV) : 4' x 5'
Wavelength Range (15 steps) : 1.4 Angstroms to both sides of H-alpha
Cycle Time : 42 seconds

II. FOV scanned over entire solar disc in 102 overlapping steps
Wavelength Range (5 steps) : 1.0 Angstroms to both sides of H-alpha
Cycle Time : 25 minutes

III. Fixed FOV : 4' x 5'
Wavelength Range (9 steps) : 1.0 Angstroms to both sides of H-alpha in steps suited to prominence studies
Cycle Time : 30 seconds

IV. FOV scanned over 10' x 10' target area in 6 overlapping steps
Wavelength Range : (a) +/- 1.0 Angstroms, 5 steps
(b) +/- 1.4 Angstroms, 15 steps
Cycle Time : (a) 2.5 minutes
(b) 7.0 minutes

Modes III and IV are new since the SMY campaign. Other new capabilities include automatic target setting from coordinates (needed in studies of quiet areas), and cycling between 2, 3, or 4 targets in sequence.

The major new instrumentation since SMY includes a digitizer for 35 mm film and an image processing system. The digitizing camera is an Eikonix Model 78/99 System which mechanically scans a 2048-element Reticon array across an image in about 5 minutes for maximum resolution. The dynamic range in practice is 10 bits (a range in density of 3.0). A Mekel 35-mm film transport advances each frame into the measuring stage which is uniformly illuminated with special optics. The image display and graphics operations are controlled by a Parallax Graphics Videographic Processor (Model 1280) installed in a Microvax II. The programming language used to analyse images is VMS-based IDL (Interactive Data Language). Processed images are stored on Exabyte 8-mm tape cartridges, and can be made available in FITS format. Work is under way to provide movies of processed images on S-VHS video tapes.

Mees Solar Observatory, University Of Hawaii

R. C. Canfield

Institute for Astronomy, Honolulu, Hawaii

Summer hours of Operation: ~ 1700 – 0200 GMT

Stokes Polarimeter

Type of data:	Vector magnetograms
Spectral coverage and resolution:	Fe 6303Å ±1.6Å, 25mÅ
Spatial coverage and resolution:	2 × 3 arcmin, 6" pixels
Temporal coverage and resolution:	Daily, ~ 1 - 2 hours

Hα Imaging Spectrograph

Type of data:	Combined spectra and spectroheliograms
Spectral coverage and resolution:	Hα ±5 Å, 200mÅ (typ)
Spatial coverage and resolution:	150 x 180", 2.5" pixels (typ)
Temporal coverage and resolution:	Campaign mode, 9 seconds (typ)

K-line Imager

Type of data:	Digital chromospheric images
Spectral coverage and resolution:	Ca II 3933 ± 0.15 Å
Spatial coverage and resolution:	Full disk, 6" pixels
Temporal coverage and resolution:	Campaign mode, one per minute

Radio Observatory BLEIEN of ETH Zurich, Switzerland

Markus J. Aschwanden[1] *and Arnold O. Benz*[2]

[1]NASA/GSFC, [2]Institute for Astronomy, ETH

In June 1989, simultaneously with the campaign of coordinated SMM/VLA observations, a new frequency range of the radio spectrometer PHOENIX is put in operation at the ETH radio station in Zurich. The frequency range of 100 MHz - 1 GHz, which was used during the last solar cycle, has been extended to 100 MHz - 3 GHz. With this upgrading, this broadband digital radio spectrometer represents an ideal complementation to VLA observations, especially for the covered 330 MHz and 1.5 GHz VLA frequencies. The frequency-agile sweep spectrometer allows high frequency resolution up to 2000 different frequency measurments with filters of 1,3 or 10 MHz, recording intensity and circular polarization. The frequency resolution is compromising with time resolution, which is dt[sec]=N/2000 (N=number of frequencies). Observation time overlap from Zurich with the VLA site is up to 6 hours in June/July, but 5 hours in August. The performance of the PHOENIX instrument is expected to start mid of June. A dedicated VLA/PHOENIX/SMM observation is scheduled for July 29-August 13. PHOENIX will continue routine observations and special high time resolution observations in the decimetric and lower microwave range of 1-3 GHz during the entire campaign FLARES 22.

Research at C.U. related to Max '91: Observational

George A. Dulk

Department of Astrophysical, Planetary and Atmospheric Research
University of Colorado, Boulder CO 80309-0391

The solar atmosphere and solar flares are being studied using ground and space-based radio observations combined with X-ray, EUV and visible-light observations from space: SMM, ISEE–3, Solar A, rockets and balloons. The research is in four areas:

1) In a study of the *quiet transition region and corona,* we have a joint project with the P.I.'s of rocket and spacecraft experiments in a joint investigation of soft X-ray, EUV and radio data from the VLA and other telescopes. This part of the solar atmosphere is imperfectly understood, and there remains a puzzle because the density-temperature structure derived from EUV data does not account for observed radio brightnesses. Another objective is to derive the abundance of iron relative to hydrogen in the corona. The C.U. rocket payload consists of a low resolution (20 arcsec) imager of high photometric accuracy and a high resolution spectrograph with absolute wavelength referencing. (Participants: Rottman, Orrall, Jones, Dulk, Kucera, Bastian)

2) We are making *observations of flares* using the VLA (recently improved for such studies) and utilizing the joint radio–hard X-ray analysis techniques that we have developed, expanded to take advantage of the imaging capabilities of the Solar–A and GRID experiments. Excellent information on the energy distribution of accelerated electrons and properties of the magnetic field can be derived from the combined data. We have installed the NASA-sponsored, high speed digital camera system to observe at three optical wavelengths with high temporal (0.1 s) and spatial (0.85″) resolution. In addition, we are making a statistical study of impulsive flares observed by HXRBS on SMM to examine the relative role of thermal and nonthermal processes and the temporal and spatial relations between hard X-ray and microwave emissions. (Participants: Kiplinger, Kucera, Dulk, Winglee)

3) The *cyclotron maser mechanism* has been proposed by us to be a means of converting substantial energy from fast electrons into radio waves and then into heating of coronal plasma distant from the site of energy release. This mechanism is being investigated in three ways: i) We are attempting to observe microwave spike bursts with the VLA and the VLBA in order to establish their properties. ii) We will examine images taken in hard and soft X rays, Hα and radio waves to check one of the predictions of the maser theory that has no counterpart in any other: transport of large amounts of energy across magnetic field lines at the speed of light. iii) As the maser mechanism seems to occur very often in the Earth's magnetosphere and on certain other stars, we are devoting a small amount of

effort to studying these objects and clarifying the relation between the processes there and those on the Sun. (Participants: Dulk, Kucera, Winglee, McKean)

4) We are examining *radio bursts due to streams of fast electrons in the outer corona and solar wind* observed by ISEE–3 and Voyager at kilometer wavelengths. The aim is explain why radiation originating at any location, even directly behind the Sun, can be seen on the near side. Also to be investigated are the anamolous delays in burst arrival times at one spacecraft or another of 500 s and more, and whether real-time observations could serve to measure the level of solar activity on the far side of the Sun. (Participants: Dulk, Steinberg, Lecacheux, Hoang)